2012

QCD
and
High Energy Interactions

Sponsored by

. CNRS (Centre National de la Recherche Scientifique)
. CEA (Commissariat à l'Énergie Atomique)
. IN2P3 (Institut National de Physique Nucléaire et de Physique des Particules)
. NSF (National Science Foundation)
. FNRS (Fond National de la Recherche Scientifique)
. BSP (Belgian Science Policy)

XLVIIth Rencontres de Moriond
La Thuile, Aosta Valley, Italy – March 10-17, 2012

2012 QCD and High Energy Interactions

web

Proceedings of the XLVIIth RENCONTRES DE MORIOND

QCD and High Energy Interactions

La Thuile, Aosta Valley Italy *March 10-17, 2012*

2012

QCD and High Energy Interactions

edited by

Etienne Augé,

Jacques Dumarchez

Boaz Klima,

Bolek Pietrzyk,

and

Jean Trân Thanh Vân

The XLVIIth Rencontres de Moriond

2012 QCD and High Energy Interactions

was organized by :

Etienne Augé (IN2P3, Paris)
Jacques Dumarchez (LPNHE, Paris)

with the active collaboration of :

E. Berger (A.N.L. Argonne)
S. Bethke (M.P.I. Munich)
A. Capella (L.P.T. Orsay)
A. Czarnecki (U. Alberta)
D. Denegri (C.E.A. Saclay)
N. Glover (Durham)
B. Klima (Fermilab)
M. Krawczyk (University of Warsaw)
L. McLerran (Brookhaven Nat. Lab.)
B. Pietrzyk (L.A.P.P. Annecy)
L. Schoeffel (CEA - IRFU/SPP - Saclay)
Chung-I Tan (Brown University)
J. Trân Thanh Vân (L.P.T. Orsay)
U. Wiedemann (CERN)

2012 RENCONTRES DE MORIOND

The XLVIIth Rencontres de Moriond were held in La Thuile, Valle d'Aosta, Italy.

The first meeting took place at Moriond in the French Alps in 1966. There, experimental as well as theoretical physicists not only shared their scientific preoccupations, but also the household chores. The participants in the first meeting were mainly french physicists interested in electromagnetic interactions. In subsequent years, a session on high energy strong interactions was added.

The main purpose of these meetings is to discuss recent developments in contemporary physics and also to promote effective collaboration between experimentalists and theorists in the field of elementary particle physics. By bringing together a relatively small number of participants, the meeting helps develop better human relations as well as more thorough and detailed discussion of the contributions.

Our wish to develop and to experiment with new channels of communication and dialogue, which was the driving force behind the original Moriond meetings, led us to organize a parallel meeting of biologists on Cell Differentiation (1980) and to create the Moriond Astrophysics Meeting (1981). In the same spirit, we started a new series on Condensed Matter physics in January 1994. Meetings between biologists, astrophysicists, condensed matter physicists and high energy physicists are organized to study how the progress in one field can lead to new developments in the others. We trust that these conferences and lively discussions will lead to new analytical methods and new mathematical languages.

The XLVIIth Rencontres de Moriond in 2012 comprised three physics sessions:

- March 3 - 10: "Electroweak Interactions and Unified Theories"
- March 10 - 17: "QCD and High Energy Hadronic Interactions"
- March 10 - 17: "Cosmology"

We thank the organizers of the XLVIIth Rencontres de Moriond:

- A. Abada, E. Armengaud, J. Conrad, S. Davidson, P. Fayet, J.-M. Frère, P. Hernandez, L. Iconomidou-Fayard, P. Janot, M. Knecht, J. P. Lees, S. Loucatos, F. Montanet, L. Okun, J. Orloff, A. Pich, S. Pokorski, D. Wood for the "Electroweak Interactions and Unified Theories" session,

- E. Augé, E. Berger, S. Bethke, A. Capella, A. Czarnecki, D. Denegri, N. Glover, B. Klima, M. Krawczyk, L. McLerran, B. Pietrzyk, L. Schoeffel, Chung-I Tan, J. Trân Thanh Vân, U. Wiedemann for the "QCD and High Energy Hadronic Interactions" session,

- R. Ansari, P. Astier, F. Bernardeau, Ch. Charmousis, J. Dumarchez, K. Ganga, Y. Giraud-Héraud, Ch. Magneville, H. McCracken, J. Silk, B. Wandelt for the "Cosmology" session

and the conference secretariat and technical staff:

V. de Sá-Varanda and C. Bareille, I. Cossin, G. Dreneau, D. Fligiel, N. Ribet, S. Vydelingum.

We are also grateful to Andrea Righetto, Gioacchino Romani,Matteo Tuzzi, Roberta Musio and the Planibel Hotel staff who contributed through their hospitality and cooperation to the well-being of the participants, enabling them to work in a relaxed atmosphere.

The Rencontres were sponsored by the Centre National de la Recherche Scientifique, the Institut National de Physique Nucléaire et de Physique des Particules (IN2P3-CNRS), the Commissariat à l'Energie Atomique (DSM and IRFU), the Fonds de la Recherche Scientifique (FRS-FNRS), the Belgium Science Policy and the National Science Foundation. We would like to express our thanks for their encouraging support.

It is our sincere hope that a fruitful exchange and an efficient collaboration between the physicists and the astrophysicists will arise from these Rencontres as from previous ones.

E. Augé, J. Dumarchez and J. Trân Thanh Vân

Contents

5. Heavy Ion

6. From Space

7. QCD

8. Structure function, Spin, Diffraction, and Forward Physics

9. Summary Talks

1.
Higgs

Precise measurements of the W mass at the Tevatron and indirect constraints on the Higgs mass

Rafael C. Lopes de Sá
(on behalf of the DØ and CDF collaborations)
Department of Physics and Astronomy, Stony Brook University
Stony Brook, New York 11794, USA
rafael.lopesdesa@stonybrook.edu

I describe the latest DØ and CDF W boson mass measurements. The DØ measurement is performed with $4.3\,fb^{-1}$ of integrated luminosity in the electron decay channel with a data set of 1.68×10^8 W candidates. The value of the W boson mass measured by DØ is $M_W = 80.375 \pm 0.023\,GeV$ when combined with the previously analyzed $1\,fb^{-1}$ of integrated luminosity. The CDF measurement uses $2.2\,fb^{-1}$ of integrated luminosity in both electron and muon decay channels with a total of 1.1×10^8 W candidates. The value of the W boson mass measured by CDF is $M_W = 80.387 \pm 0.019\,GeV$. I report the combination of these two measurements with previous Tevatron measurements and with the LEP measurements of the W boson mass. The new world average is $M_W = 80.385 \pm 0.015\,GeV$. I discuss the implications of the new measurement to the indirect measurement of the Standard Model Higgs boson mass.

PACS numbers: 12.15.-y, 13.38.Be, 14.70.Fm

1 Introduction

The electroweak sector of the Standard Model is described by a $SU(2) \times U(1)$ gauge theory with symmetry spontaneously broken by a Higgs doublet to account for the observed mass of the gauge bosons. All particles in the spectrum of this theory have been experimentally observed but the physical Higgs boson. Direct searches limit at $95\%\,C.L.$ the possible values to the low-mass range of $115 - 127\,GeV$ or to masses above $600\,GeV$ [1].

Due to gauge structure of the symmetry-broken theory, the value of masses and coupling constants are not independent. The Standard Model prediction for the value of the W boson mass has been calculated to full two-loop order [2] and, due to their large masses, is strongly dependent on the values of the Z boson, Higgs boson and top quark masses. This prediction together with other electroweak observables can be used to indirectly measure any electroweak parameter and, in particular, the yet to be measured value of the Higgs boson mass [3].

Among all observables in global electroweak fits, the W boson and top quark masses play the most important roles, since their direct and indirect measurements have similar uncertainties and, therefore, small improvements in either have a strong impact on indirect constraints of the Higgs boson mass and on the determination of the overall consistency of the electroweak sector of the Standard Model.

Precision measurements of the W boson mass were performed by all LEP experiments and by both DØ and CDF experiments at the Tevatron collider [4]. The Tevatron was a $p\bar{p}$ collider working at $1.96\,TeV$ of center of mass energy. The impossibility of fully reconstructing the final state with the undetected neutrino is a major challenge that has to be dealt with when measuring the W boson mass in a hadron collider. However, due to the large number of events recorded, both CDF and DØ are now able to measure the W boson mass more precisely than the final LEP combined result. The world average before the results presented in this note was $80.401 \pm 0.023\,GeV$.

2 Measurement strategy

As discussed in Sec. 1, the main feature of measuring the W boson mass in a hadron collider is the impossibility of knowing the initial longitudinal momentum of the parton collision. This not only implies that the uncertainty in the measured value of the W boson mass will have a large contribution from the uncertainties in the parton distribution functions inside the proton, but also that the measured phase-space of the W leptonic decay is always incomplete because it is impossible to determine the neutrino longitudinal momentum.

Both DØ and CDF measurements explore the measured lepton and neutrino transverse momenta to determine the W boson mass. Binned maximum-likelihood fits to transverse kinematical distributions are used to extract the value of the W boson mass and its uncertainty. DØ uses both the electron transverse momentum and the transverse mass distributions. The transverse mass is defined as:

$$M_T(e,\nu) = \sqrt{2\left[p_T(e)\not{E}_T(e) - \vec{p}_T(e)\cdot\vec{\not{E}}_T(e)\right]} \tag{1}$$

where $\vec{\not{E}}_T(e)$ is the missing transverse momentum of the event.

The CDF measurement uses six different distributions to extract the W boson mass: the lepton and neutrino transverse momenta distribution and the transverse mass distribution in both electron and muon decay channels.

The different observables are not fully correlated since their measured distributions are shaped by different effects. Transverse momenta distributions are heavily shaped by the W boson transverse momentum and, therefore, are sensitive to details of the initial state radiation that needs to be carefully modeled. The transverse mass distribution, on the other hand, is less sensitive to the W boson transverse momentum but is shaped by detector resolution effects.

With the increasing experimental precision of the measurements, the more systematically limited extraction of the W boson mass using the neutrino transverse momentum distribution becomes irrelevant in the final combination and DØ does not use this measurement, although it was performed and shown to be statistically consistent with the two others.

3 Event selection

In their measurement, CDF analyzes $2.2\,fb^{-1}$ of integrated luminosity. Events are required to have a single central ($|\eta| < 1$) muon or electron with transverse momentum in the range $30 < p_T(\ell) < 55\,GeV$. The neutrino transverse momentum is required to be in the same range $30 < \not{E}_T(\ell) < 55\,GeV$ and the pair transverse mass in $60 < M_T(\ell,\nu) < 100\,GeV$. Events with large W transverse momentum, when the mass information is too diluted, are suppressed by requiring that the hadronic recoil transverse momentum satisfies $u_T < 15\,GeV$.

The final CDF sample consists of 470,126 $W \to e\nu$ candidates and 624,708 $W \to \mu\nu$ candidates.

DØ in their measurement, analyzes $4.3\,fb^{-1}$ of integrated luminosity with requirements similar to the CDF event selection but uses only the electron decay channel. DØ selects central ($|\eta| < 1.05$) electrons with large transverse energy $E_T(e) > 25\,GeV$. The neutrino transverse energy is required to be $\not\!\!E_T(e) > 25\,GeV$ and the pair transverse mass to be in the range $50 < M_T(e,\nu) < 200\,GeV$. As in the case of CDF's event selection, highly boosted W candidates are suppressed by requiring $u_T < 15\,GeV$.

The final DØ sample consists of 1,677,394 $W \to e\nu$ candidates. DØ had previously analyzed another $1\,fb^{-1}$ of data in the same channel, but acquired in lower luminosity runs of the Tevatron Collider. The higher instantaneous luminosity and corresponding higher pile-up of the $4.3\,fb^{-1}$ data acquisition period presents formidable experimental challenges to this kind of precision measurement that had to be overcome in this DØ analysis and will be faced by CDF in their next analysis.

4 Calibration strategy

The usual GEANT based simulation of the detector response is neither fast nor precise enough to generate mass templates of the kinematical distributions to which data is compared. Both DØ and CDF develop dedicated Parametrized Monte Carlo Simulations (PMCS) to describe their detector response and resolution to the lepton from the W boson decay.

DØ and CDF calibrate the parameters in the simulation *in-situ* by using similar control samples, but very different strategies.

4.1 DØ calibration

The DØ measurement is based on a precise determination of the electron energy scale in the uranium-liquid argon (U-LAr) electromagnetic calorimeter. The central tracker is only used for direction measurement and electron identification.

The material upstream of the electromagnetic calorimeter is determined by measuring the energy fraction of the electron shower in each layer of the calorimeter. Due to the higher instantaneous luminosity of the Tevatron Collider during the data taking period of the sample analyzed by DØ the underlying energy flow and luminosity dependence of the calorimeter gain have to be more precisely determined than in previous measurements to correctly model the response and energy deposition in each layer of the calorimeter. The high granularity of the DØ calorimeter is explored to measure the underlying energy flow in $W \to e\nu$ events and the dependence of the electron identification efficiency with the overall soft activity in each event. The luminosity dependence of the calorimeter response is described by a model of the ionization charge collection in the LAr gaps as a function of the luminosity.

The overall energy scale and offset are determined using $Z \to ee$ events by a two-dimensional binned maximum likelihood fit to the invariant mass M_Z and f_Z distributions. The observable f_Z is defined as:

$$f_Z = \frac{[E(e_1) + E(e_2)]\,(1 - \cos\gamma)}{M_Z} \tag{2}$$

where γ is the measured angle between the electron-positron pair and M_Z is their invariant mass. The energy scale and offset are determined in bins of luminosity to validate the luminosity dependence modeling of the detector response and the results are found to be statistically consistent. The DØ electron energy scale is known to a precision of 0.021% with uncertainty dominated by the statistical power of the $Z \to ee$ sample.

Since only the $Z \to ee$ mass is used in the determination of the overall electron energy scale, the DØ measurement is a measurement of the ratio M_W/M_Z. This statement relies on the hypothesis that all the calibrations done in the somewhat more energetic Z pole is valid on the W pole. This hypothesis is carefully checked in each step of the calibration and, when needed, the non-linearity between the two close energy regimes is accordingly modeled. Measuring the ratio M_W/M_Z is not only what allows the precise calibration to be made, since the Z boson mass was measured to high precision by the LEP experiments, but also grants experimental stability against uncontrolled variations of the detector condition, since systematic variations tend to cancel in the ratio.

4.2 CDF calibration

The CDF measurement is based on a precise determination of the lepton momentum in the their central drift chamber (COT) immersed in a $1.4\,T$ solenoid. The interaction of the charged particles with the innermost silicon detector is modeled by a highly granular lookup table that describes ionization and radiative energy losses, multiple Coulomb scattering and Compton scattering in the tracker volume. The alignment is performed with a high-purity sample of cosmic rays muons whose trajectory is fitted to a single helix through the entire detector. Further weakly constrained modes of alignment are removed by the observed difference in the E/p distributions of electrons and positrons in events that pass the W boson sample selection.

The overall momentum scale is determined by binned maximum-likelihood fit to mass templates around the $J/\psi \to \mu\mu$, $\Upsilon(1S) \to \mu\mu$, and $Z \to \mu\mu$ resonances. Non-uniformities of the magnetic field are corrected by measuring the dependence of the J/ψ mass with the mean polar angle. Further ionization energy losses are corrected by measuring the dependence of the momentum scale with the mean $1/p_T$ of the muons.

Using the calibrated tracker momentum scale, the peak of the E/p distribution from $W \to e\nu$ and $Z \to ee$ events is fitted in bins of E_T to determine electron energy scale of the calorimeter response. The amount of radiative material upstream of the COT is determined by a fit to the tail of the E/p distribution. The tracker momentum scale is determined with a precision of $0.009\,\%$, dominated by uncertainties in the QED radiative corrections and magnetic field non-uniformities.

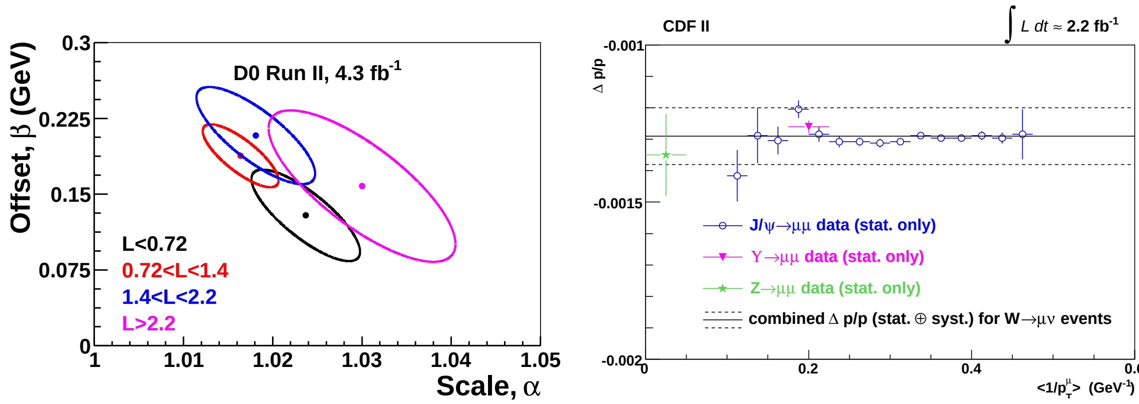

Figure 1: DØ energy scale and offset determined in 4 different luminosity bins. CDF momentum scale determine in bins of mean $1/p_T(\mu)$ to constrain the non-linearities of the detector response.

5 Results

Both DØ and CDF perform blinded measurements. That means that throughout the analysis, a constant unknown offset is applied to the result of the fitting algorithm. The DØ analysis also includes an unblinded closure test where GEANT-simulated events, with known W boson mass input, are treated as data. The goal is to test the accuracy of the analysis procedure with a high statistics sample. For this measurement, a sample equivalent to $24\,fb^{-1}$ was used and closure was obtained within the statistical uncertainty of $6\,MeV$.

5.1 DØ results

After unblinding, the W boson mass fit results from the DØ data are given in Table 1.

Table 1: DØ and CDF results from the fits to data. The uncertainty is only that from the W sample statistics. The fitting range is $65 < M_T < 90\,GeV$ for transverse mass and $32 < p_T < 48\,GeV$ for transverse momentum distributions .

DØ measurements

Variable	Result (GeV)
$M_T(e,\nu)$	80.371 ± 0.013
$p_T(e)$	80.343 ± 0.014
$\not{E}_T(e)$	80.355 ± 0.015

CDF measurements

Variable	Result (GeV)
$M_T(e,\nu)$	80.408 ± 0.019
$p_T(e)$	80.393 ± 0.021
$\not{E}_T(e)$	80.431 ± 0.025
$M_T(\mu,\nu)$	80.379 ± 0.016
$p_T(\mu)$	80.348 ± 0.018
$\not{E}_T(\mu)$	80.406 ± 0.022

The distributions of each variable showing the data and PMCS template with background for the best fit value are shown in Figs 2. These figures also show the bin-by-bin χ values defined as the difference between the data and template divided by the data uncertainty.

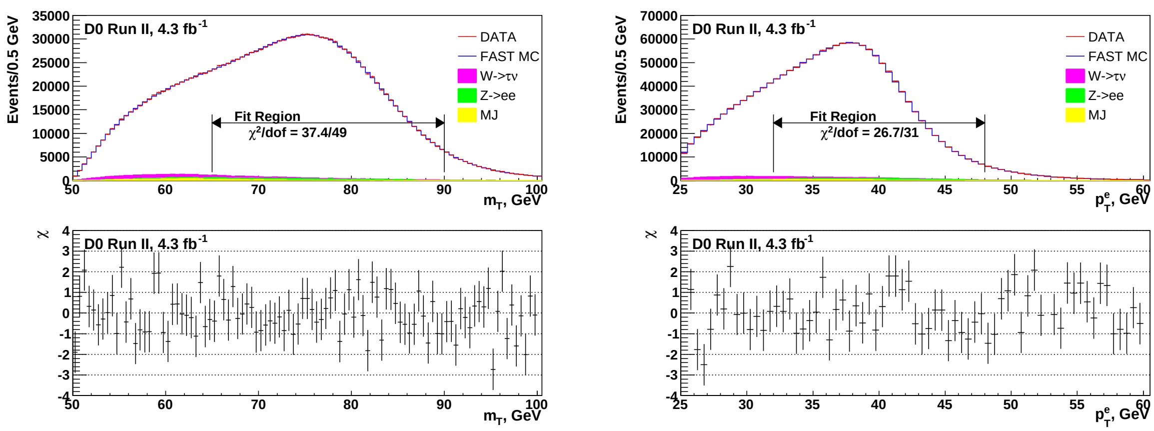

Figure 2: DØ $M_T(e,\nu)$ and $p_T(e)$ distributions for data and PMCS simulation with backgrounds added (top) and the χ value for each bin (bottom).

The combination of the M_T and p_T measurements yield a value for the W boson mass of $80.367 \pm 0.026\,GeV$ using only the $4.3\,fb^{-1}$ analyzed in this work. Further combining with the $1\,fb^{-1}$ previously analyzed, the new DØ Run II ($5.3\,fb^{-1}$) result is:

$$M_W(\text{DØ}) = 80.375 \pm 0.023\,GeV \tag{3}$$

Table 2 summarizes the systematic uncertainties associated to the DØ measurement. Although the uncertainties are already systematically dominated, all experimental systematic uncertainties can be reduced by using a larger data sample. In the DØ case, a larger $Z \to ee$ sample will reduce the dominating electron energy scale uncertainty. Production uncertainties, on the other hand, are not reduced with more events and depend on further theoretical and experimental work to be better controlled.

Table 2: Systematic uncertainties of the M_W measurement. The left table shows the uncertainties for the DØ measurement and the right one for the CDF measurement.

	Unc. (MeV)		
DØ systematics	M_T	$p_T(e)$	$\not{E}_T(e)$
Electron energy scale	16	17	16
Electron resolution	2	2	3
Electron shower modeling	4	6	7
Electron energy loss model	4	4	4
Hadronic recoil model	5	6	14
Electron efficiencies	1	3	5
Backgrounds	2	2	2
Parton distribution	11	11	14
QED radiation	7	7	9
$p_T(W)$ model	2	5	2

CDF systematics	Unc. (MeV)
Lepton energy scale and resolution	7
Recoil scale and and resolution	6
Lepton removal	2
Backgrounds	3
Parton distributions	10
QED radiation	4
$p_T(W)$ model	5

5.2 CDF results

After unblinding, the W boson mass fit results from the CDF data are also given in Table 1. Combining the six measurements, the new CDF Run II ($2.2\,fb^{-1}$) result is:

$$M_W(\text{CDF}) = 80.387 \pm 0.019\,GeV \tag{4}$$

Table 2 summarizes the systematic uncertainties. The CDF uncertainty is no longer dominated by lepton energy scale, but by the W sample statistics and the parton distribution functions uncertainties.

5.3 Combination

The two measurements described in this note were combined using the BLUE method with the older Run I and Run 0 measurements of the W boson mass done by DØ and CDF [5]. The statistical uncertainties and systematic uncertainties, except those associated with production modeling, are taken to be uncorrelated.

Production model and theory uncertainties are partially correlated. The minimum value of the CDF and DØ uncertainties for each source is assumed to be 100% correlated, and the remainder for that source is assumed to be uncorrelated. One exception is the parton distribution function uncertainty for the DØ measurement in Run I. This measurements used wider eta coverage and is only 70% correlated with the other measurements. In each measurement, the assumed value of the W boson width is slightly different and corrected to the Standard Model predicted value of $2.0922 \pm 0.0015\,GeV$ in the running-width scheme using the newly obtained W boson mass world average. After all corrections, the new Tevatron combination for the value of the W boson mass is:

$$M_W(\text{Tevatron}) = 80.387 \pm 0.016\,GeV \tag{5}$$

Further combining this result with the LEP direct measurements, which are considered to be completely uncorrelated with the Tevatron result, the new world average value of the W boson mass is:

$$M_W(\text{WA}) = 80.385 \pm 0.015\,GeV \tag{6}$$

The χ^2 of the combination is 4.3 for 7 degrees of freedom with a probability of 74%. The results is strongly dominated by the DØ and CDF Run II measurements.

6 Model and theoretical uncertainties

In the DØ, but even more so in the CDF measurement, the uncertainty in the W boson mass is dominated by model and theoretical uncertainties. In particular, the parton distribution function (PDF) uncertainty is already the most important uncertainty in the CDF measurement and will be in the next DØ measurement. To further improve the precision of the measurements, these uncertainties have to be controlled by improving both experimental techniques and theoretical understanding of the processes involved.

The PDF uncertainties are, to a large extent, an acceptance uncertainty that are introduced by the lepton acceptance requirement made by both DØ and CDF. In Run I, DØ extended the η coverage of the W sample in the W boson mass measurement [4]. The forward region brings other experimental challenges, such as the larger amount of underlying energy flowing through the detector, but the wide coverage of the DØ calorimeter must be explored in the near future. The relevant u and d quarks PDF can also be constrained at high mass scales by measuring the W charge asymmetry at the Tevatron and introducing the result in global QCD fits. Improved calculations of W production and decay in hadron colliders can also be used to reduce uncertainties associated to higher order QED and QCD corrections [6]. Finally, recently proposed kinematical distributions that carry more mass information than the transverse mass can be attempted to extract the W boson mass with less sensitivity to the systematic uncertainties [7].

7 Higgs constraints from global electroweak fit

The updated W boson mass world average can be used together with the electroweak precision measurements performed at LEP, Tevatron and SLC [3] to indirectly measure the Standard Model Higgs boson mass. The value, prior to the two measurements described in this note was $M_H = 92^{+34}_{-26}\,GeV$. With the Tevatron W boson mass measurements presented here, the new *Tevatron Electroweak Working Group* indirect value of the Higgs boson mass is [5]:

$$M_H(\text{indirect}) = 94^{+29}_{-24}\,GeV \tag{7}$$

Using the full $10\,fb^{-1}$ recorded by both DØ and CDF, the Tevatron experiments can reduce the uncertainty in the W boson mass to $10\,MeV$. Such precision, together with the planned improvements on the top quark mass measurement, will allow a confrontation between the indirect and potential direct measurement of the Higgs boson mass with similar precisions. Even after the Higgs boson mass has been measured to high precision, the W boson mass will continue to be the most important parameter in the determination of the global consistency of the electroweak sector of the Standard Model.

8 Conclusions

The W boson mass was measured by both DØ and CDF collaborations with precision at least as good as the world average average prior to these measurements [8,9]. Despite using very different calibration procedures, all DØ and CDF measurements are consistent. The new W boson mass world average is consistent with the Standard Model prediction for a low mass Higgs boson and strongly disfavors a high mass Higgs, as can be seen in Fig. 3.

Acknowledgments

I would like to thank the organizers of the Moriond QCD conference for the opportunity to give the talk in such nice scientific environment. I would also like to acknowledge the DØ and CDF

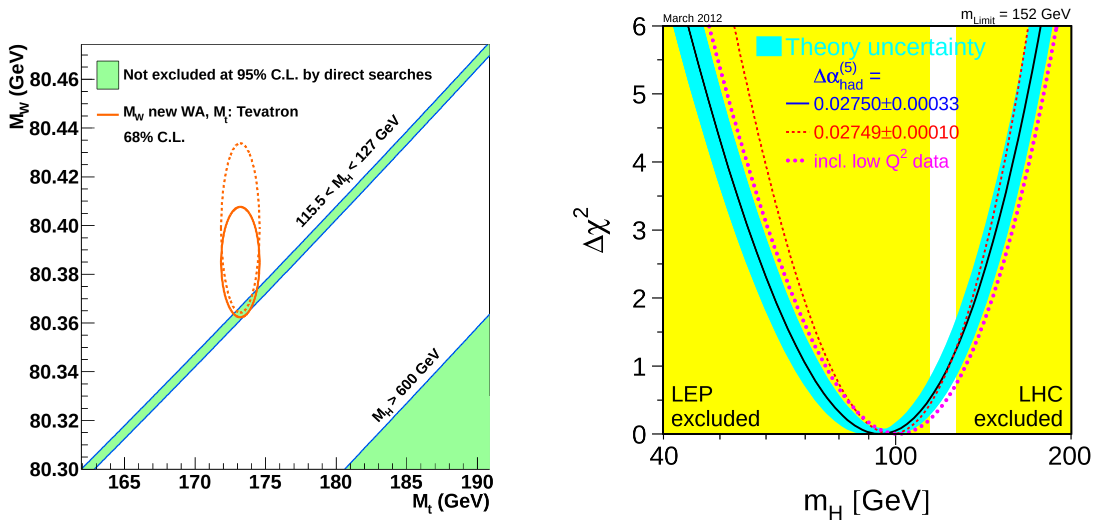

Figure 3: On the left, comparison of the Standard Model prediction of the W boson mass for varying values of the Higgs boson mass compared to the direct measurement. The previous world average, prior to the measurements presented in this note, is marked by the dashed ellipse. The green band is a purely experimental exclusion and does not include limits from perturbative unitarity. On the right, the χ^2 of the updated global electroweak fit prediction of the Higgs boson mass.

collaborations, the Tevatron Accelerator Division and the corresponding funding agencies, for the outstanding work for more than 20 years that allowed works like these ones to be produced.

References

1. G. Aad *et al.* [ATLAS Collaboration], Phys. Lett. B **710**, 49 (2012) [arXiv:1202.1408]; S. Chatrchyan *et al.* [CMS Collaboration], Phys. Lett. B **710**, 26 (2012) [arXiv:1202.1488].
2. M. Awramik, M. Czakon, A. Freitas and G. Weiglein, Phys. Rev. D **69**, 053006 (2004) [hep-ph/0311148].
3. The ALEPH Collaboration, the DELPHI Collaboration, the L3 Collaboration, the OPAL Collaboration, the SLD Collaboration, the LEP Electroweak Working Group, the SLD electroweak, heavy flavour groups, Phys. Rept. **427**, 257 (2006).
4. S. Schael *et al.* [ALEPH Collaboration], Eur. Phys. J. C **47**, 309 (2006); J. Abdallah *et al.* [DELPHI Collaboration], Eur. Phys. J. C **55**, 1 (2008); P. Achard *et al.* [L3 Collaboration], Eur. Phys. J. C **45**, 569 (2006); G. Abbiendi *et al.* [OPAL Collaboration]; V. M. Abazov *et al.* [D0 Collaboration], Phys. Rev. Lett. **103**, 141801 (2009); T. Aaltonen *et al.* [CDF Collaboration], Phys. Rev. D **77**, 112001 (2008).
5. Tevatron Electroweak Working Group, CDF and D0 Collaborations, arXiv:1204.0042 [hep-ex].
6. C. Bernaciak and D. Wackeroth, [arXiv:1201.4804]; L. Barze, G. Montagna, P. Nason, O. Nicrosini and F. Piccinini, [arXiv:1202.0465].
7. A. Rujula and A. Galindo, JHEP **1108**, 023 (2011) [arXiv:1106.0396].
8. V. M. Abazov *et al.* [D0 Collaboration], Phys. Rev. Lett. **108**, 151804 (2012) [arXiv:1203.0293].
9. T. Aaltonen *et al.* [CDF Collaboration], Phys. Rev. Lett. **108**, 151803 (2012) [arXiv:1203.0275].

Searches for the Standard Model Higgs Boson at the Tevatron

D. Bortoletto
Department of Physics, Purdue University
West Lafayette, Indiana, U.S.A.

The results from the search for a standard model Higgs boson using entire data delivered by the Fermilab Tevatron collider are presented. The data corresponding to 10 fb^{-1} of proton-antiproton collisions at a center-of-mass energy of 1.96 TeV were recorded by the CDF and D0 Detectors between March 2001 and September of 2011. A broad excess between $115 < m_H <$ 145 GeV/c^2 with a global significance of 2.2 standard deviations relative to the background-only hypothesis is observed.

1 Introduction

The Higgs boson is a critical missing element of the standard model (SM) of elementary particles and interactions. Within the SM, vector boson masses arise from the spontaneous breaking of electroweak symmetry due to the existance of the Higgs particle. Although the value of the Higgs mass is not predicted by the SM indirect constraints can be set through precision measurements of electroweak observabled such as m_{top} and m_W. These measurements indicates m_H to be less than $\approx$ 145 GeV/c^2 at 95% confidence level (C.L.). The latest results from the LHC and the Tevatron experiments have excluded wide regions of the possible m_H ranges. The most interesting region to search for the Higgs is the mass range between 115 and 127 GeV/c^2 where the both the ATLAS and the CMS experiments have found some excesses with respect to the background-only hypothesis. The Tevatron experiments can contribute to the understanding of this region by studying the production of the Higgs boson in association with an W or a Z boson followed by the decay $H \to b\bar{b}$.

Here, we present the latest results for the $H \to b\bar{b}$ searches at the Tevatron. Both CDF and D0 have developed new advanced analysis techniques to improve the sensititivity of their searches and have almost completed the analysis of the full data sample of 10 fb^{-1} of data delivered by the Tevatron. Multivariate techniques have been implemented to separate signal from QCD and electroweak backgrounds. To obtain the best expected sensitivities to SM Higgs production, the b-tagging, dijet invariant mass, and lepton identification algorithms have been re-optimized to improve the discriminantion of the Higgs signal from background processes. At CDF, a new b-tagging algorithm called HOBIT [8] has been used in most of the mainstream $H \to b\bar{b}$ search channels. This multivariate algorithm, trained on $H \to b\bar{b}$ events for a Higgs mass of $m_H = 120$ GeV/c^2, increases the Higgs sensitivity by roughly 10% for a given search channel. Many analysis improvements were also made by the D0 collaboration, including increasing signal acceptance by relaxing variable definitions and futher optimization of their b tagging algorithm.

2 Low Mass Higgs Searches at the Tevatron

Both CDF and D0 are searching for the Higgs in a variaty of final states [4, 5] . The complete list of channels entering the Higgs Tevatron combination is given in [6], along with a complete description of the limit-setting procedure and handling of systematic uncertainties. The most sensititive low-mass Higgs searches at the Tevatron rely on three optimized analysis according to the decay of the W and Z boson produced in association with the Higgs. The first considers decays of the $Z \to \ell^+\ell^-$ and therefore requires final states with two leptons. The second requires a lepton from the W decay and transverse missing energy ($\not\!\!E_T$). The last one studies final states with large $\not\!\!E_T$. This includes ZH production where $Z \to \nu\overline{\nu}$ and the neutrinos ν escape detection or $Z \to \ell\ell$ when both leptons ℓ are undetected or give rise to jets. For WH production it accepts events where $W \to e\bar{\nu}_e$ when the electron e is misidentified as a jet, $W \to e\nu/\mu\nu$ when the e or the muon μ is undetected and $W \to \tau\bar{\nu}$ when the τ lepton decays hadronically and is detected as a jet.

The $H \to boverlineb$ search sensitivity is consirably increased by requiring the two leading jets in the event to be b-tagged. Additional sensitivity can be gained by also considering events where one but not both leading jets are tagged. Several analyses also accept events with a third jet in the final state in addition to the two b jets from the Higgs boson decay. The third jet is produced either from radiation from initial or final state partons or when an e or τ from the W boson decay is reconstructed as a jet. Note that the $\not\!\!E_T$ final state at CDF [7] is not yet using HOBIT and it will be updated for the Summer 2012 conferences.

In this contribution I will highlight a few analysis were new techniques or significant improvements have occurred and I will present the results of the latest TEVATRON combination.

2.1 The dilepton final state at CDF

One of the latest major improvement to this CDF analysis has been the utilization of new multivariate algorithms to distinguish between ZH signal and background processes. To isolate ZH signal from $t\bar{t}$ an *expert NN*, trained to distinguish ZH from top is employed. Similarly a second *expert NN* , denoted as Z+jet expert, separates ZH from Z + light flavor jets and $Z + c\bar{c}$ backgrounds. CDF has now introduced a third *expert NN* trained to distinguish ZZ and WZ from ZH signal. The three expert networks are utilized to assign events to distinct regions in the final event discriminant used in the extraction of upper limits.

In addition to the three *expert NN*, an additional network is trained to simultaneously separate ZH signal from all backgrounds. CDF emploies 26 versions of this NN, designated as *final discriminants*, optimized for different values of M_H and separately for 2 and 3 jet events. Once an event receives a region classification, it is evaluated by the final discriminant and assigned to a bin corresponding to the final discriminant score within the region.

CDF does not observe a significant excess over the number of events predicted by the background model and uses MCLIMIT quantify the maximum allowed ZH component. CDF evaluates 95% C.L. upper limits on $ZH \times BR(H \to b\bar{b})$ and computes observed limits for Higgs masses between 90 and 150 GeV/c^2 in 5 GeV intervals. For a Standard Model Higgs boson mass of 120 GeV, the expected 95% C.L. is 3.1 times the Standard Model prediction with an observed limit of 5.7.

2.2 The $\not\!\!E_T$ final state at D0

The D0 collaboration has significantly refined the b-tagging and the multivariate techniques used in the $\not\!\!E_T$ final state. A multivariate b-tagging discriminant [9], using several boosted decision trees as inputs, is used to select events with one or more b quark candidates. The new algorithm includes more information relating to the lifetime of the jet and results in a better discrimination between b and light jets. It provides an output between 0 and 1 for each jet, with a value closer to one indicating a higher probability that the jet originated from a b quark. From this continuous output, twelve operating points (L_b) are defined, with untagged jets having $L_b = 0$ and b purity increasing with L_b from 1 to 12. The typical per-jet efficiency and fake rate for the loosest (tightest) b-tag operating point are about 80% (50%) and 10% (1%), respectively. To improve the sensitivity of the analysis, two high signal purity samples are defined from the analysis sample using the variable $L_{bb} = L_{b,L} + L_{b,NL}$. A tight (medium) b-tag sample: $L_{bb} \geq 18 (17 \geq L_{bb} \geq 11)$ The medium b-tag sample contains events with two loosely b-tagged jets, as well as events with one tightly b-tagged jet and one untagged jet. The signal-to-background ratios for a Higgs-boson mass of 115 GeV in the pre, medium and tight b-tag samples, after applying a multijet veto, are respectively 0.05%, 0.3% and 1.5%.

Since 50% of the signal in this final states is from WH, D0 has improved the efficiency of this search by excluding isolated tracks from the definition of the missing p_T, a variable similar to $\not\!\!E_{\mathrm{T}}$, calculated from the reconstructed charged particle tracks. The combination of these changes increase the sensititvity by 25% while luminosity alone would have given increase of only 6%. For $m_H = 115$ GeV, the observed and expected limits on the combined cross section of ZH and WH production are factors of 2.5 and 3.0 larger than the theoretical standard-model value, for an expected factor of 3.0.

3 The TEVATRON combination

The results from CDF and D0 on all direct searches for the standard model (SM) Higgs boson have been analyized by the TEVATRON combination group and the current status is presented in [6]. All analyses provide binned histograms of the final discriminant variables for the signal and background predictions. In order to preserve most sensitivity data and predictions are aggregated in bins of signal-to-background ratio, s/b. These distributions can be integrated from the high-s/b side downwards, showing the sums of signal, background, and data for the most pure portions of the selection of all channels added together. The integrated plots of the 100 highest s/b events show an excess consistent with signal for the analyses seeking a Higgs boson mass of 125 GeV/c^2, and a deficit of events in the highest-s/b bins for the analyses seeking a Higgs boson of mass 165 GeV/c^2 as shown in Fig. 1.

To gain confidence that the final result does not depend on the details of the statistical formulation, two types of combinations, using Bayesian and Modified Frequentist approaches are used to find the limits on the Higgs boson production rate. The two techniquese agree within 10% at each value of m_H, and within 1% on average. Systematic uncertainties enter on the predicted number of signal and background events as well as on the distribution of the discriminants in each analysis. Limits on the SM Higgs boson production $\sigma \times B(H \to X)$ in $p\bar{p}$ collisions at $\sqrt{s} = 1.96$ TeV for $100 < m_H < 200$ GeV/c^2 are extracted. The comparisons with the SM is facilitated by dividing them by the SM Higgs boson production cross section, as a function of Higgs boson mass. A value of the combined limit ratio which is less than or equal to one indicates that that particular Higgs boson mass is excluded at the 95% C.L. The combinations of results [4, 5] of each single experiment, as used in the Tevatron combination [6], yield the following ratios of 95% C.L. observed (expected) limits to the SM cross section: 2.37 (1.16) for CDF and 2.17 (1.58) for D0 at m_H= 115 GeV/c^2, 2.90 (1.41) for CDF and 2.53 (1.85) for D0 at $m_H = 125$ GeV/c^2, and 0.42 (0.69) for CDF and 0.94 (0.76) for D0 at $m_H = 165$ GeV/c^2.

With up to 10 fb^1 of luminosity analyzed, the 95% C.L. median expected upper limits on Higgs boson production are factors of 0.94, 1.10, and 0.49 times the values of the SM cross section for Higgs bosons of mass m_H =115 GeV/c^2, 125 GeV/c^2,and 165 GeV/c^2, respectively. The TEVATRON experiments exclude, at the 95% C.L., a new and larger region at high mass

Figure 1: Integrated distributions of s/b, starting at the high s/b side, for Higgs boson masses of 125, and 165 GeV/c^2 . The total signal+background and background-only integrals are shown separately, along with the data sums. Data are only shown for bins that have data events in them.

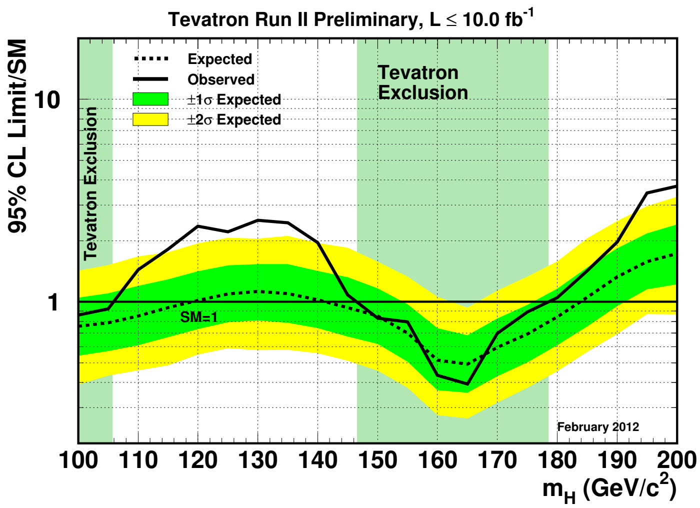

Figure 2: Observed and expected (median, for the background-only hypothesis) 95% C.L. upper limits on the ratios to the SM cross section, as functions of the Higgs boson mass for the combined CDF and D0 analyses. The bands indicate the 68% and 95% probability regions where the limits can fluctuate, in the absence of signal. The limits displayed in this figure are obtained with the Bayesian calculation.

between $147 < m_H < 179$ GeV/c^2, with an expected exclusion region of $100 < m_H < 119$ GeV/c^2 and $141 < m_H < 184$ GeV/c^2. There is an excess of data events with respect to the background estimation in the mass range $115 < m_H < 135$ GeV/c^2 which causes the limits to not be as stringent as expected. At $m_H = 120$ GeV/c^2, the p-value for a background fluctuation to produce this excess is $\approx 3.5 \times 10^3$, corresponding to a local significance of 2.7 σ. The global significance for such an excess anywhere in the full mass range is approximately 2.2 σ. The searches for $H \to b\bar{b}$ and $H \to W^+W^-$ are also combined separately and show that the excess is concentrated in the $H \to b\bar{b}$ channel, although the results in the $H \to W^+W^-$ channel are also consistent with the possible presence of a low-mass Higgs boson.

4 Conclusions

The CDF and D0 Collaborations have combined their results to give a Tevatron-wide combination of the upper limits of the SM Higgs production at 95% C.L. After combining all channels across the range $100 < m_H < 200$ GeV/c^2, a broad excess is observed in data relative to the background-only hypothesis, corresponding to a 2.2 standard-deviatios is found in the region of

M_H between 120-130 GeV/c^2 If one considers only the $H \to b\bar{b}$ final state the excess correspnds to a 2.6 standard-deviation departure from the background-only prediction. The two collaborations are still improving their tools. The final Tevatron combination will be presented in summer 2012.

Acknowledgments

The author thanks the Moriond QCD workshop organizers and conveners for an enjoyable and rewarding experience. She acknowledges support from the DOE and thanks her colleaguses from CDF and D0.

References

1. F. Englert and R. Brout, *Phys. Rev.* D **13**, 321 (1964); P. W. Higgs, *Phys. Rev. Lett.* **13**, 508 (1964); G. S. Guralnik et al., *Phys. Rev. Lett.* **13**, 585 (1964).
2. CMS Collaboration, S. Chatrchyan et al., "Combined results of searches for the standard model Higgs boson in pp collisions at $\sqrt{s} = 7$ TeV", arXiv:1202.1488v1 [hep-ex], submitted to PRL.
3. ATLAS Collaboration, "An update to the combined search for the Standard Model Higgs boson with the ATLAS detector at the LHC using up to 4.9 fb^{-1} of pp collision data at $\sqrt{s} = 7$TeV", 2012. ATLAS-CONF-2012-019
4.] CDF Collaboration, "Combination of CDF's searches for the standard model Higgs boson with up to 10.0 fb^{-1} of data", 2012. CDF Note 10804
5. D0 Collaboration, "Combined Search for the Standard Model Higgs Boson from the D0 Experiment in up to 9.7 fb^{-1} of Data", 2012. D0 Note 6304-CONF
6. The TEVNPH Working Group, for the CDF and D0 Collaborations, "Combined CDF and D0 Search for Standard Model Higgs Boson Production with up to 10.0 fb^{-1} of Data", arXiv:1203.3774v1 [hep-ex].
7. The CDF collboration, "Seach for the SM Higgs boson in the $\not\!\!E_{\mathrm{T}}+b$-jets signature with relaxed kinematic cuts in 9.45 fb^1 of data at CDF". CDF Note 10798.
8. J. Freeman et al., "Introduction to HOBIT, a b-Jet Identification Tagger at the CDF Experiment Optimized for Light Higgs Boson Searches", arXiv:1205.1812v1 [hep-ex].
9. L. Breiman et al., Classification and Regression Trees (Wadsworth, Belmont, CA, 1984). Y. Freund and R.E. Schapire, Experiments with a new boosting algorithm, in Machine Learning: Proceedings of the Thirteenth International Conference, Bari, Italy, 1996, edited by L. Saitta (Morgan Kaufmann, San Francisco, 1996), p148.

Searches for the Standard Model Higgs Boson with the ATLAS Detector

Ralf Bernhard
on behalf of the ATLAS collaboration
Physikalisches Institut, Albert-Ludwigs Universität Freiburg, Germany

The most recent results for searches for the Standard Model Higgs boson at a center-of-mass energy of $\sqrt{s}$ =7 TeV using 4.9 fb^{-1} of data collected with the ATLAS detector at CERNs Large Hadron Collider are presented.

1 Introduction

In the Standard Model (SM) of particle physics the Higgs mechanism is responsible for breaking electroweak symmetry, thereby giving mass to the W and Z bosons. It predicts the existence of a heavy scalar boson, the Higgs boson, with a mass that can not be predicted by the SM. Direct searches for the Higgs Boson were performed at the LEP experiments and yielded a direct mass limit of $m_H > 114.4$ GeV [1] and at the Tevatron excluding the region $156 < m_H < 177$ GeV [2]. Indirect limits have been placed on the Higgs boson mass by the LEP, SLD and Tevatron experiments from electroweak precision measurements [3]. The SM fit yields a best value of $m_H = 94^{+29}_{-24}$ [4]. The corresponding upper limit on the Higgs mass at 95% CL is $m_H < 152$ GeV.

2 Search Channels

In contrast to the combination of searches presented in [5] all analyses now use the full dataset of 4.9 fb^{-1} recorded in 2011, as shown in Tab. 1 which also indicates the mass range of the analysis. To enhance the sensitivity, the analysis channels under study are divided into sub-channels with different signal to background ratios or with a different sensitivity to various systematic uncertainties. In the following the search channels are described.

2.1 $H \to \gamma\gamma$

Despite the low branching ratio (≈0.2%) the diphoton decay mode is one of the most important channels in the search for the SM Higgs boson in the low mass region. The analysis separates events into nine independent categories based on the pseudo-rapidity of the photons, whether it was reconstructed as a converted or unconverted photon, and on the momentum component of the diphoton system transverse to the thrust axis (p_{T_t}) The diphoton invariant mass $m_{\gamma\gamma}$ is used as a discriminating variable to distinguish signal and background, to take advantage of the mass resolution of approximately 1.4% for m_H around 120 GeV. The distribution of $m_{\gamma\gamma}$ in the data is fit to a smooth function to estimate the background. Figure 1 (left) shows the inclusive invariant mass distribution of the observed candidates, summing over all categories.

Higgs Decay channel	Additional Sub-Channels	m_H Range [GeV]	L [fb^{-1}]	Ref.
low-m_H, good mass resolution				
$H \to \gamma\gamma$	9 sub-channels ($p_{\mathrm{T}_t} \otimes \eta_\gamma \otimes$ conversion)	110-150	4.9	[6]
$H \to ZZ \to \ell\ell\ell'\ell'$	$\{4e, 2e2\mu, 2\mu 2e, 4\mu\}$	110-600	4.8	[7]
low-m_H, limited mass resolution				
$H \to WW \to \ell\nu\ell\nu$	$\{ee, e\mu, \mu\mu\} \otimes$ {0-jet, 1-jet, VBF}	110-300-600	4.7	[8]
$VH \to b\bar{b}$	$Z \to \nu\bar{\nu}$ $W \to \ell\nu$ $Z \to \ell\ell$	110-130	4.6	[9]
$H \to \tau^+\tau^- \to \ell\ell 4\nu$	$\{e\mu\} \otimes$ {0-jet} $\oplus$ {1-jet, VBF, VH}	110-150	4.7	[10]
$H \to \tau^+\tau^- \to \ell\tau_{\mathrm{had}} 3\nu$	$\{e, \mu\} \otimes$ {0-jet} $\otimes$ $\{E_T^{\mathrm{miss}} \gtrless 20$ GeV$\}$ $\oplus$ $\{e, \mu\} \otimes$ {1-jet, VBF}	110-150	4.7	[10]
$H \to \tau^+\tau^- \to \tau_{\mathrm{had}}\tau_{\mathrm{had}} 2\nu$	{1-jet}	110-150	4.7	[10]
high-m_H				
$H \to ZZ \to \ell\ell\nu\bar{\nu}$	$\{ee, \mu\mu\} \otimes$ {low pile-up, high pile-up}	200-280-600	4.7	[11]
$H \to ZZ \to \ell\ell q\bar{q}$	{b-tagged, untagged}	200-300-600	4.7	[12]
$H \to WW \to \ell\nu q\overline{q'}$	$\{e, \mu\} \otimes$ {0-jet, 1-jet}	300-600	4.7	[13]

Table 1: Summary of the individual channels under study in ATLAS and contributing to the combination.

2.2 $H \to ZZ^{(*)} \to \ell^+\ell^-\ell^+\ell^-$

In this search the events are categorised according to the lepton flavour combinations. The main irreducible $ZZ^{(*)}$ background is estimated using Monte Carlo simulation and the reducible Z+jets is estimated from control regions in the data. The mass resolutions are approximately 1.5% in the four-muon channel and 2% in the four-electron channel for m_H∼120 GeV. The four-lepton invariant mass is used as a discriminating variable and its distribution for events selected after all cuts shown in Fig.1 on the right side.

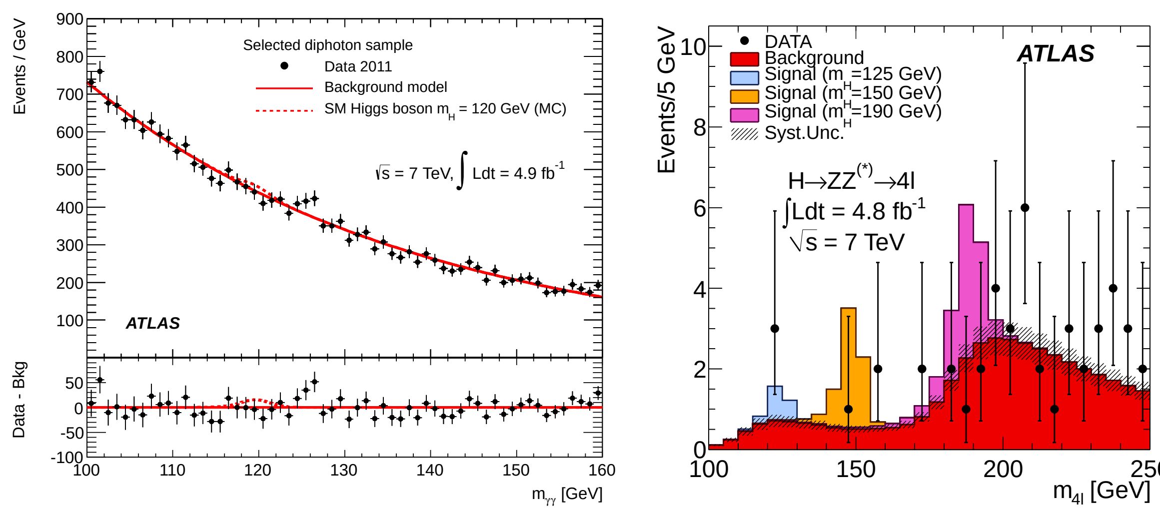

Figure 1: Distributions of the reconstructed invariant mass for the selected candidate events and for the total background and signal expected in the $H \to \gamma\gamma$ (left) and the $H \to ZZ^{(*)} \to \ell^+\ell^-\ell^+\ell^-$ (right).

2.3 $H \to WW^{(*)} \to \ell^+\nu\ell^-\overline{\nu}$

The analysis is separated into 0-jet, 1-jet and 2-jet categories as well as according to lepton flavour. The main backgrounds are estimated from the data using control regions and extrapolating into the signal region using Monte Carlo simulation. As a discriminating variable the WW transverse mass (m_T) distribution is used, which is shown for events with 0-jets and 1-jets in Fig. 2 on the left and right side, respectively.

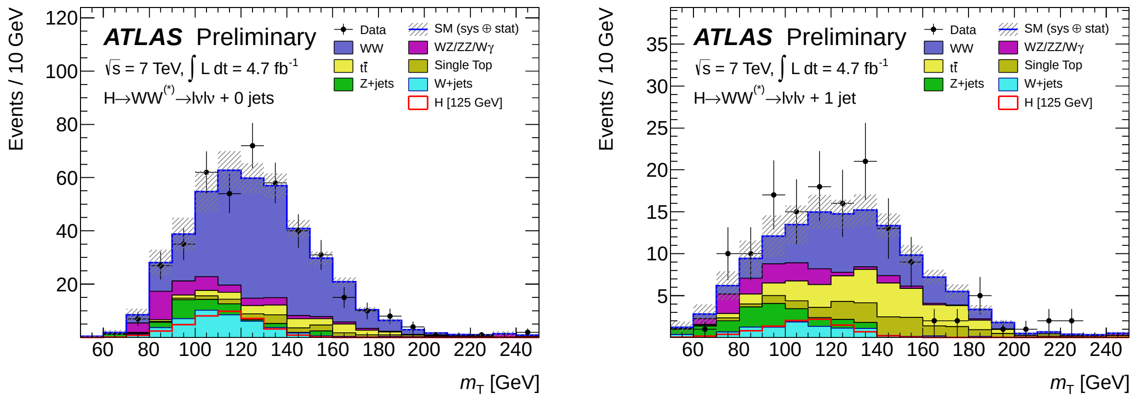

Figure 2: Distributions of the reconstructed transverse mass for the selected candidate events and for the total background and signal expected in the $H \to WW^{(*)} \to \ell^+\nu\ell^-\overline{\nu}$ channel for events with 0-jets (left) and1-jets (left).

2.4 $ZH \to \ell^+\ell^- b\overline{b}$, $WH \to \ell\nu b\overline{b}$, $ZH \to \nu\overline{\nu}b\overline{b}$

All three analyses require exactly two b-tagged jets and the invariant mass of the two b-jets, m_{bb}, is used as a discriminating variable. To increase the sensitivity of the search, the m_{bb} distribution is examined in sub-channels with different signal-to-background ratios. In the searches with one or two charged leptons, the division is made according to four bins in transverse momentum of the reconstructed vector boson. The individual channels are not broken into distinct lepton-flavour categories.

2.5 $H \to \tau\tau \to \ell^+\ell^- 4\nu$, $H \to \tau\tau \to \ell\tau_{had}3\nu$, $H \to \tau\tau \to \tau_{had}\tau_{had}2\nu$

In the $H \to \tau^+\tau^-$ channel any combination of events with leptonic decaying taus or hadronic decaying taus are considered. For the $H \to \tau\tau \to \tau_{had}\tau_{had}2\nu$ + jet channel and $H \to \tau\tau \to \ell^+\ell^- 4\nu$ channel as a discriminating variable the $\tau\tau$ invariant mass is used and estimated using the collinear approximation. As a discriminating variable in the $H \to \tau\tau \to \ell\tau_{had}3\nu$ channel a Missing Mass Calculator technique is used to estimate the ditau invariant mass which does not assume a strict collinearity between the visible and invisible decay products of the tau leptons.

2.6 $H \to ZZ \to \ell^+\ell^-\nu\overline{\nu}$, $H \to ZZ \to \ell^+\ell^- q\overline{q}$, $H \to WW \to \ell\nu q\overline{q}'$

The $H \to ZZ \to \ell^+\ell^-\nu\overline{\nu}$ is split into two lepton flavour categories and analysed in the mass range from 200 to 600 GeV and is sensitive to a SM Higgs boson in the range of $260 \leq m_H \leq 490$ GeV. The $H \to ZZ \to \ell^+\ell^- q\overline{q}$ analysis is divided into events where the two jets are b-tagged and into events with less than two b-tags. This analysis is expected to exclude a SM Higgs boson in the range of $360 \leq m_H \leq 400$ GeV at the 95% CL. In the $H \to WW \to \ell\nu q\overline{q}'$ channel the $\ell\nu q\overline{q}'$ mass distribution is used as a discriminating variable imposing mass constraints on both W bosons. The analysis reaches the best sensitivity of two times the SM Higgs boson cross section around m_H= 400 GeV.

3 Combination

The combination procedure is based on the profile likelihood ratio test statistic. The signal strength, μ, is defined as the ratio of a given Higgs boson production cross section (σ) to its SM value (σ_{SM}), $\mu = \sigma/\sigma_{\mathrm{SM}}$. Exclusion limits are based on the CL_s prescription [14]; a value of μ is regarded as excluded at the 95% (99%) CL when CL_s takes on the corresponding value. Figure 3 (left) shows the expected and observed limits from the individual channels as described above entering the combination. For the low mass region (below $m_H < 150$ GeV) the combined 95% CL exclusion limits [15] on μ are shown in Fig. 3 (right) as a function of m_H. An excess of events is observed near $m_H \sim 126$ GeV in the $H \rightarrow \gamma\gamma$ and $H \rightarrow ZZ^{(*)} \rightarrow \ell^+\ell^-\ell^+\ell^-$ channels, both of which provide fully reconstructed candidates with high-resolution in invariant mass.

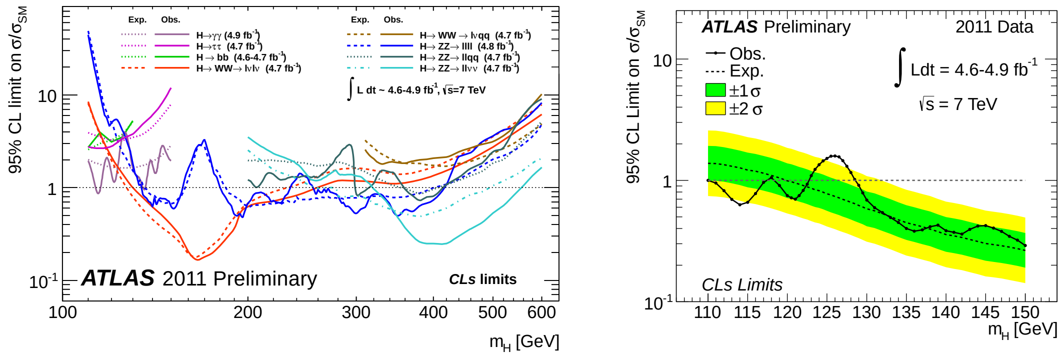

Figure 3: Left: The observed (solid) and expected (dashed) 95% CL cross section upper limits for the individual search channels as a function of the Higgs boson mass. Right: The observed and expected 95% CL combined upper limits on the SM Higgs boson production cross as a function of m_H in the low mass range.

4 Conclusions

The full dataset recorded in 2011 by the ATLAS experiment has been used to update searches for the SM Higgs boson. A Higgs boson with a mass in the ranges from 110.0 GeV to 117.5 GeV, 118.4 GeV to 122.7 GeV, and 128.6 GeV to 529.3 GeV is excluded at the 95% CL, while in the absence of a signal the range 119.8 GeV to 567 GeV is expected to be excluded. Between 130 GeV and 486 GeV the exclusion is even at the 99% CL. Around m_H of 126 GeV an excess of events is observed with a local significance of 2.5σ. The expected significance in the presence of a SM Higgs boson at that mass hypothesis is 2.8σ. The global probability for such an excess to occur anywhere in the explored Higgs boson mass region is estimated to be approximately 30%, in the range not excluded at the 99% CL, it amounts to approximately 10%.

References

1. R. Barate *et al*, *Phys. Lett.* B **565**, 61 (2003).
2. CDF and D0 Collaborations, arXiv:1203.3774.
3. Tevatron Electroweak Working Group, August 2009, `http://tevewwg.fnal.gov/`.
4. LEP Electroweak Working Group, March 2012, `http://lepewwg.web.cern.ch/LEPEWWG/`.
5. ATLAS Collaboration, *Phys. Lett.* B **710**, 49 (2012).
6. ATLAS Collaboration, *Phys. Rev. Lett.* **108**, 111803 (2012).
7. ATLAS Collaboration, *Phys. Lett.* B **710**, 383 (2012).
8. ATLAS Collaboration, ATLAS-CONF-2012-012, http://cdsweb.cern.ch/record/1429660.
9. ATLAS Collaboration, ATLAS-CONF-2012-015, http://cdsweb.cern.ch/record/1429664.
10. ATLAS Collaboration, ATLAS-CONF-2012-014, http://cdsweb.cern.ch/record/1429662.
11. ATLAS Collaboration, ATLAS-CONF-2012-016, http://cdsweb.cern.ch/record/1429665.
12. ATLAS Collaboration, ATLAS-CONF-2012-017, http://cdsweb.cern.ch/record/1429666.
13. ATLAS Collaboration, ATLAS-CONF-2012-018, http://cdsweb.cern.ch/record/1429667.
14. A. L. Read J. Phys. **G28** (2002) 2693–2704.
15. ATLAS Collaboration, ATLAS-CONF-2012-019, http://cdsweb.cern.ch/record/1430033.

Search for the Standard Model Higgs Boson at CMS

Adolf Bornheim for the CMS Collaboration

Charles C. Lauritsen Laboratory, 1200 E. California Blvd., Pasadena CA, 91125, USA

We searched for the standard model Higgs boson in 11 different decay channels using approximately 5 fb^{-1} of 7 TeV pp collisions data collected with the CMS detector at LHC. Combining the results we exclude at 95% confidence level the standard model Higgs boson with a mass between 127.5 and 600 GeV. The expected 95% confidence level exclusion if the Higgs boson is not present is from 114.5 and 543 GeV. The observed exclusion is weaker than expected at low mass because of some excess of events observed in the data. The most significant excess is found at 125 GeV with a local significance of 2.8σ, a global significance of 0.8σ in the full search range and of 2.1σ in the range 110–145 GeV. The excess is consistent both with background fluctuation and a standard model Higgs boson with mass of about 125 GeV. More data are needed to investigate its origin.

1 Analysis strategy

A search for the Standard Model (SM) Higgs Boson [1,2] is carried out in the mass range from 110 and 600 GeV in the decay modes summarized in Table 1, along with the corresponding integrated luminosity, the number of subchannels, the investigated mass range and the approximate Higgs boson mass resolution. At mass below approximately 130 GeV the sensitivity is dominated by $\gamma\gamma$ and $ZZ^{(*)} \to 4\ell$ decay channels, between 130 and 200 GeV by the WW channel and above 200 GeV various ZZ channels.

Table 1: The 11 Higgs boson search channels. The most relevant information is indicated for each of the analyses.

Channel	m_H range (GeV)	Luminosity (fb^{-1})	Sub-channels	$m_{\rm H}$ resolution	Comment
$H \to \gamma\gamma$	110–150	4.8	2	1–2%	updated
$H \to \tau\tau \to e\tau_{\rm h}/\mu\tau_{\rm h}/e\mu + X$	110–145	4.6	9	20%	
$H \to \tau\tau \to \mu\mu + X$	110–140	4.5	3	20%	new
$WH \to e\mu\tau_h/\mu\mu\tau_h + \nu$'s	100–140	4.7	2	20%	new
$(W/Z)H \to (\ell\nu/\ell\ell/\nu\nu)(bb)$	110–135	4.7	5	10%	
$H \to WW^* \to 2\ell 2\nu$	110–600	4.6	5	20%	
$WH \to W(WW^*) \to 3\ell 3\nu$	110–200	4.6	1	20%	new
$H \to ZZ^{(*)} \to 4\ell$	110–600	4.7	3	1–2%	
$H \to ZZ^{(*)} \to 2\ell 2q$	130–164 200–600	4.6	6	3% 3%	
$H \to ZZ \to 2\ell 2\tau$	190–600	4.7	8	10–15%	
$H \to ZZ \to 2\ell 2\nu$	250–600	4.6	2	7%	

2 Low mass channels

2.1 $H \to \gamma\gamma$ channel

The Higgs boson branching ratio for the decay into two photons is approximately 2×10^{-3} between 110 and 150 GeV. A signal in this channel would appear as a small, narrow peak on a large background. The background is dominated by the irreducible two photon QCD production, from events in which jets are misidentified as a photon. The sensitivity of this analysis depends crucially on a very good mass resolution of the detector which ranges between approximately 1 the pseudorapidity of the photons and the extend to which they interact with the material in front of the electromagnetic calorimeter. As reported in [8,9], the sensitivity of the analysis is increased by splitting the data set into four non overlapping event classes based on the photon pseudorapidity and shape of the shower in the electromagnetic calorimeter. In the new analysis that we present here, categories are defined in a more optimal way using a multi variant analysis technique (MVA) based approach that results in a higher sensitivity. Specifically the event by event mass resolution, photon identification discriminant, di-photon kinematic variables and vertex probability are combined using a boosted decision tree (BDT). This exploits the detector performance and the differences in the kinematics of the di-photon system between signal and background. The event by event mass resolution as well as the actual energy reconstruction of the photons are also based on a BDT to optimally utilize the information of the electromagnetic calorimeter. To enhance the sensitivity of the analysis further, events which are produced via Vector Boson Fusion (VBF) are treated in one separate event class which features an enhanced signal to background ratio, resulting in an improvement on the combined exclusion sensitivity of approximately 10% in cross section. Table 2 shows the number of expected signal events, the number of data events per GeV and the estimate of the mass resolution in all classes for the MVA analysis.

Table 2: Number of selected events in different event classes, for a SM Higgs boson signal (m_{H}=120 GeV), for data in a one GeV window around 120 GeV as well as the mass resolution in each event class.

m_{H}=120 GeV	Class 0	Class 1	Class 2	Class 3	Dijet class
Total signal expected events	3.4	19.3	18.7	33.0	2.8
Data (events/GeV)	4.5	55.1	81.3	229.1	2.1
Resolution FWHM/2.35 (%)	0.9	0.9	1.2	1.7	1.1

The background shape is estimated by fitting the di-photon mass spectrum to a polynomial in of (3^{rd} to 5^{th} order, depending on the event class) over the mass range 100 to 180 GeV. We found that the possible bias in the background estimation is always less than about 20% of the statistical error. As a cross check a background model based on side bands around the signal hypothesis is used, yielding consistent results. The signal line shape is dominated by the detector resolution. The line shape from MC used in the extraction of the result is adjusted to match the detector resolution measured in data on $Z \to ee$ events. Figure 1 shows the results in terms of 95% CL exclusion on the cross section normalized to the SM cross section and the local p-value where the p-value is the probability that a background only fluctuation is more signal-like than the observation. The expected 95% CL exclusion varies between 1.2 and 2 times the SM. We observe the largest excess around 125 GeV with a local significance of 2.9σ. Its global significance is 1.6σ when taking into account the look elsewhere effect (LEE) estimated in the full mass range 110–150 GeV. The p-values are also shown for the inclusive and the VBF categories separately. The minima of the p-value at 125 GeV has a strong contribution from the VBF category.

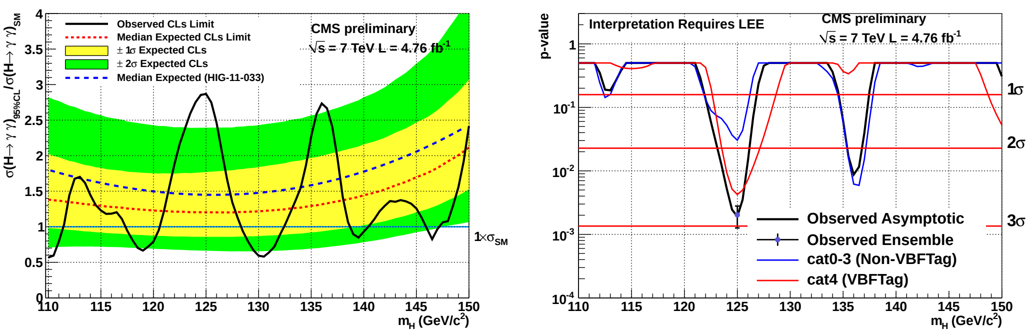

Figure 1: Left: 95% exclusion on the relative signal strength to the SM in the $\gamma\gamma$ channel for the MVA based analysis (red dotted line) and the cut based analysis (blue dashed line). as well as the 1 and 2σ (yellow and green band) expectations around the median expected result for the MVA analysis. Right: Local, combined p-value as function of the Higgs mass as well as the contribution from the individual classes.

2.2 $H \to ZZ \to 4\ell$ channel

In this channel, the cleanest and often referred to as the "golden channel", the signal consists of four isolated leptons. For high mass both pairs of opposite charge and same flavor leptons are consistent with Z decays while for lower masses at least one of the pairs has lower mass. The Higgs branching ratio for this channel is small, approximately one per mille at high mass and lower for masses below $2 \times m_{\mathrm{W}}$. The background however is very small, consisting mainly of irreducible continuum ZZ production and, to a lesser extent, Z plus jets and especially Zbb. The mass resolution is very good and ranges between 1 and 2%. The p_{T} of the lower p_{T} leptons is rather small and one of the most important features of the analysis is the achievement of a very high lepton efficiency down to very low p_{T}. Figure 2 shows the invariant mass spectrum of the selected data compared to the background expectations in the mass range 110 to 600 GeV [16] . We do not observe any significant excess of the data and we exclude at 95% CL the SM Higgs boson with M_{H} in 134–158, 180–305 and 340–465 GeV. The most significant excess is at a mass of approximately 119.5 GeV with a local significance of 2.5σ and a global significance of 1.0σ in the full mass range and 1.6σ in the range 100–160 GeV. In this mass range we observe 13 event with an expected background of 9.7 ± 1.3 events while in the full mass range up to 600 GeV we observe 72 events with 67 ± 6 events expected.

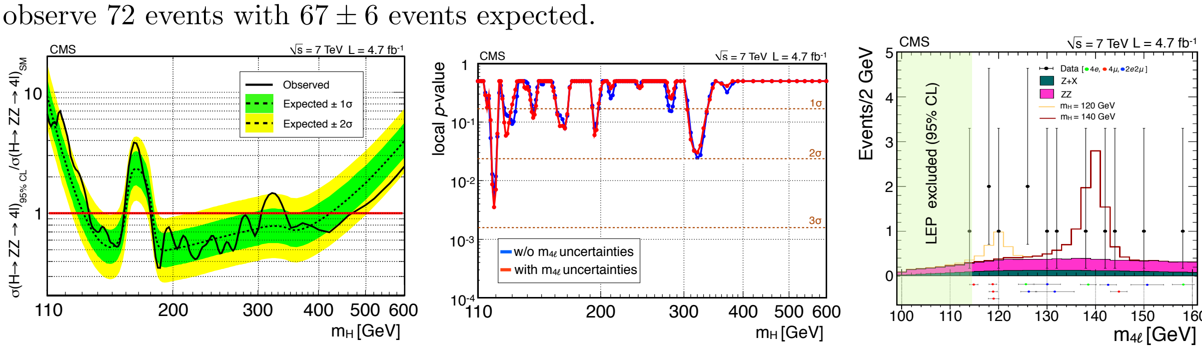

Figure 2: 95% exclusion limit on the relative signal strength to the SM (left) and local p-value computed with and without the individual candidate errors on the reconstructed mass in the $H \to ZZ \to 4\ell$ channel.

2.3 $H \to \tau\tau$ and $H \to bb$ channels

In both channels the background for the inclusive searches is huge and sensitivity is improved by requiring additional final state tags such as jets or charged leptons from VBF or VH production. The mass resolution is approximately 20% due to the presence of neutrinos in the final state for the $\tau\tau$ final state. For the bb final state the mass resolution becomes about 10% by requiering the final state to be boosted which also improves the background rejection.

In the $\tau\tau$ final state we search in the mass range between 110 and 150 GeV [10]. The expected sensitivity for exclusion is approximately 3 times the SM and we do not observe any significant excess in the data. We have recently extended the search to cases where the both τ leptons decay into muons [11] and to the channel WH→ e$\mu\tau_h$, $\mu\mu\tau_h$ [12] for which we use same sign eμ and $\mu\mu$ to reduce the background from Z plus jets. In the $H \to bb$ final state we exploit the VH associated production with W and Z decaying leptonically and we analyze separately all channels: $e\nu$, $\mu\nu$, ee, $\mu\mu$ and $\nu\nu$ [13]. We search in the mass range between 110 and 135 GeV and the expected sensitivity for exclusion ranges from 3 to 6 times the SM. We do not find a significant excess in data in this channel.

3 Channels sensitive at intermediate and high masses

The $H \to WW \to 2\ell 2\nu$ channel is very sensitive from around 120 GeV up to 600 GeV. The signature is two isolated high p_{T} leptons and the presence of missing transverse energy (MET). The Higgs mass resolution is of the order of 20%. The main backgrounds in this channel are irreducible WW production, Z plus jets, WZ, ZZ and W plus jets. Since the Higgs boson is a scalar and due to the V-A structure of the W decay, the two charged leptons tend to be aligned. This favours a small difference in azimuthal angle $\Delta\phi$ and provides some handle to discriminate the signal from the irreducible background. The analysis [14] is performed in exclusive jet multiplicities (0, 1 and 2-jet bins) and flavour (ee, $\mu\mu$, eμ) to profit from the different sensitivities and background contributions. The 2-jet bin corresponds to the VBF analysis and again exploits the characteristics of the VBF jets such as large p_{T}, large $\Delta\eta$ and di-jet invariant mass. Two variants of analyses are carried out: the first is a cut-and-count for all sub channels and the second is a multivariate analysis that is applied to the 0 and 1-jet bins that are the most sensitive ones. Figure 3 shows the the final distribution of the BDT discriminant for the opposite flavor 0 (left) and 1-jet bin (center) that is used to derive the final confidence level and the 95% exclusion confidence level (right) for the the MVA shape analysis. The opposite flavour signature yields sensitive since the signal is larger, the signal/background is favorable and the background is dominated by the irreducible WW that has less uncertainties than the Z plus jets or tt contributions. We observe no significant excess in the full mass range. At low masses there is only a small upward trend of the observed limit with respect to the expected ones. For the MVA shape analysis the 95% C.L. expected exclusion is for a Higgs boson mass between 127 and 270 GeV while the observed exclusion range is 129–270 GeV at 95% CL. The results of the cut-and-count analysis are very similar.

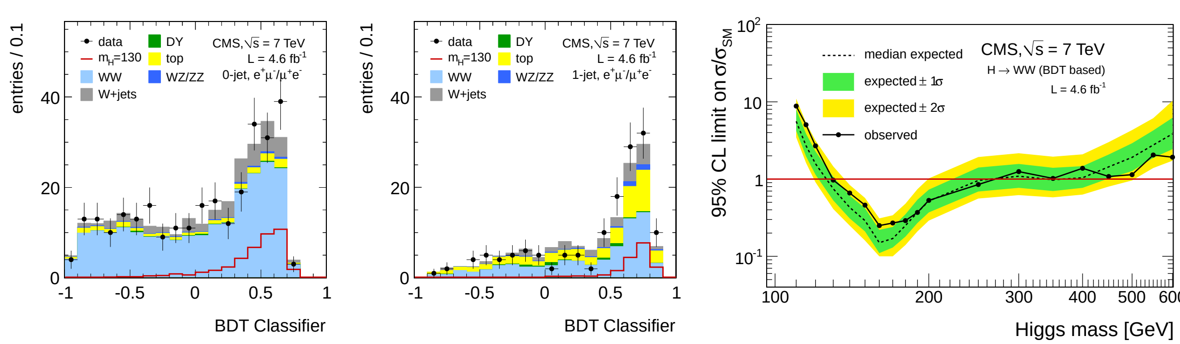

Figure 3: 95% exclusion limit on the relative signal strength to the SM for the cut based analysis(left) and for the MVA analysis (right) in the $H \to WW \to 2\ell 2\nu$ channel.

We recently added the WH→WWW→ $3\ell 3\nu$ channel [15]. This analysis is very similar to the WW channel with the main backgrounds estimated from data. It is a mass independent cut-and-count analysis and it is sensitive to about 4 times the SM in the most sensitive region around $2 \times m_{\mathrm{W}}$.

A SM Higgs boson above a mass of approximately 200 GeV almost exclusively decays into WW and ZZ and above about 300 GeV the Higgs boson width starts to be larger than the detector resolution in the ZZ channels. Beyond the previously described channels $H \to WW \to 2\ell 2\nu$ and $H \to ZZ \to 4\ell$, we searched in the channels where one Z decays into ν, quark and τ pairs. In the $H \to ZZ \to \ell\ell\nu\nu$ channel we did not observe any excess in the data and the observed exclusion from this channel alone is similar to the one expected in presence of background only. The expected 95% CL exclusion using this channel alone is M_{H} in 290–480 GeV and the observed is M_{H} in 270–440 GeV. The $H \to ZZ \to \ell\ell$qq channel [18] is used both for the high mass, where its sensitivity is similar but a little lower than the other ZZ channels, and for lower masses where it only gives a small contribution to the sensitivity.

4 Combination of all channels

All channels are combined to obtain the final exclusion and discovery confidence levels using the so-called CLs method described in [20]. The combination of the previously published results is reported in [21]. Here we present the combination that includes the new preliminary results presented at this conference [22]. SM cross sections and branching ratios are assumed for the combination with their theoretical uncertainties [5,6]. An overall signal strength multiplier $\mu = \sigma/\sigma_{\mathrm{SM}}$ is introduced and limits on its value are derived. Figure 4 shows the SM exclusion confidence level as function of the Higgs boson mass. The SM Higgs boson is excluded by our search at 95% confidence level in the range 127.5–600 GeV and at 99% confidence level in the range 129–525 GeV. The expected 95% exclusion is 114.5–543 GeV. The observed CMS upper limit on the Higgs boson mass is higher than expected because of an excess of event observed in the data in the region between 115 and 128 GeV. Figure **??** shows the 95% exclusion limit on the signal strength multiplier μ in the different Higgs decay channels.

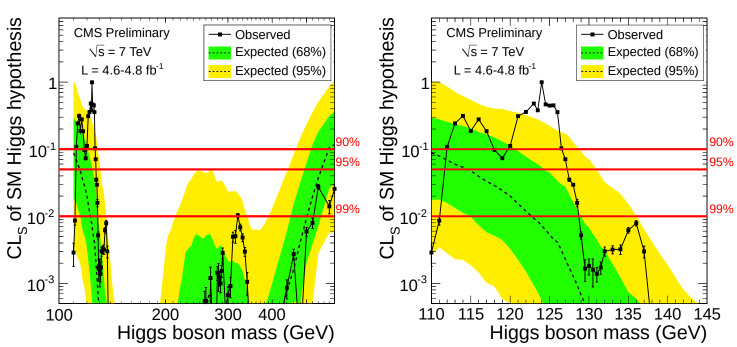

Figure 4: Exclusion confidence level for the combined SM Higgs search in the full mass range 110–600 GeV (left) and low mass zoom (center). The solid line indicates the observed confidence level and the dashed line the expected one. 95% exclusion confidence level on the signal strength multiplier for the SM Higgs search in the 5 Higgs decay channels (right). The solid lines indicate the observed exclusion and the dashed lines the expected.

Figure 5 shows the local p-value as function of the Higgs boson mass in the low mass region. The minimum combined p-value is observed at a mass of 125 GeV with a local significance of 2.8σ. If we consider the probability of observing a local significance larger than 2.8σ anywhere in the search range, we obtain a global significance of 0.8σ relative to the full mass range 110–600 GeV and of 2.1σ for the mass range 110–145 GeV. The observed significance fitted μ of the excess near 125 GeV is consistent with the SM scalar boson expectation.

5 Summary

We searched for the SM Higgs boson in 11 independent channels using approximately 5 fb^{-1} of 7 TeV pp collision data collected with the CMS detector at LHC. Combining the results of the different searches we exclude at 95% confidence level a SM Higgs boson with mass between 127.5 and 600 GeV. The expected 95% confidence level exclusion if the Higgs boson is not present is from 114.5 and 543 GeV. The observed exclusion is weaker than expected at low mass because

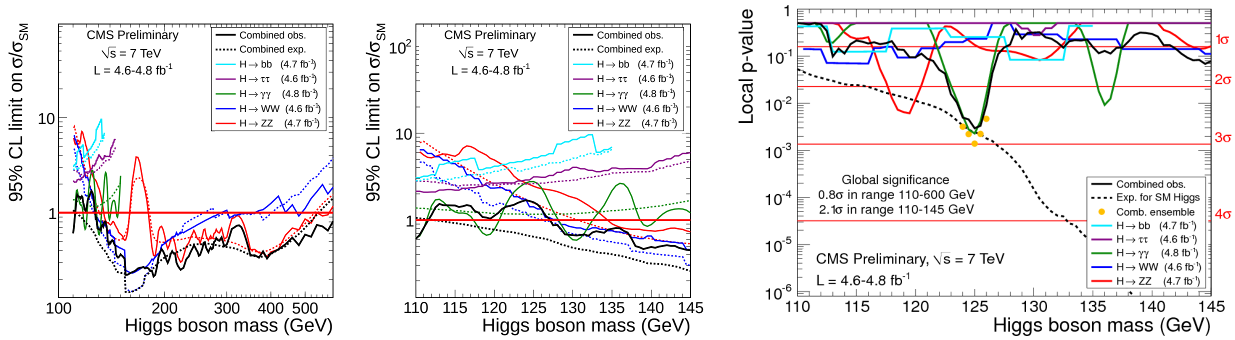

Figure 5: 95% exclusion confidence level on the signal strength multiplier for the SM Higgs search in the 5 Higgs decay channels. The solid lines indicate the observed exclusion and the dashed lines the expected.

of some excess that is observed below about 128 GeV. The most significant excess is found at 125 GeV with a local significance of 2.8σ, a global significance of 0.8σ when evaluated in the full search range and of 2.1σ in the range 110–145 GeV. The excess is consistent both with background fluctuation and a SM Higgs boson with mass of about 125 GeV and more data are needed to investigate its origin. As of the writing of these proceedings the first 5 fb^{-1} of 2012 data are being analysed.

References

1. S. Weinberg, “A Model of Leptons”, *Phys. Rev. Lett.* **19** (1967) 1264. ; A. Salam, “Elementary Particle Theory”, p. 367. Almquist and Wiksells, Stockholm, 1968.
2. P. W. Higgs, “Broken symmetry and the mass of gauge vector mesons”, *Phys. Rev. Lett.* **13** (1964) 508. ; F. Englert and R. Brout, “Broken symmetries and the masses of gauge bosons”, *Phys. Rev. Lett.* **13** (1964) 321.
3. R. Barate and others (LEP Higgs Working Group [ALEPH, DELPHI, L3, and OPAL Coll.]), “Search for the SM Higgs boson at LEP”, *Phys. Lett.* **B565** (2003) 61–75.
4. M. Baak *et al.*, arXiv:1107.0975 [hep-ph].
5. S. Dittmaier *et al.*, arXiv:1201.3084 [hep-ph].
6. S. Dittmaier *et al.* [LHC Higgs Cross Section Working Group], arXiv:1101.0593 [hep-ph].
7. CMS Collaboration,”The CMS experiment at the CERN LHC”, *JINST* **3** (2008) S08004.
8. S. Chatrchyan *et al.* [CMS Coll.], Phys. Lett. B **710**, 403 (2012) [arXiv:1202.1487 [hep-ex]].
9. CMS Collaboration, CMS Physics Analysis Summary CMS-PAS-HIG-12-001 (2012).
10. S. Chatrchyan *et al.* [CMS Coll.], arXiv:1202.4083 [hep-ex].
11. CMS Collaboration, CMS Physics Analysis Summary CMS-PAS-HIG-12-007 (2012).
12. CMS Collaboration, CMS Physics Analysis Summary CMS-PAS-HIG-12-006 (2012).
13. S. Chatrchyan *et al.* [CMS Coll.], Phys. Lett. B **710**, 284 (2012) [arXiv:1202.4195 [hep-ex]].
14. S. Chatrchyan *et al.* [CMS Coll.], Phys. Lett. B **710**, 91 (2012) [arXiv:1202.1489 [hep-ex]].
15. CMS Collaboration, CMS Physics Analysis Summary CMS-PAS-HIG-11-034 (2011).
16. S. Chatrchyan *et al.* [CMS Coll.], arXiv:1202.1997 [hep-ex].
17. S. Chatrchyan *et al.* [CMS Coll.], JHEP **1203**, 040 (2012) [arXiv:1202.3478 [hep-ex]].
18. S. Chatrchyan *et al.* [CMS Coll.], arXiv:1202.1416 [hep-ex].
19. S. Chatrchyan *et al.* [CMS Coll.], JHEP **1203**, 081 (2012) [arXiv:1202.3617 [hep-ex]].
20. ATLAS and CMS Collaborations, ATLAS-CONF-2011-157, CMS HIG-11-023 (2011).
21. S. Chatrchyan *et al.* [CMS Coll.], Phys. Lett. B **710**, 26 (2012) [arXiv:1202.1488 [hep-ex]].
22. CMS Collaboration, CMS Physics Analysis Summary CMS-PAS-HIG-12-008 (2012).

Optimizing Higgs Identification at the LHC

Seung J. Lee
Department of Physics, Korea Advanced Institute of Science and Technology, 335 Gwahak-ro, Yuseong-gu, Daejeon 305-701, Korea

Template overlaps are a class of infrared safe jet observables, based on functional comparison of the energy flow in data with the flow in selected sets (the templates) of partonic states. In a recent work with Leandro G. Almeida, Ozan Erdoğan, José Juknevich, Gilad Perez, and George Sterman, we have shown that template overlap offers the promise of a successful boosted Higgs tagger, have demonstrated how the inclusion of three particle templates allows us to test the influence of gluon emission and color flow, through their effect on energy flow, and have illustrated its use through the construction of partonic template observables.

1 Introduction

The search for the Higgs boson at the Large Hadron Collider is now in the discovery phase with the di-photon signal hinting the existence of $\sim$ 125 GeV Higgs-like particle, and it becomes important to really make sure whether this is indeed the Higgs particle of the Standard Model (SM). It is also very interesting to figure out whether the decay branching ratio of the could-be-Higgs boson is what we expect from the SM, specially in the absence of discovery of any signal for New Physics beyond the SM at the current experimental stage. While $H \to b\bar{b}$ channel is the dominant decay mode for such mass range of the Higgs, the detector sensitivity of this channel is much less than other decay channels due to the swamping QCD background. A jet substructure method was first employed to provide a useful handle to distinguish the signal from the QCD background for the case of boosted Higgs [1] (which is often referred as "BDRS" method). We apply the template method to the same production of a Higgs boson in association with a W boson, $p+p \to W+H$, followed by the dominant light Higgs boson decay, to two b-tagged jets, including schemes for generating templates and for discretizing the data. We investigate the tagging efficiency for this process, and the fake rates from the background process $p+p \to W+jets$.

2 The Template Overlap Method

A template overlap method was developed for the quantitative comparison of the energy flow of observed jets at high-p_T with the flow from selected sets (the templates) of partonic states [2], which can be summarized as follows[2,3]. We denote by $|j\rangle$ the set of particles or calorimeter towers that make up a jet, identified by some algorithm, and take $|f\rangle$ to represent a set of partonic momenta $p_1 \dots p_n$ that represent a boosted decay, found by the same algorithm. We introduce a functional measure $\mathcal{F}(j,f) \equiv \langle f|j\rangle$ that quantifies how well the energy flow of $|j\rangle$ matches $|f\rangle$. In practice, we find good results with a simple construction of functional overlap based on a Gaussian in energy differences within angular regions surrounding the template partons. Any region of partonic phase space for the boosted decays, $\{f\}$, defines a template. We use our knowledge of the signal and background to design a custom analysis for each resonance, to make use of differences in energy flow between signal and background. We define the template overlap of observed jet j as $Ov(j, f[j]) = \max_{\{f\}} \mathcal{F}(j, f)$, the maximum functional overlap of j to a state $f[j]$ within the template region. We use the notation $f[j]$ for the state of maximum overlap to emphasize that the value of the overlap functional depends not only on the physical state $|j\rangle$, but also on the choice for the set of template functions f.

As a simple working example, for an N-particle final state, we represent our template overlap (dropping the superscript (F)) as [2]

$$Ov_N(j, p_1, \ldots, p_N) = \max_{\tau_N^{(R)}} \exp\left[- \sum_{a=1}^{N} \frac{1}{2\sigma_a^2} \left(\int d^2\hat{n}\, \frac{dE(j)}{d^2\hat{n}} \theta_N(\hat{n}, \hat{n}_a^{(f)}) - E_a^{(f)} \right)^2 \right], \quad (1)$$

where the direction of template particle a is $\hat{n}_a$ and its energy is $E_a^{(f)}$. In applications below, we will use these energies to set the widths of the Gaussians. The functions $\theta_N(\hat{n}, \hat{n}_a^{(f)})$ restrict the angular integrals to (nonintersecting) regions surrounding each of the template momenta. We will refer to the corresponding state as the "peak template" $f[j]$ for state j. The peak template $f[j]$ provides us with potentially valuable information on energy flow in j. The output of the peak template method for any physical state j is the value of the overlap, $Ov(j, f)$, and also the identity of the template state $f[j]$ to which the best match is found.

2.1 Construction of template functions for the Higgs

Here we have adopted the expectation that a good rejection power is obtained when we simply use the signal (Higgs) distribution itself to construct our templates[2]. Then, we want our template overlaps to be functionals of the energy flow of any specific event (usually involving jets), which we label j, and a model, or template, for the energy flow in a signal, referred to as f . The number of particles in the templates is not necessarily fixed, and templates with more than the minimum number of particles are possible. We find, however, that combining templates in the full phase space for $N = 3$ and $N = 2$ already delivers encouraging results for the Higgs [3]. Our templates will be a set of discretized partonic states corresponding to given points in phase space. We generate a large number of template states enough to sufficiently cover both two- and three-particle phase space for Higgs decay.

2.2 Selection and Discretization of the Data

We generate events for $W^+ + H \to l^+\nu_l\, b\bar{b}$ and $W^+ + jets \to l^+\nu_l + jets$ in a configuration with large transverse momentum, using Pythia 8.150[4], Sherpa 1.3.0[5] (with CKKW matching [6]), and Madgraph[7] interfaced to Pythia 6 [8] (with MLM matching[9]). Jets are reconstructed using Fastjet [10], and the anti-k_T algorithm [11] with large effective cone size $R = 0.7$. We have chosen plausible value for R, based on a combination of physics input and a trial-and-error, but have not attempted to optimize them systematically. For each event, we find the jet with the highest transverse momentum and impose a jet mass window for the Higgs. We choose the jet mass window to be 110 GeV $\leq m_J \leq$ 130 GeV, with our reference Higgs boson mass chosen to be $m_H = 120$ GeV, and jet energy 950 GeV $\leq P_0 \leq$ 1050 GeV. This gives us a set of final states j.

We compute the overlap between data state j and two- or three-body template f from the unweighted sum of the energy in the nine cells of state j surrounding and including the occupied cells of template state f [2],

$$Ov_N(j,f) = \max_{\tau_N^{(R)}} \exp\left[-\sum_{a=1}^{N} \frac{1}{2\sigma_a^2} \left(\sum_{k=i_a-1}^{i_a+1} \sum_{l=j_a-1}^{j_a+1} E(k,l) - E(i_a,j_a)^{(f)} \right)^2 \right], \tag{2}$$

where $N = 2$ or 3. Here, $E(i_a, j_a)^{(f)}$ is the energy in the template state for particle a whose direction is labelled by indices i_a and j_a. If one of the sums extends outside the jet cone, we set the corresponding energies $E(k,l)$ to zero. We fix σ_a (for the ath parton) by that parton's energy, $\sigma_a = E(i_a, j_a)^{(f)}/2$.

3 Summary of template overlaps for Higgs and QCD jets

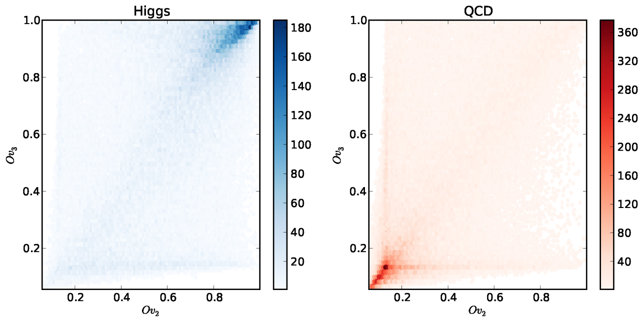

Figure 1: Density plots of 2-body overlap *vs.* 3-body overlap for boosted Higgs and QCD jets with $R = 0.7$.

Both two- and thee-body template overlap have substantial discriminating power, which can be seen in the scatter plots, shown in Fig. 1, of Ov_2 and Ov_3 for Higgs signal (left panel) and dijet production (right panel) [3]. While the signal events cluster around the upper right corner of the plot, most QCD jet events are localized diagonally opposite in the lower left. It follows immediately that making tight cuts on each observable, by drawing a rectangular window in the upper right corner of the scatter plot, makes a good discriminator to separate signal from background.

Table 1: Efficiencies and fake rates for jets with $R = 0.7$ (using anti-k_T: $D = 0.7$), 950 GeV$\leq P_0 \leq$1050 GeV, 110 GeV$\leq m_J \leq$130 GeV and $m_H = 120$ GeV. We have imposed various cuts on Ov, $\bar\theta$ and Pf variables: f$Ov_2 > 0.8$, $Ov_3 > 0.8$, $\bar\theta < 0.4$ and $Pf < 0.2$ (for Sherpa, we had $Ov_3 > 0.7$, $\bar\theta < 0.45$ and $Pf < 0.3$ for comparable results).

MC	Jet mass cut only		Mass cut + Ov ($+\bar\theta+$ Pf)	
	Higgs-jet efficiency [%]	fake rate [%]	Higgs-jet efficiency [%]	fake rate [%]
Pythia 8	70	10	10	0.05
MG/ME	70	10	10	0.05
Sherpa	60	10	10	0.05

The final results for the Higgs jet case are summarized in Tables 1 [3] for the three event generators and $R = 0.7$, that result from including these simple, naive one-dimensional cuts in Ov_2, Ov_3 (with the three-body angular variable vaiable $\bar\theta$ [a] and planar flow Pf [12,13]) at fixed

[a] The three-body angular variable $\bar\theta$ is defined as $\bar\theta = \sum_i \sin\theta_{iJ}$ where θ_{iJ} is the angles between the jet axis and the template momenta. It is a partonic level variable, which becomes a physical observable when it is associated with the peak template.

signal efficiency of $S = 10\%$. We find a large enhancement of signal compared to background, typically of the order of fifteen or more. Taking into account the rejection of QCD jets by imposing a mass window, these numbers (for a single massive jet) are multiplied by factors of ten to twenty.

The template-based approach yields, without optimization, moderately improved numbers compared with those found from other methods in the literature (see for example Ref. [1,14]). Our template overlap method has an advantage for dealing with pile-up issue, as it is based on parton-hadron dulaity where the spikiness of the jet energy distribution naturally avoids the complication of pile-up issue, as well as it provides a method based on first principle. The template overlap method is quite general, and it can be used for other massive object searches as well. Note that our event selection was chosen in a kinematical regime that at present is unrealistic for the LHC. However, our findings should serve as a proof of concept for many of the ideas, and, based on ongoing research[15,16], we expect an extended phenomenological analysis to deliver similar qualitative behaviour in terms of rejection power. As the LHC continues to explore the energy frontier of particle physics, template overlap provides us with an interesting tool for further development of jet substructure techniques.

References

1. J. M. Butterworth, A. R. Davison, M. Rubin and G. P. Salam, Phys. Rev. Lett. **100**, 242001 (2008) [arXiv:0802.2470 [hep-ph]].
2. L. G. Almeida, S. J. Lee, G. Perez, G. Sterman, I. Sung, Phys. Rev. **D82**, 054034 (2010). [arXiv:1006.2035 [hep-ph]].
3. L. G. Almeida, O. Erdogan, J. Juknevich, S. J. Lee, G. Perez and G. Sterman, arXiv:1112.1957 [hep-ph].
4. T. Sjostrand, S. Mrenna and P. Skands, Comput. Phys. Commun. **178**, 852 (2008) [arXiv:0710.3820 [hep-ph]].
5. T. Gleisberg, S. Hoche, F. Krauss, M. Schonherr, S. Schumann, F. Siegert and J. Winter, JHEP **0902**, 007 (2009) [arXiv:0811.4622 [hep-ph]].
6. S. Hoeche, F. Krauss, S. Schumann and F. Siegert, JHEP **0905**, 053 (2009) [arXiv:0903.1219 [hep-ph]].
7. F. Maltoni and T. Stelzer, JHEP **0302**, 027 (2003) [arXiv:hep-ph/0208156]; T. Stelzer and W. F. Long, Comput. Phys. Commun. **81**, 357 (1994) [arXiv:hep-ph/9401258]. JHEP **0709**, 028 (2007) [arXiv:0706.2334 [hep-ph]].
8. T. Sjostrand, S. Mrenna and P. Skands, JHEP **0605**, 026 (2006) [arXiv:hep-ph/0603175].
9. M. L. Mangano, M. Moretti, F. Piccinini and M. Treccani, JHEP **0701**, 013 (2007) [arXiv:hep-ph/0611129].
10. M. Cacciari and G.P. Salam, Phys. Lett. B 641 (2006) 57 [hep-ph/0512210]; M. Cacciari, G.P. Salam and G. Soyez, http://fastjet.fr/
11. M. Cacciari, G. P. Salam and G. Soyez, JHEP **0804**, 063 (2008) [arXiv:0802.1189 [hep-ph]].
12. J. Thaler and L. T. Wang, JHEP **0807**, 092 (2008) [arXiv:0806.0023 [hep-ph]].
13. L. G. Almeida, S. J. Lee, G. Perez, G. Sterman, I. Sung and J. Virzi, Phys. Rev. D **79**, 074017 (2009) [arXiv:0807.0234 [hep-ph]].
14. D. E. Soper and M. Spannowsky, Phys. Rev. D **84**, 074002 (2011) [arXiv:1102.3480 [hep-ph]].
15. M. Backovic, J. Juknevich, G. Perez and J. Winter, In preparation.
16. G. Gur-Ari, M. Field, D.A. Kosower, L. Manelli and G. Perez, In preparation.

DIPHOTON SPECTRUM IN THE MASS RANGE 120-140 GEV AT THE LHC

L.J CIERI

INFN, Sezione di Firenze, Via Sansone 1, I-50019 Sesto Fiorentino, Florence, Italy

We consider direct diphoton production in hadron collisions. We compute the next-to-next-to-leading order (NNLO) QCD radiative corrections at the fully-differential level. Our calculation uses the q_T subtraction formalism and it is implemented in a parton level Monte Carlo program, which allows the user to apply arbitrary kinematical cuts on the final-state photons and the associated jet activity, and to compute the corresponding distributions in the form of bin histograms. We present selected numerical results related to Higgs boson searches at the LHC, and we show how the NNLO corrections to diphoton production are relevant to understand the main background of the decay channel $H \to \gamma\gamma$.

1 Introduction

Diphoton production is a relevant process in hadron collider physics. It is both a classical signal within the Standard Model (SM) and an important background for Higgs boson and new-physics searches. Recent results from the LHC indicates that the Higgs boson mass m_H must be low (114 GeV$< m_H <$ 130 GeV), and thus the preferred search mode involves Higgs boson production via gluon fusion followed by the rare decay into a pair of photons. We are interested in the process $pp \to \gamma\gamma X$, which, at the lowest order in perturbative QCD, occurs *via* the quark annihilation subprocess $q\bar{q} \to \gamma\gamma$. The QCD corrections at the next-to-leading order (NLO) in the strong coupling α_S involve the quark annihilation channel and a new partonic channel, *via* the subprocess $qg \to \gamma\gamma q$. These corrections have been computed and implemented in the fully-differential Monte Carlo codes `DIPHOX`,[1] `2gammaMC` [2] and `MCFM`.[3] A calculation that includes the effects of transverse-momentum resummation is implemented in `RESBOS`.[4] At the next-to-next-to-leading order (NNLO), the gg channel starts to contribute, and the large gluon–gluon luminosity makes this channel sizeable. Part of the contribution from this channel, the so called *box contribution*, was computed long ago [5] and its size turns out to be comparable to the lowest-order result. Besides their *direct* production from the hard subprocess, photons can also arise from fragmentation subprocesses of QCD partons. The computation of fragmentation subprocesses requires (poorly known) non-perturbative information, in the form of parton fragmentation functions of the photon. The complete NLO single- and double-fragmentation contributions are implemented in `DIPHOX`.[1] The effect of the fragmentation contributions is sizeably reduced by the photon isolation criteria that are necessarily applied in hadron collider experiments to suppress the very large irreducible background (e.g., photons that are faked by jets or produced by hadron decays). The standard cone isolation and the 'smooth' cone isolation proposed by Frixione [6] are two of these criteria. The standard cone isolation is easily implemented in experiments, but it only suppresses a fraction of the fragmentation contribution. The smooth cone isolation (formally) eliminates the entire fragmentation contribution, but its experimental implementation is still under study.[7] However, it is important to anticipate (work to appear), that in some kinematical regions (e.g for Higgs boson searches), the standard cone and the Frixione isolation criteria give basically the same theoretical answer.[a]

2 Diphoton production at NNLO

We consider the inclusive hard-scattering reaction $h_1 + h_2 \to \gamma\gamma + X$, where the collision of the two hadrons, h_1 and h_2, produces the diphoton system $F \equiv \gamma\gamma$ with high invariant mass $M_{\gamma\gamma}$. The evaluation of the NNLO corrections to the this process requires the knowledge of the corresponding partonic scattering amplitudes with $X = 2$ partons (at the tree level, [8]) $X = 1$ parton (up to the one-loop level [9]) and no additional parton (up to the two-loop level [10]) in the final state. The implementation of the separate scattering amplitudes in a complete NNLO (numerical) calculation is severely complicated by the presence of infrared (IR) divergences that occur at intermediate stages. The q_T subtraction formalism [11] is a method that handles and cancels these unphysical IR divergences up to the NNLO. The formalism applies to generic hadron collision processes that involve hard-scattering production of a colourless high-mass system F. Within that framework,[11] the corresponding cross section is written as:

$$d\sigma^F_{(N)NLO} = \mathcal{H}^F_{(N)NLO} \otimes d\sigma^F_{LO} + \left[d\sigma^{F+\text{jets}}_{(N)LO} - d\sigma^{CT}_{(N)LO} \right] \ , \tag{1}$$

where $d\sigma^{F+\text{jets}}_{(N)LO}$ represents the cross section for the production of the system F plus jets at (N)LO accuracy [b], and $d\sigma^{CT}_{(N)LO}$ is a (IR subtraction) counterterm whose explicit expression [13] is obtained from the resummation program of the logarithmically-enhanced contributions to q_T distributions. The 'coefficient' $\mathcal{H}^F_{(N)NLO}$, which also compensates for the subtraction of $d\sigma^{CT}_{(N)LO}$, corresponds to the (N)NLO truncation of the process-dependent perturbative function

$$\mathcal{H}^F = 1 + \frac{\alpha_S}{\pi}\,\mathcal{H}^{F(1)} + \left(\frac{\alpha_S}{\pi}\right)^2 \mathcal{H}^{F(2)} + \dots \ . \tag{2}$$

The NLO calculation of $d\sigma^F$ requires the knowledge of $\mathcal{H}^{F(1)}$, and the NNLO calculation also requires $\mathcal{H}^{F(2)}$. The general structure of $\mathcal{H}^{F(1)}$ is explicitly known;[14] exploiting the explicit results of $\mathcal{H}^{F(2)}$ for Higgs [11,15] and vector boson [16] production we have generalized the process-independent relation of Ref.[14] to the calculation of the NNLO coefficient $\mathcal{H}^{F(2)}$.

3 Quantitative results

We have performed our fully-differential NNLO calculation [17] of diphoton production according to Eq. (1). The NNLO computation is encoded in a parton level Monte Carlo program, in which we can implement arbitrary IR safe cuts on the final-state photons and the associated jet activity. We concentrate on the direct production of diphotons, and we rely on the smooth cone isolation criterion.[6] Considering a cone of radius $r = \sqrt{(\Delta\eta)^2 + (\Delta\phi)^2}$ around each photon, we require the total amount of hadronic (partonic) transverse energy E_T inside the cone to be smaller than $E_{T\,max}(r)$,

$$E_T < E_{T\,max}(r) \equiv \epsilon_\gamma\, p_T^\gamma \left(\frac{1-\cos r}{1-\cos R}\right)^n \ , \tag{3}$$

where p_T^γ is the photon transverse momentum; the isolation criterion $E_T < E_{T\,max}(r)$ has to be fulfilled for all cones with $r \leq R$. We use the MSTW 2008 [18] sets of parton distributions,

[a] The use of the same parameters in both criteria is understood.

[b] In the case of diphoton production, the NLO calculation of $d\sigma^{\gamma\gamma+\text{jets}}_{NLO}$ was performed in Ref.[12]

with densities and α_S evaluated at each corresponding order, and we consider $N_f = 5$ massless quarks/antiquarks and gluons in the initial state. The default renormalization (μ_R) and factorization (μ_F) scales are set to the value of the invariant mass of the diphoton system, $\mu_R = \mu_F = M_{\gamma\gamma}$. The QED coupling constant α is fixed to $\alpha = 1/137$.

To present some quantitative results, we consider diphoton production at the LHC ($\sqrt{s}$ =

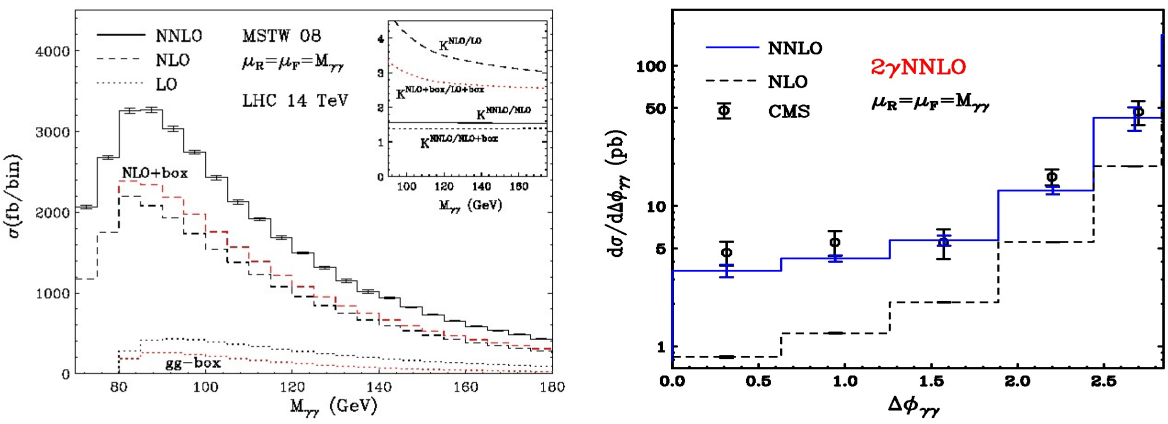

Figure 1: *Left: Invariant mass distribution of the photon pair at the LHC ($\sqrt{s}$ = 14 TeV): LO (dots), NLO (dashes) and NNLO (solid) results. We also present the results of the box and NLO+box contributions. The inset plot shows the corresponding* K*-factors. Right: Diphoton cross section as a function of the azimuthal separation of the two photons. Data from CMS*[19] *($\sqrt{s} = 7$ TeV) are compared to the NNLO calculation.*[17]

14 TeV). We apply typical kinematical cuts used by ATLAS and CMS Collaborations in their Higgs search studies. We require the harder and the softer photon to have transverse momenta $p_T^{\rm harder} \geq 40$ GeV and $p_T^{\rm softer} \geq 25$ GeV, respectively. The rapidity of both photons is restricted to $|y_\gamma| \leq 2.5$, and the invariant mass of the diphoton system is constrained to lie in the range $20\,{\rm GeV} \leq M_{\gamma\gamma} \leq 250\,{\rm GeV}$. The isolation parameters are set to the values $\epsilon_\gamma = 0.5$, $n = 1$ and $R = 0.4$. We observe [17] that the value of the cross section remarkably increases with the perturbative order of the calculation. This increase is mostly due to the use of *very asymmetric* (unbalanced) cuts on the photon transverse momenta. At the LO, kinematics implies that the two photons are produced with equal transverse momentum and, thus, both photons should have $p_T^\gamma \geq 40$ GeV. At higher orders, the final-state radiation of additional partons opens a new region of the phase space, where 40 GeV $\geq p_T^{\rm softer} \geq$ 25 GeV. Since photons can copiously be produced with small transverse momentum,[17] the cross section receives a sizeable contribution from the enlarged phase space region. This effect is further enhanced by the opening of a new large-luminosity partonic channel at each subsequent perturbative order. In Fig. 1 (left) we compare the LO, NLO and NNLO invariant mass distributions at the default scales. The inset plot shows the K-factors defined as the ratio of the cross sections at two subsequent perturbative orders. We note that $\mathrm{K}^{NNLO/NLO}$ is sensibly smaller than $\mathrm{K}^{NLO/LO}$, and this fact indicates an improvement in the convergence of the perturbative expansion. We find that about 30% of the NNLO corrections is due to the gg channel (the *box contribution* is responsible for more than half of it), while almost 60% still arises from the next-order corrections to the qg channel.

Recent results from the LHC [19,20] and the Tevatron [21] show some discrepancies between the data and NLO theoretical calculations of diphoton production. Basically, discrepancies were found in kinematical regions where the NLO calculation is *effectively* a LO theoretical description of the process. Such phase space regions [c] are accesible at NLO for the first time, due to the

[c] Away from the back-to-back configuration.

final-state radiation of the additional parton.[d] Figure 1 (right) shows a measurement by CMS,[19] of the diphoton cross section as a function of the azimuthal angle $\Delta\phi_{\gamma\gamma}$ between the photons. The data are compared with our NLO and NNLO calculations.[17] The acceptance criteria used in this analysis ($\sqrt{s} = 7$ TeV) require of: $p_T^{\rm harder} \geq 23$ GeV and $p_T^{\rm softer} \geq 20$ GeV. The rapidity of both photons is restricted to $|y_\gamma| \leq 2.5$, and the invariant mass of the diphoton system is constrained to be $M_{\gamma\gamma} > 80\,$GeV. The isolation parameters are set to the values $\epsilon_\gamma = 0.05$, $n = 1$ and $R = 0.4$. We note that the CMS data are selected by using the standard cone isolation criterion and the constraint in Eq. (3) is applied only to the cone of radius $r = R$. Since the smooth isolation criterion used in our calculation (we apply Eq. (3) for all cones with $r \leq R$) is stronger than the photon isolation used by CMS, we remark that our NLO and NNLO results cannot overestimate the corresponding theoretical results for the CMS isolation criterion. The histograms in Fig. 1 (right) show that the NNLO QCD results remarkably improve the theoretical description of the CMS data throughout the entire range of $\Delta\phi_{\gamma\gamma}$.

The results illustrated in this contribution show that the NNLO description of diphoton production is essential to understand the phenomenology associated to this process, and therefore, the NNLO calculation is a relevant tool to describe the main background for Higgs boson searches.

References

1. T. Binoth, J. P. Guillet, E. Pilon and M. Werlen, Eur. Phys. J. **C16**, 311 (2000).
2. Z. Bern, L. J. Dixon and C. Schmidt, Phys. Rev. **D66**, 074018 (2002).
3. J. M. Campbell, R. K. Ellis and C. Williams, JHEP **1107**, 018 (2011).
4. C. Balazs, E. L. Berger, P. M. Nadolsky and C. -P. Yuan, Phys. Rev. **D76**, 013009 (2007).
5. D. A. Dicus and S. S. D. Willenbrock, Phys. Rev. **D37**, 1801 (1988).
6. S. Frixione, Phys. Lett. **B429**, 369 (1998).
7. R. Blair, B. Brelier, F. Bucci, S. Chekanov, M. Stockton and M. Tripiana, CERN-OPEN-2011-041, (2011).
8. V. D. Barger, T. Han, J. Ohnemus and D. Zeppenfeld, Phys. Rev. **D41**, 2782 (1990); V. Del Duca, W. B. Kilgore and F. Maltoni, Nucl. Phys. **B566**, 252 (2000).
9. Z. Bern, L. J. Dixon and D. A. Kosower, Nucl. Phys. **B437**, 259 (1995); A. Signer, Phys. Lett. **B357**, 204 (1995).
10. C. Anastasiou, E. W. N. Glover and M. E. Tejeda-Yeomans, Nucl. Phys. **B629**, 255 (2002).
11. S. Catani and M. Grazzini, Phys. Rev. Lett. **98**, 222002 (2007).
12. V. Del Duca, F. Maltoni, Z. Nagy and Z. Trocsanyi, JHEP **0304**, 059 (2003).
13. G. Bozzi, S. Catani, D. de Florian and M. Grazzini, Nucl. Phys. **B737**, 73 (2006).
14. D. de Florian and M. Grazzini, Phys. Rev. Lett. **85**, 4678 (2000), Nucl. Phys. **B616**, 247 (2001).
15. S. Catani and M. Grazzini, report ZU-TH-12-11 (arXiv:1106.4652 [hep-ph]).
16. S. Catani, L. Cieri, G. Ferrera, D. de Florian and M. Grazzini, Phys. Rev. Lett. **103**, 082001 (2009).
17. S. Catani, L. Cieri, D. de Florian, G. Ferrera and M. Grazzini, Phys. Rev. Lett. **108** (2012) 072001.
18. A. D. Martin, W. J. Stirling, R. S. Thorne and G. Watt, Eur. Phys. J. **C63**, 189 (2009).
19. S. Chatrchyan *et al.* [CMS Collaboration], arXiv:1110.6461 [hep-ex].
20. G. Aad *et al.* [ATLAS Collaboration], Phys. Rev. D **85** (2012) 012003.
21. T. Aaltonen *et al.* [CDF Collaboration], Phys. Rev. D **84** (2011) 052006.

[d] The low-mass region ($M_{\gamma\gamma} \leq 80 GeV$) in Figure 1 also belongs to this case.

THE SM AND SUSY AFTER THE 2011 LHC RESULTS

G. ALTARELLI
Dipartimento di Fisica 'E. Amaldi', Università di Roma Tre and INFN, Sezione di Roma Tre, I-00146 Rome, Italy
and
CERN, Department of Physics, Theory Unit, CH–1211 Geneva 23, Switzerland

We present a short review of the LHC results at 7 TeV and their implications on the Standard Model (SM) and on its Supersymmetric (SUSY) extension. In particular we discuss the exclusion range for the SM Higgs mass, the tantalizing hint of an excess at $m_H \sim 125$ GeV, the negative results of searches for SUSY particles (as well as for any other new physics) and the present outlook

1 The first LHC results

The main LHC results so far (with more than 5.5 fb^{-1} of integrated luminosity collected by each large experiment at 7 TeV) are listed here, as presented at Moriond 2012.

1) A robust exclusion interval for the SM Higgs has been established which greatly extends the previous range; precisely at 95 % c.l. the excluded intervals of mass are ATLAS: 110 -117.5, 118.5 -122.5, 129 - 539 GeV and CMS: 127.5 - 600 GeV (note that ATLAS also excludes at 95% c.l. a large part of the mass range 110-122.5 GeV, while CMS has some excess in that region). In addition, there is some tantalizing indication for $m_H \sim 125$ GeV. In this respect, what is encouraging is that an excess is seen in the $\gamma\gamma$ mass distribution both in ATLAS (2.8 σ at 126.5 GeV) and CMS (2.9 σ at 125 GeV). Also there is a hint for $ZZ \to 4l^{\pm}$ in ATLAS (2.1σ at 125 GeV: 3 events) and the Tevatron reports a small excess spread over a large interval in $b\bar{b}$ and WW (2.7 σ in 115 -135 GeV). These accumulations are all compatible with $m_H \sim 125$ GeV. Further encouragement has been missed because in CMS a possible hint in $ZZ \to 4l^{\pm}$ is at a different mass (2.1σ at 119.5 GeV: 3 events) and in ATLAS the number of WW events is less than expected. Overall the evidence for $m_H \sim 125$ GeV could still evaporate and we need to wait for the outcome of the 2012 run, that, with an expected additional integrated luminosity of 15 fb^{-1} per experiment at 8 TeV, should either definitely confirm or exclude $m_H \sim 125$ GeV.

2) No evidence of new physics has been found although a big chunk of new territory has been explored.

3) Important results on B and D decays have been obtained mainly by LHCb, whose performance has been exceedingly good (but also on some issues by ATLAS and CMS), e.g. $B_s \to J\psi\phi$, $B_s \to \mu\mu$, ... CP violation in D decay.... Most of the results go in the direction of the SM. For CP violation in D decay, it could indeed be a sign of new physics but, in view of the uncertainty in the SM prediction, it is difficult to be sure.

2 The Higgs Problem

The experimental verification of the Standard Model (SM) [?] cannot be considered complete until the predicted physics of the Higgs sector [?] is not established by experiment. Indeed the Higgs problem is really central in particle physics today [?]. In fact, the Higgs sector is directly related to most of the major open problems of particle physics, like the flavour problem [?] and the hierarchy problem [?], the latter strongly suggesting the need for new physics near the weak scale, which could also clarify the Dark Matter identity.

It is clear that the fact that some sort of Higgs mechanism is at work has already been established. The W and Z longitudinal degrees of freedom are borrowed from the Higgs sector and are an evidence for it. In fact the couplings of quarks and leptons to the weak gauge bosons $W^{\pm}$ and Z are indeed experimentally found to be precisely those prescribed by the gauge symmetry [?,?]. To a lesser accuracy the triple gauge vertices γWW and ZWW have also been found in agreement with the specific predictions of the $SU(2) \bigotimes U(1)$ gauge theory. This means that it has been verified that the gauge symmetry is unbroken in the vertices of the theory: all currents and charges are indeed symmetric. Yet there is obvious evidence that the symmetry is instead badly broken in the masses. The W or the Z with longitudinal polarization that are observed are not present in an unbroken gauge theory (massless spin-1 particles, like the photon, are transversely polarized). Not only the W and the Z have large masses, but the large splitting of, for example, the top-bottom quark doublet shows that even the global weak SU(2) is not at all respected by the fermion spectrum. Symmetric couplings and totally non symmetric spectrum is a clear signal of spontaneous symmetry breaking and its implementation in a gauge theory is via the Higgs mechanism. The big remaining questions are about the nature and the properties of the Higgs particle(s). The LHC has been designed to solve the Higgs problem.

And indeed the SM Higgs is close to be observed or excluded! Either the SM Higgs is very light ($\lesssim$ 128 GeV) or rather heavy (i.e. $\gtrsim$ 600 GeV). The range m_H = 122 - 128 GeV, where possibly there is a signal, is in agreement with precision tests, compatible with the SM (the data are in fair agreement with the SM Higgs cross-sections [?]) and also with the SUSY extensions of the SM. Actually, $m_H \sim 125$ GeV is what one expects from a direct interpretation of EW precision tests: no fancy conspiracy with new physics to fake a light Higgs while the real one is heavy. On the contrary, $m_H \gtrsim 600$ GeV would point to the conspiracy alternative (but no conspirators have been found nearby!). Thus there is really a great suspense on the LHC run this year.

What if the evidence $m_H \sim 125$ GeV evaporates in 2012? Can we do without the Higgs? Suppose we take the gauge symmetric part of the SM and put masses by hand. What is the fatal problem at the LHC scale? The most immediate disease that needs a solution is that in the absence of a Higgs particle or of an alternative mechanism, violations of unitarity appear in scattering amplitudes involving longitudinal gauge bosons (those most directly related to the Higgs sector) at energies in the few TeV range [?]. A crucial question for the LHC is to identify the mechanism that avoids the unitarity violation: is it one or more Higgs bosons or some new vector boson (like additional gauge bosons W', Z' or Kaluza-Klein recurrences or resonances from a strong sector)? Thus something must happen at the few TeV scale! It is not possible that neither the Higgs nor new physics are present at the Electro-Weak (EW) scale (the only caution is whether the LHC can completely explore the EW scale).

It is well known that there are theoretical bounds on the Higgs mass valid if one assumes that the SM, with only one Higgs doublet, is valid up to a large energy scale Λ where eventually new physics appears. An upper limit on m_H (with mild dependence on m_t and α_s) is obtained, as described in [?], from the requirement that no Landau pole appears, up to the scale Λ, in the Higgs quartic coupling λ, or in simpler terms, that the perturbative description of the theory remains valid up to Λ. The Higgs mass enters because it fixes the initial value of the quartic

Higgs coupling λ in the running from the EW scale up to Λ. Even if Λ is as small as a few TeV the limit is well within the LHC range $m_H < 600 - 800$ GeV and becomes $m_H < 180$ GeV for $\Lambda \sim M_{Pl}$. This upper limit on the Higgs mass in the SM has played a crucial role in the LHC design whose mission requires that the whole allowed range is within reach of the machine. A lower limit on m_H is derived from the requirement of vacuum stability [?], i.e. that the quartic Higgs coupling λ does not turn negative in its running up to Λ (if so the energy would become negative and unbound at large absolute values of the field). Actually, in milder form, one can tolerate a moderate instability, compatible with the present age of the Universe [?]. A recent thorough reanalysis of this issue [?] has concluded that, given the experimental values of m_t and α_s, for $\Lambda \sim M_{GUT} - M_{Pl}$ the stability bound is very close to $m_H = 130$ GeV . The value $m_H \sim 125$ GeV would imply that, in the absence of new physics, our Universe becomes metastable at a scale $\Lambda \sim 10^{10}$ GeV. But the lifetime of our vacuum, for scales up to the Planck mass, would be larger than the age of the Universe. The SM remains viable with some early Universe implications. The vacuum could be stabilized by very little additional new physics (like, for example a heavy singlet S with a large VEV below the metastability scale [?]). Large Majorana neutrino masses can also have an impact on the running [?]. On the basis of this discussion we can conclude that a 125 GeV Higgs would be nearly perfect for a pure and simple SM up to M_{Pl}, just a little bit below the optimal range $130 \lesssim m_H \lesssim 180$ GeV. Incidentally, the possibility that $m_H \sim 130$ GeV, so that the SM becomes unstable precisely at around the Planck mass, and its implications have been studied in the literature [?].

3 Outlook on Avenues beyond the Standard Model

No signal of new physics has been found neither in EW precision tests nor in flavour physics. Given the success of the SM why are we not satisfied with that theory? Why not just find the Higgs particle, for completeness, and declare that particle physics is closed? As well known, the reason is that there are both conceptual problems and phenomenological indications for physics beyond the SM. On the conceptual side the most obvious problems are the proliferation of parameters, the puzzles of family replication and of flavour hierarchies, the fact that quantum gravity is not included in the SM and the related hierarchy problem. Among the main phenomenological hints for new physics we can list the constraints from coupling constant merging in Grand Unified Theories (GUT's), Dark Matter, neutrino masses (explained in terms of L non conservation), baryogenesis and the cosmological vacuum energy (a gigantic naturalness problem). The computable evolution with energy of the effective gauge couplings clearly points (better in SUSY than in the SM) towards the unification of the electro-weak and strong forces at scales of energy $M_{GUT} \sim 10^{15} - 10^{16}\ GeV$ which are close to the scale of quantum gravity, $M_{Pl} \sim 10^{19}\ GeV$. One is led to imagine a unified theory of all interactions also including gravity (at present superstrings provide the best attempt at such a theory). Thus GUT's and the realm of quantum gravity set a very distant energy horizon that modern particle theory cannot ignore. Can the SM without new physics be valid up to such large energies? Indeed, some of the SM problems could be postponed to the more fundamental theory at the Planck mass. For example, the explanation of the three generations of fermions and the understanding of fermion masses and mixing angles can be postponed. But other problems must find their solution in the low energy theory. In particular, the structure of the SM could not naturally explain the relative smallness of the weak scale of mass, set by the Higgs mechanism at $1/\sqrt{G_F} \sim 250\ GeV$ with G_F being the Fermi coupling constant. This so-called hierarchy problem [?] is due to the instability of the SM with respect to quantum corrections. This is related to the presence of fundamental scalar fields in the theory with quadratic mass divergences and no protective extra symmetry at $\mu = 0$, with μ the scalar mass. For fermion masses, first, the divergences are logarithmic and, second, at $m = 0$ an additional symmetry, i.e. chiral symmetry, is restored. Here, when talking of divergences, we are not worried of actual infinities. The theory is renormalizable and finite once the dependence on the cut-off Λ is absorbed in a redefinition of masses and couplings. Rather the hierarchy problem is one of naturalness. We can look at the cut-off as a parameterization of our ignorance on the new physics that will modify the theory at large energy scales. Then it is relevant to look at the dependence of physical quantities on the cut-off and to demand that no unexplained enormously accurate cancellations arise.

The hierarchy problem can be put in less abstract terms: loop corrections to the Higgs mass squared are quadratic in the cut-off Λ. The most pressing problem is from the top loop (the heaviest particle, hence the most coupled to the Higgs). If we demand that the correction does not exceed the light Higgs mass indicated by the precision tests, Λ must be close, $\Lambda \sim o(1\ TeV)$. So a crucial question for the LHC to answer is: what damps the top loop contribution? Similar constraints arise from the quadratic Λ dependence of loops with gauge bosons and scalars, which, however, lead to less pressing bounds. So the hierarchy problem demands new physics to be very close. Actually, this new physics must be rather special, because it must be very close, yet its effects are not clearly visible in EW precision tests (the "LEP Paradox" [?]) now also accompanied by a similar "flavour paradox" [?]. Examples [?] of proposed classes of solutions for the hierarchy problem are SUSY, technicolor, "Little Higgs" models, extra dimensions, effective theories for compositeness etc or the alternative, extreme, point of view given by the anthropic solution. In the following, after a comment on the anthropic route, I will discuss the quest for SUSY in some detail, while the alternative solutions to the hierarchy problem will be considered in the companion presentation by Mariano Quiros [?].

4 An extreme solution: the anthropic way

The observed value of the cosmological constant Λ poses a tremendous, unsolved naturalness problem [?]. Yet the value of Λ is close to the Weinberg upper bound for galaxy formation [?]. Possibly our Universe is just one of infinitely many bubbles (Multiverse) continuously created from the vacuum by quantum fluctuations. Different physics takes place in different Universes according to the multitude of string theory solutions [?] ($\sim 10^{500}$). Perhaps we live in a very unlikely Universe but the only one that allows our existence [?,?]. I find applying the anthropic principle to the SM hierarchy problem somewhat excessive. After all one can find plenty of models that easily reduce the fine tuning from 10^{14} to 10^2: why make our Universe so terribly unlikely? If to the SM we add, say, supersymmetry, does the Universe become less fit for our existence? In the Multiverse there should be plenty of less fine tuned Universes where more natural solutions are realized and yet are suitable for our living. By comparison the case of the cosmological constant is a lot different: the context is not as fully specified as the for the SM (quantum gravity, string cosmology, branes in extra dimensions, wormholes through different Universes....). While I remain skeptical I would like here to sketch one possibility on how the SM can be extended in agreement with the anthropic idea. If we ignore completely the hierarchy problem and only want to reproduce the most compelling data that demand new physics beyond the SM, a possible scenario is the following one. The SM is to be completed by a light Higgs and no other new physics is in the LHC range (how sad!) except perhaps a Z', for example a Z'_{B-L}. In particular there is no SUSY in this model. At the GUT scale of $M_{GUT} \gtrsim 10^{16}$ GeV the unifying group is $SO(10)$, broken at an intermediate scale, typically $M_{int} \sim 10^{10} - 10^{12}$ down to a subgroup like the Pati-Salam group $SU(4) \bigotimes SU(2)_L \bigotimes SU(2)_R$ or some other one [?]. Note that unification in $SU(5)$ would not work because we need a group of rank larger than 4 in order to allow for a two step (at least) breaking needed, in the absence of SUSY, to restore coupling unification and to avoid a too fast proton decay. The Dark Matter problem should be solved by axions [?]. Lepton number violation, Majorana neutrinos and the see-saw mechanism give rise to neutrino mass and mixing. Baryogenesis occurs through leptogenesis [?]. One should one day observe proton decay and neutrino-less beta decay. None of the alleged indications for new physics at colliders should survive (in particular even the claimed muon (g-2) [?] discrepancy should be attributed, if not to an experimental problem, to an underestimate of the theoretical errors or, otherwise, to some specific addition to the above model [?]). This model is in line with the non observation of $\mu \to e\gamma$ at MEG [?], of the electric dipole moment of the neutron [?] etc. It is a very important challenge to experiment to falsify this scenario by establishing a firm evidence of new physics at the LHC or at another "low energy" experiment.

5 Supersymmetry

In the limit of exact boson-fermion symmetry [?] the quadratic divergences of bosons cancel so that only log divergences remain. However, exact SUSY is clearly unrealistic. For approximate SUSY (with soft breaking terms), which is the basis for all practical models, Λ is essentially replaced by the splitting of SUSY multiplets. In particular, the top loop is quenched by partial cancellation with s-top exchange, so, to limit the fine-tuning the s-top cannot be too heavy. The existing limits on SUSY particles (even before the LHC), EW precision tests, success of the Cabibbo-Kobayashi-Maskawa theory of quark mixing and of CP violation, absence of Flavour Changing Neutral Currents, all together, impose sizable fine tuning particularly on minimal realizations. Yet SUSY is a completely specified, consistent, computable model, perturbative up to M_{Pl}. Important phenomenological indications in favour of SUSY are that coupling unification takes place with greater accuracy in SUSY than in the SM and that proton decay bounds are not in contradiction with the predictions. Grand Unification (GUT's) and SUSY go very well together: this is unique among new physics models. Other non standard models [?,?] (little Higgs, composite Higgs, Higgsless....) all become strongly interacting and non perturbative at a multi-TeV scale. Two Higgs doublets are expected in SUSY [?]. The EW symmetry breaking can be triggered by the H_u mass becoming negative at low energy in the running down from the GUT scale, due to the large top Yukawa coupling. SUSY offers a good Dark Matter candidate: the neutralino (actually more than one candidate, e.g. also the gravitino). In summary SUSY remains the reference model for new physics. But the negative result of the search for SUSY at the LHC, where a big chunk of new territory has been explored in the last year run, has imposed new strong constraints on SUSY models. And the hint of $m_H = 125$ GeV, if confirmed, does even more restrict the parameter space of these models ($m_H = 125$ GeV is a bit too heavy: near the upper bound on m_H in the MSSM).

Even the Minimal SUSY Model (MSSM) [?] has more than 100 parameters (mostly from the SUSY soft breaking terms). Simplified versions with a drastic reduction of parameters are used for practical reasons, e.g. the CMSSM, where C stands for Constrained, or mSUGRA, i.e. minimal SuperGravity (often the two names are confused): with universal gaugino and scalar soft terms at the GUT scale, the set of parameters is drastically reduced down to $m_{1/2}$, m_0, A_0 (the s-top mixing parameter), $\tan\beta$ and sign(μ). Similarly in the Non Universal Higgs Mass models NUHM1,2: masses for Hu, Hd (1 or 2 masses) different from m_0 are added. It is only these oversimplified models that are now cornered. A more flexible setup but, apparently still manageable, is the MSSM with CP and R conservation (pMSSM: p for phenomenological) [?] in terms of 19 parameters (M_A, $\tan\beta$, 3 gaugino masses, 3 mixing parameters A_u, A_d, A_e, μ and 10 s-fermion masses, with degenerate first 2 generations) recently studied in several works.

Many different new physics signatures have been searched at the LHC at 7 TeV with no positive outcome in a variety of channels involving combinations of charged leptons, jets and missing energy. All kinds of models for new physics can be compared with these data, not only SUSY. For SUSY the resulting limits depend on the assumptions on the spectrum, but, in the CMSSM, generically imply that gluinos and degenerate s-quarks are heavier than 500 - 1000 GeV. In addition to these limits the impact of $m_H \sim 125$ GeV on SUSY models is important

[?]. For example, minimal models with gauge mediation or anomaly mediation are disfavoured [?] (predict m_H too light) although some versions, like gauge mediation with extra vector like matter [?], could still work. Specific models that give up naturalness but remain predictive like split SUSY or heavy SUSY have seen their allowed domain restricted [?]. Gravity mediation [?] is in better shape but CMSSM, mSUGRA, NUHM1,2 are only marginally consistent and need s-quarks heavy, A_t large and lead to tension with the muon (g-2). In fact the muon magnetic moment would point to light SUSY, more precisely to light EW gauginos and s-leptons. This type of light SUSY would also improve the EW precision fit (by predicting a heavier m_W than the SM for the experimental value of m_t and a light Higgs). Several groups (for example, see [?]) have repeated the fit to EW precision tests in the CMSSM, also including the additional data on the muon $(g-2)$, the Dark Matter relic density and rare $b \to s\gamma$ decay modes. Before the LHC results the promising outcome of this exercise was that the central value of the lightest Higgs mass m_H went up (in better harmony with the bound from direct searches) with moderately large $\tan\beta$ and relatively light SUSY spectrum [?]. After the LHC bounds one finds that the best fit Higgs mass is 125 GeV only if the result on the muon (g-2) is removed from the fit, while, with the (g-2) included, the best fit Higgs mass value is 119 GeV. In other words, in the CMSSM there is a sizable tension between the muon (g-2) and $m_H \sim 125$ GeV. Also normally too much Dark Matter is predicted in the CMSSM or mSUGRA for $m_H = 125$ GeV. In comparison, the upper limit on m_H is larger in the pMSSM: $m_H \lesssim 135$ GeV [?].

The problem with SUSY is that one expected its discovery already at LEP2 on the basis of complete naturalness applied to minimal models. With the recent LHC data ever increasing fine tuning appears to be needed in the minimal versions. However less fine tuning is necessary if non minimal models are assumed. One must go beyond the CMSSM, mSUGRA, NUHM1,2. And indeed there is still plenty of room for more sophisticated versions of SUSY as a solution to the hierarchy problem. The simplest new ingredients that are studied at present are either heavy first 2 generations [?,?] and/or an extra Higgs singlet [?].

The first option is still within the MSSM framework. Note that, on the one hand, it is mostly gluinos and 1-2 generation s-quarks that are affected by the LHC limits while EW s-particles and s-tops are less constrained. On the other hand, what is really needed for naturalness in the MSSM [?] is that the s-tops (they directly enter at one loop in the radiative corrections to the Higgs mass), their isospin partners the s-bottoms, as well as the lightest higgsino (related to the μ parameter), and also gluinos (that contribute, with a strong coupling, in the radiative corrections at two loops) must be relatively light (below, say, 1 TeV). As remarked already long ago [?] an inverted s-quark spectrum with heavier 1st-2nd and lighter 3rd generation s-quarks has several advantages in flavour and CP violation problems. This option has been widely reanalysed recently in the present context. If gluinos are forced to only decay into final states involving s-tops or s-bottoms, their mass limits are considerably less stringent. Similarly the present lower limit on the lightest s-top mass is a few hundred GeV.

By adding an extra singlet Higgs [?] one goes beyond the MSSM. In a promising class of models a singlet Higgs S is added with coupling $\lambda S H_u H_d$. The μ term arises from the S Vacuum Expectation Value (VEV) and the μ problem is solved in that the S VEV can naturally be of order of the soft terms that break SUSY. Mixing with S can modify the Higgs mass and couplings at tree level. In particular, the restrictions on the Higgs mass, valid at tree level in the MSSM that demand substantial corrections from loops, can be relaxed (no need of large s-top mixing, less fine tuning). The new coupling λ grows with the scale. If we impose that the theory remains perturbative up to M_{GUT} then we must have $\lambda \lesssim\sim 0.7$. This is the case of the NMSSM (Next to Minimal SSM). For $m_H \sim 125$ GeV larger values of λ allow for lighter s-tops, no large s-top mixing and much less fine tuning. For $\lambda \sim 1-2$ we are in the so-called λ-SUSY regime (for $\lambda \gtrsim 2$ the theory becomes non perturbative already at 10 TeV). The fine tuning can be really reduced to a few percent even with a s-top of mass above 1 TeV. The presence of an extra

Higgs singlet adds one more neutral scalar particle to the spectrum. After symmetry breaking the mixing between S and the doublet Higgs leads to two eigenstates of mass that replace the single lightest Higgs h (for not too large λ a 2 by 2 matrix mixing approximation is valid while for $\lambda \gtrsim 0.7$ the full mixing matrix must be considered). The state at 125 GeV could be the lightest, but it is not excluded that at 125 GeV the heaviest of the two is seen while the lightest escaped detection at LEP [?]. In fact the mixing also modifies the couplings and may be that the lightest eigenstate has suppressed couplings to gauge bosons. In this case the heavier one at 125 GeV would get enhanced couplings to gauge bosons. Indeed there is a tenuous indication that the 125 GeV state may have a slightly enhanced coupling to $\gamma\gamma$.

6 Conclusion

The most exciting result of the 2011 LHC run is that the SM Higgs is close to be observed or excluded! The present, very solid, exclusion ranges for the SM Higgs have much restricted the mass interval for the SM Higgs: either the SM Higgs is very light (115 - 128 GeV) or very heavy (i.e. $\gtrsim 600$ GeV). The range $m_H = 122$ - 128 GeV where some excess is observed is in agreement with precision tests, compatible with the SM and also with the SUSY extensions of the SM. This hint is very exciting but could still disappear with more statistics. Thus the outcome of the 2012 LHC run at 8 TeV is of extreme interest for particle physics.

The search for new physics is the other big issue. No signals have shown up so far in spite of the many channels explored and of the large slice of parameter space that has been for the first time explored. Optimistic expectations of an early success have been deceived. But the LHC experiments are just at the start and larger masses can be reached in 2012 and even more in the 14 TeV phase. Still supersymmetry remains the standard way beyond the SM. It is true that we could have expected the first signals of SUSY already at LEP, based on naturality arguments applied to the most minimal models like the CMSSM or mSUGRA. But the general MSSM is still very much viable, for example in the versions with heavy 1 - 2 generation s-quarks [?]. Among non minimal models the most studied possibility are based on the addition of an extra singlet S to the Higgs sector [?] (NMSSM and λ - SUSY). The absence of SUSY signals has also stimulated the development of new ideas like those of extra dimensions and composite Higgs (discussed in the talk by M. Quiros [?]). The extreme anthropic proposal that naturalness could be irrelevant for the very particular physics that is valid in our exceptional Universe, just one among many in the Multiverse, is boosted now by the absence of new physics signals at the LHC. Only experiment can choose among these and other possibilities. Supersymmetry? Compositeness? Extra dimensions? Anthropic? We shall see!

I am very grateful to J. Tran Thanh Van and the Organisers of the 2012 Rencontres de Moriond, in particular B. Klima and B. Pietrzyk, for inviting me to give this talk. My related research has been funded by the COFIN program (PRIN 2008), the INFN- Roma Tre, and by the European Commission, under the networks “LHCPHENONET” and “Invisibles”.

References

1. A review of the SM can be found in G. Altarelli, in Elementary Particles (Landolt-Brnstein, New Series / Elementary Particles, Nuclei and Atoms), ed. by H. Schopper, Springer, Berlin, 2008, chap. 2, 3 and 4.
2. See, for example, A. Djouadi, Phys. Rept. **457** 1 (2008), ArXiv:hep-ph/0503172.
3. For a pedagogical review, see J.D. Wells, ArXiv:0909.4541.
4. For a review, see G. Isidori, Y. Nir and G. Perez, ArXiv:1002.0900.

5. E. Gildener, Phys. Rev. D 14, 1667 (1976); L. Maiani, in *Vector bosons and Higgs bosons in the Weinberg-Salam theory of weak and electromagnetic interactions. Proc. of the Summer School on Particle Physics*, Gif-sur-Yvette, 3-7 Sep 1979, Ed. by M. Davier *et al.*, IN_2P_3, Paris, France (1979); M. Veltman, Acta Phys. Polon. **B12** (1981) 437; E. Witten, Nucl. Phys. **B 188** (1981) 513 and Phys. Lett. **B 105** (1981) 267.
6. The LEP Electroweak Group, http://lepewwg.web.cern.ch/LEPEWWG/.
7. For s review see, for example, G. Altarelli and M. Grunewald, Phys.Rept., **1**89403 (2004), ArXiv: hep-ph/0404165.
8. J.R. Espinosa et al, ArXiv:1202.3697, P.P. Giardino et al, ArXiv:1203.4254.
9. B. W. Lee, C. Quigg and H.B. Thacker, Phys.Rev. **D**16 1519 (1977).
10. T. Hambye and K. Riesselmann, Phys.Rev.**D**55 7255 (1997) and references therein.
11. N. Cabibbo, L. Maiani, G. Parisi and R. Petronzio, *Nucl. Phys.* **B 158** (1979) 295; P.Q. Hung, *Phys. Rev. Lett.* **42** (1979) 873; M. Lindner, *Z. Phys.* **C 31** (1986) 295; M. Lindner, M. Sher and H. Zaglauer, *Phys. Lett.* **B 228** (1989) 139. M. Sher, *Phys. Rep.* **179** (1989) 273; B. Schrempp and M. Wimmer, *Prog. Part. Nucl. Phys.* **37** (1996) 1. M. Sher, *Phys. Lett.* **B 317** (1993) 159; *addendum ibid.* **331** (1994) 448; G. Altarelli and G. Isidori, *Phys. Lett.* **B 337** (1994) 141; J.A. Casas, J.R. Espinosa and M. Quirós, *Phys. Lett.* **B 342** (1995) 171.
12. G. Isidori, G. Ridolfi and A. Strumia , Nucl. Phys. **B**609387 (2001) and references therein.
13. J. Elias-Mir et al, ArXiv:1112.3022.
14. J. Elias-Mir et al, ArXiv:1203.0237.
15. C. Wetterich, ArXiv:1112.2910; F. Bezrukov et al, ArXiv:1205.2893 and references therein.
16. R. Barbieri and A. Strumia, ArXiv:hep-ph/0007265.
17. For an overview see C. Grojean, ArXiv:0910.4976.
18. M. Quiros, these Proceedings.
19. J. Frieman, M. Turner and D. Huterer, Ann.Rev.Astron.Astrophys. **46** 385 (2008), ArXiv:0803.0982.
20. S. Weinberg, Phys. Rev. Lett. **59**, 2607 (1987).
21. M. R. Douglas, ArXiv:hep-th/0602266; ArXiv:1204.6626.
22. N. Arkani-Hamed and S. Dimopoulos, *JHEP* **0**506, 073 (2005), ArXiv:hep-th/0405159; N. Arkani-Hamed et al, **N**ucl.Phys. **B**709 3 (2005), ArXiv:hep-ph/0409232; G. Giudice and A. Romanino, *Nucl.Phys.* **B**699, 65 (2004), Erratum-ibid. **B**706, 65 (2005), ArXiv:hep-ph/0406088; N. Arkani-Hamed, S. Dimopoulos, S. Kachru, ArXiv:hep-ph/0501082; G. Giudice, R. Rattazzi, *Nucl.Phys.* **B**757, 19 (2006), ArXiv:hep-ph/0606105.
23. G. Giudice, in "Perspectives on LHC Physics", ed. by G. Kane and A. Pierce, World Sci., ArXiv:0801.2562.
24. S. Bertolini, L. Di Luzio and M. Malinsky, ArXiv:1205.5637 and references therein.
25. R. D. Peccei and H. R. Quinn, Phys. Rev. D 16 (1977) 1791; R. D. Peccei and H. R. Quinn, Phys. Rev. Lett. 38 (1977) 1440; S. Weinberg, Phys. Rev. Lett. 40 (1978) 223; F. Wilczek, Phys. Rev. Lett. 40 (1978) 279.
26. For a general review, see, for example, W. Buchmuller, R.D. Peccei and T. Yanagida, Ann.Rev.Nucl.Part.Sci.**5**5311 (2005), ArXiv:hep-ph/0502169.
27. Muon g-2 Collab., G.W. Bennett *et al.*, Phys. Rev.**D**73072003 (2006).
28. K. Kannike et al, ArXiv:1111.2551.
29. The MEG Collaboration, J. Adam et al, ArXiv:1107.5547.
30. C. A. Baker et al, Phys. Rev. Lett.97:131801,2006; ArXiv:hep-ex/0602020v3.
31. For a review, see, for example, A. Hoecker, ArXiv:1201.5093.
32. For recent pedagogical reviews see, for example, S.P. Martin, hep-ph/9709356; I.J. R. Aitchison, ArXiv:hep-ph/0505105; M. Drees, R. Godbole and P. Roy, *Theory and Phenomenology of Sparticles*, World Sci. (2005).

33. A. Djouadi, Phys. Rept. **459** 1 (2008), ArXiv:hep-ph/0503173.
34. A. Djouadi and S. Rosiers-Lees et al., hep-ph/9901246; A. Djouadi, Phys. Rept. 459, 1 (2008), A. Arbey, M. Battaglia and F. Mahmoudi, Eur.Phys.J. C72 (2012) 1847, ArXiv:1110.3726; Eur.Phys.J. C72 (2012) 1906, ArXiv:1112.3032; ArXiv:1205.2557.
35. F. Mahmoudi, ArXiv:1205.3100.
36. A. Arbey et al, Phys.Lett. B708 (2012) 162, ArXiv:1112.3028; P. Draper et al, ArXiv:1112.3068.
37. M. Endo et al, ArXiv:1112.56.53, J. L. Evans et al, ArXiv:1201.2611.
38. G. Giudice and A. Strumia, ArXiv:1108.7067.
39. M. Holthausen, K. S. Lim and M. Lindner, ArXiv:1112.2415; H. Baer, V. Barger and A. Mustafayev, ArXiv:1112.3017; S. Heinemeyer, O. Stal and G. Weiglein, ArXiv:1112.3026; M. Carena et al, ArXiv:1112.3336; O. Buchmueller et al, ArXiv:1112.3564; S. Akula et al, ArXiv:1112.3645; ArXiv:1202.4038; M. Kadastik et al, ArXiv:1112.3647; C. Strege et al, ArXiv:1112.4192; C. Beskidt et al, ArXiv:1202.3366; J. L. Feng and D. Sanford, ArXiv:1205.2372.
40. O. Buchmueller *et al.*, JHEP **0**809 117 (2008), ArXiv:0808.4128; Eur.Phys.J. **C**64 391 (2009), ArXiv:0907.5568.
41. S. Dimopoulos and G. Giudice, Phys.Lett. B357, 573 (1995), ArXiv:hep-ph/9507282; A.Pomarol and D. Tommasini, Nucl.Phys. B466 (1996) 3, ArXiv:hep-ph/9507462; A. G. Cohen, D. Kaplan, and A. Nelson, Phys.Lett. B388, 588 (1996), ArXiv:hep-ph/9607394; R. Barbieri, G.R. Dvali, L. J. Hall; Phys.Lett. B377 (1996) 76, ArXiv:hep-ph/9512388.
42. R. Essig et al, ArXiv:1110.6443; Y. Kats et al, ArXiv:1110.6444; ArXiv:1110.6443; M.Papucci, J.T. Ruderman and A. Weiler, ArXiv:1110.6926; C. Brust et al, ArXiv:1110.6670; C. Csaki, L. Randall and J. Terning, ArXiv:1201.1293; G. Larsen, Y. Nomura and H. L.L. Roberts, ArXiv:1202.6339.
43. R. Barbieri et al, Phys. Rev. D 75, 035007 (2007), ArXiv:hep-ph/0607332; L. Cavicchia, R. Franceschini and V. S. Rychkov, Phys. Rev. D77, 055006 (2008), ArXiv:0710.5750; R. Barbieri et al, JHEP 0803, 005 (2008), ArXiv:0712.2903;J. Cao and J. M. Yang, Phys. Rev. D78, 115001 (2008), ArXiv:0810.0989; P. Lodone, JHEP 1005, 068 (2010), ArXiv:1004.1271; R. Barbieri et al, JHEP 1008, 024 (2010), ArXiv:1004.2256; R. Franceschini and S. Gori, JHEP 1105, 084 (2011), ArXiv:1005.1070; Y. Nomura, D. Poland and B. Tweedie, Phys. Lett. B 633, 573 (2006), ArXiv:hep-ph/0509244; M. Bastero-Gil et al, Phys. Lett. B 489, 359 (2000), ArXiv:/0006198; A. Delgado, C. Kolda, J. P. Olson and A. de la Puente, Phys. Rev. Lett. 105, 091802 (2010), ArXiv:1005.1282; G. G. Ross and K. Schmidt-Hoberg, ArXiv:1108.1284; U. Ellwanger and C. Hugonie, Mod. Phys. Lett. A 22, 1581 (2007), ArXiv:hep-ph/0612133; U. Ellwanger, C. Hugonie and A. M. Teixeira, Phys. Rept. 496, 1-77 (2010), ArXiv:0910.1785; L. J. Hall, D. Pinner and J. T. Ruderman, ArXiv:1112.2703; S. F. King, M. Muhlleitner and R. Nevzorov, ArXiv:1201.2671.
44. U. Ellwanger, ArXiv:1112.3548.

HIGGS SEARCHES AND EXTRA DIMENSIONS

M. QUIROS
Institució Catalana de Recerca i Estudis Avançats (ICREA), Barcelona, Catalonia, Spain
and
Institut de Fisica d'Altes Energies (IFAE), Universidad Autònoma de Barcelona
08193 Bellaterra, Barcelona, Spain

We present a short review of theories based on warped extra dimensions (motivated by the hierarchy problem of the Standard Model) which can accomodate a Higgs boson in the range suggested by the recent LHC results at 7 TeV. Using the AdS/CFT correspondence the Higgs is composite and can be described in the dual theory by a bound state of the 4D CFT. We have classified the theories in those with a scalar Higgs (5D SM) and those where the Higgs is the fifth component (gauge-Higgs unification) of a bulk gauge field.

1 Introduction

The Large Hadron Collider (LHC) is trying to answer the most fundamental question in particle physics: what is the nature of the electroweak symmetry breaking? Is it a perturbative mechanism, as the Brout-Englert-Higgs (BEH) mechanism, or a non-perturbative one, as in QCD? From the experimental point of view everything seems to be consistent with the Standard Model (SM) with the BEH mechanism (also known as Higgs mechanism) and possibly with a Higgs scalar around 124-126 GeV. However from the theoretical point of view such electroweak vacuum is not stable under quantum corrections (also known as hierarchy problem) which provide

$$\Delta m_H^2 = -\frac{3h_t^2}{8\pi^2}\Lambda^2 \tag{1}$$

where Λ is the SM cutoff. In the absence of any tuning this implies an upper bound on the cutoff scale as

$$\Lambda < 600\ \text{GeV}\frac{m_H}{200\ \text{GeV}} \tag{2}$$

and therefore for a larger cutoff there should exist new physics to stabilize it. In fact uncover the nature of the electroweak symmetry breaking should amount to uncovering the kind of new physics (if any) which stabilizes the electroweak vacuum!

There are two main avenues for solving the hierarchy problem:

Elementary Higgs

In this case there should exist an extra symmetry, and new particles with couplings dictated by this symmetry, such that the quadratic sensitivity to high scale cancels. The typical and paradigmatic example is supersymmetry : the stops cancel the quadratic divergence generated by the top quark. This solution has been covered at this Conference by G. Altarelli's talk [1] and we will concentrate ourselves in the next alternative solution.

Composite Higgs

The hierarchy problem is also solved provided that at some scale the Higgs dissolves, and the theory of its constituents is at work. This case is similar to QCD where the pions dissolve into quarks and gluons beyond Λ_{QCD}. In fact the compositeness scale acts as a cutoff of quadratic divergences. The typical example of compositeness is technicolor. Modern theories of compositeness involve an extra dimension through the Anti-de-Sitter/Conformal-Field-Theory (AdS/CFT) correspondence [2].

2 Extra dimensions and Composite Higgs

The original AdS/CFT correspondence in string theory [2] related type IIB string theory on $AdS_5 \times S^5$ with $\mathcal{N} = 4$ $SU(N)$ 4D gauge theory, the parameters of the correspondence being

$$\left(\frac{M_s}{k}\right)^4 = 4\pi g^2 N \tag{3}$$

where M_s is the string scale, k the AdS curvature and g the gauge coupling constant of the $\mathcal{N} = 4$ $SU(N)$ supersymmetric theory which is known to be a CFT. In the regime where we can decouple the string excitations and describe the theory by pure gravity $k \ll M_s$ it turns out that $g^2 N \gg 1$ which implies that the 4D field theory is non-perturbative. Moreover if the S^5 radius is small enough we can decouple its heavy modes and the gravity theory corresponds just to AdS_5.

In the case of a slice of AdS [with two branes, one in the ultraviolet (UV) $y = 0$ and another one in the infrared (IR) $y = y_1$ region] a similar correspondence can also be formulated: The UV boundary corresponds to a UV cutoff in the 4D CFT. The IR boundary corresponds to an IR cutoff. Matter localized towards the UV boundary is mainly elementary: e.g. light fermions. Matter localized towards the IR boundary is mainly composite: e.g. heavy fermions, Higgs boson and Kaluza-Klein (KK) excitations. Although the CFT picture is useful for understanding some qualitative aspects of the theory it is useless for obtaining quantitative predictions since the theory is strongly coupled.

An AdS 5D theory with two branes was proposed long ago [3]. In order to solve the hierarchy problem the Higgs should be either: **i)** Localized on the IR brane (i.e. composite). In that case the theory is disfavored by electroweak precision tests (EWPT); **ii)** Propagating in the bulk of the fifth dimension but with a profile leaning towards the IR brane (i.e. with a certain degree of compositeness). In all cases the hierarchy problem is solved because the Planckian Higgs mass is warped down to the weak scale by the geometry.

A Higgs propagating in the bulk can be:

Scalar-Higgs: H

In this case EWPT require either:

- An extra (custodial) gauge symmetry in the bulk generating *non-minimal* models [4].
- A deformation of the AdS metric in the IR [5]. In this case we can consider the *minimal* 5D SM propagating in the bulk.

Here we will only consider the latter case as the former one is already covered by the (next) gauge-Higgs unification case.

Gauge-Higgs: A_5

In this case the Higgs is the fifth component of the gauge boson of an extended gauge group which can possibly contain a custodial symmetry. Now the Higgs bulk mass is doubly protected by the warp factor and by gauge invariance.

3 Scalar Higgs

The first and simplest possibility is to consider a SM-like Higgs propagating in the 5D space

$$H(x,y) = \frac{1}{\sqrt{2}} e^{i\chi(x,y)} \begin{pmatrix} 0 \\ h(y) + \xi(x,y) \end{pmatrix}, \quad h(y) = h(0)e^{aky} \tag{4}$$

with an arbitrary metric $A \equiv A(ky)$. The parameters of the effective Lagrangian for the Higgs boson,

$$\mathcal{L}_{\text{eff}} = -|D_\nu \mathcal{H}|^2 + \mu^2 |\mathcal{H}|^2 - \lambda |\mathcal{H}|^4 \tag{5}$$

are related to 5D quantities as

$$\lambda \sim Z^{-2}; \quad \rho = k e^{-A(y_1)}; \quad m_H^2 = \frac{2}{Z}(M_1/k - a)\rho^2; \quad Z = k \int_0^{y_1} dy \frac{h^2(y)}{h^2(y_1)} e^{-2A(y)+2A(y_1)} \tag{6}$$

where ρ is the warped down AdS curvature scale ($\sim$ TeV) and Z is a wave-function renormalization of the Higgs field which appears from integration over the extra dimension. We can see from (6) that the natural value of the Higgs mass is ρ, so that a light Higgs requires a certain amount of fine-tuning, unless the factor $Z \gg 1$ as we will see it happens in deformed models.

3.1 RS model

In the RS model [3] the metric is conformally symmetric $A(y) = ky$, $Z = \mathcal{O}(1)$ and the natural value of the Higgs mass is TeV. Moreover confronting the model with EWPT implies heavy KK modes (unless extra custodial gauge symmetry in the bulk) and a little fine-tuning problem. As

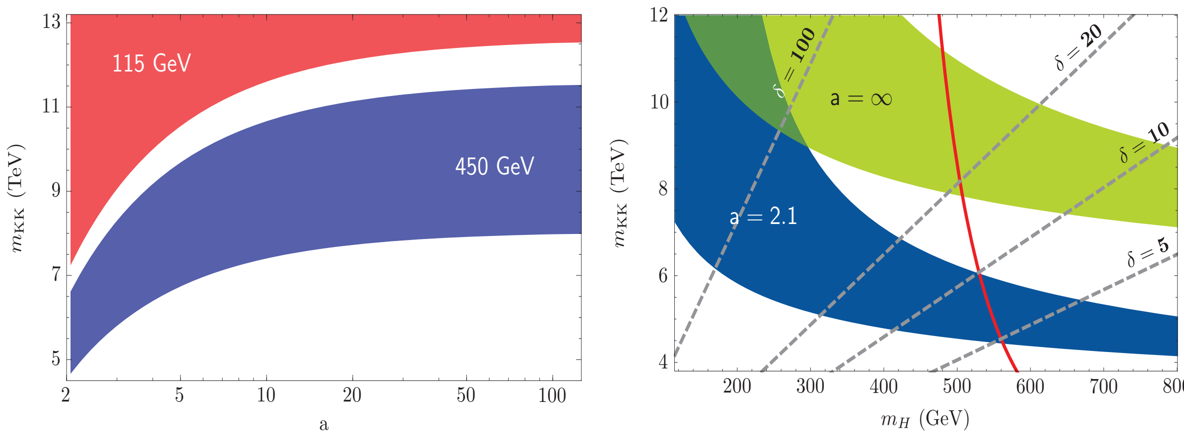

Figure 1: Left panel: Constraints imposed by EWPT on the mass of the first KK mode as a function of a for different values of the Higgs mass. Right panel: The same as a function of m_H for different values of the parameter a. We also exhibit the contour lines of constant δ, the sensitivity, defined such that the fine-tuning is $100/\delta$ %.

we can see from Fig. 1 for a Higgs mass $m_H = 125$ GeV: **i)** There is no hope to detect KK modes at LHC since they are too heavy; **ii)** The fine tuning is at the level of a few per mille.

3.2 Deformed metric model

A possible solution to the previous problem is deforming the metric [5], as in the soft-walls used in AdS/QCD theories. In particular we will consider the metric

$$A(y) = ky - \frac{1}{\nu^2} \log(1 - y/y_s) \tag{7}$$

where ν is a real ($\nu > 0$) parameter and which has a singularity at $y = y_s > y_1$, outside the physical interval. One recovers the AdS metric in the limit $\nu \to \infty$ and/or $y_s \to \infty$. Notice also that AdS and the deformed metric (7) differ only in the IR region while in the UV the metric behaves as AdS and the main features of AdS/CFT duality hold.

In the deformed metric theory the warping is more efficient and consequently the compactification volume is smaller than in the RS theory. This helps in reducing the electroweak precision observables, in particular the oblique observable T which is volume enhanced. Moreover the wave function renormalization parameter is $Z \gg 1$ which helps in: **i)** Having a light Higgs mass without any fine-tuning, as can be seen from (6); **ii)** Reducing the observables T (which scales as $1/Z^2$) and S (which scales as $1/Z$). As we can see from Fig. 2 for $m_H = 125$ GeV the

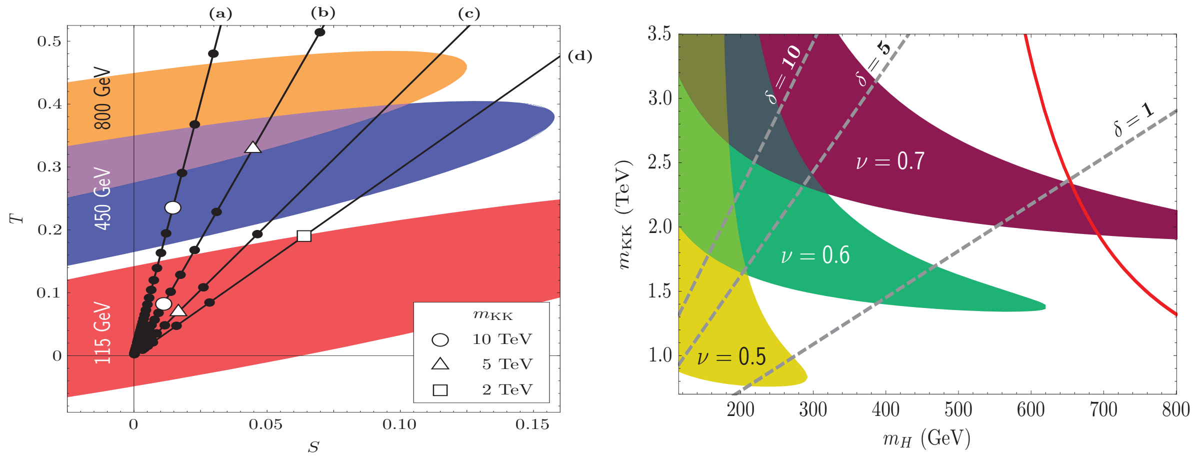

Figure 2: Left panel: Constraints imposed by EWPT on the mass of the first KK mode in the plane (S, T) for different values of the Higgs mass. $\Delta m_{KK} = 1$ TeV. Right panel: Constraints imposed by EWPT on the mass of the first KK mode as a function of m_H for different values of the parameter a and contour lines of constant δ.

required fine-tuning is better than 10% and KK-modes have masses of a few TeV so that they can in principle be detected at the LHC. Production of KK modes in this scenario has been analyzed in Refs.[6] which focus on signals involving the third generation and study in particular $\bar{t}t$ production, which is dominated by the KK gluon exchange, as well as $\bar{t}b$ in the case of the charged KK gauge bosons. After making adequate cuts, the LHC should be able to probe the existence of the KK gluons for $\sqrt{s} = 8$ TeV and integrated luminosity of $10 fb^{-1}$ while testing the charged electroweak KK gauge bosons would require $\sqrt{s} = 14$ TeV and larger luminosities.

To analyze perturbative unitarization of the theory one can compute the coupling of the Higgs to gauge bosons and in particular one can prove that[5]

$$h^2_{WWH} = h^2_{WWH,SM}\,(1-\xi)\,, \quad \xi = \mathcal{O}(m_H^2/m_{KK}^2) \simeq 0.01 \tag{8}$$

so a light Higgs unitarizes the theory in a similar way as the SM Higgs.

4 Gauge-Higgs

Gauge-Higgs unification is another alternative to supersymmetry where the gauge symmetry in the bulk $\mathcal{G}$ protects the mass of extra-dimensional components of gauge bosons. This solution to the hierarchy problem requires: **i)** An extended space-time, for instance a 5D space. **ii)** An extended gauge group with respect to the SM $SU(3) \otimes SU(2)_L \otimes U(1)_Y$ group. It can be constructed in flat or warped space, although in warped space the GIM-RS mechanism protects the theory with differently localized fermion fields from huge flavor violation, which otherwise would require severe constraints on the mass of KK modes[7]. Four dimensional components of gauge bosons (A^a_μ) of $\mathcal{G}$ contain the four-dimensional gauge bosons while the fifth components ($A^{\hat{a}}_5$) contain the four-dimensional Higgs fields in a number equal to the number of Pseudo Goldstone Bosons (PGB) which are left out in the four dimensional theory. In general $\mathcal{G}$ will be broken by boundary conditions to $\mathcal{H}_{UV}$ ($\mathcal{H}_{IR}$) on the UV (IR) brane. For $\mathcal{H}_{UV} = SU(2)_L \otimes U(1)_Y$ the number of PGB is $\dim(\mathcal{G}/\mathcal{H}_{IR})$ so different models differ by different choices for $\mathcal{G}$ and $\mathcal{H}_{IR}$. Some models [8] are defined in the table below.

Model	# Goldstones ($A^{\hat{a}}_5$)
SO(4)/SO(3)	6-3=3 (Higgsless SM)
SU(3)/SU(2)×U(1)	8-4=4(H_{SM})
SO(5)/SO(4)	10-6=4 (H_{SM})
SO(6)/SO(5)	15-10=5 (H_{SM} + singlet)
SO(6)/SO(4)×SO(2)	15-6-1=8 (H_u, H_d)

Some of the models in the table contain the custodial $SO(4)$ group on the IR brane and so their contribution to the T parameter is protected. In these theories $SU(2)_L \otimes U(1)_Y$ breaking is radiative through the kind of diagrams [11] exhibited in Fig. 3. It turns out that triggering

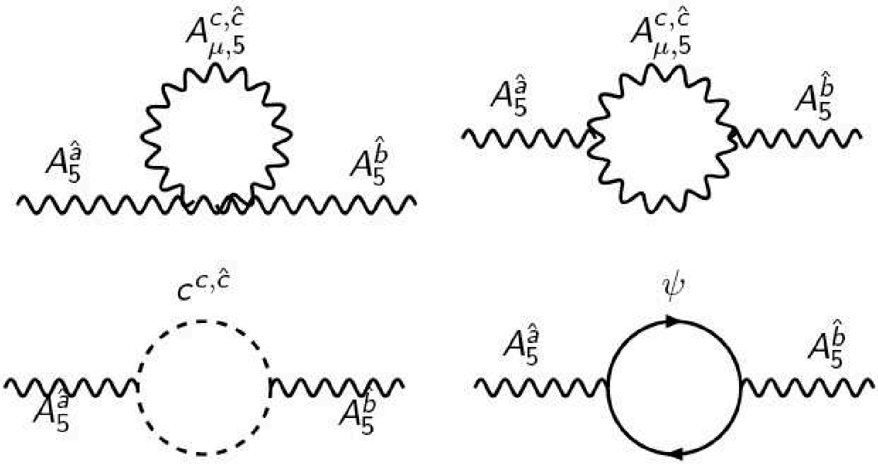

Figure 3: One-loop diagrams contributing to electroweak breaking in gauge-Higgs unification models.

electroweak breaking will depend on the nature and localization of bulk matter fields.

In the dual theory $\mathcal{G}/\mathcal{H}_{IR}$ is characterized by the spontaneous breaking scale f such that the expansion parameter in the theory is ξ

$$\xi \equiv \left(\frac{v}{f}\right)^2 \quad \begin{cases} \bullet \quad \xi \to 0 \Rightarrow \text{SM limit} \\ \bullet \quad \xi \to 1 \Rightarrow \text{Technicolor limit} \end{cases} \tag{9}$$

where $v \simeq 246$ GeV is the electroweak breaking parameter. The ξ parameter controls perturbative unitarity through the relation (8). However unlike in the models presented in Sec. 3 with a scalar Higgs, where the parameter $\xi \ll 1$, in the models presented in this section ξ depends on f and can thus be considered as a free parameter. For instance in the limit $\xi \to 0$ the SM result is obtained and the Higgs unitarizes the theory without the need of any extra particle. On the other extreme in the Technicolor limit $\xi \to 1$ all unitarity must be provided by new TeV resonances at scales close to the electroweak scale. For intermediate values of $0 < \xi < 1$ unitarity must be partially restored by resonances at scales which depend on the value of ξ.

One can consider in general an effective theory [9] parametrized by ξ, which measures the degree of compositeness of the Higgs. In this theory all Higgs couplings (cubic, quartic, HWW, ...) depart from the SM values by quantities which are proportional to ξ. These models have been confronted to EWPT and direct searches [10]. The former ones provide the strongest constraints which yield typical bounds $\xi < 0.18$ at 99% CL in the absence of additional contributions to the S and T parameters.

5 Conclusions

It is clear at the moment of this Conference that the next step in Higgs search belongs to the LHC Collaborations, in particular ATLAS and CMS, so that confronting different theories on electroweak breaking with experimental data should wait till the excess of events found at 125 GeV, which hints on the presence of a Higgs boson, be eventually confirmed. We can only speculate about the different possibilities. If Higgs is confirmed at $m_H \simeq 125$ GeV and cross sections in different channels are consistent with the SM expectations, then the SM is a good candidate and there should be no problem with perturbative unitarity or (meta)stability of the electroweak vacuum. If Higgs is confirmed at $m_H \simeq 125$ GeV and cross sections in some channels are *not* consistent with the SM expectations (as it seems to be the case now with $\gamma\gamma_{ggF}$ excess) then one should consider to extend the SM to theories with a light Higgs and extra matter which can eventually modify some of the relevant production cross sections (supersymmetry, composite Higgs, extra dimensions, unexpected physics, ...). Finally if it turns out that the Higgs is not found then it might be heavy in which case extra states should soon appear.

Acknowledgments

Work supported in part by the Spanish Consolider-Ingenio 2010 Programme CPAN (CSD2007-00042) and by CICYTFEDER-FPA2008-01430 and FPA2011-25948.

References

1. G. Altarelli, *The SM and the MSSM after the 2011 LHC results*, arXiv:1206.1476 [hep-ph].
2. J. M. Maldacena, Adv. Theor. Math. Phys. **2** (1998) 231 [hep-th/9711200].
3. L. Randall and R. Sundrum, Phys. Rev. Lett. **83** (1999) 3370 [hep-ph/9905221].
4. K. Agashe, A. Delgado, M. J. May and R. Sundrum, JHEP **0308**, 050 (2003) [hep-ph/0308036].
5. J. A. Cabrer, G. von Gersdorff and M. Quiros, New J. Phys. **12** (2010) 075012 [arXiv:0907.5361 [hep-ph]]; Phys. Lett. B **697** (2011) 208 [arXiv:1011.2205 [hep-ph]]; JHEP **1105** (2011) 083 [arXiv:1103.1388 [hep-ph]]; Phys. Rev. D **84** (2011) 035024 [arXiv:1104.3149 [hep-ph]]; arXiv:1104.5253 [hep-ph]; JHEP **1201** (2012) 033 [arXiv:1110.3324 [hep-ph]].
6. A. Carmona, E. Ponton and J. Santiago, JHEP **1110** (2011) 137 [arXiv:1107.1500 [hep-ph]]; J. de Blas, A. Delgado, B. Ostdiek and A. de la Puente, arXiv:1206.0699 [hep-ph].
7. A. Delgado, A. Pomarol and M. Quiros, JHEP **0001** (2000) 030 [hep-ph/9911252].
8. R. Contino, Y. Nomura and A. Pomarol, Nucl. Phys. B **671** (2003) 148 [hep-ph/0306259]; K. Agashe, R. Contino and A. Pomarol, Nucl. Phys. B **719** (2005) 165 [hep-ph/0412089]; R. Contino, L. Da Rold and A. Pomarol, Phys. Rev. D **75** (2007) 055014 [hep-ph/0612048].
9. J. R. Espinosa, C. Grojean and M. Muhlleitner, JHEP **1005** (2010) 065 [arXiv:1003.3251].
10. J. R. Espinosa, C. Grojean and M. Muhlleitner, arXiv:1202.1286 [hep-ph].
11. G. von Gersdorff, N. Irges and M. Quiros, Nucl. Phys. B **635** (2002) 127 [hep-th/0204223]; G. von Gersdorff, N. Irges and M. Quiros, hep-ph/0206029.

High order QCD predictions of the Higgs boson production cross-section at the LHC

Achilleas Lazopoulos, Stephan Bühler

1 Introduction

The LHC is marching through its third year of operation and the first tantalizing hits for a Higgs boson have already appeared. The corresponding experimental analyses rely crucially on theory predictions for the number of Higgs events expected within the Standard Model (SM) or theories beyond it that contain one or more Higgs bosons.

The number of Higgs events expected from each channel is currently evaluated in an involved way. the overall normalization is retrieved from very precise higher order inclusive calculations that have reached the level of next-to-next-to-leading order (NNLO) in the QCD and next-to-leading order (NLO) in the electroweak coupling for all production processes of immediate interest for the LHC discovery phase. Kinematic distributions are, on the other hand, predicted with the help of parton showers matched with hard matrix elements at the LO or NLO level. The distributions thus produced have been cross-checked against fixed order NNLO differential computations for the case of the (dominant) gluon fusion production mode. When such NNLO computations are available, they can be used to compare directly with distributions from experimental data under the assumption that showering and hadronization effects are negligible so that the parton level description of the fixed order calculation is a good approximation.

In what follows the focus will be on Higgs production cross-sections for the LHC and the precision with which we know them as of the time of writing of this proceeding.

2 Associated production and vector boson fusion

The associated production mechanism is not as prominent at the LHC as it has been at Tevatron and until recently it was not considered a viable discovery channel. The situation has changed thanks to various insightful proposals on how to improve the signal to background ratio, and the channel is now contributing to exclusion or discovery combinations for both full-range LHC experiments. The focus is on configurations with kinematically boosted Higgs bosons decaying to a pair of bottom quarks. The inclusive production rate is known at NNLO [?]. The NLO EW corrections are also known [?]. The perturbative expansion is very stable leading to K-factors of 1.27 at NLO and 1.28 at NNLO, similarly to what happens in Drell-Yan. The uncertainty due to factorization and renormalization scales is reduced to $\sim 3\%$. Recently the fully differential NNLO calculation was completed [?] including the LO decay to bottom pairs which allows for studies in the boosted region of interest. First phenomenological studies show that, as in the case of gluon

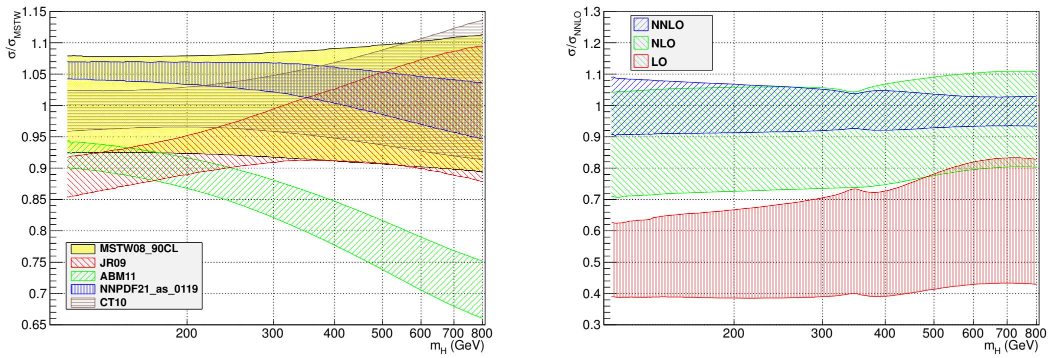

Figure 1: Higgs in gluon fusion. Left: production cross sections with various PDF sets and their uncertainty bands, normalized to the cross section calculated with the central MSTW08 grid. Note that the MSTW08 uncertainty band is at 95%CL and that the bands for NNPDF and CT10 do **not** include the induced error due to α_s variation. Right: Scale uncertainty per QCD order in the interval $\mu_f = \mu_r = \mu \in [m_H/4, m_H]$.

fusion, the presence of aggressive kinematical cuts can alter significantly the acceptance rates at the LHC. We have recently completed [?] the fully differential decay $H \to b\bar{b}$ which will be soon interfaced with the production computation.

The vector boson fusion channel is of particular interest since it is an indirect probe of vector boson scattering. Its production cross section is known to NLO QCD[?] as well as NLO EW[?]. The DIS-like component of the NNLO calculation is also known [?] and the perturbative convergence is excellent, as demonstrated at fig.4.1 of the work by Bolzoni et al. [?].

3 Gluon fusion $gg \to H$

This is the dominant production mode at the LHC and the one that has been studied most extensively. The NNLO QCD corrections are know already for a decade now, in the heavy quark effective theory (HQET) approximation [?,?,?] which has recently been shown [?,?] to be an excellent approximation. At the NLO level the production rate is known exactly (i.e. including finite top and bottom mass effects as well as their interference). Electroweak corrections at the two-loop level [?,?,?] and mixed QCD electroweak corrections [?,?] are also known. Threshold [?] and soft gluon [?] re-summation have also been performed to the NNLL level and the soft terms of the NNNLO have been calculated [?]. We have recently implemented [?] all known fixed order contributions up to NNLO in a new publicly available program for the inclusive cross-section at hadron colliders, `ihixs`. We have added to the existing literature the possibility to account for finite top width effects in the calculation, which were found to be negligible below the top threshold and only of the order of $\sim 2.5\%$ around the threshold and $\sim 1\%$ for a heavy Higgs. Moreover, `ihixs` delivers predictions for an arbitrary number of SM-like quarks and arbitrary rescalings of their Yukawa couplings. This allows for BSM predictions, an example of which is the cross section for an extended SM with four quark generations [?].

The SM cross-section predictions we recommend for the LHC at 8TeV have been published recently [?] and include uncertainties due to the factorization and renormalization scales, as well as the imprecise knowledge of the parton distribution functions.

3.1 PDF uncertainties

An impressive progress has been achieved in recent years towards increasing the precision and the reliability of parton density functions (PDF). There are currently five PDF providers using different data sets, theoretical assumptions, parameterizations and fitting techniques to predict

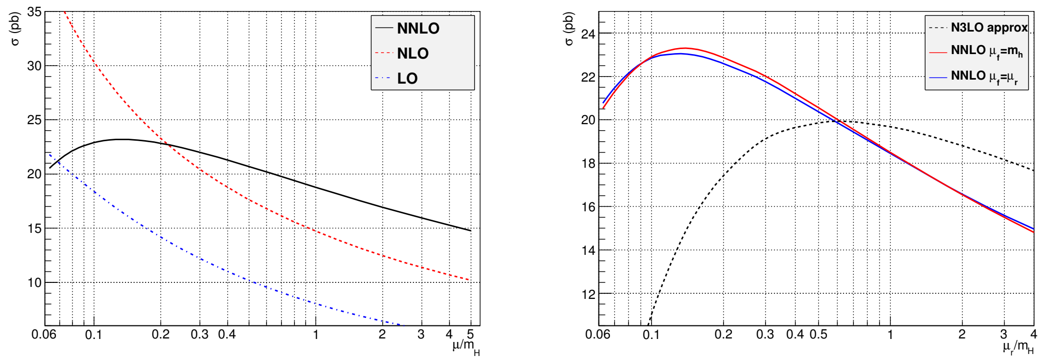

Figure 2: Higgs in gluon fusion: cross-section as a function of the ratio μ/m_H of the scale over the Higgs mass for fixed order (left) and the gluon fusion channel alone in NNLO with $\mu_r = m_H$, NNLO with $\mu_r = \mu_f = \mu$, and the NNNLO approximate soft terms from ref.24 (right).

the parton densities, that have already reached the NNLO level of accuracy. The resulting central values and uncertainty bands [a] for MSTW08, NNPDF, ABM11, JR09, as well as the recently released CT10NNLO PDFs, normalized to the central value for MSTW08, are shown in fig. **??**. It is seen that all "global" PDF sets agree within their uncertainties, while the ABM set clearly disagrees for all Higgs masses, with the discrepancy increasing with the Higgs mass. The difference can be partly attributed to the lower value for α_s used by the ABM collaboration (the value is an outcome of their fitting procedure and not an input parameter) but comparison to the NNPDF set adopting the lowest available value for α_s shows that there are further differences of a systematic nature. The issue should be resolved shortly, as predictions for SM processes using the different PDF sets will be compared with the LHC measurements with increasingly diminishing experimental uncertainty. Until then we find it prudent to provide cross section rates with the ABM11 set as our second benchmark set.

3.2 Scale uncertainty

Another important source of uncertainty comes from the arbitrary choice of renormalization and factorization scales used in the calculation. This uncertainty would vanish in an all orders computation and is therefore an artifact of the truncation of the perturbative series. It is usually taken as an indication of the size of the remaining, unknown, higher order corrections, beyond NNLO in the case of gluon fusion. However, such an estimate includes a certain degree of arbitrariness, as the choice of both the central scale used and the interval in which the scale is varied are only dictated by past experience and tradition.

In fig. **??** we show the cross section at LO, NLO, NNLO as a function of the scale μ. For the fixed order predictions up to NNLO, we keep the two scales equal, $\mu_f = \mu_r$ but it should be kept in mind that the dependence of the fixed order result on μ_f is very mild. This is reflected in fig. **??**(right) where the gluon fusion channel of the NNLO cross section in the EFT approximation for $\mu_f = m_H$ as a function of μ_r/m_H is shown and it is seen to almost completely overlap with the $\mu_f = \mu_r = \mu$ prediction. In fig. **??** we compare the fixed order result with the NNNLO approximate soft contributions [?].

Our choice of the central scale is $\mu = \mu_f = \mu_r = m_H/2$. This leads to a scale uncertainty per fixed order shown in fig. **??**. The motivation for choosing the central scale at $m_H/2$ comes from considerations on the convergence of the perturbative expansion:

[a]Note however that the MSTW08 uncertainty band reflects the 90%CL while for all other PDF sets it's at the 68%CL, and that the NNPDF and CT10 uncertainty bands do **not** include the uncertainty induced by α_s variation.

- We find it unnatural to separate μ_f from μ_r, thus inducing a further artificial dependence on $\log(\mu_f/\mu_r)$ that would vanish in an all orders result.

- Typical emission of extra partons happen at a scale $m_H/2$ or below and the average transverse momentum of the Higgs is between $m_H/4$ and $m_H/2$ for all Higgs masses. This indicates that a reasonable scale is $m_H/2$.

- At NLO the logarithmic dependence on μ is through the ratio $\log\left(\frac{\mu}{m_H(1-z)}\right)$ where z parametrizes the distance from threshold production. Choosing a scale equal or higher than the Higgs mass artificially enhances the contribution of this logarithm, as it was already noticed a decade ago [?].

- As shown in fig. **??** the convergence of the perturbative series in the low μ region is improved. That is reflected in the fact that the NLO scale uncertainty band fully engulfs the NNLO band.

- The NNNLO soft contributions, shown for the gg initial state channel in fig. **??**, whose variation lies within the NNLO scale uncertainty band when the scale is chosen low, lead to a similar conclusion.

Moreover, comparison with the NNLO prediction with threshold re-summation shows that it agrees below the per cent level with the fixed order result when $\mu = m_H/2$ and below and starts deviating from it for $\mu > m_H/2$. We have checked that the relative deviation of the threshold re-summation calculation and the fixed order one remains at the per mille level for all collider energies up to 20TeV, while for $\mu = m_H$ the two results differ by 5% or more at the entire energy range up to 20TeV.

3.3 High Higgs mass

If the Higgs boson is light, i.e. its mass is smaller than ~ 300 GeV, its line shape, measured as the invariant mass distribution of its decay products, is an uneventful spike well thinner than the corresponding experimental resolution in both the diphoton and the four leptons decay channel. If, on the contrary, the mass of the Higgs boson lies in the near TeV scale (i.e. if $m_H > 800$GeV) the width becomes comparable to its mass and the customary factorization of cross-sections in production and decay phases is not valid any more. Two related features call for our attention: (a) the zero width approximation used for low masses is not a valid approximation any more. Hence the off-shell contributions of the Higgs boson have to be included and the exact treatment of the Higgs propagator becomes a delicate issue in which Dyson resummation and gauge invariance have to be combined in a consistent way. (b) Signal-background (SB) interference with background diagrams cannot be ignored any more, especially in the experimentally interesting vector boson decay channels. In particular, as the mass of the Higgs approaches the TeV range, the cancellations between diagrams involving the Higgs boson and diagrams involving the longitudinal mode of the vector bosons, which ensure the unitarization of vector boson scattering, become stronger. Therefore ignoring the latter is no longer possible.

Using `ihixs` we have shown [?] that the treatment of the propagator has a severe impact on the line shape and the total cross section. An attempt to quantify the SB interference effects, using a prescription for the propagator based on the re-summation of $VV \to VV$ scattering amplitudes [?] (with the dominant contributions from both resonant and non-resonant Feynman diagrams) at the high energy regime shows that the distortions on both line shape and cross-section are too large to ignore for $m_H \geq 400$GeV. Studies of the impact of different propagator prescriptions on exclusion plots [?] show that including the emulated SB interference effects through the above

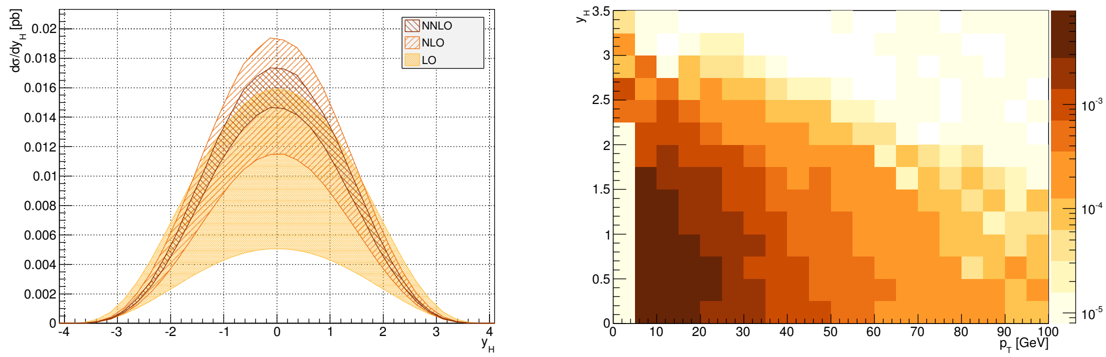

Figure 3: Higgs from bottom quark annihilation: Higgs rapidity distribution per QCD order with scale uncertainty bands (left) and doubly differential distribution in rapidity and transverse momentum(right).

prescription [?] as part of the signal hypothesis would lead to differences in exclusion limits for masses higher than 600GeV.

For these reasons we have refrained [?] from providing NNLO predictions for the Higgs production cross section for $m_H > 400$GeV. We believe that for Higgs bosons heavier than that, the SB interference, known at LO [?,?,?] should be included in the cross-section prediction and the corresponding LO uncertainty should be assigned to it. Since the NNLO K-factor for the signal diagrams alone is known to be ~ 2, one would in practice prefer to assign a SB related uncertainty to the full NNLO cross-section based on LO information, but it should be clear that this would be based on unwarranted assumptions on the magnitude of the NLO and NNLO SB diagrams.

4 Bottom quark annihilation: $b\bar{b} \to H$

In new physics models where the Higgs sector is non-minimal, the Yukawa coupling to bottom quarks is enhanced by a potentially large factor and the bottom quark annihilation becomes competitive to gluon fusion as a Higgs production mode. Moreover it is experimentally indistinguishable from gluon fusion and therefore its production rates add to those of the gluon fusion channel. The inclusive cross-section of the process is known to NNLO in QCD [?] as well as at NLO EW [?]. We have recently completed the fully differential NNLO calculation [?]. The rapidity distribution for the Higgs boson and its uncertainty band due to the factorization scale choice shows that the perturbative expansion in this channel is, as expected, smooth, see fig. **??**. In fig. **??** we can also see the doubly differential distribution over the rapidity and the transverse momentum of the Higgs boson. We have further implemented the diphoton decay channel and produced distributions in the presence of realistic experimental cuts, which demonstrates the fully differential nature of our calculation.

5 Conclusions

The inclusive cross-sections for Higgs production at the LHC have in general been studied extensively and are therefore known to relatively high precision. However there are several salient features in Higgs production via gluon fusion that deserve further attention and are currently the focus of theoretical investigations. In this short proceeding we point to some of those features, in anticipation of further developments.

References

1. O. Brein, A. Djouadi and R. Harlander, Phys. Lett. B **579** (2004) 149 [hep-ph/0307206].
2. M. L. Ciccolini, S. Dittmaier and M. Kramer, Phys. Rev. D **68** (2003) 073003
3. M. Ciccolini, A. Denner and S. Dittmaier, Phys. Rev. Lett. **99** (2007) 161803
4. M. Ciccolini, A. Denner and S. Dittmaier, Phys. Rev. D **77** (2008) 013002
5. P. Bolzoni, F. Maltoni, S. -O. Moch and M. Zaro, Phys. Rev. Lett. **105** (2010) 011801
6. P. Bolzoni, F. Maltoni, S. -O. Moch and M. Zaro, Phys. Rev. D **85** (2012) 035002
7. G. Ferrera, M. Grazzini and F. Tramontano, Phys. Rev. Lett. **107** (2011) 152003
8. C. Anastasiou, F. Herzog and A. Lazopoulos, JHEP **1203** (2012) 035
9. R. V. Harlander and W. B. Kilgore, Phys. Rev. Lett. **88**, 201801 (2002)
10. C. Anastasiou and K. Melnikov, Nucl. Phys. B **646**, 220 (2002)
11. V. Ravindran, J. Smith and W. L. van Neerven, Nucl. Phys. B **665**, 325 (2003)
12. R. V. Harlander and K. J. Ozeren, JHEP **0911** (2009) 088
13. A. Pak, M. Rogal and M. Steinhauser, JHEP **1002** (2010) 025
14. S. Actis, G. Passarino, C. Sturm and S. Uccirati, Nucl. Phys. B **811**, 182 (2009)
15. S. Actis, G. Passarino, C. Sturm and S. Uccirati, Phys. Lett. B **670**, 12 (2008)
16. U. Aglietti, R. Bonciani, G. Degrassi and A. Vicini, Phys. Lett. B **595**, 432 (2004)
17. W. Y. Keung and F. J. Petriello, Phys. Rev. D **80**, 013007 (2009)
18. C. Anastasiou, R. Boughezal and F. Petriello, JHEP **0904**, 003 (2009)
19. S. Catani, D. de Florian, M. Grazzini and P. Nason, JHEP **0307** (2003) 028
20. D. de Florian and M. Grazzini, Phys. Rev. Lett. **85** (2000) 4678
21. C. Anastasiou, S. Buehler, F. Herzog and A. Lazopoulos, JHEP **1112** (2011) 058
22. C. Anastasiou, S. Buehler, F. Herzog and A. Lazopoulos, JHEP **1204** (2012) 004
23. C. Anastasiou, S. Buehler, E. Furlan, F. Herzog and A. Lazopoulos, Phys. Lett. B **702** (2011) 224
24. S. Moch and A. Vogt, Phys. Lett. B **631** (2005) 48
25. M. H. Seymour, Phys. Lett. B **354** (1995) 409
26. A. Aeberli, F. Dulat and B. Mistlberger, Master Thesis
27. E. W. N. Glover and J. J. van der Bij, Phys. Lett. B **219** (1989) 488.
28. T. Binoth, M. Ciccolini, N. Kauer and M. Kramer, JHEP **0612** (2006) 046
29. J. M. Campbell, R. K. Ellis and C. Williams, JHEP **1110** (2011) 005
30. R. V. Harlander, W. B. Kilgore, Phys. Rev. **D68** (2003) 013001.
31. S. Dittmaier, M. Kramer, 1, A. Muck and T. Schluter, JHEP **0703** (2007) 114
32. S. Buehler, F. Herzog, A. Lazopoulos and R. Mueller, arXiv:1204.4415 [hep-ph].

Higher order QCD predictions for the Higgs p_T distribution

D. de Florian
Departamento de Física, FCEYN, Universidad de Buenos Aires, (1428) Pabellón 1 Ciudad Universitaria, Capital Federal, Argentina

G. Ferrera
Dipartimento di Fisica, Università di Milano and INFN, Sezione di Milano, I-20133 Milan, Italy

M. Grazzini [a]
Institut für Theoretische Physik, Universität Zürich, CH-8057 Zürich, Switzerland

D. Tommasini
University of Debrecen and Institute of Nuclear Research of the Hungarian Academy of Sciences, H-4001 Debrecen, Hungary

We consider Standard Model Higgs boson production through gluon–gluon fusion in hadron collisions. We combine the calculation of the next-to-next-to-leading order QCD corrections to the inclusive cross section with the resummation of multiple soft-gluon emissions at small transverse momenta up to next-to-next-to-leading logarithmic accuracy. We extend previous results including exactly all the perturbative terms up to order α_S^4 in our computation. We present numerical predictions for the Higgs boson spectrum at the LHC, together with an estimate of the corresponding uncertainties. We introduce the novel numerical program `HRes` that allows us to retain the full kinematics of the Higgs boson and of its decay products in the $H \to \gamma\gamma$, $H \to WW \to l\nu l\nu$ and $H \to ZZ \to 4l$ decay channels. We show explicit results in the $H \to \gamma\gamma$ decay mode, by using the nominal cuts applied in current Higgs boson searches by the ATLAS and CMS collaborations.

1 Introduction

One of the main tasks of the LHC program is the search for the Higgs boson [?] and the study of its properties (mass, couplings, decay widths). The experimental data already collected at the LHC in 2011 [?] considerably reduce the allowed mass range for the Standard Model (SM) Higgs boson H by essentially excluding the Higgs bosons in the mass range $\mathcal{O}(130$ GeV$) < m_H < \mathcal{O}(600$ GeV$)$, while observing an excess of Higgs boson candidate events around $m_H = 125$ GeV. More data from the ongoing LHC 2012 run, being operated at a centre-of-mass energy of 8 TeV, are needed to say whether these excesses really correspond to a Higgs signal or are just statistical fluctuations.

In this contribution we consider the production of the SM Higgs boson by the gluon fusion mechanism and its decays $H \to \gamma\gamma$, $H \to WW$ and $H \to ZZ$. The gluon fusion process $gg \to H$ [?], through a heavy-quark loop, is the main production mechanism of the SM Higgs boson at hadron colliders, and, as a consequence, it is crucial to achieve reliable theoretical predictions for

[a] On leave of absence from INFN, Sezione di Firenze, Sesto Fiorentino, Florence, Italy.

the cross section and the associated distributions. The dynamics of the gluon fusion mechanism is driven by strong interactions. Thus, accurate studies of the effect of QCD radiative corrections are mandatory to obtain precise theoretical predictions.

Here we consider the transverse momentum (p_T) spectrum of the SM Higgs boson produced by the gluon fusion mechanism. This observable is of direct importance in the experimental search. When studying the p_T distribution of the Higgs boson in QCD perturbation theory we define two different regions of p_T. In the large-p_T region ($p_T \sim m_H$), where the transverse momentum is of the order of the Higgs boson mass m_H, perturbative QCD calculations based on the truncation of the perturbative series at a fixed order in α_S are theoretically justified. In this region, the QCD radiative corrections are known up to $\mathcal{O}(\alpha_S^4)$, i.e., the next-to-leading order (NLO) [?,?,?] for the p_T spectrum and the next-to-next-to-leading-order (NNLO) as far as the inclusive cross section is considered. In the small-p_T region ($p_T \ll m_H$), the convergence of the fixed-order expansion is spoiled by the presence of large logarithmic terms, $\alpha_S^n \ln^m(m_H^2/p_T^2)$. To obtain reliable predictions, these logarithmically-enhanced terms have to be systematically resummed to all perturbative orders [?,?,?,?,?]. It is then important to consistently match the resummed and fixed-order calculations at intermediate values of p_T, in order to obtain accurate QCD predictions for the entire range of transverse momenta. In this contribution we present a selection of numerical results obtained by our group for the Higgs p_T spectrum [?] and discuss the effects of transverse-momentum resummation on the Higgs decay products [?].

2 The Higgs p_T spectrum

The numerical program `HqT` [?] implements the most accurate perturbative information that is available at present: soft-gluon resummation up to next-to-next-to-leading-logarithmic (NNLL) accuracy [?] combined with fixed-order perturbation theory up to $O(\alpha_S^4)$ in the large-p_T region [?]. The program is used by the Tevatron and LHC experimental collaborations to reweight the p_T spectrum of the Monte Carlo event generators used in the analysis and is thus of direct relevance in the Higgs boson search. The program `HqT` is based on the transverse-momentum resummation formalism described in Refs. [?,?,?], which is valid for a generic process in which a high-mass system of non strongly-interacting particles is produced in hadron–hadron collisions.

In Ref. [?] we performed some improvements with respect to the work of Ref. [?]. In particular, we have implemented the exact value of the NNLO hard-collinear coefficients $\mathcal{H}_N^{H(2)}$ computed in Ref. [?,?], and the recently derived value of the NNLL coefficient $A^{(3)}$ [?]. We have presented numerical results for Higgs production at the LHC and performed a study of the perturbative uncertainties. Our calculation for the p_T spectrum is implemented [?] in the updated version of the numerical code `HqT`, which can be downloaded from [?].

In Fig. **??**-left we consider Higgs boson production by gluon fusion at the LHC ($\sqrt{s} = 7$ TeV) and $m_H = 165$ GeV. We present our resummed results at NNLL+NLO accuracy, and we compare them with the NLL+LO results. The bands represent the scale uncertainty evaluated as explained in Ref. [?]. We find that the scale dependence at NNLL+NLO (NLL+LO) is about $\pm 10\%$ ($\pm 22\%$) at the peak, it decreases to about $\pm 8\%$ ($\pm 19\%$) in the region up to $p_T = 30$ GeV, and becomes $\pm 10\%$ ($\pm 18\%$) at $p_T = 60$ GeV. In the region beyond $p_T \sim 120$ GeV the resummed result looses predictivity, and its perturbative uncertainty becomes large. In Fig. **??**-right we compare the NLO and NNLL+NLO bands. At large values of p_T the NLO and NNLL+NLO scale uncertainty bands overlap, and the NLO result has smaller uncertainty. The new version of `HqT` implements a switching procedure, such that the fixed order NLO result is recovered at large p_T, where resummation is not any more relevant.

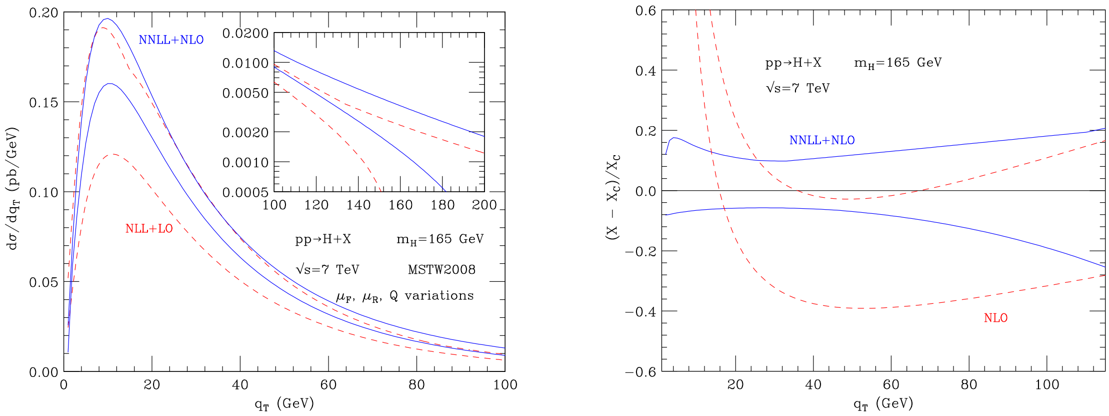

Figure 1: *The p_T spectrum of Higgs boson at the LHC: NNLL+NLO (solid) and NLL+LO (dashes) uncertainty bands (left panel); NNLL+NLO (solid) and NLO (dashes) uncertainty bands relative to the central NNLL+NLO result (right panel).*

3 Inclusion of Higgs boson decay products

In Ref.[?] we made a step forward with respect to previous work by including the Higgs boson decay products. We start from the doubly differential cross section, including transverse-momentum resummation and rapidity dependence [?] at full NNLL accuracy. We then include the Higgs boson decay and implement the ensuing result into an efficient Higgs event generator, that is able to simulate the full kinematics of the Higgs boson and of its decay products. This calculation is implemented in a new numerical program[?] called `HRes`, that embodies the features of `HNNLO` [?,?] and `HqT`. The decay modes that are implemented are $H \to \gamma\gamma$, $H \to WW \to l\nu l\nu$ and $H \to ZZ \to 4l$.

Here, we present just an example of the predictions that can be obtained with our program for Higgs boson production at the LHC ($\sqrt{s} = 8$ TeV) up to NNLL+NNLO accuracy. We focus on the $H \to \gamma\gamma$ decay channel and compare the resummed results with the corresponding fixed order results, obtained with the `HNNLO` numerical code. We consider the production of a SM Higgs boson with mass $m_H = 125$ GeV. We apply the following cuts on the photons. For each event, we classify the photon transverse momenta according to their minimum and maximum value, $p_{T\rm min}$ and $p_{T\rm max}$. The photons are required to be in the central rapidity region, $|\eta| < 2.5$, with $p_{T\rm min} > 25$ GeV and $p_{T\rm max} > 40$ GeV. A variable that is often studied is $\cos\theta^*$, where θ^* is the polar angle of one of the photons with respect to the beam axis in the Higgs boson rest frame. A cut on the photon transverse momentum p_T^γ implies a maximum value for $\cos\theta^*$ at LO. For example for $m_H = 125$ GeV and $p_T^\gamma \geq 40$ GeV we obtain $|\cos\theta^*| \leq |\cos\theta^*_{\rm cut}| \simeq 0.768$. At the NLO and NNLO the Higgs transverse momentum is non vanishing and events with $|\cos\theta^*| > |\cos\theta^*_{\rm cut}|$ are kinematically allowed. In the region of the kinematical boundary higher-order perturbative distributions suffer of logarithmic singularities. As expected [?], resummed results do not suffer of such instabilities in the vicinity of the LO kinematical boundary; the resummed distributions are smooth and the shape is rather stable when going from NLL+NLO to NNLL+NNLO. In Fig. **??** we report both the distributions (normalized to unity) obtained by fixed order and the resummed calculations. We see that the resummed results are smooth in the region around the kinematical boundary. Away from such region, fixed order and resummed results show perfect agreement.

The program `HRes` is built upon the fully exclusive calculation implemented in `HNNLO` and includes soft-gluon resummation at small transverse momenta of the Higgs boson. It thus provides a result which is everywhere as good as the NNLO result but much better in the small p_T region. These features should make our program a useful tool for Higgs searches and studies at the Tevatron and the LHC.

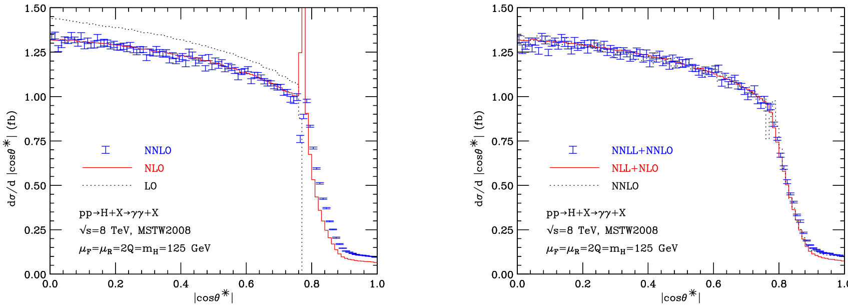

Figure 2: *Normalised* $\cos\theta^*$ *distribution at the LHC. On the left: LO, NLO and NNLO results. On the right: resummed predictions at NLL+NLO and NNLL+NNLO accuracy are compared with the NNLO result.*

References

1. F. Englert and R. Brout, Phys. Rev. Lett. **13** (1964) 321; P. W. Higgs, Phys. Lett. **12** (1964) 132, Phys. Rev. Lett. **13** (1964) 508.
2. G. Aad *et al.* [ATLAS Collaboration], Phys. Lett. B **710** (2012) 49; S. Chatrchyan *et al.* [CMS Collaboration], Phys. Lett. B **710** (2012) 26.
3. H. M. Georgi, S. L. Glashow, M. E. Machacek and D. V. Nanopoulos, Phys. Rev. Lett. **40** (1978) 692.
4. D. de Florian, M. Grazzini and Z. Kunszt, Phys. Rev. Lett. **82** (1999) 5209.
5. V. Ravindran, J. Smith and W. L. Van Neerven, Nucl. Phys. B **634** (2002) 247.
6. C. J. Glosser and C. R. Schmidt, JHEP **0212** (2002) 016.
7. Y. L. Dokshitzer, D. Diakonov and S. I. Troian, Phys. Lett. B **79** (1978) 269, Phys. Rep. **58** (1980) 269; G. Parisi and R. Petronzio, Nucl. Phys. B **154** (1979) 427; G. Curci, M. Greco and Y. Srivastava, Nucl. Phys. B **159** (1979) 451; J. C. Collins and D. E. Soper, Nucl. Phys. B **193** (1981) 381 [Erratum-ibid. B **213** (1983) 545]; J. C. Collins and D. E. Soper, Nucl. Phys. B **197** (1982) 446; J. C. Collins, D. E. Soper and G. Sterman, Nucl. Phys. B **250** (1985) 199; J. Kodaira and L. Trentadue, Phys. Lett. B **112** (1982) 66, report SLAC-PUB-2934 (1982), Phys. Lett. B **123** (1983) 335.
8. S. Catani, E. D'Emilio and L. Trentadue, Phys. Lett. B **211** (1988) 335.
9. S. Catani, D. de Florian and M. Grazzini, Nucl. Phys. B **596** (2001) 299.
10. G. Bozzi, S. Catani, D. de Florian and M. Grazzini, Nucl. Phys. B **737** (2006) 73.
11. S. Catani, M. Grazzini, Nucl. Phys. **B845** (2011) 297.
12. D. de Florian, G. Ferrera, M. Grazzini and D. Tommasini, JHEP **1111** (2011) 064.
13. D. de Florian, G. Ferrera, M. Grazzini and D. Tommasini, arXiv:1203.6321 [hep-ph].
14. D. de Florian and M. Grazzini, Phys. Rev. Lett. **85** (2000) 4678, Nucl. Phys. B **616** (2001) 247.
15. S. Catani and M. Grazzini, Phys. Rev. Lett. **98**, 222002 (2007).
16. S. Catani and M. Grazzini, arXiv:1106.4652 [hep-ph].
17. T. Becher and M. Neubert, Eur. Phys. J. C **71** (2011) 1665.
18. `http://theory.fi.infn.it/grazzini/codes.html`
19. G. Bozzi, S. Catani, D. de Florian and M. Grazzini, Nucl. Phys. B **791** (2008) 1.
20. M. Grazzini, JHEP **0802** (2008) 043 [arXiv:0801.3232 [hep-ph]].
21. S. Catani and B. R. Webber, JHEP **9710** (1997) 005.

Searches for Beyond Standard Model Higgs bosons at the Tevatron

F. COUDERC
CEA-Saclay/Irfu/SPP,
91191 Gif-Sur-Yvette Cedex, France

This paper presents recent searches for minimal supersymmetric standard model (MSSM) Higgs bosons in $p\bar{p}$ collisions at $\sqrt{s} = 1.96$ TeV. These results have been obtained by the D0 and CDF experiments. We show analyses with up to 7.3 fb^{-1} of integrated luminosity. They probe a significant portion of the MSSM parameter space, being able to exclude $\tan\beta > 25$ for low mass Higgs bosons $m_A < 170$ GeV. We also report for Fermiophobic (FP) Higgs bosons searches in the $\gamma\gamma$, WW channels and their combination, which excludes FP Higgs bosons with masses $m_{h_{FP}} < 119$ GeV.

1 MSSM Higgs bosons searches

While in the standard model (SM) only one Higgs boson doublet breaks the $SU(2)$ symmetry, there are two Higgs boson doublets in the minimal supersymmetric standard model (MSSM) [1]. This leads to five physical Higgs bosons remaining after electroweak symmetry breaking; three neutrals: h, H, and A, collectively denoted as ϕ, and twxo charged, $H^{\pm}$. At the tree level, the mass spectrum of the Higgs bosons is determined by two parameters conventionally chosen to be $\tan\beta$, the ratio of the two Higgs doublet vacuum expectation values, and M_A, the mass of the pseudoscalar Higgs boson A. Although $\tan\beta$ is a free parameter in the MSSM, large values ($\tan\beta \gtrsim 20$) are preferred. The top quark to bottom quark mass ratio suggests $\tan\beta \approx 35$ [2], and the observed density of dark matter also points towards high $\tan\beta$ values [3]. In this large $\tan\beta$ case, two of the neutral Higgs bosons (A and h or H) are approximately degenerate in mass. They share similar couplings to quarks, enhanced by $\tan\beta$ compared to the SM couplings for down-type fermions. The consequences of this enhanced coupling are first, that the main Higgs boson decay modes are $\phi \to b\bar{b}$ and $\phi \to \tau\tau$ with $\mathcal{B}(\phi \to b\bar{b}) \approx 90\%$ and $\mathcal{B}(\phi \to \tau\tau) \approx 10\%$, respectively, and then, that their production in association with b quarks is enhanced by approximately $\tan^2\beta$ compared to the SM.

Experiments at the CERN e^+e^- Collider (LEP) excluded MSSM Higgs boson masses below 93 GeV/c^2 [4]. More recently, LHC experiments have also set stringent constraints on MSSM Higgs bosons properties [5,6]. We present here recent searches from the D0 and CDF experiments which extend the exclusion to higher masses for high $\tan\beta$. These experiments exploit the two Higgs boson decay modes $\phi \to \tau\tau$ and $\phi \to b\bar{b}$ to perform several searches with different sensitivity and backgrounds, the $\phi \to b\bar{b}$ searches are nevertheless more sensitive to radiative corrections, hence to the MSSM parameters.

1.1 Inclusive searches in the di-tau channels

Both D0 and CDF experiments exploits the different τ lepton decay modes: $\tau \to \mu\nu_\mu\nu_\tau$ (τ_μ), $\tau \to e\nu_e\nu_\tau$ (τ_e) and hadronic τ decays (τ_h) to do the search in different sub-channels: $\tau_\mu\tau_\mathrm{h}$, $\tau_\mathrm{e}\tau_\mathrm{h}$, and $\tau_\mu\tau_\mathrm{e}$. The different analyses follow a similar strategy requiring exactly two oppositely

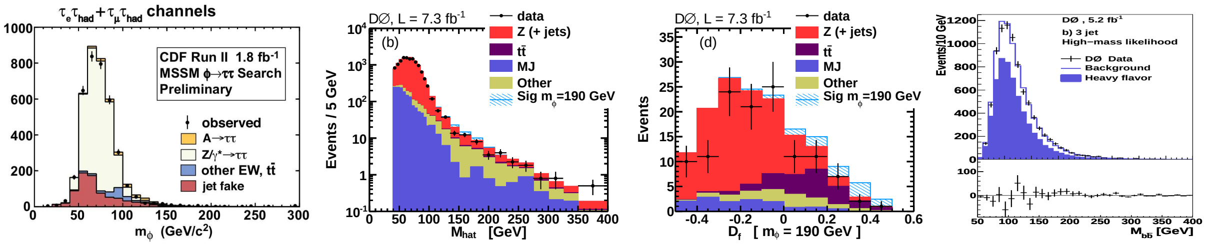

Figure 1: Left M_{vis} distribution at CDF in the combined $\tau_e\tau_h+\tau_\mu\tau_h$ channel. Middle left: M_{vis} distribution at D0 in the $\tau_\mu\tau_h$ channel. Middle right: Invariant mass of the best Higgs jet-pair at D0, background is fitted assuming no Higgs signal. Right: $\mathcal{D}_f$ discriminant in $b\tau_\mu\tau_h$ analysis for a Higgs boson mass of 190 GeV/c^2.

charged well identified leptons. In addition μ and e must be isolated while τ_h are required to be τ_h-tagged. CDF searches employ $\mathcal{L} = 1.8$ fb^{-1} of integrated luminosity [9]. D0 results [10] are based on $\mathcal{L} = 7.3$ fb^{-1} but limited to the most sensitive channel $\phi \to \tau_\mu\tau_h$.

A set of cuts are imposed to suppress multijets (MJ), W+jets and, $t\bar{t}$ backgrounds, the $Z \to \tau\tau$ background being irreducible. Both experiments search for an excess in the $M_{\rm vis} = \sqrt{(p_{\tau\tau} + \not{p}_T)^2}$ distribution, where $p_{\tau\tau}$ with $\not{p}_T \equiv (\not{E}_T, \not{E}_x, \not{E}_y, 0)$. $M_{\rm vis}$ distributions are shown on Fig. 1 for D0 and CDF experiments.

For both experiments no excess of data over expected background is observed. They both proceed to set model independent limits on $\sigma(\phi \to \tau\tau) \times \mathcal{B}(\phi \to \tau\tau)$ as a function of the Higgs boson mass (assuming its natural width is negligible compared to the experimental resolution) and translate these constraints in different MSSM scenarii.

1.2 $b\phi \to bb\bar{b}$ searches

An inclusive search $\phi \to b\bar{b}$ is extremely difficult due to the abundant MJ background. Therefore, both experiments focus on the $bb\bar{b}$ final state where an additional b quark in the acceptance greatly reduces the MJ background. They require three b-tagged jets in the final selection. The MJ background dominates the sample and is modeled from a data-driven method. Both D0 and CDF search for a peak in the the Higgs jet-pair invariant mass distribution. The Higgs jet-pair is selected at D0 using a likelihood ($\mathcal{LH}$) method while CDF selects the two leading jets. The selected jet-pair invariant mass distribution is modelled by using the MJ sample with exactly two b-tagged jets corrected for the presence of a third b-tagged jet. In both experiment, the composition of the signal sample is determined from a fit to data. See Fig. 1 for an example of the selected di-jet pair invariant mass at D0.

The analysis is performed with an integrated luminosity of 2.6 fb^{-1} by CDF [11] and 5.2 fb^{-1} at D0 [12]. Both experiments does not observe any significant excess of data over the predicted background and set limit on the $\sigma(bg \to b\phi) \times \mathcal{B}(\phi \to b\bar{b})$. Limits on the different MSSM scenarii are also derived (taking into account the Higgs natural width).

1.3 $b\phi \to b\tau\tau$ searches

This channel is studied for by the D0 experiment in two different final states: $b\tau_e\tau_h$ and $b\tau_\mu\tau_h$. The former [13] uses an integrated luminosity of 3.7 fb^{-1} while the latter [14] analyses 7.3 fb^{-1}.

The dominant backgrounds are coming from $Z \to \tau\tau$, W+jets, MJ and $t\bar{t}$. The two analysis employs a similar strategy. The W+jets background is efficiently suppressed by a cut on the transverse mass formed by the $\ell \equiv \mu/e$ and the $\not{E}_T$. Then, they developed multivariate discriminants against the main backgrounds, *i.e.* MJ and $t\bar{t}$, and combined them in a final discriminant $\mathcal{D}_f$ which is used to perform for the search for a potential signal. In the case of the $b\tau_\mu\tau_h$ analysis, b-tagging information are also included in $\mathcal{D}_f$. For this channel, the Z background is

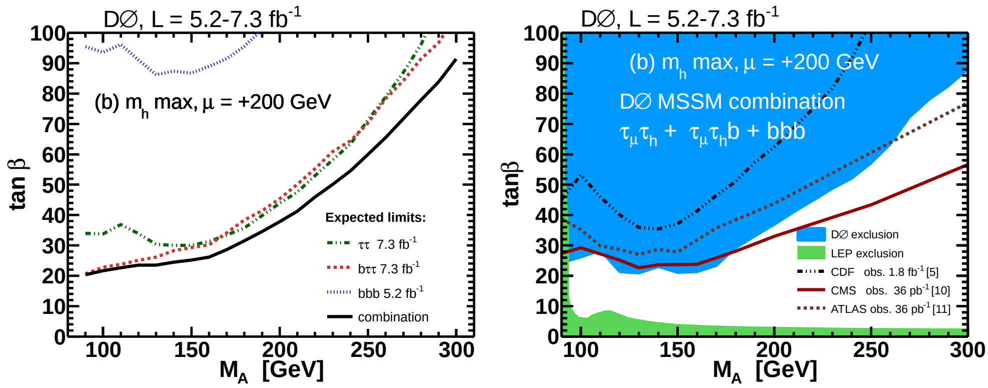

Figure 2: Left : Expected constraints in the $(\tan\beta, M_A)$ plane from the D0 MSSM combination in the $m_{\rm h}$-max scenario. Right: Observed constraints in the $(\tan\beta, m_A)$ plane in the MSSM $m_{\rm h}$-max scenario $(\mu < 0)$ from the D0 MSSM combination.

constrained from data using a $Z \to \mu\mu$ control sample. Such a $\mathcal{D}_f$ discriminant distribution is presented on Fig. 1 for the $b\tau_\mu\tau_{\rm h}$ channel.

No excess of data over predicted background is observed and limits are placed on $\sigma(bg \to b\phi) \times \mathcal{B}(\phi \to \tau\tau)$, and subsequently converted into constraints on the MSSM benchmark scenarii.

1.4 D0 MSSM combination and conclusion

The D0 collaboration combined the three channels: $\tau\tau$, $b\tau\tau$ and $b\bar{b}b$ to increase further the MSSM Higgs boson search sensitivity [10]. The expected constraints for each channels as well as the expected combined sensitivity are shown on Fig. 2 for the$m_{\rm h}$-max MSSM scenario [15] with $\mu > 0$. The D0 collaboration does not observe any significant excess over the expected background and places constraint in the $(\tan\beta, M_A)$ plane, taking into account the Higgs natural width. Examples are given on Fig. 2

D0 and CDF have actively searched for MSSM Higgs bosons. We presented here results with up to 7.3 fb^{-1} of integrated luminosity. In the absence of excess of data over expected background from SM processes, we set limits, strongly constraining the MSSM parameter space. We reach sensitivities down to $\tan\beta \approx 20$ for low mass MSSM Higgs bosons.

2 Fermiophobic Higgs searches

In several beyond the standard model scenarii, the Higgs couplings to fermions are reduced. We study the extreme case where these couplings are cancelled. In this case, the Higgs production is restrained to vector-boson fusion (VBF) and vector-boson associated production (VH) while the $\mathcal{B}(h_{\rm FP} \to \gamma\gamma)$ is increased. Therefore the $h_{\rm FP} \to \gamma\gamma$ is enhanced by an order of magnitude compared to the SM which makes this final state the most promising channel at low mass to discover such a Higgs boson. The $VH \to VWW^*$ is also very important at higher masses. Both collaboration uses the full Tevatron integrated luminosity ($L \approx 10$ fb^{-1}) to study the $\gamma\gamma$ final state.

The search strategy uses the peculiar kinematic of this boosted production to optimize the sensitivity compared to the SM case. The CDF collaboration splits the sample into different categories depending on the diphoton mass resolution and on the transverse momentum of the diphoton pair while the D0 collaboration uses the same information combined with the invariant diphoton mass in a multivariate discriminant. The $m_{\gamma\gamma}$ distribution in the most sensitive CDF channel and the D0 discriminant for $m_{h_{FP}} = 120$ GeV are shown on Fig. 3 . The SM background is mainly coming from prompt di-photon production but also from γ+jets

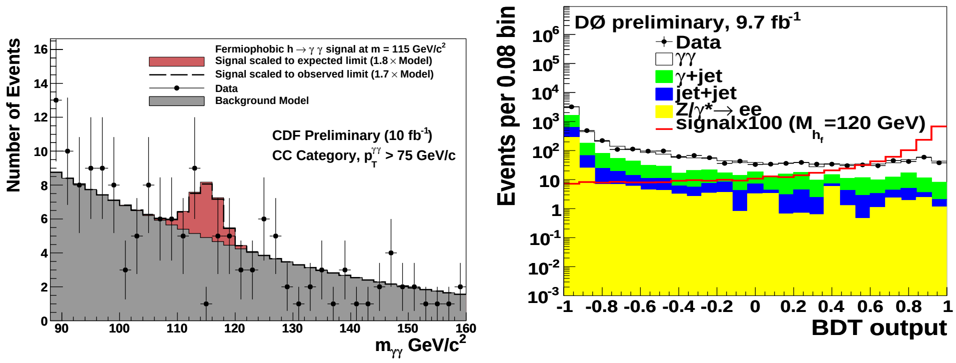

Figure 3: Left : CDF $m_{\gamma\gamma}$ invariant mass for 2 isolated photons in the electromagnetic calorimeter barrel with $p_T[\gamma\gamma] > 75$ GeV. Right: D0 final discriminant for $m_{h_{FP}} = 120$ GeV.

production. It is estimated with a sliding window technique at CDF and a combination of a data-driven method (for γ+jets) and MC at D0. Both collaborations have similar sensitivity and none of them observe any significant excess over the expected background. Assuming the SM cross sections for VBF and VH productions, they set limits at: $m_{h_{FP}} > 114$ GeV (CDF [17]) and $m_{h_{FP}} > 111$ GeV (D0 [16]).

The CDF collaboration has also combined this search in the $\gamma\gamma$ final state with searches in WW and WWW^* channels which are also enhanced in FP models. They reach an expected sensitivity of $m_{h_{FP}} > 119$ GeV while the observed limit is: $m_{h_{FP}} > 115$ GeV.

References

1. H. P. Nilles, Phys. Rep. **110**, 1 (1984); H. E. Haber and G. L. Kane, Phys. Rep. **117**, 75 (1985).
2. B. Ananthanarayan, G. Lazarides, and Q. Shafi, Phys. Rev. D **44**, 1613 (1991).
3. V. Barger and C. Kao, Phys. Lett. B **518**, 117 (2001).
4. S. Schael *et al.* (ALEPH, DELPHI, L3, and OPAL Collaborations), Eur. Phys. J. C **47**, 547 (2006).
5. S. Chatrchyan *et al.* (CMS Collaboration), Phys. Rev. Lett. **106**, 231801 (2011).
6. G. Aad *et al.* (ATLAS Collaboration), Phys. Lett. B **705**, 174 (2011).
7. V. M. Abazov *et al.* (D0 Collaboration), Phys. Lett. B **670**, 292 (2009).
8. A. Abulencia *et al.* (CDF Collaboration), Phys. Rev. Lett. **96**, 011802 (2006); D. E. Acosta *et al.* (CDF Collaboration), Phys. Rev. Lett. **95**, 131801 (2005).
9. T. Aaltonen *et al.*, (CDF Collaboration), Phys. Rev. Lett. **103**, 201801 (2009).
10. V. M. Abazov *et al.* (D0 Collaboration), Phys. Lett. B **710**, 569 (2012).
11. T. Aaltonen *et al.*, (CDF Collaboration), arXiv: 1106.4782, submitted to PRD.
12. V. M. Abazov *et al.* (D0 Collaboration), Phys. Lett. B **698**, 97 (2011).
13. V. M. Abazov *et al.* (D0 Collaboration), D0 Notes 5974-CONF.
14. V. M. Abazov *et al.* (D0 Collaboration), Phys. Rev. Lett. **107**, 121801 (2011)
15. M. Carena, S. Heinemeyer, C. E. M. Wagner, and G. Weiglein, Eur. Phys. J. C **45**, 797 (2006).
16. D0 Collaboration, Conference Note D0 Note 6297-CONF
17. CDF Collaboration, Conference Note CDF-10731

Searches for Non-Standard Model Higgs Bosons at CMS

Paolo SPAGNOLO on behalf of the CMS Collaboration
INFN Pisa, Italy

These proceedings report the results on the Higgs Searches beyond the Standard Model at the CMS experiment with data collected during the 2011 LHC run at 7 TeV, corresponding to an integrated luminosity of about 5 fb^{-1}. Many analyses performed by the CMS collaboration are reviewed and results for several models are shown. Most of these analyses are based on the same signature, like a resonance in the invariant mass of two b-quarks, muons or taus or an excess in the $\gamma\gamma$ spectrum. No significant deviation from the Standard Model is found and limits on the Higgs mass are set for each physics scenario.

1 Introduction

The Standard Model (SM) of Particle Physics describes very precisely the experimental measurements up to now but one of its key ingredients has not yet been observed: the Higgs boson, which is at the source of the electro-weak symmetry breaking and provides a mechanism to assign mass to particles. It is clear, however, that the SM theory breaks at larger scales and some major open points are the unification of couplings, hierarchy problem, dark matter issue and neutrino masses. Theories have been proposed that attempt to answer to some of these open questions such as supersymmetry (SUSY) or other Beyond Standard Model (BSM) scenarios and are currently under experimental test. The CMS experiment, a multi-purpose detector [1] operating at the CERN LHC pp collider, has been designed to investigate a wide range of physical phenomena. In these proceedings, the latest BSM Higgs searches at the CMS experiment will be briefly described. These results are achieved by the CMS collaboration with datasets collected in 2011 with a corresponding luminosity of about 5 fb^{-1}.

2 The MSSM Higgs

In the Minimal Supersymmetric Standard Model, the standard scalar Higgs boson is substituted by three neutral ϕ = (h,H,A) and two charged ($H^{\pm}$) Higgs particles. Neutral MSSM Higgs bosons are searched in the ditau final state. In the MSSM, all decays to "down-type" fermions are enhanced by a factor of tanβ. For relatively high tanβ the BR ($\phi \rightarrow \tau^+\tau^-$) is about 10% which is much lower then the corresponding branching ratio of the b-decay mode. The ditau channel is however preferred for its clear signature in the two leptons final states (electrons or muons) and in the lepton plus an hadronic decaying τ final state. The signature is an isolated high p_T lepton and a hadronic τ or an opposite sign lepton. The dilepton channel was searched in dimuons and in electron-muon final states. The hadronic τ is reconstructed in 1 and 3 prongs (+N π^0). The background is mostly due to Z decays, W+jets and $t\bar{t}$ with a lower contribution of WW and ZZ decays. A kinematic fit is applied on the reconstructed Higgs mass, in order to take into account the missing energy, with an improvement of about 20% on the measured mass [2]. In fig. 1 is shown the exclusion plot for the neutral MSSM Higgs mass versus tanβ. For tanβ = 20 Higgs masses up to 300 GeV/c^2 are excluded.

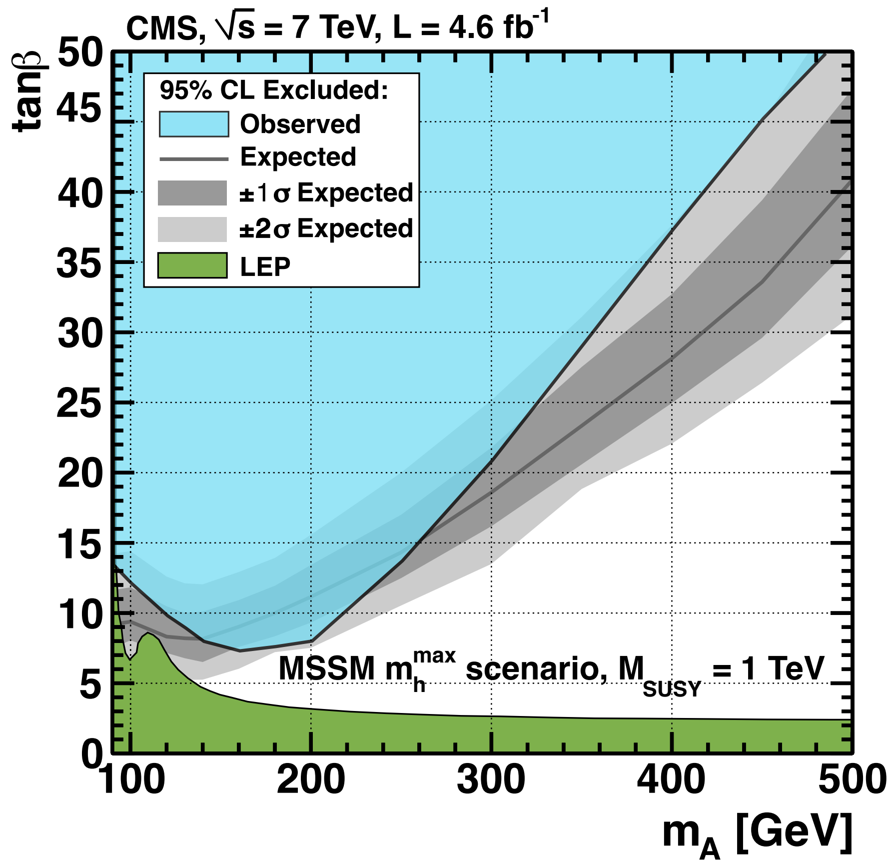

Figure 1: Region in the parameter space of tanβ versus m_A excluded at 95% CL in the context pf the MSSM scenario. The expected one- and two-standard-deviation ranges and the observed 95% CL upper limits are shown together with the observed excluded region.

The charged MSSM Higgs bosons are searched in the top decays t $\rightarrow$ H$^+$ with the tau final states a H$^+$ $\rightarrow$ $\tau^+\nu$. The $t\bar{t}$ production yields with tau final states are modified by Higgs diagrams if the Higgs mass is lower than the top mass. The Higgs particle is searched in isolated τ decays plus b-jets and possibly an isolated lepton in the final state, depending on the second top decay chain in the $t\bar{t}$ events. The analysis is described here [3] and results on BR(t $\rightarrow$ H$^+$) are shown in fig. 2 and fig. 3 together with the mass limits. Values of BR(t $\rightarrow$ H$^+$) > 4% are excluded for all the possible Higgs mass values.

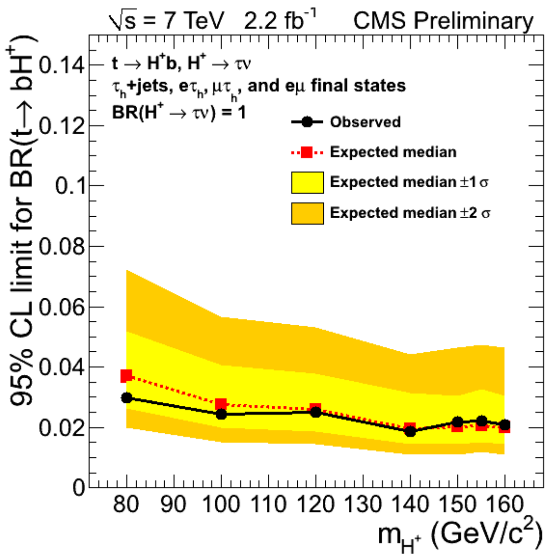

Figure 2: Upper limit on BR(t $\rightarrow$ H$^+$) assuming BR($H^+ \rightarrow \tau^+\nu$)=1 as a function of m(H$^+$). The yellow bands show the one and two sigma bands around the expected limit.

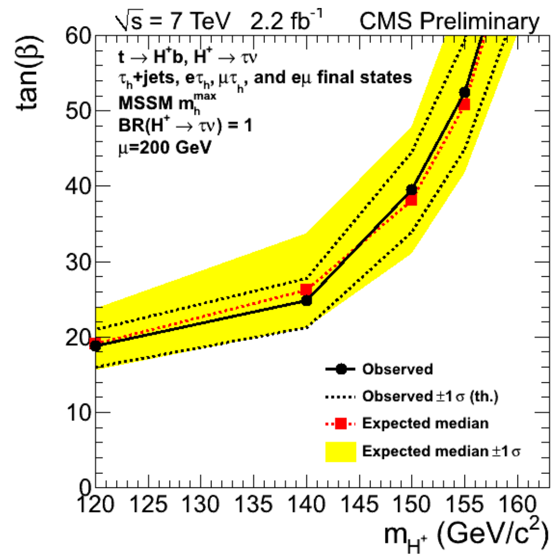

Figure 3: Exclusion plot of the H$^+$ mass vs tanβ obtained for the MSSM scenario.

3 Doubly charged H$^{\pm\pm}$

These exotic Higgs bosons are predicted within the "type II" see-saw model and are related to the presence of a light neutrino mass. H$^{\pm\pm}$ decay to two same charged resonant leptons and obviously do not have any physical background in the Standard Model. They are produced in pairs or together with a single charged Higgs through the processes: Z/$\gamma^* \rightarrow H^{++}H^{--}$ and W$^+$ $\rightarrow H^{++}H^{-}$ (charge conjugates included), giving a final states with four or three leptons, same charge resonant. No excess is observed in the CMS data. In fig. 4 the invariant mass of the same charge leptons is shown for the 3 leptons analysis. Fig. 5 shows the mass limits for the different leptonic final states and four benchmark points of the see-saw mechanism described in [4].

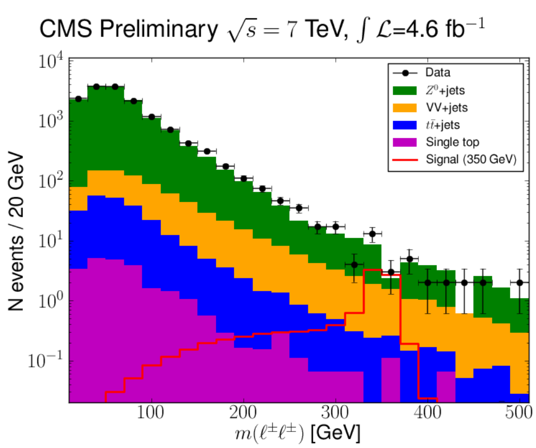

Figure 4: Invariant mass distribution from three lepton final state for backgrounds and data. We also show the expected contribution of a H^{++} with a mass of 350 GeV

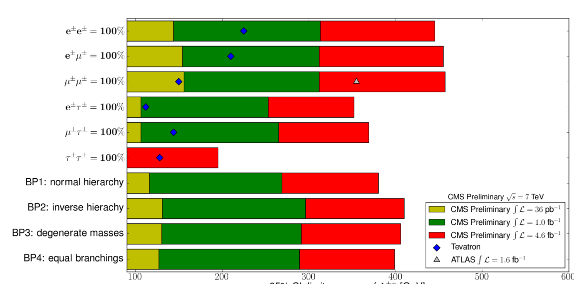

Figure 5: Limits on the mass of the doubly charged Higgs bosons for different final states

4 Light pseudoscalar Higgs boson

The presence of a light pseudoscalar CP-odd Higgs a is predicted within the Next to Minimal Supersymmetric extension to the Standard Model. This search [5] has been performed in the sidebands of the $\Upsilon \rightarrow \mu^+\mu^-$ dimuon decays, namely $5.5 < M(\mu\mu) < 9$ GeV/c^2 and $11.5 < M(\mu\mu) < 14$ GeV/c^2. A special high level trigger conceived for charmonium states studies was set up and this analysis was performed with a data sample corresponding to a luminosity of 1.3 fb^{-1}. Results are shown in fig. 6 with no excess found in the dimuon spectrum. An upper limit on the cross-section $\sigma(pp \rightarrow a \rightarrow \mu^+\mu^-)$ below 5 pb is set for all the masses in the two search intervals.

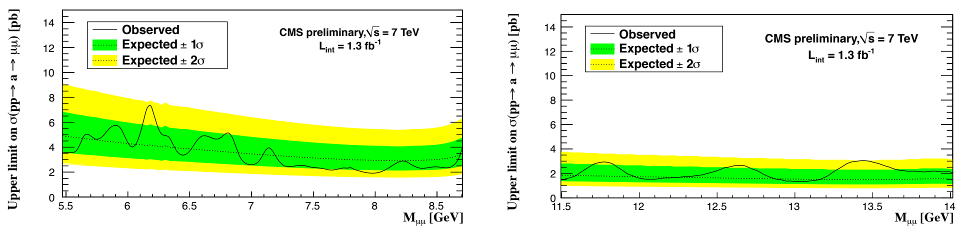

Figure 6: Limits on the cross-section $\sigma(pp \rightarrow a \rightarrow \mu^+\mu^-)$ for the two mass intervals in the Υ sidebands

5 Fermiophobic Higgs boson decays

In the Fermiophobic model the gluon-gluon process of Higgs production is forbidden and the production cross-section is suppressed by an order of magnitude with the Vector Boson Fusion (VBF) and the Higgs-strahlung (VH) that become the two most important contributions to Higgs production. On the other hand, the diphoton decay $H \rightarrow \gamma\gamma$ is enhanced by another order of magnitude, with the result of a total $\sigma\times$ BR that is of the same size of the standard Higgs diphoton decays . This analysis is based on the selection of two high p$_T$ photons and three tag classes with electron, muon or dijets in the final states [6] corresponding to different decays in the associate production. Furthermore four inclusive samples based on different Ecal regions and leading to four different Higgs mass resolutions are taken into account. The results are presented in fig. 7 and show a small excess at 126 GeV/c^2 corresponding to 2.7σ of local significance, reducing to 1.2σ of global significance taking into account of the "Look Elsewhere" effect. Two intervals of Higgs mass are excluded @95% of C.L.: $110 < M_H < 124$ GeV/c^2 and $128 < M_H < 136$ GeV/c^2. The excess at 126 GeV/c^2 is even more diluted when the diphoton channel is combined[7] with $H \rightarrow WW, ZZ$ as shown in fig. 8.

6 Other results

Other results to be mentioned here are the analysis of the long lived neutrals [8] where the Higgs particle is searched in exotic neutral particles decaying at long distance from the beam-line and Standard Model SM4 extensions searches obtained including a fourth quark generation [7] that significantly increase the Higgs bosons production rate. The SM4 model is excluded @95% CL from 120 up to 600 GeV/c^2 of Higgs masses.

7 Conclusions

A broad program of BSM Higgs bosons searches with CMS has been presented in this talk. Model independent inclusive searches together with well defined new physics scenarios have

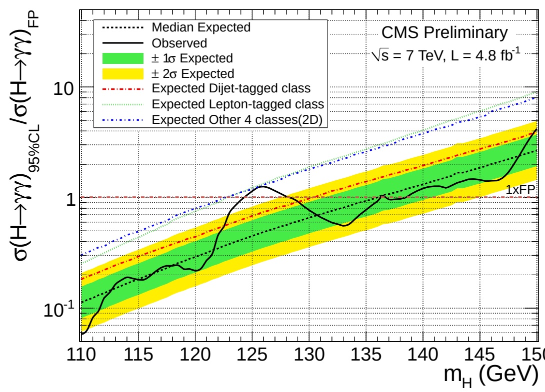

Figure 7: The 95% CL upper limits on the signal strength parameter $\mu = \sigma/\sigma_{FP}$ for the fermiophobic Higgs boson hypothesis as function of the Higgs boson mass for the di-photon channel. The observed values are shown by the solid line. The dashed line indicates the expected median of results for the background only hypothesis, while the green (dark) and yellow (light) bands indicate the ranges that are expected to contain 68% and 95% of all observed excursions from the median, respectively. The limits are obtained with the asymptotic CLs approximation.

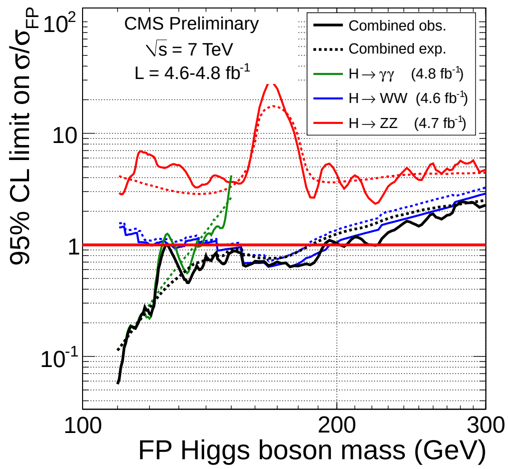

Figure 8: The 95% CL upper limits on the signal strength parameter $\mu = \sigma/\sigma_{FP}$ for the fermiophobic Higgs boson hypothesis as function of the Higgs boson mass for the three explored Higgs boson decay modes and their combination. Observed limits are shown with solid lines, while expected limits are shown with dashed lines. The limits are obtained with the asymptotic CLs approximation.

been probed during 2011 with a luminosity of about 5 fb^{-1}. A large fraction of the MSSM Higgs parameters are constrained by the $H \to \tau^+\tau^-$ analyses. A small excess on the $H \to \gamma\gamma$ is registered, compatible with a statistical fluctuation. No evidence for new BSM Higgs bosons is observed. The 2012 run, with about 15 fb^{-1} of data collected, will help to improve these searches.

References

1. "The CMS experiment at the CERN LHC" [CMS Collaboration], JINST 0803:S08004,(2008).
2. "Search for Neutral Higgs Bosons Decaying to Tau Pairs in pp Collisions at $\sqrt{s} = 7$ TeV" [CMS Collaboration], arXiv:1202.4083, submitted to PLB
3. "Search for the light charged Higgs boson in top quark decays in pp collisions at $sqrts =$ 7 TeV" [CMS Collaboration], CMS-PAS-HIG-11-019
4. "Search for Doubly Charged Higgs" [CMS Collaboration], CMS-PAS-HIG-12-005
5. "Search of a light pseudoscalar Higgs boson in the dimuon channel" [CMS Collaboration], CMS-PAS-HIG-12-004
6. "Search for the fermiophobic model Higgs boson decaying into two photons" [CMS Collaboration], CMS-PAS-HIG-12-002
7. "Combination of SM, SM4, FP Higgs boson searches", [CMS Collaboration], CMS-PAS-HIG-12-008
8. "Search for Long-Lived Exotica Decaying to Displaced Leptons" [CMS Collaboration], CMS-PAS-EXO-11-004

Higgs Boson Searches Beyond the Standard Model with ATLAS

J. Kroseberg (on behalf of the ATLAS Collaboration)
Physikalisches Institut der Universität Bonn, Nußallee 12, D-53115 Bonn, Germany

Recent searches for Higgs bosons in the context of extensions to the Standard Model of Particle Physics with the ATLAS detector at the Large Hadron Collider are discussed. All presented analyses use data recorded at a pp center-of-mass energy of 7 TeV in 2011 with integrated luminosities between 1 and 5 fb^{-1}. No significant deviations from the background expectations are found and corresponding constraints on physics beyond the Standard Model are obtained.

1 Introduction

While much of the current interest in Higgs boson searches is focussed on the Standard Model (SM) case [2], a number of important Higgs sector scenarios beyond the SM are also being investigated. In the following, selected searches with the ATLAS experiment at the Large Hadron Collider for beyond-SM neutral, charged and doubly-charged Higgs boson are discussed. The analyses are based on data recorded in 2011 at a pp center-of-mass energy of 7 TeV. Signal expectations are derived using information compiled by the LHC Higgs Cross Section WG [1].

2 Search for a fermiophobic Higgs boson via $H \to \gamma\gamma$

The decay $H \to \gamma\gamma$ is searched for within a simple fermiophobic Higgs benchmark model in which the Higgs-fermion couplings are zero and SM couplings to bosons are assumed. The production cross section times the decay branching ratio for a fermiophobic $H \to \gamma\gamma$ is larger than in the SM for Higgs boson masses below 120 GeV. The experimental sensitivity is further enhanced due to the fact that a fermiophobic Higgs boson can only be produced through vector boson fusion and associated production with vector bosons, leading to typically larger transverse momenta of the Higgs boson and its decay products than for the dominant SM production via gg fusion. The analysis [3] uses 4.9 fb^{-1} of ATLAS data and follows the same procedure as the SM Higgs search in this decay channel [4] . Pairs of isolated high-p_T photons in the invariant mass range 100 GeV$< m_{\gamma\gamma} <$160 GeV are analyzed in nine categories according to the presence of photon conversions, the photon calorimeter impact point, and the diphoton transverse momentum p_{Tt} orthogonal to the diphoton thrust axis in the transverse plane. Signal events are expected to typically have a larger p_{Tt} than the background. Figure 1(a) shows the $m_{\gamma\gamma}$ distribution for high-p_{Tt} events compared to the background and signal expectations. The resulting cross section limits, see Fig. 1(b), exclude a fermiophobic Higgs boson in the mass ranges [110.0,118.0] and [119.5,121.0], with an expected exclusion range of [110.0,123.5]. The largest excess over the background-only hypothesis is found at a Higgs mass $m_H = 125.5$ GeV, which however corresponds to only 1.6σ when the look-elsewhere effect is considered. Since this conference, the corresponding final results of this analysis have been submitted for publication [5].

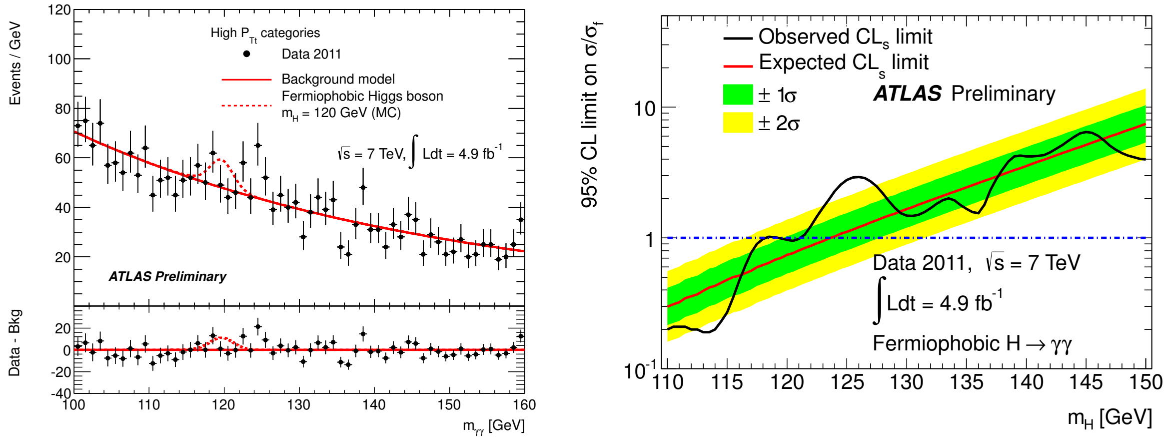

(a) (b)

Figure 1: Fermiophobic $H \to \gamma\gamma$ search[3]: (a) diphoton invariant mass spectra for the high p_{Tt} categories, overlaid with the background-only fit and signal expectation for m_H =120 GeV; (b) expected and observed 95% confidence level limits normalized to the fermiophobic cross section times branching ratio expectation as a function of m_H.

3 Search for MSSM neutral Higgs bosons via $H/A/h \to \tau\tau$

The minimal supersymmetric extension to the Standard Model (MSSM) comprises two Higgs doublets of opposite weak hypercharge. This results in five observable Higgs bosons, three of which (the CP-even h, H, and the CP-odd A) are electrically neutral and two are charged ($H^{\pm}$). The decays to τ leptons provide particularly important search channels because the Higgs couplings to third-generation down-type fermions are strongly enhanced for large regions of the MSSM parameter space. The most recent ATLAS results [6] on the search for MSSM neutral Higgs bosons decaying into a pair of τ leptons are based on 2011 data corresponding to an integrated luminosity of $\mathcal{L}$=1.06 fb^{-1}. The analysis considers the final states $\tau\tau \to e\mu$,

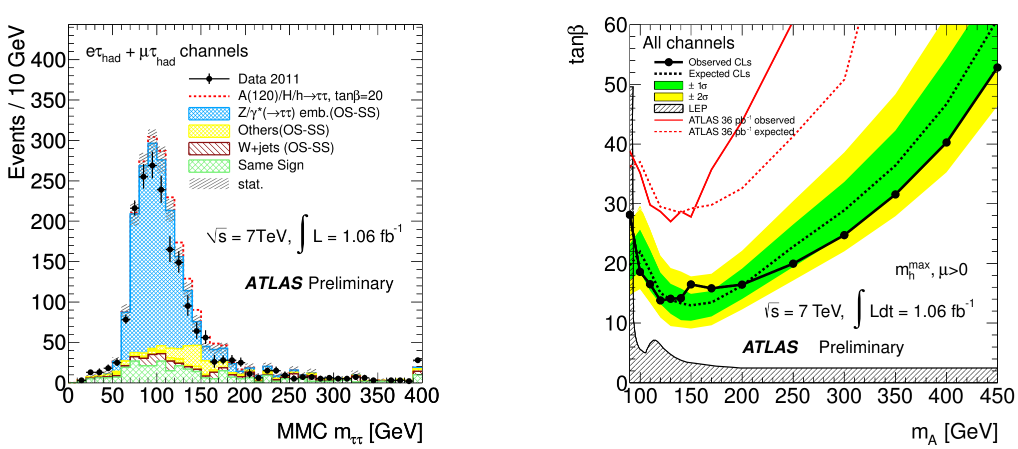

(a) (b)

Figure 2: MSSM $Higgs \to \tau\tau$ search[6]: (a) $\tau\tau$ (MMC) mass distribution for the $\ell\tau_{had}$ final state. The data are compared with the background expectation and an added hypothetical MSSM signal (m_A = 120 GeV, $\tan\beta = 20$); (b) expected and observed exclusion limits in the m_A-$\tan\beta$ plane of the MSSM derived from the combination of all channels. The region above the limit curve is excluded at the 95% confidence level.

$\ell\tau_{had}$ ($\ell = e$ or μ), and $\tau_{had}\tau_{had}$, where τ_{had} denotes a hadronically decaying τ lepton. After signal selection, 4630 events are observed in this data sample. The observed number of events is consistent with the expected background of 4900 ± 600 events. Corresponding exclusion limits are obtained from the $m_{\tau\tau}$ distribution, which for the dominant $\ell\tau_{had}$ channel is reconstructed using the so-called missing-mass calculator (MMC) technique [7], see Fig. 2(a). Data control samples are used, where possible, to estimate or validate the background distributions; this is particularly relevant for the irreducible $Z \to \tau\tau$ background, which is modeled by embedding simulated τ decays in selected $Z \to \mu\mu$ data events. Fig. 2(b) shows the resulting limits in the context of the MSSM $m_h^{\max}$ scenario [8] as a function of the CP-odd Higgs boson mass m_A and the ratio $\tan\beta$ of the vacuum expectation values of the two Higgs doublets.

4 Search for a MSSM charged Higgs boson via $H^\pm \to \tau\nu_\tau$

The discovery of a charged Higgs boson $H^\pm$ would clearly establish physics beyond the SM. For charged Higgs masses smaller than the top quark mass, the dominant production mechanism is the production of a $t\bar{t}$ pair with subsequent decay of one of the top quarks to a b quark and a charged Higgs boson, which in turn predominantly decays via $H^\pm \to \tau\nu_\tau$ if $\tan\beta > 3$. A recent ATLAS search [9], based on the entire 2011 data set ($\mathcal{L} = 4.6$ fb^{-1}), considers the decays $t\bar{t} \to b\bar{b}W^\mp H^\pm \to b\bar{b}(q\bar{q}')(\tau_{lep}\nu_\tau)$, $b\bar{b}(\ell\nu_\ell)(\tau_{had}\nu_\tau)$, and $b\bar{b}(q\bar{q}'))(\tau_{had}\nu_\tau)$, which in the context of this analysis are referred to as lepton+jets, τ+lepton and τ+jets channels, respectively. Different discriminating variables are used for the individual channels. For lepton+jets final states, the angular correlation between the b jet and the charged lepton coming from the same top quark candidate is exploited; also, a transverse mass m_T^H is reconstructed providing an event-by-event lower bound on the mass of the leptonically decaying charged (Wor Higgs) boson produced in the top quark decay. In the τ+lepton and τ+jets channels, the distributions of the missing transverse energy (E_T^{miss}) and the transverse mass m_T of the τ-E_T^{miss} system (cf. Fig. 3(a)), respectively, are used for the statistical analysis. In all cases the data are found to be consistent with the expected SM background. Assuming that the branching fraction $B(H^\pm \to \tau\nu)$ is 100%, this leads to upper limits on $B(t \to bH^\pm)$ between 5% and 1% for charged Higgs boson masses m_{H^+} ranging from 90 to 160 GeV, respectively. Within the $m_h^{\max}$ scenario of the MSSM, values of $\tan\beta$ larger than 13-26 are excluded for charged Higgs boson masses in the range

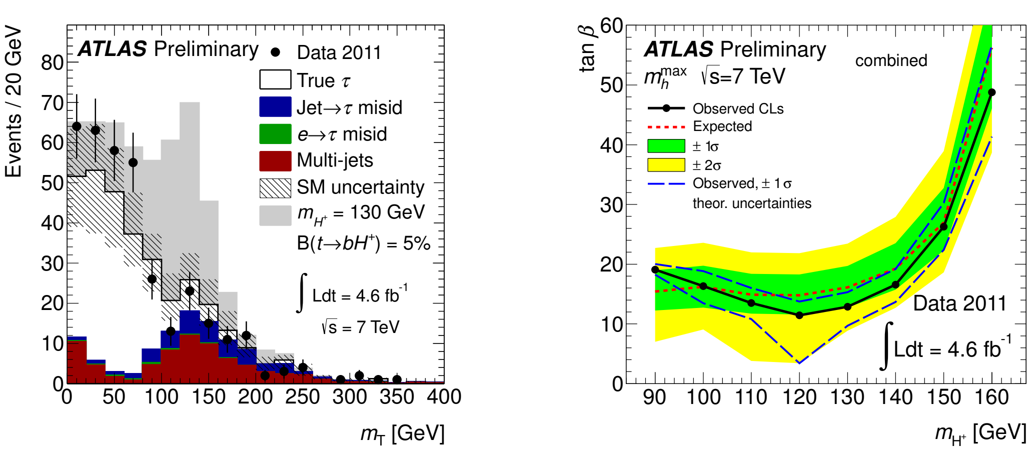

(a) (b)

Figure 3: MSSM $H^\pm \to \tau\nu_\tau$ search[9]: (a) distribution of m_T after all selection cuts in the τ+jets channel. The stacked histogram shows the predicted contribution of signal+background for $m_{H^+} = 130$ GeV, assuming $\mathcal{B}(t \to bH^\pm) = 5\%$ and $\mathcal{B}(H^\pm \to \tau\nu_\tau) = 100\%$; (b) 95% CL exclusion limits on $\tan\beta$ as a function of $m_{H^\pm}$.

90 GeV< $m_{H^\pm}$ <150 GeV as shown in Fig. 3(b). Since this conference, the corresponding final results of this analysis have been submitted for publication [10].

5 Search for a doubly-charged Higgs boson in same-sign dimuon final states

Going beyond the MSSM, there are a number of scenarios, such as Higgs triplet and left-right-symmetric models, predicting doubly-charged Higgs bosons $H^{\pm\pm}$. ATLAS has performed a search [11] for the decay $H^{\pm\pm} \to \mu^\pm\mu^\pm$ using 2011 data corresponding to a luminosity of 1.6 fb^{-1} in the context of an inclusive analysis of dimuon pairs with the same electric charge, where a doubly-charged Higgs boson could be observed as a narrow resonance in the dimuon mass spectrum. Figure 4(a) shows the $m_{\mu\mu}$ distribution for selected pairs of same-sign muons with $p_T > 20$ GeV and $|\eta| < 2.5$; no significant deviation from the background expectation is observed. Assuming pair production of $H^{\pm\pm}$ bosons and a branching ratio to muons of 100% (33%), this analysis excludes masses below 355 (244) GeV and 251 (209) GeV for $H^{\pm\pm}$ bosons coupling to left-handed and right-handed fermions, respectively, cf. Fig. 4(b).

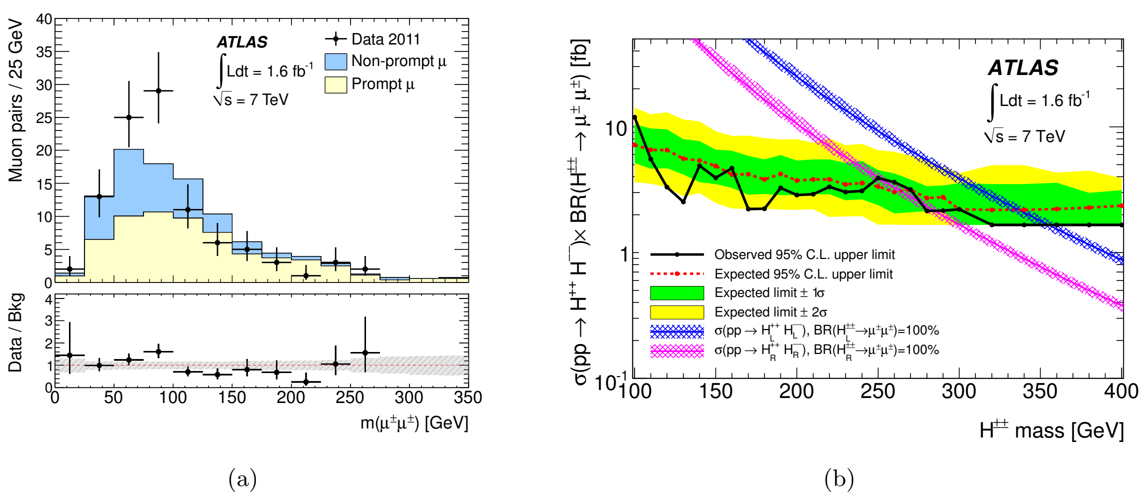

Figure 4: $H^{\pm\pm} \to \mu^\pm\mu^\pm$ search[11]: (a) distribution of the dimuon invariant mass for $\mu^\pm\mu^\pm$ pairs. The data are compared to the estimated background; (b) Upper limit at 95% C.L. on the cross section times branching ratio for pair production of doubly charged Higgs bosons decaying to two muons. Superimposed is the predicted cross section for $H_R^{++}H_R^{--}$ and $H_L^{++}H_L^{--}$ production assuming a branching ratio to muons of 100%. The bands on the predicted cross sections corresponds to the theoretical uncertainty of 10%.

References

1. The LHC Higgs Cross Section Working Group, arXiv:1101.0593, arXiv:1201.3084.
2. D. Bortoletto, R. Bernhard, A. Bornheim, contributions to this conference.
3. ATLAS Collaboration, ATLAS-CONF-2012-013, https://cdsweb.cern.ch/record/1429661.
4. ATLAS Collaboration, *Phys. Rev. Lett.* **108**, 111803 (2012).
5. ATLAS Collaboration, arXiv:1205.0701, submitted to EPJC.
6. ATLAS Collaboration, ATLAS-CONF-2011-132, https://cdsweb.cern.ch/record/1383835.
7. A. Elagin, P. Murat, A. Pranko, A. Safonov, *Nucl. Instrum. Methods* A **654**, 481 (2011).
8. M. Carena, S. Heinemeyer, C. E. M. Wagner, and G. Weiglein, EPJC **26**, 601 (2003).
9. ATLAS Collaboration, ATLAS-CONF-2012-011, https://cdsweb.cern.ch/record/1429659.
10. ATLAS Collaboration, arXiv:1204.2760[hep-ex], submitted to JHEP.
11. ATLAS Collaboration, *Phys. Rev.* D **88**, 032004 (2012).

LHC Searches and Higgs Portal Dark Matter

Oleg Lebedev
DESY Theory Group,
Notkestrasse 85, D-22607 Hamburg, Germany

We discuss implications of the tentative 125 GeV Higgs signal at the LHC for Higgs portal dark matter (DM) of different spins. We find that light scalar and vector DM, i.e. with masses below ≈ 60 GeV, is strongly disfavored by the invisible Higgs decay. The fermionic DM is practically ruled out by the combination of the XENON100 and WMAP data.

The ATLAS and CMS collaborations have recently reported on the search of the Standard Model (SM) Higgs boson with 5 fb^{-1} data [1]. Higgs bosons have been excluded in a significant mass range and, ignoring the unlikely possibility of a very heavy particle, only the very narrow window $m_h \approx 115$–130 GeV is now left over. There is even a slight excess of events in the data which could correspond to a SM like Higgs boson with a mass of 125 ± 1 GeV. Although the statistics are not sufficient for the experiments to claim discovery, one is tempted to take this piece of evidence seriously and analyze its consequences.

In this contribution, we study the implications of these LHC results for Higgs-portal models of dark matter (DM). The Higgs sector of the SM enjoys a special status since it allows for a direct coupling to the hidden sector that is renormalizable. Hence, determination of the properties of the Higgs boson would allow us to gain information about the hidden world. The latter is particularly important in the context of dark matter since hidden sector particles can be stable and couple very weakly to the SM sector, thereby offering a viable dark matter candidate [2]. In principle, the Higgs boson could decay into light DM particles which escape detection. However, given the fact that the ATLAS and CMS signal is close to what one expects for a Standard Model–like Higgs particle, there is little room for invisible decays. In what follows, we will assume that 10% is the upper bound on the invisible Higgs decay branching ratio, although values up to 20% will not significantly change our conclusions.

The relevant terms in the Lagrangians are

$$\begin{aligned}
\Delta\mathcal{L}_S &= -\frac{1}{2}m_S^2 S^2 - \frac{1}{4}\lambda_S S^4 - \frac{1}{4}\lambda_{hSS} H^\dagger H S^2 \ , \\
\Delta\mathcal{L}_V &= \frac{1}{2}m_V^2 V_\mu V^\mu + \frac{1}{4}\lambda_V (V_\mu V^\mu)^2 + \frac{1}{4}\lambda_{hVV} H^\dagger H V_\mu V^\mu , \\
\Delta\mathcal{L}_f &= -\frac{1}{2}m_f \bar{\chi}\chi - \frac{1}{4}\frac{\lambda_{hff}}{\Lambda} H^\dagger H \bar{\chi}\chi \ . \qquad (1)
\end{aligned}$$

Here S is a real scalar, V_μ is a vector and χ is a Majorana fermion. Although in the fermionic case the Higgs–DM coupling is not renormalizable, we still include it for completeness. The self–interaction terms S^4 in the scalar case and the $(V_\mu V^\mu)^2$ term in the vector case are not essential for our discussion and we will ignore them. After electroweak symmetry breaking, the neutral component of the doublet field H is shifted to $H^0 \to v + h/\sqrt{2}$ with $v = 174$ GeV and the physical masses of the DM particles will be given by

$$\begin{aligned} M_S^2 &= m_S^2 + \frac{1}{2}\lambda_{hSS} v^2 \ , \\ M_V^2 &= m_V^2 + \frac{1}{2}\lambda_{hVV} v^2 \ , \\ M_f &= m_f + \frac{1}{2}\frac{\lambda_{hff}}{\Lambda} v^2 \ . \end{aligned} \tag{2}$$

The relic abundance of the DM particles is obtained through the s–channel annihilation via the exchange of the Higgs boson. For instance, the annihilation cross section into light fermions of mass $m_{\rm ferm}$ is given by

$$\begin{aligned} \langle \sigma^S_{\rm ferm} v_r \rangle &= \frac{\lambda^2_{hSS} m^2_{\rm ferm}}{16\pi} \frac{1}{(4M_S^2 - m_h^2)^2} \ , \\ \langle \sigma^V_{\rm ferm} v_r \rangle &= \frac{\lambda^2_{hVV} m^2_{\rm ferm}}{48\pi} \frac{1}{(4M_V^2 - m_h^2)^2} \ , \\ \langle \sigma^f_{\rm ferm} v_r \rangle &= \frac{\lambda^2_{hff} m^2_{\rm ferm}}{32\pi} \frac{M_f^2}{\Lambda^2} \frac{v_r^2}{(4M_f^2 - m_h^2)^2} \ , \end{aligned} \tag{3}$$

where v_r is the DM relative velocity. We should note that in our numerical analysis, we take into account the full set of relevant diagrams and channels, and we have adapted the program micrOMEGAs to calculate the relic DM density.

The properties of the dark matter particles can be studied in direct detection experiments. The DM interacts elastically with nuclei through the Higgs boson exchange. The resulting nuclear recoil is then interpreted in terms of the DM mass and DM–nucleon cross section. The spin–independent DM–nucleon interaction can be expressed as [3]

$$\begin{aligned} \sigma^{SI}_{S-N} &= \frac{\lambda^2_{hSS}}{16\pi m_h^4} \frac{m_N^4 f_N^2}{(M_S + m_N)^2} \ , \\ \sigma^{SI}_{V-N} &= \frac{\lambda^2_{hVV}}{16\pi m_h^4} \frac{m_N^4 f_N^2}{(M_V + m_N)^2} \ , \\ \sigma^{SI}_{f-N} &= \frac{\lambda^2_{hff}}{4\pi \Lambda^2 m_h^4} \frac{m_N^4 M_f^2 f_N^2}{(M_f + m_N)^2} \ , \end{aligned} \tag{4}$$

where m_N is the nucleon mass and f_N parameterizes the Higgs–nucleon coupling.

If the DM particles are light enough, $M_{\rm DM} \leq \frac{1}{2} m_h$, they will appear as invisible decay products of the Higgs boson. For the various cases, the Higgs partial decay widths into invisible DM particles are given by

$$\begin{aligned} \Gamma^{\rm inv}_{h\to SS} &= \frac{\lambda^2_{hSS} v^2 \beta_S}{64\pi m_h} \ , \\ \Gamma^{\rm inv}_{h\to VV} &= \frac{\lambda^2_{hVV} v^2 m_h^3 \beta_V}{256\pi M_V^4} \left(1 - 4\frac{M_V^2}{m_h^2} + 12\frac{M_V^4}{m_h^4}\right) , \\ \Gamma^{\rm inv}_{h\to \chi\chi} &= \frac{\lambda^2_{hff} v^2 m_h \beta_f^3}{32\pi \Lambda^2} \ , \end{aligned} \tag{5}$$

where $\beta_X = \sqrt{1 - 4M_X^2/m_h^2}$. We have adapted the program HDECAY which calculates all Higgs decay widths and branching ratios to include invisible decays.

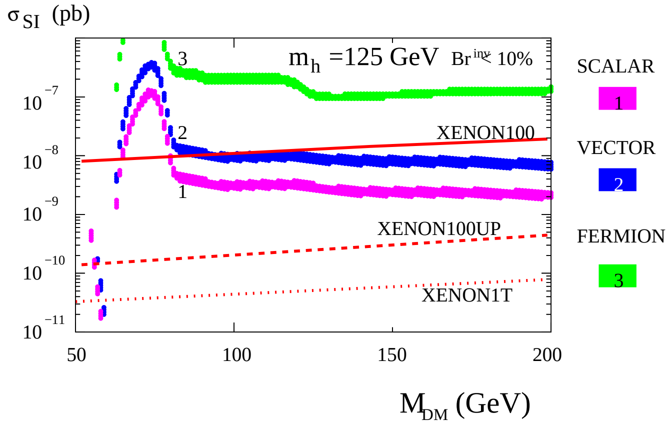

Figure 1: Spin independent DM–nucleon cross section versus DM mass. The upper band (3) corresponds to fermion DM, the middle one (2) to vector DM and the lower one (1) to scalar DM. The solid, dashed and dotted lines represent XENON100, XENON100 upgrade and XENON1T sensitivities, respectively.

Our main results[4] are presented in Fig. 1 which displays predictions for the spin–independent DM–nucleon cross section $\sigma_{\rm SI}$ (based on the lattice f_N) subject to the WMAP and $\text{BR}^{\rm inv} < 10\%$ bounds. The upper band corresponds to the fermion Higgs-portal DM and is excluded by XENON100. On the other hand, scalar and vector DM are both allowed for a wide range of masses. Apart from a very small region around $\frac{1}{2}m_h$, this parameter space will be probed by XENON100–upgrade and XENON1T. The typical value for the scalar $\sigma_{\rm SI}$ is a few times 10^{-9} pb, whereas $\sigma_{\rm SI}$ for vectors is larger by a factor of 3 which accounts for the number of degrees of freedom.

We conclude that the entire class of Higgs-portal DM models will be probed by the XENON100–upgrade and XENON1T direct detection experiments, which will also be able to discriminate between the vector and scalar cases. The fermion DM is essentially ruled out by the current data, most notably by XENON100. Furthermore, we find that light Higgs-portal DM $M_{\rm DM} \lesssim 60$ GeV is excluded independently of its nature since it predicts a large invisible Higgs decay branching ratio, which should be incompatible with the production of an SM–like Higgs boson at the LHC.

References

1. F. Gianotti (for ATLAS) and G. Tonelli (for CMS), talks given at the CERN seminar on update on the Standard Model Higgs searches, CERN, 13/12/2011.
2. V. Silveira, A. Zee, Phys. Lett. **B161**, 136 (1985).
3. S. Kanemura, S. Matsumoto, T. Nabeshima, N. Okada, Phys. Rev. **D82** (2010) 055026.
4. A. Djouadi, O. Lebedev, Y. Mambrini and J. Quevillon, Phys. Lett. B **709**, 65 (2012).

2.
New Phenomena

Searches from ep energy frontier at HERA

H. Pirumov on behalf of the H1 and ZEUS Collaborations
Heidelberg Physikalisches Institut, Philosophenweg 12, D-69120 Heidelberg, Germany

The latest results on a variety of searches for new physics at HERA by the H1 and ZEUS Collaborations are presented. HERA, the worlds only ep collider, was ideally suited for searches for physics beyond the Standard Model due to its unique initial state. The searches use the complete HERA data sample of the H1 and ZEUS experiments corresponding to a total integrated luminosity of about $0.5fb^{-1}$ per experiment. The following topics are covered: a search for *eqeq* contact interactions, a search for first generation leptoquarks, a search for lepton flavour violation, and a search for single-top production. The data is in a good agreement with the Standard Model predictions and limits on various new physics models are derived

1 Introduction

HERA, the world's only ep collider, provides a unique opportunity to search for new physics beyond the Standard Model. Two collider experiments, the H1 and ZEUS, have collected $0.5fb^{-1}$ of data each during the operation time from 1994 till 2007. HERA operation was divided in two phases. HERA I phase $(1994-2000)$ followed by an upgrade of the collider which increased the significantly luminosity. Another innovation during the HERA II running phase $(2003-2007)$ was that the lepton beam got a longitudinal polarisation which together with higher luminosity increased the sensitivity of the experiments to new physics.

2 Search for Contact Interactions

New physics may modify the neutral current (NC) deep inelastic scattering cross section at the highest values of the negative four-momentum transfer squared (Q^2). The concept of four-fermion contact interactions provides a convenient method to investigate those effects.

Searches for deviations from the Standard Model (SM) predictions in measured NC cross sections are performed by the H1 and ZEUS collaborations [1,2]. Since data show good agreement with the SM predictions varios new physics models are constrained. Limits at 95% confidence level (CL) are derived on the effective mass scale Λ in compositeness models ($\Lambda > 3.8-8.9$ TeV), on the effective Planck-mass scale in models with large extra dimensions ($M_S > 0.90-0.94$ TeV) and on the electroweak charge distribution radius of the quark ($R_q < 0.63 \cdot 10^{-18}$m). Both H1 and ZEUS limits are comparable. Exclusion ranges for different compositeness models obtained by H1 are shown on Figure 1.

3 Search for First Generation Leptoqurks

The full H1 and ZEUS data sample is analysed in a search for fist generation scalar and vector leptoquarks [3,4]. No evidence for the production of leptoquarks is observed. Limits on the

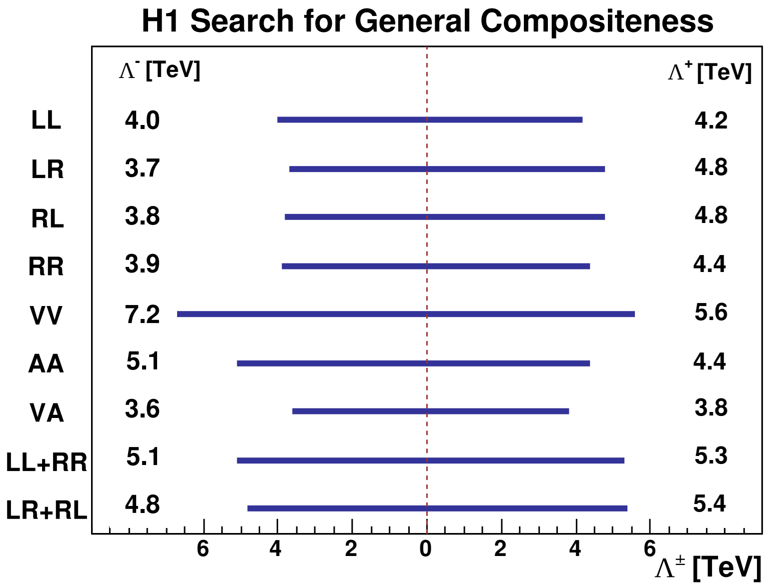

Figure 1: Lower limits on the compositeness scale Λ for both interference signs obtained by the H1.

masses and the couplings of leptoquarks in the Buchmüller-Rückl-Wyler (BRW) framework are derived. Exclusion limits on the coupling λ as a function of the leptoquark mass for vector type leptoquarks are shown on Figure 1. Assuming a coupling of electromagnetic strength ($\lambda \approx 0.3$) leptoquarks with masses up to 800 GeV are excluded.

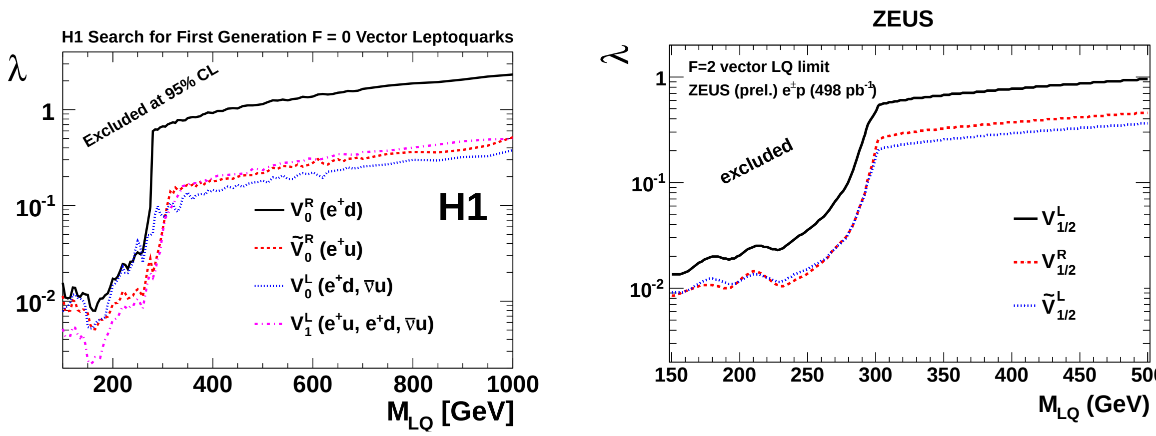

Figure 2: Exclusion limits for vector type leptoquarks described by the Buchmüller, Rückl and Wyler (BRW) model. The $95\% CL$ limits on the coupling λ as a function of leptoquark mass are shown. The left plot corresponds to the limits set by the H1 and the right plot indicates the limits obtained by ZEUS collaboration.

4 Search for Lepton Flavor Violation

Second and third generation leptoquarks, appearing in extensions of the BRW model, might induce lepton flavour violating (LFV) processes in ep collisions. A search for the processes $ep \to \mu X$ and $ep \to \tau X$, is performed by the H1 [5] using a data sample corresponding to an integrated luminosity of $0.41 fb^{-1}$. The data is consistent with the SM expectations and the results are interpreted in terms of exclusion limits on the masses and the couplings of second and third generation leptoquarks. Exclusion limits of coupling λ as a function of leptoquark mass for both channels are shown in Figure 3.

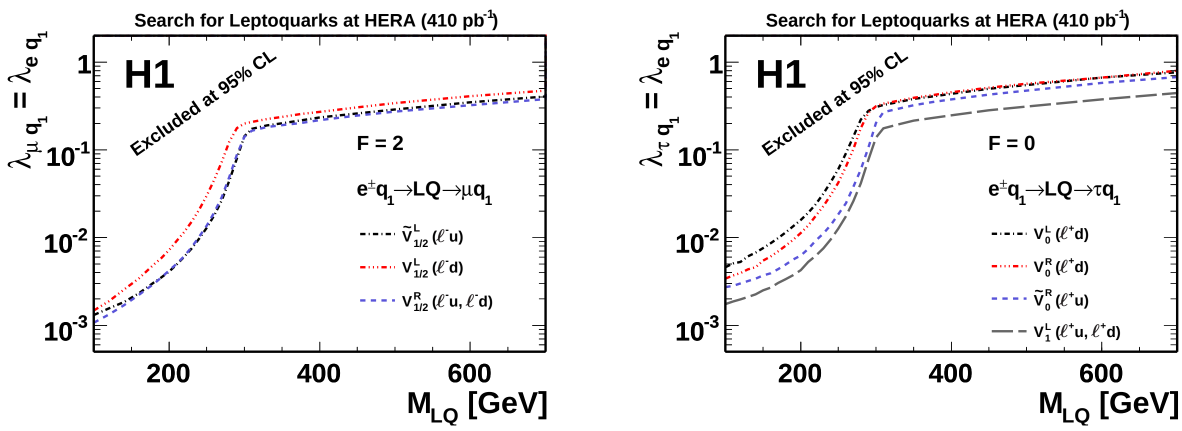

Figure 3: Exclusion limits on the coupling constants $\lambda_{\mu q} = \lambda_{eq}$ (left plot) and $\lambda_{\tau q} = \lambda_{eq}$ (right plot) as a function of the leptoquark mass M_{LQ} for vector type LQs. Regions above the lines are excluded at 95% CL. The notation $q1$ indicates that only processes involving first generation quarks are considered. The parentheses after the LQ name indicate the fermion pairs coupling to the LQ, where pairs involving anti-quarks are not shown.

5 Search for Single-top Production

The cross section of the single top quark production at HERA predicted by the SM is very small (less then $1fb$). However flavour changing neutral current (FCNC) processes could enhance the top production. The full data sample collected by ZEUS is used in a search for deviations from the SM due to FCNC top production [6]. No significant deviation from the SM expectations is observed and the results are used to set constraints on anomalous top production. An upper limit for a single-top production cross section at HERA is set $\sigma < 0.13pb$. Limits on the top anomalous branching ratios to the up quark and a photon ($BR_{u\gamma}$) or a Z boson (BR_{uZ}) is shown in the Figure 4.

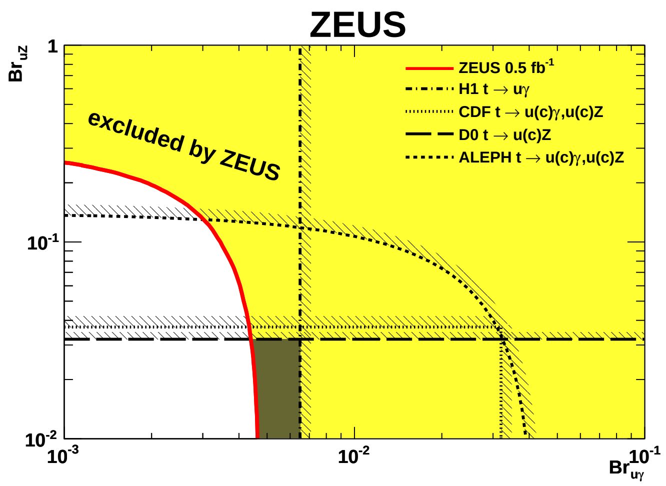

Figure 4: ZEUS boundary in the $(Br_{u\gamma}, Br_{uZ})$ plane. Also shown are the boundaries of the H1, CDF, D0, ALEPH experiments. The shaded area is excluded. The dark shaded region denotes the area uniquely excluded by ZEUS.

6 Summary

The complete HERA data sample of the H1 and ZEUS experiments with a total integrated luminosity of about $0.5 fb^{-1}$ per experiment is analyzed in searches for new physics. The data show good agreement with the SM predictions. Limits on contact interactions, first generation leptoquarks, lepton flavour violating processes are derived.

References

‘

1. F. D. Aaron *et al.* [H1 Collaboration], *Phys. Lett.* B **705**, 52 (2011) [arXiv:1107.2478].
2. [ZEUS Collaboration], “Search for Contact Interactions at HERA ”, ZEUS-prel-09-013.
3. F. D. Aaron *et al.* [H1 Collaboration], *Phys. Lett.* B **704**, 388 (2011) [arXiv:1107.3716].
4. [ZEUS Collaboration], “A search for resonance decays to lepton+jet at HERA and limits on leptoquarks”, ZEUS-prel-11-008.
5. F. D. Aaron *et al.* [H1 Collaboration], Eur. Phys. J. C **71**, 1572 (2011) [arXiv:1011.6359].
6. H. Abramowicz *et al.* [ZEUS Collaboration], *Phys. Lett.* B **708**, 27 (2012) [arXiv:1111.3901v2].

NEW PHENOMENA SEARCHES AT THE TEVATRON

L. ZIVKOVIC
Department of Physics, Brown University, Providence, RI 02912

In this article results from the searches for the new phenomena at D0 and CDF are reported. SUSY searches for the charginos and neutralinos, and the GMSB models are described. In addition, searches for the new resonances, and the dark matter are shown. As no signs of the new physics for these models are observed, the most stringent limits to date are presented.

1 Introduction

In spite of the great success of the standard model in description of the natural phenomena, many questions still remained unanswered. Thus many new models have been proposed in the past. Experiments at the Tevatron collider, CDF and D0 developed vigorous program to search for many models over the years. Even after the first successful year of the LHC experiments, some of the results from the CDF and D0 are the most stringent. Some of these results are presented in this report.

2 SUSY Searches

CDF [1] updated the search for the production of charginos ($\tilde{\chi}^{\pm}$) and neutralinos ($\tilde{\chi}^{0}$) in the final states with at least three leptons with 5.8 fb^{-1} of data. The final states under consideration are eel and $\mu\mu l$, where l is an electron or a muon or a hadronic tau or an isolated track. Events are selected if they have at least one central electron or muon with the $p_T > 20$ GeV. The second and the third leptons are required to have $p_T > 5$ GeV. Main background is the Drell-Yan process, with smaller contributions from diboson and $t\bar{t}$ production. Background model is verified in dedicated control regions. Signal region is obtained requiring that missing E_T, $\not\!\!E_T > 15$ GeV, that there is no more than one jet in the event, and that the invariant mass of the two leptons is $M_{ll} < 76$ GeV and $M_{ll} > 106$ GeV. Figure 1(left) shows dielectron mass of the selected events, and Fig. 1(middle) $\not\!\!E_T$ in dimuon channel. In the absence of the signal, limits interpreted in mSUGRA, benchmark with $m_0 = 60$ GeV, $tan\beta = 3$, $A_0 = 0$, and $M_{1/2} = 160$ GeV are set (Figure 1(right)).

CDF [2] searched for the chargino and neutralino supersymmetric particles with the same signed dilepton and one hadronically decaying τ-lepton in the final state using 6.0 fb^{-1} of data. Results of this search are interpreted in simplified models of SUSY, where limits are set on the particle masses. Two models of the simplified SUSY were considered, one similar to the mSUGRA and another, similar to the GMSB. In the simplified gravity model, $\tilde{\chi}_1^{\pm} - \tilde{\chi}_2^0$ pairs are produced via electroweak interaction, and further decay into slepton ($\tilde{l}^{\pm}$) and neutrino (ν), and $\tilde{l}^{\pm}$ and lepton ($l^{\pm}$). To enhance production of the τ-leptons in final state, two branching ratios were selected: $BR(\tilde{\chi}_2^0, \tilde{\chi}_1^{\pm} \rightarrow \tilde{\tau}^{\pm} + X = 1, 1/3$. In a simplified gauge model, the LSP

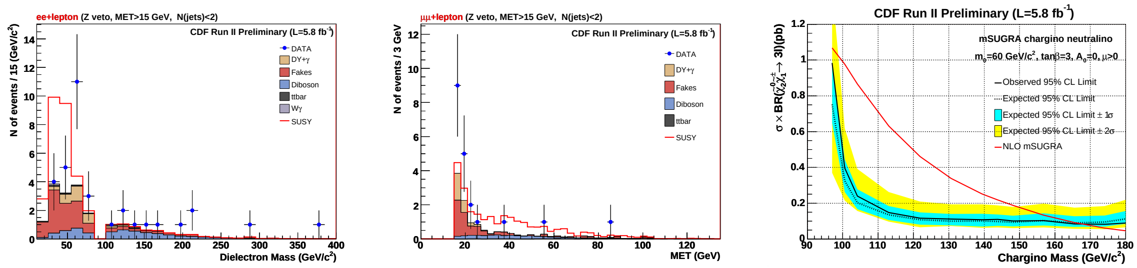

Figure 1: Invariant mass of the two leptons (left), the missing ET (middle) and the limit on chargino neutralino production as a function of chargino mass (right).

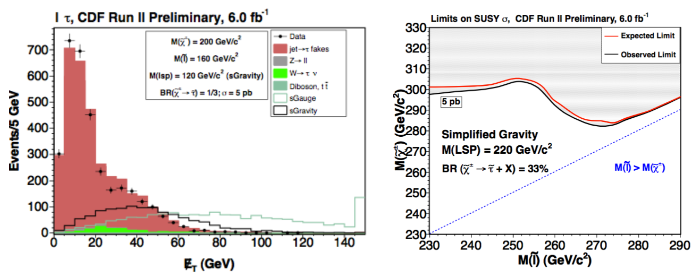

Figure 2: The $\not{E}_T$ (left) and the limit on the $\tilde{\chi}_1^{\pm}, \tilde{l}^{\pm}$ masses.

is gravitino which is very light, and charginos don't couple to the right handed leptons, thus $BR(\tilde{\chi}^{\pm}1 \to \tilde{\tau}_1^{\pm}\nu_\tau) = 1$. Events are selected if they contain pair of electrons and muons with $p_T > 10$ GeV with the same charge, and hadronic τ with $p_T > 15$ GeV. It is further required that the scalar sum of the p_T of the leptons, hadronic τ and missing E_T is greater than 45 GeV. Signal is searched in events with $\not{E}_T > 20$ GeV (Figure 2(left)), and since no significant excess is observed, limits on the masses of the $\tilde{\chi}_1^{\pm}, \tilde{l}^{\pm}$ (Figure 2(right)).

D0 [3] presented the first search for SUSY in $Z\gamma$ final states with large missing transverse energy using 6.2 fb^1. These signatures are predicted by GMSB SUSY models where the lightest neutralino, $NLSP$, is produced in pairs. They decay to either a Z boson or a photon and to a gravitino that escapes detection. The model considered in this search is parametrized by an effective SUSY breaking scale Λ. Events are selected if they contain pair of oppositely charged leptons consistent with a Z-boson, γ and large $\not{E}_T$ (Figure 3 (left)). Signal is further separated from backgrounds using Boosted Decision Tree (BDT) technique (Figure 3 (middle)). In the absence of any significant excess limits are set. A model with the $\Lambda < 87$ TeV is excluded and also the lightest neutralino with $m < 151$ GeV is excluded (Figure 3 (right)).

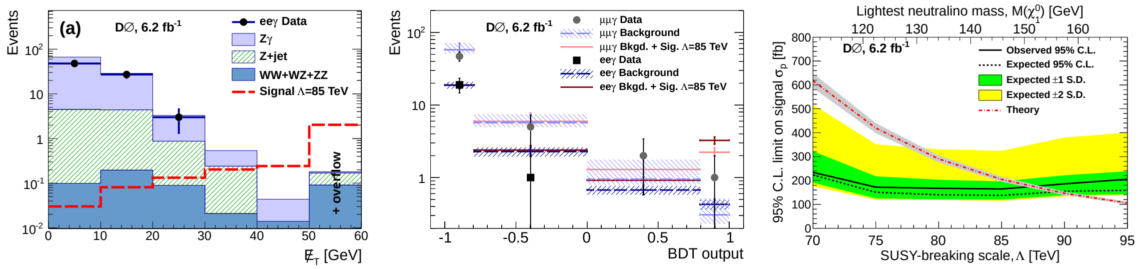

Figure 3: The missing E_T (left), output of the BDT middle, and the limit of the signal cross section as a function of the Λ (right).

3 Non SUSY Searches

3.1 Searches for resonances

CDF [4] searched for a high-mass resonances decaying into the Z boson pairs using data corresponding to the 6 fb^{-1}. Many theories present models with a resonance decaying to a pair of the Z bosons, for instance Randall Sundrum graviton (G^*), where the G^* couplings to light fermions and photons are heavily suppressed. The process examined in this search is $G^* \to ZZ \to ll + X$, where $X = ll$, jj or $\nu\nu$. Leptons are selected with $p_T > 20$ GeV, and jets with $p_T > 25$ GeV. In the $ZZ \to ll$ channel, it is required that leptons with the same flavor are consistent with a Z boson. Signal is searched as an in M_{ZZ}. In the $ZZ \to ll\nu\nu$ signal events are selected if $\not{E}_T > 100$ GeV and excess is looked for in the visible mass of the ZZ system, defined as the invariant mass of the sum of the two charged lepton four-momenta and the four-vector representing the $\not{E}_T, (\not{E}_T(x), \not{E}_T(y), 0, \not{E}_T)$ (Figure 4(middle)). In $ZZ \to lljj$ channel, selection of the $Z \to jj$ is done in the two steps. First, all pairs of jets with invariant mass between 70 and 110 GeV are kept. Then, the constrained fit is used to select the best candidate. The invariant mass of the two Z bosons is then used to search for the excess (Figure 4 in the $lljj$ final state (left) and $ll\nu\nu$ final state (middle)). Since no significant excess has been observed, the limit is set as shown on Figure 4(right).

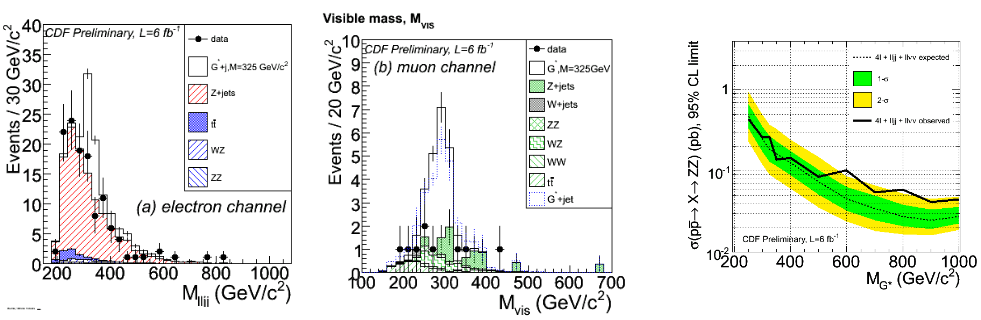

Figure 4: Invariant mass of the ZZ system in the $lljj$ final state (left) and the visible mass of the ZZ system $ll\nu\nu$ final state (middle). Limit on the graviton production as a function of its mass.

3.2 Searches for dark matter

CDF [5] searched for dark matter production in the monojet + missing transverse energy signature in 6.7 fb^{-1} of data. The process under study is $p\bar{p} \to \bar{\chi}\chi + jet$, where χ is the dark matter particle and the jet originates from initial state radiation. Events with significant missing E_T, $\not{E}_T > 60$ GeV and one energetic jet, $p_T > 60$ GeV are selected. Main background processes are multijets production obtained from data, and electroweak (W and Z) obtained from simulation, but normalized to data in the dedicated control region. Signal is searched in the the region of the high p_T of the jet as shown in Figure 5(left). In the absence of a significant excess, upper limits are set Figure 5(right). These limits are converted into constraints on the dark matter-nucleon cross section and they are comparable to the results of direct searches (Figure 6).

Acknowledgements

We thank the staffs at Fermilab and collaborating institutions, and acknowledge support from the DOE and NSF (USA); CEA and CNRS/IN2P3 (France); FASI, Rosatom and RFBR (Russia); CNPq, FAPERJ, FAPESP and FUNDUNESP (Brazil); DAE and DST (India); Colciencias

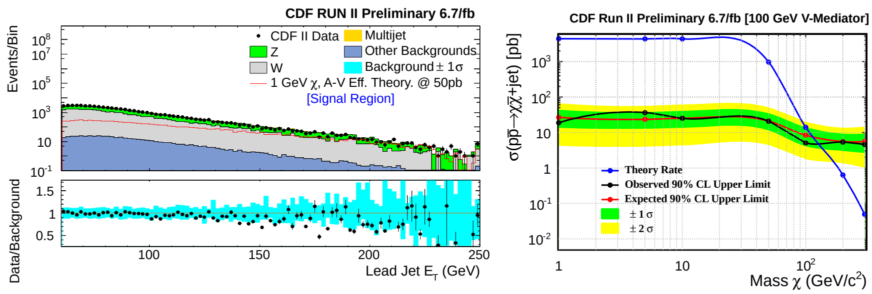

Figure 5: The leading jet p_T (left) and the limit on dark matter production as a function of its mass (right).

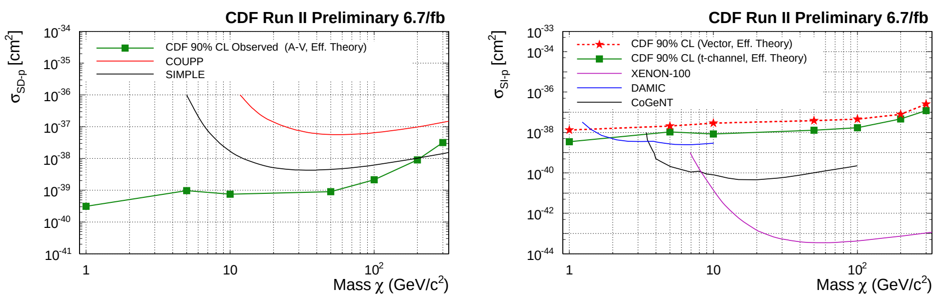

Figure 6: Limits on the dark matter-nucleon cross section compared with the results from direct searches.

(Colombia); CONACyT (Mexico); KRF and KOSEF (Korea); CONICET and UBACyT (Argentina); FOM (The Netherlands); STFC and the Royal Society (United Kingdom); MSMT and GACR (Czech Republic); CRC Program and NSERC (Canada); BMBF and DFG (Germany); SFI (Ireland); The Swedish Research Council (Sweden); and CAS and CNSF (China). Author in particular thanks NSF for a support to attend the conference.

References

1. T. Aaltonen *et al.* [CDF Collaboration], CDF Note 10636 (2011).
2. T. Aaltonen *et al.* [CDF Collaboration], CDF Note 10611(2011).
3. V. M. Abazov *et al.* [D0 Collaboration], arXiv:1203.5311 [hep-ex].
4. T. Aaltonen *et al.* [CDF Collaboration] *Phys. Rev.* D **85**, 012008 (2012)
5. T. Aaltonen *et al.* [CDF Collaboration], arXiv:1203.0742 [hep-ex].

LEPTONIC SUSY SEARCHES AT THE LHC

GEORGIA KARAPOSTOLI
Department of Physics,
Imperial College London, London, UK

This paper summarizes recent results from the LHC on Supersymmetry searches using leptonic signatures. The public results were produced using data collected within 2011 and correspond to $4.7fb^{-1}$ and $2.05fb^{-1}$ of integrated luminosity from the CMS and ATLAS collaborations respectively. The searches cover a wide range of leptonic analyses using single-lepton, double-lepton final states, the latter split in Opposite- and Same-sign di-lepton final states, multi-lepton ones, as well as their extensions by requiring b-tagged jets in some cases. Overall, no New Physics excess has been observed with respect to the Standard Model expectations, whereas Exclusion limits have been produced to set constraints to a number of such physics models.

1 Introduction

The CMS [1] and ATLAS [2] collaborations have developed a robust set of analyses using the latest 2011 LHC data, in the search of New Physics and particularly the discovery of Supersymmetry (SUSY). In this proceedings, we give an overview of the SUSY analyses with leptons in the final state, accompanied by jets and Missing Transverse Energy (MET), and present their public results which were produced using data collected in 2011 and correspond to $4.7fb^{-1}$ and $2.05fb^{-1}$ of integrated luminosity, for CMS and ATLAS respectively.

Both CMS and ATLAS analyses have been evolved following standard cut-and-count techniques, whereas many of them have been extended in a non-standard way, for example using Artificial Neural Networks (ANN) or adding b-tagging information to probe more exclusive signatures. With respect to the Summer 2011, the present Analyses have acquired a factor 2 to 3 increase in luminosity, whereas in addition new methodologies that were not pursued before appear in a complementry way to extend the coverage of the SUSY phase space.

2 Single-lepton SUSY searches

The one-lepton + MET + jets signature is prominent in models based on SUSY. Such searches are complicated by the presence of Standard Model (SM) backgrounds that can share many of the features of SUSY events. These backgrounds arise mainly from the production of $t\bar{t}$ and W+jets, with smaller contributions from Z+jets, single-top production and QCD multijet events. To determine the contribution of these backgrounds, CMS and ATLAS use methods that are primarily based on control samples in the data, sometimes in conjunction with certain reliable information from simulated event samples.

The CMS analysis comprises two methods have been used to probe the event data sample [3]. One of them, the Lepton Spectrum (LS) method, uses the observed lepton transverse momentum (p_T) spectrum and other control samples to predict the MET spectrum associated with the SM backgrounds (figure 1), which applies to SUSY models in which the MET distribution is decoupled from the lepton

p_T spectrum. Twelve signal regions are considered, specified by three thresholds on H_T and four bins of MET. In the absence of any significant excess of observed events in the data, the results of the above analyses have been interpreted in the framework of the Constrained Minimal Supersymmetric SM (cMSSM), reporting exclusion regions as a function of $m_{1/2}$ and m_0, for $\tan\beta = 10$ (see figure 2). These results exclude gluino masses below ≈ 1.1 TeV for m_0 below ≈ 750 GeV.

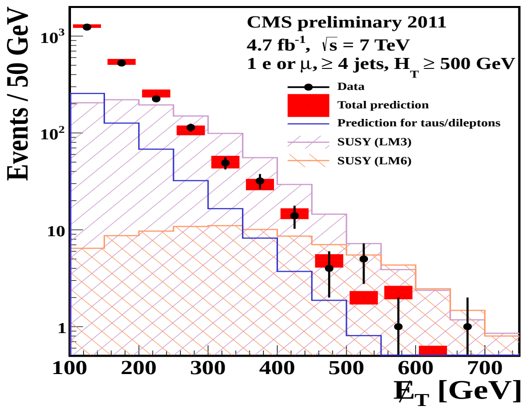

Figure 1: Observed MET distributions in data compared with predicted distributions (red bars) in the combined electron and muon channels, for $H_T > 500$ GeV.

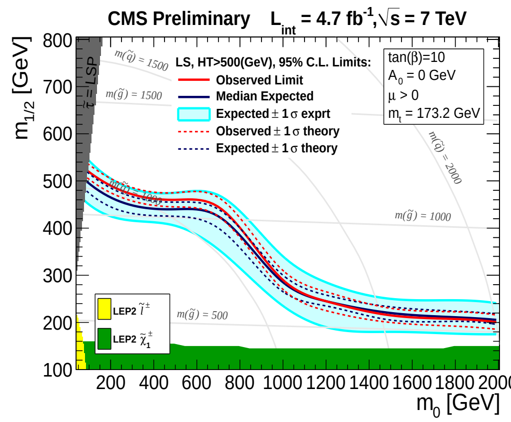

Figure 2: The 95% CL exclusion contours obtained from the $H_T > 500$ GeV search region are shown in the cMSSM $m_{1/2}$ vs m_0 plane.

The corresponding ATLAS analysis used 1.04 fb^{-1} of data of the first half of 2011. The search [4] is carried out in four distinct signal regions with either three or four jets and variations on the (missing) transverse momentum and effective mass cuts, resulting in optimized limits for various supersymmetry models.

3 Di-lepton SUSY searches in the opposite-sign and same-sign channels

We then proceed to the searches in final states with opposite-sign (OS) isolated lepton pairs accompanied by hadronic jets and missing transverse energy.

Because beyond the SM (BSM) physics is expected to have large hadronic activity and MET, the CMS analysis [5] defines two signal regions that reject all but $\approx 0.1\%$ of the dilepton $t\bar{t}$ events, by adding requirements of large MET and H_T. We perform counting experiments in these signal regions, and compare the observed yields with the predictions from two independent background estimation techniques based on data control samples, as well as with SM and BSM MC expectations. A complementary analysis is the search for a di-lepton edge which is sensitive to new physics models which do not have very large MET and H_T. Such analyses probe more exclusive signatures arising for example from SUSY events with the χ_2^o decaying to $\tilde{\ell}\ell \to \chi_1^o \ell^+\ell^-$. The OS di-lepton inclusive analysis has also been extended to use ANN [6], which allowed complementarity in the SUSY phase space to probe lower MET/H_T regions[a].

An additional CMS search looks for evidence of BSM physics in final states containing a Z boson that decays to a pair of oppositely-charged isolated electrons or muons [7]. This strategy is favored in the search for SUSY models with the production of a Z boson in the decay $\chi_2^o \to \chi_1^o Z$. The dominant background consists of SM Z production accompanied by jets from initial-state radiation (Z + jets). Two complementary strategies are used to suppress the dominant Z + jets background, -arising primarily when jet energies are mismeasured-, and to estimate the remaining background from data control samples: the jet-Z balance method (JZB) and the MET template method.

[a] Public results correspond to an integrated luminosity of 2.2 fb^{-1}.

Overall, the above analyses find no evidence for anomalous yields beyond the SM expectations and place upper limits on the non-SM contributions to the yields in their signal regions. The results have been interpreted in the context of the CMSSM and simplified model spectra.

We turn now to the SUSY searches with same-sign (SS) isolated lepton pairs (including taus decaying hadronically), missing transverse energy, and hadronic jets. Such events in hadron collisions are very rare in the SM but appear very naturally in many new physics scenarios. A baseline selection region has been defined for each of the following three dilepton categories: inclusive di-leptons, high-p_T leptons, and tau di-leptons, each binned in the H_T-MET plane. Backgrounds in all of these searches are dominated by one or two jets mimicking the lepton signature ("fake" lepton background), which are estimated from data using multijet control samples with two SS leptons. Overall, no evidence for an excess over the background prediction has been observed. A search for SUSY with two same-sign leptons, jets and missing transverse momentum has also been performed using 2.05 fb^1 of ATLAS data[8]. With no events observed in the selected signal regions, limits have been derived in the context of simplified models where top quarks are produced in gluino decays and mSUGRA/CMSSM scenarios (see figure 3). In all these signal models, gluino masses below 550 GeV are excluded within the parameter space considered and gluino masses up to 700-750 GeV can be excluded depending on the model parameters.

While in general the hadronic jets in these anomalous processes can originate from light flavor, there is a range of well-established models predicting the presence of two to four b-quark jets in such events. These appear naturally in signatures of SUSY where bottom- and top- quark superpartners are lighter than other squarks, enhancing the fraction of strongly produced SUSY events with top and bottom quarks in the final states. A counting signature-based experiment[9] is performed by comparing the event yield with the expected signal and backgrounds. We observe no significant deviations from the SM expectations. We have used these results to set limits on the parameter space of two models of same-sign top pair production, two models of gluino decay into virtual or real stop quarks, a model of sbottom pair production, and a model of sbottom production from gluino decay (see figure 4).

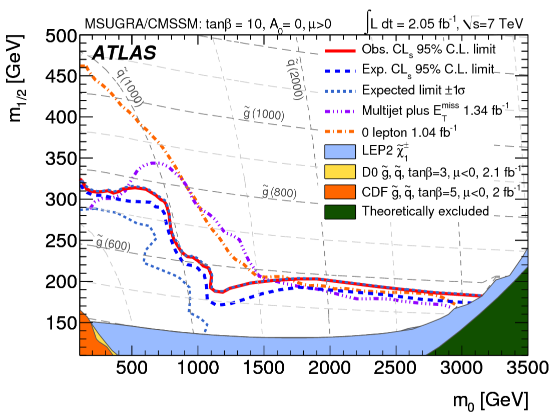

Figure 3: Expected and observed 95% CL exclusion limits in the MSUGRA/CMSSM (m_0, $m_{1/2}$) plane for $\tan\beta = 10$, $A_0 = 0$ and $\mu > 0$.

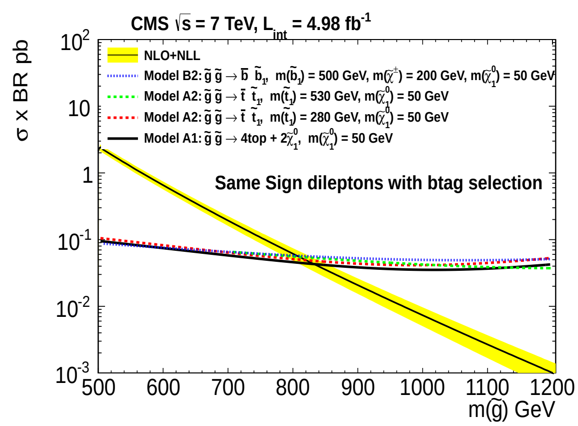

Figure 4: Gluino pair-production cross-section as a function of gluino mass compared with limits on the cross-section from various models.

4 Multi-lepton searches and the EWK interpretation

This following search focuses on the associated production and leptonic decays of charginos and neutrali- nos. The direct production of light charginos and neutralinos, at the LHC, can be abundant which in turn can give rise to a low-background signature with three SM leptons and sizable missing transverse momentum. The analysis has been based on $2.06 fb^1$ of data collected with the ATLAS detector[10]. No significant excess of events has been found in data. The null result is interpreted in the pMSSM and in simplified models. For the simplified models, degenerate lightest chargino and next-to-lightest neutralino masses are excluded up to 300 GeV for mass differences to the lightest neutralino up to 250 GeV.

Multilepton final states can also be produced in R-parity violating (RPV) scenarios. A relevant search looks for supersymmetric particles in final states with four or more leptons (electrons or muons) and missing transverse momentum. The ATLAS analysis [11] uses a sample corresponding to an integrated luminosity of 2.06 fb^1 of proton-proton data. After applying a Z boson veto for leptons pairs with the same flavour and opposite charge, no events are observed for 0.7 ± 0.8 events expected. Within the selection acceptance, we determine 95% C.L. exclusion limits in the cMSSM, as shown in figure 5.

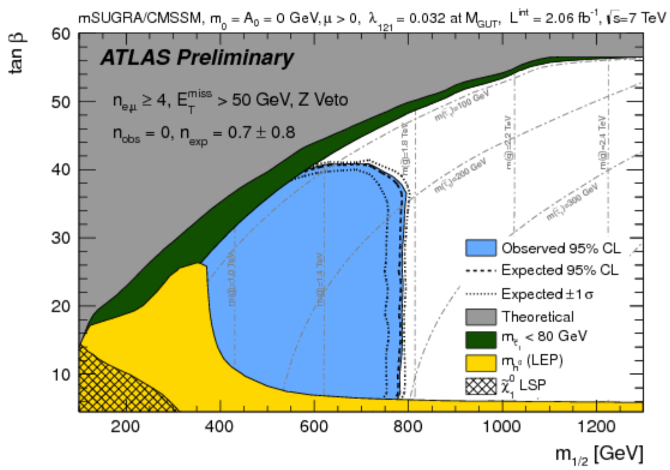

Figure 5: Expected and observed 95% CL exclusion limits in the mSUGRA/CMSSM ($m_{1/2}$, $\tan\beta$) plane for $m_0 = A_0 = 0$ and $\mu > 0$, as derived with the ATLAS multi-lepton analysis at $2.06 fb^{-1}$.

5 Tau channels

This note reports on the search for events with large MET, jets, and at least two hadronically decaying τ leptons [12], [13]. The dominant backgrounds are from top-pair plus single top events and W events, in which one real τ is correctly reconstructed and the other τ candidates are mis-reconstructed from hadronic activity in the final state. This background contribution is determined in a control region defined by inverting the effective mass (Meff) cut. No excess above the SM background expectation is observed and a 95 % CL visible cross section upper limit for new phenomena at 2.9 fb^{-1} is set. For a minimal model of gauge-mediated supersymmetry breaking (GMSB), limits on the production cross section are set. A 95 % CL lower limit of 32 TeV is set on the GMSB breaking scale Λ independent of $\tan\beta$. Finally, ATLAS results from a search in final states with one or more τ leptons, are interpreted in the context of GMSB models with Mmess = 250 TeV, $N_5 = 3$, $\mu > 0$, and $C_{grav} = 1$, excluding the production of supersymmetric particles up to $\Lambda = 40$ TeV for $\tan\beta > 15$ at 95% C.L.

References

1. The CMS Collaboration, JINST 3 S08004 (2008).
2. The ATLAS Collaboration, JINST 3 S08003 (2008).
3. CMS Collaboration, CMS-PAS-SUS-12-010.
4. ATLAS Collaboration, Phys.Rev. D85 (2012) 012006.
5. CMS Collaboration, CMS-PAS-SUS-11-011.
6. CMS Collaboration, CMS-PAS-SUS-11-018.

7. CMS Collaboration, CMS-SUS-11-021, submitted to PLB: arXiv:1204.3774.
8. ATLAS Collaboration, ATLAS-CONF-2012-004, submitted to Phys Rev Lett., arXiv:1203.5763.
9. CMS Collaboration, CMS-PAS-SUS-11-020, submitted to JHEP: arXiv:1205.3933.
10. ATLAS Collaboration, ATLAS-CONF-2012-035, arXiv:1204.5638.
11. ATLAS Collaboration, ATLAS-CONF-2012-001.
12. ATLAS Collaboration, arXiv:1204.3852.
13. ATLAS Collaboration, arXiv:1203.6580.

Searches for Resonances at the LHC

Edward Moyse
Department of Physics, University of Massachusetts, 710 North Pleasant St, Amherst, USA

On behalf of the ATLAS and CMS Collaborations

Data taken in 2011 with the ATLAS and CMS detectors at the LHC have been used to search for resonances. Results are presented based on up to 5 fb^{-1} of $\sqrt{(s)} = 7$ TeV proton-proton collisions in final states which include dileptons, diphotons, dijets, jets+photons, dibosons, MET+charged lepton and $t\bar{t}$. No evidence of new physics is seen, but limits have been placed on various benchmark models.

1 Introduction

Many proposed extensions to the Standard Model (SM) of particle physics are expected to be expressed in heavy resonances visible at the LHC. These proceedings detail the search for resonances with the ATLAS [1] and CMS [2] detectors, using data taken from the 2011 LHC run.

No excesses were seen, so the following will concentrate on documenting the latest limits, grouped together via various final state topologies (and which are listed in approximate order of experimental complexity): dileptons; diphotons; dijets; jets+photons; diboson; MET+charged leptons; ditop ($t\bar{t}$).

The results are interpreted in terms of benchmark models, but most limits are presented in a general way and can therefore be interpreted in other models. The benchmarks used include: the Randall-Sundrum (RS) model, which predicts a tower of Kaluza-Klein (KK) excitations of the graviton/gluon; a Z', either from the Sequential Standard Model (SSM), where the new gauge bosons are assumed to have SM-like couplings, or from additional large symmetry groups (such as E6); or finally, a generic resonance with a mass and width.

2 Dilepton resonances

Dilepton final states are characterised by very clean signatures and are predicted by SM-extensions including: extra heavy gauge bosons, techni-mesons, and RS gravitons. Figure 1 shows the $\mu\mu$ mass spectra for ATLAS using 5 fb^{-1} of data, as well as the stacked sum of background processes (of which Drell-Yan is the most significant component) [3]. Mass spectra are consistent with expectations from SM, and so in Table 1 the newest limits are shown, whilst Figure 2 shows the CMS 95% Confidence Limits (CL) for various benchmark models in 4.9 fb^{-1} [4].

3 Diphoton resonances

In addition to their clean signature, the branching ratio (BR) for spin-2 gravitons decaying to diphotons is double that to lepton final states. The main irreducible background is SM

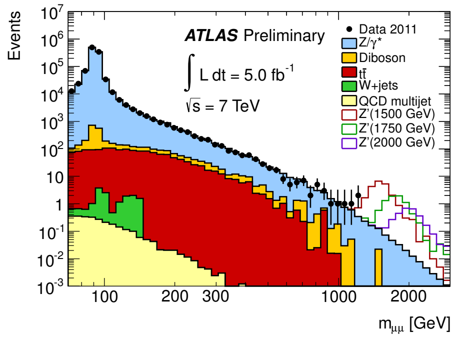

Figure 1: Invariant mass spectrum of dimuon events for ATLAS. The points with error bars represent the data. The uncertainties on the data points (stat. only) represent 68% confidence intervals for the Poisson means. The histograms represent the SM expectation [3].

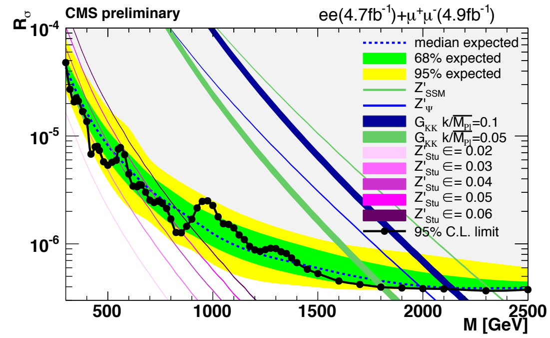

Figure 2: Upper limits on the production ratio $\sigma \times BR$ of cross section times branching fraction into $\mu\mu$/ee pairs for Z'_{SSM}, Z'_{Ψ}, and G_{KK} production. Shaded yellow(red) bands correspond to the 68%(95%) quantiles for the expected limits [4].

$\gamma\ \gamma$ production (estimated by simulation), whilst the reducible component consists mainly of γ+jet and jet+jet (estimated from data). With 2.2 fb^{-1} CMS excludes a RS graviton with mass less than 0.86(1.84) TeV for couplings $k/\bar{M}_{PL} = 0.01(0.1)$ [5], whilst with 2.12 fb^{-1} (and in combination with the dilepton result) ATLAS excludes masses less than 0.80 (1.95) TeV for $k/\bar{M}_{PL} = 0.01(0.1)$ [6].

4 Dijet resonances

Dijets are sensitive to a variety of beyond-SM physics, such as string resonances, excited quarks, RS gravitons etc. The exclusions for excited quarks in ATLAS [7] are shown in Table 1 (CMS has also excluded: m_{q^*} <2.49 TeV; String Resonances < 4.00 TeV; E6 Diquarks< 3.52 TeV; and Axigluons/Colorons < 2.47 TeV [8]). ATLAS's invariant mass distribution and CL are shown in Figures 3 and 4 respectively. ATLAS used 4.8 fb^{-1} of data, whilst CMS used 1.0 fb^{-1}.

5 Photon plus Jet resonances

The benchmark model is an excited quark, and with this final state and 2.11 fb^{-1} of data, ATLAS has excluded [9] a q^* with mass less than 2.46 TeV.

6 Diboson resonances

For the beyond-SM graviton mediated ZZ resonances, there are two final states consider: $llll$ and $lljj$. The ATLAS graviton mass limits [10], produced with 1.02 fb^{-1}, are shown in Table 1, whilst the CL plot is shown in Figure 5. It is also possible to look for resonant structure in decay of $WZ \to ll l\nu$, predicted, for example, by Low Scale Technicolor Model. The CMS ρ_{TC} mass limits [11], produced with 4.7 fb^{-1}, are shown in Table 1, whilst the CL plot is shown in Figure 6. ATLAS has also excluded [12] a ρ_{TC} with mass less than 467 GeV (using 1.02 fb^{-1}).

7 $t\bar{t}$ resonances

Topcolor Z' decays preferentially to t or u, whilst the chosen RS KK gluon models couple more strongly to the top than other SM particles. Various final states have been considered: all-hadronic (6 jets); semi-leptonic $(qqb)(\mu\nu b)$; dilepton. As the decay products are boosted, jets can merge so the analyses must look for 'subjets' and use different algorithms depending on

Table 1: Some of the newer limits set at the LHC. See the referenced texts for more details.

Final state	Experiment	Mass Limits (GeV)	
Dilepton	ATLAS	$Z'_{SSM} > 2210$	$RS\ G_{KK} > 2160$ for $k/\bar{M}_{PL} = 0.1$
	CMS	$Z'_{SSM} > 2320$	$RS\ G_{KK} > 1810(2140)$ for $k/\bar{M}_{PL} = 0.05(0.1)$
Dijet	ATLAS	$q^* > 3350$	
Diboson	ATLAS ZZ	$RS\ G_{KK} > 845$ or < 325 for $k/\bar{M}_{PL} = 0.1$	
	CMS WZ	$W'_{SSM} > 1141$	$\rho_{TC} > 935$ or < 180
$t\bar{t}$	ATLAS l+jets	$Z'_{SSM} > 860$ or < 500	$g_{KK} > 1025$ or < 500
	CMS all-had.	$Z'_{TC} < 1000$ or > 1600 (width $\Gamma_{Z'}/m_{Z'} = 3\%$	

the event topology. Figure 7 shows the CMS limits for Z' for the all-hadronic channel [13] in 4.6 fb^{-1}, whilst new ATLAS limits using lepton+jets [14] and 2.05 fb^{-1} are shown in Table 1 and Figure 8. Using 4.33 fb^{-1} of data in the e+jets channel, CMS has put a limit of 2.51 pb for Z' mass of 1 TeV [15]. Finally, with 1.04 fb^{-1} ATLAS [16] has used the dilepton channel to exclude $m_{g_{KK}} < 840$ GeV.

References

1. ATLAS Collaboration, *The Atlas Experiment at the CERN Large Hadron Collider*, JINST **3** (2008) S08003.
2. CMS Collaboration, *The CMS Experiment at the CERN Large Hadron Collider*, JINST **3** (2008) S08004.
3. ATLAS Collaboration, ATLAS-CONF-2012-007, `https://cdsweb.cern.ch/record/1428547`.
4. CMS Collaboration, PAS EXO-11-019, `https://twiki.cern.ch/twiki/bin/view/CMSPublic/PhysicsResultsEXO11019Winter2012`.
5. CMS Collaboration, arXiv:1112.0688
6. ATLAS Collaboration, *Phys. Lett.* B **710**, 538-556 (2012)
7. ATLAS Collaboration, ATLAS-CONF-2012-038, `https://cdsweb.cern.ch/record/1432206`
8. CMS Collaboration, *Phys. Lett.* B **704**, 123 (2011)
9. ATLAS Collaboration, arXiv:1112.3580 (submitted to *Phys. Rev. Lett.*)
10. ATLAS Collaboration, arXiv:1203.0718 (submitted to *Phys. Lett.* B)
11. CMS Collaboration, CMS-PAS-EXO-11-041, `https://twiki.cern.ch/twiki/bin/view/CMSPublic/PhysicsResultsEXO11041Winter2012`
12. ATLAS Collaboration, arXiv:1204.1648 (submitted to *Phys. Rev.* D)
13. CMS Collaboration, arXiv:1204.2488
14. ATLAS Collaboration, ATLAS-CONF-2012-029, `https://cdsweb.cern.ch/record/1430738`
15. CMS Collaboration, CMS-PAS-EXO-11-092, `https://cdsweb.cern.ch/record/1423037`
16. ATLAS Collaboration, ATLAS-CONF-2011-123, `https://cdsweb.cern.ch/record/1376423`

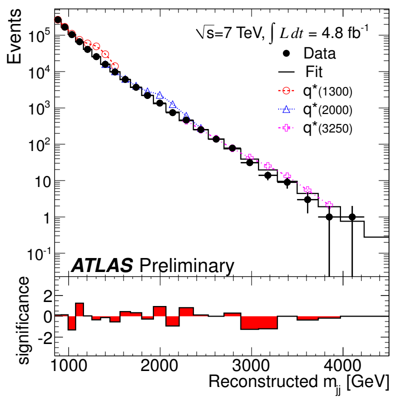

Figure 3: The reconstructed dijet mass distribution (filled points) fitted with a smooth functional form (solid line). Mass distribution predictions for three excited quark masses are shown above the background. The bin-by-bin significance of the data-background difference is shown in the lower panel [7].

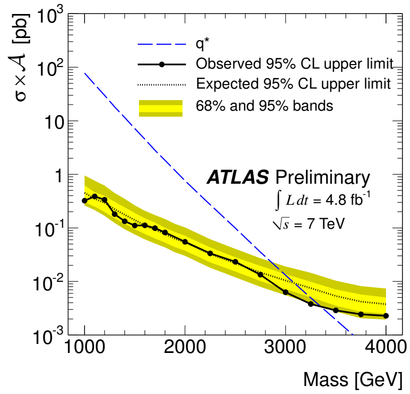

Figure 4: The 95% CL upper limits on $\sigma \times$A as a function of particle mass (black filled circles) for excited quarks. The black dotted curve shows the 95% CL upper limit expected from Monte Carlo and the light(dark) yellow shaded bands represent the 68% (95%) contours of the expected limit [7].

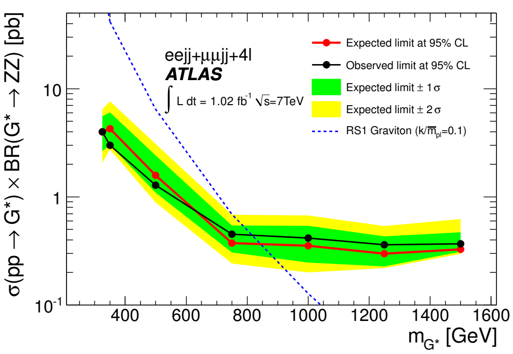

Figure 5: Expected and observed 95% CL limits for G* to ZZ for the combined lljj+llll channels. The leading-order theoretical prediction is also shown for $k/m_{pl} = 0.1$ [10].

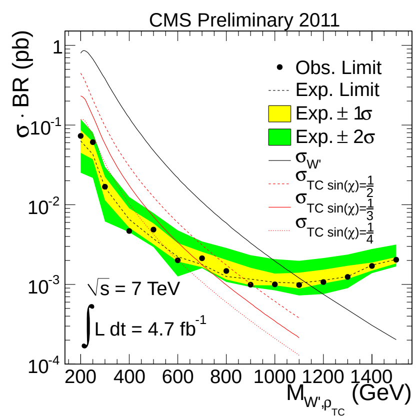

Figure 6: Expected and observed upper limit on $\sigma \times BR$ for W' and ρ_{TC} [11].

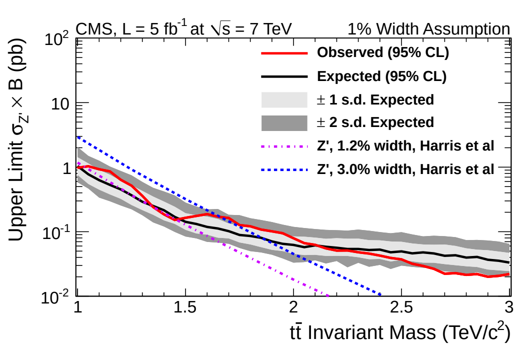

Figure 7: Limits on the possible cross section times branching ratio of $t\bar{t}$ resonances. This plot uses Z' sample with 1% width assumption [13].

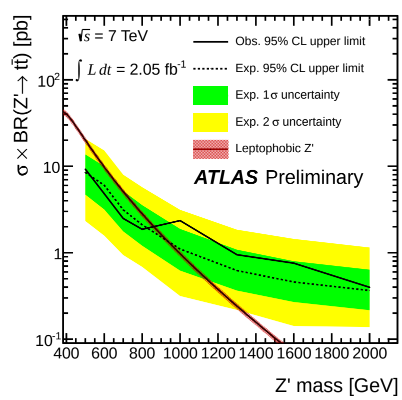

Figure 8: Limits on the possible $\sigma \times$BR of $t\bar{t}$ resonances. This plot uses Z' sample with 1% width assumption. Expected (dashed line) and observed (solid line) upper limits on $\sigma \times$BR ($Z \to t\bar{t}$). The red lines correspond to the predicted $\sigma \times$BR for the leptophobic model [14].

Searches for New Phenomena at the LHC

Lars Sonnenschein
on behalf of the CMS and ATLAS collaborations
RWTH Aachen University, III. Phys. Inst. A,
52056 Aachen, Germany

Searches for physics beyond the Standard Model (SM) with the CMS [1] and ATLAS [2] experiments in pp collisions at a centre of mass energy of $\sqrt{s} = 7$ TeV at the LHC are presented. The discussed results are based on data taken in 2011, making use of integrated luminosities between $\mathcal{L}$ =1.1 and 4.9 fb^{-1}. Various important theories, encompassing TeV scale gravity, quark/lepton compositeness, contact interactions, new heavy vector bosons and other exotic signatures are probed.

1 Introduction

In the following is focused on non-resonant search channels where the invariant mass of a new particle can not be fully reconstructed due to its decay modes including undetected daughter particles or where the signal does not consist of the production of a resonant particle. Only new results (after the HCP conference in November 2011) are presented. A complete list of public analysis results in exotic searches for new physics (preliminary, published and submitted or accepted for publication) can be found in ref. [3] and ref. [4].

The next section covers the search for TeV scale gravity. The subsequent searches are dedicated to numerous different model interpretations and are categorised according to their final states into lepton production (section 3), lepton plus jet production (section 4) and jet production (section 5). In each category only one analysis is discussed here exemplarily. Further presented analyses are cited accordingly. Throughout this article the convention $c \equiv 1$ is adopted for the speed of light.

2 TeV scale gravity

The CMS search [5] for microscopic black holes is based on $\mathcal{L} = 4.7$ fb^{-1}. Energetic multiparticle final states including jets, bosons and leptons are selected by means of the scalar transverse momentum sum S_T, taking into account also the missing transverse energy E_T^{miss} of the event. The left plot in Fig. 1 shows the S_T distribution of the data for the $N \geq 3$ final state object multiplicity bin, together with the predicted background which is dominated by multijet production and has been estimated by means of the data.

Limits are set on production cross sections (Fig. 1, right) as a function of the minimum black-hole mass. These limits are interpreted in terms of minimal Quantum Black Hole masses $m_{\text{QBH}}^{\text{min}}$ as a function of the multidimensional Planck mass M_D for several extra dimensions. Further

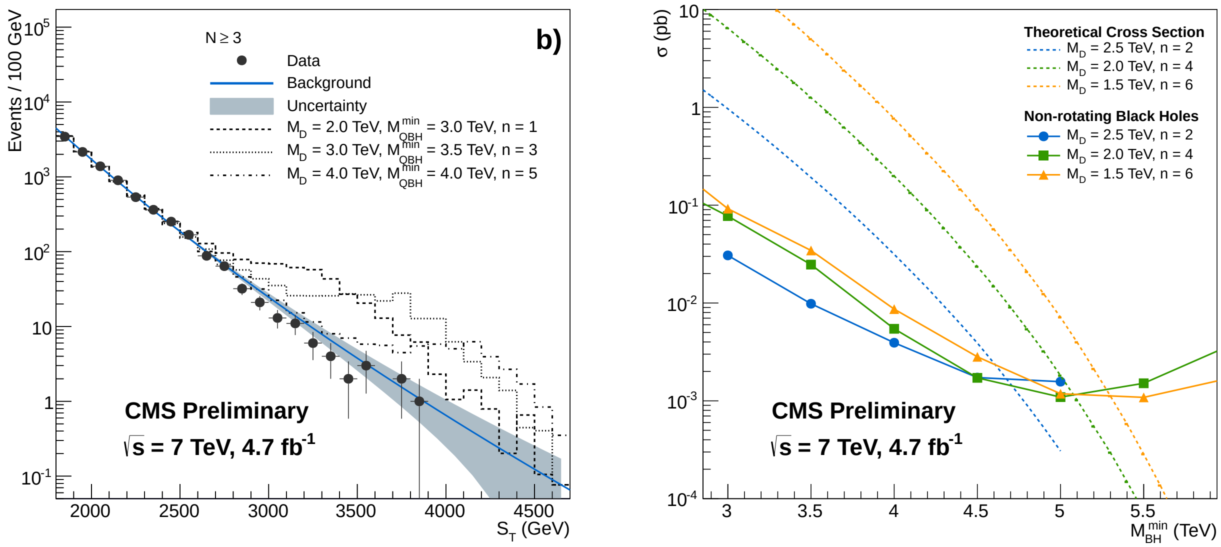

Figure 1: Left: S_T distribution in the $N \geq 3$ final state objects bin for data superposed by the background prediction with uncertainties. Some simulated signals with multidimensional Planck scale $M_D = 2 - 4$ TeV are indicated, too. At the right are shown cross section limits at 95% C.L. as a function of minimum black-hole mass for various black hole parameter sets.

limits on minimum string-ball mass and semi-classical black hole mass $m_{\mathrm{BH}}^{\mathrm{min}}$ are estimated, keeping in mind that the model validity breaks down for $m_{\mathrm{BH}}^{\mathrm{min}} \simeq 3 - 5M_D$.

Further new results in search of black holes, extra dimensions, dark matter and unparticles [6] [7] [8] [9] [10] [11] [12] [13] have been presented.

3 Searches in lepton production

The ATLAS search [14] for excited leptons $\ell^* \to \ell\gamma, \ell = e, \mu$ is an update of the previous measurement [15] and makes use of $\mathcal{L}_{ee(\mu\mu)} = 4.9(4.8)$ fb^{-1}. The excited leptons are expected in the electromagnetic radiative decay channel $\ell^* \to \ell\gamma$, produced together with a charge conjugated same flavour lepton via a four-fermion contact interaction at a given compositeness scale Λ. The dominant background consists of Drell-Yan production plus an additional photon or jet. All background predictions are evaluated with simulated samples. Background from multijets and semileptonic heavy flavour decays is heavily suppressed by isolation requirements. In Fig. 2 left plot the invariant dilepton photon mass distribution is shown for the electron channel. The signal search region is defined by a sliding lower threshold of $m_{\ell\ell\gamma} > m_{\ell^*} + 150$ GeV. 95% C.L. exclusion limits on the production cross section times branching ratio as a function of the excited muon invariant mass are shown in Fig. 2, right plot. For $m_{\ell^*} > 0.9$ TeV the observed upper limits on $\sigma \times BR$ are 1.0 fb and 1.9 fb in the e^* and μ^* channels, respectively. These limits are translated into bounds on the compositeness scale Λ as a function of the excited lepton mass. For $\Lambda = m_{\ell^*}$ masses below 2.0 TeV and 1.9 TeV are excluded for the e^* and μ^* channels, respectively.

Further new results in lepton production [16] [17] [18] have been presented.

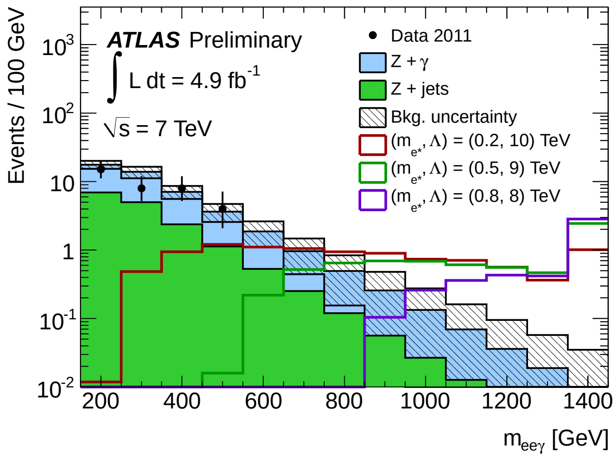

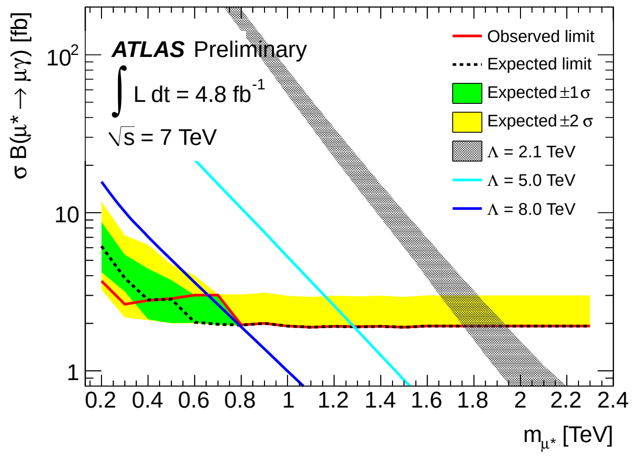

Figure 2: Left: $ee\gamma$ invariant mass distribution of data in comparison to simulation. In the right plot are shown the 95% C.L. exclusion limits on the excited muon production cross section times branching ratio as a function of its mass. Indicated are also three different compositeness scales Λ.

4 Searches in lepton + jet production

The CMS search [19] for heavy bottom like quarks is based on $\mathcal{L} = 4.6$ fb^{-1}. These b' quarks are assumed to decay exclusively to tW. Lighter b' quarks are disfavoured by results form previous experiments. The pair production $b'\bar{b}' \to tW^-\bar{t}W^+$ can be identified by the distinctive signatures of trileptons or same-sign dileptons, both accompanied by at least one b-jet. Jets are reconstructed with the anti-k_T jet algorithm making use of the distance measure $R = 0.5$ in rapidity y, azimuthal angle ϕ space. For a jet to be tagged as a b-jet the impact parameter significance of tracks is considered. The scalar sum of transverse object momenta and missing transverse energy has to exceed 500 GeV. The signal region is defined by at least four (two) jets in the same-sign dilepton (trilepton) channel. Top quark and Drell-Yan production constitute the dominant backgrounds which are determined by means of data. Top quark plus boson and diboson production background is determined by simulation. Exclusion limits at 95% C.L. on the $b'\bar{b}' \to tW^-\bar{t}W^+$ production cross section are set and translated into an exclusion limit of b' masses below 600 GeV.
Further searches in lepton plus jet production [20] [21] [22] [23] have been discussed.

5 Searches in jet production

The ATLAS search [24] for heavy vector-like quarks Q makes use of $\mathcal{L} = 1.04$ fb^{-1}. The analysis is sensitive to the charged current via the process $pp \to Qq \to Wqq'$ and the neutral current via the process $pp \to Qq \to Zqq'$ with leptonic decay of the vector boson. If vector-like quarks exist they are expected to couple in general only to the third generation sizably. A coupling $\tilde{\kappa}_{qQ}$ is introduced to describe the model dependence of the qVQ vertex, with V being one of the vector bosons W or Z. Events with at least two jets and a leptonically decaying vector boson are selected. The dominating background is vector boson plus jet production, followed by top and diboson production which are determined from simulation. Multijet background is estimated from data. Jets are determined by means of the anti-k_T algorithm with distance measure $R = 0.4$. 95% C.L. exclusion limits on the production cross section times branching ratio into a vector boson plus jet have been set. Assuming the coupling strengths $\tilde{\kappa}^2_{uD} = 1$ and $\tilde{\kappa}^2_{uU} = 1$ and the branching ratio $BR(Q \to W/Z + \text{jet}) = 100\%$, heavy quark masses m_Q below 900 GeV in the charged current and below 760 GeV in the neutral current can be excluded.

Further new searches [25,26] in jet production have been presented as well as the long-lived particle searches [27,28].

6 Conclusions

Various CMS and ATLAS searches for new phenomena have been presented here. Complete tables of exclusion limits for all existing analysis channels can be found in ref. [29], pp31.

References

1. CMS Collaboration, JINST **3** S08004 (2008).
2. ATLAS Collaboration, J. High Energy Phys. 09 (2010) 056.
3. CMS Collaboration, Exotica group public results, `https://twiki.cern.ch/twiki/bin/view/CMSPublic/PhysicsResultsEXO`.
4. ATLAS Collaboration, Exotica group public results, `https://twiki.cern.ch/twiki/bin/view/AtlasPublic/ExoticsPublicResults`.
5. CMS Collaboration, CMS PAPER EXO-11-071, submitted to JHEP.
6. ATLAS Collaboration, ATLAS-CONF-2011-147, `http://cdsweb.cern.ch/record/1390798`.
7. CMS Collaboration, CMS-EXO-11-038, arXiv:1112.0688 [hep-ex], accepted by Phys. Rev. Lett.
8. CMS Collaboration, JHEP **5** (2011) 85, arXiv:1103.4279 [hep-ex].
9. ATLAS Collaboration, arXiv:1112.2194v1 [hep-ex], submitted to Phys. Lett. **B**.
10. CMS Collaboration, CMS PAPER EXO-11-087, arXiv:1202.3827 [hep-ex], accepted by Phys. Lett. **B**.
11. CMS Collaboration, CMS PAPER EXO-11-096.
12. CMS Collaboration, CMS PAPER EXO-11-059.
13. CMS Collaboration, CMS PAS EXO-11-061.
14. ATLAS Collaboration, ATLAS-CONF-2012-008.
15. ATLAS Collaboration, arXiv:1201.3293 [hep-ex], submitted to Phys. Rev. Lett.
16. CMS Collaboration, CMS PAPER EXO-11-024.
17. CMS Collaboration, CMS PAPER EXO-11-045.
18. ATLAS Collaboration, arXiv:1112.4462 [hep-ex], submitted to Phys. Lett. **B**.
19. CMS Collaboration, CMS PAPER EXO-11-036.
20. ATLAS Collaboration, Phys. Lett. B709 (2012) 158-176, arXiv:1112.4828 [hep-ex].
21. ATLAS Collaboration, arXiv:1203.3172 [hep-ex], submitted to Eur. Phys. Journal C.
22. ATLAS Collaboration, arXiv:1204.1265 [hep-ex], submitted to Phys. Rev. Lett.
23. ATLAS Collaboration, arXiv:1203.5420 [hep-ex], submitted to Eur. Phys. Journal C.
24. ATLAS Collaboration, arXiv:1112.5755 [hep-ex], submitted to Phys. Lett. **B**.
25. CMS Collaboration, CMS PAPER EXO-11-017.
26. CMS Collaboration, Phys. Rev. Lett. **106**, 201804 (2011), arXiv:1102.2020 [hep-ex].
27. CMS Collaboration, CMS PAPER EXO-11-022.
28. ATLAS Collaboration, arXiv:1203.1303 [hep-ph], submitted to Phys. Rev. Lett.
29. L. Sonnenschein, `http://moriond.in2p3.fr/QCD/2012/MondayMorning/Sonnenschein.pdf`, talk given at the Moriond QCD 2012 conference, La Thuile, Italy.

Searches for New Physics in Top Events at the Tevatron

A.W. Jung for the CDF and DØ collaboration
FERMILAB-CONF-12-141-PPD
Fermi National Accelerator Laboratory,
P.O. Box 500, Batavia, IL, 60510, USA

Recent results of searches for new physics in top events at the Tevatron are presented. In case of CDF three searches are discussed using 6.0 to 8.7 fb^{-1} of data, with the latter being the final CDF data sample available for this kind of analysis. CDF carried out a search for Top + jet resonance production, dark matter production in association with single top and boosted tops. No signs of new physics are observed and instead upper limits are derived. DØ used 5.3 fb^{-1} of data and searched for a narrow resonance in $t\bar{t}$ production and a time dependent $t\bar{t}$ cross section, which would reveal a violation of Lorentz invariance. However, no signs for deviations from Standard Model are seen and instead upper limits for non-Standard Model contributions are calculated.

1 Introduction

The *top* quark is the heaviest known elementary particle and was discovered at the Tevatron $p\bar{p}$ collider in 1995 by the CDF and DØ collaboration [1,2] with a mass around 173 GeV. The production is dominated by the $q\bar{q}$ annihilation process with 85% as opposed to gluon-gluon fusion which contributes only 15%. The measurements presented here are performed using either the all-jets final state or the ℓ+jets channel. Within the ℓ+jets final state one of the W bosons (stemming from the decay of the *top* quarks) decays leptonically, the other W boson decays hadronically. For the all-jets final state both W bosons decay hadronically. The branching fraction for top quarks decaying into Wb is almost 100%. Jets containing a beauty quark (b-jets) are identified by means of a neural network (NN) built by the combination of variables describing the properties of secondary vertices and of tracks with large impact parameters relative to the primary vertex.

1.1 Top + jet resonance (CDF)

A search for a heavy new particle M produced in association with a top quark using 8.7 fb^{-1} of CDF data [3] is discussed. The data sample represents the final data sample for this kind of analysis. One of the motivations of this search is the deviation of the measurement of the forward-backward asymmetry A_{FB} from the SM prediction as recently reported by CDF and DØ [4]. The measured value of A_{FB} is significantly larger than the Standard Model (SM) prediction and many models explain this by adding a new heavy particle M. The final state is the ℓ+jets decay final state with five or more jets with at least one identified as b-jet, and missing transverse momentum $\not{E}_T$. The resonance mass m_{tj} is reconstructed by using a top kinematic reconstruction followed by a likelihood scan for the best match to the $t\bar{t}$ topology. The remaining jets are paired with the $t/\bar{t}$ with m_{tj} being the combination with the highest mass. No signal is observed and instead limits on the production of $t\bar{t}+j$ via a new heavy mediator M are set. Upper limits as a function of m_{tj} range between 0.61 and 0.02 pb at 95% confidence level (C.L.). The results have also been used to exclude two specific models in mass-coupling space. Figure 1 shows the

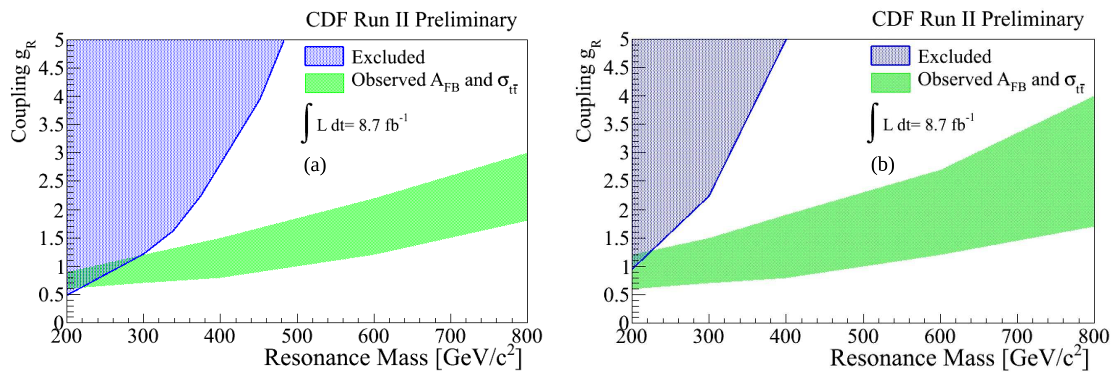

Figure 1: (a) shows the excluded region in mass-coupling space (hashed blue) where the new heavy particle M is part of a singlet or colored triplet (b). In addition the regions consistent with the observed A_{FB} and $t\bar{t}$ and single top cross section measurements are indicated (green band).

excluded regions (hashed blue) in the case that M is part of a new singlet (a) or colored triplet (b). In addition the regions consistent with the observed A_{FB} and $t\bar{t}$ and single top cross section measurements (green band) are indicated.

1.2 Narrow resonance (DØ)

DØ used 5.3 fb^{-1} of data to search for a narrow resonance produced in $t\bar{t}$ events [5]. The final state used for the analysis is the ℓ+jets decay final state of $t\bar{t}$ events with a lepton (e/μ) and at least three additional jets with at least one of them identified as a b-jet, and $\not{E}_T$. Figure 2a) shows the distribution of the invariant mass of the $t\bar{t}$ system $m(t\bar{t})$ with at least four jets. No

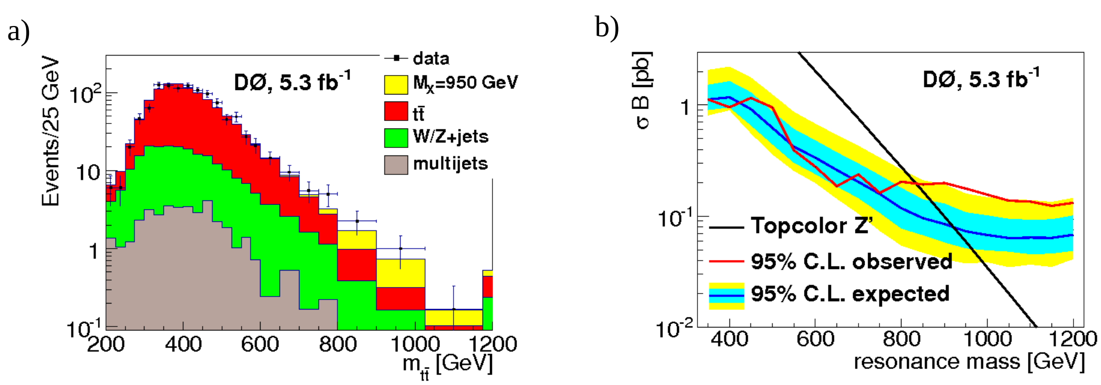

Figure 2: a) compares data from events with at least four jets to expectations from SM processes and a 950 GeV/c^2 resonance signal with the best fitted cross section times branching fraction of $\sigma \cdot BR = 0.10$ pb. b) shows upper limits at 95% C.L. on $\sigma \cdot BR$ for a narrow resonance as a function of the resonance mass. More details in the text.

observation of a narrow resonance has been made, but a slight excess of 2 standard deviations (s.d.) of events around 950 GeV/c^2 is seen. The best fit yields a cross section times branching fraction of $\sigma \cdot BR(M_X) = 0.10 \pm 0.05$ pb. The absence of a narrow resonance allows to calculate limits for the NLO production cross section of a topcolor Z' boson. The intrinsic width Γ_X of the

Z' has been set to $0.012 \cdot M_X$ and a branching fraction for $Z' \to t\bar{t}$ of 100% is assumed. Figure 2b) shows the upper limit on $\sigma \cdot BR$ for a narrow resonance as a function of the resonance mass. The shaded regions around the expected limit represent the one and two standard deviation bands. The solid line shows the predicted topcolor Z' production cross section. The observed cross section limits exclude Z' boson masses below 835 GeV/c^2 (95% C.L).

1.3 Single top + dark matter candidate (CDF)

A dark matter candidate can be produced in association with a single top quark. CDF used 7.7 fb^{-1} of data to perform the first search for this specific signature [6]. The final state consists of three jets with at least one identified as a b-jet. The dark matter signal is expected to contribute significantly at high $\not{E}_T$. In absence of a signal upper cross section limits are calculated as a function of the mass of the dark matter candidate. Figure 3 shows the upper cross section limit at 95% C.L. which is about 0.5 pb for dark matter candidate masses of $0 - 150$ GeV/c^2. The

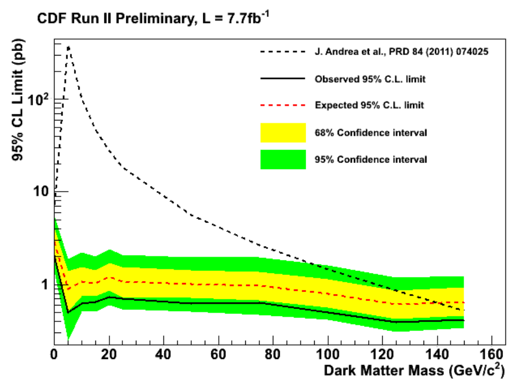

Figure 3: The figure shows the upper cross section limit at 95% C.L. as a function of the dark matter candidate mass. More details in the text.

shaded regions around the expected limit represent the one and two s.d. bands. In addition the predicted dark matter candidate production cross section is indicated by the dashed black line.

1.4 Boosted top quarks (CDF)

CDF used 6.0 fb^{-1} to search for a signature corresponding to boosted tops in a sample of one or two high transverse momentum massive jets with additional $\not{E}_T$ [7]. The substructure of high transverse momentum objects (or jets) had not been studied extensively at Tevatron before this search. The term boosted top refers to the fact that the decay products of these top quarks are collimated into one single massive jet. The background estimation is done using data-driven methods. The predicted top cross section for $p_T > 400$ GeV/c using the MSTW2008NNLO [8] parton density distribution function (PDF) is $4.55^{+0.50}_{-0.41}$ fb. No signal is observed and an upper cross section limit of 38 fb at 95% C.L. is set for $p_T > 400$ GeV/c. It is also possible to search for the pair production of a massive object, in this case an upper cross section limit of 20 fb at 95% C.L. is derived.

1.5 Lorentz Invariance Violation (DØ)

DØ searched for a time dependent $t\bar{t}$ production cross section using 5.3 fb^{-1} of data [9]. For the analysis $t\bar{t}$ events in the ℓ+jets final state are selected with a lepton (e/μ), additional at least four jets, exactly one jet identified as a b-jet and $\not{E}_T$. In addition the analysis relies on the timestamp of the data at production time. The Standard Model Extension (SME) [10] is an effective field theory and implements terms that violate Lorentz and CPT invariance. The modified SME matrix element adds Lorentz invariance violating terms for the production and decay of $t\bar{t}$ events to the Standard Model terms. The SME predicts a cross section dependency on siderial time as the orientation of the detector changes with the rotation of the earth relative to the fixed stars. The background and luminosity corrected ratio R is expected to be flat within the Standard Model, i.e. no time dependency of the $t\bar{t}$ production cross section. Figure 4 shows this ratio as a function of the siderial phase, i.e. 1 corresponds to one siderial day. There is

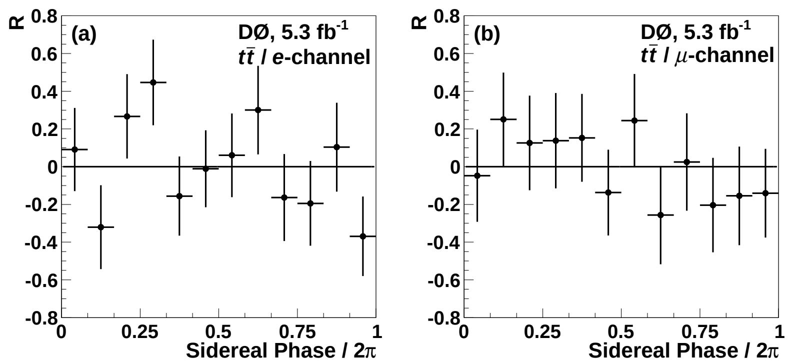

Figure 4: (a) shows the background and luminosity corrected ratio R as a function of the siderial phase (one siderial day) for events containing electrons, whereas (b) shows the same ratio R for the muon case.

no indication of a time dependent $t\bar{t}$ production cross section. Instead this measurement sets the first constraints on Lorentz invariance violation in the top sector. As the top quark decays before it can hadronize the constraints are also the first ones for a bare quark.

2 Conclusions

Various recent searches in top events at the Tevatron have been discussed. More details and results are given at the DØ and CDF webpage [11]. There is no significant evidence for non-Standard Model signals or contributions. CDF and DØ continue to provide unique results in the top sector and more top analyzes using the final data sample are expected to come out soon.

References

1. F. Abe *et al.* (CDF), Phys. Rev. Lett. **74**, 2626 (1995) [arXiv:hep-ex/9503002].
2. S. Abachi *et al.* (DØ), Phys. Rev. Lett. **74**, 2632 (1995) [arXiv:hep-ex/9503003].
3. http://www-cdf.fnal.gov/physics/new/top/confNotes/cdf10776_ttj.pdf (2012).
4. http://www-cdf.fnal.gov/physics/new/top/2012/LepJet_AFB_Winter2012/CDF10807.pdf (2012); Phys. Rev. D 84, 112055, [arXiv:1107.4995] (2011).
5. Phys. Rev. D 85, 051101, [arXiv:1111.1271] (2012).
6. CDF [arXiv:1202.5653] (2011).
7. http://www-cdf.fnal.gov/physics/new/top/confNotes/cdf10234_BoostedTopConf.pdf (2011).
8. A. D. Martin, W. J. Stirling, R. S. Thorne and G. Watt, Eur. Phys. J. C63 189-285 [arXiv:0901.0002] (2009).
9. DØ, Submitted to Phys. Rev. Lett., [arXiv:1203.6103] (2012).
10. D. Colladay and V.A. Kostelecky, Phys. Rev. D 58, 116002 (1998); V.A. Kostelecky, Phys. Rev. D 69, 105009 (2004).
11. CDF: http://www-cdf.fnal.gov/physics/new/top/top.html;
DØ: http://www-d0.fnal.gov/Run2Physics/top/top_public_web_pages/top_public.html

Effective Theory Descriptions of Dark Matter Interactions

Tim M.P. Tait
Department of Physics and Astronomy, University of California, Irvine, CA 92697

This write-up covers an invited talk prepared for the Rencontres de Moriond QCD conference in 2012. It provides some theoretical thoughts regarding searches for new phenomena at high energy colliders, with some specific reference to signatures including missing transverse momentum, which provide natural probes of the nature of dark matter.

1 Introduction

There is over-whelming evidence that the Universe contains a large fraction of dark non-baryonic matter [1], yet its nature remains elusive. Among the variety of possibilities, weakly interacting massive particles (WIMPs) remain the most compelling vision for dark matter, because they offer a natural explanation of the observed abundance of dark matter which is roughly independent of the detailed thermal history of the Universe. WIMPs are also an interesting candidate because they have "large" (very roughly weak scale) interactions with ordinary matter, leading to good prospects for their detection by particle physics experiments.

Given a specific model containing a dark matter candidate particle, such as the neutralino [2] in a model of supersymmetry with R-parity, or the lightest Kaluza-Klein particle [3] in a model with Universal Extra Dimensions,[4] one can make detailed predictions for any observable (such as relic density, direct scattering rate, indirect annihilation rate, or production of a signature at colliders) in terms of the underlying model parameters. However, in the absence of a clear indication as to which model is correct, such predictions are difficult to put together into a coherent picture of the constraints on dark matter and interrelation of the various null searches for its presence.

2 Effective Theory Descriptions of WIMP Interactions

While the details of a given WIMP model are usually involved and depend sensitively on the nature of the particles which mediate interactions between WIMPs and the Standard Model (SM) particles, a particular simplification takes place when the mediating particles are heavy compared to the momentum transfer of the processes of interest. In this limit, the mediators never appear on-shell in processes, and their effects are well approximated by an effective field theory containing contact interactions between the WIMP and the SM fields. While there is no guarantee that nature need work this way, nonetheless the effective field theory offers the possibility to capture classes of similar models in a common framework, and to compare different kinds of WIMP searches in a consistent language which allows one to highlight the strengths and weaknesses of each one.

Table 1: The list of the operators defined in Eq. (1).

Name	Type	G_χ	Γ^χ	Γ^q
M1	qq	$m_q/2M_*^3$	1	1
M2	qq	$im_q/2M_*^3$	γ_5	1
M3	qq	$im_q/2M_*^3$	1	γ_5
M4	qq	$m_q/2M_*^3$	γ_5	γ_5
M5	qq	$1/2M_*^2$	$\gamma_5\gamma_\mu$	γ^μ
M6	qq	$1/2M_*^2$	$\gamma_5\gamma_\mu$	$\gamma_5\gamma^\mu$
M7	GG	$\alpha_s/8M_*^3$	1	-
M8	GG	$i\alpha_s/8M_*^3$	γ_5	-
M9	$G\tilde{G}$	$\alpha_s/8M_*^3$	1	-
M10	$G\tilde{G}$	$i\alpha_s/8M_*^3$	γ_5	-

The effective theory is constructed to contain the WIMP and the SM fields, and is subject to Lorentz invariance and the gauge invariance of the SM. In practice we realize only the $SU(3)_C \times U(1)_{EM}$ gauge symmetries and leave the electroweak $SU(2)_W \times U(1)_Y$ implicit. As an example, in Table 1 we present the leading interactions (in an expansion in the momentum transfer) of a Majorana WIMP χ which is a SM singlet interacting with quarks and/or gluons.[5] (see also [6,7]). The operators are specified as,

$$\mathcal{L}_{int} = \sum_q G_\chi \; [\bar{\chi}\Gamma^\chi\chi] \; [\bar{q}\Gamma^q q] + G_\chi \; [\bar{\chi}\Gamma^\chi\chi] \; \left(G^a_{\mu\nu}G^{a\mu\nu} \text{ or } G^a_{\mu\nu}\widetilde{G}^{a\mu\nu}\right) \qquad (1)$$

where each G_χ, parameterized by a scale M_* to some power, is a separate coefficient for each operator. It is a simple (and similar) exercise to write down effective theories applicable to WIMPs which are real or complex scalars,[6,9], Dirac fermions,[6,8,9] or vector bosons.[10]

3 Monojet Searches

Interactions of the type shown in Eq. 1 allow WIMPs to be produced at hadron colliders. Since they escape undetected from a typical detector, the strategy is to look for events containing additional hadronic radiation from which the presence of the WIMPs can be inferred due to an imbalance in the transverse momentum of the visible particles.[11,12] Since a typical event contains one jet of hadrons as well as the undetected WIMPs, this signature is known as a "mono-jet search". The null results of past searches allow one to place upper limits on the value of M_* for each operator that mediates WIMP-SM interactions. An example of typical limits placed on the operators M5 and M6 are shown in Figure 1.[13] (Similar results have also been derived independently in Refs.[14,15] from mono- and di-jet plus missing momentum signatures). At Moriond this year, it was very heartening to see that the experimental collaborations themselves are now working in the EFT framework, with news results shown from CDF[16] and CMS.[17] By re-optimizing the search strategy (rather than repurposing existing mono-jet limits designed to search for large extra dimensions), better limits on M_* are possible.

3.1 Applicability of the EFT Formalism

One legitimate concern that was raised during the discussion was how well the effective theory description is expected to capture the physics of WIMP production at a hadron collider. The essential assumption underlying the EFT is that the masses of the particles mediating the

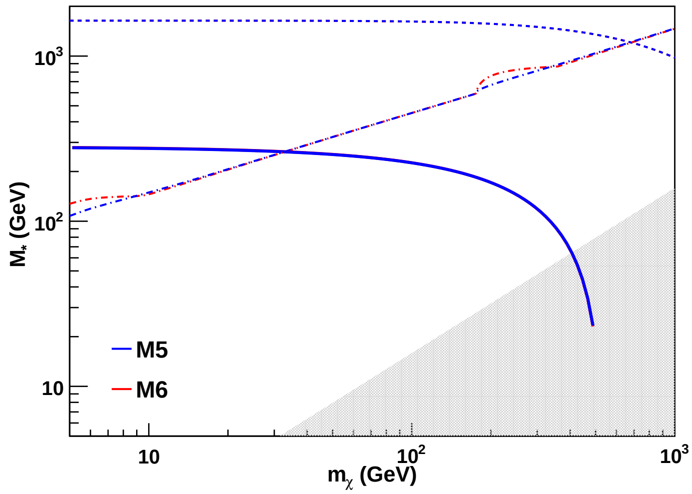

Figure 1: Tevatron bounds (solid curves) on M_* for the operators M5 (red) and M6 (blue) as a function of WIMP mass m_χ. Also shown are the M_* leading to the correct thermal relic density (dot-dashed curves) and long term (14 TeV, ~ 100 fb^{-1}) LHC prospects.

interaction (generically denoted M_ψ) are large compared to the momentum transfer of any process. In a collider mono-jet search, this requirement boils down to,

$$M_\psi \gg \max\left\{m_\chi, p_T^j\right\} \tag{2}$$

where p_T^j is the transverse momentum of the jet, which will typically cluster around the minimum jet p_T selected by the analysis (though perhaps with tails which reach higher p_T, the extent of which will depend on the collected luminosity).

For simple UV completions, one can imagine the coupling to quarks is mediated either by a neutral particle with interactions to pair of WIMPs as well as with a pair of SM quarks, or by exchange of a colored mediator which has interacts with a WIMP together with a SM quark. In the former case (which includes WIMPs whose primary interaction with the SM is by exchange of either a Z or light SM Higgs boson), the neutral mediator could either be heavy enough to use the EFT description or light enough that it will break down (for some specific investigations, see Refs.[8,14,18,19,20]) which will typically result in the EFT over-estimating the bound on M_*. A colored mediator must be heavier than the WIMP (or the WIMP would decay into it). It can be copiously produced at the LHC (and its rate is determined purely by QCD, together with the mass of the colored particle), and can decay into jets and a WIMP, resulting in jets + missing p_T signatures. Based on the null searches for new colored particles decaying into missing p_T, the LHC places bounds on the masses of such particles to be greater than about 1 TeV,[21] indicating that in this case the EFT formalism is likely to work for the current mono-jet analyses provided the WIMP mass is sufficiently below ~ 1 TeV.

It is also worth pointing out that "integrating out" the mediators is not a necessary requirement of the EFT formalism. One can build an effective theory containing the WIMP and the mediating particle, and since there are relatively few such candidate theories, one can still cover the space of such "simplified models".[22] From this point of view, the EFT as formulated here is just exploiting a universal behavior in the limit of heavy mediators inside the space of simplified models.

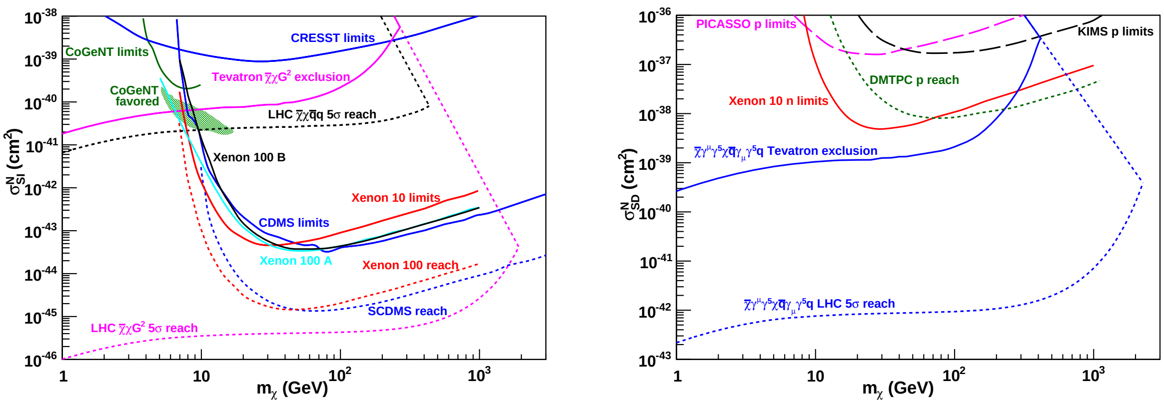

Figure 2: Bounds on the plane of spin-independent (left figure) and spin-dependent (right figure) scattering of WIMPs with nucleons versus m_χ, coming from Tevatron data and direct detection experiments, as labelled.

4 Implications for Direct and Indirect Detection

As a common language to talk about dark matter interactions with SM particles, the EFT also provides a means to translate the results of one experiment into the observables measured by another. Thus, the EFT allows one to directly compare searches at colliders with those from direct and indirect detection of dark matter. To illustrate these points, in Figure 2, we show the constraints on the direct detection plane, for dark matter interacting both independently dependently with the spin of the target nucleus.[5] A few important points of comparison emerge in the figures:

- For low mass WIMPs (m_χ less than about 10 GeV), direct detection has difficult registering the scattering, because the WIMPs carry too little energy to substantially affect the target nuclei. Colliders fill this region in, because for low masses the rate for producing relativistic WIMPs (needed for the mono-jet search) increases.

- Colliders see the colliding protons incoherently, implying that they are not subject to interference effects between dark matter interacting with quarks of various flavors (unlike in direct scattering, which sees the nucleus coherently). One side effect of this feature is that each operator for each quark flavor has a separate bound in the direct scattering plane, so one needs to label the collider bounds with the operator assumption when showing them in the direct detection parameter space.

- Collider constraints are stronger for gluon than for quark operators, which could potentially be used to learn more about a given observation in direct detection given what the LHC results turn out to be.

- Colliders are typically providing weaker bounds for theories where the WIMP interactions are coherent over the entire nucleus and WIMP masses are of order 100 GeV.

- For spin-dependent interactions, colliders provide the best bounds up to WIMP masses of order TeV, beyond which the LHC becomes energy-limited to produce dark matter relativistically (unlike direct detection experiments, which receive the dark matter for free).

This last point may be expanded: many operators lead to velocity-suppressed direct scattering for non-relativistic WIMPs. Collider searches do particularly well in such cases because they must produce the WIMPs relativistically to see them at all.

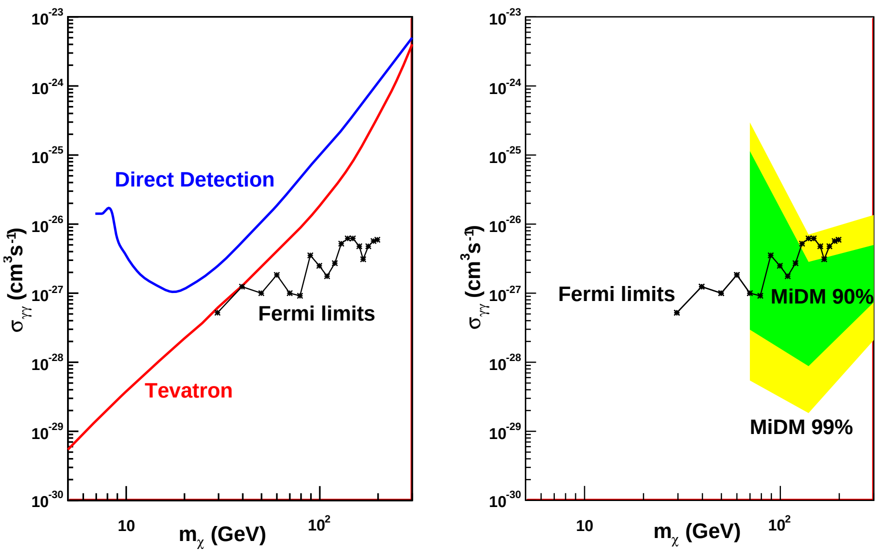

Figure 3: Bounds on the plane of the cross section for WIMP annihilation into two photons versus m_χ, coming from Tevatron data, the Fermi LAT line search, and direct detection experiments, as labelled.

Similarly, one may map collider and direct searches into the plane of indirect detection, including production of gamma rays,[23,24,25] and anti-protons.[25,26]. As an illustrative example, we compute the (loop) process of $\chi\chi \to \gamma\gamma$ for the operator M5 (which mediates spin-dependent direct scattering), closing the quarks into a loop and attaching photons. Though loop-suppressed, this process is considered a promising means to search for dark matter at a gamma ray observatory such as the Fermi LAT, because astrophysical processes have difficulty mimicking a line signal. In Figure 3, we show the line cross section for this operator, including bounds from direct searches, CDF, and Fermi itself (assuming the dark matter is distributed in an NFW profile in the galaxy).[23] The three experiments are largely complementary, with colliders providing the best bounds at low masses, the Fermi line search providing the best coverage of 30 GeV $\leq m_\chi \leq$ 200 GeV, and the direct detection experiments taking over for masses larger than around 2 TeV.

5 Outlook

Effective theories are new weapon in the theoretical arsenal to look for dark matter. Though every theory of dark matter may not be accurately parameterized in this language, it covers the limiting case of heavy mediators in a wide class of theories. Effective theories provide a powerful language through which results of different kinds of experiments may be compared, and ultimately can be used to build coherent picture of how dark matter interacts with the Standard Model.

Acknowledgments

I am grateful to the organizers for the invitation to participate in the wonderful conference, and to Sarah Malik for clarifying some details regarding the CMS plots. This work was partially supported by the US National Science Foundation through Grant PHY-0970171.

References

1. G. Bertone, D. Hooper and J. Silk, Phys. Rept. **405** (2005) 279 [hep-ph/0404175].
2. H. Goldberg, Phys. Rev. Lett. **50** (1983) 1419 [Erratum-ibid. **103** (2009) 099905].
3. G. Servant and T. M. P. Tait, Nucl. Phys. B **650** (2003) 391 [hep-ph/0206071].
4. T. Appelquist, H. -C. Cheng and B. A. Dobrescu, Phys. Rev. D **64** (2001) 035002 [hep-ph/0012100].
5. J. Goodman, M. Ibe, A. Rajaraman, W. Shepherd, T. M. P. Tait and H. -B. Yu, Phys. Lett. B **695** (2011) 185 [arXiv:1005.1286 [hep-ph]].
6. M. Beltran, D. Hooper, E. W. Kolb and Z. C. Krusberg, Phys. Rev. D **80**, 043509 (2009) [arXiv:0808.3384 [hep-ph]].
7. Q. -H. Cao, C. -R. Chen, C. S. Li and H. Zhang, JHEP **1108** (2011) 018 [arXiv:0912.4511 [hep-ph]].
8. Y. Bai, P. J. Fox and R. Harnik, JHEP **1012** (2010) 048 [arXiv:1005.3797 [hep-ph]].
9. J. Goodman, M. Ibe, A. Rajaraman, W. Shepherd, T. M. P. Tait and H. -B. Yu, Phys. Rev. D **82** (2010) 116010 [arXiv:1008.1783 [hep-ph]].
10. Z. -H. Yu, J. -M. Zheng, X. -J. Bi, Z. Li, D. -X. Yao and H. -H. Zhang, Nucl. Phys. B **860** (2012) 115 [arXiv:1112.6052 [hep-ph]]; J. Hisano, K. Ishiwata, N. Nagata and M. Yamanaka, Prog. Theor. Phys. **126** (2011) 435 [arXiv:1012.5455 [hep-ph]].
11. J. L. Feng, S. Su and F. Takayama, Phys. Rev. Lett. **96** (2006) 151802 [hep-ph/0503117].
12. M. Beltran, D. Hooper, E. W. Kolb, Z. A. C. Krusberg and T. M. P. Tait, JHEP **1009** (2010) 037 [arXiv:1002.4137 [hep-ph]].
13. A. Rajaraman, W. Shepherd, T. M. P. Tait and A. M. Wijangco, Phys. Rev. D **84** (2011) 095013 [arXiv:1108.1196 [hep-ph]].
14. P. J. Fox, R. Harnik, J. Kopp and Y. Tsai, Phys. Rev. D **85** (2012) 056011 [arXiv:1109.4398 [hep-ph]].
15. P. J. Fox, R. Harnik, R. Primulando and C. -T. Yu, arXiv:1203.1662 [hep-ph].
16. See the contribution from Lidija Zivkovic, these proceedings.
17. See the contribution from Lars Sonnenschein, these proceedings.
18. J. Goodman and W. Shepherd, arXiv:1111.2359 [hep-ph].
19. M. T. Frandsen, F. Kahlhoefer, A. Preston, S. Sarkar and K. Schmidt-Hoberg, arXiv:1204.3839 [hep-ph].
20. I. M. Shoemaker and L. Vecchi, arXiv:1112.5457 [hep-ph].
21. See the contribution from Laurent Duflot, these proceedings.
22. D. Alves *et al.* [LHC New Physics Working Group Collaboration], arXiv:1105.2838 [hep-ph].
23. J. Goodman, M. Ibe, A. Rajaraman, W. Shepherd, T. M. P. Tait and H. -B. Yu, Nucl. Phys. B **844** (2011) 55 [arXiv:1009.0008 [hep-ph]].
24. K. Cheung, P. -Y. Tseng and T. -C. Yuan, JCAP **1106** (2011) 023 [arXiv:1104.5329 [hep-ph]].
25. K. Cheung, P. -Y. Tseng, Y. -L. S. Tsai and T. -C. Yuan, arXiv:1201.3402 [hep-ph].
26. K. Cheung, P. -Y. Tseng and T. -C. Yuan, JCAP **1101** (2011) 004 [arXiv:1011.2310 [hep-ph]].

3.
Heavy Flavour

Heavy Flavour Production at $\sqrt{s} = 7$ TeV

E. Aguiló
Physik-Institut, Universität Zürich, Winterthurerstr. 190,
CH-8057 Zürich, Switzerland

The measurements of b quark, quarkonium and exotic state production performed with the ATLAS and CMS experiments at $\sqrt{s} = 7$ TeV are presented. The b-quark production cross section is measured both in inclusive and fully reconstructed B hadron decays. The results are compared with QCD expectations at tree-level and NLO.

1 Introduction

The data analyzed for the presented results were collected by the multi-purpose experiments ATLAS [?] and CMS [?] at the LHC, which provides since Spring 2010 proton-proton collisions at $\sqrt{s} = 7$ TeV. The collected luminosity by each experiment was close to 40 pb^{-1} in 2010 and 5 fb^{-1} in 2011.

The study of heavy quark production cross section in high-energy hadronic interactions plays a critical role as precision tests of next-to-leading order (NLO) Quantum Chromodynamics (QCD) calculations [?] at a higher energy scale than before. Measurements of b-hadron production at the higher energies provided by the Large Hadron Collider (LHC), which are possible thanks to the large $b\bar{b}$ cross section at $\sqrt{s} = 7$ TeV, represent an important test of theoretical calculations [?,?]. In addition, a good understanding of b-quark production is necessary, since it is an important background to several other analyses, *i.e.* top quark physics, Higgs or Supersymmetry searches, *etc.* These measurements also serve as a validation of the tracking and muon systems.

Both experiments have produced several results on several heavy flavor production subjects, which can be divided in the following three categories: quarkonium production, exclusive heavy flavor hadron cross-section measurements and inclusive $\mathrm{b\bar{b}}$ cross-section measurements using b-tagged jets or muons. The latest results on each category will be presented here.

2 Observation of the χ_b(3P)

The χ_b mesons are the P-wave function excitation of $\mathrm{b\bar{b}}$ quark system. They decay radiating a photon into the Υ(1S) or the Υ(2S). These mesons can appear in different spin projections, resulting in a hyperfine splitting of the spectrum. The ATLAS experiment has analyzed the whole 2011 data sample reconstructing $\Upsilon \to \mu^+\mu^-$, and matching them to either calorimeter reconstructed photons or converted photons, from the $\mathrm{e^+e^-}$ tracks reconstructed in the tracker. Calorimeter photons can be reconstructed more efficiently than converted photons, but in addition to the fact that the converted photons allow the reconstruction of lower energy photons, they also have better energy resolution than those reconstructed in the calorimeter. The spectrum when using converted photons can be seen in Fig. **??**, where the right-most peak corresponds to a never observed before χ_b state: the $\chi_b(3P)$. The spectrum is fitted to crystal ball functions for the signal peaks, including the hyperfine mass splitting structure predicted by Ref. [?], and an empirical function for the background. The $\chi_b(3P)$ peak significance is larger than 6 standard deviations and the measured mass barycenter is 10.530 ± 0.005 (stat.) ± 0.009 (syst.) GeV [?].

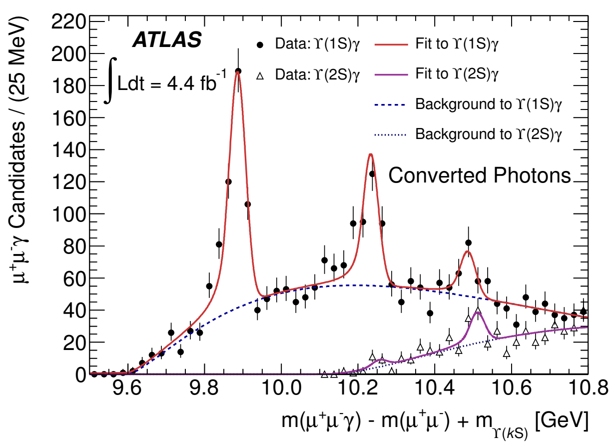

Figure 1: The mass distributions of the $\chi_b \to \Upsilon(kS)\gamma$ (k = 1, 2) candidates formed using photons which have converted and have been reconstructed in the tracker. Data are shown before the correction for the energy loss from the photon conversion electrons due to bremsstrahlung and other processes. The data for decays of $\chi_b \to \Upsilon(1S)\gamma$ and $\chi_b \to \Upsilon(2S)\gamma$ are plotted using circles and triangles respectively. Solid lines represent the total fit result for each mass window. The dashed lines represent the background components only.

3 Λ_b production cross section

CMS has measured the Λ_b baryon production differential cross section [?] in transverse momentum (p_T) and rapidity (y) using the decay chain $\Lambda_b \to J/\psi\Lambda$, $J/\psi \to \mu^+\mu^-$, and $\Lambda \to p\pi$ with 1.9 fb^{-1} of the 2011 data sample. As seen in Fig. **??** (left), the measured differential cross section shows a steeper slope than the Monte Carlo (MC) predictions. The production ratio between Λ_b and $\bar{\Lambda}_b$ is also measured and no significant deviations from theory are found over the measured p_T and y ranges. In Fig. **??** (right) this result is compared to the differential cross sections of the B^+, B^0 and B_s, as measured by CMS.

4 Production of heavy flavor with b-jets and with muons

ATLAS and CMS have measured the inclusive beauty cross section for pp collisions at $\sqrt{s} =$ 7 TeV by means of jets tagged by an algorithm using secondary vertex information with 2010 data [?,?]. A displaced vertex is a good tag of the presence of a b-quark originated jet. The same measurement has been preformed using muons within the jets. As discriminating variable the transverse momentum relative to the jet axis ("p_T rel") has been used. In both experiments good agreement between the measurement and theory calculations is seen, as shown in Fig. **??**, except for some discrepancies at large p_T and y. The ATLAS result includes a measurement of the di-jet cross section, which also agrees with theory calculations, as seen in **??** (left), except for low azimuthal angles (ϕ) between the two b-jets. A similar discrepancy, seen in Fig. **??** (right), was observed in a previous CMS result which studied the separation in the (η,ϕ) plane (ΔR) between the directions of the two b hadrons (BB), found using only information from the tracker.

5 Conclusions

There are many high quality results on heavy flavor production by both ATLAS and CMS. The observation of the new $\chi_b(3P)$ particle has been presented. The measurement of the exclusive Λ_b production cross section shows discrepancies with MC predictions. Open heavy flavor production is well described by theory calculations, although some discrepancies with the measurements can be seen at high p_T and , and at low di-jet separation angles.

References

1. ATLAS Collaboration, JINST **3**, S08003 (2008)
2. CMS Collaboration, JINST **3**, S08004 (2008)
3. P. Nason, S. Dawson and R.K. Ellis, *Nucl. Phys.* B **303**, 607 (1988).
4. M. Cacciari, M. Greco and P. Nason, JHEP **9805**, 107 (1998)
5. B.A. Kniehl, G. Kramer, I. Schienbein and H. Spiesberger, *Phys. Rev.* D **77**, 014011 (2008)
6. L. Motyka and K. Zalewski, *Eur. Phys. J.* C **4**, 107 (1998)
7. ATLAS Collaboration, *Phys. Rev. Lett.* **108**, 152001 (2012)
8. CMS Collaboration, arXiv:1205.0594 [hep-ex], submitted to *Phys. Lett.* B (2012)
9. ATLAS Collaboration, *Eur. Phys. J.* C **71**, 1846 (2011)
10. CMS Collaboration, arXiv:1202.4617v1 [hep-ex] submitted to JHEP (2012)
11. CMS Collaboration, JHEP **3**, 136 (2011)

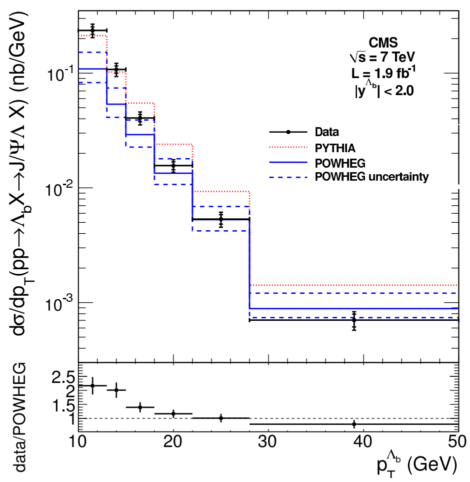

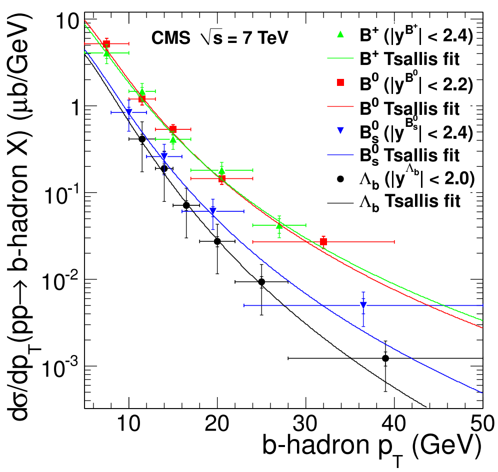

Figure 2: (Left) Upper: measured differential cross sections times branching fraction vs. $p_T^{\Lambda_b}$ compared to the theoretical predictions from PYTHIA and POWHEG. The inner error bars correspond to the statistical uncertainties and the outer ones represent the uncorrelated systematic uncertainties added in quadrature to the statistical uncertainties. The dashed lines show the uncertainties on the POWHEG predictions. Overall uncertainties of 2.2% for the luminosity and 1.3% for the $J/\psi \to \mu^+\mu^-$ and $\Lambda \to p\pi$ are not shown, nor is the 54% uncertainty due to $\mathcal{B}(\Lambda_b \to J/\psi\Lambda)$ for the PYTHIA and POWHEG predictions. Lower: The ratio of the measured values to the POWHEG predictions. The error bars include the statistical and uncorrelated systematic uncertainties on the data and the uncertainties affecting only the distribution shapes on the POWHEG predictions. (Right) Comparison of b-hadron production rates versus hadron p_T, where the inner error bars correspond to the bin-to-bin uncertainties, while the outer error bars represent the bin-to-bin plus normalization uncertainties added in quadrature. The large normalization uncertainties for Λ_b and B_s are dominated by the poorly measured $\Lambda_b \to J/\psi\Lambda$ and $B_s \to J/\psi\phi$ branching fractions for the decay channels used in the analysis.

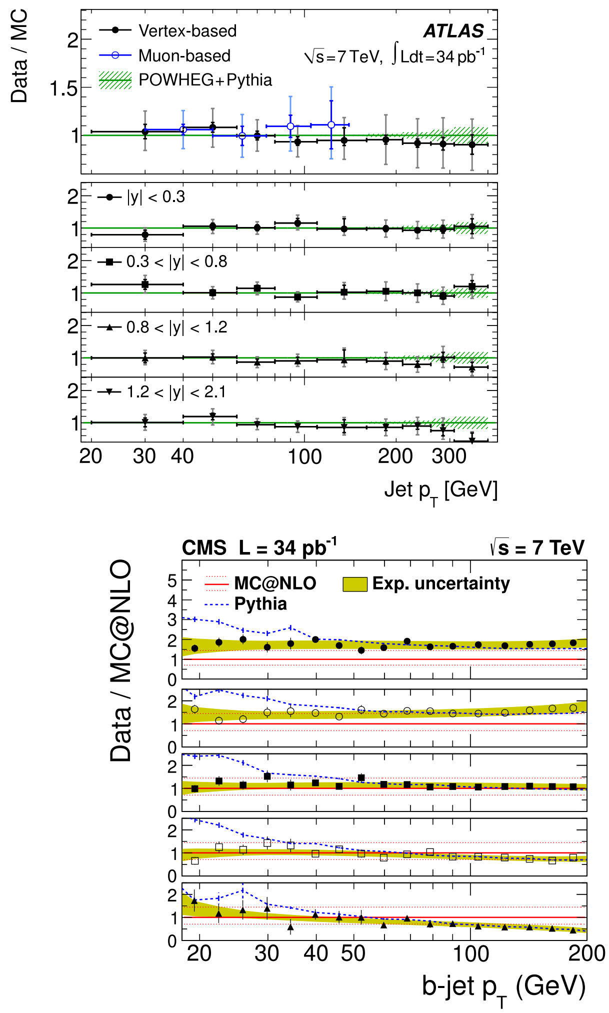

Figure 3: (Left) Ratio of the ATLAS measured cross sections to the theory predictions of POWHEG. In the region where the displaced vertex based measurement overlaps with the muon "p_T rel" measurement both results are shown. The top plot shows the full y acceptance, while the four smaller plots show the comparison for each of the y ranges separately. The data points show both the statistical uncertainty (dark colour) and the combination of the statistical and systematic uncertainty (light colour). The shaded regions around the theoretical predictions reflect the statistical uncertainty only. (Right) CMS measured b-jet cross section shown as a ratio to the MC@NLO calculation, for the ranges $|y| < 0.5$, $0.5 < |y| < 1$, $1 < |y| < 1.5$, $1.5 < |y| < 2$, $2 < |y| < 2.2$. The experimental systematic uncertainties are shown as a shaded band and the statistical uncertainties as error bars. The MC@NLO uncertainty is shown as dotted lines. The PYTHIA prediction is also shown as a dashed line.

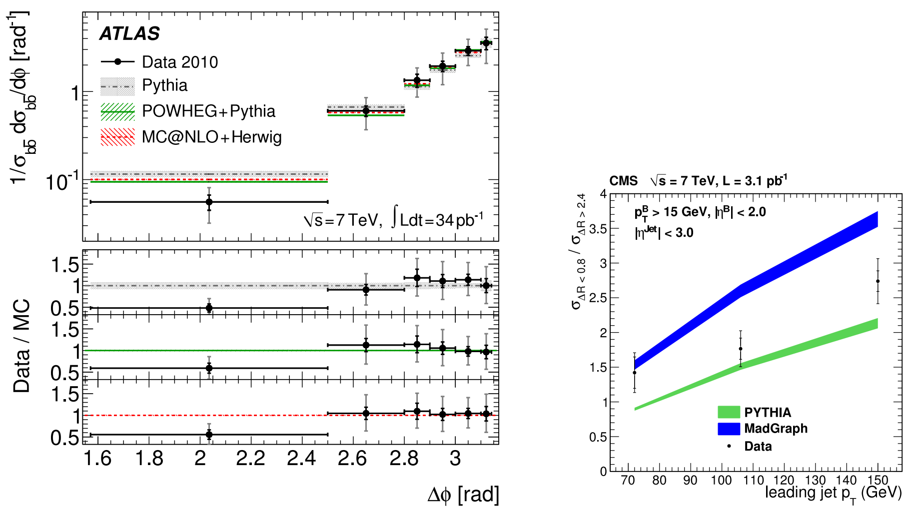

Figure 4: (Left) The ATLAS $b\bar{b}$-dijet cross section as a function of the azimuthal angle difference between the two jets for b-jets with $p_T > 40$ GeV, $|y| < 2.1$ and a dijet invariant mass of $m_{jj} > 110$ GeV. The data are compared to the theory predictions of Pythia, POWHEG and MC@NLO. The shaded regions around the MC predictions reflect the statistical uncertainty only. (Right) ratio between the BB production cross sections in $\Delta R < 0.8$ and $\Delta R > 2.4$ as a function of the leading jet p_T. For the data points, the error bars show the statistical (inner bars) and the total (outer bars) errors. Also shown are the predictions from the pythia and MadGraph simulations, where the widths of the bands indicate the uncertainties arising from the limited number of simulated events.

HEAVY FLAVOUR PRODUCTION AND SPECTROSCOPY AT LHCB

A. KOZLINSKIY
Nikhef National Institute for Subatomic Physics,
Amsterdam, The Netherlands

At the Moriond QCD conference LHCb has presented results on heavy flavour production and spectroscopy. Here the latest results are discussed, which include the first observation and measurement of the branching fraction of the hadronic decay $B_c^+ \to J/\psi\pi^+\pi^-\pi^+$, the mass measurement of the excited B mesons and the mass measurement of the Ξ_b and Ω_b baryons.

1 Introduction

In the high energy pp collisions at the LHC all kind of mesons and baryons containing b- and c-quarks are produced. The production and spectroscopy of these particles is an important input for other measurements and for many theoretical calculations.

The LHCb detector is a single-arm forward spectrometer [1]. The detector is dedicated to flavour physics at the LHC and its main goal is the measurement of CP-violating observables and rare decays of heavy flavour to search for 'New Physics' beyond the Standard Model in the decays of b- and c- hadrons. In 2010 and 2011 the LHC has delivered an integrated luminosity of 1.1 fb^{-1} of data to LHCb at a center-of-mass energy of 7 TeV of which about 90% was recorded.

The open charm (D^0, D^{*+}, D^+ and D_s^+) production was measured by the LHCb collaboration using 1.4 nb^{-1} of 2010 data and is reported elsewhere [2].

The B^+ production was measured using 35 pb^{-1} of 2010 in the decay $B^\pm \to J/\psi K^\pm$ [3]. The production of other b-mesons (B_s and B_c) is determined through the fragmentation functions f_u, f_d, f_c and f_s. The measurement of f_s/f_d ratio was performed by LHCb with 2010 data [4] and it is a crucial ingredient for branching fraction measurements. Recently, the relative yield (production times branching fraction) of B_c^+ to B^+ mesons was measured [5].

The results discussed here include the first observation and the measurement of the branching fraction of the hadronic decay $B_c^+ \to J/\psi\pi^+\pi^-\pi^+$, which is discussed in Section 2, and the mass measurement of excited B mesons, generically referred to as $B_{(s)}^{**}$, which is discussed in Section 3. Finally, the measurement of the Ξ_b and Ω_b baryon masses is discussed in Section 4.

2 First observation of the hadronic decay $B_c^+ \to J/\psi\pi^+\pi^-\pi^+$

The B_c^+ meson is the lightest state composed of two heavy quarks, $\bar{b}$ and c. It was discovered by the CDF collaboration in the semileptonic decay $B_c^+ \to J/\psi l^+\nu X$ [6]. The same decay was also used for a lifetime measurement of the B_c^+ meson, which is a factor three smaller than the B^+ lifetime. Only one hadronic decay of the B_c^+ meson has been observed so far, $B_c^+ \to J/\psi\pi^+$.

Since the B_c^+ meson contains two heavy quarks, its production rate at the LHC is about three orders of magnitude smaller than for light B mesons.

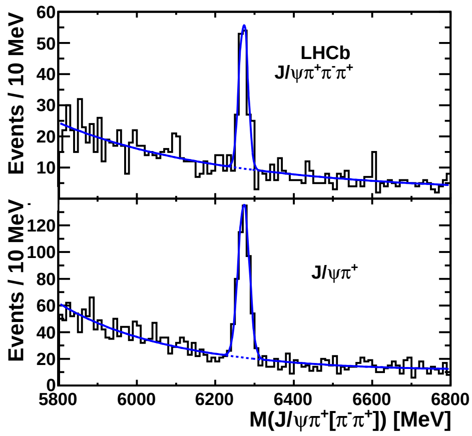

Figure 1: Invariant mass distributions of $B_c^+ \to J/\psi\pi^+\pi^-\pi^+$ and $B_c^+ \to J/\psi\pi^+$ candidates with the fit overlaid.

With an integrated luminosity of 0.8 fb^{-1} the LHCb collaboration has observed the hadronic decay $B_c^+ \to J/\psi\pi^+\pi^-\pi^+$ for the first time and measured its branching fraction relative to the branching fraction of the decay $B_c^+ \to J/\psi\pi^+$. The branching fraction for this decay is expected to be 1.5-2.3 time larger than for the decay $B_c^+ \to J/\psi\pi^+$.

The invariant mass distribution of $B_c^+ \to J/\psi\pi^+(\pi^-\pi^+)$ candidates is shown in Fig. 1.

The ratio of branching fractions is found to be [7]

$$\frac{B(B_c^+ \to J/\psi\pi^+\pi^-\pi^+)}{B(B_c^+ \to J/\psi\pi^+)} = 2.41 \pm 0.30 \pm 0.33,$$

where the first uncertainty is statistical and the second is systematic. The main sources of systematic uncertainty are the tracking efficiency, trigger, kaon veto and B_c^+ lifetime.

3 Measurement of the mass of the excited $B_{(s)}^{**}$ mesons

The properties of excited B mesons are predicted by the Heavy Quark Effective Theory (HQET). There are four excited B mesons with orbital angular momentum $L = 1$. These excited states are generically labelled as $B_{(s)}^{**}$, whereas the individual particles follow the PDG notation $B_{(s)J}^{(*)}$.

LHCb performed the search for $B_{(s)}^{**}$ states in the B^+K^-, $B^+\pi^-$ and $B^0\pi^+$ invariant mass distributions. Fig. 2 shows the invariant mass distributions relative to the threshold (Q value) of B^+K^-, $B^+\pi^-$ and $B^0\pi^+$ combinations with the fit overlaid. The peaks correspond to different $B_{(s)}^{**}$ states. The $B_{(s)1}$ and $B_{(s)2}^*$ resonances are observed with a significance greater than 5σ for all decays except for the $B_2^{*+} \to B^0\pi^+$ decay, which has a significance of more than 3σ. The decay $B_1^+ \to B^{*0}\pi^+$ is observed for the first time.

The masses measured for these six excited B mesons are [8]

$$\begin{aligned}
M_{B_{s1}^0} &= (5828.99 \pm 0.08 \pm 0.13 \pm 0.45)\ \mathrm{MeV}/c^2 & M_{B_{s2}^0} &= (5839.67 \pm 0.13 \pm 0.17 \pm 0.29)\ \mathrm{MeV}/c^2 \\
M_{B_1^0} &= (5724.1 \pm 1.7 \pm 2.0 \pm 0.5)\ \mathrm{MeV}/c^2 & M_{B_2^{*0}} &= (5738.6 \pm 1.2 \pm 1.2 \pm 0.3)\ \mathrm{MeV}/c^2 \\
M_{B_1^+} &= (5726.3 \pm 1.9 \pm 3.0 \pm 0.5)\ \mathrm{MeV}/c^2 & M_{B_2^{*+}} &= (5739.0 \pm 3.3 \pm 1.6 \pm 0.3)\ \mathrm{MeV}/c^2
\end{aligned}$$

where the first uncertainty is statistical, the second is systematic and the third is the B mass uncertainty from PDG. The masses of B_1^+ and B_2^{*+} are measured for the first time.

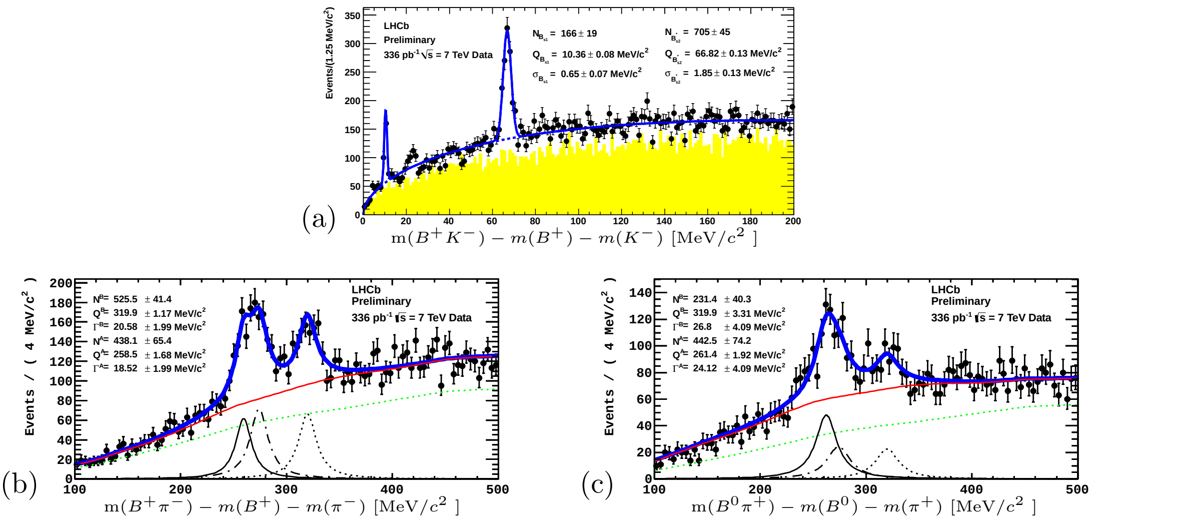

Figure 2: Fits to the Q distributions of the (a) B^+K^-, (b) $B^+\pi^-$ and (c) $B^0\pi^+$ final states. The full histogram (a) shows the distribution of wrong sign combinations.

4 Mass measurement of b-baryons, Ξ_b and Ω_b

The quark model predicts fifteen different ground states of b-baryons. There are seven ground states with $J^P = \frac{1}{2}^+$, containing one b quark and two light quarks (u, d or s). These states are the Λ_b^0 singlet, the Σ_b triplet, the Ξ_b doublet and the Ω_b singlet. Except for the Σ_b^0 baryon, all these states have already been observed and their masses have been measured. On the other hand, the quantum numbers and other properties for all these states have not yet been determined experimentally.

LHCb can improve the understanding of the baryon properties, such as masses and lifetimes, and their production. LHCb has performed the measurement of masses of two b-baryons: $\Xi_b(bsd)$ and $\Omega_b(bss)$. The mass of the Ω_b baryon was measured by CDF[9] and D0[10], showing a discrepancy of 6σ. The Ξ_b baryon has also been observed by Tevatron[11] and there is good agreement between the mass measurements.

The analysis done by LHCb is based on data corresponding to an integrated luminosity of 0.62 fb^{-1} recorded with the LHCb detector in the first half of 2011. Fig. 3 shows the invariant mass distributions of the Ξ_b and Ω_b candidates.

The measured masses of the Ξ_b and Ω_b baryons[12] are shown in Table 1 and are compared with the CDF and D0 results. The first uncertainty is statistical and the second is systematic.

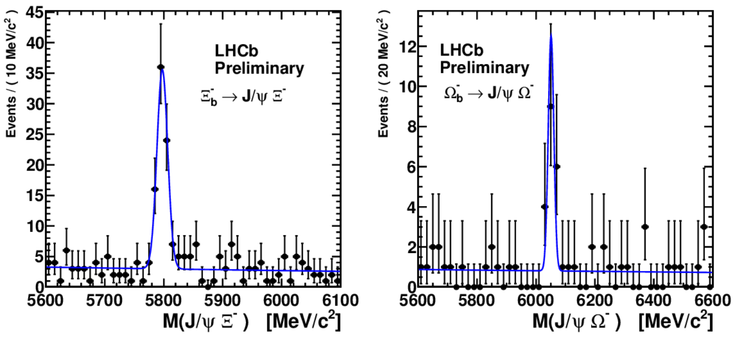

Figure 3: Invariant mass distribution of Ξ_b and Ω_b with the fit projections overlaid.

Table 1: LHCb results compared with results from CDF and D0.

	$M(\Xi_b)$ [MeV/c^2]	$M(\Omega_b)$ [MeV/c^2]
LHCb	$5796.5 \pm 1.2 \pm 1.2$	$6050.3 \pm 4.5 \pm 2.2$
D0	$5774 \quad \pm 19$	$6165 \quad \pm 16$
CDF	5790.9 ± 2.7	6054.4 ± 6.9

The systematic uncertainty is dominated by the momentum scale uncertainty.

The Ξ_b result is compatible with CDF and D0, while the Ω_b result is in good agreement with the CDF measurement but not with the D0 measurement.

5 Summary

Heavy flavour production and spectroscopy is a wide topic in LHCb. The recent results presented at the Moriond QCD conference include the first observation and the measurement of the branching fraction of the hadronic decay $B_c^+ \to J/\psi\pi^+\pi^-\pi^+$, the mass measurement of the excited B mesons and the mass measurement of the Ξ_b and Ω_b baryons.

References

1. A. A. Alves, Jr. *et al.* [LHCb Collaboration], "The LHCb Detector at the LHC," JINST **3**, S08005 (2008).
2. R. Aaij *et al.* [LHCb Collaboration], "Prompt charm production in pp collisions at $\sqrt{s} = 7$ TeV," CERN-LHCb-CONF-2010-013.
3. R. Aaij *et al.* [LHCb Collaboration], "Measurement of the $B^{\pm}$ production cross-section at LHCb," LHCb-CONF-2011-033.
4. R. Aaij *et al.* [LHCb Collaboration], "Measurement of the relative yields of decay modes $B^0 \to D^-\pi^+$, $B^0 \to D^-K^+$, $B_s^0 \to D_s^-\pi^+$, and determination of f_s/f_d for 7 TeV pp collisions," LHCb-CONF-2011-013.
5. R. Aaij *et al.* [LHCb Collaboration], "Measurement of the B_c^+ to B^+ production cross-section ratio at $\sqrt{s} = 7$ TeV in LHCb," LHCb-CONF-2011-017.
6. F. Abe *et al.* [CDF Collaboration], "Observation of the B_c meson in $p\bar{p}$ collisions at $\sqrt{s} = 1.8$ TeV," Phys. Rev. Lett. **81**, 2432 (1998) [hep-ex/9805034].
7. R. Aaij *et al.* [LHCb Collaboration], "First observation of the decay $B_c^+ \to J/\psi\pi^+\pi^-\pi^+$," arXiv:1204.0079 [hep-ex].
8. R. Aaij *et al.* [LHCb Collaboration], "Observation of Orbitally Exited $B_{(s)}^{**}$ Mesons," LHCb-CONF-2011-053.
9. T. Aaltonen *et al.* [CDF Collaboration], "Observation of the Ω_b^- Baryon and Measurement of the Properties of the Ξ_b^- and Ω_b^- Baryons," Phys. Rev. D **80**, 072003 (2009) [arXiv:0905.3123 [hep-ex]].
10. V. M. Abazov *et al.* [D0 Collaboration], "Observation of the doubly strange b baryon Ω_b^-," Phys. Rev. Lett. **101**, 232002 (2008) [arXiv:0808.4142 [hep-ex]].
11. V. M. Abazov *et al.* [D0 Collaboration], "Direct observation of the strange b baryon Ξ_b^-," Phys. Rev. Lett. **99**, 052001 (2007) [arXiv:0706.1690 [hep-ex]]. T. Aaltonen *et al.* [CDF Collaboration], "Observation and mass measurement of the baryon Ξ_b^-," Phys. Rev. Lett. **99**, 052002 (2007) [arXiv:0707.0589 [hep-ex]].
12. R. Aaij *et al.* [LHCb Collaboration], "Measurement of the masses of the Ξ_b^- and Ω_b^-," LHCb-CONF-2011-060.

Hadronic B Decays at LHCb

C.R. Jones
HEP Group, Cavendish Laboratory, JJ Thomson Avenue, Cambridge, CB3 0HE. United Kingdom

The article outlines three new or updated LHCb[1] results[2,3,4] presented at Moriond QCD 2012, using $1.0\,\mathrm{fb}^{-1}$ of data collected in 2011.

1 $\overline{B}{}^0_s$ to double-charm final states

Double charm decays of B mesons provide an interesting avenue to search for signs of new physics beyond the Standard Model (SM). For example, the decays $\overline{B}{}^0 \to D^+D^-$ and $\overline{B}{}^0_s \to D_s^+D_s^-$ can be used to measure the weak phase γ, assuming U-spin symmetry and the decay $\overline{B}{}^0 \to D^+D^-$ provides an alternate way to measure $\sin(2\beta)$, which can in principle differ from the values determined in $\overline{B}{}^0 \to (c\bar{c})K^0_{\mathrm{S}}$ because of penguin contributions.

1.1 Event Selection and Analysis

Signal candidates are formed using reconstructed $D^0 \to K^-\pi^+$, $D^+ \to K^-\pi^+\pi^+$ and $D_s^+ \to K^+K^-\pi^+$ decays[2]. The B candidates are then reconstructed from the appropriate pair of charm mesons, applying both mass and vertex constraints to the assumed decay chain and loose particle identification requirements on the D children. To further improve the signal purity, a multivariate selection is then applied, trained on data using clean signals of D mesons obtained from background subtracted $\overline{B}{}^0_{(s)} \to D^+_{(s)}\pi^-$ and $B^- \to D^0\pi^-$ decays. Background for the training is taken from the D mass sideband regions. In addition to including kinematical quantities of the D and the D children, a number of track-quality and particle-identification variables are also used to maximize the discriminating power.

The mass spectra are fitted using a single Crystal Ball function which is used for all $\overline{B} \to D\overline{D}'$ modes. Simulated events are used to derive Gaussian parametrizations for the backgrounds due to mis-reconstructed decays. An exponential combinatoric background term is also included. Examples of the fitted mass spectra are shown in Figures 1 and 2.

The results for the branching ratios, computed from the fitted signal yields, are

$$\begin{aligned}
&\frac{\mathcal{B}(\overline{B}{}^0_s \to D^+D^-)}{\mathcal{B}(\overline{B}{}^0 \to D^+D^-)} = 1.00 \pm 0.18 \pm 0.09 \quad , && \frac{\mathcal{B}(\overline{B}{}^0_s \to D_s^+D^-)}{\mathcal{B}(B^0 \to D_s^+D^-)} = 0.048 \pm 0.008 \pm 0.004, \\
&\frac{\mathcal{B}(\overline{B}{}^0_s \to D_s^+D_s^-)}{\mathcal{B}(\overline{B}{}^0 \to D^+D_s^-)} = 0.508 \pm 0.026 \pm 0.043, && \frac{\mathcal{B}(\overline{B}{}^0_s \to D^0\overline{D}{}^0)}{\mathcal{B}(B^- \to D^0D_s^-)} = 0.015 \pm 0.004 \pm 0.002,
\end{aligned} \tag{1}$$

where the errors are statistical and systematic respectively. See[2] for details on the determination of the systematic uncertainities.

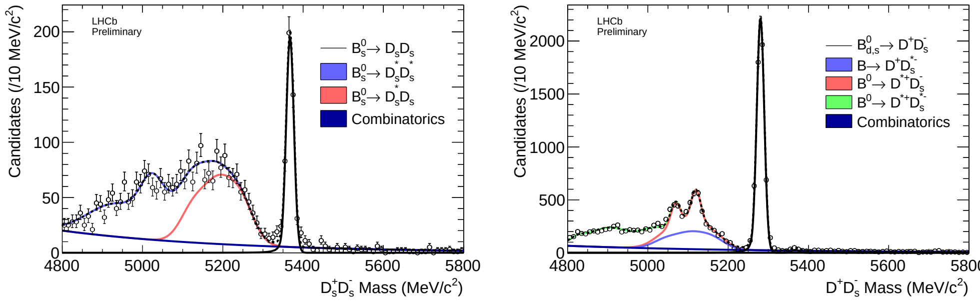

Figure 1: Invariant mass distributions for $\overline{B}{}^0_s \to D_s^+ D_s^-$ (left) and $\overline{B}{}^0 \to D^+ D_s^-$ (right) candidates.

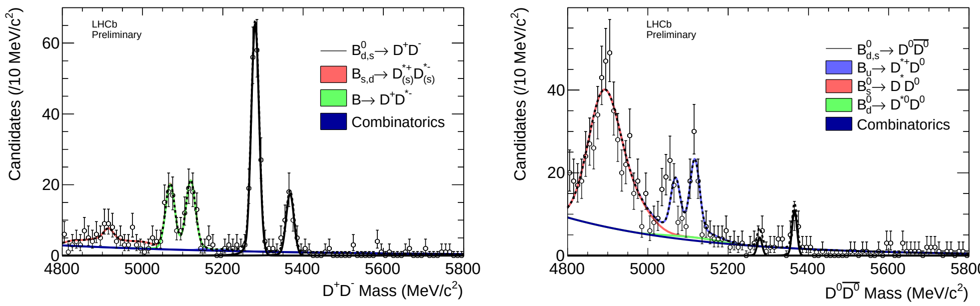

Figure 2: Invariant mass distributions for $\overline{B}{}^0_{(s)} \to D^+ D^-$ (left) and $\overline{B}{}^0_{(s)} \to D^0 \overline{D}{}^0$ (right).

1.2 Summary

First observations and relative branching fractions measurements of the decays $\overline{B}{}^0_s \to D^+ D^-$, $\overline{B}{}^0_s \to D_s^+ D^-$ and $\overline{B}{}^0_s \to D^0 \overline{D}{}^0$ have been made [2]. A new result on the branching fraction of $\overline{B}{}^0_s \to D_s^+ D_s^-$ relative to $\overline{B}{}^0_s \to D_s^+ D^-$, which has a precision about 5 times better than the current world average value [5] has also been presented.

2 Observation of CP violation in $B^\pm \to DK^\pm$ decays

Testing the unitary of the CKM quark mixing matrix, by verifing the condition $V_{ud}V_{ub}^* + V_{cd}V_{cb}^* + V_{td}V_{tb}^* = 0$, is a powerful check of the SM. This condition describes a triangle in the complex plane, whose area is proportional to the amount of *CP* violation in the model, and the unitary of which can be tested by making over-constraining measurements of its sides and angles.

Measurements of the partial widths of $B^\pm \to DK^\pm$ decays, with D either a D^0 or $\overline{D}{}^0$ meson, provide one of the most powerful methods for determining the currently least-well determined observable, the CKM phase $\gamma = \arg\left(-V_{ud}V_{ub}^*/V_{cd}V_{cb}^*\right)$. If the same D final state is accessible for both D^0 and $\overline{D}{}^0$ mesons, the interference of these two processes gives sensitivity to γ and may exhibit direct *CP* violation. This feature of open-charm B^- decays was first recognised in its application to *CP* eigenstates, such as $D \to K^+K^-$, $\pi^+\pi^-$ [6,7] but can be extended to other decays, *e.g.* $D \to \pi^- K^+$, labelled “ADS” modes in reference to the authors [8,9].

2.1 Event Selection and Analysis

All sixteen combinations of $B^\pm \to Dh^\pm$, $D \to h^\pm h^\mp$ with $h = K, \pi$ are formed with the candidate D mass within $1765 - 1965$ MeV/c^2. P and Pt cuts are applied to the D daughter tracks, in order to ensure best pion versus kaon discrimination.

A multi-variate selection is then trained using a simulated sample of $B^\pm \to [K^\pm\pi^\mp]_D K^\pm$ and background events from the D sideband ($35 < |m(hh) - m_{\rm PDG}^{D^0}| < 100$ MeV/c^2) of an independent sample collected in 2010. The selection uses a combination of track and vertex quality variables, $B^{\pm}$ and D flight distance and the angle between the $B^{\pm}$ momentum vector and the line joining its decay vertex to the primary interaction vertex. For futher details see [3].

The observables of interest are determined from a fit to the invariant mass distributions of selected B candidates, as shown in Figure 3.

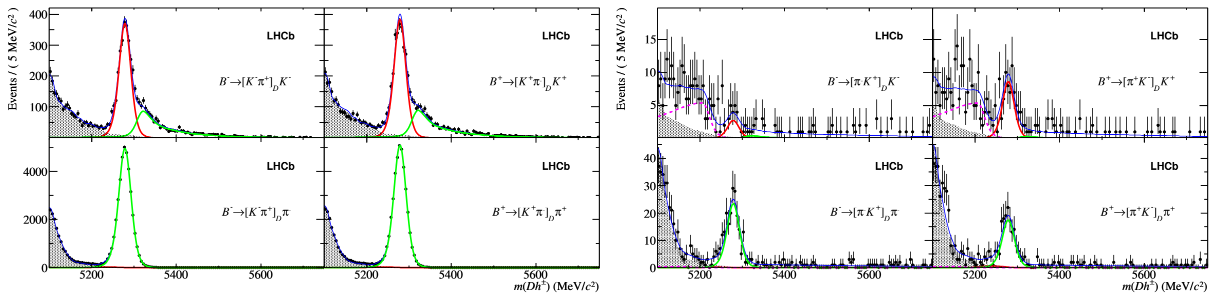

Figure 3: Invariant mass distributions of $B^{\pm} \to [K^{\pm}\pi^{\mp}]_D h^{\pm}$ (left) and $B^{\pm} \to [\pi^{\pm}K^{\mp}]_D h^{\pm}$ (right) candidates.

In total, thirteen observables are measured in the fit:

$$R^f_{K/\pi} = \frac{\Gamma(B^- \to [f]_D K^-) + \Gamma(B^+ \to [f]_D K^+)}{\Gamma(B^- \to [f]_D \pi^-) + \Gamma(B^+ \to [f]_D \pi^+)}, \qquad R^{\pm}_h = \frac{\Gamma(B^{\pm} \to [\pi^{\pm}K^{\mp}]_D h^{\pm})}{\Gamma(B^{\pm} \to [K^{\pm}\pi^{\mp}]_D h^{\pm})}$$
$$A^f_h = \frac{\Gamma(B^- \to [f]_D h^-) - \Gamma(B^+ \to [f]_D h^+)}{\Gamma(B^- \to [f]_D h^-) + \Gamma(B^+ \to [f]_D h^+)} \tag{2}$$

where f represents KK, $\pi\pi$ and the favoured $K\pi$ mode. The following quantities are deduced:

$$\begin{aligned}
R_{CP+} \approx \; < R^{KK}_{K/\pi}, R^{\pi\pi}_{K/\pi} > / R^{K\pi}_{K/\pi} &= 1.007 \pm 0.038(\text{stat}) \pm 0.012(\text{syst}) \\
A_{CP+} = \; < A^{KK}_{K}, A^{\pi\pi}_{K} > &= 0.145 \pm 0.032(\text{stat}) \pm 0.010(\text{syst}) \\
R_{\text{ADS}(K)} = (R^-_K + R^+_K)/2 &= 0.0152 \pm 0.0020(\text{stat}) \pm 0.0004(\text{syst}) \\
A_{\text{ADS}(K)} = (R^-_K - R^+_K)/(R^-_K + R^+_K) &= -0.52 \pm 0.15(\text{stat}) \pm 0.02(\text{syst}) \\
R_{\text{ADS}(\pi)} = (R^-_\pi + R^+_\pi)/2 &= 0.00410 \pm 0.00025(\text{stat}) \pm 0.00005(\text{syst}) \\
A_{\text{ADS}(\pi)} = (R^-_\pi - R^+_\pi)/(R^-_\pi + R^+_\pi) &= 0.143 \pm 0.062(\text{stat}) \pm 0.011(\text{syst}),
\end{aligned}$$

2.2 Summary

The $B^{\pm} \to DK^{\pm}$ ADS mode has been observed with a statistical significance of $\sim 10\sigma$ and displays evidence (4.0σ) of a large negative asymmetry. The $B^{\pm} \to D\pi^{\pm}$ ADS mode shows a hint of a positive asymmetry with 2.4σ significance. The KK and $\pi\pi$ modes both show positive asymmetries. The statistical significance of the combined asymmetry, A_{CP+}, is 4.5σ. With a total significance of 5.8σ, direct *CP* violation in $B^{\pm} \to DK^{\pm}$ decays is observed.

3 Polarization amplitudes and triple product asymmetries in the decay $B^0_s \to \phi\phi$

In the SM, the flavour-changing neutral current decay $B^0_s \to \phi\phi$ proceeds via a $b \to s\bar{s}s$ penguin process. These decays can be used to investigate new sources of CP violation in the comparison of their time-dependent CP asymmetry with the charmonia modes (e.g $B_s \to J/\Psi\phi$).

As the decay is a pseudoscalar to vector-vector transition, three possible spin configurations of the vector meson pair are allowed by angular momentum conservation, namely H_{+1}, H_{-1} and H_0. From these states, three linear polarization amplitudes can be defined

$$A_0 = H_0\,, \qquad A_{\perp} = \frac{H_{+1} - H_{-1}}{\sqrt{2}}\,, \qquad A_{\parallel} = \frac{H_{+1} + H_{-1}}{\sqrt{2}}\,. \tag{3}$$

The $\phi\phi$ final state can be a mixture of *CP*-even and *CP*-odd eigenstates. The longitudinal (A_0) and parallel ($A_{\parallel}$) components are *CP*-even and the perpendicular component ($A_{\perp}$) is

CP-odd. From the V–A structure of the weak interaction, the longitudinal component, $f_L = |A_0|^2/(|A_0|^2 + |A_\perp|^2 + |A_\parallel|^2)$, is expected to be dominant. The revelant decay angles are defined in Figure 4 .

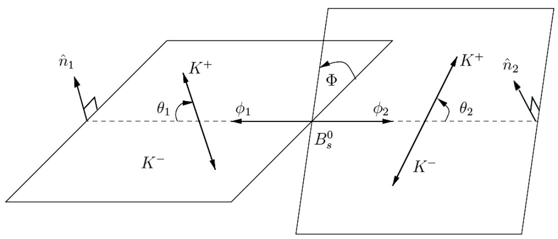

Figure 4: Decay angles for the $B_s^0 \to \phi\phi$ decay.

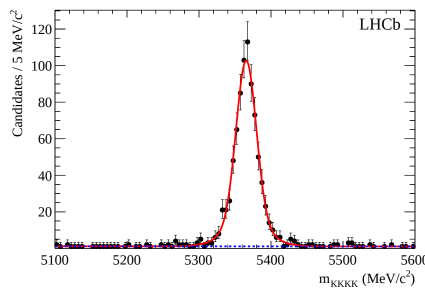

Figure 5: Invariant $K^+K^-K^+K^-$ mass distribution.

A search for physics beyond the SM can also be performed by studying the triple products $U = \sin(2\Phi)/2$ and $V = \pm\sin(\Phi)$. Non zero values of the asymmetries in these variables (0 in the SM), A_U and A_V, can be either due to T-violation or final-state interactions.

3.1 Event Selection and Analysis

$B_s^0 \to \phi\phi$ candidates are reconstructed[4] using events where both ϕ mesons decay into a K^+K^- pair. Excellent signal purity (Figure 5) is achieved using cuts on the minimum impact parameter of the tracks to all reconstructed pp interaction vertices, and by requiring the tracks also are identified as kaons.

3.2 Summary

The polarization amplitudes ($|A_0|^2$, $|A_\perp|^2$, $|A_\parallel|^2$) and triple product asymetries A_U and A_V are determined by performing an unbinned maximum likelihood fits to data. The results are :-

$$\begin{aligned}
|A_0|^2 &= 0.365 \pm 0.022\,(\text{stat}) \pm 0.012\,(\text{syst})\,, \\
|A_\perp|^2 &= 0.291 \pm 0.024\,(\text{stat}) \pm 0.010\,(\text{syst})\,, & A_U &= -0.055 \pm 0.036\,(\text{stat}) \pm 0.018\,(\text{syst})\,, \\
|A_\parallel|^2 &= 0.344 \pm 0.024\,(\text{stat}) \pm 0.014\,(\text{syst})\,, & A_V &= 0.010 \pm 0.036\,(\text{stat}) \pm 0.018\,(\text{syst})\,. \\
\cos(\delta_\parallel) &= -0.844 \pm 0.068\,(\text{stat}) \pm 0.029\,(\text{syst})\,.
\end{aligned}$$

and are consistent previous measurements and do not exhibit any T-odd violation effects.

1. A.Augusto Alves et al. The LHCb Detector at the LHC. *JINST*, 3:S08005, 2008.
2. First observations and branching fraction measurements of $\overline{B}_s^0$ to double-charm final states LHCb-CONF-2012-009.
3. Observation of CP violation in $B^\pm \to DK^\pm$ decays LHCb-PAPER-2012-001.
4. Measurement of the polarization amplitudes and triple product asymmetries in the $B_s^0 \to \phi\phi$ decay LHCb-PAPER-2012-004.
5. K. Nakamura et al. Review of particle physics. *J. Phys.*, G37:075021, 2010.
6. Michael Gronau and David London. How to determine all the angles of the unitarity triangle from $B_d^0 \to DK_S^0$ and $B_s^0 \to D\phi$. *Phys. Lett.*, B253:483, 1991.
7. Michael Gronau and Daniel Wyler. On determining a weak phase from CP asymmetries in charged B decays. *Phys. Lett.*, B265:172, 1991.
8. David Atwood, Isard Dunietz, and Amarjit Soni. Enhanced CP violation with $B \to KD^0(\overline{D}^0)$ modes and extraction of the CKM angle γ. *Phys.Rev.Lett.*, 78:3257, 1997.
9. David Atwood, Isard Dunietz, and Amarjit Soni. Improved methods for observing CP violation in $B^\pm \to KD$ and measuring the CKM phase γ. *Phys.Rev.*, D63:036005, 2001.

Baryonic B decays at BABAR

O. GRUENBERG (for the BABAR collaboration)
University of Rostock, Institute for Physics,
Uniplatz 3, 18055 Rostock, Germany

We report on the analyses of the baryonic B decays $\overline{B}^0 \to \Lambda_c^+ \, \overline{p}p\overline{p}$ and $B^- \to \Sigma_c^{++}\overline{p}\pi^-\pi^-$. The underlying data sample consists of 470×10^6 $B\overline{B}$ pairs generated in the process $e^+e^- \to \Upsilon(4S) \to B\overline{B}$ and collected with the BABAR detector at the PEP-II storage ring at SLAC. We find $\mathcal{B}(\overline{B}^0 \to \Lambda_c^+ \, \overline{p}p\overline{p}) \cdot \mathcal{B}(\Lambda_c^+ \to pK^-\pi^+)/5\% < 6.2 \cdot 10^{-6}$ @ 90 % CL and $\mathcal{B}(B^- \to \Sigma_c^{++}\overline{p}\pi^-\pi^-) = (2.98 \pm 0.16_{(\mathrm{stat})} \pm 0.15_{(\mathrm{syst})} \pm 0.77_{(\Lambda_c)}) \times 10^{-4}$, where the last error is due to the uncertainty in $\mathcal{B}(\Lambda_c^+ \to pK^-\pi^+)$. The data suggest the existence of resonant subchannels $B^- \to \Lambda_c(2595)^+ \, \overline{p}\pi^-$ and, possibly, $B^- \to \Sigma_c^{++}\overline{\Delta}^{--}\pi^-$. We see unexplained structures in $m(\Sigma_c^{++}\pi^-\pi^-)$ at 3.25 GeV/c^2, 3.8 GeV/c^2, and 4.2 GeV/c^2.

1 Introduction

Approximately 7 % [1] of all B mesons have baryons among their decay products. This is a substantial fraction that justifies further investigations which may allow better understanding of baryon production in B decays and, more generally, hadron fragmentation into baryons. The measurement and comparison of exclusive branching fractions of baryonic B decays as well as systematic studies on the dynamic of the decay, i.e. the fraction of resonant subchannels, is a direct way to study the mechanisms of baryonization. In the following, we present the results of two recently completed BABAR analyses of the decays $B^- \to \Sigma_c^{++}\overline{p}\pi^-\pi^-$ and $\overline{B}^0 \to \Lambda_c^+ \, \overline{p}p\overline{p}$ [2].

2 $B^- \to \Sigma_c^{++}\overline{p}\pi^-\pi^-$

The decay $B^- \to \Sigma_c^{++}\overline{p}\pi^-\pi^-$ is a resonant subchannel of the five body final state $B^- \to \Lambda_c^+ \, \overline{p}\pi^+\pi^-\pi^-$, which has, until now, the largest known branching fraction among all baryonic B decays and hence is a good starting point for further investigations.

2.1 Reconstruction

We reconstruct the decay in the subchannel $\Sigma_c^{++} \to \Lambda_c^+ \, \pi^+$, and $\Lambda_c^+ \to p \, K^- \, \pi^+$. For the signal selection we use the missing energy of the B candidate in the e^+e^- rest frame: $\Delta E = \sqrt{\mathrm{E_B^{2*}} - \sqrt{s}/2}$. Figure 1 shows the distribution of ΔE from the sample of reconstructed B events in data after selections for background suppression. From a fit we find 787 ± 43 signal events. The reconstruction efficiency is $(11.3 \pm 0.2_{(\mathrm{stat})})\%$. The branching fraction is $\mathcal{B}(B^- \to \Sigma_c^{++}\overline{p}\pi^-\pi^-) = (2.98 \pm 0.16_{(\mathrm{stat})} \pm 0.15_{(\mathrm{syst})} \pm 0.77_{(\Lambda_c)}) \times 10^{-4}$.

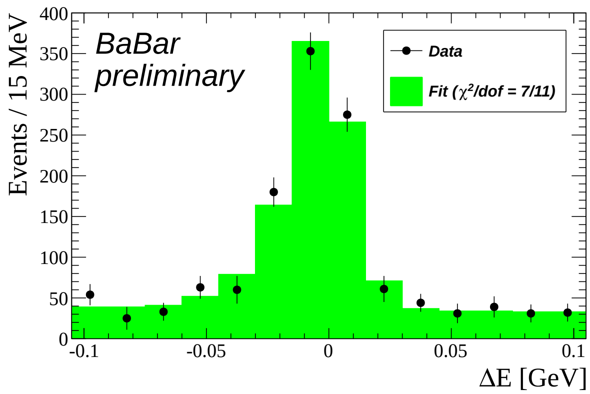

Figure 1: The distribution of ΔE from the *BABAR* data.

2.2 Resonant subchannels

We see large deviations between data and the prediction of four-body phase space (PS) in the two-body and three-body masses of the B daughters. These deviations may be attributed to the resonant intermediate states $\Lambda_c^{*+} \rightarrow \Sigma_c^{++}\pi^-$ and $\overline{\Delta}^{--} \rightarrow \overline{p}\pi^-$.
Figure 2(a) shows the invariant mass distribution of $\Sigma_c^{++}\pi^-$ after a sideband subtraction in ΔE and efficiency correction. The large number of events at the threshold is compatible with the existance of the resonance Λ_c^+ $(2595)^+$. There are no significant signals for other Λ_c^{*+} resonances.
Figure 2(b) shows the invariant mass distribution of $p\pi^-$ after a sideband subtraction in ΔE and efficiency correction. The differences between data and PS in the range of $m(\overline{p}\pi^-) \in (1.2, 1.7)\,\mathrm{GeV}/c^2$ could be due to the existance of the resonances $\overline{\Delta}^{--}(1232, 1600, 1620)$.

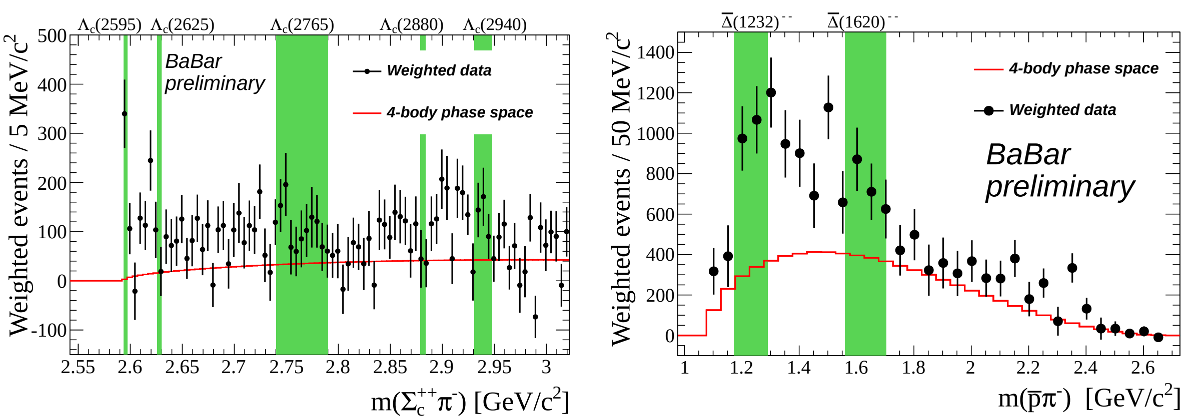

(a) (b)

Figure 2: The distribution of m($\Sigma_c^{++}\pi^+$) and m(p π^-) from *BABAR* data and four-body PS.

Figure 3(a) shows the invariant mass distribution of $\Sigma_c^{++}\pi^-\pi^-$ after a sideband subtraction in ΔE and efficiency correction. We see unexplained structures at $3.25\,\mathrm{GeV}/c^2$, $3.8\,\mathrm{GeV}/c^2$, and $4.2\,\mathrm{GeV}/c^2$. In figure 3(b) we present the result of a fit in the range $m(\Sigma_c^{++}\pi^-\pi^-) = 2.750\ldots3.725\,\mathrm{GeV}/c^2$. We choose an ad-hoc parametrization that consists of a Breit-Wigner function with two parameters (width: Γ, mean: μ) for the signal and a two-body phase space distribution with the parameters $m_1 = m(\Sigma_c^{++})$ and $m_2 = 2 \cdot m(\pi^-)$ for the background. The fitted parameters are $\mu = (3245 \pm 20_{(\mathrm{stat})})\,\mathrm{MeV}/c^2$ and $\Gamma = (108 \pm 60_{(\mathrm{stat})})\,\mathrm{MeV}/c^2$.

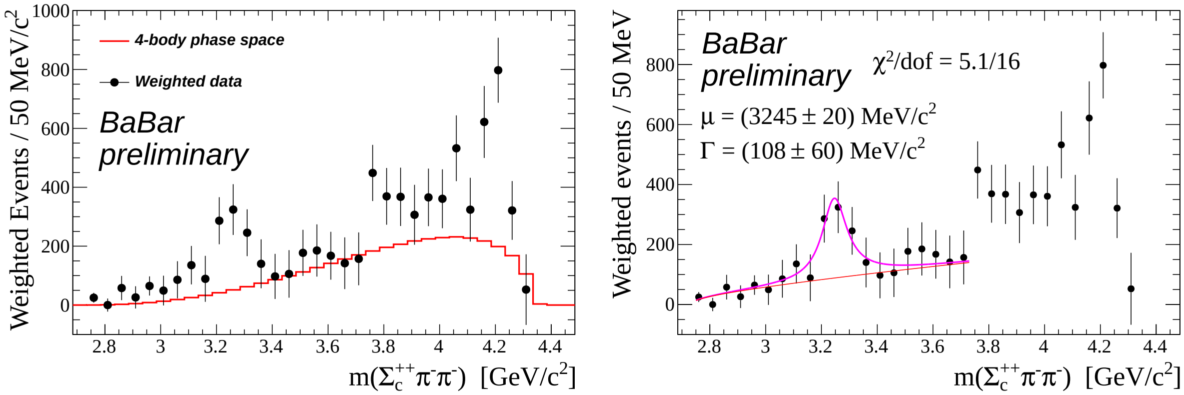

(a) (b)

Figure 3: The distribution of m($\Sigma_c^{++}\pi^-\ \pi^-$) from *BABAR* data and four-body PS.

2.3 Conclusion

Comparing the branching fractions $\mathcal{B}(B^- \to \Sigma_c^{++}\overline{p}\pi^-\pi^-) = (2.98 \pm 0.8) \times 10^{-4}$ and $\mathcal{B}(B^- \to \Sigma_c^0\overline{p}\pi^+\pi^-) = (4.4 \pm 1.7) \times 10^{-4}$ [3] one finds that the decay $B^- \to \Sigma_c^0\overline{p}\pi^+\pi^-$ is 50% more frequent. This could be due to a number of additional resonant subchannels that contribute to $B^- \to \Sigma_c^0\overline{p}\pi^+\pi^-$, i.e. $B^- \to \Sigma_c^0\overline{N}\pi^-$ and $B^- \to \Sigma_c^0\overline{p}\rho^0$, and would indicate the importance of resonant subchannels in baryonic B decays. Furthermore, the combined branching fraction of $B^- \to \Sigma_c^{++}\overline{p}\pi^-\pi^-$ and $B^- \to \Sigma_c^0\overline{p}\pi^+\pi^-$ makes about 30% of the branching fraction of the five body decay $\mathcal{B}(B^- \to \Lambda_c^+\ \overline{p}\pi^+\pi^-\pi^-) = (22.5 \pm 6.8) \times 10^{-4}$ [3], which also stresses the large impact of intermediate states.

3 $\overline{B}^0 \to \Lambda_c^+\ \overline{p}p\overline{p}$

The decay $\overline{B}^0 \to \Lambda_c^+\ \overline{p}p\overline{p}$ is one of a few allowed B decays with a $b \to c$ transition and four baryons in the final state. It is closely connected to $\overline{B}^0 \to \Lambda_c^+\ \overline{p}\pi^+\pi^-$ ($\mathcal{B} = (1.12 \pm 0.32) \times 10^{-3}$ [4]) and $B^- \to \Lambda_c^+\ \overline{p}\pi^+\pi^-\pi^-$, which have similar quark contents and the (so far) largest measured branching fractions among the baryonic B decays with a Λ_c^+ in the final state. The main differences between the sought decay and the other two decay channels are the absence of possible resonant subchannels and the much smaller phase space ($Q(\overline{B}^0 \to \Lambda_c^+\ \overline{p}p\overline{p}) = 176\,\mathrm{MeV}/c^2, Q(\overline{B}^0 \to \Lambda_c^+\ \overline{p}\pi^+\pi^-) = 1776\,\mathrm{MeV}/c^2$ with $Q = m(\text{mother}) - \sum m(\text{daughter})$. The latter may favour the decay $\overline{B}^0 \to \Lambda_c^+\ \overline{p}p\overline{p}$, in that baryons are more likely to form when quarks are close to each other in momentum space [5], [6]. An example of this behavior is the ratio of $\mathcal{B}(B^- \to \Lambda_c^+\ \overline{\Lambda}_c^-\ K^-)/\mathcal{B}(B^- \to \Lambda_c^+\ \overline{p}\pi^-) \approx 3$ [1], preferring the more massive final state that mainly differs by the size of phasespace since $|V_{cs}| \approx |V_{ud}|$. On the other hand the decay $\overline{B}^0 \to \Lambda_c^+\ \overline{p}p\overline{p}$ may be suppressed by the fact that it does not have resonant subchannels which could play an important role for baryonic B decays, i.e. $\mathcal{B}(\overline{B}^0 \to \Lambda_c^+\ \overline{p}\pi^+\pi^-)_{\text{resonant}}/\mathcal{B}(\overline{B}^0 \to \Lambda_c^+\ \overline{p}\pi^+\pi^-) \approx 40\%$ [1]. The size of the branching fraction may allow to balance the relevance of resonant subchannels against momentum space in baryonic B decays.

3.1 Reconstruction

We reconstruct the decay $\overline{B}^0 \to \Lambda_c^+ \overline{p} p \overline{p}$ in the subchannel $\Lambda_c^+ \to p\, K^-\, \pi^+$. Besides ΔE, we use the energy substituted mass $m_{\rm ES}$ of the B candidate for the signal selection. In a simplified form, it can be written as $m_{\rm ES}\prime = \sqrt{(\sqrt{s}/2)^2 - |\vec{p}_{\rm B}^{\,*}|^2}$, where $\vec{p}_{\rm B}^{\,*}$ is the momentum of the B candidate in the e^+e^- rest frame. The complete formular of $m_{\rm ES}$ also takes into account the asymmetric energies of e^+ and e^-. $m_{\rm ES}$ is centered at the true B mass for correctly reconstructed B decays. Figure 4 shows the distribution of ΔE vs. $m_{\rm ES}$ with a selection in $m_{pK^-\pi^+}$ for background suppression. There are two B candidates within a signal window that is chosen on the basis of an analysis of simulated signal events. The efficiency in this range is $\varepsilon = (3.66 \pm 0.03_{\rm (stat)})\,\%$. For background estimation we analyze sidebands in $m_{pK^-\pi^+}$ and $m_{\rm ES}$ from the data sample as well as a set of simulated *BABAR* events and find no reliable prediction due to large systematic uncertainties. Therefore we calculate a conservative upper limit by taking the two B candidates as signal. In addition, we exclude the large uncertainty of $\mathcal{B}(\Lambda_c^+ \to pK^-\pi^+) = (5.0 \pm 1.3)\,\%$ [1]. Consequently, we determine:

$$\mathcal{B}(\overline{B}^0 \to \Lambda_c^+ \overline{p} p \overline{p}) \cdot \frac{\mathcal{B}(\Lambda_c^+ \to pK^-\pi^+)}{5\,\%} < \frac{N_{up}}{\varepsilon \cdot N_B \cdot 5\,\%} = 6.2 \cdot 10^{-6} \quad @\, CL = 90\% \qquad (1)$$

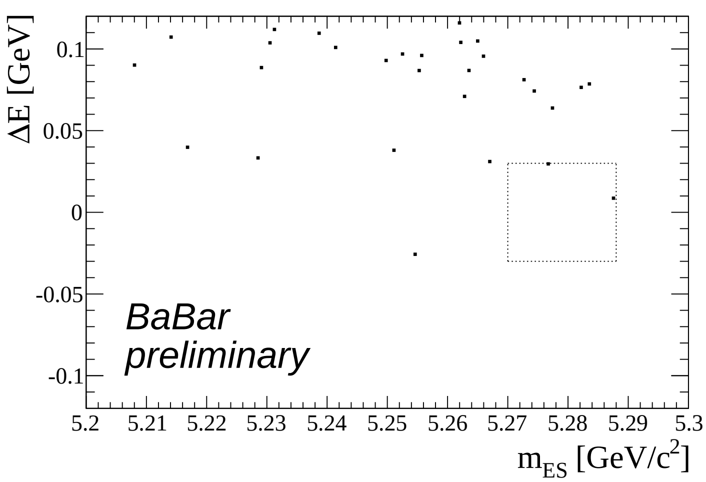

Figure 4: The distribution of ΔE vs. $m_{\rm ES}$ from the *BABAR* data.

As a result we find that $\mathcal{B}(\overline{B}^0 \to \Lambda_c^+ \overline{p} p \overline{p})$ is at least two orders of a magnitude smaller than $\mathcal{B}(\overline{B}^0 \to \Lambda_c^+ \overline{p}\pi^+\pi^-)$ and $\mathcal{B}(B^- \to \Lambda_c^+ \overline{p}\pi^+\pi^-\pi^-)$ @ $CL = 90\%$. This could indicate, that the phase space of $\overline{B}^0 \to \Lambda_c^+ \overline{p} p \overline{p}$ is too small to favor baryonisation of the quarks and thus increase the decay rate. Furthermore, the nonappearance of resonant subchannels may additionally affect the branching fraction.

References

1. K. Nakamura *et al.* (Particle Data Group), J. Phys. **G37**, 075021 (2010).
2. Throughout this paper, all decay modes represent that mode and its charge conjugate.
3. S. A. Dytman *et al.* (CLEO Collaboration), Phys. Rev. **D66**, 091101 (2002).
4. K. S. Park *et al.* (Belle Collaboration), Phys. Rev. D **75**, 011101 (2007).
5. J. L. Rosner, Phys. Rev. D **68** (2003) 014004 [hep-ph/0303079].
6. M. Suzuki, J. Phys. G G **34** (2007) 283 [hep-ph/0609133].

Studies of Charmonium States in Two-photon fusion at *BABAR*

Nir Guttman
(On behalf of the *BABAR* Collaboration)
Tel Aviv University, Department of High Energy Physics, Israel

We report on two studies using two-photon fusion events, $\gamma\gamma \to J/\psi\omega$ and $\gamma\gamma \to \eta_c\pi^+\pi^-$, performed on a data sample of around 500 fb^{-1} collected by the *BABAR* experiment at the PEP-II asymmetric energy e^+e^- storage ring at the SLAC National Accelerator Laboratory at center-of-mass energies at or around the $\Upsilon(2S)$, $\Upsilon(3S)$, and $\Upsilon(4S)$ resonances.

1 Introduction

In recent years, experiments have collected evidence for new charmonium-like states that do not fit well with the conventional $c\bar{c}$ picture [?]. Two-photon fusion events are a useful production mode for studying such states. The e^+ and e^- are scattered at small angles and are therefore undetected implying that the photons are quasi-real. This allows production of final state with the quantum numbers $J^{PC} = 0^{\pm+}$, $2^{\pm+}$, $4^{\pm+}$, ...,3^{++}, 5^{++},... [?]. A further consequence is that the transverse momentum (p_T) of the hadronic system is expected to be low. In addition, these events are characterized by low particle multiplicity and low energy. Any additional energy (E_{extra}) in the calorimeter not associated with the final state is expected to be small. A process that mimics the characteristics of two-photon events is the initial state radiation (ISR) process. A powerful discriminate against such events is a requirement of large values of $M^2_{miss} \equiv (p_{e^+e^-} - p_{rec})^2$ where the $p_{e^+e^-}$ (p_{rec}) is the four momentum of the initial state (reconstructed final state).

2 Analysis of $\gamma\gamma \to J/\psi\omega$

The charmonium-like state $X(3915)$ was first observed [?] by Belle in two-photon fusion events decaying into $J/\psi\omega$. In addition, it was seen decaying into $J/\psi\omega$ in B decay analysis, along with the $X(3872)$ [?]. The nature of the $X(3872)$ is still unclear. It is commonly accepted [?] that its quantum numbers can be 1^{++} or 2^{-+}.

This analysis is performed to search for the $X(3915)$ and the $X(3872)$ resonances via the decay to $J/\psi\omega$, using a data sample of 519.2 ± 5.7 fb^{-1}. The J/ψ is reconstructed using the l^+l^- final state, with $l = e$ or μ. The J/ψ signal region is defined as $2.95 < m(e^+e^-) < 3.14$ GeV/c^2 or $3.05 < m(\mu^+\mu^-) < 3.14$ GeV/c^2. The ω is reconstructed using its $\pi^+\pi^-\pi^0$ decay. The neutral pions are reconstructed via the decay to two photons. The ω signal region is defined as $740 < m(\pi^+\pi^-\pi^0) < 820$ MeV/c^2. A candidate $J/\psi\omega$ is reconstructed by fitting the J/ψ and the ω to a common vertex. The main event selection criteria require the number of tracks in the event to be four, $p_T < 0.2$ GeV/c, $E_{extra} < 0.3$ GeV, and $M^2_{miss} > 2$ (GeV/c^2)^2. Fig. **??**

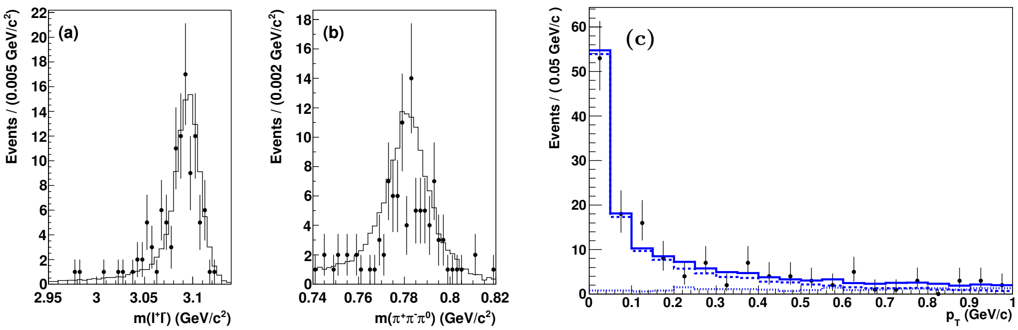

Figure 1: The solid points represents the data, and the histogram represents normalized MC. (a) Distribution of $m(l^+l^-)$ for events in the ω signal region. (b) Distribution of $m(\pi^+\pi^-\pi^0)$ for events in the J/ψ signal region. (c) The p_T distribution. The solid points represents the data and the solid histogram represents the result of a fit to the sum of the simulated signal (dashed) and background (dotted) contributions.

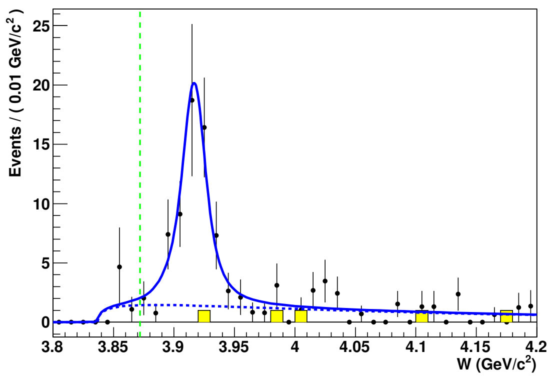

Figure 2: The efficiency-corrected W spectrum. The solid line represents the total fit function. The dashed line represent the background contribution. The histogram is the background estimated from sidebands. The vertical dashed line is placed at the mass peak of the $X(3872)$.

presents the p_T distribution of the final sample after the event selection, and the invariant mass distributions for the J/ψ and ω in the signal regions.

We calculate the $J/\psi\omega$ candidate mass from $m(J/\psi\omega) = m(l^+l^-\pi^+\pi^-\pi^0) - m(l^+l^-) + m(J/\psi)^{PDG}$ using the known J/ψ mass $m(J/\psi)^{PDG}$? to improve the mass resolution. The detection efficiency is parameterized as a function of $m(J/\psi\omega)$ and θ_l, where θ_l is defined as the angle between the direction of the positively-charged lepton and the beam axis in the $J/\psi\omega$ rest frame. An extended unbinned maximum likelihood fit is performed to the efficiency-corrected spectrum W. The probability density function describe three event types: combinatorial background, $X(3915)$ signal, and $X(3872)$ signal. Fig. **??** presents the result of the fit. A large peak at near 3915 MeV/c^2 is observed with a significance of 7.6σ. The measured resonance parameters are $m[X(3915)] = (3919.4 \pm 2.2 \pm 1.6)\,\mathrm{MeV}/c^2$, $\Gamma[X(3915)] = (13 \pm 6 \pm 3)\,\mathrm{MeV}$. The measured value of the two-photon width times the branching fraction, $\Gamma_{\gamma\gamma}[X(3915)] \times \mathcal{B}(X(3915) \to J/\psi\omega)$, is $(52 \pm 10 \pm 3)$ eV and $(10.5 \pm 1.9 \pm 0.6)$ eV for two spin hypotheses $J = 0$ and $J = 2$, respectively, where the first error is statistical and the second is systematic. This measurement confirms Belle's observation of the $X(3915)$? and finds a consistent value for $\Gamma_{\gamma\gamma}[X(3915)] \times \mathcal{B}(X(3915) \to J/\psi\omega)$ assuming $J = 0$ and a somewhat lower value for the $J = 2$ assumption. In addition, a Bayesian upper limit (UL) at 90% confidence level (CL) is obtained for the $X(3872)$, $\Gamma_{\gamma\gamma}[X(3872)] \times \mathcal{B}(X(3872) \to J/\psi\omega) < 1.7$ eV, assuming $J = 2$.

3 Analysis of $\gamma\gamma \to \eta_c\pi\pi$

Studies of charmonium-like states in recent years have been performed using the $J/\psi\pi^+\pi^-$ final state[?], but no search using the $\eta_c\pi^+\pi^-$ final state has been conducted. Such a search may shed light on the internal dynamic of these states.

This analysis is designed to search for resonances decaying into $\eta_c\pi^+\pi^-$, using a data sample of 473.9 ± 2.1 fb^{-1}. The η_c was reconstructed via its decay to $K^0_S K^+\pi^-$, with $K^0_S \to \pi^+\pi^-$. η_c candidates must satisfy $2.77 < m(K^0_S K^+\pi^-) < 3.22$ GeV/c^2, and the K^0_S signal range is $0.491 < m(\pi\pi) < 0.503$ GeV/c^2. A candidate is reconstructed by fitting the η_c and two pions to a common vertex. The main event selection criteria require the number of tracks in the event to be six, $p_T < 1.5$ GeV/c, $E_{extra} < 0.8$ GeV, and $M^2_{miss} > 10$ (GeV/c^2)^2. Additional background suppression is obtained by using the Dalitz plot for the η_c candidates. The invariant mass distribution for a control sample of $\gamma\gamma \to \eta_c \to K^0_S K^+\pi^-$ events is shown in Fig. **??** (a). The Dalitz plot for the control sample in the η_c peak region is shown Fig. **??**(b). In Fig. **??**(c) and (d) the Dalitz plot is shown for the $\eta_c\pi^+\pi^-$ sample in the lower and upper $m(K^0_S K^+\pi^-)$ sidebands. Further background suppression is achieved by combining six variables (p_T, E_{extra}, and four particle identification algorithm outputs for the kaon and pions not originating from the K^0_S) in a neural-network discriminator. The neural-network output variable is shown in Fig. **??**(e).

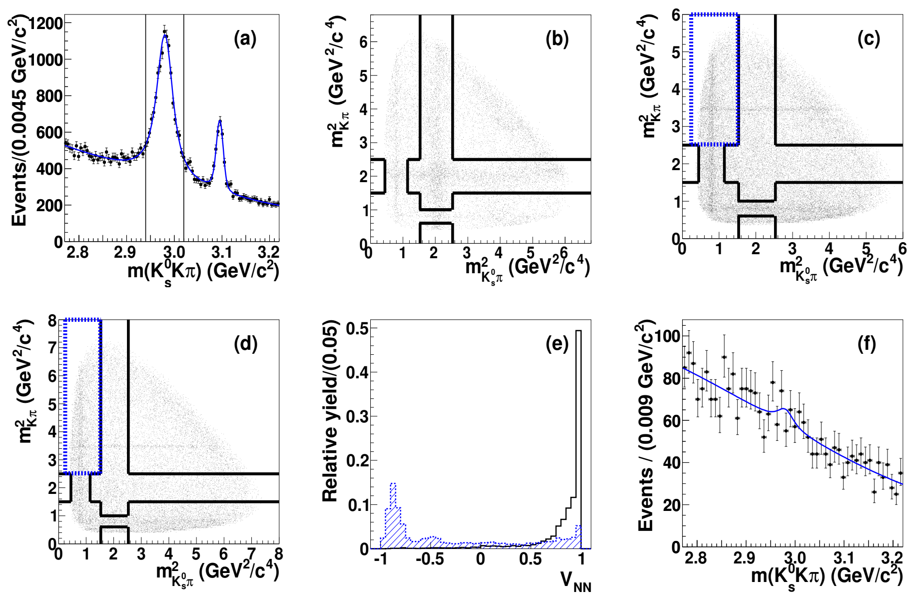

Figure 3: (a) The $m(K^0_S K^+\pi^-)$ distribution for the $\gamma\gamma \to \eta_c$ control sample. The vertical lines indicate the η_c peak mass region used in figures (b, c, d). Also shown are the $K^0_S K^+\pi^-$ Dalitz-plots for (b) the control-sample in the η_c peak mass region and for the $\eta_c\pi^+\pi^-$ sample in the (c) lower and (d) upper η_c mass sidebands. Solid black lines indicate the regions defined by the Dalitz-plot selection criteria. The dotted blue box in the upper left corner of (c) and (d) indicates the Dalitz-plot-sideband background region used for the neural-network training. (e) The neural-network output-variable distributions for the Dalitz-plot sideband (hatched) and signal MC. (f) One-dimensional fit to the $m(K^0_S K^+\pi^-)$ distribution for the $\eta_c\pi^+\pi^-$ sample.

We determine the polynomial parameters of the $m(K^0_S K^+\pi^-)$ background distribution, along with the inclusive η_c yield with a one-dimensional fit to $m(K^0_S K^+\pi^-)$ without restrictions on $m(K^0_S K^+\pi^-\pi^+\pi^-)$. Fig. **??**(f) shows the one-dimensional fit which determines the inclusive η_c yield to be 50 ± 37. Based on this value it was decided not to search for new resonance but to focus on established resonances. The signal yield for each X resonance is extracted from a two-dimensional fit to $m(K^0_S K^+\pi^-)$ and $m(K^0_S K^+\pi^-\pi^+\pi^-)$. This fit include four categories

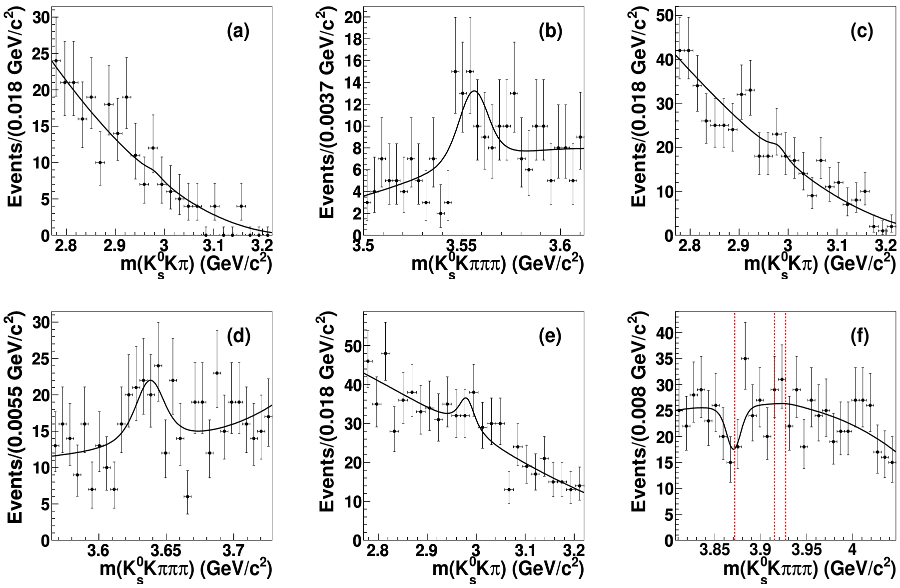

Figure 4: Distributions of (a,c,e) $m(K_S^0 K^+ \pi^-)$ and (b,d,f) $m(K_S^0 K^+ \pi^- \pi^+ \pi^-)$ with the fit function overlaid for the fit regions of the (a,b) $\chi_{c2}(1P)$, (c,d) $\eta_c(2S)$, and (e,f) $X(3872)$, $X(3915)$ and $\chi_{c2}(2P)$. The vertical dashed lines in (f) indicate the peak mass positions of the $X(3872)$, $X(3915)$, and $\chi_{c2}(2P)$.

of events: non-peaking background in both variables, peaking background in $m(K_S^0 K^+ \pi^-)$, peaking background in $m(K_S^0 K^+ \pi^- \pi^+ \pi^-)$, and signal events. Correlation between the non-peaking background distributions of $m(K_S^0 K^+ \pi^-)$ and $m(K_S^0 K^+ \pi^- \pi^+ \pi^-)$ are due to phase-space, and accounted for in the fit. Fig. **??** presents the two-dimensional fits around each of the resonances. No significant signal is observed in any of the fits, and a Bayesian ULs at 90% CL is obtained on the two-photon width times the branching fraction for each resonance. Table **??** summarizes these results. In addition, ULs are obtained on the branching fractions $\mathcal{B}(\eta_c(2S) \to \eta_c \pi^+ \pi^-) < 7.4\%$ and $\mathcal{B}(\chi_{c2}(1P) \to \eta_c \pi^+ \pi^-) < 2.2\%$ at 90% CL. This measurement is the first study of the process $\gamma\gamma \to \eta_c \pi^+ \pi^-$.

Table 1: Results of the $\gamma\gamma \to \eta_c \pi^+ \pi^-$ fits. For each resonance X, we show the peak mass and width used in the fit; the product of the two-photon partial width $\Gamma_{\gamma\gamma}$ and the $X \to \eta_c \pi\pi$ branching fraction, and the 90% CL upper limit on this product. For the $X(3872)$ and the $X(3915)$ we assume $J = 2$.

Resonance	M_X (MeV/c^2)	Γ_X (MeV)	$\Gamma_{\gamma\gamma}\mathcal{B}$(eV)	
			Central value	UL
$\chi_{c2}(1P)$	3556.20 ± 0.09	1.97 ± 0.11	$7.2^{+5.5}_{-4.4} \pm 2.9$	15.7
$\eta_c(2S)$	3638.5 ± 1.7	13.4 ± 5.6	$65^{+47}_{-44} \pm 18$	133
$X(3872)$	3871.57 ± 0.25	3.0 ± 2.1	$-4.5^{+7.7}_{-6.7} \pm 2.9$	11.1
$X(3915)$	3915.0 ± 3.6	17.0 ± 10.4	$-13^{+12}_{-12} \pm 8$	16
$\chi_{c2}(2P)$	3927.2 ± 2.6	24 ± 6	$-16^{+15}_{-14} \pm 6$	19

Acknowledgments

I would like to thank my *BABAR* collaborators.

References

1. S.K. Choi *et al.* (Belle Collaboration), Phys. Rev. Lett. **91**, 262001 (2003); B. Aubert *et al.* (*BABAR* Collaboration), Phys. Rev. Lett. **95**, 142001 (2005).
2. C. N. Yang, Phys. Rev. **77**, 242 (1950).
3. S. Uehara *et al.* (Belle Collaboration), Phys. Rev. Lett. **104**, 092001 (2010)
4. P. del Amo Sanchez *et al.* (*BABAR* Collaboration), Phys. Rev. D. **82**, 011101(R) (2010).
5. A. Abulencia *et al.* (CDF Collaboration), Phys. Rev. Lett. **99**, 132002 (2007).
6. K. Nakamura *et al.* (Particle Data Group), J. Phys. G **37**, 075021 (2010), and partial update for the 2012 edition (URL: http://pdg.lbl.gov).
7. B. Aubert *et al.* (*BABAR* Collaboration), Phys. Rev. Lett. **95**, 142001 (2005); C. Z. Yuan *et al.* (Belle Collaboration), Phys. Rev. Lett. **99**, 182004 (2007); D. Acosta *et al.* (CDF Collaboration), Phys. Rev. Lett. **93**, 072001 (2004); V.M. Abazov *et al.* (D0 Collaboration), Phys. Rev. Lett. **93**, 162002 (2004).

Charmonium and -like states from Belle

V. Bhardwaj (for the Belle Collaboration)
Physics Department, Nara Women's University,
Kitauoya Nishi-machi, Nara, Japan -630 8506.

Large data collected at e^+e^- asymmetric B-factories has resulted in addition of many new states in the charmonium spectrum. Few states agrees well with the prediction of the charmonium models (conventional $c\bar{c}$ states), while others are totally unexpected (candidates for tetraquark or molecular-interpretation). In this paper, we report the recent results from Belle Collaboration on the searches for isospin triplet partner of $X(3872)$ in $J/\psi\pi\pi$, $J/\psi\eta$ and $\chi_{c1}\gamma$. Along with this first evidence of ψ_2 candidate around 3820 MeV/c^2 is also presented.

1 Introduction

Belle detector is a general purpose detector build to test Standard Model mechanism for CP-violation in B decays to charmonium (golden channel) [1]. Parallel to this, Belle has also proven to be an ideal place to carry charmonium spectroscopy due to very clean environment. Many new $c\bar{c}$ and $c\bar{c}$-like states such as $\eta_c(2S)$, $X(3872)$, $X(3915)$, $Z(3930)$, $X(3940)$, $Z_1(4050)^+$, $Z_2(4250)^+$, $Y(4260)$, $Z(4430)^+$ and $Y(4660)$ have been found. Out of these states, $X(3872)$ is the most interesting state. It was first observed in $B^\pm \to (J/\psi\pi^+\pi^-)K^\pm$ at Belle [2]. Soon after it's discovery, it was confirmed by CDF, D0 and BaBar. Recently, it has also been observed in LHCb and CMS. The observation of $X(3872)$ in the same final states ($J/\psi\pi^+\pi^-$) in the six different experiments, reflects the eminent status of the $X(3872)$. $X(3872)$ narrow width and the proximity of its mass, 3871.5 ± 0.2 MeV/c^2 to the $D^{*0}\bar{D}^0$ threshold makes it a good candidate for a $D\bar{D}^*$ molecule [3]. Other possibilities have also been proposed for the $X(3872)$ state, such as tetraquark[4], $c\bar{c}g$ hybrid meson [5] and vector glueball models [6].

Mass, width, J^{PC} and branching ratio ($\mathcal{B}$) plays an important role in identifying its nature. Using 772 Million $B\bar{B}$ pairs (full and final $\Upsilon(4S)$ data sample), Belle updated[7] these properties. We also carried search for the charged partner of $X(3872)$ ($X(3872)^+$). Radiative decays of $X(3872)$ provide us an opportunity to understand the nature of $X(3872)$. One such decay, $X(3872) \to J/\psi\gamma$ resulted in the confirmation of C-even ($C = +$) parity for $X(3872)$[8,9,10]. However, a similar decay mode $X(3872) \to \psi'\gamma$; important as it can help in identifying $X(3872)$ as a charmonium, molecular or molecular with charmonium mixing [3,11,12], is under conflict due to Belle's no evidence of the signal (disagree with the BaBar's evidence) [9,10]. If $X(3872)$ is tetraquark than it has a C-odd parity ($C = -$) partner, which can dominantly decay into $X(3872) \to J/\psi\eta$ and $X(3872) \to \chi_{c1}\gamma$. Along with this search for a new narrow state is also carried out in these final states. In this search, we find first evidence of $X(3823) \to \chi_{c1}\gamma$, most probably the missing ψ_2 ($^3D_2$ $c\bar{c}$ state).

For update on the properties of $X(3872)$, B reconstruction is done using $(J/\psi\pi^+\pi^-)K$ decay mode, while in our search of the charged $X(3872)$, B is reconstructed using $(J/\psi\pi^+\pi^0)K^-$.

$B^{\pm} \to (J/\psi\eta(\to \gamma\gamma))K^{\pm}$ and $B^{\pm} \to (\chi_{c1}(\to J/\psi\gamma)\gamma)K^{\pm}$ decay modes are used in the search for C-odd partner of the $X(3872)$ and other new narrow resonances. In all the decay modes, J/ψ is reconstructed via e^+e^- and $\mu^+\mu^-$. B candidates are identified using: energy difference $\Delta E \equiv E_B^* - E_{beam}^*$ and beam-energy constrained mass $M_{\rm bc} \equiv \sqrt{(E_{beam}^*)^2 - (p_B^{cms})^2}$, where E_B^* is the cms beam energy, and E_B^* and p_B^* are the cms energy and momentum of the reconstructed particles. Invariant mass of the final state (of interest) is used to identify the resonance.

2 Update on the properties of $X(3872)$

To extract the signal yield 3-dimension unbinned maximum likelihood (UML) fit to ΔE, $M_{\rm bc}$ and $M_{J/\psi\pi\pi}$, is used. Table 1 summarizes the mass, $\mathcal{B}$ and the signal yield extracted by the fit.

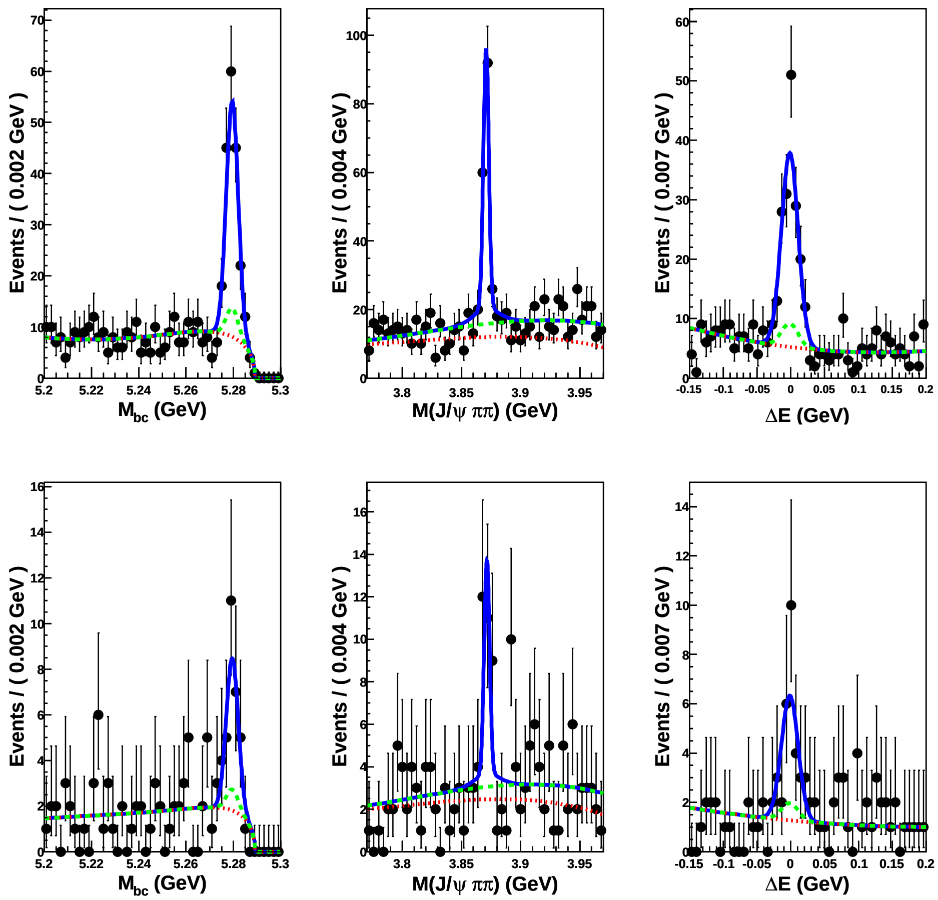

Figure 1: 3D UML fit to $M_{\rm bc}$ (left), $M_{J/\psi\pi\pi}$ (center) and ΔE (right) to extract signal yield for $B^{\pm} \to X(3872)K^{\pm}$ (top) and $B^0 \to X(3872)K_S^0$ (bottom) within the signal regions of other two quantities. In the fit, combinatorial background is shown as red dotted line, combinatorial plus peaking background by green dashed line and the total fit (background plus signal is shown by blue solid line). Signal region is defined as $M_{\rm bc} > 5.27$ GeV/c^2, $-35 < \Delta E < 30$ MeV and $3.863 < M_{J/\psi\pi\pi} < 3.881$ GeV/c^2.

After applying mass correction determined from $B^+ \to \psi' K^+$ sample, mass of $X(3872)$ is estimated to be : $M_{X(3872)} = (3871.85 \pm 0.27 \pm 0.19)$ MeV. First uncertainty is due to statistics while second due to systematics. Width of $X(3872)$ is estimated using likelihood scan and after including systematics it comes out to be as $\Lambda_{X(3872)} < 1.2$ MeV. If $X(3872)$ is tetraquark then few model predicts the mass of $X(3872)$ in the charged B and neutral B to have measurable difference of ΔM $(M_{X(B^+)} - M_{X(B^0)})$ $= (8 \pm 3)$ MeV. We measure this difference

Table 1: $\mathcal{B}$ estimated from the 3D UML fits.

Channel	Yield	Mass (MeV)	$\mathcal{B}(B \to XK)\mathcal{B}(X \to J/\psi\pi\pi)$ (10^{-6})
$X(3872)K^+$	152 ± 15	3870.85 ± 0.28	$8.61 \pm 0.82 \pm 0.52$
$X(3872)K^0$	21.0 ± 5.7	3871.56 ± 0.92	$4.3 \pm 1.2 \pm 0.4$
Combined	173 ± 16	3870.92 ± 0.27	

and found it to be consistent with zero $(-0.69 \pm 0.97 \pm 0.19)$ MeV. Also, tetraquark model predicts the existence of isospin triplet : $X(3872)^+$ (charged $X(3872)$) having large $\mathcal{B}$ such that $\mathcal{B}(B^\pm \to X(3872)^+K^0) = 2 \times \mathcal{B}(B^0 \to X(3872)K^0)$. We search for the charged $X(3872)^+$ using $J/\psi\pi^+\pi^0$ and found no signal in the 2D ($M_{\rm bc}$ and $M_{J/\psi\pi^+\pi^0}$) UML fit, as shown in Figure 2. We provide the world best U.L. (@ 90% C.L.) on the $\mathcal{B}$ of the production of $X(3872)^+$ in B decays as:

- $\mathcal{B}(\bar{B}^0 \to X(3872)^+K^-)\mathcal{B}(X(3872)^+ \to J/\psi\rho^+) < 4.2 \times 10^{-6}$
- $\mathcal{B}(\bar{B}^+ \to X(3872)^+K^0)\mathcal{B}(X(3872)^+ \to J/\psi\rho^+) < 6.2 \times 10^{-6}$

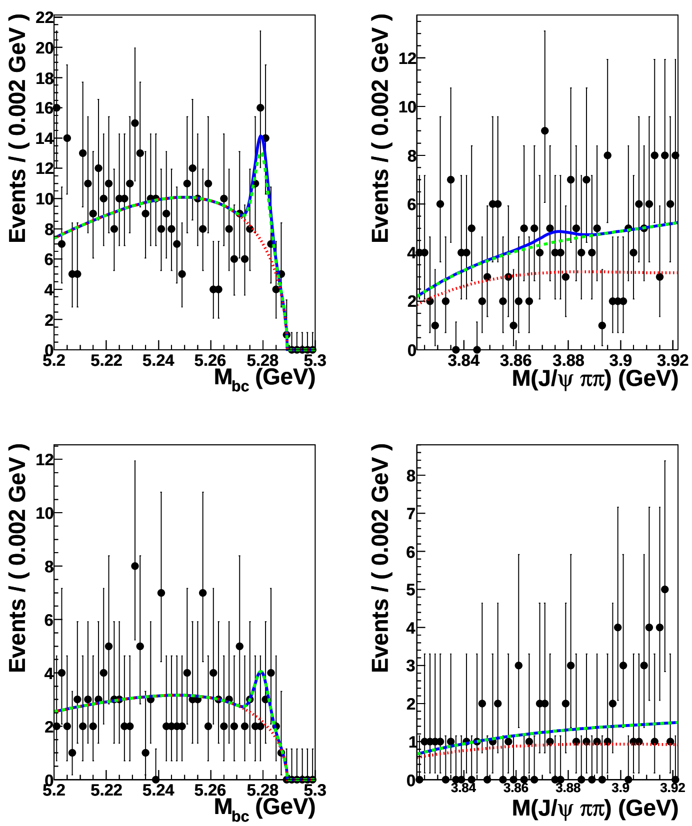

Figure 2: 2D UML fit to $M_{\rm bc}$ (left), $M_{J/\psi\pi^+\pi^0}$ (right) distributions for $B^0 \to X(3872)^+K^+$ (top) and $B^+ \to X(3872)^+K^0$ (bottom) within the signal regions of other quantity.

The angular study is carried out using $\cos\theta_X(J/\psi, K^\pm)$, $\cos\chi(\pi^+, K^\pm)$ and $\cos\theta_\ell(\ell, K^\pm)$, which suggests J^{PC} to be 1^{++} along with 2^{-+}. Fits to $M_{\pi^+\pi^-}$ distribution suggest J^{PC} to be 1^{++} without $\rho-\omega$ interference and when $\rho-\omega$ interference is taken into account, 2^{-+} also gives agreeable fit to $M_{\pi\pi}$ distribution. With current statistics, the most probable J^{PC} of $X(3872)$ is suggested to be either 1^{++} or 2^{-+} [7].

3 Search of C-odd partner of $X(3872)$ in $B^{\pm} \to J/\psi\eta K^{\pm}$

In the search of charged tetraquark partner of $X(3872)$, no signal is seen. Still it is hard to rule out $X(3872)$ as tetraquark, as some tetraquark model predicts $X(3872)^{+}$ to be broad resulting in non-observation at low statistics [13]. $X(3872)$'s C-odd partner can dominantly decay into J/ψ η and search of $X(3872)$'s $C-$odd partner can either result in the observation or provide much tighter constraint to the tetraquark interpretation of $X(3872)$. Previous study of $B \to J/\psi\eta K$ was carried out by BaBar [14].

We use ΔE to estimate the MC/data difference. We cut in the signal region defined as $M_{\rm bc} > 5.27$ GeV/c^2 and -35 MeV $< \Delta E <$ 30 MeV and look at the $M_{J/\psi\eta}$ for any resonance. Figure 3 shows the fit to $M_{J/\psi\eta}$. Difference between data and MC above 3.8 GeV/c^2 is found but once we include phase space component for $B^{\pm} \to J/\psi\eta K^{\pm}$, we are able to describe MC/data very well. No hint of a narrow resonance is evident from the current statistics. No $X(3872)$ signal is seen and U.L. (@ 90% CL) is provided using frequentist method. We also provide U.L. (@90% CL) at different masses using narrow width hypothesis, result shown in Figure 4. Table 2 summarizes the result from $B^{\pm} \to (J/\psi\eta)K^{\pm}$ study.

Table 2: Preliminary $\mathcal{B}$ for $B^{\pm} \to J/\psi\eta K^{\pm}$ analysis.

Channel	Yield	$\mathcal{B}(10^{-4})$
$B^{\pm} \to \psi'(\to J/\psi\eta)K^{\pm}$	52 ± 8.2	$5.81 \pm 0.92 \pm 0.44$
$B^{\pm} \to J/\psi\eta K^{\pm}$ (phase space)	395 ± 26	$1.17 \pm 0.07 \pm 0.11$
		$\mathcal{B}(B^{\pm} \to X(3872)K^{\pm})\mathcal{B}(X(3872) \to J/\psi\eta)(10^{-6})$
$B^{\pm} \to X(3872)(\to J/\psi\eta)K^{\pm}$	2.3 ± 5.2	< 3.8 (@ 90% CL)

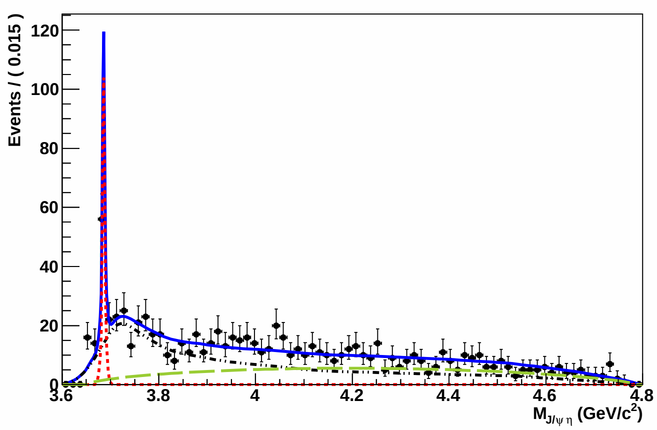

Figure 3: 1D UML fit to $M_{J/\psi\eta}$ distribution in order to extract the signal yield for the mode of interest. Red dashed (green long dashed) curve shows the signal for $B^{\pm} \to \psi'(\to J/\psi\eta)K^{\pm}$ (phase space component $B^{\pm} \to J/\psi\eta K^{\pm}$), while black dashed-dotted curve shows the background parameterized using $B \to J/\psi X$ MC sample.

4 First evidence of ψ_2 around 3823 MeV/c^2

Complimentary to $B^{\pm} \to (J/\psi\eta)K^{\pm}$ study, $X(3872)$'s C-odd partner search is also carried in $B^{\pm} \to (\chi_{c1}\gamma)K^{\pm}$ decay. Along with this search, we also look for any other narrow charmonium or charmonium-like candidate. Charmonium model predict that there should be a narrow state

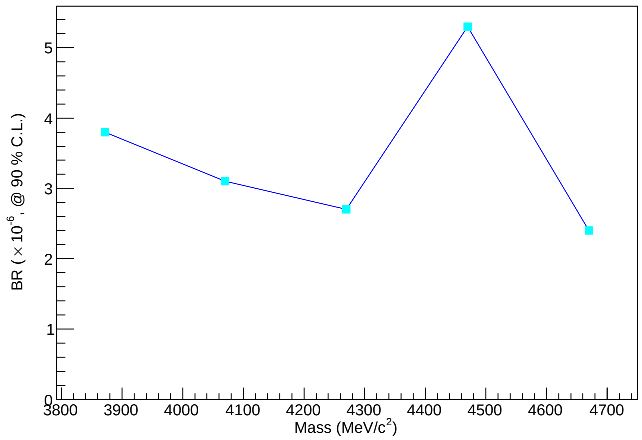

Figure 4: U.L. (@90% C.L.) on the $\mathcal{B}$ estimated at different masses using narrow width hypothesis.

($^3D_2\ c\bar{c}$) which lies around 3810-3840 MeV[15]. In our search, we find a clear evidence of a narrow peak at 3823 MeV in $M_{\chi_{c1}\gamma}$ with a significance of 4.2 σ (syst. included). We extract the signal yield using 2D UML fit to $M_{\chi_{c1}\gamma}$ and $M_{\rm bc}$ distribution. While estimation of the width, we find data to be insensitive enough to provide a proper width estimation (4 ± 6 MeV) due to low statistics. The mass of the peak is estimated to be 3823.5 ± 2.1 MeV/c^2. Figure 5 shows the 2D UML fit to extract signal yield. Table 3 summarizes the result from $B^{\pm} \to (\chi_{c1}\gamma)K^{\pm}$ study.

Table 3: Preliminary $\mathcal{B}$ for $B^{\pm} \to \chi_{c1}\gamma K^{\pm}$ analysis.

Channel	Yield	$\mathcal{B}(10^{-4})$
$B^{\pm} \to \psi'(\to \chi_{c1}\gamma)K^{\pm}$	193 ± 19	$7.74^{+0.77+0.87}_{-0.74-0.83}$
		$\mathcal{B}(B^{\pm} \to XK^{\pm}) \times \mathcal{B}(X \to \chi_{c1}\gamma)(10^{-6})$
$B^{\pm} \to X(3823)(\to \chi_{c1}\gamma)K^{\pm}$	33.2 ± 9.1	$9.70^{+2.84+1.06}_{-2.52-1.03}$
$B^{\pm} \to X(3872)(\to \chi_{c1}\gamma)K^{\pm}$	-0.9 ± 5.1	< 2.0 (@ 90% CL)

5 Summary

Belle updated the mass, width and $\mathcal{B}$ of the $X(3872)$ using the full data sample. In search for charged partner of the $X(3872)$, no signal is seen. Also, in the search of C- odd partner, no signal is seen for $B^{\pm} \to (J/\psi\eta)K^{\pm}$ and $B^{\pm} \to (\chi_{c1}\gamma)K^{\pm}$ decays and provided much tighter constraint to the tetraquark interpretation of $X(3872)$. Along with this, Belle also provided the first evidence for a narrow state having mass of 3823.5 ± 2.1 MeV/c^2. This narrow state seems to be the missing ψ_2 of the charmonium spectrum.

Acknowledgments

We thank the KEKB group for excellent operation of the accelerator; the KEK cryogenics group for efficient solenoid operations; and the KEK computer group, the NII, and PNNL/EMSL for valuable computing and SINET4 network support. We acknowledge support from MEXT, JSPS and Nagoya's TLPRC (Japan); ARC and DIISR (Australia); NSFC (China); MSMT (Czechia); DST (India); INFN (Italy); MEST, NRF, GSDC of KISTI, and WCU (Korea);

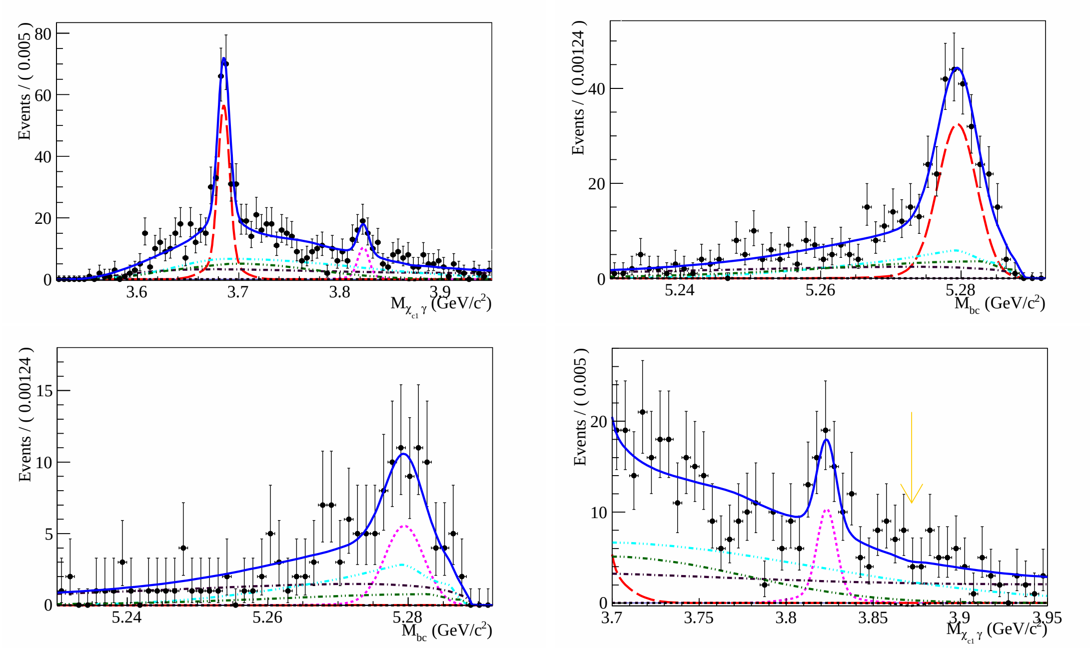

Figure 5: 2D UML fit projections in $M_{\chi_{c1}\gamma}$ (top left), $M_{\rm bc}$ (top right), $M_{\rm bc}$ (bottom left) and $M_{\chi_{c1}\gamma}$ (bottom right) for the signal region $M_{\rm bc} > 5.27$ GeV/c^2, $3.66 < M_{\chi_{c1}\gamma} < 3.708$ GeV/c^2 (ψ' signal region), $3.805 < M_{\chi_{c1}\gamma} < 3.845$ GeV/c^2 ($X(3823)$ signal region) and $M_{\rm bc} > 5.27$ GeV/c^2 [yellow arrows shows the $X(3872)$ position]. The curves shows the signal [red large-dashed for ψ' and pink dashed for ψ_2] and the background component [black dotted-dashed for combinatorial, dark green two dottted-dashed for $B^{\pm} \to \psi'$(other than $\chi_{c1}\gamma)K^{\pm}$ and cyan three dotted-dashed for peaking component] as well as the overall fit [blue solid].

MNiSW (Poland); MES and RFAAE (Russia); ARRS (Slovenia); SNSF (Switzerland); NSC and MOE (Taiwan); and DOE and NSF (USA).

References

1. I. Adachi *et al.* (Belle Collaboration), *Phys. Rev. Lett.* **108**, 171802 (2012).
2. S.-K. Choi *et al.* (Belle Collaboration), *Phys. Rev. Lett.* **91**, 262001 (2003).
3. E.S. Swanson, *Phys. Lett.* B **598**, 197 (2004); E.S. Swanson, *Phys. Rep.* **429**, 243 (2006).
4. L. Maiani, *Phys. Rev.* D **71**, 014028 (2005).
5. B.A. Li, *Phys. Lett.* B **605**, 306 (2005).
6. K.K. Seth, *Phys. Lett.* B **612**, 1 (2005).
7. S.-K. Choi *et al* (Belle Collaboration), *Phys. Rev.* D **85**, 052004 (2011).
8. K. Abe *et al* (Belle Collaboration), arXiv:hep-ex/0408116.
9. B. Aubert *et al* (BaBar Collaboration), *Phys. Rev. Lett.* **102**, 132001 (2009).
10. V. Bhardwaj *et al* (Belle Collaboration), *Phys. Rev. Lett.* **107**, 091803 (2011).
11. T. Mehen and R. Springer, *Phys. Rev.* D **83**, 094009 (2011).
12. T.H. Wang, G.L. Wang, *Phys. Lett.* B **697**, 3 (2011).
13. K. Terasaki, *Prog. Theor. Phys.* **127**, 577-582 (2012).
14. B. Aubert *et al*, (BaBar Collaboration), *Phys. Rev. Lett.* **93**, 041801 (2004).
15. S. Godfrey and N. Isgur, *Phys. Rev.* D **32**, 189 (1985), E. Eichten *et al*, *Phys. Rev. Lett.* **89**, 162002 (2002), E. Eichten *et al*, *Phys. Rev.* D **69**, 094019 (2004).

BOTTOMONIUM AND BOTTOMONIUM-LIKE STATES AND DECAYS AT BELLE

G. TATISHVILI [a]
Pacific Northwest National Laboratory
902 Battelle Boulevard, Richland, WA, USA

Recent results from the Belle experiment are presented. We report the results of the first observation of P-wave spin-singlet Bottomonium states, observation of two charged Bottomonium-like resonances and the first observation of the radiative transition $h_b(1P) \rightarrow \eta_b(1S)\gamma$ at the $\Upsilon(5S)$ resonance region.

We report the results of the first observation of P-wave spin-singlet Bottomonium states $h_b(1P)$ and $h_b(2P)$ produced in the $\Upsilon(5S)$ region. We used a 121.4 fb^{-1} data sample collected near the peak of the $\Upsilon(5S)$ resonance with the Belle detector at the KEKB asymmetric-energy e^+e^- collider. The Belle detector is a large-solid-angle magnetic spectrometer consisting of a central drift chamber, an array of aerogel threshold Cherenkov counters, electromagnetic calorimeter composed of CsI(Tl) crystals located inside a superconducting solenoid with 1.5 T magnetic field. The detector is described in detail elsewhere [1].

The $h_b(nP)$ states were produced via $e^+e^- \rightarrow h_b(nP)\pi^+\pi^-$ and observed in the $\pi^+\pi^-$ missing mass spectrum of hadronic events [2]. The $\pi^+\pi^-$ missing mass was calculated by formula $M^2_{\text{miss}}=(P_{\Upsilon(5S)} - P_{\pi+\pi-})^2$, where $P_{\Upsilon(5S)}$ (4-momentum of the $\Upsilon(5S)$) was determined from the beam momenta. $P_{\pi+\pi-}$ is the 4-momentum of the $\pi^+\pi^-$ system. The background subtracted inclusive M_{miss} spectrum is presented in Fig.1. To determine the number of produced resonant decays the M_{miss} spectrum was fitted separately into three adjacent regions. The measured masses of $h_b(1P)$ and $h_b(2P)$ states are $M=(9898.2^{+1.1+1.0}_{-1.0-1.1})$ MeV/c^2 and $M=(10259.8\pm0.6^{+1.4}_{-1.0})$ MeV/c^2, respectively. Using the measured h_b and world average masses of $\chi_{bJ}(nP)$ states we determine the hyperfine

---

[a] On behalf of the Belle Collaboration

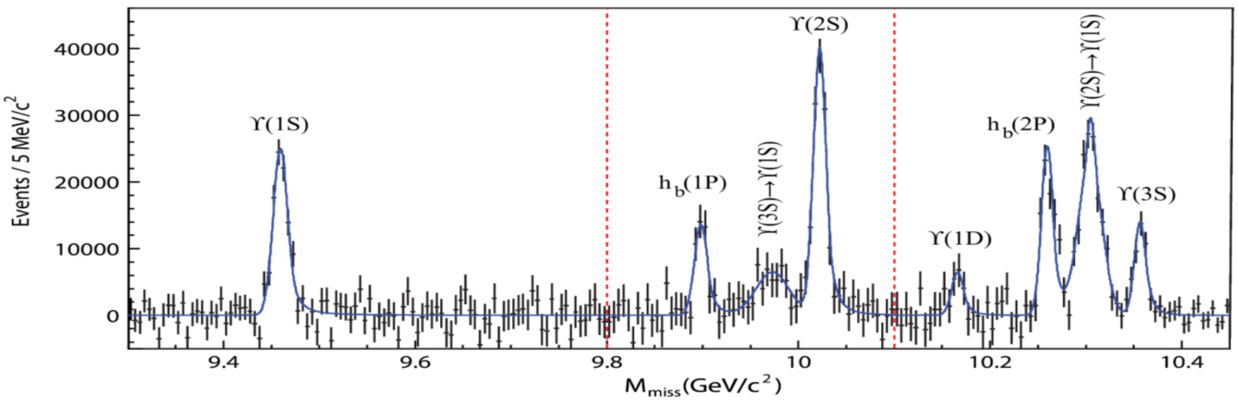

FIG. 1 The background subtracted inclusive $M_{\rm miss}$ spectrum (points with errors). The vertical lines indicate boundaries of the fit regions. Overlaid smooth curve is the resulting fit function.

splittings to be $\Delta M_{\rm HF}$ = (+1.7 ± 1.5) and $(+0.5\ ^{+1.6}_{-1.2})$ MeV/c^2 for $h_b(1P)$ and $h_b(2P)$, respectively which are consistent with zero. We measured the ratio of cross sections $R = \sigma(h_b(nP)\pi^+\pi^-) / \sigma(\Upsilon(2S)\pi^+\pi^-)$ to be $0.45\pm0.08\ ^{+0.07}_{-0.12}$ for the $h_b(1P)$ and $0.77\pm0.08\ ^{+0.22}_{-0.17}$ for the $h_b(2P)$, which indicates that $h_b(nP)\pi^+\pi^-$ and $\Upsilon(2S)\pi^+\pi^-$ proceed at similar rates despite the fact that the production of $h_b(nP)$ requires a spin flip of a b quark. The angular analysis of the $\Upsilon(5S) \to h_b(1P)\pi^+\pi^-$ transition indicates spin parity of $J^P=1^+$ for the $h_b(1P)$ state. We also analyzed 711fb^{-1} data at the $\Upsilon(4S)$ resonance to search for $h_b(1P)\pi^+\pi^-$ transition and set an upper limit on the ratio of $\sigma(e^+e^-\to h_b(1P)\pi^+\pi^-)$ at the $\Upsilon(4S)$ to that at the $\Upsilon(5S)$ of 0.27 at 90% C.L.

The analysis of di-pion transition of $\Upsilon(5S)$ resonance shows a high rates of $\Upsilon(5S) \to \Upsilon(nS)\pi^+\pi^-$ (n=1,2,3) and $\Upsilon(5S) \to h_b(mP)\pi^+\pi^-$ (m=1,2) which indicates contribution of exotic mechanisms in the $\Upsilon(5S)$ decays. We report results of study of resonant substructure in the decays of $\Upsilon(5S)\to\Upsilon(nS)\pi^+\pi^-$ (n=1,2,3) and $\Upsilon(5S)\to h_b(mP)\pi^+\pi^-$ (m=1,2) [3]. Fig.2 (a) and 2(b) show Dalitz distributions – the maximum value of the two $M^2[\Upsilon(2S)\pi^\pm]$ versus $M^2(\pi^+\pi^-)$ for $\Upsilon(2S)$ sideband and signal regions, respectively. Two horizontal bands in Fig. 2(b) indicate existence of structures in $\Upsilon(nS)\pi$ system near 10.61 GeV/c^2 ($Z_b(10610)$) and 10.65 GeV/c^2 ($Z_b(10650)$). Fig.3 show the yield of $\Upsilon(5S)\to h_b(mP)\pi^+\pi^-$ (m=1,2) as a function of pion missing mass. A clear two-peak structure indicates the production of $Z_b(10610)$ and $Z_b(10650)$. In total we observed two $Z_b(10610)$ and $Z_b(10650)$ Bottomonium-like resonances in five different decay channels $\Upsilon(nS)\pi^\pm$ (n=1,2,3) and $h_b(mP)\pi^\pm$ (m=1,2). The minimal quark content of the $Z_b(10610)$

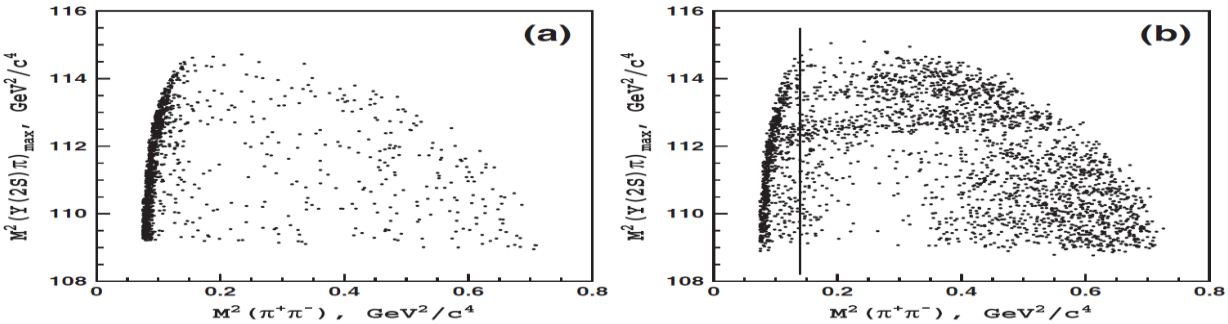

FIG. 2 Dalitz plots for the $\Upsilon(2S)$ sideband (a) and $\Upsilon(2S)$ signal (b) regions. Vertical line shows the cut which allows to remove a background from photon conversions in the detector elements.

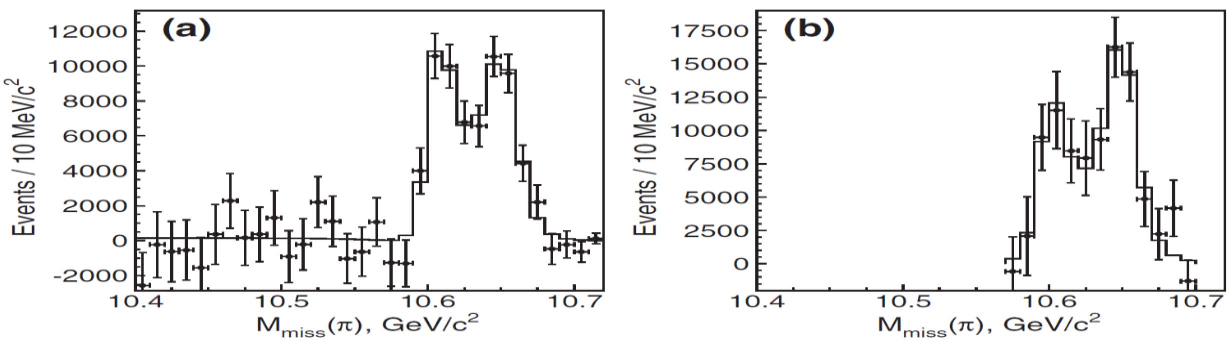

FIG. 3. The $h_b(1P)$ (a) and $h_b(2P)$ (b) yields as a function of the missing mass recoiling against the pion. Fit results are presented as a histograms.

and $Z_b(10650)$ requires a four quark combination. Weighted average values of masses and widths over all five channels are M=10607.2±2.0 MeV/c^2, Γ=18.4±2.4 MeV for the $Z_b(10610)$ and M=10652.2±1.5 MeV/c^2, Γ=11.5±2.2 MeV for the $Z_b(10650)$. The measured masses of these states are a few MeV/c^2 above the thresholds for the open beauty channels which suggests that their internal dynamics is dominated by the coupling to B meson pairs [4].

The radiative transition to the $\eta_b(1S)$ is expected to be one of the dominant decay modes of the $h_b(1P)$. We report the first observation of the radiative transition $h_b(1P) \to \eta_b(1S)\gamma$ [5]. In the decay chain $\Upsilon(5S) \to Z^+_b\,\pi^-$, $Z^+_b \to h_b(1P)\pi^+$, $h_b(1P) \to \eta_b(1S)\gamma$ we reconstruct only the π^-, π^+ and γ. We search for the $\eta_b(1S)$ signal in the distribution of $\Delta M_{miss}(\pi^+\pi^-\gamma) - M_{miss}(\pi^+\pi^-) + m[h_b(1P)]$ (see Fig.4). Observed signal parameterized by a non-relativistic Breit-Wigner function, the combinatorial background – by an exponential function.

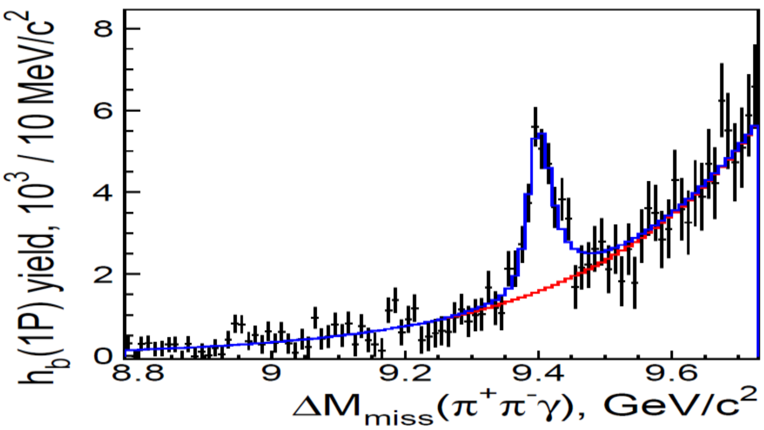

FIG. 4 $\Delta M_{miss}(\pi^+\pi^-\gamma)$ distribution of the $h_b(1P)$ yield with fit result superimposed.

We obtained the single most precise measurement of the $\eta_b(1S)$ mass, $(9401.0\pm1.9\,^{+1.4}_{-2.4})$ MeV/c^2, which corresponds to the hyperfine splitting $\Delta M_{HF}[\eta_b(1S)] = (59.3\pm1.9\,^{+2.4}_{-1.4})$ MeV/c^2. We report the first measurement of the $\eta_b(1S)$ width $(12.4\,^{+5.5+11.5}_{-4.6-3.4})$ MeV. For the branching fraction we find $B[h_b(1P) \to \eta_b(1S)\gamma] = (49.8\pm6.8\,^{+10.9}_{-5.2})$ % which agrees with the theoretical expectations [6].

Acknowledgments

We thank the KEKB group for excellent operation of the accelerator; the KEK cryogenics group for efficient solenoid operations; the KEK computer group and the NII for valuable computing and SINET4 network support. We acknowledge support from MEXT, JSPS and Nagoya's TLPRC (Japan); ARC and DIISR (Australia); NSFC (China); MSMT (Czechia); DST (India); MEST, NRF, NSDC of KISTI, and WCU (Korea); MNiSW (Poland); MES and RFAAE (Russia); ARRS (Slovenia); SNSF (Switzerland); NSC and MOE (Taiwan); and DOE and NSF (USA).

References

1. S.Kurokawa and E.Kikutani, *Nucl. Instrum. Methods Phys. Res.* Sect. A 499, 1(2003).
2. I. Adachi *et al*, *Phys. Rev. Lett.* 108, 032001 (2012).
3. A. Bondar *et al*, *Phys. Rev. Lett.* 108, 122001 (2012).
4. A. Bondar *et al*, *Phys. Rev.* D 84, 054010 (2011).
5. I. Adachi *et al*, *arXiv:*1110.3934v1 [hep-ex] 18 Oct 2011.
6. S. Godfrey and J. L. Rosner, *Phys. Rev.* D 66, 014012 (2002).

$e^+e^- \to J/\Psi + \eta_c$ in Bethe-Salpeter framework

LI Shi-Yuan
Department of Physics, Shandong University, Jinan 250100, P.R. China

It is shown that the off-shell states as well as the relative movement of the $c\bar{c}$ in bound states are important for this exclusive production process.

1 Introduction

Heavy quarkonium physics has been the traditional arena of Quantum Chromodynamics (QCD) since J/Ψ was discovered, in both perturbative (PT) and non-perturbative (NPT) aspects. The heavy quark mass provides a hard scale for PT QCD calculations. The mass term of fermions in the QCD Lagrangian is irrelevant to the colour symmetry, so that the confinement and NPT QCD mechanism for heavy and light quarks could be similar. These facts make the heavy quark a good tool in investigating the unsolved NPT QCD. A further simplification is expected from the large mass of heavy quark, that it may be non-relativistic (NR) in the bound states. As a matter of fact, not only the relative momentum between heavy quarks in the bound states are considered small, but also these quarks are treated as almost on shell. The off shell states and the creation/annihilation of the heavy quarks are not taken into account in the static bound state. This is justified for the *rest* quarkonia, as investigating their decay widths. In these processes, the largest energy scale is the quarkonium mass M. However, in the hard production processes of heavy quarkonium at high energies, the hard scale are much larger than M. If there is no well justified factorization formula[a] for a certain process, the NR description of the bound states could not be straightforward applicable. In this case, more general framework, which is relativistic and robust to introduce enough number of parameters to describe the bound system, especially the off shell states of the heavy quarks, is needed. The Bethe-Salpeter (BS) wave function framework is one of the good choices. If various relativistic effects are found to be small or could be factorized from the static bound state, the BS framework will naturally leads to the NR descriptions.

In this paper, the cross section of the exclusive production process $e^+e^- \to J/\Psi + \eta_c$ at B factories [1,2,3] is studied in the BS framework. The various relativistic effects, especially the off-shell heavy quark states and large relative momentum are taken into account.

The double charm pair production process in B factory energies is of special significance. These four (anti)charms can be respectively grouped into two colour-singlet pairs, hence the colour-octet mechanism never plays important rôle because of the relatively much smaller colour-octet matrix elements. One can concentrate on the effects of relative movement and heavy

[a] factorization here means that all the effects of the off shell states and creation/annihilation of the heavy quarks, as well as the large relative momentum between them, are well separated into the hard part which is calculable via PT QCD, so that the bound state can be described by NR effective theories, such as [4].

quark off shell states without considering the indefinte colour-octet matrix element paremeters. It has been found that the decay width, as well as the energy distribution of the J/Ψ in $\Upsilon \to J/\Psi + X$ process [5,6] can be easily understood by considering such kind of process [7,8]. It has also been suggested [9] double charm pair production is helpful to analyze the Tevatron polarization 'paradox', which is refreshed by Tevatron RUNII [10] recently. When the discrepancy between the data and the lowest order NRQCD calculation for the exclusive process $e^+e^- \to J/\Psi + \eta_c$ was presented, Many groups recognized the importance of the relativistic corrections, besides the higher order PT QCD corrections. It has been generally adopted that exclusive process could be more sensitive to the inner movements and more difficult to factorize.

The ways of incorporating the relativistic corrections can be grouped into two: One is in the NRQCD framework, the other is to employ various relativistic wave functions of J/Ψ and η_c. Works in the NRQCD frameworks [11,12] show that the relativistic correction is important, at the same time the $O(\alpha_s^3)$ PQCD corrections are found also very large. The large higher order corrections [13,14] indicate the requirement of all order summations. For the to-date review of works in this framework, one refers to [15]. Works in the framework of light-cone wave functions [16,17,18,19,20], employ the same hard partonic process as the lowest order NRQCD approach. When the scale parameter in the wave function is large, the momentum fraction difference $|x_1 - x_2|$ is of $O(1)$, and this approach can explain the data well. In both the above frameworks, the charm quarks in the bound states are treated as almost on shell, i.e., factorization is assumed.

On the other hand, the bound states can be described by BS wave functions [21,22], with the heavy quark limit (HQL) employed and the partonic process the same as that of the lowest order NRQCD approach. But the results [21,22] are consistent with data, i.e., much larger than that of the NRQCD. The HQL generally is considered as to make NR description of the quarks in the bound states valid. This fact implies that different approaches for 'NR limit' (HQL vs. NRQCD) could lead to completely different results. There could be effects of the full BS approach not incorporated in the NRQCD framework (but kept in HQL) which enhance the cross section. Such experiences have been seen in history. For the electron in the hydrogen atom, the most important 'relativistic effect' comes from the generators of the little group of the Lorentz group, i.e., spin. Such a quantum number can only be naturally deduced from the relativistic wave function/equation of the electron, i.e., the Dirac spinor/equation. The Sommerfeld relativistic corrections to the Bohr theory can never incorporate this.

Of course by the mention of this history we do not imply NRQCD can not properly incorporate the spin effect of the bound state, but want to point out that it could be better to start from the completely relativistic framework, i.e., the full BS wave function *without HQL*, to investigate the relativistic effects in bound state, namely the off-shell states and the large relative movement of $c\bar{c}$. The off-shell states are never covered in all the above approaches, while the large relativistic corrections in NRQCD and wide $|x_1 - x_2|$ spectrum in light cone approaches indicate that the large relative movement is important. Once taking such a step, the Feynman diagram in Figure 1 ($O(\alpha_s^0)$) naturally comes up. These three charm quark lines can never be all on shell at the same time that the four-momenta are all conserved for the two quark-hadron vertices (requiring at least one of the charm propagators off-shell at the order of $\sqrt{s}$). Hence all the above mentioned approaches, which neglect the consideration of off-shell states of $c\bar{c}$, set this diagram to be zero by hand. On the contrary, taking into account the the off-shell state and the large relative movement of $c\bar{c}$ in a self-consistent BS wave function framework, one has to make clear the contribution of this diagram. Its contribution is not necessarily the leading, but depending on how large the effects of the off-shell states and relative movements. So we need the concrete calculations. Details of Section 2,3 are referred to the long write up.

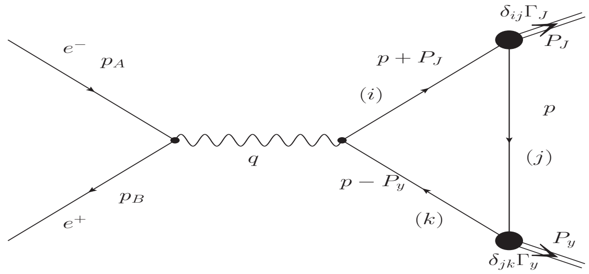

Figure 1: One of two Feynman diagrams.

2 The BS WF framework for the calculation

The BS wave function is

$$\chi(P,q)=\int\frac{d^4x}{(2\pi)^4}e^{-iqx}\frac{1}{\sqrt{3}}\delta_{ij}<0\mid T\psi^i(\frac{x}{2})\bar{\psi}^j(-\frac{x}{2})\mid B>=:S_F(p_1)\Gamma(P,q)S_F(-p_2) \qquad (1)$$

where $p_1=\frac{P}{2}+q,\ p_2=\frac{P}{2}-q,\ P=p_1+p_2,\ q=\frac{1}{2}(p_1-p_2)$. Eq. 1 defines the BS vertex for the coupling of the bound state particle with the composite particles. $S_F(p)$ denotes the quark propagator. For incorporation of the information of the bound states from their decay processes, we employ the Covariant Instantaneous Ansatz (CIA) framework as [23,24,25] in calculations.

3 The calculation procedure and the result

The invariant amplitude is proportional to $\int\frac{d^4p}{(2\pi)^4}\frac{D(\hat{q}_J)D(\hat{q}_y)\phi(\hat{q}_J)\phi(\hat{q}_y)}{((p-P_y)^2-m^2)(p^2-m^2)((p+P_J)^2-m^2)}$, lepton current l_μ, and $h^\mu=4m\varepsilon_{\mu\alpha\beta\sigma}P_y^\alpha\epsilon_\lambda^\beta P_J^\sigma$. The EM (U(1)) gauge invariance is explicit. When replacing the four-vector l_μ by the total four-momentum of the virtual photon, which equals to $(P_J+P_y)_\mu$, the amplitude is zero. The reason is $(P_J+P_y)_\mu h^\mu=0$, because of the totally antisymmetric tensor $\varepsilon_{\mu\alpha\beta\sigma}$. We first integrate over the poles and then do the numerical integral for the remaining 3-dimensional momentum. This provides a calculation procedure other than the Feynman parameters when the vertices are very complex. The cross section as function of β is shown in the Table. Here β is parameter for the distribution of $c\bar{c}$ relative momentum.

4 summary and discussion

The results show that the off shell states of $c\bar{c}$ in bound states can contribute significantly in this production process, when the relative movement is large enough (but because of the normalization factor, the results are static even β very large); no other framework can take into account this effect. Higher order calculations are straightforward, but the treating of the propagator and vertices need to be investigated.

Acknowledgments

The author thanks Shashank and Ming for Collaboration. This work is partially supported by NSFC, NSF of Shandong Province, and funds of Shandong University based on MoE.

References

1. K. Abe *et al.* [Belle Collaboration], Phys. Rev. Lett. **89** (2002) 142001.
2. K. Abe *et al.* [Belle Collaboration], Phys. Rev. D **70** (2004) 071102.

β	I^2	N^2	I^2/N^2	$\sigma(fb)$
$1/2$	3.39×10^{-14}	1.29×10^{6}	2.63×10^{-20}	1.4×10^{-6}
$1/\sqrt{2}$	7.90×10^{-9}	1.47×10^{7}	5.37×10^{-16}	2.9×10^{-2}
1	1.36×10^{-6}	1.52×10^{8}	8.95×10^{-15}	4.9×10^{-1}
1.15	8.00×10^{-6}	2.83×10^{8}	2.83×10^{-14}	1.5
1.3	9.80×10^{-6}	8.06×10^{7}	1.22×10^{-13}	6.6
$\sqrt{2}$	9.80×10^{-5}	1.08×10^{9}	9.09×10^{-14}	5.0
1.5	1.00×10^{-4}	3.36×10^{9}	2.97×10^{-14}	1.6
1.6	3.59×10^{-4}	8.85×10^{9}	4.05×10^{-14}	2.2
1.7	1.08×10^{-3}	1.89×10^{10}	5.73×10^{-14}	3.1
1.8	2.95×10^{-3}	3.40×10^{10}	8.69×10^{-14}	4.7
1.9	7.32×10^{-3}	4.96×10^{10}	1.48×10^{-13}	8.1
2	1.05×10^{-2}	4.72×10^{10}	2.23×10^{-13}	12.2
2.1	3.41×10^{-2}	2.50×10^{10}	1.37×10^{-12}	74.6
2.25	8.59×10^{-2}	5.73×10^{11}	1.50×10^{-13}	8.2
2.5	1.81×10^{-1}	6.59×10^{12}	2.75×10^{-14}	1.5
3	1.41	2.08×10^{14}	6.81×10^{-15}	0.4

3. B. Aubert *et al.* [BABAR Collaboration], Phys. Rev. D **72** (2005) 031101.
4. G. T. Bodwin, E. Braaten and G. P. Lepage, Phys. Rev. D **51** (1995) 1125.
5. R. Fulton *et al.* [CLEO Collaboration], Phys. Lett. B **224** (1989) 445.
6. R. A. Briere *et al.* [CLEO Collaboration], Phys. Rev. D **70** (2004) 072001.
7. S. Y. Li, Q. B. Xie and Q. Wang, Phys. Lett. B **482** (2000) 65.
8. W. Han and S. Y. Li, Phys. Rev. D **74** (2006) 117502.
9. Q. B. Xie and S. Y. Li, *Prepared for 3rd Joint Meeting of Chinese Physicists Worldwide: Role of Physics in the New Millenium: Research, Education and Society, Hong Kong, China, 31 Jul - 4 Aug 2000*
10. A. Abulencia *et al.* [CDF Collaboration], Phys. Rev. Lett. **99** (2007) 132001.
11. G. T. Bodwin, J. Lee and C. Yu, Phys.Rev. D77 (2008) 094018.
12. Z. G. He, Y. Fan and K. T. Chao, Phys. Rev. D **75** (2007) 074011.
13. B. Gong and J. X. Wang, Phys.Rev. D77 (2008) 054028.
14. Y. J. Zhang, Y. j. Gao and K. T. Chao, Phys. Rev. Lett. **96** (2006) 092001.
15. H. R. Dong, F. Feng and Y. Jia, arXiv:1204.4128 [hep-ph].
16. J. P. Ma and Z. G. Si, Phys. Rev. D **70** (2004) 074007.
17. A. E. Bondar and V. L. Chernyak, Phys. Lett. B **612** (2005) 215.
18. V. V. Braguta, A. K. Likhoded and A. V. Luchinsky, Phys. Rev. D **72** (2005) 074019.
19. V. V. Braguta, A. K. Likhoded and A. V. Luchinsky, Phys. Lett. B **646** (2007) 80.
20. G. T. Bodwin, D. Kang and J. Lee, Phys. Rev. D **74** (2006) 114028.
21. E. Mengesha and S. Bhatnagar, Int.J.Mod.Phys. E20 (2011) 2521-2533.
22. X. H. Guo, H. W. Ke, X. Q. Li and X. H. Wu, arXiv:0804.0949 [hep-ph].
23. S. Bhatnagar and S. Y. Li, arXiv:hep-ph/0612084.
24. S. Bhatnagar and S. Y. Li, J. Phys. G **32** (2006) 949.
25. S. Bhatnagar, S. Y. Li and J. Mahecha, Int.J.Mod.Phys. E20 (2011) 1437-1454.

RECENT HEAVY FLAVOR RESULTS FROM THE TEVATRON

M. DORIGO on behalf of the CDF and D0 Collaborations.
University of Trieste and INFN Trieste

The CDF and D0 experiments at the Tevatron $p\bar{p}$ collider have pioneered and established the role of flavor physics in hadron collisions. A broad program is now at its full maturity. We report on three new results sensitive to physics beyond the standard model, obtained using the whole CDF dataset: a measurement of the difference of CP asymmetries in K^+K^- and $\pi^+\pi^-$ decays of D^0 mesons, new bounds on the B_s^0 mixing phase and on the decay width difference of B_s^0 mass-eigenstates, and an update of the summer 2011 search for $B_{(s)}^0$ mesons decaying into pairs of muons. Finally, the D0 confirmation of the observation of a new hadron, the $\chi_b(3P)$ state, is briefly mentioned.

1 Measurement of CP violation in charm in the final CDF dataset

Violation of the CP symmetry in tree-dominated decays $D^0 \to \pi^+\pi^-$ and $D^0 \to K^+K^-$ is a sensitive probe of physics beyond the standard model (SM). Both the D^0–$\bar{D}^0$ mixing amplitude and the SM-suppressed penguin amplitude can be greatly enhanced by new dynamics, which can also increase the size of the CP violation over that expected from to the Cabibbo-Kobayashi-Maskawa (CKM) hierarchy. Last year, using 5.9 fb^{-1} of data, CDF produced the world's most precise measurements of the CP asymmetries $A_{\rm CP}(KK) = (-0.24\pm0.22\pm0.09)\%$ and $A_{\rm CP}(\pi\pi) = (0.22\pm0.24\pm0.11)\%$.[1] In spite of the hadronic uncertainties, there is broad consensus that direct CP asymmetries of $D^0 \to K^+K^-$ and of $D^0 \to \pi^+\pi^-$ should be of opposite sign. Therefore, a measurement of the difference between asymmetries of those decays is maximally sensitive to detect CP violation. Indeed, the LHCb collaboration reported recently the first evidence of CP violation in charm measuring $\Delta A_{\rm CP} = A_{\rm CP}(KK) - A_{\rm CP}(\pi\pi) = (-0.82 \pm 0.21 \pm 0.11)\%$.[2] An independent measurement is crucial to establish the effect, and the 10 fb^{-1} sample of hadronic D decays collected by CDF is the only one currently available to attain sufficient precision.

The analysis follows closely the measurement of individual asymmetries.[3] The flavor of the D^0 meson is tagged from the charge of the soft pion in the strong $D^{\star+} \to D^0\pi^+$ decay. Since $D^{\star+}$ and $D^{\star-}$ mesons are produced in equal number in strong $p\bar{p}$ interactions, any asymmetry between the number of D^0 and $\bar{D}^0$ decays is due to either CP violation or instrumental effects. The latter can be induced only by the difference in reconstruction efficiency between positive and negative soft pions. Provided that the relevant kinematic distributions are equalized in the two decay channels, the instrumental asymmetry cancels to an excellent level of accuracy in the difference between the observed asymmetries between signal yields. Such cancellation allows one to increase the sensitivity on $\Delta A_{\rm CP}$ by loosening some selection criteria with respect to the measurement of individual asymmetries and double the signal yields. The trigger is fired by two charged particles with transverse momenta greater than 2 GeV/c. The excellent CDF momentum resolution yields precise mass resolution ($\sim$8 MeV/c^2 for D mesons) which provides good signal-to-background. The typical resolution (50 μm) on the impact parameter (IP) of the tracks is effective to trigger on good kaon or pion candidates, that are required to have IP>100 μm. The offline selection adds some basic additional requirements on track and vertex quality. The numbers of D^0 and $\bar{D}^0$ decays are determined with a simultaneous fit to the $D^0\pi$-mass distribution of positive and negative $D^\star$ decays (see Fig. 1, left). About 1.21 million $D^0 \to K^+K^-$ decays and 550 thousand $D^0 \to \pi^+\pi^-$ decays are reconstructed, yielding the following observed asymmetries between signal yields, $A_{\rm raw}(KK) = (-2.33 \pm 0.14)\%$ and

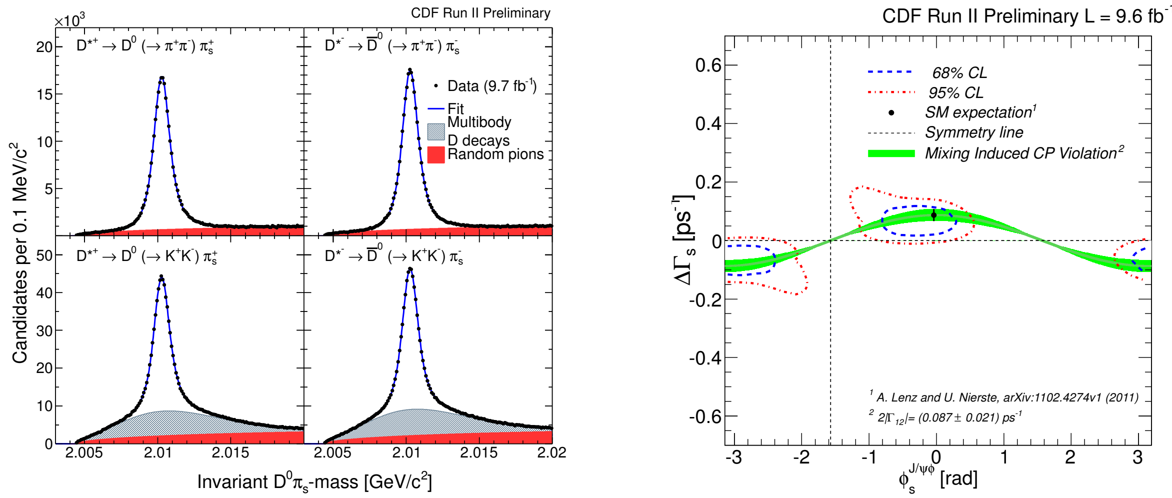

Figure 1: Left: $D^0\pi$-mass distributions of positive and negative $D^\star$ decays with fit projections overlaid. Right: 68% and 95% confidence regions in the plane (ϕ_s,$\Delta\Gamma_s$) from profile-likelihood of CDF data.

$A_{\rm raw}(\pi\pi) = (-1.71 \pm 0.15)\%$. Residual systematic uncertainties total 0.10% and are driven by differences between distributions associated with charm and anticharm decays. The final result is $\Delta A_{\rm CP} = (-0.62 \pm 0.21 \pm 0.10)\%$, which is 2.7σ different from zero. This provides strong indication of CP violation in CDF charm data, supporting the LHCb earlier evidence with same resolution. The combination of CDF, LHCb and B-factories measurements deviates by approximately 3.8σ from the no CP violation point.

2 Measurement of the $B_s^0 \to J/\psi\varphi$ time-evolution in the final CDF dataset

The B_s^0–$\bar{B}_s^0$ mixing is a promising process where to search for new physics (NP), given the D0 3.9σ anomaly in dimuon charge asymmetry.[4] If the anomaly is due to new dynamics in the B_s^0 sector, the phase difference between the B_s^0–$\bar{B}_s^0$ mixing amplitude and the amplitude of B_s^0 and $\bar{B}_s^0$ decays into common final states, ϕ_s, would be significantly altered with respect to its nearly vanishing value expected in the SM. A non-CKM enhancement of ϕ_s can also decrease the decay width difference between the heavy and light mass-eigenstate of the B_s^0 meson, $\Delta\Gamma_s$. The analysis of the time evolution of $B_s^0 \to J/\psi\varphi$ decays is the most effective experimental probe of such a CP-violating phase. Since the decay is dominated by a single real amplitude, the phase difference equals the mixing phase to a good approximation. Early Tevatron measurements have shown a mild discrepancy of about 2σ with the SM expectation.[5] Latest updates by CDF and D0 are in better agreement with the SM, as well as first measurements provided by LHCb.[6,7,8]

Here we report the new CDF update using the final dataset of 10 fb^{-1} which comprises about 11000 $B_s^0 \to J/\psi\varphi$ decays collected by a low-momenta dimuon trigger.[9] The decays are fully reconstructed through four tracks that fit to a common displaced vertex, two matched to muon pairs consistent with a J/ψ decay, and two consistent with a $\phi \to K^+K^-$ decay. A joint fit that exploits the candidate-specific information given by the B mass, decay time and production flavor, along with the decay angles of kaons and muons, is used to determine both ϕ_s and $\Delta\Gamma_s$. The analysis closely follows the previous measurement obtained on a subset of the data.[6] The only major difference is the use of an updated calibration of the tagging algorithm that uses information from the decay of the "opposite side" bottom hadron in the event to determine the flavor of the B_s^0 at its production, with tagging power $(1.39 \pm 0.01)\%$. The information from the tagger that exploits charge-flavor correlations of the neighboring kaon to the B_s^0 is instead restricted to only half of the sample, in which has tagging power $(3.2 \pm 1.4)\%$. This degrades the statistical resolution on ϕ_s by no more than 15%. A decay-resolution of ∼90 fs allows resolving the fast B_s^0 oscillations to increase sensitivity on the mixing phase. The 68% and 95% confidence regions in the plane $(\phi_s, \Delta\Gamma_s)$ obtained from the profile-likelihood of the CDF data are reported in Fig. 1 (right). The confidence interval for the mixing phase is $\phi_s \in [-0.60, 0.12]$ rad at 68% C.L., in agreement with the CKM value and recent D0 and LHCb determinations.[7,10] This is the final CDF measurement on the B_s^0 mixing phase, and provides a factor 35% improvement in resolution with respect to the latest determination. CDF also reports $\Delta\Gamma_s = (0.068 \pm 0.026 \pm 0.007)$ ps^{-1} under the hypothesis of a SM value for ϕ_s, along with the measurement of the B_s^0 lifetime, $\tau_s = (1.528 \pm 0.019 \pm 0.009)$ ps, in agreement with other experiments' results.[7,10]

3 Final search for dimuon decays of B mesons at CDF

The $B^0_{(s)} \to \mu^+\mu^-$ decays involve flavor changing neutral currents and the observation of an abnormal decay rate can provide excellent evidence of NP since in the SM they can occur only through high-order loop diagrams. Enhancements to the SM expectation of their branching ratios (BR) can indeed occur in a variety of different NP models. Last summer CDF reported an intriguing $\sim 2.5\sigma$ fluctuation over background in 7 fb^{-1} of data. Even if compatible with the SM and other experiments' results, it allowed the first two sided bound on the $B_s^0 \to \mu^+\mu^-$ rate.[11]

Here we report the CDF update of the analysis with the final 10 fb^{-1} dataset.[12] The analysis methods are not changed from the previous iteration to ensure the unbiased processing of new data. The events are collected using a set of dimuon triggers and are divided in two categories: "CC" events have both muon candidates in the central region of the detector, while "CF" events have one central muon and another muon in the forward region. The signal candidates are fully reconstructed with a secondary vertex due to the long B_s^0 lifetime (∼450 μm). They also feature a primary-to-secondary vertex vector aligned with the B_s^0 candidate momentum and a very isolated B_s^0 candidate. There are two sources of background: combinatorial background and peaking background. The former tends to be partially reconstructed and shorter-lived than signal. It is estimated by extrapolating the number of events in the sideband regions of the B mass distribution to the signal window using a linear fit. The peaking background are due to decays of B_s^0 and B^0 mesons to pions and kaons that are misreconstructed as muons, and it is ten times greater in the B^0 search with respect to the B_s^0 analysis. It is carefully taken into account with simulation (mass shape) and with $D^0 \to K\pi$ decays from data (misidentification probability). A neural network (NN) classifier is optimized to reject the background using 14 event variables. The background estimates are checked to be consistent in many control samples. Finally, when the background is well understood, the number of observed events is compared to the number expected. The data are found to be consistent with the background expectations for the $B^0 \to \mu^+\mu^-$ decay and yield an observed limit of BR $< 4.6 \times 10^{-9}$ at 95% C.L (with expected limit 4.2×10^{-9}). In the case of $B_s^0 \to \mu^+\mu^-$ the summer 2011 excess is not reinforced, even though it is still present as shown in the most sensitive (top-right) bin of the NN in Fig. 2. The resulting bounds at 95% C.L. are $0.8 \times 10^{-9} <$ BR $< 3.4 \times 10^{-8}$, which is still compatible both with the SM expectation and the latest limits from LHC experiments.[13] An upper limit at 95% C.L. of BR $< 3.1 \times 10^{-8}$ (expected 1.3×10^{-8}) is also derived.

4 A new state decaying into $\Upsilon(1S) + \gamma$

Using data corresponding to an integrated luminosity of 1.3 fb^{-1}, the D0 collaboration observes a narrow mass state decaying into $\Upsilon(1S) + \gamma$, where the $\Upsilon(1S)$ meson is detected by its decay

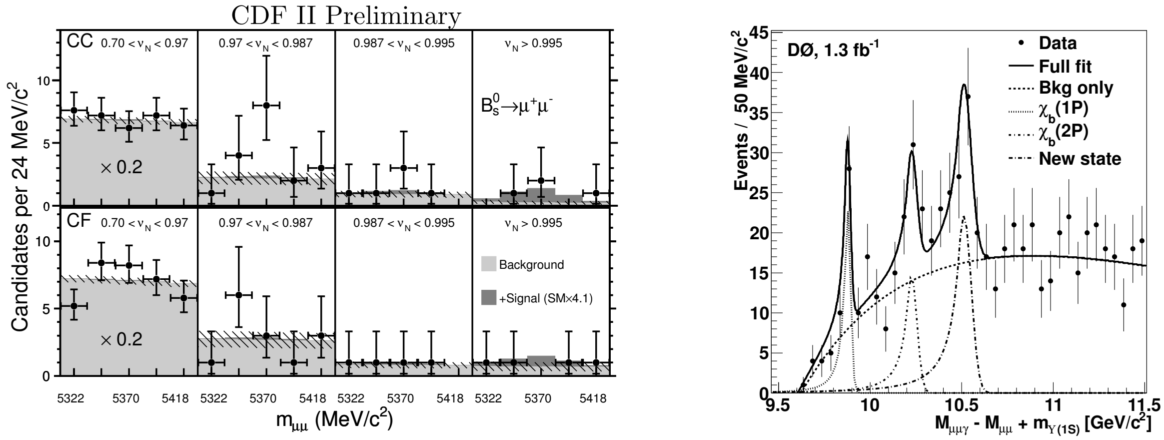

Figure 2: Left: comparison of the CDF $B_s^0 \to \mu^+\mu^-$ data (points) and expected background (solid grey) for CC and CF muons. Right: mass distribution of $M_{\mu\mu\gamma} - M_{\mu\mu} + M_{\Upsilon(1S)}$ of D0 data with fit overlaid.

into a muons pair, and the photon through its conversion into an e^+e^- pair.[14] The fit to the mass spectrum in Fig. 2 (right) shows three structures above a smooth, threshold-like background. The one at the highest mass has a statistical significance of 5.6σ. It is interpreted as the state $\chi_b(3P)$ and is centered at $10.551 \pm 0.014 \pm 0.017$ GeV/c^2, consistent with the recent ATLAS observation.[15]

5 Conclusions

We reported the final CDF results on three flagship measurements in the indirect search for NP at Tevatron, and the confirmation of a new hadron ($\chi_b(3P)$) by the D0 collaboration. The CP asymmetries of D^0 meson decays reported by CDF confirm the first evidence of CP violation in charm reported by LHCb; in the B_s^0 sector, tensions with SM predictions are now softened by latest updates of ϕ_s and $\Delta\Gamma_s$ bounds, making the D0 A_{sl} anomaly even harder to depuzzle. The final CDF update on the $B_s^0 \to \mu^+\mu^-$ rate is concluding a decade-long program of Tevatron searches that improved the experimental bounds on the rate down to the 10^{-8} range, nearing now the sensitivity to observe a SM signal. Analyses of the unique ($p\bar{p}$ charge-symmetric), rich (*e.g.*, millions of charm decays), and well-understood (10-years expertise) data sample acquired by CDF and D0 are still in progress and may reserve interesting results in the near future.

References

1. T. Aaltonen *et al.* (CDF Collaboration), *Phys. Rev.* D **85**, 012009 (2012).
2. R. Aaij *et al.* (LHCb Collaboration), *Phys. Rev. Lett.* **108**, 111602 (2012).
3. T. Aaltonen *et al.* (CDF Collaboration), CDF Note 10784 (2012).
4. V. M. Abazov *et al.* (D0 Collaboration), *Phys. Rev.* D **84**, 052007 (2011).
5. CDF and D0 Collaborations, CDF Note 9787, D0 Note 5928 (2009).
6. T. Aaltonen *et al.* (CDF Collaboration), *Phys. Rev.* D **85**, 072002 (2012).
7. V. M. Abazov *et al.* (D0 Collaboration), *Phys. Rev.* D **85**, 032006 (2012).
8. R. Aaij *et al.* (LHCb Collaboration), *Phys. Rev. Lett.* **108**, 101803 (2012)
9. T. Aaltonen *et al.* (CDF Collaboration), CDF Note 10778 (2012).
10. R. Aaij *et al.* (LHCb Collaboration), LHCb-CONF-2012-002.
11. T. Aaltonen *et al.* (CDF Collaboration), *Phys. Rev. Lett.* **107**, 191801 (2011).
12. http://www-cdf.fnal.gov/physics/new/bottom/120209.blessed-bmumu10fb.
13. CMS PAS BPH-11-020; ATLAS-CONF-2012-010; LHCb-PAPER-2012-007.
14. V. M. Abazov *et al.* (D0 Collaboration), arXiv:1203.6034 [hep-ex].
15. Georges Aad *et al.* (ATLAS Collaboration), *Phys. Rev. Lett.* **108**, 152001 (2012).

Forward-backward asymmetry of $B \to K_J l^+ l^-$ decays in SM and new physics models

Cai-Dian Lü[a] and Wei Wang[b]
[a] *Institute of High Energy Physics Chinese Academy of Sciences, P.O. Box 918, Beijing 100049, China*
[b] *Deutsches Elektronen-Synchrotron DESY, Hamburg 22607, Germany*

We report on our studies of $B \to K_J l^+ l^-$ in the standard model and several new physics variations, with K_J denoting a kaonic resoanance. In terms of helicity amplitudes, we derive a compact form for the full angular distributions, and use them to calculate the branching ratios, forward-backward asymmetries and polarizations. We have updated the constraints on effective Wilson coefficients and/or free parameters in these new physics scenarios by making use of the $B \to K^* l^+ l^-$ and $b \to s l^+ l^-$ experimental data. Their impact on $B \to K_J^* l^+ l^-$ is subsequently explored and in particular the zero-crossing point for forward-backward asymmetry in new physics scenarios can sizably deviate from the standard model.

1 Introduction

Flavor changing neutral currents are forbidden at tree level in the standard model (SM). Such rare B-decays into dileptons are precision probes of the SM and provide constraints on new physics beyond the standard model [1]. Important semileptonic modes in terms of experimental accessibility and theory control are those into K_J [2,3,4,5,6], in which K_J can be K^*, $K_1(1270), K_1(1410),\ K^*(1410), K_0^*(1430), K_2^*(1430), K^*(1680), K_3^*(1780)$ and $K_4^*(2045)$. These decays exhibit a rich phenomenology through the angular analysis of subsequent decays of K_J, through which the forward-backward asymmetry (FBA) can be extracted. As opposed to the branching ratios which suffer from large hadronic uncertainties, the FBA is theoretically clean and sensitive to NP. Therefore it is one of the major goals of LHCb to precisely explore FBA as a hunt for new physics signals [7].

2 Form factor relations

The $B \to K_J^*$ form factors are nonperturbative in nature and the application of QCD theory to them mostly resorts to the Lattice QCD simulations, which has large limitation at the current stage. An important observation is that, in the heavy quark limit $m_b \to \infty$ and the large energy limit $E \to \infty$, interactions of the heavy and light systems can be expanded in small ratios Λ_{QCD}/E and Λ_{QCD}/m_B. At the leading power in $1/m_b$, the large energy symmetry is obtained and such symmetry greatly simplifies the heavy-to-light transition [8].

As a concrete application, the current $\bar{s}\Gamma b$ in QCD can be matched onto the current $\bar{s}_n \Gamma b_v$ constructed in terms of the fields in the low-energy effective theory. Here v denotes the velocity of the heavy meson and n is a light-like vector along the K_J^* moving direction. This procedure constrains the independent Lorentz structures and reduces the seven independent hadronic form

Table 1: $B \to K_J^*$ form factors derived from the large recoil symmetry.

K_J^*	$\xi_{\|\|}$	$\xi_\perp$
$K^*(1410)$	0.22 ± 0.03	0.28 ± 0.04
$K_0^*(1430)$	0.22 ± 0.03	–
$K_2^*(1430)$	0.22 ± 0.03	0.28 ± 0.04
$K^*(1680)$	0.18 ± 0.03	0.24 ± 0.05
$K_3^*(1780)$	0.16 ± 0.03	0.23 ± 0.05
$K_4^*(2045)$	0.13 ± 0.03	0.19 ± 0.05

factors for each $B \to K_J^*$ $(J \geq 1)$ type to two universal functions $\xi_\perp$ and $\xi_{||}$. Explicitly, we have

$$
\begin{aligned}
A_0^{K_J^*}(q^2)\left(\frac{|\vec{p}_{K_J^*}|}{m_{K_J^*}}\right)^{J-1} &\equiv A_0^{K_J^*,\text{eff}} \simeq (1-\frac{m_{K_J^*}^2}{m_B E})\xi_{||}^{K_J^*}(q^2)+\frac{m_{K_J^*}}{m_B}\xi_\perp^{K_J^*}(q^2),\\
A_1^{K_J^*}(q^2)\left(\frac{|\vec{p}_{K_J^*}|}{m_{K_J^*}}\right)^{J-1} &\equiv A_1^{K_J^*,\text{eff}} \simeq \frac{2E}{m_B+m_{K_J^*}}\xi_\perp^{K_J^*}(q^2),\\
A_2^{K_J^*}(q^2)\left(\frac{|\vec{p}_{K_J^*}|}{m_{K_J^*}}\right)^{J-1} &\equiv A_2^{K_J^*,\text{eff}} \simeq (1+\frac{m_{K_J^*}}{m_B})[\xi_\perp^{K_J^*}(q^2)-\frac{m_{K_J^*}}{E}\xi_{||}^{K_J^*}(q^2)],\\
V^{K_J^*}(q^2)\left(\frac{|\vec{p}_{K_J^*}|}{m_{K_J^*}}\right)^{J-1} &\equiv V^{K_J^*,\text{eff}} \simeq (1+\frac{m_{K_J^*}}{m_B})\xi_\perp^{K_J^*}(q^2),\\
T_1^{K_J^*}(q^2)\left(\frac{|\vec{p}_{K_J^*}|}{m_{K_J^*}}\right)^{J-1} &\equiv T_1^{K_J^*,\text{eff}} \simeq \xi_\perp^{K_J^*}(q^2),\\
T_2^{K_J^*}(q^2)\left(\frac{|\vec{p}_{K_J^*}|}{m_{K_J^*}}\right)^{J-1} &\equiv T_2^{K_J^*,\text{eff}} \simeq (1-\frac{q^2}{m_B^2-m_{K_J^*}^2})\xi_\perp^{K_J^*}(q^2),\\
T_3^{K_J^*}(q^2)\left(\frac{|\vec{p}_{K_J^*}|}{m_{K_J^*}}\right)^{J-1} &\equiv T_3^{K_J^*,\text{eff}} \simeq \xi_\perp^{K_J^*}(q^2)-(1-\frac{m_{K_J^*}^2}{m_B^2})\frac{m_{K_J^*}}{E}\xi_{||}^{K_J^*}(q^2).
\end{aligned}
\tag{1}
$$

In the case of B to scalar meson transition, the large energy limit gives

$$
\frac{m_B}{m_B+m_{K_0^*}}F_T(q^2)=F_1(q^2)=\frac{m_B}{2E}F_0(q^2)=\xi^{K_0^*}(q^2).
\tag{2}
$$

The results for $\xi_{||}^{K_J^*}$ and $\xi_\perp^{K_J^*}$ obtained from the Bauer-Stech-Wirbel (BSW) model [9] in Ref. [10] are used in our work and we collect these results in Tab. 1. For the $B \to K_0^*$ transition, it is plausible to employ $\xi^{B\to K_0^*}=\xi_{||}^{B\to K_2^*}$ since both K_0^* and K_2^* are p-wave states.

In addition, we have employed the perturbative QCD approach to directly compute these form factors [11,12,13] and find many agreements with the large recoil symmetries, for instance the PQCD results for $B \to K_2^*$ transition are shown in Table 2 (See Ref. [5] for a more detailed comparison).

3 New physics contributions

We choose several kinds of new physics models, such as family non-universal Z' model, Supersymmetric model and vector-like quark model. All of them can induce extra contributions to the branching ratios, polarizations and forward-backward asymmetry parameters, through the effective operators O_9 and/or O_{10}. Via modifying the Wilson coefficients C_9 and C_{10}, these

Table 2: $B \to K_2^*$ form factors at $q^2 = 0$ in the ISGW2 model, the covariant light-front quark model and the light-cone QCD sum rules and perturbative QCD approach.

	ISGW2	CLFQM	LCSR	LEET+BSW	PQCD
$V^{BK_2^*}$	0.38	0.29	0.16 ± 0.02	0.21 ± 0.03	$0.21^{+0.06}_{-0.05}$
$A_0^{BK_2^*}$	0.27	0.23	0.25 ± 0.04	0.15 ± 0.02	$0.18^{+0.05}_{-0.04}$
$A_1^{BK_2^*}$	0.24	0.22	0.14 ± 0.02	0.14 ± 0.02	$0.13^{+0.04}_{-0.03}$
$A_2^{BK_2^*}$	0.22	0.21	0.05 ± 0.02	0.14 ± 0.02	$0.08^{+0.03}_{-0.02}$
$T_1^{BK_2^*}$		0.28	0.14 ± 0.02	0.16 ± 0.02	$0.17^{+0.05}_{-0.04}$
$T_3^{BK_2^*}$		-0.25	$0.01^{+0.02}_{-0.01}$	0.10 ± 0.02	$0.14^{+0.05}_{-0.03}$

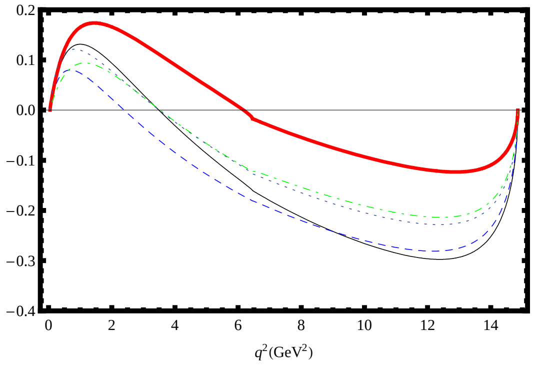

Figure 1: Impacts of the NP contributions on normalized forward-backward asymmetry of $B \to K_2^* l^+ l^-$. Black (solid) line denotes the SM result, while the dashed (blue) and thick (red) lines correspond to the modification of C_9. Dot-dashed (green) and dotted lines are obtained by modifying C_{10}.

contributions affect the observables in $B \to K^* l^+ l^-$ as well and the comparison of theory with data derive the constraints on C_9 and C_{10}.

We adopt a least χ^2-fit method and make use of the experimental data on $B \to K^* l^+ l^-$. Embedded in the vector-like quark model, the free two parameters, real part and imaginary part of the FCNC coupling λ_{sb}, are found as

$$\mathrm{Re}\lambda_{sb} = (0.07 \pm 0.04) \times 10^{-3}, \quad \mathrm{Im}\lambda_{sb} = (0.09 \pm 0.23) \times 10^{-3}, \tag{3}$$

from which we obtain $|\lambda_{sb}| < 0.3 \times 10^{-3}$ but the phase is less constrained again. The corresponding constraint on Wilson coefficients are

$$|\Delta C_9| = |C_9 - C_9^{SM}| < 0.2, \quad |\Delta C_{10}| = |C_{10} - C_{10}^{SM}| < 2.8. \tag{4}$$

Turning to family nonuniveral Z' model in which the coupling between Z' and a lepton pair is unknown, the two Wilson coefficients, C_9 and C_{10}, can be chosen as independent parameters. Assuming ΔC_9 and ΔC_{10} as real, we find

$$\Delta C_9 = 0.88 \pm 0.75, \quad \Delta C_{10} = 0.01 \pm 0.69. \tag{5}$$

Removal of the above assumption leads to

$$\Delta C_9 = -0.81 \pm 1.22 + (3.05 \pm 0.92)i, \quad \Delta C_{10} = 1.00 \pm 1.28 + (-3.16 \pm 0.94)i. \tag{6}$$

For illustration, we choose $\Delta C_9 = 3e^{i\pi/4, i3\pi/4}$ and $\Delta C_{10} = 3e^{i\pi/4, i3\pi/4}$ as the reference points and give the plots of FBAs in Fig. 1. The black (solid) line denotes the SM result, while the dashed (blue) and thick (red) lines correspond to the modification of C_9. The dot-dashed (green) and dotted lines are obtained by modifying C_{10}. From the figure for A_{FB}, we can see that the zero-crossing point s_0 can be sizably changed, which can be tested on the future collider or can be further constrained.

4 Summary

Heavy flavor physics has entered a precision era as large samples of flavor physics data have been brought to us from B factories and the LHC. As a result, we are able to reach a multitude of observables from exclusive $b \to sl^+l^-$ processes, which allow to map out the structure of the underlying physics.

In this talk we have concentrated on the $B \to K_1(K_0^*, K_2^*, K_3^*, K_4^*)l^+l^-$ in the standard model. Their branching ratios are predicted to have the order 10^{-6} or 10^{-7} which are large enough for observation of these processes. Using the experimental data on $B \to K^*l^+l^-$, we have also presented an update of the constraints on new physics parameters in two specific scenarios and elaborated on the impact on $B \to K_Jl^+l^-$. We expect more and more results from the LHCb quite soon, which may lead to success of the justification of new physics degree of freedoms from flavor physics.

Acknowledgments

We are very grateful to M.Jamil Aslam, Run-Hui Li and Yu-Ming Wang for collaboration. This work is partly supported by the National Science Foundation of China under the Grant No.11075168.

References

1. A. Ali, P. Ball, L. T. Handoko and G. Hiller, Phys. Rev. D **61** (2000) 074024 [hep-ph/9910221].
2. M.Jamil Aslam, Cai-Dian Lu, Yu-Ming Wang, Phys. Rev. D79 (2009) 074007 e-Print: arXiv:0902.0432 [hep-ph]
3. Run-Hui Li, Cai-Dian Lu, Wei Wang, Phys. Rev. D79 (2009) 094024 e-Print: arXiv:0902.3291 [hep-ph]
4. Run-Hui Li, Cai-Dian Lu, Wei Wang, Phys. Rev. D83 (2011) 034034 e-Print: arXiv:1012.2129 [hep-ph]
5. Cai-Dian Lu, Wei Wang, Phys. Rev. D85 (2012) 034014, e-Print: arXiv:1111.1513 [hep-ph]
6. Cheng-Wei Chiang, Run-Hui Li, Cai-Dian Lu, Chin. Phys. C36 (2012) 14-24 e-Print: arXiv:0911.2399 [hep-ph]
7. RAaij *et al.* [LHCb Collaboration], Phys. Rev. Lett. **108** (2012) 181806 [arXiv:1112.3515 [hep-ex]].
8. J. Charles, A. Le Yaouanc, L. Oliver, O. Pene and J. C. Raynal, Phys. Rev. D **60**, 014001 (1999) [hep-ph/9812358].
9. M. Wirbel, B. Stech, M. Bauer, Z. Phys. **C29**, 637 (1985).
10. H. Hatanaka and K. C. Yang, Phys. Rev. D **79**, 114008 (2009) [arXiv:0903.1917 [hep-ph]]; Eur. Phys. J. C **67**, 149 (2010) [arXiv:0907.1496 [hep-ph]].
11. R. -H. Li, C. -D. Lu, W. Wang and X. -X. Wang, Phys. Rev. D **79** (2009) 014013 [arXiv:0811.2648 [hep-ph]].
12. R. -H. Li, C. -D. Lu and W. Wang, Phys. Rev. D **79** (2009) 034014 [arXiv:0901.0307 [hep-ph]].
13. W. Wang, Phys. Rev. D **83** (2011) 014008 [arXiv:1008.5326 [hep-ph]].

DECAYS OF BEAUTY HADRONS MEASURED IN CMS AND ATLAS

Maria Smizanska for ATLAS and CMS collaborations
Department of Physics,Lancaster University, Lancaster, LA1 4YB, UK

The ATLAS and CMS data collected in pp collisions during 2010 and 2011 allowed a good quality of B-physics measurements, reproducing essential b-hadron properties, such as masses and lifetimes, and demonstrating a good performance of the two detectors within an increasing instantaneous luminosity of the LHC machine. These features enabled in particular a measurement of rare B decays with a precision that contributes to the LHC potential along with the LHCb experiment dedicated to B-physics. The CMS and ATLAS results on searches for $B_s^0 \to \mu^+\mu^-$and $B^0 \to \mu^+\mu^-$decays with 2011 data are reported here.

1 Introduction

The ATLAS[?] and CMS[?] experiments have rich and competitive heavy flavor programs including measurements of b-quark production, studies of b-hadron decays, as well as measurements of quarkonium and exotic states production. Both are ready to perform indirect searches for new physics, such as the rare decays of $B_s^0 \to \mu^+\mu^-$, $B^0 \to \mu^+\mu^-$, and measurements of CP-violating phase in the B_s^0 decay, that provide important constraints to the Standard Model (SM) and are complementary to direct searches for new physics. In 2010, the CMS and ATLAS have collected 40 pb^{-1} of data with a peak instantaneous luminosity of 2×10^{32} $cm^{-2}s^{-1}$. In 2011 the data taking was characterized by an increase of the LHC instantaneous luminosity reaching values of 3.5×10^{33} $cm^{-2}s^{-1}$ and the total integrated recorded luminosity was about 5 fb^{-1}.

The ATLAS and CMS B-physics trigger strategies are based on muon signatures. Due to bandwidth limitations the trigger menus in 2011 were mainly based on di-muon signatures at the first level trigger, combined at the higher trigger levels with a precise tracking and a vertex reconstruction capabilities.

A good track reconstruction performance with increasing instantaneous luminosity is important. For b-hadrons, decays trajectories of secondary particles are displaced from the primary vertex and the reconstruction of their shortest distances from the primary vertex (impact parameters) is of key importance. CMS measured the resolution of the track transverse impact parameter as a function of the track p_{T}[?]. This resolution, shown in Figure **??** was measured from data and compared with predictions from simulations. A precise test of these capabilities was made in ATLAS by reconstructing transverse impact parameters of tracks originating (mostly) from primary vertex for three different values of average number of interactions per beam crossing during 2011 data taking, Figure **??**, right. It was demonstrated that the resolution with increasing luminosity is preserved. The tails are potentially sensitive to the rate of secondaries and fakes and the results show no significant increase in the fake rate.

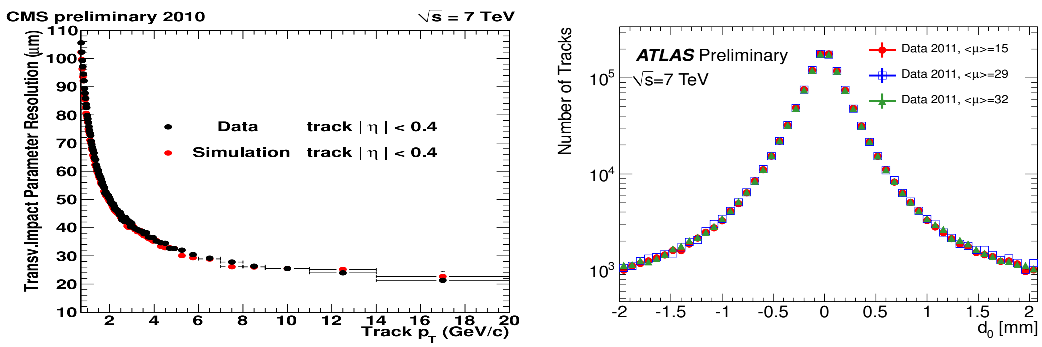

Figure 1: Left: CMS measured resolution of the track transverse impact parameter as a function of the track p_{T} [?]. Only central tracks with $|\eta| < 0.4$ are considered. Black and red symbols correspond to results from data and simulation, respectively. Right: ATLAS transverse impact parameter of reconstructed track with respect to primary vertex for three different values of average number of interactions per beam crossing during 2011 data taking [?].

2 b-hadron masses and lifetimes in decays with $J/\psi \to \mu^+\mu^-$ in final state.

Using 2010 and 2011 data most of b-hadron species have been extracted in ATLAS and CMS using exclusive decays with $J/\psi \to \mu^+\mu^-$ in final state, and masses and most of lifetimes were measured. These measurements showed a consistency with PDG values and thus provided a precise test of p_{T}-scale calibration in low p_{T} region, a precise test of detector alignment and a validation of vertexing algorithms.

High precision lifetime measurements performed by ATLAS and CMS using 2010 data were an important milestone on the way towards high precision time-dependent CP violation measurements. An overview of lifetime measurements using decay channels with $J/\psi \to \mu^+\mu^-$ in final state is given in Table **??** showing good agreement with PDG values. Figure **??** is showing fits to proper-decay times; the ATLAS measurement of average B-meson in inclusive decay $B \to J/\psi$ (left) [?] and CMS measurement of B^0 lifetime in $B^0 \to J/\psi K^0$ decay (right) [?]. An

		measured lifetime	PDG
$B^0 \to J/\psi K^0$	CMS [?]	$c\tau$ = 479 ± 22 μm	457 ± 3 μm
$B^0 \to J/\psi K^{*0}$	ATLAS [?]	τ = 1.51 ± 0.04 (stat) ± 0.04 (syst)	1.525 ± 0.009 ps
$B_s^0 \to J/\psi\phi$	CMS [?]	$c\tau$ = 478 ± 26 μm	491.0 ± 8.7 μm
$B_s^0 \to J/\psi\phi$	ATLAS [?]	τ =1.41 ± 0.08 (stat) ± 0.05 (syst) ps	1.472 ± 0.026 ps
$B \to J/\psi$	ATLAS [?]	τ =1.489 ± 0.016 (stat) ± 0.043 (syst) ps	1.544 ± 0.014 ps

Table 1: b-hadron lifetimes measured in CMS and ATLAS using 40 pb^{-1} of 2010 data.

example of two mass signals using 2011 data is given in Figure **??**. First is a Λ_b^0 signal in decay channel $\Lambda_b^0 \to \Lambda^0 J/\psi$ measured in CMS using 1.8 fb^{-1} of 2011 data [?], the extraction of this signal was used for a production cross section measurement. Second example is the ATLAS measurement of B_c meson mass, through its decay into $B_c^\pm \to J/\psi\pi^+(\pi^-)$, using 4.3 fb^{-1} of data in 2011 [?]. The B_c mass distribution is fitted with an unbinned maximum likelihood fit. The fitted mass of 6.282±0.007 (stat.) GeV is consistent with the PDG value m(B_c)= 6.277±0.006 GeV.

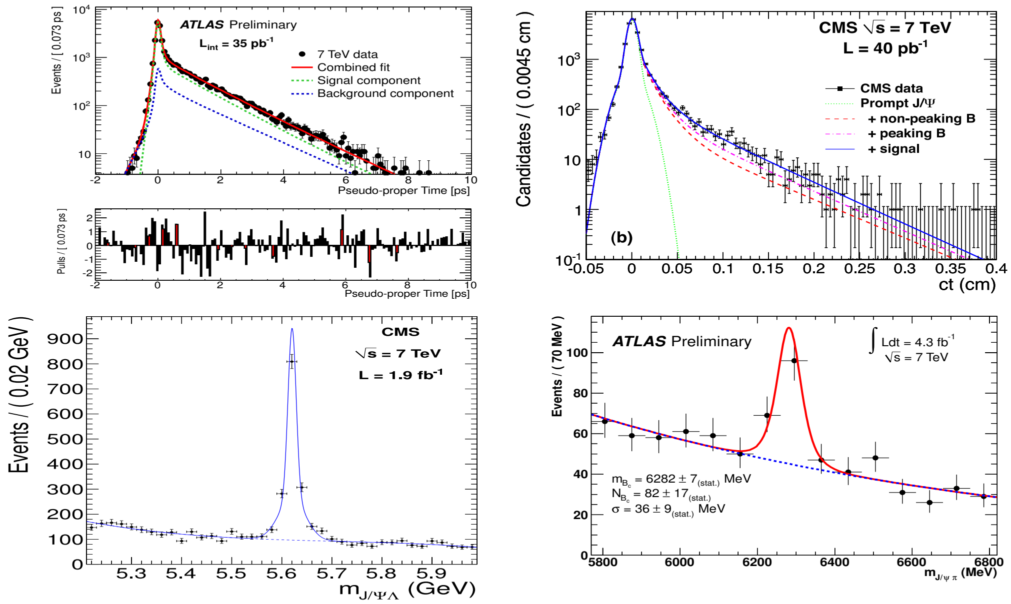

Figure 2: Left, top: ATLAS measurement of average b-hadron lifetime in inclusive decay $B \to J/\psi\ \mathrm{X}$? . The signal component (green hashed line), background components (blue dotted line) and the sum of signal and backgrounds (red solid line). Right, top: CMS measurement of B^0 lifetime ? , the sum of all contributions (blue solid line); the prompt J/ψ (green dotted); the sum of the prompt and non-prompt J/ψ (red dashed), and the sum of all backgrounds (purple dot-dashed). Left, down CMS Λ_b^0 mass ?. Right, down: ATLAS $B_c^\pm \to J/\psi\pi^+(\pi^-)$ mass ?. Red (full) line shows a fit projection to signal and background, blue (hash) line to background.

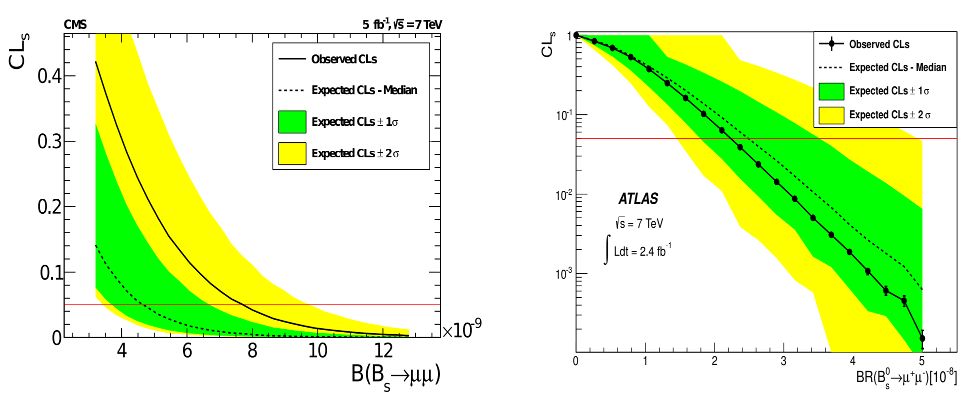

Figure 3: The expected and observed CLs functions of BR($B_s^0 \to \mu^+\mu^-$) for CMS ? (left) and ATLAS ? (right). Details given in the text.

3 Searches for rare B-meson decays

The rare decays $B_s^0 \to \mu^+\mu^-$and $B^0 \to \mu^+\mu^-$offer a profound probe into the effects of physics beyond the Standard Model (SM). The decays are flavour-changing neutral-current processes which are forbidden in the SM at tree level, occurring only via higher order diagrams. In the SM, these di-muonic B-decays have been calculated with high precision and with minimal non-perturbative uncertainties. These decays are also helicity suppressed, resulting in expected branching ratios (BR) of $(3.2 \pm 0.2) \times 10^{-9}$ and $(1.0 \pm 0.1) \times 10^{-10}$, respectively [?].

The results of CMS and ATLAS are using 4.9 fb^{-1} and 2.4 fb^{-1} of 2011 data respectively. The obtained CMS upper limits on BR at 95% C.L. are 7.7×10^{-9} and 1.8×10^{-9} for the $B_s^0 \to \mu^+\mu^-$and $B^0 \to \mu^+\mu^-$decays, respectively [?]. ATLAS determined the upper limit on the BR($B_s^0 \to \mu^+\mu^-$) 2.2×10^{-8} at 95% C.L. [?]. The expected and obtained CLs functions of branching ratios for $B_s^0 \to \mu^+\mu^-$decay are given for CMS and ATLAS in Figures **??**.

In both cases, the 95% CL limit is indicated by the red line and the solid black curves are the observed CLs. The yellow and green bands are the $\pm$ 1 σ and $\pm$ 2 σ fluctuations on the expected CLs (dashed black line) based on pseudo experiments with setting the counts in the search window to the interpolated background including the resonant one - before unblinding the region.

4 Conclusions

The CMS and ATLAS experiments have a rich program in the field of b-hadron decays. Precise measurements of lifetimes and masses of b-hadrons demonstrated that these experiments are well equipped for coming CP violation measurements. Searches for the rare decays $B_s^0 \to \mu^+\mu^-$and $B^0 \to \mu^+\mu^-$have been conducted, setting stringent constraints on extensions to the Standard Model.

1. ATLAS Collaboration, *The ATLAS Experiment at the CERN Large Hadron Collider.* JINST **3**, S08003 (2-8)
2. CMS Collaboration, *The CMS experiment at the CERN Large Hadron Collider.* JINST **3**, S08004 (1748-0221) 2008
3. CMS Collaboration, *Tracking and Primary Vertex Results in First 7 TeV Collisions.* CMS PAS TRK-10-005, 2010.
4. ATLAS Collaboration, *Performance of the ATLAS Inner Detector Track and Vertex Reconstruction in the High Pile-Up LHC Environment.* ATLAS-CONF-2012-042.
5. ATLAS Collaboration, *Measurement of the average B lifetime in inclusive $B \to J/\psi X$ decays with the ATLAS detector.* ATLAS-CONF-2011-145.
6. CMS Collaboration, *Phys. Rev. Lett.* **106**, 252001 (2011) .
7. ATLAS Collaboration, *Measurement of the average B lifetime in inclusive $B \to J/\psi X$ decays with the ATLAS detector.* ATLAS-CONF-2011-092.
8. CMS Collaboration, *Phys. Rev.* D **84**, 052008 (2011) .
9. CMS Collaboration, *Measurement of the $\Lambda_b^0 \to \Lambda^0 J/\psi$ differential cross section*, CERN-PH-EP-2012-124
10. ATLAS Collaboration, *Observation of the $B_c$meson in the decay $B_c^\pm \to J/\psi\pi^+(\pi^-)$ with the ATLAS detector at the LHC* , ATLAS-CONF-2012-028.
11. A.J.Buras: arXiv:1012.1447, E. Gamiz et al: Phys.Rev.D **80**, 014503 (2009).
12. ATLAS Collaboration, *Search for the decay $B_s^0 \to \mu^+\mu^-$with the ATLAS detector*, CERN-PH-EP-2012-067, arXiv:1204.0735v2.
13. CMS Collaboration, *Search for $B_s^0 \to \mu^+\mu^-$ and $B^0 \to \mu^+\mu^-$ decays.* JHEP **04**, 033 (2012).

CP VIOLATION WITH B_s

G. RICCIARDI
Dipartimento di Scienze Fisiche, Università di Napoli Federico II
and I.N.F.N., Sezione di Napoli
Complesso Universitario di Monte Sant'Angelo, Via Cintia,
80126 Napoli, Italy

The observation of CP violation effects is becoming more and more significant in a variety of channels, due to the impressive experimental effort of the last years. We review recent progress in B_s^0 semileptonic decays and in B_s^0 decays into CP eigenstates.

1 Introduction

There are well known differences between the B_s^0 and the B^0 system. The mixing parameter $x_s \equiv \Delta m_s/\Gamma_s$ is about 30 times larger than x_d, and the mass and width difference are sizable. Another important difference is that the CP violating mixing phase probes the angle β_s in the unitarity triangle, which is about two order of magnitudes smaller than β in the Standard Model, and hence negligibly small. Any large variation due to new physics can produce observable effects, and that alone would be enough to motivate the study of CP violation in the B_s^0 system. We will review a few decays where the observation of CP violation effects has recently become accessible and significant, due to the impressive experimental effort of the last years.

1.1 Flavour-specific decays

The mass eigenstates can be written in terms of the flavour eigenstates

$$|B_{s,H}>= p\,|B_s^0> +q\,|\bar{B}_s^0> \qquad\qquad |B_{s,L}>= p\,|B_s^0> -q\,|\bar{B}_s^0> \tag{1}$$

where $|p|^2 + |q|^2 = 1$, by normalization condition. Evidence for CP violation in B_s^0 mixing has been searched for, with flavor-specific decays, in samples where the initial flavor state is tagged. Flavour-specific final states are states which, due to some selection rule, can be reached directly only by B_s^0 and not by $\bar{B}_s^0$ or conversely. CP violation in the interference of mixing and decay clearly cannot occur, as only one of the two flavour eigenstates can feed the final state. Instead, CP violation in the mixing and in the decay are both possible. However, in some cases, the decay is dominated by a single amplitude, and/or there are no different strong scattering phases as required to observe CP violation in the decay. In that case, when the final state tag is also available, we can write the following asymmetry

$$a_{fs}^s = \frac{\Gamma(\bar{B}_s^0(t) \to f) - \Gamma(B_s^0(t) \to \bar{f})}{\Gamma(\bar{B}_s^0(t) \to f) + \Gamma(B_s^0(t) \to \bar{f})} = \frac{1 - |q/p|^4}{1 + |q/p|^4} \tag{2}$$

testing the "wrong" final state, accessible only through mixing. The asymmetry a_{fs} measures CP violation in mixing and it is independent from time and from the final state (to within a sign), as it can be ascribed to a property of the decaying states. In the Standard Model, one expects $|\Gamma_{12}/M_{12}| \sim m_b^2/m_t^2 \sim 10^{-3} \ll 1$. At lowest order in $|\Gamma_{12}/M_{12}|$, we have

$$\left|\frac{q}{p}\right|^2 = 1 - a \qquad\qquad a \equiv \mathrm{Im}\left(\frac{\Gamma_{12}}{M_{12}}\right) = \frac{\Delta\Gamma_s}{\Delta m_s}\tan\phi_s \tag{3}$$

where $\phi_s \equiv \arg\left(-M_{12}/\Gamma_{12}\right)$, $\Delta m_s \equiv m_H - m_L = 2|M_{12}|$ and $\Delta\Gamma_s = \Gamma_L - \Gamma_H = 2|\Gamma_{12}|\cos\phi_s$. Notice that the symbol ϕ_s is overloaded, since in literature it is also used for the mixing phase induced by M_{12} only. Whatever the definition, the CP violating phase can be related to β_s, that is $\beta_s \equiv \arg\left[-V_{tb}^\star V_{ts}/V_{cb}^\star V_{cs}\right]$ in the Standard Model, since the dispersive term M_{12} is mainly driven by box diagrams involving virtual top quarks and the absorptive term Γ_{12} is dominated by on-shell charmed intermediate states. An additional phase, e. g. $\beta_s(SM) \to \beta_s(SM) + \tilde{\beta}_s$, it is often used to parameterize effects of new physics or non-leading hadronic contributions.

The phase $\phi_s \neq 0, \pi$ implies $|q/p| \neq 1$. The parameter a, that is small irrespective of the value of ϕ_s, implies small CP violation in the mixing. At lowest order $a \simeq a_{fs}^s$, and the measured value of a_{fs}^s can be translated into a constraint for both $\Delta\Gamma_s$ and ϕ_s. In the case of semileptonic decays, when the final state contains also a charged meson, a_{fs}^s is called semileptonic charge asymmetry. It has been directly measured by the experiment DØ via the decay $B_s^0 \to D_s^- \mu^+ X$ [1]

$$a_{sl}^s = \left[-1.7 \pm 9.1(\mathrm{stat})^{+1.2}_{-2.3}(\mathrm{syst})\right] \times 10^{-3} \tag{4}$$

A related observable is the (like-sign) dimuon charge asymmetry $\mathcal{A}_{sl}^b$, which is the difference in the number of events with a pair of positive muons minus the number with a pair of negative muons divided by the sum. Since it arises from the meson mixing, if there is not a separation of the asymmetry due to B^0 and B_s^0, $\mathcal{A}_{sl}^b$ can be written as

$$\mathcal{A}_{sl}^b = C_d a_{sl}^d + C_s a_{sl}^s \tag{5}$$

where the coefficients depend on mean mixing probability and the production rates of B^0 and B_s^0 mesons. Here a_{sl}^d is the semileptonic charge asymmetry in the B^0 system, which has been measured since 2001 at e^+e^- machines; the actual averaged value is $a_{sl}^d = 0.0105 \pm 0.0064$ [2]. In 2010 the experiment DØ, with $6\,\mathrm{fb}^{-1}$ of data, showed evidence for anomalous $\mathcal{A}_{sl}^b$, deviating 3.2σ from the SM [3]. The 2011 DØ update at $9\,\mathrm{fb}^{-1}$ shows again a deviation, at $3.9\,\sigma$ [4], from the Standard Model value [5]

$$\mathcal{A}_{sl}^b = \left[-0.787 \pm 0.172(\mathrm{stat}) \pm 0.093(\mathrm{syst})\right]\% \qquad\qquad \mathcal{A}_{sl}^b(\mathrm{SM}) = (-0.028^{+0.005}_{-0.006})\% \tag{6}$$

The extracted value for a_{sl}^s is in agreement with the direct determination, but improved precision or, even better, independent measurements of semileptonic asymmetries are needed to establish evidence of CP violation due to new physics. The latter could come from the LHCb experiment, which has the potential for measurements of $B^0 \to D^\pm \mu^\mp \nu$ and $B_s^0 \to D_s^\pm \mu^\mp \nu$ asymmetries.

1.2 Decays into CP eigenstates

The values of $\Delta\Gamma_s$ and ϕ_s obtained by the semileptonic charge asymmetries have to be compared with independent measurements from other channels. Particularly interesting are the so-called golden modes, which are defined as decays where the final state is a CP eigenstate and where all contributing Feynman diagrams carry the same CP violating phase. That ensures the absence of CP violation in the decays, which is often plagued by large hadronic uncertainties in the theoretical estimates. Neglecting also the small CP violation in the mixing, golden modes exhibit interference CP violation only. A well studied process is the $B_s \to J/\psi\phi$ decay, whose final state is an admixture of different CP eigenstates, which can be disentangled through an angular analysis of the $J/\psi(\to l^+l^-)\,\phi(\to K^+K^-)$ decay products. This decay tests directly the $B_s^0 - \bar{B}_s^0$ mixing phase, that is $\phi_M = -2\beta_s$ in the Standard Model. In this channel, the actual world's most precise measurement of ϕ_M comes from the LHCb experiment at about 1 fb^{-1} of pp collisions and it is in good agreement with Standard Model predictions [6]. The conflict between the DØ measurement of $\mathcal{A}_{sl}^b$ and the newest LHCb data does not appear to be theoretically solvable with the addition of a new phase $\tilde{\phi}_M$, originated by new physics contributions to M_{12}, but it seems to require non-standard additions to Γ_{12} as well [7].

A recent player, first observed in 2011 by the LHCb [8] and Belle experiments [9], is the $B_s^0 \to J/\psi f_0(980)$ decay. Data have been reported for $B_s^0 \to J/\psi f_0(980)$ with $f_0(980) \to \pi^+\pi^-$, which is the dominant channel. LHCb has not measured the branching ratio directly, but instead its fraction, $R_{f_0/\phi}$, with respect to the branching ratio for $B_s^0 \to J/\psi\phi$ with $\phi \to K^+K^-$. The same ratio has been measured afterwards by the DØ [10] and CDF [11] collaborations. All these results are in general agreement and point to a fraction $R_{f_0/\phi}$ between about 1/5 and 1/3. The disadvantage of a smaller branching ratio is compensated by the fact that the $B_s^0 \to J/\psi f_0(980)$ channel, unlike the $B_s^0 \to J/\psi\phi$ one, does not require a time-dependent angular analisys. Indeed, because the $f_0(980)$ is a scalar state with quantum numbers $J^{PC} = 0^{++}$, the final state of $B_s^0 \to J/\psi f_0(980)$ is a p-wave state with the CP eigenvalue -1.

In addition to the branching ratio result, the CDF collaboration has reported a first measurement for the effective $B_s^0 \to J/\psi f_0(980)$ lifetime [11], and the LHCb collaboration has presented a first analysis of CP violation in $B_s^0 \to J/\psi f_0(980)$ [12]. Experimental investigations are still progressing, leading towards more and more precise measurements of relevant observables. It should be noted that the composition of the scalar $f_0(980)$ as a conventional $\bar{q}q$ meson is still under debate as of today, since alternative interpretations, e.g. as a tetraquark or a molecular state, are deemed possible. The dominant contributions to the amplitude of $B_s^0 \to J/\psi f_0$ is given by the color-suppressed tree diagram $b \to c\bar{c}s$, where $f_0(980)$ is originated by the couple $\bar{s}s$. Penguin and exchange diagrams give additional contributions, that add to hadronic uncertainties. The details of the composition of $f_0(980)$ affect the amplitudes, introducing additional topologies [13]. It becomes important to look for observables that are quite robust with respect to hadronic effects and thereby allow searching for a large (i.e. non-standard) CP violating mixing phase. It has been demonstrated [13] that useful candidates in that respect are the effective lifetime of $B_s^0 \to J/\psi f_0(980)$ and the CP violating observable S. The effective lifetime is defined as

$$\tau_{J/\psi f_0} \equiv \frac{\int_0^\infty t\,\langle\Gamma(B_s(t) \to J/\psi f_0(980))\rangle\,dt}{\int_0^\infty \langle\Gamma(B_s(t) \to J/\psi f_0(980))\rangle\,dt}. \tag{7}$$

and it can be written in terms of $y_s \equiv \Delta\Gamma_s/2\Gamma_s$, which in turn depends on the mixing phase. One can investigate the dependence on the hadronic uncertainties, finding a robust behavior under a generous range of the parameters describing contributions from topologies different than the tree diagram [13]. The dominant uncertainty comes from the theoretical error on $\Delta\Gamma_s$ in the Standard Model.

A tagged analysis, from which we can distinguish between initially present B_s^0 or $\bar{B}_s^0$ mesons, allows to measure the time-dependent, CP-violating rate asymmetry

$$\frac{\Gamma(B_s(t) \to J/\psi f_0(980)) - \Gamma(\bar{B}_s(t) \to J/\psi f_0(980))}{\Gamma(B_s(t) \to J/\psi f_0(980)) + \Gamma(\bar{B}_s(t) \to J/\psi f_0(980))} = \frac{C\cos(\Delta M_s t) - S\sin(\Delta M_s t)}{\cosh(\Delta\Gamma_s t/2) + \mathcal{A}_{\Delta\Gamma}\sinh(\Delta\Gamma_s t/2)}, \tag{8}$$

where the "mixing-induced" CP-violating observable S

$$S \equiv \frac{-2\,\mathrm{Im}\,\lambda_{J/\psi f_0}}{1 + |\lambda_{J/\psi f_0}|^2} \qquad \lambda_{J/\psi f_0} \equiv \frac{q}{p}\,\frac{A(\bar{B}_s^0 \to J/\psi f_0(980))}{A(B_s^0 \to J/\psi f_0(980))} \tag{9}$$

originates from interference between B_s^0–$\bar{B}_s^0$ mixing and decay processes, and depends on the mixing phase. The Standard Model prediction gives[13] $S(B_s^0 \to J/\psi f_0(980))|_{\rm SM} \in [-0.086, -0.012]$, and a measurement of a sizably different $|S|$ would give us unambiguous evidence for new physics. Still, should its value fall into the range $-0.1 \lesssim S \lesssim 0$, the Standard Model effects related to the hadronic parameters would preclude conclusions on the presence or absence of CP violating new physics contributions to B_s^0 mixing. It should be noted that the decay $B^0 \to J/\psi f_0(980)$, which has not yet been observed, may be used to obtain insights into the size of such hadronic parameters. The leading contributions of the $B^0 \to J/\psi f_0(980)$ decay emerge from the $d\bar{d}$ component of the $f_0(980)$. Its estimated branching ratio with $f_0(980) \to \pi^+\pi^-$ is at the few times 10^{-6} level[13], which is not outside the reach of future experimental data taking.

New terrain for exploring CP violation is provided by the $B_{(s)}^0 \to J/\psi\eta^{(\prime)}$ decays. The only data come from the Belle Collaboration, that this year has given the measured values for branching fractions (of order $\sim 10^{-4}$) with 121.4 fb^{-1} of data at the $\Upsilon(5S)$ resonance[14], following the first observation for $B_s^0 \to J/\psi\eta$ and the first evidence for $B_s^0 \to J/\psi\eta'$ in 2009[15]. As before, CP violation can be investigated analyzing the effective lifetimes and mixing-induced CP asymmetries. As far as the latter are concerned, measured values within the range $0.03 \lesssim S_{J/\psi\eta^{(\prime)}} \lesssim 0.09$ would not allow us to distinguish CP violating new physics contributions to B_s^0–$\bar{B}_s^0$ mixing from Standard Model effects, unless we can control the hadronic Standard Model corrections. This can be accomplished by using e.g. the $B^0 \to J/\psi\eta^{(\prime)}$ as a control channel and the $SU(3)_{\rm F}$ flavour symmetry. Very recently Belle has analyzed the branching fractions of $B^0 \to J/\psi\eta^{(\prime)}$ decays with the complete Belle data sample of 772×10^6 $B\bar{B}$ events collected at the $\Upsilon(4S)$ resonance[16]. Only an upper limit is obtained for $B^0 \to J/\psi\eta'$, while the branching fractions of $B^0 \to J/\psi\eta$ is measured to be of order $O(10^{-6})$, in agreement with theoretical predictions[17]. The most prominent $\eta^{(\prime)}$ decays involve photons or neutral pions in the final states, which is a very challenging signature for B-decay experiments at hadron colliders and appears well suited for the future e^+e^- SuperKEKB and SuperB projects.

References

1. V. M. Abazov *et al* [DØ Collaboration], *Phys. Rev.* D **82**, 012003 (2010) [Erratum-ibid. D **83** 119901 (2011)].
2. D. Asner *et al* , *Averages of b-hadron, c-hadron, and tau-lepton Properties*, arXiv:1010.1589 and online update at http://www.slac.stanford.edu/xorg/hfag.
3. V. M. Abazov *et al* [DØ Collaboration], *Phys. Rev. Lett.* **105**, 081801 (2010).
4. V. M. Abazov *et al* [DØ Collaboration], *Phys. Rev.* D **84**, 052007 (2011).
5. A. Lenz and U. Nierste, *J. High Energy Phys.* **0706**, 072 (2007).
6. R. Aaij *et al* [LHCb Collaboration], *Phys. Rev. Lett.* **108**, 101803 (2012); ; updated in LHCb-CONF-2012-002.
7. A. Lenz *et al*, arXiv:1203.0238 [hep-ph].
8. R. Aaij *et al* [LHCb Collaboration], *Phys. Lett.* B **698**, 115 (2011).
9. J. Li *et al* [Belle Collaboration], *Phys. Rev. Lett.* **106**, 121802 (2011).
10. V. M. Abazov *et al.* [DØ Collaboration], *Phys. Rev.* D **85**, 011103 (2012).
11. T. Aaltonen *et al* [CDF Collaboration], *Phys. Rev.* D **84**, 052012 (2011).
12. R. Aaij *et al* [LHCb Collaboration], *Phys. Lett.* B **707**, 497 (2012).
13. R. Fleischer, R. Knegjens and G. Ricciardi, *Eur. Phys. J. C* **71** 1832 (2011).
14. J. Li *et al* [Belle Collaboration], arXiv:1202.0103 [hep-ex].
15. I. Adachi *et al* [Belle Collaboration], BELLE-CONF-0902, arXiv:0912.1434 [hep-ex].
16. M. C. Chang *et al*, arXiv:1203.3399 [hep-ex].
17. R. Fleischer, R. Knegjens and G. Ricciardi, *Eur. Phys. J.* C **71**, 1798 (2011).

DIRECT CP VIOLATION IN D-MESON DECAYS

JOACHIM BROD

Department of Physics, University of Cincinnati, Cincinnati, OH 45221, USA

Recently, the LHCb and CDF collaborations reported a surprisingly large difference between the direct CP asymmetries, $\Delta\mathcal{A}_{CP}$, in the $D^0 \to K^+K^-$ and $D^0 \to \pi^+\pi^-$ decay modes. An interesting question is whether this measurement can be explained within the standard model. In this review, I would like to convey two messages: First, large penguin contractions can plausibly account for this measurement and lead to a consistent picture, also explaining the difference between the decay rates of the two modes. Second, "new physics" contributions are by no means excluded; viable models exist and can possibly be tested.

1 Introduction

The $D^0 \to K^+K^-$ and $D^0 \to \pi^+\pi^-$ decays are induced by the weak interaction via an exchange of a virtual W boson and suppressed by a single power of the Cabibbo angle. Direct CP violation in singly Cabibbo-suppressed (SCS) D-meson decays is sensitive to contributions of new physics in the up-quark sector, since it is expected to be small in the standard model: the penguin amplitudes necessary for interference are down by a loop factor and small Cabibbo-Kobayashi-Maskawa (CKM) matrix elements, and there is no heavy virtual top quark which could provide substantial breaking of the Glashow-Iliopoulos-Maiani (GIM) mechanism. Naively, one would thus expect effects of order $\mathcal{O}([V_{cb}V_{ub}/V_{cs}V_{us}]\alpha_s/\pi) \sim 0.01\%$.

We define the amplitudes for final state f as

$$\begin{aligned} A_f &\equiv A(D \to f) = A_f^T\left[1 + r_f e^{i(\delta_f - \phi_f)}\right], \\ \overline{A}_f &\equiv A(\bar{D} \to f) = A_f^T\left[1 + r_f e^{i(\delta_f + \phi_f)}\right]. \end{aligned} \tag{1}$$

Here A_f^T is the dominant tree amplitude and r_f the relative magnitude of the subleading amplitude, carrying the weak phase ϕ_f and the strong phase δ_f. We can now define the direct CP asymmetry as

$$\mathcal{A}_f^{\mathrm{dir}} \equiv \frac{|A_f|^2 - |\bar{A}_f|^2}{|A_f|^2 + |\bar{A}_f|^2} = 2r_f \sin\gamma \sin\delta_f\,, \tag{2}$$

where the last equality holds up to corrections of $\mathcal{O}(r_f^2)$. LHCb and CDF measure a time-integrated CP asymmetry. The approximately universal contribution of indirect CP violation cancels to good approximation in the difference

$$\Delta\mathcal{A}_{CP} = \mathcal{A}_{CP}(D \to K^+K^-) - \mathcal{A}_{CP}(D \to \pi^+\pi^-)\,. \tag{3}$$

The measurements of LHCb, $\Delta\mathcal{A}_{CP} = (-0.82 \pm 0.21 \pm 0.11)\%$ [1], CDF, $\Delta\mathcal{A}_{CP} = (-0.62 \pm 0.21 \pm 0.10)\%$ [2], and inclusion of the indirect CP asymmetry A_Γ [5,6], lead to the new world average (including the Babar [3], Belle [4], and CDF [7] measurements) $\Delta\mathcal{A}_{CP} = (-0.67 \pm 0.16)\%$ [2]. In the following, we will try to answer three questions: Can this measurement be accounted for by the standard model? Can it be new physics? Can we distinguish the two possibilities?

2 Setting the stage

As a first step, we take the size of the tree amplitudes A^T from data and then relate the tree amplitudes to the penguin amplitudes A^P to estimate the size of the latter [8]. The starting point of our analysis is the weak effective Hamiltonian

$$\begin{aligned} H_{\rm eff}^{\rm SCS} = \frac{G_F}{\sqrt{2}} \Bigg\{ & (V_{cs}V_{us}^* - V_{cd}V_{ud}^*) \sum_{i=1,2} C_i \left(Q_i^{\bar{s}s} - Q_i^{\bar{d}d} \right) /2 \\ & - V_{cb}V_{ub}^* \left[\sum_{i=1,2} C_i \left(Q_i^{\bar{s}s} + Q_i^{\bar{d}d} \right) /2 + \sum_{i=3}^{6} C_i Q_i + C_{8g} Q_{8g} \right] \Bigg\} + \text{h.c.}\,. \end{aligned} \tag{4}$$

The Wilson coefficients of the tree operators $Q_1^{\bar{p}p'} = (\bar{p}u)_{V-A} \otimes (\bar{c}p')_{V-A}$, $Q_2^{\bar{p}p'} = (\bar{p}_\alpha u_\beta)_{V-A} \otimes (\bar{c}_\beta p'_\alpha)_{V-A}$, the penguin operators $Q_{3\ldots6}$, and the chromomagnetic operator Q_{8g}, can be calculated in perturbation theory. The hadronic matrix elements are harder to compute; we will estimate their size using experimental data. They receive leading power contributions and power corrections in $1/m_c$, which are expected to be large.

A leading power estimation, using naive factorization and $\mathcal{O}(\alpha_s)$ corrections, yields for the ratio $r_f^{\rm LP} \equiv |A_f^P(\text{leading power})/A_f^T(\text{experiment})|$: $r_{K^+K^-}^{\rm LP} \approx (0.01 - 0.02)\%$, $r_{\pi^+\pi^-}^{\rm LP} \approx (0.015 - 0.028)\%$. This is consistent with, yet slightly larger than the naive scaling estimate. We expect the signs of $\mathcal{A}_{K^+K^-}^{\rm dir}$ and $\mathcal{A}_{\pi^+\pi^-}^{\rm dir}$ to be opposite, if $SU(3)$ breaking is not too large; so for $\phi_f = \gamma \approx 67^\circ$ and $\mathcal{O}(1)$ strong phases we obtain $\Delta\mathcal{A}_{CP}(\text{leading power}) = \mathcal{O}(0.1\%)$, an order of magnitude smaller than the measurement.

However, we know from $SU(3)$ fits [9,10,11,12,13] that power corrections can be large. To be specific, we look at insertions of the penguin operators Q_4, Q_6 into power-suppressed annihilation amplitudes. The associated penguin contractions of Q_1 cancel the scale and scheme dependence. Estimating their size using the loop functions G, defined in [15], and using naive N_c counting to relate the penguin to the tree amplitudes, we arrive at $r_{f,1}^{\rm PC} \approx (0.04 - 0.08)\%$, $r_{f,2}^{\rm PC} \approx (0.03 - 0.04)\%$, where $r_{f,i}^{\rm PC} \equiv |A_f^P(\text{power correction})/A_f^T(\text{experiment})|$ and the subscripts $1, 2$ correspond to the insertions of Q_4, Q_6, respectively. Again assuming $\mathcal{O}(1)$ strong phases, this leads to $\Delta\mathcal{A}_{CP}(r_{f,1}) = \mathcal{O}(0.3\%)$ and $\Delta\mathcal{A}_{CP}(r_{f,2}) = \mathcal{O}(0.2\%)$ for the two insertions. Thus, a standard model explanation seems plausible.

Of course, the extraction of the annihilation amplitudes from data, neglected contributions to the annihilation amplitudes, N_c counting, the modeling of the penguin contraction amplitudes, and the neglected additional penguin contractions lead to an uncertainty of a factor of a few. So, can we trust the estimate?

3 A consistent picture

Another interesting observation is the large difference of SCS branching ratios, $\text{Br}(D^0 \to K^+K^-) \approx 2.8 \times \text{Br}(D^0 \to \pi^+\pi^-)$. It implies that the ratio of amplitudes (normalized to phase space) is $A(D^0 \to K^+K^-) \approx 1.8 \times A(D^0 \to \pi^+\pi^-)$, whereas they would be equal in the $SU(3)$ limit. This has often been interpreted as a sign of large $SU(3)$ breaking. On the other hand, the ratio of the Cabibbo-favored (CF) to the doubly Cabibbo-suppressed (DCS) amplitude is $A(D^0 \to K^-\pi^+) \approx 1.15 \times A(D^0 \to K^+\pi^-)$, after accounting for CKM factors, in accordance with nominal $SU(3)$ breaking of $\mathcal{O}(20\%)$.

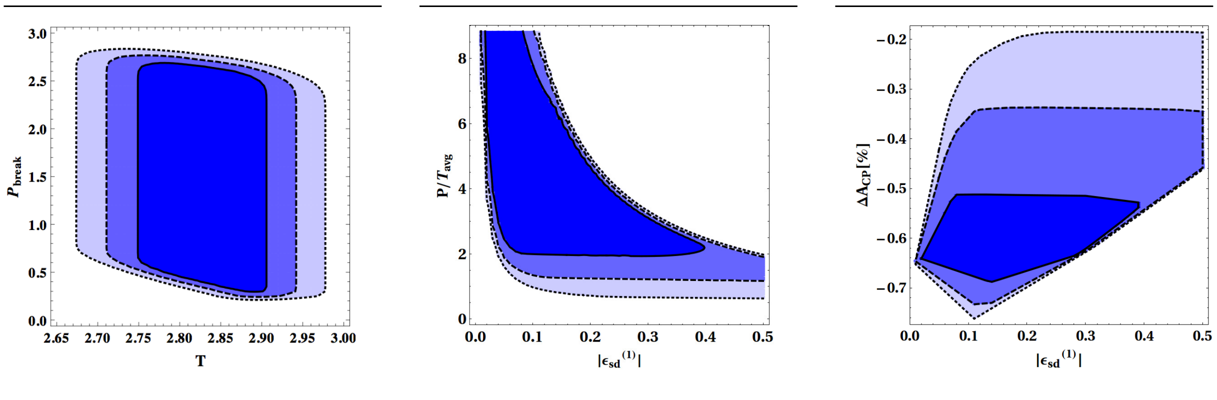

Figure 1: The results of our fit. Solid, dashed, and dotted lines denote one-, two-, and three-sigma contours, respectively. Left panel: A fit to the branching ratios only yields $P_{\rm break} \equiv \epsilon_{sd}^{(1)} P \sim T$, assuming nominal U-spin breaking. T is the tree amplitude. The lower bound of $P/T_{\rm avg}$ in the middle panel is directly related to the large difference of decay rates for the SCS modes. ($T_{\rm avg}$ is the average value of T from the fit). It translates into the upper bound on $\Delta\mathcal{A}_{CP}$ – the fit results can naturally accommodate the measured value (right panel).

A glance at the effective Hamiltonian (4) shows that the combination P of penguin contractions of $Q_{1,2}^{\bar{s}s}$ and $Q_{1,2}^{\bar{d}d}$ proportional to $V_{cb}V_{ub}^*$ is U-spin invariant, while $P_{\rm break}$, the combination contributing to the tree amplitude vanishes in the U-spin limit. $P_{\rm break}$ contributes with opposite sign to the two SCS decay rates, and P gives rise to a nonvanishing $\Delta\mathcal{A}_{CP}$. Guided by the considerations exposed in Section 2, we perform a U-spin decomposition of the amplitudes to all four (CF, SCS, DCS) decays, and fit these amplitudes to the data (branching ratios and CP asymmetries) under the additional assumption that penguin contractions are large, of order $\mathcal{O}(1/\epsilon)$, where $\epsilon \ll 1$.

Our main point is [14] that under the assumption of nominal U-spin breaking, a broken penguin $P_{\rm break}$ which explains the difference of the $D^0 \to K^+K^-$ and $D^0 \to \pi^+\pi^-$ decay rates implies a $\Delta U = 0$ penguin P that naturally[a] yields the observed $\Delta\mathcal{A}_{CP}$. The scaling $P_{\rm break} \sim \epsilon_U P$ together with our fit result $P_{\rm break} \sim T/2$ (see Fig. 1) yields the estimate

$$r_{\pi^+\pi^-,K^+K^-} \simeq \left|\frac{V_{cb}V_{ub}}{V_{cs}V_{us}}\right| \cdot \left|\frac{P}{T \pm P_{\rm break}}\right| \sim \frac{|V_{cb}V_{ub}|}{|V_{cs}V_{us}|}\frac{1}{2\,\epsilon_U} \sim 0.2\%, \tag{5}$$

for $\epsilon_U \sim 0.2$. This is consistent with the measured $\Delta\mathcal{A}_{CP}$ for $\mathcal{O}(1)$ strong phases. Some results of our fit are shown in Figure 1.

By the same reasoning, exchanging the spectator quark we expect direct CP asymmetries of the same order ($\approx 0.5\%$) in the decay modes $D^+ \to K^+\overline{K^0}$, $D_s^+ \to \pi^+K^0$.

4 Can it be new physics?

Whereas a standard-model explanation seems plausible, it is not excluded that new physics contributes partly to $\Delta\mathcal{A}_{CP}$. Any new-physics explanation has to respect constraints from other observables like D- and K-meson mixing, or direct searches, but substantial contributions are still possible [16,17]. Can we discriminate them from the standard-model contributions?

Models of new physics that have $\Delta I = 3/2$ contributions could be separated from the standard-model background (an example would be a scalar color-singlet weak doublet [18]). To see this, note that the standard-model tree operators have both $\Delta I = 1/2$ and $\Delta I = 3/2$ contributions, while the standard-model penguin operators are pure $\Delta I = 1/2$ (apart from neglegible electroweak contributions). For instance, the $I = 2$ final state in $D^+ \to \pi^+\pi^0$ cannot

[a] An important side remark is that no fine tuning of strong phases is required [14].

be reached by standard-model penguin operators, so any observed direct CP asymmetry in this decay would be a clear signal of new physics. More sophisticated isospin sum rules can be constructed [19].

If new physics induces only $\Delta I = 1/2$ transitions, it seems necessary to build explicit models and look for their collider signatures. The most plausible models include chirally enhanced chromomagnetic penguin operators [20,21].

5 Conclusion

Large penguin contractions in the standard model can naturally explain both the large difference of decay rates in the $D^0 \to K^+K^-$ and $D^0 \to \pi^+\pi^-$ modes and the observed $\Delta\mathcal{A}_{CP}$. However, new-physics contributions are not excluded. Viable models exist and can possibly tested.

Acknowledgments

I thank Yuval Grossman, Alexander Kagan, and Jure Zupan for the pleasant and fruitful collaboration, the organizers of "Recontres de Moriond" for the invitation to this inspiring conference, Emmanuel Stamou for proofreading the manuscript, and the NFS for travel support. The work of J. B. is supported by DOE grant FG02-84-ER40153.

References

1. R. Aaij *et al.* [LHCb Collaboration], arXiv:1112.0938 [hep-ex].
2. A. Di Canto, talk at XXVI Rencontres de Physique de la Vallee d'Aoste Feb 26th-Mar 3rd 2012, La Thuile, Italy; CDF Note 10784.
3. B. Aubert *et al.* [BaBar Collaboration], Phys. Rev. Lett. **100**, 061803 (2008)
4. M. Staric *et al.* [Belle Collaboration], Phys. Lett. B **670**, 190 (2008)
5. B. Aubert *et al.* [BABAR Collaboration], Phys. Rev. D **78**, 011105 (2008)
6. M. Staric *et al.* [Belle Collaboration], Phys. Rev. Lett. **98**, 211803 (2007)
7. T. Aaltonen *et al.* [CDF Collaboration], Phys. Rev. D **85**, 012009 (2012)
8. J. Brod, A. L. Kagan and J. Zupan, arXiv:1111.5000 [hep-ph].
9. H. Y. Cheng and C. W. Chiang, Phys. Rev. D **81** (2010) 074021 [arXiv:1001.0987 [hep-ph]].
10. D. Pirtskhalava and P. Uttayarat, arXiv:1112.5451 [hep-ph].
11. H. Y. Cheng and C. W. Chiang, arXiv:1201.0785 [hep-ph].
12. B. Bhattacharya, M. Gronau and J. L. Rosner, arXiv:1201.2351 [hep-ph].
13. T. Feldmann, S. Nandi and A. Soni, arXiv:1202.3795 [hep-ph].
14. J. Brod, Y. Grossman, A. L. Kagan and J. Zupan, arXiv:1203.6659 [hep-ph].
15. M. Beneke, G. Buchalla, M. Neubert and C. T. Sachrajda, Nucl. Phys. B **606**, 245 (2001)
16. G. Isidori, J. F. Kamenik, Z. Ligeti and G. Perez, Phys. Lett. B **711**, 46 (2012)
17. W. Altmannshofer, R. Primulando, C. -T. Yu and F. Yu, JHEP **1204**, 049 (2012)
18. Y. Hochberg and Y. Nir, arXiv:1112.5268 [hep-ph].
19. Y. Grossman, A. L. Kagan and J. Zupan, arXiv:1204.3557 [hep-ph].
20. Y. Grossman, A. L. Kagan and Y. Nir, Phys. Rev. D **75**, 036008 (2007)
21. G. F. Giudice, G. Isidori and P. Paradisi, JHEP **1204**, 060 (2012)

RARE BEAUTY AND CHARM DECAYS AT LHCB

C. PARKINSON, on behalf of the LHCb collaboration
Imperial College London, South Kensington Campus, London SW7 2AZ, England

New results are presented using a data sample with an integrated luminosity of $\sim 1\,\mathrm{fb}^{-1}$ collected in 2011 with the LHCb detector. The $B \to \mu^+\mu^-$ and $D^0 \to \mu^+\mu^-$ results have been presented at a previous conference. The angular distributions and (partial) branching fractions of selected radiative penguin decays are studied using a data sample with an integrated luminosity of $\sim 1\,\mathrm{fb}^{-1}$ collected in 2011 with the LHCb detector. The partial branching fraction and theoretically clean observables of the decay $B^0 \to K^{*0}\mu^+\mu^-$ have been extracted as a function of the dimuon invariant mass. The partial branching fraction of the decay $B_s^0 \to \phi\mu^+\mu^-$ has also been extracted as a function of the dimuon invariant mass. The branching fraction and first observation of the decay $B^+ \to \pi^+\mu^+\mu^-$ is reported. New limits were set on the decay $B \to \mu^+\mu^-\mu^+\mu^-$. Improved limits on the decays $B \to \mu^+\mu^-$ and $D^0 \to \mu^+\mu^-$ are also presented.

1 Introduction

In the Standard Model (SM), B and D mesons can decay via Flavour-Changing Neutral Current (FCNC) processes mediated by loop diagrams. Competing diagrams involving New Physics (NP) phenomena may significantly affect the total amplitude and the Lorentz structure of the decay. These properties may be accessed through measurement of the branching fraction $\mathcal{B}$ or through an angular analysis. New results are presented using a data sample with an integrated luminosity of $\sim 1\,\mathrm{fb}^{-1}$ collected in 2011 with the LHCb detector.

The presented results comprise: the worlds most precise measurement of angular observables in $B^0 \to K^{*0}\mu^+\mu^-$, including the worlds first measurement of q_0^2 [1]; the worlds best measurements of the $B^0 \to K^{*0}\mu^+\mu^-$ [1] and $B_s^0 \to \phi\mu^+\mu^-$ [2] partial branching fractions; the worlds first measurement of the $B^+ \to \pi^+\mu^+\mu^-$ total branching fraction [3]; the worlds first limits on $B \to \mu^+\mu^-\mu^+\mu^-$ [4] and the worlds best limits on $B \to \mu^+\mu^-$ [5] and $D^0 \to \mu^+\mu^-$ [6].

2 The angular analysis of $B^0 \to K^{*0}\mu^+\mu^-$

The angular distribution of the decay $B^0 \to K^{*0}\mu^+\mu^-$ may be parameterised by 6 complex amplitudes. These may be combined to form theoretically clean and experimentally accessible angular observables; F_{L}, the fraction of K^{*0} longitudinal polarisation; A_{FB}, the forward-backward asymmetry of the dimuon system; $S_3 = A_{\mathrm{T}}^2(1 - F_{\mathrm{L}})/2$, where A_{T}^2 is the asymmetry in the K^{*0} transverse polarisation [7 8]; A_{IM}, a T-odd CP asymmetry. These observables allow separation between the SM and a variety of NP models. The results of this analysis and the SM theory prediction [9] are shown in Fig. 1 [1]. No significant deviation from the SM theory prediction is observed.

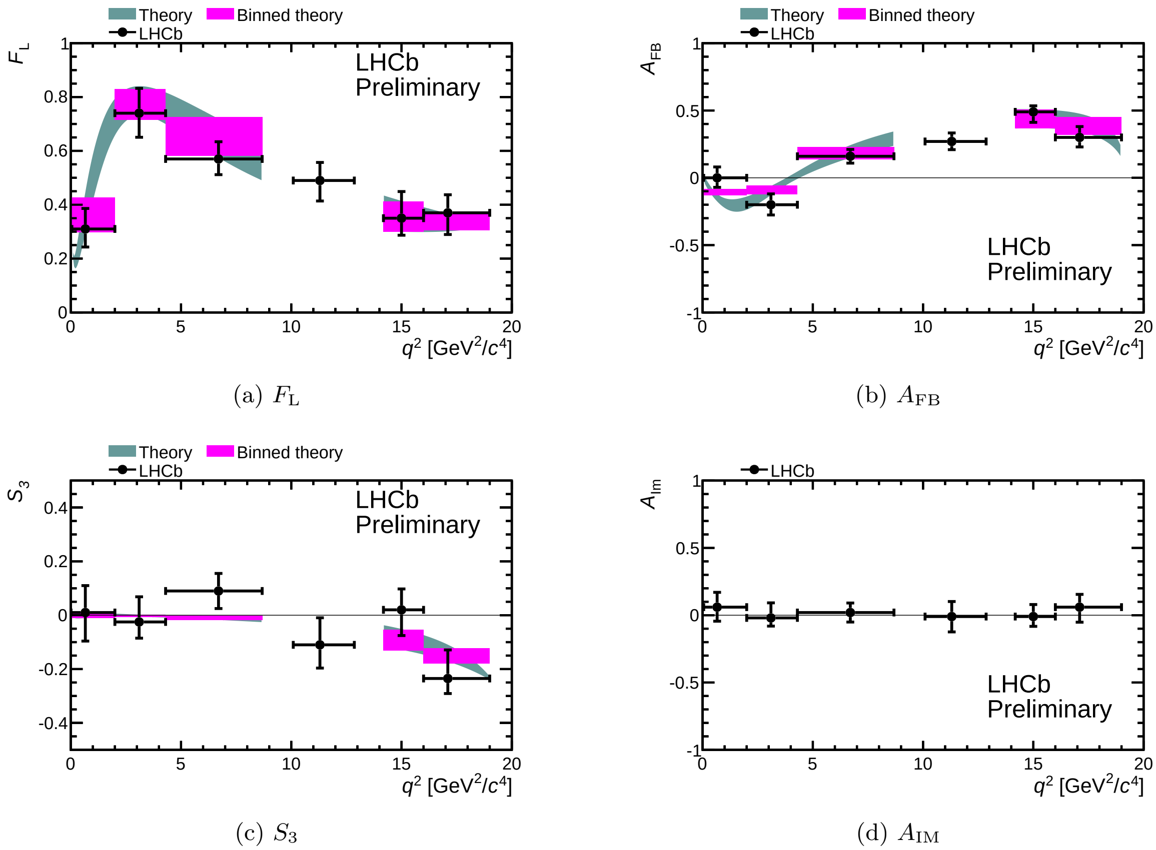

(a) F_{L} (b) A_{FB} (c) S_3 (d) A_{IM}

Figure 1: $B^0 \to K^{*0}\mu^+\mu^-$ angular analysis results. Black points are results of a fit to the data sample. The error bars include both statistical and systematic uncertainties. The SM theory prediction is shown as a continuous band (grey) and binned according to the experimental binning scheme (pink) [9]. In (d) the SM theory prediction is close to zero. No significant deviation from the SM theory prediction is observed.

In the SM, the A_{FB} observable changes sign at a well defined point in q^2 that is largely free from form-factor uncertainties. This zero-crossing point q_0^2 was measured to be $q_0^2 = 4.9^{+1.1}_{-1.3}$ GeV$^2/c^4$ [1]. This is consistent with a the available SM theoretical predictions [9,10,11].

3 Branching fraction of $b \to \{s,d\}\mu^+\mu^-$ decays

3.1 *Partial Branching Fraction of the Decays $B^0 \to K^{*0}\mu^+\mu^-$ and $B_s^0 \to \phi\mu^+\mu^-$*

The $B^0 \to K^{*0}\mu^+\mu^-$ partial branching fraction measurement and SM theory prediction [9] is presented in Fig. 2b [1]. No significant deviation from the SM prediction is observed.

The theoretical estimate for the $B_s^0 \to \phi\mu^+\mu^-$ branching fraction is 1.61×10^{-6} [12]. The total branching fraction was extracted by normalising to $B_s^0 \to J/\psi\,\phi$ events, and was measured to be $(0.78 \pm 0.10(\mathrm{stat}) \pm 0.06(\mathrm{syst}) \pm 0.28(\mathcal{B})) \times 10^{-6}$, where the third error is due to the uncertainty on $\mathcal{B}(B_s^0 \to J/\psi\,\phi)$. The $B_s^0 \to \phi\mu^+\mu^-$ partial branching fraction is presented in Fig. 2a [2]. No significant deviation from the SM prediction is observed.

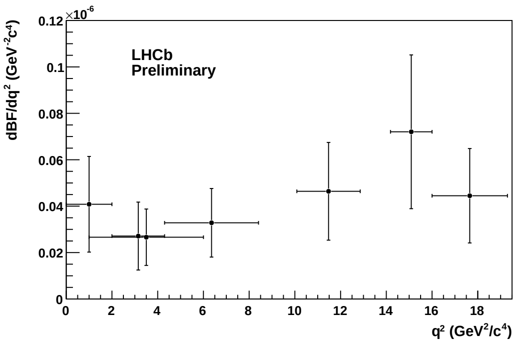

(a)

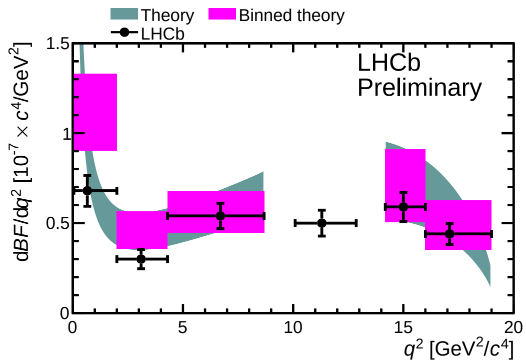

(b)

Figure 2: Results of the $B_s^0 \to \phi\mu^+\mu^-$ (a) and $B^0 \to K^{*0}\mu^+\mu^-$ (b) partial branching fraction measurements. The error bars include both statistical and systematic uncertainties. In (b), the SM theory prediction is shown as a continuous band (grey) and binned according to the experimental binning scheme (pink). No significant deviation from the SM theory prediction is observed.

3.2 Total brancing fraction of the decay $B^+ \to \pi^+\mu^+\mu^-$

Unlike $b \to s\ell^+\ell^-$ transitions, no $b \to d\ell^+\ell^-$ has previously been observed. In the SM $B^+ \to \pi^+\mu^+\mu^-$ decays are suppressed with respect to $B^+ \to K^+\mu^+\mu^-$ decays by a factor of ~ 25, from the ratio of the CKM elements $|V_{td}|/|V_{ts}|$. The theoretical estimate for the total branching fraction in the SM is $(1.96 \pm 0.21) \times 10^{-8}$ [13]. The distribution of $B^+ \to \pi^+\mu^+\mu^-$ candidates observed in data is presented in Fig. 3. The measured branching fraction is $2.4 \pm 0.6\,(\text{stat}) \pm 0.2\,(\text{syst})) \times 10^{-8}$. This is consistent with the SM theory prediction and is the first observation of the $B^+ \to \pi^+\mu^+\mu^-$ decay; the rarest B decay ever observed [3].

4 Branching fraction of purely leptonic B^0 and D^0 decays

4.1 New limits on the decay $B \to \mu^+\mu^-\mu^+\mu^-$

The dominant contribution for a B meson decaying to a four muon final state comes from the decay $B_s^0 \to J/\psi\,\phi$ with both the J/ψ and ϕ decaying into two muons. The branching fraction estimate for this process is $(2.3 \pm 0.9) \times 10^{-8}$ [14]. The combined branching fraction from other sources is expected to be $< 10^{-10}$ [15, 16]. This can be significantly enhanced in NP models through FCNC processes mediated by new particles that decay into $\mu^+\mu^-$ pairs. The distribution of $B \to \mu^+\mu^-\mu^+\mu^-$ candidates observed in data, after J/ψ and ϕ vetoes are applied, is presented in Fig. 4. The observed events are consistent with the expectation from background. A branching fraction limit was set at $< 5.4 \times 10^{-9}$ and $< 1.3 \times 10^{-8}$ at 95% C.L. for the B^0 and B_s^0 mode respectively [4]. These limits are consistent with the SM theory predictions.

4.2 Improved limits on the decay $B \to \mu^+\mu^-$ and $D^0 \to \mu^+\mu^-$

The decays of B mesons to muon pair final states are highly suppressed in the SM. Theoretical predictions for the branching fractions for $B \to \mu^+\mu^-$ decays are $(3.2 \pm 0.2) \times 10^{-9}$ [17] and $(0.10 \pm 0.01) \times 10^{-9}$ [18] for the B_s^0 and B^0 decays respectively. Improved branching fraction limits were set at $< 4.5 \times 10^{-9}$ and 1.03×10^{-9} at 95% C.L. respectively [5]. These limits are consistent with the SM theory predictions.

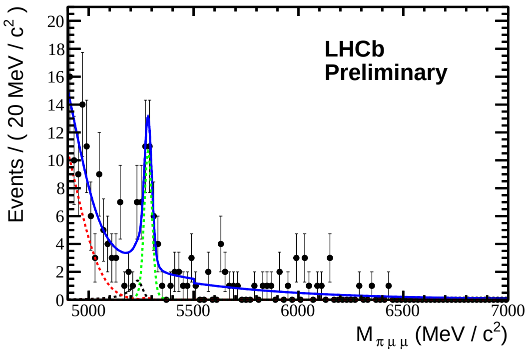

Figure 3: The $\pi^+\mu^+\mu^-$ invariant mass distribution of $B^+ \to \pi^+\mu^+\mu^-$ candidates in the data. The fitted shape (solid blue) comprises signal (green dash), background (red dash) and $B^+ \to K^+\mu^+\mu^-$ (black dash) components.

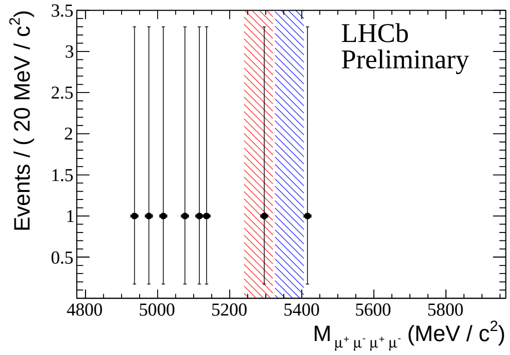

Figure 4: The $\mu^+\mu^-\mu^+\mu^-$ invariant mass distribution of $B \to \mu^+\mu^-\mu^+\mu^-$ candidates in the data. The B^0 (red striped) and B_s^0 (blue striped) search regions are indicated.

The branching fraction of the $D^0 \to \mu^+\mu^-$ is dominated by long distance contributions; the SM theory prediction has an upper limit of 6×10^{-11} at 90% C.L. [19]. The best experimental limit was previously set by BELLE at $< 1.4 \times 10^{-7}$ at 90% C.L. [20]. Improved experimental limits were set at $< 1.3 \times 10^{-8}$ at 95% C.L. using $\sim 0.9\,\text{fb}^{-1}$ of integrated luminosity. This is consistent with the SM theory prediction and improves the current world best limit by more than an order of magnitude.

References

1. LHCb Collaboration, CERN-LHCb-CONF-2012-008 (2012).
2. LHCb Collaboration, CERN-LHCb-CONF-2012-003 (2012).
3. LHCb Collaboration, CERN-LHCb-CONF-2012-006 (2012).
4. LHCb Collaboration, CERN-LHCb-CONF-2012-010 (2012).
5. LHCb Collaboration, CERN-PH-EP-2012-072 (2012).
6. LHCb Collaboration, CERN-LHCb-CONF-2012-005 (2012).
7. F. Kruger *et al*, Phys. Rev. **D71**, 094009 (2005).
8. W. Altmannshofer *et al*, JHEP **01**, 019 (2009).
9. C. Bobeth *et al*, JHEP **07**, 067 (2011).
10. M. Beneke *et al*, Eur. Phys. J. **C41**, 173-188 (2005).
11. A. Ali *et al*, Eur. Phys. J. **C47**, 625-641 (2006).
12. C.Q. Geng *et al*, J. Phys. G **G29**, 1103-1118 (2003).
13. S. Hai-Zhen *et al*, Commun. Theor. Phys. **50**, 696 (2008).
14. K. Nakamura et al. (Particle Data Group), J. Phys. G **37**, 075021 (2010).
15. D. Melikhov *et al*, Phys. Rev. **D70**, 114028 (2004).
16. D. Melikhov *et al*, Phys. At. Nucl. **68**, 1842 (2005).
17. A. J. Buras *et al*, JHEP **10**, 009 (2010).
18. A. J. Buras, Acta Phys. Polon. **B41**, 2487-2561 (2010).
19. G. Buchalla *et al*, Rev. Mod. Phys. **68**, 1125-1144 (1996).
20. BELLE Collaboration, Phys. Rev. **D81**, 091102 (2010).

Direct and indirect searches for New Physics

F. Mahmoudi
CERN Theory Division, Physics Department, CH-1211 Geneva 23, Switzerland

Clermont Université, Université Blaise Pascal, CNRS/IN2P3, LPC, BP 10448, 63000 Clermont-Ferrand, France

An overview of the indirect constraints from flavour physics on supersymmetric models is presented. We study in particular constraints from $B_s \to \mu^+\mu^-$ and $B \to K^*\mu^+\mu^-$, emphasising on the new LHCb results. We show that these rare transitions provide valuable information in the search for new physics and are complementary to the direct searches.

1 Introduction

In addition to direct searches for new physics signals, indirect searches play an important and complementary role in the quest for physics beyond the Standard Model (SM). The most commonly used indirect constraints originate from flavour physics observables, cosmological data and dark matter relic density, electroweak precision tests and anomalous magnetic moment of the muon. Precise experimental measurements and theoretical predictions have been achieved for the B meson systems in the past decade and stringent constraints due to sizeable new physics contributions to many observables can be obtained [1]. In the following, we present an overview of the most constraining flavour physics observables for supersymmetry (SUSY), with an emphasis on the recent LHCb results. The latest limit on $\mathrm{BR}(B_s \to \mu^+\mu^-)$, being very close to the SM prediction, constrains strongly the large $\tan\beta$ regime and the various angular observables from $B \to K^*\mu^+\mu^-$ decay can provide complementary information in particular for intermediate $\tan\beta$ values. We highlight here some of the implications for several SUSY scenarios and show that these indirect constraints can be superior to those which are derived from direct searches for SUSY particles in some regions of the parameter space.

2 Flavour observables

2.1 Framework

The effective Hamiltonian describing the $b \to s$ transitions has the following generic structure:

$$\mathcal{H}_{\rm eff} = -\frac{4G_F}{\sqrt{2}} V_{tb} V_{ts}^* \Big(\sum_{i=1\cdots 10} \big(C_i(\mu) O_i(\mu) + C_i'(\mu) O_i'(\mu) \big) \Big) , \tag{1}$$

where $O_i(\mu)$ are the relevant operators and $C_i(\mu)$ the corresponding Wilson coefficients evaluated at the scale μ which encode short-distance physics. The primed operators are chirality flipped compared to the non-primed operators, and they are highly suppressed in the SM. Contributions from physics beyond the SM to the observables can be described by the modification of Wilson coefficients or by the addition of new operators. The most relevant operators in rare radiative, semileptonic and leptonic B decays are:

$$
\begin{aligned}
O_1 &= (\bar{s}\gamma_\mu T^a P_L c)(\bar{c}\gamma^\mu T^a P_L b) \;, & O_2 &= (\bar{s}\gamma_\mu P_L c)(\bar{c}\gamma^\mu P_L b) \;, \\
O_3 &= (\bar{s}\gamma_\mu P_L b)\sum_q(\bar{q}\gamma^\mu q) \;, & O_4 &= (\bar{s}\gamma_\mu T^a P_L b)\sum_q(\bar{q}\gamma^\mu T^a q) \;, \\
O_5 &= (\bar{s}\gamma_{\mu_1}\gamma_{\mu_2}\gamma_{\mu_3} P_L b)\sum_q(\bar{q}\gamma^{\mu_1}\gamma^{\mu_2}\gamma^{\mu_3} q) \;, & O_6 &= (\bar{s}\gamma_{\mu_1}\gamma_{\mu_2}\gamma_{\mu_3} T^a P_L b)\sum_q(\bar{q}\gamma^{\mu_1}\gamma^{\mu_2}\gamma^{\mu_3} T^a q) \;, \\
O_7 &= \frac{e}{(4\pi)^2} m_b(\bar{s}\sigma^{\mu\nu} P_R b) F_{\mu\nu} \;, & O_8 &= \frac{g}{(4\pi)^2} m_b(\bar{s}\sigma^{\mu\nu} T^a P_R b) G^a_{\mu\nu} \;, \\
O_9 &= \frac{e^2}{(4\pi)^2}(\bar{s}\gamma^\mu P_L b)(\bar{\ell}\gamma_\mu \ell) \;, & O_{10} &= \frac{e^2}{(4\pi)^2}(\bar{s}\gamma^\mu P_L b)(\bar{\ell}\gamma_\mu\gamma_5 \ell) \;, \\
Q_1 &= \frac{e^2}{(4\pi)^2}(\bar{s} P_R b)(\bar{\ell}\,\ell) \;, & Q_2 &= \frac{e^2}{(4\pi)^2}(\bar{s} P_R b)(\bar{\ell}\gamma_5 \ell) \;,
\end{aligned}
\tag{2}
$$

where Q_1 and Q_2 are the scalar and pseudo-scalar operators arising in new physics scenarios.

The Wilson coefficients $C_i(\mu)$ are calculated at scale $\mu \sim \mathcal{O}(M_W)$ by requiring matching between the effective and full theories. They can be expanded perturbatively:

$$C_i(\mu) = C_i^{(0)}(\mu) + \frac{\alpha_s(\mu)}{4\pi} C_i^{(1)}(\mu) + \cdots \tag{3}$$

and are subsequently evolved to scale $\mu \sim \mathcal{O}(m_b)$ at which they can be used to calculate the flavour observables, using the renormalisation group equations:

$$\mu \frac{d}{d\mu} C_i(\mu) = C_j(\mu)\gamma_{ji}(\mu) \tag{4}$$

driven by the anomalous dimension matrix $\hat{\gamma}(\mu)$:

$$\hat{\gamma}(\mu) = \frac{\alpha_s(\mu)}{4\pi}\hat{\gamma}^{(0)} + \frac{\alpha_s^2(\mu)}{(4\pi)^2}\hat{\gamma}^{(1)} + \cdots \tag{5}$$

which are known to high accuracy. A review on effective methods is given in [2] and the analytical expressions for the Wilson coefficients and the renormalisation group equations can be found in [3].

2.2 Observables

The rare decays $B_s \to \mu^+\mu^-$ and $B \to K^*\mu^+\mu^-$ deserve special attention as new results have been recently announced by the LHCb collaboration using an integrated luminosity of 1 fb^{-1}. In particular, a stringent 95% C.L. limit on the branching ratio $\mathrm{BR}(B_s \to \mu^+\mu^-) < 4.5 \times 10^{-9}$ has been obtained [4]. In terms of Wilson coefficients, this branching ratio is expressed as [3,5]:

$$
\begin{aligned}
\mathrm{BR}(B_s \to \mu^+\mu^-) \;&=\; \frac{G_F^2\alpha^2}{64\pi^2} f_{B_s}^2 m_{B_s}^3 |V_{tb}V_{ts}^*|^2 \tau_{B_s}\sqrt{1-\frac{4m_\mu^2}{m_{B_s}^2}} \\
&\times \left\{\left(1-\frac{4m_\mu^2}{m_{B_s}^2}\right)|C_{Q_1}-C'_{Q_1}|^2 + \left|(C_{Q_2}-C'_{Q_2}) + 2(C_{10}-C'_{10})\frac{m_\mu}{m_{B_s}}\right|^2\right\} .
\end{aligned}
\tag{6}
$$

In the Standard Model, only C_{10} is non-vanishing and gets its largest contributions from Z penguin and box diagrams. With the input parameters of [6] we obtain $\mathrm{BR}(B_s \to \mu^+\mu^-)_{SM} =$

Observable	SM prediction	Experiment
$10^7\mathrm{GeV}^2 \times \langle dBR/dq^2\ (B \to K^*\mu^+\mu^-)\rangle_{[1,6]}$	0.47 ± 0.27	$0.42 \pm 0.04 \pm 0.04$
$\langle A_{FB}(B \to K^*\mu^+\mu^-)\rangle_{[1,6]}$	-0.06 ± 0.05	$-0.18^{+0.06+0.01}_{-0.06-0.01}$
$\langle F_L(B \to K^*\mu^+\mu^-)\rangle_{[1,6]}$	0.71 ± 0.13	$0.66^{+0.06+0.04}_{-0.06-0.03}$
$q_0^2(B \to K^*\mu^+\mu^-)/\mathrm{GeV}^2$	$4.26^{+0.36}_{-0.34}$	$4.9^{+1.1}_{-1.3}$

Table 1: SM predictions and experimental values of $B \to K^*\mu^+\mu^-$ observables [6].

$(3.53 \pm 0.38) \times 10^{-9}$. The latest experimental limit thus severely restricts the room for new physics.

The decay $B \to K^*\mu^+\mu^-$ on the other hand provides a variety of complementary observables as it gives access to angular distributions in addition to the differential branching fraction. The differential decay distribution of the $\bar{B}^0 \to \bar{K}^*(\to K^-\pi^+)\mu^+\mu^-$ decay can be written as a function of three angles θ_l, θ_{K^*}, ϕ and the invariant dilepton mass squared (q^2) [7,8]:

$$d^4\Gamma = \frac{9}{32\pi} J(q^2, \theta_l, \theta_{K^*}, \phi)\, dq^2\, d\cos\theta_l\, d\cos\theta_{K^*}\, d\phi\ . \tag{7}$$

The angular dependence of $J(q^2, \theta_l, \theta_{K^*}, \phi)$ are then expanded in terms of the angular coefficients J_i which are functions of q^2 and can be described in terms of the transversity amplitudes and form factors [9,10]. Integrating Eq. 7 over all angles, the dilepton mass distribution is obtained in terms of the angular coefficients [8,11]:

$$\frac{d\Gamma}{dq^2} = \frac{3}{4}\left(J_1 - \frac{J_2}{3}\right)\ . \tag{8}$$

The forward-backward asymmetry A_{FB}, which benefits from reduced theoretical uncertainty, is defined as:

$$A_{\mathrm{FB}}(q^2) \equiv \left[\int_{-1}^{0} - \int_{0}^{1}\right] d\cos\theta_l\, \frac{d^2\Gamma}{dq^2\, d\cos\theta_l} \Bigg/ \frac{d\Gamma}{dq^2} = -\frac{3}{8} J_6 \Bigg/ \frac{d\Gamma}{dq^2}\ . \tag{9}$$

Another clean observable is the zero–crossing of the forward-backward asymmetry (q_0^2) for which the form factors cancel out at leading order. q_0^2 depends on the relative sign of C_7 and C_9 and its measurement allow to remove the sign ambiguity.

The longitudinal polarisation fraction F_L can also be constructed as the ratio of the transversity amplitudes and contains less theoretical uncertainty from the form factors. It reads:

$$F_L(s) = \frac{-J_2^c}{d\Gamma/dq^2}\ . \tag{10}$$

The SM predictions and experimental values for these observables are given in Table 1.

Another observable which is rather independent of hadronic input parameters is the isospin asymmetry which arises from the annihilation diagrams and depends on the charge of the spectator quark. The isospin asymmetry is defined as [12]

$$\frac{dA_I}{dq^2} = \frac{d\Gamma[B^0 \to K^{*0}\mu^+\mu^-]/dq^2 - d\Gamma[B^\pm \to K^{*\pm}\mu^+\mu^-]/dq^2}{d\Gamma[B^0 \to K^{*0}\mu^+\mu^-]/dq^2 + d\Gamma[B^\pm \to K^{*\pm}\mu^+\mu^-]/dq^2}\ . \tag{11}$$

In the SM, dA_I/dq^2 is at the percent level.

The decay $B \to K^*\mu^+\mu^-$ gives access to many other observables such as transverse amplitudes, which are not yet measured but could be of interest in the near future.

In addition to the above observables, $B \to X_s\gamma$, $B \to \tau\nu$, $B \to D\tau\nu_\tau$, $B \to X_s\mu^+\mu^-$ and $D_s \to \tau\nu_\tau$ are also very sensitive to SUSY as discussed in [1].

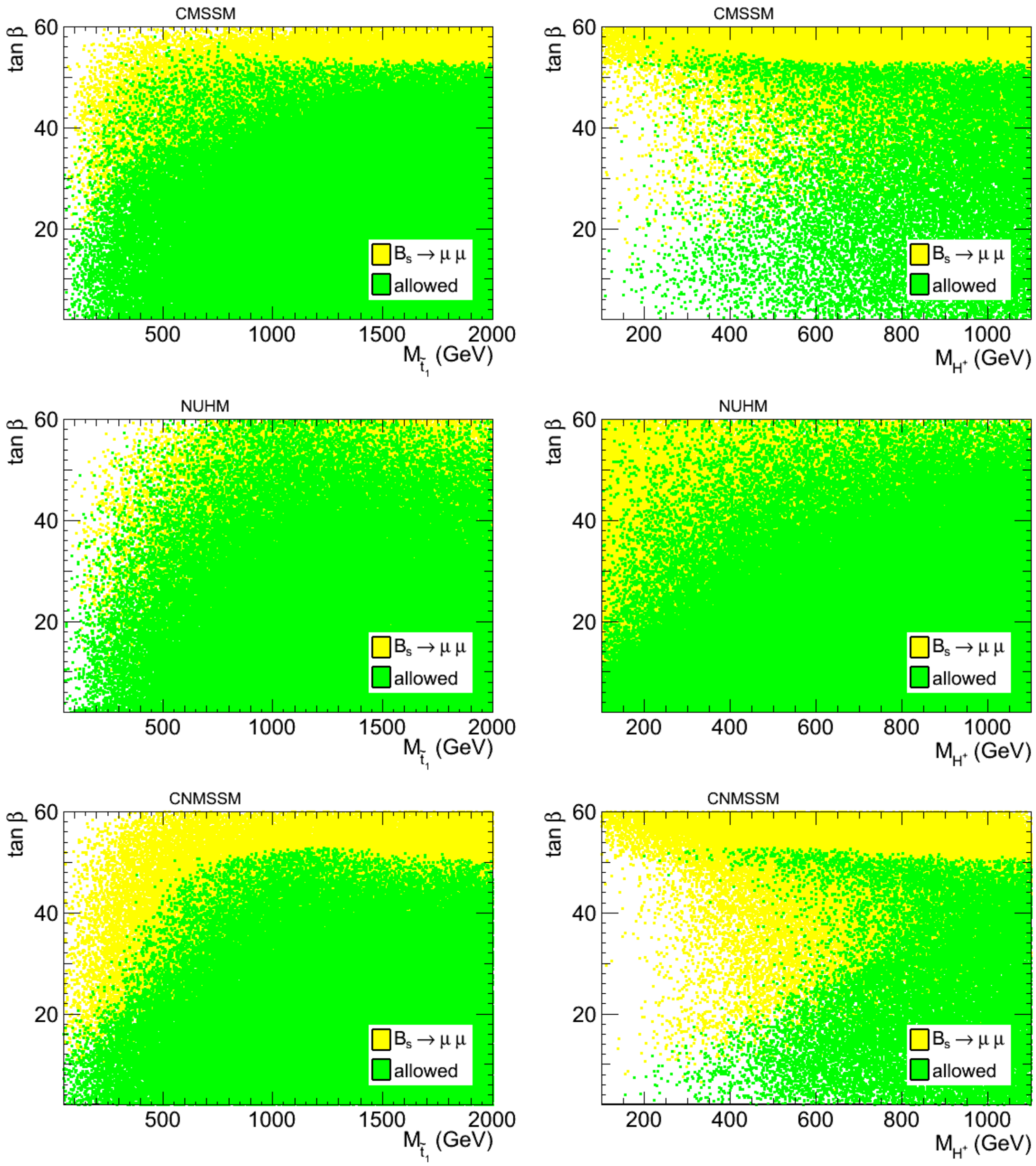

Figure 1: Constraints from BR($B_s \to \mu^+\mu^-$) in the CMSSM (upper panel), NUHM (central panel) and CNMSSM (lower panel) in the plane ($M_{\tilde{t}_1}$, $\tan\beta$) in the left and ($M_{H^\pm}$, $\tan\beta$) in the right, with the allowed points displayed in the foreground.

3 Implications for supersymmetry

To illustrate the impact of the flavour observables and in particular $B_s \to \mu^+\mu^-$ and $B \to K^*\mu^+\mu^-$, we consider several MSSM scenarios, and compare the resulting constraints to the direct search limits.

First we study the constraints from BR($B_s \to \mu^+\mu^-$) in the CMSSM, NUHM and CNMSSM by scanning over the relevant parameters as described in [6,13]. For each generated point we calculate the spectrum of SUSY particle masses and couplings using SOFTSUSY [14] or NMSSMTOOLS [15] and compute flavour observables using SuperIso v3.3 [3,16].

The constraints are shown in Fig. 1 in the planes ($M_{\tilde{t}_1}$, $\tan\beta$) and ($M_{H^\pm}$, $\tan\beta$). The region most probed by $B_s \to \mu^+\mu^-$ is at large $\tan\beta$ and small $M_{\tilde{t}_1}$ / $M_{H^\pm}$ as can be seen from the

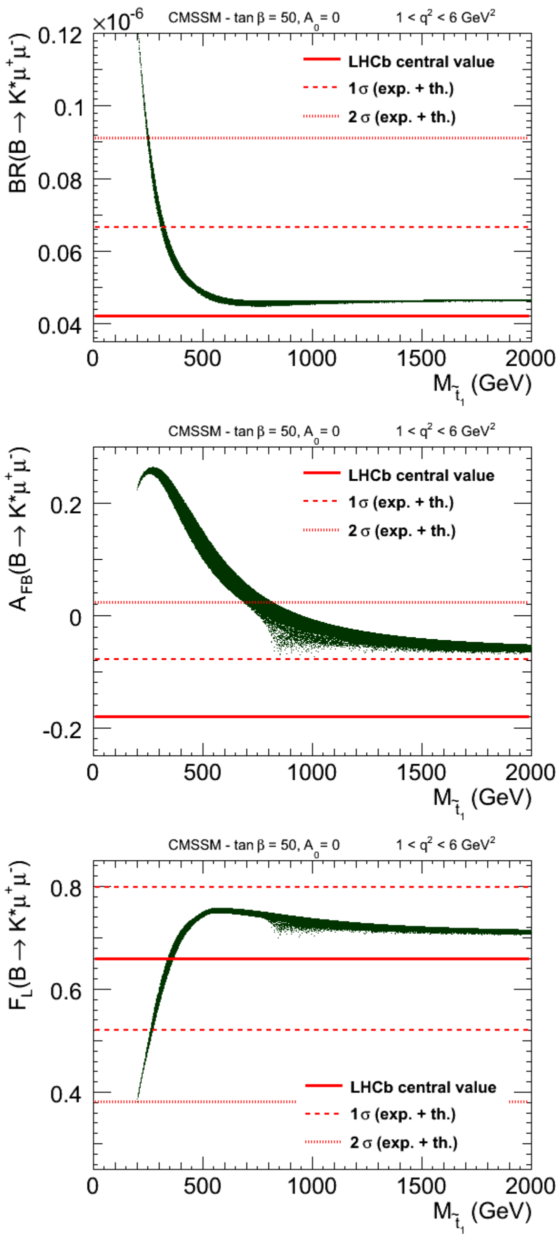

Figure 2: SUSY spread of the averaged BR($B \to K^*\mu^+\mu^-$) at low q^2 (top left), at high q^2 (top right), $A_{FB}(B \to K^*\mu^+\mu^-)$ at low q^2 (middle left), zero-crossing of $A_{FB}(B \to K^*\mu^+\mu^-)$ (middle right), $F_L(B \to K^*\mu^+\mu^-)$ at low q^2 (bottom left) and $A_I(B \to K^*\mu^+\mu^-)$ at low q^2 (bottom right), as a function of the lightest stop mass, in the CMSSM with $\tan\beta$=50 and $A_0 = 0$.

figures. Since there are two additional degrees of freedom in NUHM as compared to CMSSM, it is easier for a model point to escape the limits and the constraints are therefore weaker in NUHM. In the CNMSSM, the $B_s \to \mu^+\mu^-$ constraint is similar to the CMSSM case, but slightly stronger.

Next we consider the constraints from $B \to K^*\mu^+\mu^-$ observables. In order to study the maximal effects we consider $\tan\beta$=50 and investigate the SUSY spread as a function of the lightest stop mass. The results are displayed in Fig. 2 for the averaged differential branching ratio at low and high q^2, the forward-backward asymmetry A_{FB}, the zero-crossing q_0^2 of A_{FB}, the longitudinal polarisation F_L and the isospin asymmetry A_I. The solid red lines correspond to the LHCb central value, while the dashed and dotted lines represent the 1 and 2σ bounds

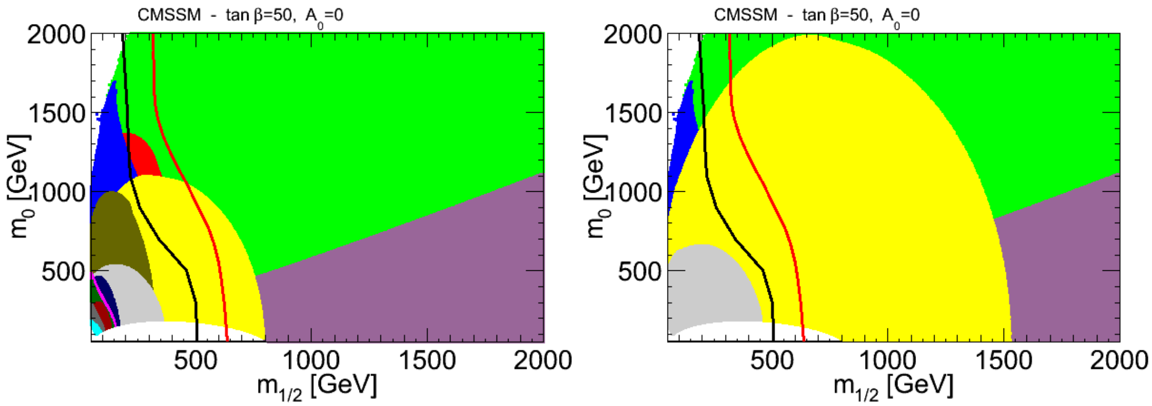

Figure 3: Constraints from flavour observables in CMSSM in the plane $(m_{1/2}, m_0)$ for $\tan\beta = 50$ and $A_0 = 0$, in the left with the 2010 results for $\mathrm{BR}(B_s \to \mu^+\mu^-)$, and in the right with the 2011 results. The black line corresponds to the CMS exclusion limit with 1.1 fb^{-1} of data [18] and the red line to the CMS exclusion limit with 4.4 fb^{-1} of data [19] . The colour legend is given below.

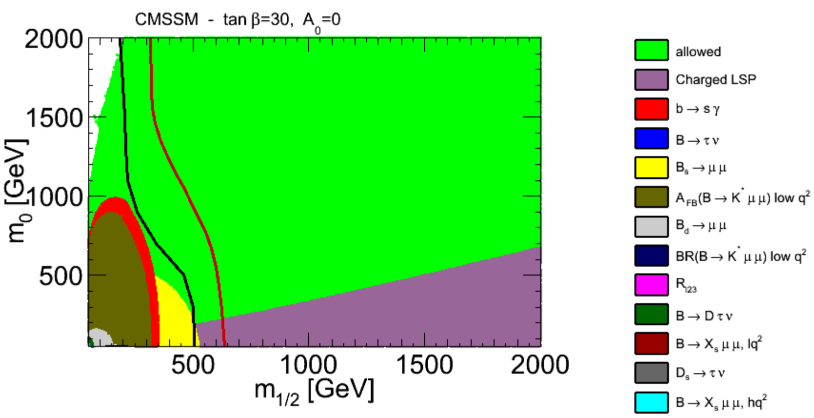

Figure 4: Constraints from flavour observables in CMSSM in the plane $(m_{1/2}, m_0)$ for $\tan\beta = 30$ and $A_0 = 0$.

respectively, including both theoretical and experimental errors (added in quadrature). As can be seen from the figure, A_{FB} is the most constraining observable and excludes $M_{\tilde{t}_1} \lesssim 800$ GeV. On the other hand, with the current experimental accuracy [17], the isospin asymmetry does not provide any information on the SUSY parameters.

A comparison between different flavour observables in the plane $(m_{1/2}, m_0)$ is given in Fig. 3, where we can also see the limits from $B \to X_s\gamma$, $B \to \tau\nu$, $R_{l23}(K \to \mu\nu_\mu)$, $B \to D\tau\nu_\tau$, $B \to X_s\mu^+\mu^-$ and $D_s \to \tau\nu_\tau$. In the left hand side, the combined CMS+LHCb limit from the 2010 data (1.1×10^{-8} at 95% C.L.) is applied for $\mathrm{BR}(B_s \to \mu^+\mu^-)$, while this limit is updated to the 2011 LHCb result (4.5×10^{-9} at 95% C.L.) in the right hand side. As can be seen, the recent LHCb limit strongly constrains the CMSSM with large $\tan\beta$. We also notice that, at large $\tan\beta$, the flavour constraints and in particular $B_s \to \mu^+\mu^-$, are superior to those from direct searches. By lowering the value of $\tan\beta$, $B_s \to \mu^+\mu^-$ significantly loses importance compared to direct searches as can be seen in Fig. 4. On the other hand, $B \to X_s\gamma$ and $B \to K^*\mu^+\mu^-$ related observables and in particular the forward-backward asymmetry lose sensitivity in a less drastic manner and they could play a complementary role in the intermediate $\tan\beta$ regime.

The study in constrained MSSM scenarios is very illustrative and allows to pin down the most important effects in a rather simple framework. However these scenarios are not representative of the full MSSM and by focussing only on the constrained scenarios one may miss some

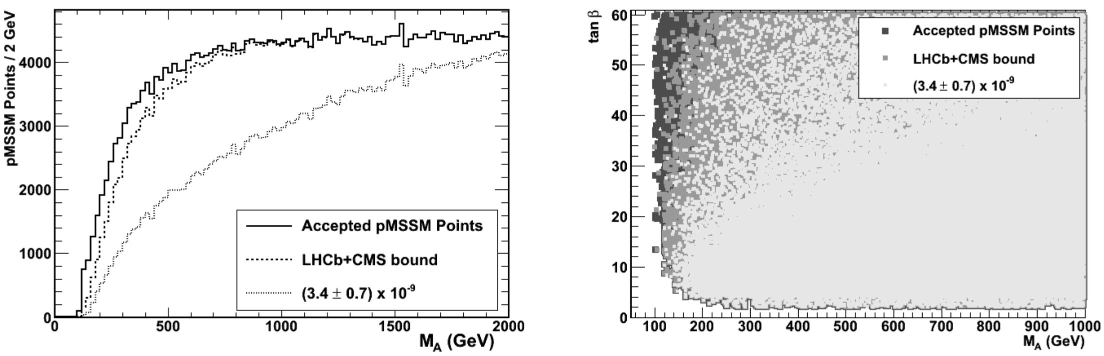

Figure 5: Distribution of pMSSM points after the $B_s \to \mu^+\mu^-$ constraint projected on the M_A (left) and $(M_A, \tan\beta)$ plane (right) for all accepted pMSSM points (medium grey), points not excluded by the combination of the 2010 LHCb and CMS analyses (dark grey) and the projection for the points compatible with the measurement of the SM expected branching fractions with a 20% total uncertainty (light grey) [21].

important features. Also the constrained scenarios are already very much squeezed, while this is not the case in more general scenarios. To go beyond the constrained scenarios, we consider the phenomenological MSSM (pMSSM) [20]. This model is the most general CP and R–parity conserving MSSM, assuming MFV at the weak scale and the absence of FCNCs at the tree level. It contains 19 free parameters: 10 sfermion masses, 3 gaugino masses, 3 trilinear couplings and 3 Higgs masses. To study the pMSSM, we perform flat scans over the parameters as described in [21,22]. The left panel of Fig. 5 shows the density of points in function of M_A before and after applying the combined 2010 LHCb and CMS limit for $B_s \to \mu^+\mu^-$, as well as the projection for an SM–like measurement with an overall 20% theoretical and experimental uncertainty. As can be seen the density of the allowed pMSSM points is reduced by a factor of 3, in the case of an SM–like measurement. The right panel shows the same distribution in the (M_A, $\tan\beta$) plane. The region with large $\tan\beta$ and small M_A is the most affected one.

4 SuperIso program

SuperIso [3,16] is a public C program dedicated mainly to the calculation of flavour physics observables. The calculations are done in various models, such as SM, 2HDM, MSSM and NMSSM with minimal flavour violation. A broad set of flavour physics observables is implemented in SuperIso. This includes the branching ratio of $B \to X_s\gamma$, isospin asymmetry of $B \to K^*\gamma$, branching ratios of $B_s \to \mu^+\mu^-$, $B_d \to \mu^+\mu^-$, $B_u \to \tau\nu_\tau$, $B \to D\tau\nu_\tau$, $K \to \mu\nu_\mu$, $D \to \mu\nu_\mu$, $D_s \to \tau\nu_\tau$ and $D_s \to \mu\nu_\mu$. In addition several observables related to $b \to s\ell^+\ell^-$ transitions, such as branching ratios of $B \to X_s\mu^+\mu^-$ and $B \to K^*\mu^+\mu^-$, the forward backward asymmetries, the zero-crossings, polarisation fractions of K^*, isospin asymmetries, transverse amplitudes, the CP averaged angular coefficients, etc..., have also been included.

The calculation of the anomalous magnetic moment of the muon is also implemented in the program. SuperIso uses a SUSY Les Houches Accord (SLHA) file [23] as input, which can be either generated automatically by the program via a call to a spectrum generator or provided by the user. The program is able to perform the calculations automatically for different SUSY breaking scenarios. An extension of SuperIso including the relic density calculation, SuperIso Relic, is also available publicly [24]. Finally, in SuperIso we make use of the Flavour Les Houches Accord (FLHA) [25], the newly developed standard for flavour related quantities.

5 Conclusions

Indirect constraints and in particular those from flavour physics are essential to restrict the new physics parameters as we have seen here. The information obtained from these low energy observables combined with the collider data opens the door to a very rich phenomenology and would help us to step forward toward a deeper understanding of the underlying physics. It is clear that with more precise measurements of flavour observables a large part of the supersymmetric parameter space could be disfavoured. In particular large $\tan\beta$ region is strongly affected by $B_s \to \mu^+\mu^-$. Also, a measurement of $\mathrm{BR}(B_s \to \mu^+\mu^-)$ lower than the Standard Model prediction would rule out a large variety of supersymmetric models. In addition, $B \to K^*\mu^+\mu^-$ observables play a complementary role specially for smaller $\tan\beta$ values. With reduced theoretical and experimental errors, the exclusion bounds in Fig. 2 for example would squeeze leading to important consequences for SUSY parameters. The $B \to K^*\mu^+\mu^-$ decay provides many other clean observables, not yet measured, which could also bring substantial additional information.

Acknowledgements

I would like to thank the organisers of the Moriond QCD 2012 for organising a great conference and for inviting me to give this talk.

References

1. See for example M. S. Carena, A. Menon, R. Noriega-Papaqui *et al.*, Phys. Rev. D **74**, 015009 (2006); D. Eriksson, F. Mahmoudi and O. Stal, JHEP **0811**, 035 (2008); A. G. Akeroyd and F. Mahmoudi, JHEP **0904**, 121 (2009); F. Mahmoudi and O. Stal, Phys. Rev. D **81**, 035016 (2010); F. Mahmoudi, Nuovo Cim. C **34S01**, 48 (2011).
2. A. J. Buras, hep-ph/9806471.
3. F. Mahmoudi, Comput. Phys. Commun. **180**, 1579 (2009).
4. R. Aaij *et al.* [LHCb Collaboration], arXiv:1203.4493 [hep-ex].
5. C. Bobeth, T. Ewerth, F. Kruger and J. Urban, Phys. Rev. D **64**, 074014 (2001).
6. F. Mahmoudi, S. Neshatpour and J. Orloff, arXiv:1205.1845 [hep-ph].
7. F. Kruger and J. Matias, Phys. Rev. D **71**, 094009 (2005).
8. W. Altmannshofer, P. Ball, A. Bharucha *et al.*, JHEP **0901**, 019 (2009).
9. M. Beneke, T. Feldmann and D. Seidel, Nucl. Phys. B **612**, 25 (2001).
10. M. Beneke, T. Feldmann and D. Seidel, Eur. Phys. J. C **41**, 173 (2005).
11. C. Bobeth, G. Hiller and G. Piranishvili, JHEP **0807**, 106 (2008).
12. T. Feldmann and J. Matias, JHEP **0301**, 074 (2003).
13. A. G. Akeroyd, F. Mahmoudi and D. Martinez Santos, JHEP **1112**, 088 (2011).
14. B. C. Allanach, Comput. Phys. Commun. **143**, 305 (2002).
15. U. Ellwanger and C. Hugonie, Comput. Phys. Commun. **175**, 290 (2006).
16. F. Mahmoudi, Comput. Phys. Commun. **178**, 745 (2008); Comput. Phys. Commun. **180**, 1718 (2009).
17. R. Aaij *et al.* [LHCb Collaboration], arXiv:1205.3422 [hep-ex].
18. S. Chatrchyan *et al.* [CMS Collaboration], Phys. Rev. Lett. **107**, 221804 (2011).
19. CMS Collaboration, CMS-PAS-SUS-12-005.
20. A. Djouadi and S. Rosiers–Lees *et al.*, hep-ph/9901246; A. Djouadi, Phys. Rept. **459**, 1 (2008).
21. A. Arbey, M. Battaglia and F. Mahmoudi, Eur. Phys. J. C **72**, 1906 (2012).
22. A. Arbey, M. Battaglia and F. Mahmoudi, Eur. Phys. J. C **72**, 1847 (2012).
23. B. C. Allanach, C. Balazs *et al.*, Comput. Phys. Commun. **180**, 8 (2009).
24. A. Arbey and F. Mahmoudi, Comput. Phys. Commun. **181**, 1277 (2010); Comput. Phys. Commun. **182**, 1582 (2011).
25. F. Mahmoudi, S. Heinemeyer *et al.*, Comput. Phys. Commun. **183**, 285 (2012).

Recent Results on Light Hadron Spectroscopy at BESIII

Zhao Haisheng (for BESIII collaboration)
Institute of High Energy of Physics, Beijing, China

Using about $2.25 \times 10^8 J/\psi$ events and $1.06 \times 10^8 \psi'$ events accumulated with BESIII detector operating at BEPCII e^+e^- collider, a partial wave analysis of $p\bar{p}$ mass threshold enhancement is used in $J/\psi(\psi') \to \gamma p\bar{p}$. $X(1835)$ is confirmed in $J/\psi \to \gamma\eta'\pi^+\pi^-$ and $X(2120)$ and $X(2370)$ are observed. A new structure $X(1870)$ is observed with a significance of 7.1σ in $J/\psi \to \omega\eta\pi^+\pi^-$. For the decays $J/\psi \to \gamma\pi^+\pi^-\pi^0$ and $J/\psi \to \gamma\pi^0\pi^0\pi^0$, the isospin violating decay $\eta(1405) \to f_0(980)\pi^0$ is observed for the first time. New measurements of the $J/\psi \to \pi^+\pi^-\pi^0$ and $\psi' \to \pi^+\pi^-\pi^0$ are presented with high precision.

1 BESIII and BEPCII

BEPCII/BESIII [1] is a major upgrade of the BEPC(Beijing Electron Positron Collider) accelerator and BESII(the Beijing Spectrometer) detector. The primary physics purposes are aimed at the study of light hadron spectroscopy and τ-charm physics. The analysis reported here are based on the data samples of $2.25 \times 10^8 J/\psi$ and $1.06 \times 10^8 \psi'$ events.

2 $p\bar{p}$ mass threshold structure

An anomalously strong $p\bar{p}$ mass threshold enhancement was first observed by BESII experiment in the radiative decay of $J/\psi \to \gamma p\bar{p}$ [2]. One intriguing feature of this enhancement structure is that the corresponding structures are absent in the relative channels, including B-meson decays [3], Υ [4], and the decay of $J/\psi \to \omega p\bar{p}$ [5].

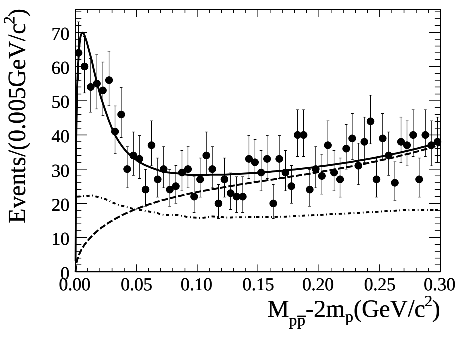

Figure 1: The $p\bar{p}$ mass spectrum for the $\psi' \to \pi^+\pi^- J/\psi(\gamma p\bar{p})$ at BESIII. The solid curve is the fit result; the dashed curve shows the fitted background function, and the dash-dotted curve indicates how the acceptance varies with $p\bar{p}$ invariant mass.

The mass threshold enhancement was confirmed by an analysis of $\psi' \to \pi^+\pi^- J/\psi, J/\psi \to$

$\gamma p\bar{p}$ by the BESIII experiment [6], shown in Fig.1 and the data were fitted by an S-wave Breit-Wigner resonance function, obtaining $M = 1861 \pm 6.13(stat) + 7.26(syst)$. Recently, a partial wave analysis(PWA) of $p\bar{p}$ mass-threshold enhancement in the reaction $J/\psi \to \gamma p\bar{p}$ is used to determine [7]: its J^{PC} quantum numbers to be 0^{-+}; its peak mass to be below threshold at $M = 1832^{+19}_{-5}(stat.)^{+18}_{-17}(syst.)19(model)\mathrm{MeV}/c^2$; and its total width to be $\Gamma < 76$ MeV at 90% CL. A similar PWA analysis is performed on $\psi' \to \gamma p\bar{p}$ decays and the $p\bar{p}$ mass threshold is observed, but it is not obvious due to limited statistics of ψ' events. The produce branching fractions for $X(p\bar{p})$ in J/ψ and ψ' decays are measured to be $Br(J/\psi \to \gamma X)Br(X \to p\bar{p}) = (9.0^{+0.4}_{-1.1}(stat.)^{+1.5}_{-5.0}(syst.) \pm 2.3(model)) \times 10^{-5}$ and $Br(\psi(2S) \to \gamma X)Br(X \to p\bar{p}) = (4.57 \pm 0.36(stat.)^{+1.23}_{-4.07}(syst.) \pm 1.28(model)) \times 10^{-6}$, respectively. And the production ratio of the $p\bar{p}$ between J/ψ and ψ' radiative decays is $R = \frac{Br(\psi(2S)\to\gamma X(p\bar{p}))}{Br(J/\psi\to\gamma X(p\bar{p}))} = (5.08^{+0.71}_{-0.45}(stat.)^{+0.67}_{-3.58}(syst.) \pm 0.12(model))\%$, which is suppressed compared with 12% rule.

3 Confirmation of $X(1835)$ and observation of two new structures in $J/\psi \to \gamma\pi\pi\eta'$

A $\pi^+\pi^-\eta'$ resonance, the $X(1835)$, was first observed in $J/\psi \to \gamma\pi^+\pi^-\eta'$ at BESII with a statistical significance of 7.7σ [8]. Extensive theoretical interpretations have been raised to settle the nature of this resonance, such as the $p\bar{p}$ bound state [9], glueball [10], radial excitation of η' [11] and so on. At BESIII, two decay modes of η', $\eta' \to \gamma\rho$ and $\eta' \to \eta\pi^+\pi^-$ are utilized to study the channel of $J/\psi \to \gamma\pi^+\pi^-\eta'$ [12]. Fig. 2(a) and Fig. 2(b) show the mass spectrum of $\pi^+\pi^-\eta'$ in both decay modes of η'. In addition to the clear $X(1835)$ peak, two structures located at around 2.1 and 2.3 GeV/c^2 are also clearly observed.

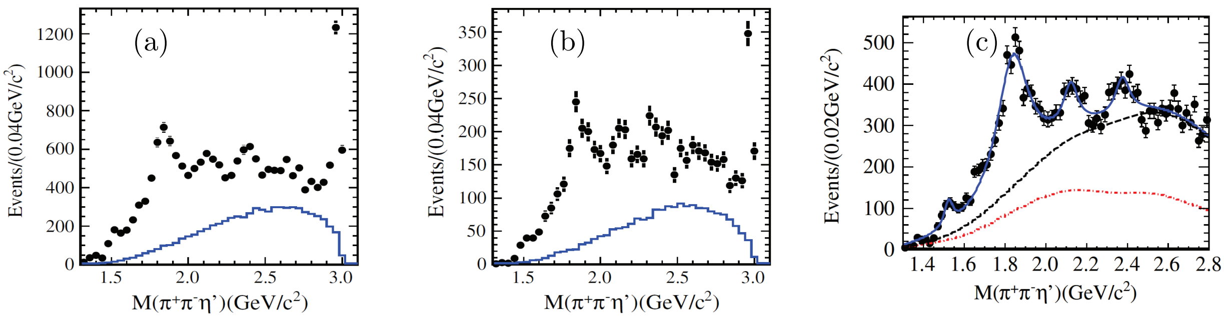

Figure 2: (a) the mass spectrum of $\pi^+\pi^-\eta'$ with $\eta' \to \gamma\rho$; (b) the mass spectrum of $\pi^+\pi^-\eta'$ with $\eta' \to \eta\pi^+\pi^-$. (c) the mass spectrum fitting with four resonances. The dots with error bars show the data, and the blue histogram in (a) and (b) stands for the distribution of arbitrarily normalized phase space Monte Carlo sample. The dash-dotted red curve in (c) is the contribution from non-η' events and $J/\psi \to \pi^0\pi^+\pi^-\eta'$ events, and the dashed black curve in (c) represents the total background.

Figure 2(c) shows the fitting result of the $\pi^+\pi^-\eta'$ mass spectrum with the contribution of two decay modes of η' combined together. The existence of $X(1835)$ is confirmed with a significance of larger than 20σ. The statistical significance of $X(2120)$ and $X(2370)$ are determined to be 7.2σ and 6.4σ respectively. $\cos\theta_\gamma$ distribution of the $X(1835)$, where θ_γ is the polar angle of the photon in the J/ψ center of mass system, agrees with $1 + \cos^2\theta_\gamma$, which is expected for a pseudoscalar meson.

4 Observation of $X(1870)$ in $J/\psi \to \omega\eta\pi^+\pi^-$

$X(1835)$ is reported in the analysis of $J/\psi \to \gamma\pi^+\pi^-\eta'$ as covered in the last section. The study of the decay patterns of the resonance, i.e. to search for similar structures in relative channels and with other side particles is very important to clarify its nature. In this sense, the analysis of $J/\psi \to \omega\eta\pi^+\pi^-$ [14] will shed light on the properties of the resonance.

Figure 3 shows the fitting result of $\eta\pi^+\pi^-$ mass spectrum within the $a_0^0(980)$ signal region in $M(\eta\pi^\pm)$. The signal peaks of $f_1(1285)$, $\eta(1405)$ and $X(1870)$ are parameterized with efficiency-corrected Breit-Wigner function convoluted with Gaussian resolution function, and the background curve is described by a floating polynomial. The mass and width of $f_1(1285)$ and $\eta(1405)$ agree quite well with their PDG values [13]. The fit yields the mass and width of $X(1870)$ to be $M = 1877.3 \pm 6.3$ MeV/c^2, and $\Gamma = 57 \pm 12$MeV/c^2. The statistical significance of $X(1870)$ is conservatively estimated as 7.1σ. Whether the $X(1870)$, $X(1860)$ and $X(1835)$ are the same particle need further study.

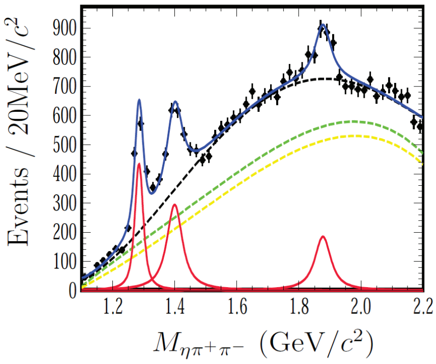

Figure 3: Mass spectrum fitting results with either $\eta\pi^+$ or $\eta\pi^-$ located in the 100 MeV/c2 mass window of $a_0(980)$. The yellow dashed curve shows the contribution of non-ω and/or non-$a_0(980)$ background, green dashed line in addition includes the contribution of $J/\psi \to b_1(1235)a_0(980)$, the black dashed curve stands for the total background with the non-resonant $J/\psi \to \omega a_0^\pm(980)\pi^\mp$ included.

5 Observation of $\eta(1405) \to f_0(980)\pi^0$ in $J/\psi \to \gamma 3\pi$

The spectrum of radial excitation states of isoscalar η and η' is still not well known. An important issue is about the nature of $\eta(1405)$ and $\eta(1475)$ states, which are not well established. The decays $J/\psi \to \gamma\pi^+\pi^-\pi^0$ and $\gamma\pi^0\pi^0\pi^0$ are analyzed at BESIII [15]. In both modes, clear $f_0(980)$ signals are observed on both $\pi^+\pi^-$ and $\pi^0\pi^0$ spectra, and the width of observed $f_0(980)$ is much narrower(about 10 MeV) than that in other processes [16]. Fig.4 shows the invariant mass of $f_0(980)\pi^0$ by taking events in the window of $f_0(980)$ on the $\pi\pi$ mass spectrum and $f_1(1285)/\eta(1295)$ can be observed with a significance of about 3.7σ for $f_1(1285)/\eta(1295) \to f_0(980)\pi^0$ in $f_0 \to \pi^+\pi^-$ mode(1.2σ in $f_0(980) \to \pi^0\pi^0$). A clear peak around 1400MeV is also observed on the mass of $f_0(980)\pi^0$ and angular analysis indicates that the peak on 1400MeV is from $\eta(1405) \to f_0(980)\pi^0$ decay. The combined branching fraction of $\eta(1405)$ production is determined to be $Br(J/\psi \to \gamma\eta(1405) \to \gamma\pi^0 f_0(980) \to \gamma\pi^0\pi^+\pi^-) = (1.50 \pm 0.11(stat.) \pm 0.11(sys.)) \times 10^{-5}$ and $Br(J/\psi \to \gamma\eta(1405) \to \gamma\pi^0 f_0(980) \to \gamma\pi^0\pi^0\pi^0) = (7.10 \pm 0.82(stat.) \pm 0.72(sys.)) \times 10^{-6}$, respectively. It is the first time that we observe anomalously large isospin violation in the strong decay of $\eta(1405) \to f_0(980)\pi^0$. A possible explanation [17] to this puzzle is an intermediate on-shell $K\bar{K}^*$+$c.c.$ rescattering to the isospin violating $f_0(980)\pi^0$ by exchanging on-shell kaon.

The decay rates for $\eta' \to 3\pi$ is determined to be $Br(\eta' \to \pi^+\pi^-\pi^0) = (3.83 \pm 0.15 \pm 0.39) \times 10^{-3}$ and $Br(\eta' \to 3\pi^0) = (3.56 \pm 0.22 \pm 0.34) \times 10^{-3}$, respectively. For $\eta' \to \pi^+\pi^-\pi^0$ decay, it is consistent with CLEO-c's measurements and precision is improved by a factor of 4. while, for $\eta' \to \pi^0\pi^-\pi^0$, it is two times larger than that in the PDG value [16].

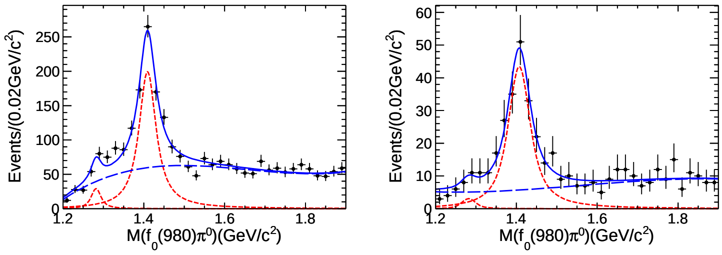

Figure 4: The invariant mass of $f_0\pi^0$ from $J/\psi \to \gamma\pi^+\pi^-\pi^0$ and $\gamma 3\pi^0$.

6 Precision measurement of the branching ratios of $J/\psi(\psi(2S)) \to \pi^+\pi^-\pi^0$

Previous studies[18 19 20] of $J/\psi \to \pi^+\pi^-\pi^0$ and $\psi(2S) \to \pi^+\pi^-\pi^0$ found not only an unexpectedly low branching fraction in the case of the $\psi(2S)$ but also a completely different shape of the di-pion mass spectrum and the Dalitz plot.

Figure 5 shows the invariant mass spectra and Dalitz plots for $J/\psi \to \pi^+\pi^-\pi^0$ and $\psi(2S) \to \pi^+\pi^-\pi^0$ at BESIII[21]. The decay $J/\psi \to \pi^+\pi^-\pi^0$ is dominated by $\rho(770)$ production; the absence of events in the center of the Dalitz plot points to negatively interfering higher ρ states. While for the $\psi(2S) \to \pi^+\pi^-\pi^0$ decay, a small $\rho(770)$ contribution can be discerned. Most of the events are however clustering around 2.2GeV/c^2 in di-pion mass. The branching fraction for $J/\psi \to \pi^+\pi^-\pi^0$ is determined to be $(2.137 \pm 0.004(stat.)^{+0.058}_{-0.056}(syst.)^{+0.027}_{-0.026}(norm.)) \times 10^{-2}$, and the branching fraction for $\psi(2S) \to \pi^+\pi^-\pi^0$ is measured as $(2.14 \pm 0.03(stat.)^{+0.08}_{-0.07}(syst.)^{+0.09}_{-0.08}(norm.)) \times 10^{-4}$. The ratio of these two branching fractions is $\frac{Br(\psi(2S)\to\pi^+\pi^-\pi^0)}{Br(J/\psi\to\pi^+\pi^-\pi^0)} = (1.00 \pm 0.01(stat.)^{+0.06}_{-0.05}(syst.))\%$.

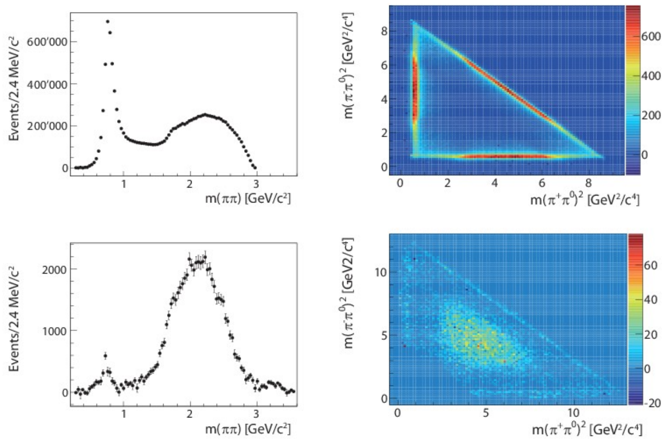

Figure 5: $\pi\pi$ invariant mass distribution(left) and Dalitz plot(right) with backgrounds subtracted and corrected for efficiency. Top and bottom graphs show the results for the $J/\psi \to \pi^+\pi^-\pi^0$ and $\psi(2S) \to \pi^+\pi^-\pi^0$ analysis, respectively.

References

1. M. Ablikim et al. (BES Collaboration), *Nucl. Instrum.Meth. A* **614**, 345 (2010).
2. J.Z.Bai et al. (BES Collaboration), *Phys. Rev. Lett.* **91**, 022001 (()2003).
3. M. A. Wang et al., *Phys. Rev. Lett.* **92**, 131801 (2004).
4. S. B. Athar et al. (CLEO Collaboration), *Phys. Rev.* D **73**, 032001 (2006).
5. M. Ablikim et al. (BES Collaboration), *Eur. Phys. J. C* **53**, 15 (2008).
6. M.Ablikim et al. (BES Collaboration), *Chin. Phys. C* **34**, 421 (2010).

7. M.Ablikim et al. (BES COllaboration), *Phys. Rev. Lett.* **108**, 112003 (2012).
8. M. Ablikim et al. (BES Collaboration), *Phys. Rev. Lett.* **95**, 262001 (2005).
9. A. Datta and P. J. ODonnel, *Phys. Lett.* B **567**, 273 (2003).
10. N. Kochelev and D. P. Min, *Phys. Lett.* B **633**, 283-288 (2006).
11. T. Huang and S. L. Zhu, *Phys. Rev.* D **73**, 014023 (2006).
12. M.Ablikim et al. (BES Collaboration), *Phys. Rev. Lett.* **106**, 072002 (2011).
13. C. Amsler et al. (Particle Data Group), *Phys. Lett.* B **667**, 1 (2008).
14. M.Ablikim et al. (BES Collaboration), *Phys. Rev. Lett.* **107**, 182001 (2011).
15. M.Ablikim et al. (BES Collaboration), *Phys. Rev. Lett.* **108**, 182001 (2012).
16. K. Nakamura et al., *Journal of Physics G* **37**, 075021 (2010).
17. J.J. Wu et al, *Phys. Rev. Lett.* **108**, 081803 (2012).
18. M.E.B. Franklin, et al., *Phys. Rev. Lett.* **51**, 963 (1983).
19. J.Z.Bai, et al., *Phys. Rev.* D **70**, 012005 (2004).
20. M.Ablikim,et al., *Phys. Rev. Lett.* **94**, 247-254 (2005).
21. M.Ablikim et al.(BES Collaboration), *Phys. Lett.* B **710**, 594 (2012).

Recent results of Charmonium decays and transitions at BESIII

Zhiyong Wang for BESIII Collaboration
Institute of High Energy Physics of Chinese Academy of Sciences, YuQuan Road, 19(2) Beijing, China

Based on 106×10^6 ψ' events collected at BESIII detector in 2009, we study charmonium decays and transition decays. We measured the branching fractions of $\psi' \to \gamma\pi^0, \gamma\eta, \gamma\eta', \chi_{cJ} \to \gamma\rho, \gamma\omega, \gamma\phi, p\bar{p}K^+K^-$, and $VV(V=\omega,\phi)$. We also search for the decay mode of $\eta_c' \to VV(V = K^{*0}, \rho)$, but no obvious signal is found. We also studied charmonium properties via hadronic and radiative transitions. For example, h_c properties study, η_c mass and width measurement, first observation of η_c' in charmonium decay as well as the multipoles analysis of $\psi' \to \gamma\chi_{c2}$.

1 Introduction

The ratio of $R_{c\bar{c}}$ is defined as $R_{c\bar{c}} \equiv (\mathcal{B}(c\bar{c} \to \gamma\eta)/\mathcal{B}(c\bar{c} \to \gamma\eta')$. CLEO-c's experiments indicates that $R_{\psi'} \ll R_{J/\psi}$ with $R_{\psi'} < 1.8\%$ at the 90% C.L. and $R_{J/\psi} = (21.1 \pm 0.9)\%$ [1]. Such a small $R_{\psi'}$ is unanticipated, and it poses a significant challenge to our understanding of the $c\bar{c}$ bound states. The two-photon transition of $\psi' \to \gamma\gamma J/\psi$ is more sensitive to the coupled-channel effect and thus provides a unique opportunity to investigate the issues [2]. Meanwhile, the two-photon spectroscopy has been a very powerful tool for the study of the excitation spectra of a variety of systems with a side range of sizes, such as molecules atomic hydrogen and positronium. Doubly radiative decays of the type $\psi' \to \gamma X \to \gamma\gamma V$, where V is either a ϕ, ρ^0, or ω meson, provide information on the flavor content of the C-even resonance X and on the gluon hadronization dynamics in the process. The spin and charge dependent couplings in radiative decays reveal detailed information which is particularly useful in the search for glueball and hybrid states. CLEO's measurement failed to find any obvious ϕ signal due to the small statistic. Decays of the χ_{c1} into $\phi\phi$,$\omega\omega$ and $\omega\phi$ violate the helicity selection rule (HSR). In addition, the decays of $\chi_{cJ} \to \omega\phi$ are doubly OZI suppressed and have yet to be observed. Recently, long-distance effects in χ_{c1} decay have been proposed to account for the HSR violation. Precise measurement of $\chi_{c1} \to VV$ decays will help clarify the influence of long-distance effects in this energy region. $\eta_c(2S) \to VV$ are supposed to be highly suppressed according to some theoretical prediction, but have a higher production in other theory. The measurement of $\eta_c(2S) \to VV$ may help in understanding the role played by charmed meson loops in $\eta_c(2S) \to VV$. h_c is firstly observed by CLEO collaboration with E1 tagged mode. However, they haven't measured its width, nor observed h_c without E1-tagged. The resonant parameter of η_c have been measured by many experiments, but the differences between them are awfully large for both mass and width. $\eta_c(2S)$ has been found in many decay modes, but haven't been observed in charmonium decay. In general, the transition amplitude of radiative decays of charmonium states is dominated by the electric dipole (E1) contribution, with higher multipoles suppressed by powers of photon energy divided by charm quark mass. The search for contributions of higher-order multipole amplitudes is of interest as a source of information on the charm quarks magnetic moment.

1.1 Charmonium decays

For the branching fraction measurements of $\psi' \to \gamma\pi^0, \gamma\eta, \gamma\eta', \chi_{cJ} \to \gamma\rho, \gamma\omega, \gamma\phi, p\bar{p}K^+K^-$, and $VV(V=\omega,\phi)$. The events selection criteria can be found in the published paper [5,6,8]. For the search for $\eta_c' \to VV$, one can refer to [9] for detail. The general selection criteria for charged track and neutral shower are below. We require that each charged track (except those from K_S decays) is consistent with originating from within 1 cm in the radial direction and 10 cm along the beam direction of the run-by-run-determined interaction point. The tracks must be within the MDC fiducial volume, $|\cos\theta| < 0.93$. Photons are reconstructed from the isolated showers in the EMC. The energy deposited in the nearby TOF counter is included to improve the reconstruction efficiency and energy resolution. Photon energies are required to be greater than 25 MeV in the EMC barrel region($|\cos\theta| < 0.8$); in the EMC end caps ($0.86 < |\cos\theta| < 0.92$) this requirement is increases to 50 MeV. The showers in the angular range between the barrel and end cap are poorly reconstructed and excluded from the analysis. Moreover, the EMC timing of the photon candidate must be in coincidence with collision events, $0 \le t \le 700$ ns , to suppress electronic noise and energy deposits unrelated to the events. π^0, η is reconstructed by $\gamma\gamma$ invariant mass and ρ, ω, and ϕ are reconstructed by $\pi^+\pi^-$, $\pi^+\pi^-\pi^0$, and K^+K^- invariant mass. Table 1 shows the measurement results for $\psi' \to \gamma P(P=\pi^0,\eta,\eta')$.

Table 1: Branching fractions($\times 10^6$) of $\psi' \to \gamma P$, where the first errors are statistical and the second ones are systematic, and the comparison with the PDG values.

Mode	BESIII	PDG
hline $\psi' \to \gamma\pi^0$	$1.58 \pm 0.40 \pm 0.13$	≤ 5
$\psi' \to \gamma\eta$	$1.38 \pm 0.48 \pm 0.09$	≤ 2
$\psi' \to \gamma\eta'$	$126 \pm 3 \pm 8$	121 ± 8

Figure 1 (a) and (b) show the fit to the recoiling mass of lower-energy photon for $\gamma\gamma e^+e^-$ and $\gamma\gamma\mu^+\mu^-$ final states. Clear χ_{cJ} signal can be seen. Figure 1 (e) and (f) shows the $\gamma\gamma$ recoiling mass with the events in the region of 3.44 GeV/c^2 < R_{sm} <3.48 GeV/c^2. Here, R_{sm} denotes the recoiling mass of lower-energy photon. Most events from the known decay modes, $\psi' \to \gamma\chi_{cJ}, \chi_{cJ} \to \gamma J/\psi$ and $\psi' \to \pi^0(\eta)J/\psi$ doesn't fall into this region. An excess of data above known background can be seen around J/ψ nominal mass in figure 1(e) and (f), which is expected from the sought after two-photon process. With the number of events from fit, we obtain the branching fraction of two-photon process $\psi' \to \gamma\gamma J/\psi$ is $(3.3 \pm 0.6^{+0.8}_{-1.1}) \times 10^{-4}$ with the statistical significance of 3.8σ. Table 2 shows the results of $\chi_{cJ} \to \gamma V$. We also list the CLEO's measurements and some theoretical predictions. The polarization of $\chi_{c1} \to \gamma V$ have been studied according to their angular distribution information, and it is found that longitudinal polarization is dominant which is consistent with theoretical prediction [7]. Table 3 shows the measured branching fractions of $\chi_{cJ} \to p\bar{p}K^+K^-$. For $\chi_{cJ} \to VV$, we confirm the previous $\chi_{c0,2} \to \phi\phi, \omega\omega$ with higher precision. Besides, we observed the decay of $\chi_{c1} \to \phi\phi, \omega\omega$ and $\chi_{cJ} \to \omega\phi$ for the first time. Table 4 shows the measurement results. In the search for $\eta_c' \to VV$, we haven't observed any obvious signal in $\rho^0\rho^0$, $K^{*0}\bar{K}^{*0}$, and $\phi\phi$. As a results we just give the upper limits on the decay fractions, which are $\mathcal{B}(\eta_c' \to \rho^0\rho^0) < 3.1 \times 10^{-3}$, $\mathcal{B}(\eta_c' \to K^{*0}\bar{K}^{*0}) < 5.4 \times 10^{-3}$, and $\mathcal{B}(\eta_c' \to \phi\phi) < 2.0 \times 10^{-3}$.

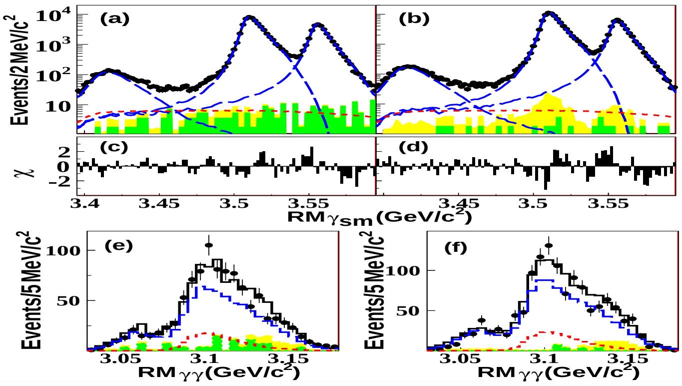

Figure 1: The distribution of the recoiling mass of lower-energy photon and $\gamma\gamma$ in $\gamma\gamma e^+e^-$ and $\gamma\gamma\mu^+\mu^-$ final states.

Table 2: Branching fractions on $\chi_{cJ} \to \gamma V$. The upper limit is set at 90% C.L.

Mode	CLEO	pQCD	QCD	QCD+QED	this experiments
hline $\chi_{c0} \to \gamma\phi$	< 9.6	1.2	3.2	2.0	< 10.5
$\chi_{c1} \to \gamma\phi$	$243 \pm 19 \pm 22$	14	41	42	$228 \pm 13 \pm 22$
$\chi_{c2} \to \gamma\phi$	< 50	4.4	13	38	< 20.8
$\chi_{c0} \to \gamma\omega$	< 8.8	0.13	0.35	0.22	< 12.9
$\chi_{c1} \to \gamma\omega$	$83 \pm 15 \pm 12$	1.6	4.6	4.7	$69.7 \pm 7.2 \pm 6.6$
$\chi_{c2} \to \gamma\omega$	< 7.0	0.5	1.5	4.2	< 6.1
$\chi_{c0} \to \gamma\phi$	< 6.4	0.46	1.3	0.03	< 16.2
$\chi_{c1} \to \gamma\phi$	< 26	14	3.6	11	$25.8 \pm 5.2 \pm 2.3$
$\chi_{c2} \to \gamma\phi$	< 13	1.1	3.3	6.5	< 8.1

2 Charmonium transitions

The event selection criteria for $\psi' \to \pi^0 h_c, \gamma\eta_c, \eta_c \to X$(X denotes a certain final state), $\psi' \to \gamma\eta_c', \eta_c' \to K_S K\pi$, and $\psi' \to \gamma\pi^+\pi^-, K^+K^-$ can be found in [10,11,12,13]. The h_c mass is confirmed with E1-tagged mode. It is found to be $3525.40 \pm 0.13 \pm 0.18$ MeV/c^2. In addition, we measure its width for the first time. It is found to be $0.73 \pm 0.45 \pm 0.28$ MeV, or < 1.44 MeV at 90% C.L. h_c signal can also be observed without E1-tagged mode. Therefore, we gave the absolute branching fraction $\mathcal{B}(\psi' \to \pi^0 h_c) = (8.4 \pm 1.3 \pm 1.0) \times 10^{-4}$ and $\mathcal{B}(h_c \to \gamma\eta_c) = (54.3 \pm 6.7 \pm 5.2)\%$. Meanwhile, h_c is also observed in 16 η_c exclusive decay channels. Figure 2 shows the π^0 recoil mass of sum 16 η_c exclusive decay channels. A global fit yields the preliminary mass and width, $3525.40 \pm 0.13 \pm 0.18$ MeV/c^2 and $0.73 \pm 0.45 \pm 0.28$ MeV. One finds that these results are very consistent with those in inclusive measurement. For η_c mass and width measurement, we investigate the transition decay of $\psi' \to \gamma\eta_c$, η_c decaying to $K_S K^+\pi^-, K^+K^-\pi^0, \eta\pi^+\pi^-, KsK^+\pi^+\pi^-\pi^0$, and $3(\pi^+\pi^-)$ final states. In the fit of mass spectrum, we have considered the interference between resonant and non-resonant state, the mass-dependent efficiency, the factors of the radiative photon energy reflect the expected energy dependence of the M1 matrix element. A global fit gives $M = 2984.3 \pm 0.6 \pm 0.6$ MeV/c^2, $\Gamma = 32.0 \pm 1.2 \pm 1.0$ MeV. η_c' has been observed in B decay, two-photon process and double charmonium production, but hasn't been reported in charmonium decay. The experimental challenge is how to search for the soft radiative photon which has a energy of about 50 MeV. We search η_c' signal in $\psi' \to K^+K^-\pi$ channel, including $K_S^0 K^\pm\pi^\mp$ and $K^+K^-\pi^0$. Figure 3 shows the invariant mass $K_S^0 K^\pm\pi^\mp$. The small bump is the η_c' signal. The fit yields $N_{\eta_c'} = 81 \pm 14$ for $K_S^0 K^\pm\pi^\mp$ channel and 46 ± 11 for $K^+K^-\pi^0$ channel. The $K_S^0 K^\pm\pi^\mp$ channel determines primarily the precision for the η_c' mass and width measurements in the simultaneous fit with

Table 3: Branching fractions($\times 10^{-4}$) on $\chi_{cJ} \to p\bar{p}K^+K^-$ final state. The upper limit is set at 90% C.L.

modes	χ_{c0}	χ_{c1}	χ_{c2}
$p\bar{p}K^+K^-$	$1.24 \pm 0.20 \pm 0.18$	$1.35 \pm 0.15 \pm 0.19$	$2.08 \pm 0.19 \pm 0.30$
$\bar{p}K^+\Lambda(1520) + c.c.$	$3.00 \pm 0.58 \pm 0.50$	$1.81 \pm 0.38 \pm 0.28$	$3.06 \pm 0.50 \pm 0.54$
$\Lambda(1520)\bar{\Lambda}(1520)$	$3.18 \pm 1.11 \pm 0.53$	< 1.00	$5.05 \pm 1.29 \pm 0.93$
$p\bar{p}\phi$	$0.61 \pm 0.12 \pm 0.09$	< 0.18	$030 \pm 0.09 \pm 0.04$

Table 4: Branching fractions($\times 10^{-4}$) on $\chi_{cJ} \to \phi\phi, \omega\omega, \omega\phi$.

modes	χ_{c0}	χ_{c1}	χ_{c2}	final state
$\phi\phi$	$8.0 \pm 0.3 \pm 0.8$	$4.4 \pm 0.3 \pm 0.5$	$10.7 \pm 0.3 \pm 1.2$	$2(K^+K^-)$
$\omega\omega$	$9.5 \pm 0.3 \pm 1.1$	$6.0 \pm 0.3 \pm 0.7$	$8.9 \pm 0.3 \pm 1.1$	$2(\pi^+\pi^-\pi^0)$
$\omega\phi$	$1.2 \pm 0.1 \pm 0.2$	$0.22 \pm 0.06 \pm 0.02$	< 0.2	$K^+K^-\pi^+\pi^-\pi^0$

the results $M_{\eta_c'} = 3637.6 \pm 2.9 \pm 1.6$ MeV/c^2 and $\Gamma_{etacp} = 16.9 \pm 6.4 \pm 4.8$ MeV, respectively. The combined statistical significance is larger than 10.2σ. The preliminary branching ratio is $\mathcal{B}(\psi' \to \gamma\eta_c') = (6.8 \pm 1.1 \pm 4.5) \times 10^{-4}$. By the simultaneous fit to the angular distribution of pion and kaon in $\psi' \to \gamma\chi_{c2}, \chi_{c2} \to \pi^+\pi^-, K^+K^-$, we obtain the normalized high-order parameter M2 and E3. They are $M2 = 0.046 \pm 0.010 \pm 0.013$ and $E3 = 0.015 \pm 0.008 \pm 0.018$. where the first errors are statistical and the second systematic.

References

1. T. K. Pedlar *et al.* (CLEO Collaboration),*Phys. Rev.* D, **79**, 111101(2009).
2. Z. G. He *et al. Phys. Rev.* D, **83**, 054028 (2011).
3. BESIII Collaboration, M. Ablikim, *et al. Phys. Rev. Lett.* **105**, 261801 (2010).
4. http://arxiv.org/abs/1204.0246
5. BESIII Collaboration, M. Ablikim, *et al. Phys. Rev.* D **83**, 112005(2011).
6. BESIII Collaboration, M. Ablikim, *et al. Phys. Rev.* D **83**, 112009(2011).
7. D. V. Amelin *et al.* (VES Collaboration), *Z. Phys.* C **66**, 71 (1995).
8. BESIII Collaboration, M. Ablikim, *et al. Phys. Rev. Lett.* **107**, 091803(2011).
9. BESIII Collaboration, M. Ablikim, *et al. Phys. Rev.* D **84**, 091102(2011)
10. BESIII Collaboration, M. Ablikim, *et al. Phys. Rev. Lett.***104**, 132002(2010).
11. BESIII Collaboration, M. Ablikim, *et al. Phys. Rev. Lett.* **100**, (2012)
12. http://xxx.itp.ac.cn/abs/1205.5103.
13. BESIII Collaboration, M. Ablikim, *et al. Phys. Rev.* D **84**, 092006(2011)

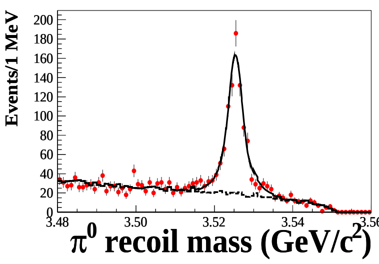

Figure 2: Sum of π^0 recoiling mass to 16 η_c exclusive decay channels

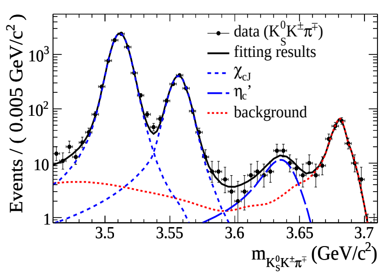

Figure 3: The fit to $K_S K\pi$ invariant mass.

4.
Top

Jet Substructure and Top Tagging

M. Spannowsky
Institute for Particle Physics Phenomenology, Department of Physics, Durham University, DH1 3LE, United Kingdom

Almost all theoretical extensions of the Standard Model predict heavy TeV-scale resonances which have to couple to electroweak-scale resonances, e.g. top quarks or electroweak gauge bosons. Therefore, boosted electroweak-scale resonances with large branching ratios into jets is a highly probable scenario in many processes probing new physics. Here, jet substructure methods can help to disentangle the sought-after signal from the backgrounds. In this brief review we classify scenarios where jet substructure methods can be beneficial for new physics searches at the LHC and discuss the application of the HEPTopTagger in some of these scenarios.

1 Jet substructure in the era of the LHC

The large potential for searches of new electroweak-scale particles by looking inside a fat jet has only been appreciated recently [1,2]. At the LHC with its targetted 14 TeV center of mass energy, particles with masses around the electroweak scale are frequently produced beyond threshold, i.e. boosted transverse to the beam direction. Either because they recoil against other energetic resonances or because they arise from decays of even heavier particles, e.g. Z or KK-gluons. If the resonances transverse momentum is bigger than their mass, their decay products tend to be collimated in the lab frame. Thus, combinatorial problems in the reconstruction of the resonances are ameliorated.

However, at the LHC many sources of hadronic radiation exist. Apart from the decay products of an electroweak-scale resonance, proton-bunch crossings give rise to radiation from the initial state (ISR), the underlying event (UE) and pileup. Initial state radiation results in relatively hard jets. They arise because the incoming partons have to bridge the gap in energy between the proton and the hard process. Underlying event is additional soft QCD activity arising from a given proton-proton interaction surrounding the hard event. It is caused by semi- or non-perturbative interactions between the proton remnants. Finally, pileup denotes multiple proton-proton collisions in one beam crossing.

For an optimal discrimination of a hadronically decaying electroweak resonance from QCD jets, the resonance's decay products have to be disentangled from ISR, UE and pileup.

Sequential jet algorithms [3,4,5], popular for their infrared safety, allow to associate a recombination history to every jet. Therefore, a jet is not only a massive object with a specific cone size and a three-momentum but has a well defined internal structure. Thus, more information is accessible to discriminate the signal from the backgrounds. Over the last few years a plethora of different methods has been proposed to use the internal structure of jets in searches for new physics [2,6]. In general they can be categorized into two classes. On the one hand, methods which extend event shape observables to jet shape observables, making use of the energy flow among the jet's constituents, and on the other hand methods which use internal scales of the recombination history. Often these procedures are combined with so-called jet grooming approaches e.g. Filtering , Pruning or Trimming. At the LHC, the amount of transverse momentum of the underlying event radiation and pileup per unit rapidity can be large [8,9] and their effect on the jet mass depends on the cone size of the fat jet [10]. Grooming procedures are generic prescriptions of how to remove uncorrelated soft radiation from the jet constituents. This goal is achieved by reducing the active area of a jet.

2 Jet grooming methods

Jet grooming methods, like filtering, trimming and pruning, remove soft uncorrelated radiation from a fat jet while retaining final state radiation off the resonance. For QCD jets grooming methods reduce the upper end of the jet mass distribution, whereas for signal events they yield a sharper peak near the true resonance mass $m_j = m_{\text{res}}$. To keep these methods generic it is implicitly assumed that for boosted heavy particles $p_{T_{\text{decay}}} > p_{T_{\text{ISR,UE,PU}}}$.

2.1 Filtering

Filtering, the first proposed jet grooming method, was introduced as part of the so-called BDRS Higgs tagger [1]. Its target application is HW and HZ production with a leptonic decay of the gauge bosons and with the Higgs boson decaying to $b\bar{b}$. A mass drop requirement identifies the vicinity of the Higgs decay products. The procedure called filtering then performs a recombination of the remaining fat jet constituents with a much smaller cone size, R_f. It results in n_f small subjets. This obviously reduces the effective area of the fat jet considered for mass reconstruction and this way tames any QCD effects scaling with R. For the Higgs boson the best mass resolution is achieved by reconstructing the Higgs mass from the $n_f = 3$ hardest filtered subjets. This means we include two b-jets and the hardest wide-angle gluon radiation. Two free parameters, R_f and n_f control the filtering performance.

2.2 Trimming

Trimming [11] targets very similar effects as filtering. In the first step we reconstruct a fat jet which will be heavily impacted by QCD radiation. Its subjets we recombine with a higher resolution R_{trim}, defining a larger number of smaller subjets. These subjets can be separated into two categories: hard and soft. This discrimination is based on the transverse momentum, so hard subjets obey $p_{T,j} > f_{\text{trim}}\Lambda_{\text{trim}}$, where f_{trim} is an adjustable parameter and Λ_{trim} is an intrinsic scale of the fat jet. It can for example be chosen as its jet mass or its transverse momentum. While we discard all soft subjets the recombined hard subjets define a trimmed (fat) jet. Just like filtering this reduces the effective size of the fat jet entering any kind of jet mass measurement. Because Λ_{trim} can be different for each fat jet the trimming procedure is self-adaptive: for a fat jet with large transverse momentum and/or mass the subjets need to have a larger transverse momentum to stay inside the trimmed jet. Just as the filtering procedure, trimming requires two input parameters.

2.3 Pruning

Unlike filtering or trimming, pruning [12] removes underlying event and pileup while building the jet, i.e. as part of the jet algorithm. In a first step it defines a fat jet which can be based on a sequential recombination algorithm. In a second step its constituents are pruned by checking in every recombination step $\min(p_{T,j_1}, p_{T,j_2})/p_{T,j_{1+2}} < z_{\text{prune}}$ and $\Delta R_{j_1,j_2} > R_{\text{prune}}$. If both conditions are met, the merging $j_1, j_2 \to j$ is vetoed. Just as filtering and trimming, pruning depends on two parameters: $z_{\rm prune}$ and $R_{\rm prune}$. $z_{\rm prune}$ ensures that recombined well separated subjets are not very asymmetric in p_T. $R_{\rm prune}$ can be determined on a jet-by-jet basis.

Unlike filtering, pruning and trimming are self-adaptive procedures, applicable to a multi-jet final state in an unbiased resonance search.

It has been shown that pruning, trimming and filtering treat QCD jets differently while yielding a strong correlation in the reconstruction of electroweak scale resonances [13]. Thus, by combining different grooming techniques we can improve the signal-to-background ratio in new physics searches.

3 Phenomenological application of Top Taggers

The reconstruction of boosted hadronically decaying top quarks was one of the first applications of jet substructure methods in searches for new physics [14,15]. In events where boosted top quarks arise from TeV scale resonances top taggers which make use of the substructure of large jets are necessary to discriminate top jets from QCD jets.

Many different approaches to tag boosted top quarks have been proposed [15,16]. It has been shown that they perform similarly on highly boosted top quarks [17]. It is worth noting that it might be possible to combine different top tagging ideas.

One example of a top tagger is the so-called HEPTopTagger (Heidelberg-Eugene-Paris) [18]. The HEPTopTagger is designed to reconstruct top quarks which are only mildly boosted. To capture the decay products of tops with $p_{T,t} \sim 200$ GeV in one fat jet, it is necessary to increase its cone size, e.g. $R = 1.5$. However, increasing the jet area poses two problems for the tagging algorithm. First, subjet combinatorics will increase and it will get more difficult to identify the top decay products. Second, ISR, UE and pileup will become a huge problem, so the HEPTopTagger includes a jet grooming stage.

The tagging algorithm proceeds along the following steps:

1. Un-doing the last clustering of the jet j the mass drop criterion min $m_{j_i} < 0.8\, m_j$ determines if we keep j_1 and j_2. Subjets with $m_{j_i} < 30$ GeV are not considered, which eventually ends the iterative un-clustering.

2. Apply a filtering stage to construct one three-subjet combination with a jet mass within $m_t \pm 25$ GeV.

3. Order these three subjets by p_T. If their jet masses (m_{12}, m_{13}, m_{23}) satisfy one of the following three criteria, accept them as a top candidate:

$$0.2 < \arctan \frac{m_{13}}{m_{12}} < 1.3 \qquad \& \quad R_{\rm min} < \frac{m_{23}}{m_{123}} < R_{\rm max}$$

$$R^2_{\rm min}\left(1+\left(\frac{m_{13}}{m_{12}}\right)^2\right) < 1-\left(\frac{m_{23}}{m_{123}}\right)^2 < R^2_{\rm max}\left(1+\left(\frac{m_{13}}{m_{12}}\right)^2\right) \quad \& \quad \frac{m_{23}}{m_{123}} > R_{\rm s}$$

$$R^2_{\rm min}\left(1+\left(\frac{m_{12}}{m_{13}}\right)^2\right) < 1-\left(\frac{m_{23}}{m_{123}}\right)^2 < R^2_{\rm max}\left(1+\left(\frac{m_{12}}{m_{13}}\right)^2\right) \quad \& \quad \frac{m_{23}}{m_{123}} > R_{\rm s}$$

The dimensionless mass windows $R_{\rm min} = 85\% \times m_W/m_t$ and $R_{\rm max} = 115\% \times m_W/m_t$ are tunable and will be optimized by the experimental collaborations.

For the HEPTopTagger the quality of the top quark's momentum reconstruction has been studied in detail. The question if the top tagger really reconstructs all top decay products is surprisingly irrelevant for this test a generic tagger will always be fairly likely to correctly assign the hardest two top decay products, while the softer W decay subjet will contribute little to the reconstructed top momentum. This is the reason why even for moderately boosted tops 95% of the tagged events show a correctly reconstructed direction within $\Delta R = 0.5$; for more than 80% of the tops the momentum is reconstructed within 20% of the Monte Carlo truth (see Fig. 1).

Tagging strategies for medium p_T top quarks can be important for a large variety of applications:

Scalar top partners can ameliorate the top quark's impact on the hierarchy problem of the Higgs, they are among the most anticipated particles to be found at the LHC. The HEPTopTagger was applied [18] to reconstruct the light top squark of the MSSM $\tilde{t}_1$ in a final-state with only jets and missing transverse energy, $pp \to \tilde{t}_1\tilde{t}_1 \to t\bar{t}\chi_1\bar{\chi}_1$. While a reconstruction with standard techniques yields $S/B \sim 1/7$, a subjet analysis in combination with mT2 can result in $S/B \sim 0.88$ and $S/\sqrt{B} \simeq 6$ after 10 fb^{-1}. If one of the tops decays leptonically a leptonic top tagger can be used [19] to separate the neutrinos MET contribution from the neutralinos MET, which allows an effective use of m_{T2}. However, already at 8 TeV and

Recently, CDF [20] and D0 [21] measured an unexpectedly large forward-backward asymmetry of the top quarks. Measurements of this quantity are subtle at the LHC, due to its proton-proton initial state. However, one can define a forward/central charge asymmetry which captures the physics. Unfortunately, for the dominating gg initial state at the LHC there is no asymmetry at all. To enhance the subdominant $q\bar{q}$ and qg production processes it is beneficial to require a large invariant mass of the $t\bar{t}$ system, i.e. require boosted tops. By reconstructing the momentum of the hadronic top and measuring the charge of the second tops lepton, it is possible to count the number of tops and anti-tops in the forward or central region. The forward charge asymmetry we define

$$\mathcal{A}_F(y_0) = \frac{N_t(y_0 < |y| < 2.5) - N_{\bar{t}}(y_0 < |y| < 2.5)}{N_t(y_0 < |y| < 2.5) + N_{\bar{t}}(|y| < y_0 < 2.5))}, \tag{1}$$

for a given rapidity y_0. As shown in the left and middle panels of Fig. 2 this approach allows to measure the Standard Model forward/central charge asymmetry at the LHC [22].

In early ATLAS and CMS reports the $t\bar{t}H$ production channel with subsequent Higgs decay to bottom quarks was one of the major discovery channels for a light Higgs boson. Further studies revealed a very poor signal-to-background ratio of 1/9 [23], making the channel very sensitive to systematic uncertainties which might prevent it from reaching a 5σ significance for any luminosity. However, at high transverse momentum, after reconstructing the boosted, hadronically decaying top quark using the HEPTopTagger as well as the Higgs boson with a modified version of the BDRS method, and requiring 3 b-tags, the signal-to-background ratio can be improved to $\sim 1/2$, while keeping the statistical significance at a similar value to that in Ref. [24], see Fig. 2.

4 Outlook

In this brief review we have given a categorization of new physics scenarios where searches using jet substructure methods can be beneficial over standard search strategies. Any machine probing the multi-TeV scale will produce electroweak scale resonances which will be highly boosted. In this context top tagging is one of the most prominent applications in searches for new physics. The HEPTopTagger is an example of a top tagger applicable in searches for mildly boosted tops. Currently, many different tagging and jet grooming methods are being evaluated on data to test their validity. Present results indicate a huge potential for new physics searches at the LHC in all discussed kinematic scenarios.

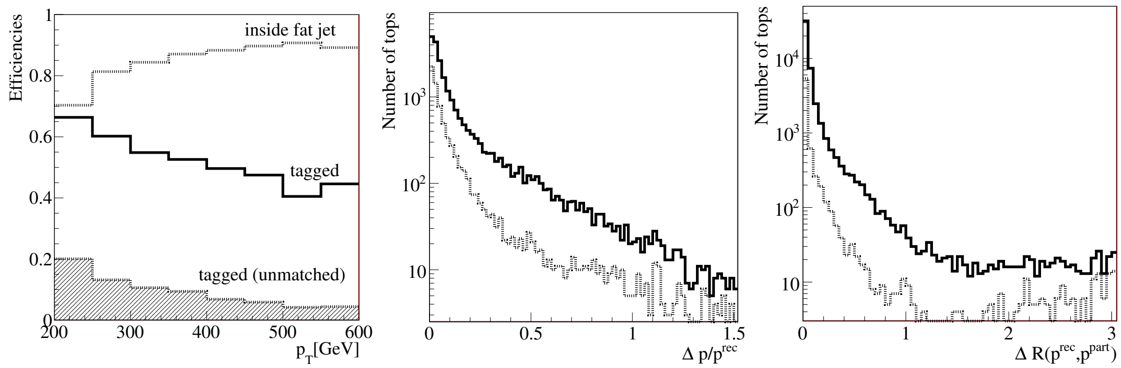

Figure 1: Left: Tagging efficiency of the HEPTopTagger in p_T slices of the fat jet. The dotted line shows the fraction of top quark's where all three decay products on parton level can be found inside the fat jet. The solid black line gives the number of tagged tops. The shaded grey area indicates the ratio of tagged jets where at least one of the subjets is not correctly assigned to the top decay products. Middle: Difference between length of top quark's and reconstructed top jet's three momentum, normalized to the reconstructed top jet's three momentum, i.e. $\Delta p = |p - p^{\mathrm{rec}}|$. Right: Angular separation between the reconstructed top jet and the partonic top quark. In the middle and right panels the thin grey line is for $p_{T,j} > 300$ GeV and the solid black line for $p_{T,j} > 200$ GeV.

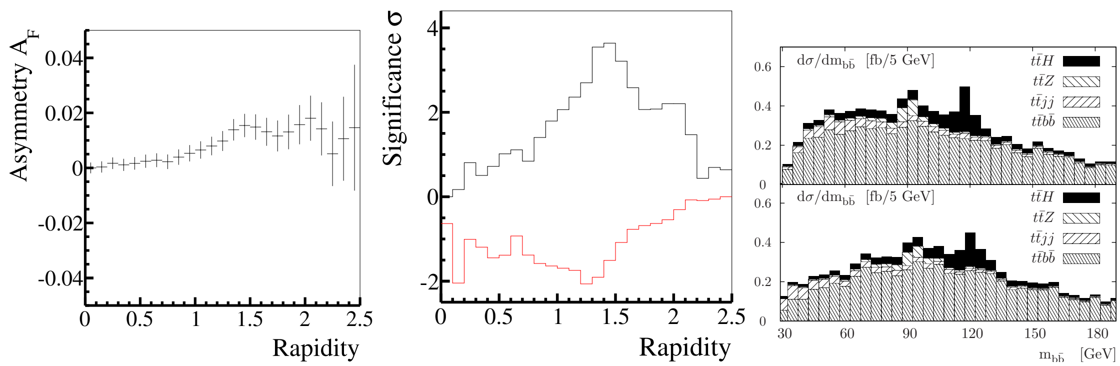

Figure 2: Left: $\mathcal{A}_F$ for a given y_0 according to Eq. (1). Middle: Black curve shows significance to measure the Standard Model $\mathcal{A}_F$. For both panels an integrated luminosity of 25 fb^{-1} at 14 TeV is assumed. Right: Reconstructed Higgs mass, $m_H = 120$ GeV, after event selection cuts and identification of the hadronic top. The upper part shows the reconstruction without underlying event, the lower part with underlying event. The Higgs (and Z boson) peak can be easily disentangled from the shapeless QCD backgrounds.

References

1. J. M. Butterworth, A. R. Davison, M. Rubin, and G. P. Salam, Phys. Rev. Lett. **100** (2008) 242001.
2. A. Abdesselam, *et al.*, Eur. Phys. J. **C71**, 1661 (2011).
3. S. Catani, Y. L. Dokshitzer, M. H. Seymour and B. R. Webber, Nucl. Phys. B **406**, 187 (1993); S. D. Ellis and D. E. Soper, Phys. Rev. D **48**, 3160 (1993).
4. Y. L. Dokshitzer, G. D. Leder, S. Moretti and B. R. Webber, JHEP **9708**, 001 (1997); M. Wobisch and T. Wengler, arXiv:hep-ph/9907280.
5. M. Cacciari, G. P. Salam, G. Soyez, JHEP **0804**, 063 (2008).
6. L. G. Almeida, R. Alon and M. Spannowsky, arXiv:1110.3684 [hep-ph].
7. ATLAS collaboration, ATL-PHYS-PUB-2009-088.
8. M. Cacciari and G. P. Salam, Phys. Lett. B **659**, 119 (2008).
9. M. Cacciari, G. P. Salam and S. Sapeta, JHEP **1004**, 065 (2010).
10. M. Dasgupta, L. Magnea and G. P. Salam, JHEP **0802**, 055 (2008).
11. D. Krohn, J. Thaler, L. -T. Wang, JHEP **1002**, 084 (2010).
12. S. D. Ellis, C. K. Vermilion and J. R. Walsh, Phys. Rev. D **80**, 051501 (2009); S. D. Ellis,

C. K. Vermilion and J. R. Walsh, Phys. Rev. D **81**, 094023 (2010).
13. D. E. Soper, M. Spannowsky, JHEP **1008**, 029 (2010).
14. K. Agashe, A. Belyaev, T. Krupovnickas, G. Perez and J. Virzi, Phys. Rev. D **77**, 015003 (2008) B. Lillie, L. Randall and L. -T. Wang, JHEP **0709**, 074 (2007).
15. T. Plehn and M. Spannowsky, arXiv:1112.4441 [hep-ph].
16. G. Brooijmans, ATL-PHYS-CONF-2008-008; J. Thaler and L.-T. Wang, JHEP **07** (2008) 092; D. E. Kaplan, K. Rehermann, M. D. Schwartz, and B. Tweedie, Phys. Rev. Lett. **101** (2008) 142001; L. G. Almeida, S. J. Lee, G. Perez, I. Sung, J. Virzi, Phys. Rev. **D79**, 074012 (2009).
17. A. Altheimer, S. Arora, L. Asquith, G. Brooijmans, J. Butterworth, M. Campanelli, B. Chapleau and A. E. Cholakian *et al.*, J. Phys. G G **39**, 063001 (2012) [arXiv:1201.0008 [hep-ph]].
18. T. Plehn, M. Spannowsky, M. Takeuchi, and D. Zerwas, JHEP **1010**, 078 (2010).
19. T. Plehn, M. Spannowsky and M. Takeuchi, arXiv:1111.5034 [hep-ph].
20. T. Aaltonen *et al.* [CDF Collaboration], Phys. Rev. **D83**, 112003 (2011).
21. V. M. Abazov *et al.* [D0 Collaboration], Phys. Rev. Lett. **100**, 142002 (2008).
22. J. L. Hewett, *et al.*, Phys. Rev. **D84**, 054005 (2011).
23. J. Cammin and M. Schumacher, ATL-PHYS-2003-024.
24. T. Plehn, G. P. Salam, and M. Spannowsky, Phys. Rev. Lett. **104** (2010) 111801.

Top Quark Pair Production at $\sqrt{s} = 7$ TeV

Ignacio Aracena on behalf of the ATLAS and CMS Collaborations
SLAC National Accelerator Laboratory, 2575 Sand Hill Road, 94025 Menlo Park, California, USA

The successful pp run at $\sqrt{s} = 7$ TeV of the Large Hadron Collider in 2010-2011, has allowed the measurement of the top-quark pair production cross section in a variety of final states and with unprecedented precision. This note presents the results of the ATLAS and CMS collaborations of the top-quark pair production cross section measurement in various final states, as well as their combination. The combination of the ATLAS measurements gives $\sigma_{t\bar{t}} = 177 \pm 3(\text{stat.})^{+8}_{-7}(\text{syst.}) \pm 7(\text{lumi.})$ pb and the CMS combination yields a value $\sigma_{t\bar{t}} = 165.8 \pm 2.2(\text{stat.}) \pm 10.6(\text{syst.}) \pm 7.8(\text{lumi.})$ pb, which are both within the Standard Model expectations.

1 Introduction

Owing to its large mass the top quark might play an important role in physics beyond the Standard Model (SM), and the measurement of its production at the Large Hadron Collider (LHC) provides important tests of perturbative quantum chromodynamics (QCD) in the multi-TeV energy regime. In pp collisions at the LHC, top quarks are dominantly produced in top-antitop pairs ($t\bar{t}$), and are classified according to its decay modes. Within the SM the top quark decays essentially always via the weak process $t \to Wb$. The decay topology is determined by the decay mode of the W boson, which decays either to a lepton and its neutrino or to a pair of quarks. The predicted SM $t\bar{t}$ cross section for pp collisions at a centre-of-mass energy of $\sqrt{s} = 7$ TeV is $\sigma_{t\bar{t}} = 167^{+17}_{-18}$ pb for a top quark mass of 172.5 GeV/c^2 as obtained from approximate NNLO QCD calculations [1].
Measurements of the $t\bar{t}$ cross section in several final states have been carried out by the ATLAS [2] and CMS [3] collaborations and are presented in this note. The results in the different channels are based on data samples corresponding to an integrated lumiosity ranging from 0.70 to 4.7 fb^{-1} recorded by the two experiments.

2 Top quark pair production cross-section

Final states of $t\bar{t}$ events contain at least two jets with secondary vertices from the B mesons decays (b-tagged jets), leptons, missing energy from the escaping neutrinos or light jets, depending on the decay mode of the two W bosons. In the following, the measurements by the ATLAS and CMS collaborations of the $t\bar{t}$ cross section for various final state topologies are presented. Thanks to the large data sample that has been recorded, all measurements presented here are limited by systematic uncertainties.

2.1 *Single lepton channel*

The single lepton channel currently provides the most precise measurement of the $t\bar{t}$ cross section. In this channel one of the two W bosons decays hadronically, while the other decays into a lepton-neutrino pair. The event trigger and selection is based on the identification of one isolated lepton. The dominant contributions to the background are due to W+jet events and QCD multi-jet events, where one jet is mis-identified as a reconstructed lepton. Since the background from these sources is difficult to simulate correctly, its modeling is based on data. A likelihood function is built from various kinematic variables and templates are constructed for signal and backgrounds, separating the sample in the electron and muon channel and different jet multiplicities. The cross section measured by ATLAS, based on an analysis without explicit identification of b jets and with a data sample corresponding to 0.70 fb^{-1}, is $\sigma_{t\bar{t}} = 179.0 \pm 3.9(\text{stat.}) \pm 9.0(\text{syst.}) \pm 6.6(\text{lumi.})$ pb [4]. The result by CMS presented here is $\sigma_{t\bar{t}} = 164.4 \pm 2.8(\text{stat.}) \pm 11.9(\text{syst.}) \pm 7.9(\text{lumi.})$ pb, which takes advantage of the b-tagging capabilities [5] and uses a data sample with 0.80-1.09 fb^{-1}.
In both cases the uncertainty on the jet energy calibration is one of the dominant contributions to the total systematic error. It is worth noting that the overall uncertainty of the measurement is below the uncertainty of the approximate NNLO calculation mentioned in Section 1.

2.2 *Dilepton channel*

In the dilepton channel, which contains two pairs of leptons with its neutrino in the final state, the background is dominated by Drell-Yan production and is estimated from data. Other background processes, such as single top quark or diboson production are estimated from Monte Carlo simulation. The event selection is based on a trigger and identification of two leptons, identifying b-tagged jets and large missing transverse energy ($E_{\mathrm{T}}^{\mathrm{miss}}$). In the dilepton channel ATLAS reports $\sigma_{t\bar{t}} = 176 \pm 5(\text{stat.})^{+14}_{-11}(\text{syst.}) \pm 8(\text{lumi.})$ pb [6] and CMS $\sigma_{t\bar{t}} = 169.9 \pm 3.9(\text{stat.}) \pm 16.3(\text{syst.}) \pm 7.6(\text{lumi.})$ pb [7]. The measurement by ATLAS is based on a total integrated luminosity of 0.70 fb^{-1}, while the one by CMS is based on 1.14 fb^{-1}. In both analyses the systematic uncertainty is dominated by the lepton identification capability.

2.3 *Tau + μ channel*

In this section the measurement of the $t\bar{t}$ cross section in events with an isolated muon and a tau lepton decaying hadronically is presented. The sample of events is selected using a single muon trigger and requiring at least one b-tagged jet and large $E_{\mathrm{T}}^{\mathrm{miss}}$. The dominant background arises from jets faking taus which is estimated from data. One of the pivotal elements of this measurement is the tau-identification algorithm. A boosted decision tree, which distinguishes between one and three-prong tau decays, is used for the measurement by ATLAS, while CMS uses the hadron-plus-strips (HPS) tau identification algorithm [8]. The cross section reported by ATLAS in this channel is $\sigma_{t\bar{t}} = 142 \pm 21(\text{stat.})^{+20}_{-16}(\text{syst.}) \pm 5(\text{lumi.})$ pb [9], the one reported by CMS is $\sigma_{t\bar{t}} = 148.7 \pm 23.6(\text{stat.}) \pm 26.0(\text{syst.}) \pm 8.9(\text{lumi.})$ pb [10]. The measurements are based on data samples corresponding to an integrated luminosity of 1.08 fb^{-1} and 1.09 fb^{-1} used by ATLAS and CMS, respectively.

2.4 *Tau + jets channel*

This channel is characterized by $t\bar{t}$ events with one hadronically decaying τ-lepton and jets ($t\bar{t} \to \tau_{\text{had}}+$ jets). Currently the measurement of the $t\bar{t}$ production cross section in this channel has only been presented by the ATLAS collaboration. Events are selected with a trigger requiring at least two b-tagged jets, which are further confirmed by the offline b-tagging reconstruction. The signal is extracted using a fit to the distribution of the number of tracks associated to the tau candidate. The background to this final state is mainly due to multi-jet events, from $t\bar{t}$ events with a different final state or from jets in $t\bar{t}$ events mis-identified as tau candidates. For the multi-jet and $t\bar{t}$ backgrounds, templates are derived from data in a background enriched region. On the other hand, the background from $t\bar{t}$ events with electrons in the final state is estimated from simulation. The result presented by ATLAS is the first measurement of the $t\bar{t}$ cross section in this channel which is found to be $\sigma_{t\bar{t}} = 200 \pm 19(\text{stat.}) \pm 43(\text{syst.})$ pb and is based on a data sample corresponding to an integrated luminosity of 1.67 fb^{-1} [11].

2.5 All hadronic channel

The all hadronic channel is the final state of $t\bar{t}$ events with the largest branching ratio ($\approx 44\%$), but suffers from a large multi-jet background. The signal extraction is based on a kinematical fit that exploits the characteristic topology of a hadronic $t\bar{t}$ event. It maximizes a likelihood function with respect to the jet energies, which are varied in the fit, and the constraints given by the Breit-Wigner distributions of the W boson and top quark. For the background modeling, the ATLAS measurement derives the shape of the multi-jet background by performing the kinematical fit on the data sample without applying the b-tagging requirement. In the CMS measurement a probability, $R(p_{\text{T}}, |\eta|)$, for b-tagging a jet is first derived as a function of the jet transverse momentum p_{T} and its absolute pseudorapidity value $|\eta|$. Then the kinematic fit is performed on all events with zero b-tagged jets and an event weight, defined as the product of $R(p_{\text{T}}, |\eta|)$ computed for the two jets assigned to the b-quarks in the kinematic fit hypothesis, is applied to estimate the multi-jet background. The measurement by ATLAS is based on a data sample corresponding to an integrated luminosity of 4.7 fb^{-1} and gives a value of $\sigma_{t\bar{t}} = 168 \pm 12(\text{stat.})^{+60}_{-57}(\text{syst.}) \pm 6(\text{lumi.})$ pb [12]. The value reported by CMS is $\sigma_{t\bar{t}} = 136 \pm 20(\text{stat.}) \pm 40(\text{syst.}) \pm 8(\text{lumi.})$ pb [13], which is based on a data sample corresponding to 1.09 fb^{-1}.

2.6 Combination of measurements

The combination takes into account correlated systematic uncertainties between the channels. The result presented by ATLAS combines the single-lepton, dilepton and all-hadronic final states, and finds a value of $\sigma_{t\bar{t}} = 177 \pm 3(\text{stat.})^{+8}_{-7}(\text{syst.}) \pm 7(\text{lumi.})$ pb [14]. CMS combines the single-lepton, dilepton, τ+μ and the all hadronic channels which yields a value of $\sigma_{t\bar{t}} = 165.8 \pm 2.2(\text{stat.}) \pm 10.6(\text{syst.}) \pm 7.8(\text{lumi.})$ pb [15]. The measurements used for the combination presented here and the comparison to the approximate NNLO calculation are shown in Fig. 1 and are in good agreement with the SM expectation.

3 Conclusions

The pp run in 2010-2011 at $\sqrt{s} = 7$ TeV of the LHC has been very successful, with up to 4.7 fb^{-1} of data recorded by the ATLAS and CMS experiments. The measured $t\bar{t}$ cross section in various final states is found to be in agreement with the SM expectation. The precision of all the measurements presented here is driven by systematic uncertainties, and reaches levels that are comparable or below the uncertainties of theoretical predictions.

References

1. M. Aliev et al., Comput. Phys. Commun.182 (2011) 1034-1046, arXiv:1007:1327 [hep-ph].
2. ATLAS Collaboration, JINST 3 (2008) S08003.
3. CMS Collaboration, JINST 3 (2008) S08004.
4. ATLAS Collaboration, ATLAS-CONF-2011-121, http://cdsweb.cern.ch/record/1376413.
5. CMS Collaboration, CMS-PAS-TOP-11-003, https://cdsweb.cern.ch/record/1386709.

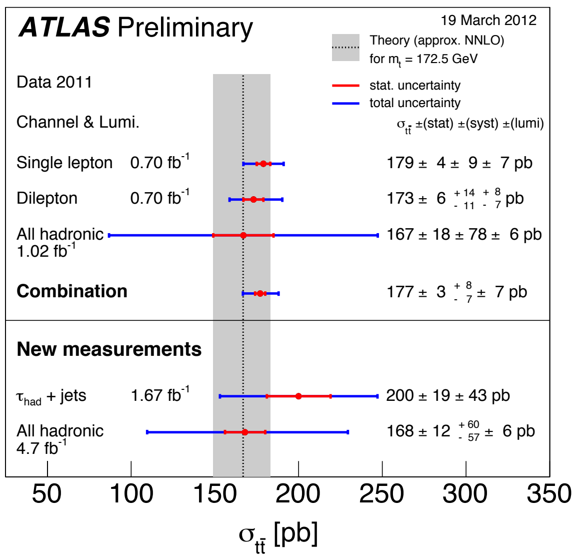

(a)

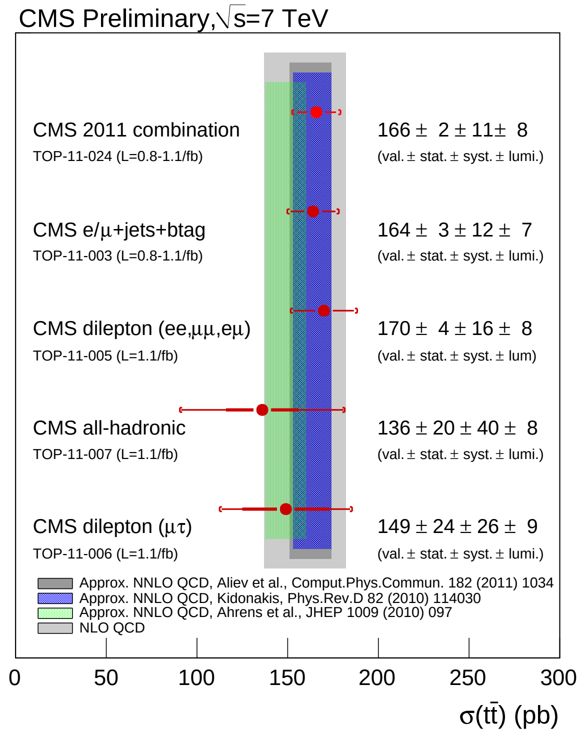

(b)

Figure 1: The measured value of $\sigma_{t\bar{t}}$ by ATLAS (a) and CMS (b) in various channels at $\sqrt{s} = 7$ TeV and the resulting combination. Error bars include statistical and systematic uncertainties. The approximate NNLO prediction with its uncertainty is also shown.

6. ATLAS Collaboration, CERN-PH-EP-2011-223, arXiv:1202.4892.
7. CMS Collaboration, CMS-PAS-TOP-11-005, http://cdsweb.cern.ch/record/1377323.
8. CMS Collaboration, CMS-PAS-PFT-10-004, https://cdsweb.cern.ch/record/1279358, CMS Collaboration, CMS-PAS-TAU-11-001, https://cdsweb.cern.ch/record/1337004.
9. ATLAS Collaboration, ATLAS-CONF-2011-119, http://cdsweb.cern.ch/record/1376411.
10. CMS Collaboration, CMS-PAS-TOP-11-006, http://cdsweb.cern.ch/record/1371010.
11. ATLAS Collaboration, ATLAS-CONF-2012-032, https://cdsweb.cern.ch/record/1432196.
12. ATLAS Collaboration, ATLAS-CONF-2012-031, http://cdsweb.cern.ch/record/1432196.
13. CMS Collaboration, CMS-PAS-TOP-11-007, http://cdsweb.cern.ch/record/1371755.
14. ATLAS Collaboration, ATLAS-CONF-2012-024, http://cdsweb.cern.ch/record/1430733.
15. CMS Collaboration, CMS-PAS-TOP-11-024, http://cdsweb.cern.ch/record/1401250.

NNLL threshold resummation for the total top-pair production cross section

Martin Beneke[a,b], Pietro Falgari[c], Sebastian Klein[b], Jan Piclum[a,b], Christian Schwinn[d]

a: Physik Department T31, Technische Universität München, James-Franck-Straße, D - 85748 Garching, Germany

b: Institut für Theoretische Teilchenphysik und Kosmologie, RWTH Aachen University, D–52056 Aachen, Germany

c: Institute for Theoretical Physics and Spinoza Institute, Utrecht University, 3508 TD Utrecht, The Netherlands

d: Albert-Ludwigs Universität Freiburg, Physikalisches Institut, D-79104 Freiburg, Germany

We present predictions for the total top-quark pair production cross section at the Tevatron and the LHC with 7, 8 and 14 TeV centre-of-mass energy, including the resummation of threshold logarithms and Coulomb corrections through next-to-next-to-leading logarithmic order, and $t\bar{t}$ bound-state contributions. The remaining theoretical and PDF uncertainties and prospects for the measurement of the top mass from the total cross section are discussed.

1 Introduction

After the discovery of the top quark at the Tevatron and the initial determination of its properties like mass, decay width, and the coupling to other particles, the LHC is currently opening the door to precision studies with hundreds of thousands of top-antitop pairs produced per year. One of the key observables is the top-quark pair production cross-section that has now been measured with an accuracy of seven percent both at Tevatron and LHC. At the LHC, the combinations of measurements in different channels yield the results [1]

$$\sigma_{t\bar{t}} = \begin{cases} 177 \;\; \pm 3 \;\; (\text{stat.}) \pm 8 \quad\;\; (\text{syst.}) \pm 7 \;\; (\text{lumi.})\ \text{pb}, & \text{ATLAS} \\ 165.8 \pm 2.2\ (\text{stat.}) \pm 10.6\ (\text{syst.}) \pm 7.8\ (\text{lumi.})\ \text{pb}, & \text{CMS} \end{cases} \tag{1}$$

Since the uncertainty of theoretical predictions based on next-to-leading order (NLO) calculations [2] in QCD and next-to-leading-logarithmic (NLL) higher-order effects [3] is larger than 10%, higher-order corrections have to be included in order to match the experimental precision. In the absence of the complete NNLO corrections that are currently being computed,[a] the theoretical precision can be improved by including higher-order QCD corrections that are enhanced in the partonic threshold limit, $\beta = \sqrt{1 - 4m_t^2/\hat{s}} \to 0$, where $\hat{s}$ is the partonic centre-of-mass energy. These contributions take the form of logarithmic corrections proportional to $(\alpha_s \log^{2,1} \beta)^n$ due to the emission of soft gluons, and of Coulomb corrections $(\alpha_s/\beta)^n$ due to the virtual exchange of gluons between the slowly moving top quarks. Both corrections can be resummed to all

[a] For a status report see. [4] The result for the quark-antiquark initial state was obtained very recently. [5]

$\sigma_{t\bar{t}}$[pb]	Tevatron	LHC ($\sqrt{s}$ =7 TeV)	LHC ($\sqrt{s}$ =8 TeV)	LHC ($\sqrt{s}$ =14 TeV)
NLO	$6.68^{+0.36+0.51}_{-0.75-0.45}$	$158.1^{+18.5+13.9}_{-21.2-13.1}$	$226.2^{+27.8+19.1}_{-29.7-17.8}$	$884^{+107+65}_{-106-58}$
NNLO$_{\text{app}}$	$7.06^{+0.27+0.69}_{-0.34-0.53}$	$161.1^{+12.3+15.2}_{-11.9-14.5}$	$230.0^{+16.7+20.5}_{-15.7-19.8}$	891^{+76+64}_{-69-63}
NNLL	$7.22^{+0.31+0.71}_{-0.47-0.55}$	$162.6^{+7.4+15.4}_{-7.5-14.7}$	$231.9^{+10.5+20.8}_{-10.3-20.1}$	896^{+40+65}_{-37-64}

Table 1: $t\bar{t}$ cross section at Tevatron and LHC in various approximations, for $m_t = 173.3\,\text{GeV}$ using the MSTW08 PDFs. The first error denotes the total theoretical uncertainty, the second the 90% c.l. PDF+α_s uncertainty.

orders in perturbation theory, leading to a representation of the partonic cross sections for the subprocesses $pp' \to t\bar{t}X$ (with $p, p' \in \{g, q, \bar{q}\}$) of the form

$$\begin{aligned}\hat{\sigma}_{pp'} &= \hat{\sigma}^{(0)}_{pp'} \sum_{k=0} \left(\frac{\alpha_s}{\beta}\right)^k \exp\Big[\underbrace{\ln\beta\, g_0(\alpha_s \ln\beta)}_{\text{(LL)}} + \underbrace{g_1(\alpha_s \ln\beta)}_{\text{(NLL)}} + \underbrace{\alpha_s g_2(\alpha_s \ln\beta)}_{\text{(NNLL)}} + \ldots\Big] \\ &\quad \times \left\{1\,(\text{LL,NLL}); \alpha_s\,(\text{NNLL}); \alpha_s^2, \beta^2\,(\text{N}^3\text{LL}); \ldots\right\}\,. \qquad (2)\end{aligned}$$

Several recent developments have made it possible to perform resummation at NNLL accuracy: the function g_2 has been computed [6] using the infrared structure of massive QCD amplitudes, [7] while the $\mathcal{O}(\alpha)$ coefficient functions [8] and the NNLO Coulomb effects [9] became available as well. The combined resummation of soft and Coulomb corrections has been established in. [10]

2 Results from NNLL resummation

In [11] we have performed the combined NNLL resummation of soft and Coulomb effects using the momentum-space approach to soft-gluon resummation [12] and results for the higher-order Coulomb corrections, [13] including would-be bound-state contributions to the cross section. We extend these results in table 1 by providing predictions for the LHC at a centre-of-mass energy of 8 TeV in addition to the results for Tevatron and the LHC at 7 and 14 TeV. Results for different values of m_t at 8 TeV (updated to include the NNLO $q\bar{q}$ partonic cross section [5]), as well as for hypothetical heavy quarks will be presented elsewhere. [14] For comparison, the table also includes the NLO cross section [2] and the approximate NNLO results [9] obtained by expanding the resummed corrections to $\mathcal{O}(\alpha_s^2)$. The theoretical uncertainty of the approximate NNLO results includes an estimate of the unknown constant NNLO contribution to the cross section; the NNLL uncertainties include in addition an estimate of higher-order ambiguities based on comparing different NNLL implementations and expansions to N^{3}LO accuracy as discussed in detail in. [11] Compared to the NLO results, the NNLL corrections increase the cross section by 8% at the Tevatron and $1-3\%$ at the LHC. The main effect of the NNLL corrections is included in the NNLO$_{\text{app}}$ result, with further higher-order corrections of about 2% at the Tevatron, and $\lesssim 1\%$ at the LHC. The NNLO$_{\text{app}}$ and NNLL results include two-loop Coulomb and soft/Coulomb interference effects of the order of $1-2\%$, while Coulomb corrections beyond NNLO and bound-state contributions of the order of 0.5% [11] are included in addition at NNLL.

In the left panel of figure 1 we compare our results (denoted by black circles) for the LHC at $\sqrt{s} = 7$ TeV to predictions by other groups and experimental measurements. The NNLL resummation of soft-gluon corrections using the traditional Mellin-space approach [15] (denoted by a green square) differs from our results in the treatment of constant NNLO and power-suppressed terms, in addition to the different resummation formalism. Further results have been obtained by integrating NNLL or approximate NNLO predictions for invariant-mass or p_T-distributions. [16,17] These calculations (denoted by a blue triangle/red diamonds) include some power suppressed contributions in β, but not the NNLO potential terms. [9] All the approximations [15,16,17] differ

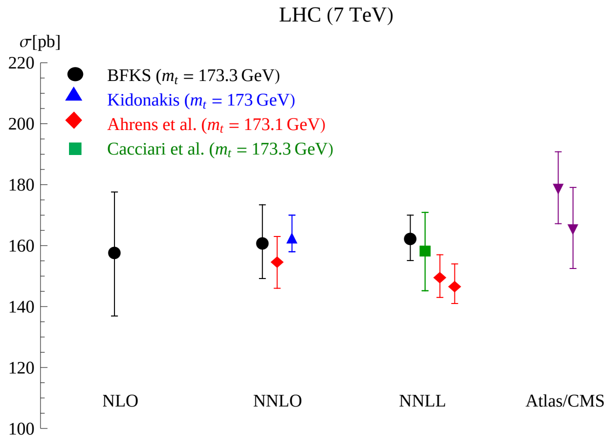

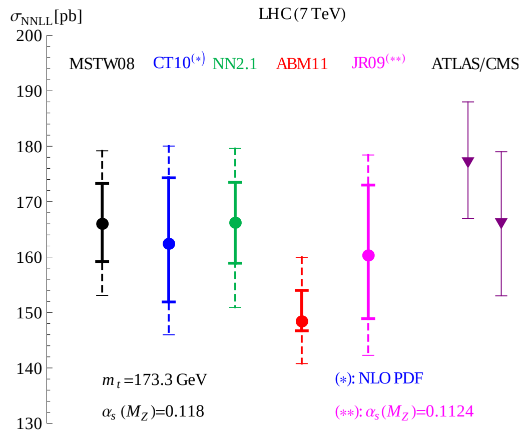

Figure 1: Left: Comparison of different NNLO and NNLL predictions, see the text for explanation and references. The error bands include theoretical uncertainties, but no PDF+α_s errors. Right: NNLL predictions for different PDF sets with fixed $\alpha_s(M_Z) = 0.118$. The inner (solid) error bar denotes the 68% confidence level PDF+α_s error, the outer (dashed) error bar includes in addition the uncertainty of the NNLL cross-section calculation. Both figures include also the most recent experimental measurements that assume $m_t = 172.5$ GeV.

from ours by neglecting the higher-order Coulomb effects. While the predictions agree within the quoted uncertainties at the LHC,[b] the different central values indicate the ambiguities inherent in threshold approximations and illustrate the possible impact of a full NNLO calculation.

In addition to the top-quark mass and the strong coupling, the top-pair cross section depends also on the parton distribution functions (PDFs). Due to the dominant gluon fusion channel, uncertainties in the determination of the gluon PDF have a large impact on the cross section at the LHC and constitute the main theoretical uncertainty. This is illustrated in the right panel of figure 1 where the results of the MSTW08NNLO PDF [18] used as our default are compared to the NNLO PDF sets by NNPDF2.1, [19] ABM11 [20] and JR09VR. [21] As illustration, results from the NLO PDF CT10 [22] are also included. In this comparison, a common central value $\alpha_s(M_Z) = 0.118$ of the strong coupling [c] is employed instead of the best-fit values used as default by the PDF sets (note that the MSTW08NNLO default $\alpha_s(M_Z) = 0.1171$ is used in the left panel of Figure 1). For the common α_s-value, the predictions of most PDFs agree within the 68% confidence level of the PDF+α_s uncertainty (denoted by the inner, solid error bar), but it is also seen that the spread is larger than estimated by the uncertainty of a single PDF set.

As an application of a precise theoretical prediction of the total top-pair cross section, the top-quark mass can be extracted in a theoretically well defined mass definition from the measured cross section, assuming the latter is free of new-physics contributions. [23] Using our NNLL predictions discussed above, we have estimated that the top-quark pole mass could be extracted with an accuracy of ±5 GeV from the currently available ATLAS data on the total cross section, and our result [11] $m_t = 169.8^{+4.9}_{-4.7}$ GeV is compatible with the direct mass determination $m_t = 173.2 \pm 0.8$ GeV at the Tevatron. [24] A CMS analysis [25] of a cross section measurement with a smaller central value but larger uncertainty, $\sigma_{t\bar{t}} = 169.90 \pm 3.9$ (stat.) ± 16.3 (syst.)± 7.6 (lumi.) pb, obtained the comparable result $m_t = 170.3^{+7.3}_{-6.7}$ GeV using the calculation of. [23]

3 Summary and outlook

We have reviewed the results of the NNLL resummation of soft and Coulomb-gluon corrections performed in [11] and extended them by including predictions for the LHC at $\sqrt{s} = 8$ TeV and

[b] Somewhat larger discrepancies are found at the Tevatron, see for instance. [11]

[c] With the exception of the JR09 PDF where $\alpha_s(M_Z) = 0.1124$ is used.

for different PDF sets. Our results are in good agreement with experimental measurements. We plan to make our calculation available in form of a public program in the near future.[14] We have discussed the impact of the uncertainty of current PDF sets on the cross-section predictions. The prospects to constrain the gluon PDF by the top-pair cross-section measurement will be investigated in.[14] It has been estimated that the top-quark pole mass could be measured with a precision of ±5 GeV from current LHC cross-section measurements.

References

1. I. Aracena, these proceedings; Conference notes ATLAS-CONF-2012-024, CMS PAS TOP-11-024.
2. P. Nason, S. Dawson, and R. K. Ellis, *Nucl. Phys.* **B303** (1988) 607.
3. N. Kidonakis and G. Sterman, *Nucl. Phys.* **B505** (1997) 321, `arXiv:hep-ph/9705234`; R. Bonciani et al.,*Nucl. Phys.* **B529** (1998) 424, `arXiv:hep-ph/9801375`.
4. R. Bonciani et al., *PoS* **ICHEP2010** (2010) 098, `arXiv:1012.0258 [hep-ph]`.
5. A. Mitov, these proceedings; P. Bärnreuther, M. Czakon and A. Mitov, `arXiv:1204.5201 [hep-ph]`.
6. M. Beneke, P. Falgari, and C. Schwinn, *Nucl. Phys.* **B828** (2010) 69, `arXiv:0907.1443 [hep-ph]`; M. Czakon, A. Mitov, and G. Sterman, *Phys. Rev.* **D80** (2009) 074017, `arXiv:0907.1790 [hep-ph]`.
7. T. Becher and M. Neubert, *Phys. Rev.* **D79** (2009) 125004, `arXiv:0904.1021 [hep-ph]`; A. Ferroglia et al., *Phys. Rev. Lett.* **103** (2009) 201601, `arXiv:0907.4791 [hep-ph]`.
8. M. Czakon and A. Mitov, *Phys. Lett.* **B680** (2009) 154, `arXiv:0812.0353 [hep-ph]`.
9. M. Beneke, M. Czakon, P. Falgari, A. Mitov, and C. Schwinn, *Phys. Lett.* **B690** (2010) 483–490, `arXiv:0911.5166 [hep-ph]`.
10. M. Beneke, P. Falgari, and C. Schwinn, *Nucl. Phys.* **B842** (2011) 414, `arXiv:1007.5414 [hep-ph]`.
11. M. Beneke, P. Falgari, S. Klein, and C. Schwinn, *Nucl.Phys.* **B855** (2012) 695, `arXiv:1109.1536 [hep-ph]`.
12. T. Becher and M. Neubert, *Phys. Rev. Lett.* **97** (2006) 082001, `hep-ph/0605050`.
13. M. Beneke, A. Signer, and V. A. Smirnov, *Phys. Lett.* **B454** (1999) 137–146, `arXiv:hep-ph/9903260`.
14. M. Beneke, P. Falgari, S. Klein, J. Piclum, C. Schwinn, M. Ubiali and F. Yan, in preperation.
15. M. Cacciari et al., Phys. Lett. B **710**, 612 (2012) `arXiv:1111.5869 [hep-ph]`.
16. N. Kidonakis, Phys. Rev. D **82** (2010) 114030 `arXiv:1009.4935 [hep-ph]`.
17. V. Ahrens et al.,Phys. Lett. B **703** (2011) 135 `arXiv:1105.5824 [hep-ph]`.
18. A. D. Martin, W. J. Stirling, R. S. Thorne, and G. Watt, *Eur. Phys. J.* **C63** (2009) 189–285, `arXiv:0901.0002 [hep-ph]`.
19. R. D. Ball *et al.*, Nucl. Phys. B **855** (2012) 153, `arXiv:1107.2652 [hep-ph]`.
20. S. Alekhin, J. Blümlein and S. Moch, `arXiv:1202.2281 [hep-ph]`.
21. P. Jimenez-Delgado and E. Reya, *Phys. Rev.* **D79** (2009) 074023, `arXiv:0810.4274 [hep-ph]`.
22. H. -L. Lai et al., Phys. Rev. D **82** (2010) 074024 `arXiv:1007.2241 [hep-ph]`.
23. U. Langenfeld, S. Moch, and P. Uwer, *Phys. Rev.* **D80** (2009) 054009, `arXiv:0906.5273 [hep-ph]`.
24. Tevatron Electroweak Working Group, `arXiv:1107.5255 [hep-ex]`, O. Brandt, these proceedings , `arXiv:1204.0919 [hep-ex]`.
25. M. Aldaya *et al.* [for the CMS Collaboration], `arXiv:1201.5336 [hep-ex]`.

MEASUREMENTS OF THE TOP QUARK MASS AT THE TEVATRON

O. Brandt on behalf of the CDF and D0 Collaborations
II. Physikalisches Institut, Friedrich-Hund-Platz 1,
Göttingen, Germany

The mass of the top quark (m_{top}) is a fundamental parameter of the standard model (SM). Currently, its most precise measurements are performed by the CDF and D0 collaborations at the Fermilab Tevatron $p\bar{p}$ collider at a centre-of-mass energy of $\sqrt{s} = 1.96$ TeV. We review the most recent of those measurements, performed on data samples of up to 8.7 fb^{-1} of integrated luminosity. The Tevatron combination using up to 5.8 fb^{-1} of data results in a preliminary world average top quark mass of $m_{\text{top}} = 173.2 \pm 0.9$ GeV. This corresponds to a relative precision of about 0.54%. We conclude with an outlook of anticipated precision the final measurement of m_{top} at the Tevatron.

PACS `14.65.Ha` – Top quarks.

1 Introduction

The pair-production of the top quark was discovered in 1995 by the CDF and D0 experiments [1] at the Fermilab Tevatron proton-antiproton collider. Observation of the electroweak production of single top quarks was presented only two years ago [2]. The large top quark mass and the resulting Yukawa coupling of almost unity indicates that the top quark could play a crucial role in electroweak symmetry breaking. Precise measurements of the properties of the top quark provide a crucial test of the consistency of the SM and could hint at physics beyond the SM.

In the following, we review measurements of the top quark mass at the Tevatron, which is a fundamental parameter of the SM. Its precise knowledge, together with the mass of the W boson (m_W), provides an important constraint on the mass of the postulated SM Higgs boson. This is illustrated in the m_{top},m_W plane in Fig. 1, which includes the recent, most precise measurements of m_W reviewed in Ref. [3]. Measurements of properties of the top quark other than m_{top} are reviewed in Ref. [4]. The full listing of top quark measurements at the Tevatron can be found in Refs. [5,6].

At the Tevatron, top quarks are mostly produced in pairs via the strong interaction. By the end of Tevatron operation, about 10.5 fb^{-1} of integrated luminosity per experiment were recorded by CDF and DØ, which corresponds to about 80k produced $t\bar{t}$ pairs. In the framework of the SM, the top quark decays to a W boson and a b quark nearly 100% of the time, resulting in a $W^+W^-b\bar{b}$ final state from top quark pair production. Thus, $t\bar{t}$ events are classified according to the W boson decay channels as “dileptonic”, “all–jets”, or “lepton+jets”. More details on the channels and their experimental challenges can be found in Ref. [7], while the electroweak production of single top quarks is reviewed in Ref. [8].

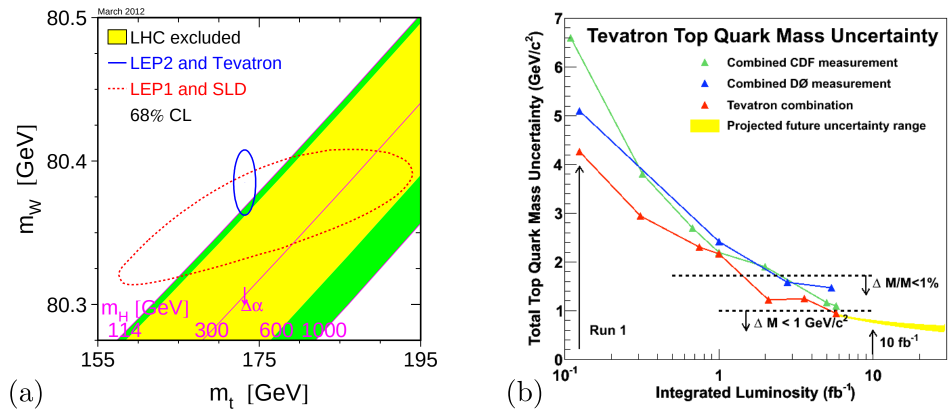

Figure 1: **(a)** The constraint on mass of the SM Higgs boson from direct $m_{\rm top}$ and m_W measurements in the $m_{\rm top}$,m_W plane. The red ellipsis indicates the 68% CL contour. **(b)** The anticipated precision on $m_{\rm top}$ measurements at D0 and the Tevatron combination versus integrated luminosity.

2 Direct measurements of the top quark mass in $\ell + $jets final states

D0's most precise measurement of $m_{\rm top}$ is performed in $\ell + 4\,$jets final state using the so-called *matrix element* (ME) method in 3.6 fb^{-1} of data [10]. This technique was pioneered by DØ in Run I of the Tevatron [9], and it calculates the probability that a given event, characterised by a set of measured observables x, comes from the $t\bar{t}$ production given an $m_{\rm top}$ hypothesis, or from a background process: $\mathcal{P}_{\rm evt}(x) \propto f\mathcal{P}_{\rm sig}(x,m_{\rm top})+(1-f)\mathcal{P}_{\rm bgr}$. The dependence on $m_{\rm top}$ is explicitly introduced by calculating $\mathcal{P}_{\rm sig}$ using the differential cross section ${\rm d}\sigma(y,m_{\rm top}) \propto |\mathcal{M}_{t\bar{t}}|^2(m_{\rm top})$, where $\mathcal{M}_{t\bar{t}}$ is the leading order (LO) matrix element for $t\bar{t}$ production:

$$\mathcal{P}_{\rm sig}(x,m_{\rm top},k_{\rm JES}) = \frac{1}{\sigma^{\rm observed}_{t\bar{t}}} \cdot \int W(x,y,k_{\rm JES})\ {\rm d}\sigma(y,m_{\rm top})\,.$$

Since ${\rm d}\sigma(y,m_{\rm top})$ is defined for a set of parton-level observables y, the transfer function $W(x,y,k_{\rm JES})$ is used to map them to the reconstruction-level set x. This accounts for detector resolutions and acceptance cuts, and introduces explicitly the dependence on the jet energy scale (JES) via an overall scaling factor $k_{\rm JES}$. The uncertainty on the JES, which is almost fully correlated with $m_{\rm top}$, is around 2% or larger. Therefore, an *in situ* calibration is performed by requiring that the mass of the dijet system assigned to the parton pair from the hadronically decaying W boson be $m_{jj} = 80.4$ GeV. Thus, $m_{\rm top}$ and $k_{\rm JES}$ are extracted simultaneously. This reduces the uncertainty from the JES to about 0.5%, decreasing with the number of selected $t\bar{t}$ events. The measurement is performed in events with four jets, resulting in 24 possible jet-parton assignments. All 24 are summed over, weighted according to the consistency of a given assignment with the b-tagging information. $\mathcal{P}_{\rm bgr}$ is calculated using the VECBOS matrix element for $W + 4$ jets production. Generally, the ME technique offers a superior statistical sensitivity as it uses the full topological and kinematic information in the event in form of 4-vectors. The drawback of this method is the high computational demand.

D0 measures $m_{\rm top} = 174.9 \pm 0.8$ (stat) $\pm\, 0.8$ (JES) $\pm\, 1.0$ (syst) GeV, corresponding to a relative uncertainty of 0.9%. The dominant systematic uncertainties are from modeling of underlying event activity and hadronisation, as well as the colour reconnection effects. On the detector modeling side, diffential uncertainties on the JES which are compatible with the overall $k_{\rm JES}$ value from *in situ* calibration, and the difference between the JES for light and b-quark jets are dominant. This picture is representative for all $m_{\rm top}$ measurements in $\ell + $jets final states shown here.

CDF employs the ME technique similar to that used at D0 to measure $m_{\rm top}$ on a dataset corresponding to 5.6 fb^{-1}and finds $m_{\rm top} = 173.0 \pm 0.7$ (stat) $\pm\, 0.6$ (JES) $\pm\, 0.9$ (syst) GeV [11].

Most notable differences from the D0 measurement are: (i) background events present in the data sample are accounted for on *average* rather than on an event-by-event basis using a likelihood based on a neural network output, (ii) the contribution of "mismeasured" signal events, where one of the jets cannot be matched to a parton, is reduced with a cut on the aforementioned likelihood.

Currently, the world's best single measurement of $m_{\rm top}$ is performed by CDF in $\ell+$jets final states using the so-called *template* method to analyse the full dataset of 8.7 fb^{-1} [12]. The basic idea of the template method is to construct "templates", i.e. distributions in a set of variables x, which are sensitive to $m_{\rm top}$, for different mass hypotheses, and extract $m_{\rm top}$ by matching them to the distribution found in data, e.g. via a maximum likelihood fit. CDF minimises a χ^2-like function to kinematically reconstruct the event for jet-parton assignments consistent with the b-tagging information. To extract $m_{\rm top}$and calibrate the JES *in-situ*, three-dimensional templates are defined in (i) the fitted $m_{\rm top}$ of the best jet-parton assignment, (ii) the fitted $m_{\rm top}$ of the second-best assignment, and (iii) the fitted invariant mass of the dijet system from the hadronically decaying W boson. CDF finds $m_{\rm top} = 172.9\ \pm 0.7$ (stat) $\pm\, 0.8$ (syst) GeV.

3 Direct measurement of the top quark mass in all-hadronic final states

The third most statistically significant contribution to the current Tevatron average of $m_{\rm top}$ comes from a measurement in $6 \leq N_{\rm jets} \leq 8$ final states by CDF using $5.8\,{\rm fb}^{-1}$ of data [13]. The main challenge is the high level of the background contribution from QCD multijet production: the $S:B$ ratio is about $1:1200$ after a multijet trigger requirement. Therefore, a discrimination variable $\mathcal{D}_{\rm NN}$ is constructed with a multilayered NN. Beyond typical kinematic and topological variables like $\not{p}_{\rm T}$, also jet shape variables like the second moment in η and ϕ which provide discrimination between quark and gluon jets, are used as inputs. To enhance the purity of the sample and to reduce the number of combinatoric possibilities, b tagging is applied. For each jet–parton assignment, a χ^2 is constructed which accounts for: the consistency of the two dijet pairs with the reconstructed m_W, the consistency of the jjb combinations with the reconstructed $m_{\rm top}$, and the consistency of the individual fitted jet momenta with the measured ones, within experimental resolutions. The final sample for top mass extraction is defined by $\mathcal{D}_{\rm NN} > 0.97$ (0.84) for events with 1 (≥ 2) b tags, yielding a signal to background ratio of $1:3$ ($1:1$). The measured value is $m_{\rm top} = 172.5\ \pm 1.4$ (stat) $\pm\, 1.4$ (syst) GeV. Beyond systematic uncertainties relevant in $\ell+$jets final states, potential biases from the data-driven background model pose a notable contribution to the total uncertainty.

4 Direct measurement of the top quark mass in dilepton final states

The world's most precise measurement of $m_{\rm top}$ in dilepton final states is performed by D0 using 4.7 fb^{-1} of data [14]. Leaving $m_{\rm top}$ as a free parameter, dilepton final states are kinematically underconstrained by one degree of freedom, and the so-called neutrino weighting algorithm is applied for kinematic reconstruction. It postulates distributions in rapidities of the neutrino and the antineutrino, and calculates a weight, which depends on the consistency of the reconstructed $\vec{p}_{\rm T}^{\,\nu\bar\nu} \equiv \vec{p}_{\rm T}^{\,\nu} + \vec{p}_{\rm T}^{\,\bar\nu}$ with the measured missing transverse momentum $\not{p}_{\rm T}$ vector, versus $m_{\rm top}$. D0 uses the first and second moment of this weight distribution to define templates and extract $m_{\rm top}$. To reduce the systematic uncertainty, the *in situ* JES calibration in $\ell+$jets final states derived in Ref. [10] is applied, accounting for differences in jet multiplicity, luminosity, and detector ageing. After calibration and all corrections, $m_{\rm top} = 174.0\ \pm 2.4$ (stat) $\pm\, 1.4$ (syst) GeV is found.

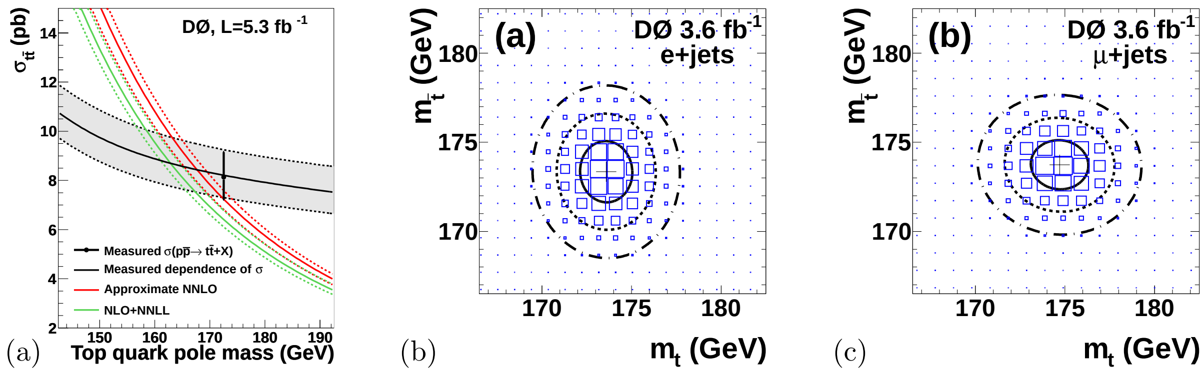

Figure 2: **(a)** $\sigma_{t\bar{t}}$ measured by D0 using 5.3 fb^{-1} (black line) and theoretical NLO+NNLL [16] (green solid line) and approximate NNLO [17] (red solid line) predictions as a function of $m_{\rm top}^{\rm pole}$, assuming $m_{\rm top}^{\rm MC} = m_{\rm top}^{\rm pole}$. The gray band corresponds to the total uncertainty on measured $\sigma_{t\bar{t}}$. The dashed lines indicate theoretical uncertainties from the choice of scales and parton distribution functions. **(b)** m_t and $m_{\bar{t}}$ measured by D0 directly and independently using 3.6 fb^{-1}in $e+$jetsfinal states. The solid, dashed, and dash-dotted lines represent the 1, 2, and 3 SD contours. **(c)** same as (b) but for $\mu+$jets.

5 Measurement of $m_{\rm top}$ from the $t\bar{t}$ production cross-section

The $t\bar{t}$ production cross section ($\sigma_{t\bar{t}}$) is correlated to $m_{\rm top}$. This can be used to extract $m_{\rm top}$ by comparing the measured $\sigma_{t\bar{t}}$ to the most complete to–date, fully inclusive theoretical predictions, assuming the validity of the SM. Such calcualtions offer the advantage of using mass definitions in well-defined renormalisation schemes like $m_{\rm top}^{\overline{\rm MS}}$ or $m_{\rm top}^{\rm pole}$. In contrast, the main methods using kinematic fits utilise the mass definition in MC generators $m_{\rm top}^{\rm MC}$, which cannot be translated into $m_{\rm top}^{\overline{\rm MS}}$ or $m_{\rm top}^{\rm pole}$ in a straightforward way. D0 uses 5.3 fb^{-1} of data to measure $\sigma_{t\bar{t}}$ and extracts $m_{\rm top}$ [15] using theoretical calculations for $\sigma_{t\bar{t}}$ like the next-to-leading order (NLO) calculation with next-to-leading logarithmic (NLL) terms resummed to all orders [16], an approximate NNLO calculation [17], and others. For this, a correction is derived to account for the weak dependence of $\sigma_{t\bar{t}}$ on $m_{\rm top}^{\rm MC}$. The results for $m_{\rm top}^{\rm pole}$are presented in Fig. 2, and can be summarised as follows: $m_{\rm top}^{\rm pole} = 163.0^{+5.1}_{-4.6}$ GeV and $m_{\rm top}^{\rm pole} = 167.5^{+5.2}_{-4.7}$ GeV for Ref. [16] and [17], respectively. The effect from interpreting $m_{\rm top}^{\rm MC}$ as $m_{\rm top}^{\overline{\rm MS}}$ or $m_{\rm top}^{\rm pole}$ is found to be about 3 GeV.

6 Measurements of the mass difference between the t and $\bar{t}$ quarks

The invariance under $\mathcal{CPT}$ transformations is a fundamental property of the SM. $m_{\rm particle} \neq m_{\rm antiparticle}$ would constitute a violation of $\mathcal{CPT}$, and has been tested extensively in the charged lepton sector. Given its short decay time, the top quark offers a possiblity to test $m_t = m_{\bar{t}}$ at the %-level, which is unique in the quark sector. D0 applies the ME technique to measure m_t and $m_{\bar{t}}$ directly and independently using 3.6 fb^{-1} of data, and finds $\Delta m \equiv m_t - m_{\bar{t}} = 0.8 \pm 1.8$ GeV [18], in agreement with the SM prediction. The results are illustrated in Fig. 2. With 0.5 GeV, the systematic uncertainty on Δm is much smaller than that on $m_{\rm top}$ due to cancellations in the difference, and is dominated by the uncertainty on the difference in calorimeter response to b and $\bar{b}$ quark jets. CDF uses a template-based method and a kinematic reconstruction similar to that in Ref. [12] to measure Δm directly given the constraint $\frac{m_t+m_{\bar{t}}}{2} \equiv 172.5$ GeV from 8.7 fb^{-1} of data, and finds $\Delta m = -2.0 \pm 1.3$ GeV [19].

7 Tevatron combination and outlook

Currently, the world's most precise measurements of $m_{\rm top}$ are performed by CDF and D0 collaborations in $\ell+$jets final states. The preliminary Tevatron combination using up to 5.8 fb^{-1}

of data results in $m_{\rm top} = 173.2 \pm 0.9$ GeV [20], corresponding to a relative uncertainty of 0.54%.

With about 10.5 $\rm fb^{-1}$ recorded, the precision on $m_{\rm top}$ is expected to further improve, especially at D0, where only 3.6 $\rm fb^{-1}$ are used in the flagship measurement in $\ell+$jets final states. This applies not only to the statistical uncertainty, but also to several systematic uncertainties due to the limited size of calibration samples, like e.g. some components of the JES. Moreover, efforts are underway to better understand systematic uncertainties from the modeling of $t\bar{t}$ signal, in particular the dominating uncertainty from different hadronisation and underlying event models. We look forward to exciting updates of $m_{\rm top}$ measurements presented here.

With uncertainties approaching $\mathcal{O}$(GeV) at the LHC [21], we strongly advocate to start preparations towards the first world-wide combination of the measurements of the top quark mass including ATLAS and CMS results.

Acknowledgments

I would like to thank my collaborators from the CDF and D0 experiments for their help in preparing this article. I also thank the staffs at Fermilab and collaborating institutions, as well as the CDF and D0 funding agencies.

References

1. F. Abe *et. al.* (CDF Coll.), Phys. Rev. Lett. **74**, 2626 (1995), S. Abachi *et. al.* (D0 Coll.), Phys. Rev. Lett. **74**, 2632 (1995).
2. T. Aaltonen *et. al.* (CDF Coll.), Phys. Rev. Lett. **103**, 092001 (2009), V. M. Abazov *et. al.* (D0 Coll.), Phys. Rev. Lett. **103**, 092002 (2009).
3. R. Lopes de Sà, these proceedings.
4. D. Mietlicki, these proceedings; A. Lister, these proceedings.
5. `http://www-cdf.fnal.gov/physics/new/top/public_mass.html`
6. `http://www-d0.fnal.gov/Run2Physics/WWW/results/top.htm`, `http://www-d0.fnal.gov/Run2Physics/WWW/documents/Run2Results.htm`.
7. I. Aracena, these proceedings.
8. W. Bu, these proceedings; R. G. Suarez, these proceedings.
9. V. M. Abazov *et. al.* (D0 Collaboration), Nature **429**, 638 (2004).
10. V. M. Abazov *et. al.* (D0 Coll.), Phys. Rev. D **84**, 032004 (2011).
11. T. Aaltonen *et. al.* (CDF Coll.), Phys. Rev. Lett. **105**, 252001 (2010).
12. T. Aaltonen *et. al.* (CDF Coll.), CDF Conf. Note 10761 (2012)
13. T. Aaltonen *et. al.* (CDF Coll.), CDF Conf. Note 10456 (2010).
14. V. M. Abazov *et. al.* (D0 Coll.), Fermilab-Pub-12/020-E, submitted to Phys. Rev. Lett., arXiv:1201.5172 [hep-ex] (2012).
15. V. M. Abazov *et. al.* (D0 Coll.), Phys. Lett. B **703**, 422 (2011).
16. V. Ahrens *et. al.*, J. High Energy Phys. **1009** (2010) 097, Nucl. Phys. B (Proc. Suppl.) 205-206 (2010) 48.
17. S. Moch, P. Uwer, Phys. Rev. D **78** (2008) 034003; U. Langenfeld, S. Moch, P. Uwer, Phys. Rev. D **80** (2009) 054009.
18. V. M. Abazov *et. al.* (D0 Coll.), Phys. Rev. D **84**, 052005 (2011).
19. T. Aaltonen *et. al.* (CDF Coll.), CDF Conf. Note 10777 (2012).
20. The Tevatron Electroweak Working Group and CDF and D0 Collaborations, arXiv:1007.5255 [hep-ex] (2011).
21. S. Blyweert, these proceedings.

TOP-QUARK MASS MEASUREMENTS AT THE LHC

S. Blyweert, on behalf of the ATLAS and CMS Collaborations
Vrije Universiteit Brussel - Interuniversity Institute for High Energies
Pleinlaan 2, 1050 Brussel, Belgium

The top-quark mass m_t is one of the fundamental parameters of the standard model (SM) of particle physics. The CDF and D0 collaborations already performed very precise measurements of m_t. Since the ATLAS and CMS collaborations already have a very large sample of top quark pairs available for analysis, they are producing results with increasing precision. An overview of the most recent measurements of m_t by ATLAS and CMS is given, using up to 4.7fb^{-1} of data in different $t\bar{t}$ decay channels. The measurement of the mass difference between top and antitop quarks is also shown. Finally, the combination of the individually measured m_t values is discussed, together with an outlook for future m_t measurements.

1 Introduction

The top quark, which was discovered in 1995 at the Tevatron, is the heaviest currently known fundamental particle. Its mass is an important parameter of the standard model, since it is an important input for the global Electro-Weak fits. These fits can be used to constrain the mass of the SM Brout-Englert-Higgs boson, and are also a consistency check of the standard model. m_t has been measured already by the CDF and D0 collaborations with great precision, resulting in $m_t = 173.2 \pm 0.9$ GeV as the current world average [1,2]. A precise measurement of m_t by the ATLAS and CMS collaborations at the Large Hadron Collider (LHC) would provide an independent cross-check of this value and would help to further reduce the total uncertainty on the world average of m_t.

In proton-proton collisions at $\sqrt{s} = 7$ TeV top quarks are dominantly produced in pairs. In 2011 the LHC delivered more than 5 fb^{-1} to both the ATLAS and CMS experiments, corresponding to about $8 \cdot 10^5$ $t\bar{t}$ pairs per experiment. This gave both ATLAS and CMS the opportunity to perform precise measurements of m_t in the different decay channels. Since top quarks decay most of the time into a b quark and a W boson, $t\bar{t}$ events can be categorized, according to the decay of the W bosons, in dileptonic ($t\bar{t} \to b\bar{b}\ell\nu_\ell\ell'\nu_{\ell'}$), all-jets ($t\bar{t} \to b\bar{b}qq'q''q'''$) and ℓ+jets ($t\bar{t} \to b\bar{b}\ell\nu_\ell qq'$) events. More information about the production and decay of $t\bar{t}$ events can be found in Ref. [3].

2 Direct measurements of the top-quark mass

2.1 Measurement of the top-quark mass in the dilepton channel

The m_t measurement from CMS in the dilepton channel is performed with 2.3 fb^{-1} of data [4]. Events in this channel are selected by requiring exactly two leptons (electrons (e) or muons (μ)) with $p_T > 20$ GeV and $|\eta| < 2.4$, at least 2 jets with $p_T > 30$ GeV and $|\eta| < 2.4$, missing transverse energy $\not{E}_{\mathrm{T}} > 30$ GeV, and at least one b-tagged jet. In the ee and $\mu\mu$ channels events with 76 GeV $< m_{\ell\ell} <$ 106 GeV are rejected. The event-by-event top-quark mass m_{KINb} is reconstructed with the KINb algorithm [5]. For each of the possible jet-quark assignments the kinematic equations are solved multiple times per event, each time varying the reconstructed kinematics within their resolutions. The jet-quark assignment with the largest number of solutions is selected. Finally, m_{KINb} is extracted by taking the mean of a Gaussian fit to the distribution of the reconstructed top quark mass for all the different solutions of the kinematic equations, for the chosen jet-quark assignment.

The extraction of m_{t} is then performed by applying the template method. Templates which are sensitive to m_{t} are constructed for different top-quark mass hypotheses. The value of m_{t} is then extracted by doing a maximum likelihood fit of these templates to the distribution of m_{KINb} observed in data. By applying this technique, CMS measures $m_{\mathrm{t}} = 173.3 \pm 1.2(\mathrm{stat})^{+2.5}_{-2.6}(\mathrm{syst})$ GeV, where the systematic uncertainty is dominated by the global Jet Energy Scale (JES) uncertainty and the uncertainty on the flavour-dependent JES. This is the most precise measurement of m_{t} in the dilepton channel, with similar precision as the most recent result from D0 [6].

2.2 *Measurement of the top-quark mass in the all-jets channel*

ATLAS performed the first measurement at the LHC of m_{t} in the all-jets channel, using 2.04 fb^{-1} of data [7]. Events are selected by asking ≥ 5 jets with $p_{\mathrm{T}} > 55$ GeV and $|\eta| < 4.5$, and a 6$^{\mathrm{th}}$ jet with $p_{\mathrm{T}} > 30$ GeV and $|\eta| < 4.5$. Two of these jets, with $p_{\mathrm{T}} > 55$ GeV and inside the inner detector acceptance ($|\eta| < 2.5$), must be b-tagged. A cut on the $\not{E}_{\mathrm{T}}$ significance is also applied: $\not{E}_{\mathrm{T}}/\sqrt{H_{\mathrm{T}}} < 3$, where H_{T} is the scalar sum of the p_{T} of all the jets in the events. The $\mathrm{t\bar{t}}$ event topology is reconstructed using a 'mass χ^2':

$$\chi^2 = \frac{(m_{j_1,j_2} - m_{\mathrm{W}})^2}{\sigma_{\mathrm{W}}^2} + \frac{(m_{j_1,j_2,b_1} - m_{\mathrm{t}})^2}{\sigma_{\mathrm{t}}^2} + \frac{(m_{j_3,j_4} - m_{\mathrm{W}})^2}{\sigma_{\mathrm{W}}^2} + \frac{(m_{j_3,j_4,b_2} - m_{\mathrm{t}})^2}{\sigma_{\mathrm{t}}^2}, \tag{1}$$

where $\sigma_{\mathrm{W}} = 10.2$ GeV and $\sigma_{\mathrm{t}} = 17.4$ GeV are the respective mass resolutions from simulation. For every event, the jet-quark assignment with the lowest χ^2 is taken, requiring 50 GeV $< m_{j_1,j_2} <$ 110 GeV and 50 GeV $< m_{j_3,j_4} <$ 110 GeV. This χ^2 is minimized as a function of m_{W} and m_{t}. Only events with $\chi^2_{\mathrm{min}} < 8$ are considered in the extraction of m_{t}.

The template method is applied to the distribution of m_{jjb} values from the selected jet-quark assignment, as observed in data. Each selected event contributes two values to this distribution. ATLAS measures $m_{\mathrm{t}} = 174.9 \pm 2.1(\mathrm{stat}) \pm 3.8(\mathrm{syst})$ GeV. The systematic uncertainty is dominated by the uncertainty on Initial and Final State Radiation (ISR/FSR), the uncertainty on the data-driven multijet background and the JES uncertainty.

2.3 *Measurement of the top-quark mass in the ℓ+jets channel*

Both ATLAS and CMS have measured m_{t} in the ℓ+jets channel [8,9]. ATLAS selects events by asking exactly 1 isolated electron ($E_{\mathrm{T}} > 25$ GeV) or muon ($p_{\mathrm{T}} > 20$ GeV). The events need to have ≥ 4 jets with $p_{\mathrm{T}} > 25$ GeV and $|\eta| < 2.5$, of which at least one is b-tagged. Multijet events are rejected by asking $\not{E}_{\mathrm{T}} > 35$ GeV and $m_{\mathrm{W}}^{\mathrm{T}} > 25$ GeV (e+jets), or $\not{E}_{\mathrm{T}} > 20$ GeV and $\not{E}_{\mathrm{T}} + m_{\mathrm{W}}^{\mathrm{T}} > 60$ GeV (μ+jets). ATLAS is using two different approaches to measure m_{t}, designed to reduce the JES uncertainty. Both analyses are based on the template method.

In the 1d-analysis, $R_{32} \equiv \frac{m_{\mathrm{t}}^{\mathrm{reco}}}{m_{\mathrm{W}}^{\mathrm{reco}}}$ is calculated for every event, where $m_{\mathrm{t}}^{\mathrm{reco}}$ and $m_{\mathrm{W}}^{\mathrm{reco}}$ are the reconstructed invariant masses of the hadronically decaying top quark and W boson, respectively. A kinematic fit is used to select a jet-quark assignment. The likelihood L of the kinematic fit of the selected jet-quark assignment has to pass: $\ln L > -50$. The jets assigned to the $\mathrm{t} \to \mathrm{bqq'}$ decay need to have $p_{\mathrm{T}} > 40$ GeV, and $m_{\mathrm{W}}^{\mathrm{reco}}$ has to fulfill 60 GeV $< m_{\mathrm{W}}^{\mathrm{reco}} <$ 100 GeV.

The 2d-analysis, a combined measurement of m_t and a global Jet energy Scale Factor (JSF), is performed by a template fit to $m_\mathrm{t}^\mathrm{reco}$ and $m_\mathrm{W}^\mathrm{reco}$. In this analysis, the jet triplet assigned to the hadronic top decay is chosen as the one with maximum p_T, considering only triplets with 50 GeV $< m_\mathrm{W}^\mathrm{reco} <$ 110 GeV. Finally a kinematic fit is performed to the chosen jet triplet.

Both analyses are applied on 1.04 fb^{-1} of data. The 2d-analysis has a slightly smaller uncertainty: $m_\mathrm{t} = 174.5 \pm 0.6(\mathrm{stat}) \pm 2.3(\mathrm{syst})$ GeV. The systematic uncertainty is dominated by the uncertainty on ISR/FSR and the uncertainty on the b-jet energy scale.

The CMS measurement of m_t uses 4.7 fb^{-1} of data in the μ+jets channel [9]. Events are selected by asking exactly 1 isolated muon with $p_\mathrm{T} > 30$ GeV and $|\eta| < 2.1$, ≥ 4 jets with $p_\mathrm{T} > 30$ GeV and $|\eta| < 2.4$, of which at least 2 are b-tagged. For every possible jet-quark assignment, a kinematic fit is applied with 3 mass constraints: an equal-mass constraint of $m_\mathrm{t}^\mathrm{lept}$ and $m_\mathrm{t}^\mathrm{hadr}$, and 2 m_W constraints. The kinematic fit returns the fitted top-quark mass $m_{\mathrm{t},i}^\mathrm{fit}$ and the fit probability P_fit^i. Wrong jet-quark assignments are rejected by asking $P_\mathrm{fit}^i > 0.2$.

To extract m_t from the data, the Ideogram method is used in a combined measurement of m_t and the Jet Energy Scale (JES). In this method, a likelihood is calculated for every event:

$$\mathcal{L}(\mathrm{event} \mid m_\mathrm{t}, \mathrm{JES}) = \left(\sum_{i=1}^{n} P_\mathrm{fit}^i \cdot P\left(m_{\mathrm{t},i}^\mathrm{fit}, m_{\mathrm{W},i}^\mathrm{reco} \mid m_\mathrm{t}, \mathrm{JES}\right)\right)^{\sum_{i=1}^{n} P_\mathrm{fit}^i} . \tag{2}$$

The distributions $P\left(m_{\mathrm{t},i}^\mathrm{fit}, m_{\mathrm{W},i}^\mathrm{reco} \mid m_\mathrm{t}, \mathrm{JES}\right)$ for all possible jet-quark assignments (correct assignments, wrong assignments and unmatched assignments) are taken from simulation. The individual event likelihoods are combined in a global likelihood, from which the measured m_t and JES values can be extracted. With this method, CMS measures $m_\mathrm{t} = 172.6 \pm 0.6(\mathrm{stat}) \pm 1.2(\mathrm{syst})$ GeV. The systematic uncertainty is dominated by the b-jet energy scale uncertainty and the uncertainty on the factorization scale. The systematic uncertainty does not include the uncertainty on color reconnection and on the underlying event.

3 Measurement of the top-quark mass from the $\mathrm{t\bar{t}}$ cross section at $\sqrt{s} = 7$ TeV

One of the problems of the direct measurements of m_t is that they use the mass definition from Monte Carlo generators, which is not related to m_t in a well-defined renormalization scheme ($m_\mathrm{t}^\mathrm{pole}$ or $m_\mathrm{t}^{\overline{\mathrm{MS}}}$) in a straightforward way. These masses can however be extracted from the measured cross section of top quark pair production $\sigma_\mathrm{t\bar{t}}$, since the theoretical dependency of $\sigma_\mathrm{t\bar{t}}$ on $m_\mathrm{t}^\mathrm{pole}$ or $m_\mathrm{t}^{\overline{\mathrm{MS}}}$ is known. ATLAS used $\sigma_\mathrm{t\bar{t}}$ measured from 35 pb^{-1} of data in the ℓ+jets channel, and obtains $m_\mathrm{t}^\mathrm{pole} = 166.4^{+7.8}_{-7.3}$ GeV for the pole mass [10]. CMS used $\sigma_\mathrm{t\bar{t}}$ measured in the dilepton final state from 1.14 fb^{-1} of data, and measures $m_\mathrm{t}^\mathrm{pole} = 170.3^{+7.3}_{-6.7}$ GeV and $m_\mathrm{t}^{\overline{\mathrm{MS}}} = 163.1^{+6.8}_{-6.1}$ GeV for the pole mass and the $\overline{\mathrm{MS}}$ mass, respectively [11]. Both the ATLAS and CMS results are in agreement with previous measurement performed by CDF and D0 [2].

4 Measurement of the mass difference between top and antitop quarks

One of the fundamental symmetries in the standard model, the invariance under CPT transformations, can be tested by measuring the difference in mass between a particle and the corresponding antiparticle. Since the top quark is the only quark that decays before hadronization can take place, this difference can be measured directly. CMS performed a measurement using 1.09 fb^{-1} of data in the μ+jets channel [12]. The events were splitted in two distinct samples according to the charge of the lepton. In each of these two samples, the mass of the hadronically decaying top quarks was measured and finally both masses were subtracted from eachother. This resulted in $\Delta m_\mathrm{t} = -1.20 \pm 1.21(\mathrm{stat}) \pm 0.47(\mathrm{syst})$ GeV. The smallness of the systematic uncertainty, when compared to m_t measurements, can be explained by the cancellation of most systematics by taking the difference.

5 Conclusion and outlook

Currently the most precise measurements of m_t are performed by the Tevatron experiments, but the ATLAS and CMS results are getting more and more precise. An overview of all these results can be found in Fig. 1. The next step is to combine all the CMS and ATLAS measurements,

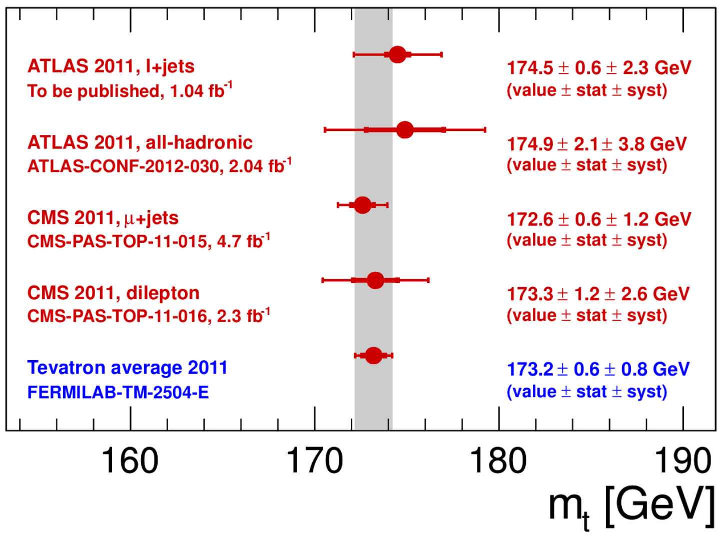

Figure 1: Overview of the m_t measurements from ATLAS and CMS, including the latest CDF and D0 combination.

on which work has already started, and finally to combine these also with the CDF and D0 results. CMS already performed a combination of its measurements, resulting in $m_t = 172.6 \pm 0.4(\text{stat}) \pm 1.2(\text{syst})$ GeV.

With the huge amount of data which will be recorded by ATLAS and CMS, the precision on m_t is expected to increase. The uncertainties are currently dominated by the jet energy scale systematic uncertainty, which can be reduced once more data is available to be analyzed.

References

1. CDF and D0 Collaboration, "Combination of CDF and DO results on the mass of the top quark using up to 5.8 fb^{-1} of data", (2011). arXiv:1107.5255.
2. O. Brandt, "Measurements of the top quark mass at the Tevatron", these proceedings. arXiv:1204.0919.
3. I. Aracena, "Top Pair Production at $E_{cm} = 7$ TeV", these proceedings.
4. CMS Collaboration, "Measurement of the top-quark mass in the dilepton channel in pp collisions at $\sqrt{s} = 7$ TeV", *CMS Physics Analysis Summary* **CMS-PAS-TOP-11-016** (2012).
5. CMS Collaboration, "Measurement of the $t\bar{t}$ production and the top-quark mass in the dilepton channel in pp collisions at $\sqrt{s} = 7$ TeV", *JHEP* **07** (2011) 049. arXiv:1105.5661.
6. D0 Collaboration, "Measurement of the top quark mass in $p\bar{p}$ collisions using events with two leptons", submitted to *Phys. Rev. Lett.* arXiv:1201.5172.
7. ATLAS Collaboration, "Determination of the Top Quark Mass with a Template Method in

the All-Hadronic Decay channel using 2.04 fb^{-1} of ATLAS data", *ATLAS Note* **ATLAS-CONF-2012-030** (2012).

8. ATLAS Collaboration, "Measurement of the top quark mass with the template method in the top antitop $\rightarrow$ lepton + jets channel using ATLAS data", submitted to *Eur. Phys. J.* **C**, `arXiv:1203.5755`.
9. CMS Collaboration, "Measurement of the top quark mass in the muon+jets channel", *CMS Physics Analysis Summary* **CMS-PAS-TOP-11-015** (2012).
10. ATLAS Collaboration, "Determination of the Top-Quark Mass from the $\mathrm{t\bar{t}}$ Cross Section Measurement in pp Collisions at $\sqrt{s} = 7$ TeV with the ATLAS detector", *ATLAS Note* **ATLAS-CONF-2011-054** (2011).
11. CMS Collaboration, "Determination of the Top Quark Mass from the $\mathrm{t\bar{t}}$ Cross Section at $\sqrt{s} = 7$ TeV", *CMS Physics Analysis Summary* **CMS-PAS-TOP-11-008** (2011).
12. CMS Collaboration, "Measurement of the mass difference between top and antitop quarks", *CMS Physics Analysis Summary* **CMS-PAS-TOP-11-019** (2011).

MEASUREMENTS OF TOP QUARK PROPERTIES AT THE TEVATRON

D. MIETLICKI
(On Behalf of the CDF and D0 Collaborations)
Department of Physics, University of Michigan,
450 Church Street, Ann Arbor, MI, USA

The top quark is the most recently discovered of the standard model quarks, and studies of its properties are important tests of the standard model. Many measurements of top properties have been produced by the CDF and D0 collaborations, which study top quarks produced in $p\bar{p}$ collisions at the Fermilab Tevatron with a center-of-mass energy $\sqrt{s} = 1.96$ TeV. We describe recent results from top properties measurements at the Tevatron using datasets corresponding to integrated luminosities up to 8.7 fb^{-1}.

1 Introduction

Since its discovery in 1995 at the Tevatron, [1] the study of the production and properties of the top quark has been one of the most active areas of research in high energy particle physics. Its extremely large mass makes the top unique among quarks, in that it decays via the electroweak interaction before hadronization. Thus, properties such as spin can be measured through their effects on the kinematic distributions of the top decay products. This offers physicists a first chance to study a “bare” quark. With a Yukawa coupling near one, the top quark could play a special role in electroweak symmetry breaking, and its large mass could potentially lead to enhanced couplings to new physics. Precision measurements of top properties are important both as tests of the standard model and as potential avenues for the discovery of new physics.

The majority of top quarks analyzed at the Tevatron are produced as $t\bar{t}$ pairs via the strong interaction, although they are also produced singly via the electroweak interaction, a mode that was not observed until 2009. [2] The standard model predicts that tops decay almost always via $t \to Wb$, so the decay modes of $t\bar{t}$ pairs are described by the two W boson decays. Two decay modes are used in the analyses described in this document: the “dilepton” mode, where both W’s decay to a lepton (electron or muon) and a neutrino, and the “lepton plus jets” mode, where one W decays leptonically and the other decays to a pair of quarks. A large portion of $t\bar{t}$ pairs decay into the “all-hadronic” channel, where both W’s decay to quark pairs, but this channel faces a very large background from QCD multi-jet production and is difficult to use in top properties measurements.

2 Asymmetry in $t\bar{t}$ Production

When top pairs are produced in $p\bar{p}$ collisions, the standard model predicts a small asymmetry, $\mathcal{O}(7\%)$ at next-to-leading order (NLO), in the number of top quarks that travel along the proton direction compared to the number that travel along the antiproton direction. Using

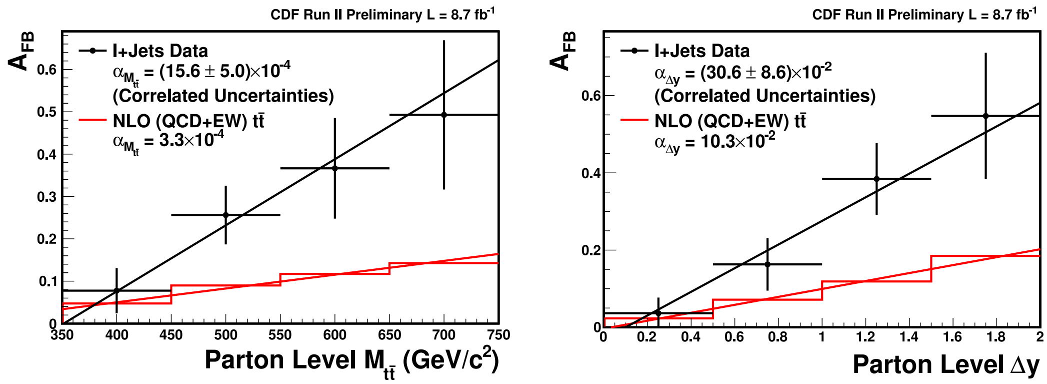

Figure 1: Parton-level A_{FB} as a function of $M_{t\bar{t}}$ (left) and $|\Delta y|$ (right) as measured at CDF.

approximately 5 fb^{-1}, analyses at CDF and D0 found asymmetries exceeding the prediction with moderate significance. [3] The CDF result in the lepton plus jets channel also observed an increase in the asymmetry as a function of the invariant mass of the $t\bar{t}$ system ($M_{t\bar{t}}$). The measurement of this asymmetry with the full Tevatron dataset is an important update and will be complementary to similar measurements at the Large Hadron Collider (LHC), where the effect must be measured in a different manner due to the symmetric pp initial state.

CDF has recently released a new measurement of the asymmetry using 8.7 fb^{-1}, corresponding to the full Tevatron dataset. [4] The asymmetry A_{FB}, defined in Equation 1, is measured using the frame-invariant variable Δy, the difference in rapidities between the top quark and the antitop quark. After removing the background contribution and correcting for acceptances and detector resolution effects, CDF measures a parton level asymmetry of $(16.2 \pm 4.7)\%$, compared to the prediction of 6.6% determined using the NLO event generator POWHEG [5] with a flat correction applied to account for electroweak contributions to the asymmetry. [6]

$$A_{FB} = \frac{N(\Delta y > 0) - N(\Delta y < 0)}{N(\Delta y > 0) + N(\Delta y < 0)} \tag{1}$$

The new CDF result also considers the mass and rapidity dependence of the asymmetry, measuring A_{FB} as a function of both $M_{t\bar{t}}$ and $|\Delta y|$, as shown in Figure 1. In both cases, the asymmetry is found to be well-fit by a linear ansatz, and the best-fit slopes are measured and compared to the prediction. At the parton level, CDF finds the slope of A_{FB} vs. $M_{t\bar{t}}$ to be $(15.6 \pm 5.0) \times 10^{-4}$, compared to a prediction of 3.3×10^{-4}. The slope of A_{FB} vs. $|\Delta y|$ is measured to be $(30.6 \pm 8.6) \times 10^{-2}$, compared to a prediction of 10.3×10^{-2}. The significance of the deviation from the prediction is determined at the background-subtracted level, before the final corrections for acceptance and resolution effects are applied. Simulated experiments are performed based on the POWHEG prediction with electroweak corrections, and a p-value is determined by finding the fraction of such experiments in which the predicted slope is at least as large as that observed in the data. A p-value of 6.46×10^{-3} is found for the $M_{t\bar{t}}$ dependence of the asymmetry, along with a p-value of 8.92×10^{-3} for the $|\Delta y|$ dependence.

3 $t\bar{t}$ Spin Correlations

When top quark pairs are produced in hadronic collisions, the individual top quarks are unpolarized, but the $t\bar{t}$ system has a definite spin state and thus the spins of the two quarks are correlated. The strength of this correlation, which is frame-dependent, is quantified as the fractional difference κ between the number of top pairs where the quark spins are aligned and the number of pairs where the spins are oppositely aligned. Because tops decay before hadronization, spin information can be measured by considering the angular distributions of the top decay products.

Both CDF and D0 have performed measurements of the spin correlation, with the spin quantization axis being defined to be along the beam direction, where the standard model predicts $\kappa = 0.78$. [7] CDF uses template fitting methods to measure κ directly, finding $\kappa = 0.72 \pm 0.69$ in the lepton plus jets decay channel [8] and $\kappa = 0.042 \pm 0.563$ in the dilepton channel. [9] The CDF results are consistent with each other and with the standard model within large uncertainties.

D0 utilizes a new matrix element approach that enhances the sensitivity by approximately 30%. A matrix element method is used to define a discriminant based on the probability that a given event contains the standard model spin correlation. Combining measurements in the dilepton [10] and lepton plus jets [11] channels, D0 finds that the fraction of events which contain the standard model spin correlation is $f = 0.85 \pm 0.29$. This result provides the first 3σ evidence for the existence of the spin correlation. The fraction of events containing the standard model correlation is then converted to a measurement of κ, giving $\kappa = 0.66 \pm 0.23$.

4 W Boson Helicity

In the standard model, top quarks decay nearly always to a W boson and a b quark, and the helicity states of the W are constrained according the the V-A nature of the $W - t - b$ coupling. The standard model predicts that the fractions of longitudinal, left-handed, and right-handed W bosons, labeled f_0,f_-, and f_+ respectively, in $t\bar{t}$ events will be approximately 0.7, 0.3, and 0.0.

D0 and CDF have both performed measurements of these helicity fractions by considering angular distributions of the W decay products - particularly the lepton - in $t\bar{t}$ candidate events. A combination of the W helicity results for the two experiments has recently been submitted for publication, [12] the first such published combination of W helicity measurements. With $f_0 + f_- + f_+ = 1$, the combined CDF and D0 measurements find $f_0 = 0.722 \pm 0.081$ and $f_+ = -0.033 \pm 0.046$.

5 Top Branching Ratio

The standard model prediction that top quarks almost always decay to Wb has also been tested in measurements by CDF and D0. Both collaborations have recently performed analyses to measure the ratio $R = \mathcal{B}(t \to Wb)/\mathcal{B}(t \to Wq)$, where $\mathcal{B}(t \to WX)$ is the branching ratio for a top to decay to WX. The standard model predicts that R should be very close to 1. If the CKM matrix is assumed to be unitary, then a measurement of R can also be converted into a measurement of the CKM matrix element $|V_{tb}|$.

In $t\bar{t}$ production and decay, the standard model expectation is that each event will contain two b quarks. Since jets originating from b quarks can be tagged by a displaced secondary vertex, and the efficiency for tagging such jets can be measured, the ratio R can be determined by dividing the sample of $t\bar{t}$ candidate events into sub-samples with 0, 1, or 2 b-tagged jets and comparing the relative sizes of each sub-sample to the predicted sizes determined from the tagging efficiency. Using a luminosity of 5.4 fb^{-1}, a recent D0 measurement in both the dilepton and lepton plus jets channels [13] finds $R = 0.90 \pm 0.04$, smaller than the standard model expectation at the level of approximately 2σ, and measures $|V_{tb}| = 0.95 \pm 0.02$. With 7.5 fb^{-1}, a new CDF result in the lepton plus jets channel [14] measures $R = 0.91 \pm 0.09$ and $|V_{tb}| = 0.95 \pm 0.05$, again somewhat below the prediction but with a significance that is smaller than the D0 result.

6 Top Width

The top quark width is expected to be approximately 1.5 GeV in the standard model, and both CDF and D0 have performed measurements to test this prediction. CDF has performed a direct measurement in the lepton plus jets decay channel with a luminosity of 4.3 fb^{-1}, using a likelihood fit to to the reconstructed top quark mass distribution based on template samples with different input top widths.[15] This analysis results in a 95% C.L. limit of $\Gamma_t < 7.6$ GeV and a 68% two-sided limit 0.3 GeV $< \Gamma_t <$ 4.4 GeV.

Using a luminosity of 5.4 fb^{-1}, D0 has performed a complementary measurement that indirectly measures the top width by combining results from other top properties measurements.[16] In particular, as shown in Equation 2, the total width of the top quark is determined from the ratio of the partial width for the process $t \to Wb$, as determined from the measured cross-section for single top production, to the branching ratio for $t \to Wb$, measured in the analysis described in Section 5. This method requires input from several measurements and from the theoretical predictions, but results in increased sensitivity compared to a direct measurement. D0 measures a width of $\Gamma_t = 2.00^{+0.47}_{-0.43}$ GeV, and converts this to a 95% C.L. limit on $|V_{tb}|$, finding $0.81 < |V_{tb}| \leq 1$.

$$\Gamma_t = \frac{\Gamma(t \to Wb)}{\mathcal{B}(t \to Wb)} \tag{2}$$

7 Conclusions

The full dataset collected at the Tevatron is now being used to measure top quark properties at CDF and D0. Many of these measurements, such as the A_{FB} measurement and the measurement of $t\bar{t}$ spin correlations, are complementary to analyses that can be performed at the LHC, where the different center-of-mass energy and initial state will provide additional information about the couplings of the top quark. Many CDF and D0 analyses, such as the W helicity measurement in $t\bar{t}$ decays described here, are now being combined to create Tevatron-wide results. Data-taking has ceased at the Tevatron, but there is still much left to be learned from analysis of the top quark samples collected at CDF and D0, and both collaborations continue to pursue precision results.

Acknowledgments

I would like to thank the members of the CDF and DO collaborations for their dedication to the study of top quark properties, especially the top group conveners and the authors of the analyses included here, as well as the CDF and D0 funding agencies who have made such research possible. I also want to thank the organizers of the 2012 Rencontres de Moriond and all contributors.

References

1. F. Abe *et al.* [CDF Collaboration], Phys. Rev. Lett. **74**, 2626 (1995). S. Abachi *et al.* [D0 Collaboration], Phys. Rev. Lett. **74**, 2632 (1995).
2. T. Aaltonen *et al.* [CDF Collaboration], Phys. Rev. Lett. **103**, 092002 (2009). V.M. Abazov *et al.* [D0 Collaboration], Phys. Rev. Lett. **103**, 092001 (2009).
3. T. Aaltonen *et al.* [CDF Collaboration], Phys. Rev. D **83**, 112003 (2011). T. Aaltonen *et al.* [CDF Collaboration], CDF Conference Note 10436 (2011). T. Aaltonen *et al.* [CDF Collaboration], CDF Conference Note 10584 (2011). V.M. Abazov *et al.* [D0 Collaboration], Phys. Rev. D **84**, 112005 (2011).

4. T. Aaltonen *et al.* [CDF Collaboration], CDF Conference Note 10807 (2012).
5. S. Frixione, P. Nason, and G. Ridolfi, J. High Energy Phys. **0709**, 126 (2007).
6. W. Hollik and D. Pagani, Phys. Rev. D **84**, 093003 (2011). J. H. Kuhn and G. Rodrigo, J. High Energy Phys. **1201**, 063 (2012). A. V. Manohar and M. Trott, arXiv:1201.3926 [hep-ph] (2012).
7. W. Bernreuther, A. Brandenburg, Z. G. Si and P. Uwer, Nucl. Phys. **B 690**, 81 (2004).
8. T. Aaltonen *et al.* [CDF Collaboration], CDF Conference Note 10211 (2010).
9. T. Aaltonen *et al.* [CDF Collaboration], CDF Conference Note 10719 (2011).
10. V. M. Abazov *et al.* [D0 Collaboration], Phys. Rev. Lett. **107**, 032001 (2011).
11. V. M. Abazov *et al.* [D0 Collaboration], Phys. Rev. Lett. **108**, 032004 (2012).
12. T. Aaltonen *et al.* [CDF and D0 Collaborations], arXiv:1202.5272 [hep-ex] (2012).
13. V. M. Abazov *et al.* [D0 Collaboration], Phys. Rev. Lett. **107**, 121802 (2011).
14. T. Aaltonen *et al.* [CDF Collaboration], CDF Conference Note In Preparation.
15. T. Aaltonen *et al.* [CDF Collaboration], Phys. Rev. Lett. **105**, 232003 (2010).
16. V. M. Abazov *et al.* [D0 Collaboration], arXiv:1201.4156 [hep-ex] (2012).

Measurements of Top Quark Properties at the LHC

A. Lister on behalf of the ATLAS and CMS Collaborations
Section de Physique, Université de Genève, Geneva, Switzerland

A total of 20 measurements carried out by the ATLAS and CMS Collaborations of the properties of top quarks were presented. These were measurements of the top quark charge, of the spin correlation between the top and the anti-top quark, of the charge asymmetry, of the polarisation of the W-boson, the measurement of the hadronic activity in the central rapidity region in $t\bar{t}$ events, and the measurement of the branching ratio of top quarks. Some direct searches for new physics were also presented: searches for fourth generation top-like and bottom-like quarks as well as more exotic T quarks with anomalous decay modes.

1 Properties of the Top Quark

Many measurement of the properties of the top quark were presented. The measurements all used data from the 2011 LHC run, using integrated luminosities ranging from 0.7 to 4.6 fb^{-1}, the latter corresponding to the full 2011 data sample.

Top charge Both the CMS [?] and ATLAS [?] Collaborations have excluded at more than 5σ the top quark having a charge 4/3e, in favour of the standard model (SM) prediction of 2/3e. The charge of the W is identified through the charge of the lepton; the charge of the b-jet is determined from the presence of a soft lepton inside the jet.

Spin correlations The measurement of the spin correlation between the top and the anti-top quark is sensitive to the fact that the life-time of the top quark is so short that it decays before it hadronises and thus for $t\bar{t}$ events, one expects the spin structure to be preserved. In top decays where both W-bosons decay leptonically, the angular separation between the two leptons is sensitive to the presence of such correlations. The ATLAS Collaboration [?] is able to exclude at more than 3 σ the scenario with no spin correlations, and measures a degree of spin correlation compatible with that predicted by the SM.

Charge asymmetry Unlike the $p\bar{p}$ collisions from the Tevatron, the LHC pp collisions cannot give a direct forward-backward asymmetry in the production of top quark pairs. Yet owing to the Parton Distribution Functions being different for quarks and anti-quarks, the difference in rapidity (y) distributions of the top and anti-top can be used to measure a form of asymmetry; indeed the top quark spectrum in y is expected to be slightly broader than for that of the anti-top. By using the difference in absolute rapidity between the top and anti-top ($\Delta|y| = |y_t| - |y_{\bar{t}}|$) one can define an asymmetry

$$A_C = \frac{N(\Delta|y| > 0) - N(\Delta|y| < 0)}{N(\Delta|y| > 0) + N(\Delta|y| < 0)}. \tag{1}$$

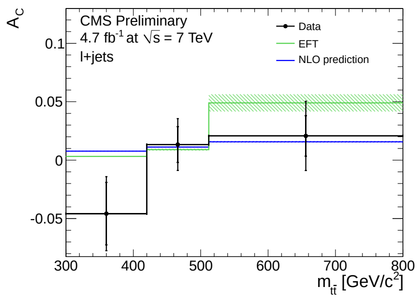

(a) Corrected asymmetry as a function of $m_{t\bar{t}}$. The measured values are compared to NLO calculations for the SM and to predictions from an effective field theory. The error bars on the differential asymmetry values indicate the staistitcal and systematic uncertainties

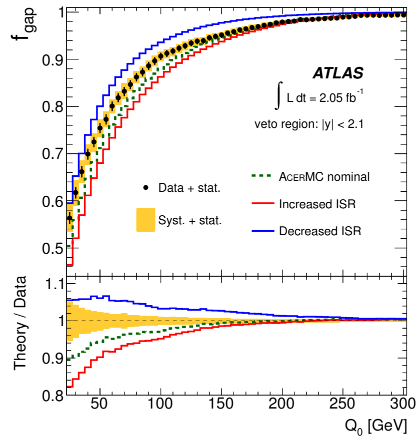

(b) The measured gap fraction as a function of Q_0 for $|y| < 2.1$ is compared with the prediction from the AcerMC generator, where different settings of the Pythia parton shower parameters are used to produce samples with nominal, increased and decreased initial state radiation (ISR).

Predictions from the MC@NLO generator are at the level of 0.006 ± 0.002. The measurement of a larger asymmetry would be an indication of new physics. Both the ATLAS [?] and CMS [?] Collaborations have studied this asymmetry in a variety of different kinematic regions. Both collaborations used the lepton+jets decay mode where one W decays leptonically and the other hadronically and both relied on the identification of at least one heavy flavour (b-tagged) jet. The measurements are corrected for detector and acceptance effects. The overall measurements of A_C are compatible with zero; ATLAS measures an overall charge asymmetry of $A_C = -0.018 \pm 0.028(stat) \pm 0.023(syst)$, while CMS measures a value of $A_C = 0.004 \pm 0.010(stat) \pm 0.012(syst)$. This asymmetry was also measured for different kinematic regions: for different values of the $t\bar{t}$ invariant mass (ATLAS and CMS) and as a function of the transverse momentum (p_T) of the $t\bar{t}$ system (CMS). The distribution as a function of the $t\bar{t}$ invariant mass from the CMS Collaboration is shown in Fig. **??**. These results disfavour many of the models developed to account for the forward-backward asymmetry observed at the Tevatron [?,?].

W boson polarisation In order the measure the three components of the polarisation of the W-boson, the distribution of the $\cos\theta^*$ is studied. This angle represents the angle between the lepton momentum in the W rest-frame and the momentum of the W in the top rest-frame. After subtracting the background distributions, the observed $\cos\theta^*$ distribution is corrected to particle-level. The resulting distribution is then fitted to templates of each of the three polarization components, with the constraint that the total fraction has to be unity. The SM predicts contribution close to zero for the right-handed polarisation, about 31% left-handed and 69% longitudinal polarisation. Both the ATLAS [?] and CMS [?] results are compatible with the SM predictions. The right handed polarisation component, F_R, is predicted to be 0.0017 ± 0.0001 at Next to Next to Leading Order, and is measured to be $0.09 \pm 0.04(stat) \pm 0.09(syst)$ and $0.040 \pm 0.035(stat) \pm 0.044(syst)$ by the ATLAS and CMS Collaborations, respectively. These results are then used to place stringent limits on anomalous couplings, described by an effective field theory, given that the scale of new physics is larger than the observable region.

$t\bar{t}$ + jet veto This measurement looks at the fraction of events that do not contain jet activity above a certain threshold in the central region. Two different types of thresholds are measured, either on the leading p_T emission from $t\bar{t}$ (Q_0), or on the sum of all emissions in that region (Q_{sum}). ATLAS [?] uses a high purity $t\bar{t}$ sample where both W-bosons decay leptonically and at least two identified heavy flavour jets. These quantities are measured in four different $|y|$ regions as a function of the Q variable, after correcting for detector effects. This measurement is extremely sensitive to the initial state radiation and can be used to constrain some parameters of Monte Carlo generators, in particular related to the parton shower. Figure **??** shows this rapidity gap fraction as a function of Q_0 for $|y| < 2.1$ in data compared to AcerMC generator with nominal and varied parton shower parameters. The data is represented as closed (black) circles with statistical uncertainties. The yellow band is the total experimental uncertainty on the data (statistical and systematic). The theoretical predictions are shown as solid and dashed coloured lines [a].

Top branching ratios In the SM, the top is expected to decay ∼100% of the time to a W-boson and a b-quark. Thus the observation of any other decay mode would be a sign of new physics. Using data in the dilepton channel and looking at the multiplicity of the identified heavy flavour jets, the CMS Collaboration was able to measure the branching ratio to Wb to a W-boson and any quark (Wq) to be 0.98 ± 0.04 and place the 95% confidence level around 0.85 [?].

Flavour changing neutral currents In addition to looking for anomalous decays to a W boson and a non-b-quark, one can look for flavour changing neutral current decay modes $t \to qZ$. Many models of new physics predict measurable branching ratios in this decay mode. Results from the ATLAS [?] and CMS [?] Collaborations have put upper limits on this fraction at 1.1% and 0.34%, respectively. In these analyses, events with three leptons are considered, where two of the leptons should be compatible with a Z-boson and the other originate from the other top quark that decays to Wb.

One can also search for flavour changing neutral currents, not in the decay mode, but in the production mode. The ATLAS Collaboration looked for production modes where a coupling between a gluon, a top quark and a light quark could exist [?]. These signatures would be similar to single top production but with different kinematics. In order to separate this new signature from the SM backgrounds, a neutral network is used. Stringent limits are placed on the maximum allowed branching ratios of top to ug and cg at the level of $5.7 \cdot 10^{-5}$ and $2.7 \cdot 10^{-4}$, respectively.

2 Searches for New Physics Using Top Quarks

While most of the measurements of the properties of the top quark can be used to place limits on anomalous behaviour and thus limits on the presence of new physics, direct searches for new physics resulting in signatures containing or resembling those of SM top quarks can be carried out.

Fourth generation top-like quarks Results for fourth generation top-like quarks were presented in both the lepton+jets and the dilepton channels [?,?,?]; in the lepton+jets analyses, there is an explicit requirement on the decay mode $t' \to Wb$, while for the ATLAS dilepton analysis, the more generic decay mode to Wq is considered. The mass of the top-quarks are reconstructed and one looks for excesses in the tails of this distribution, where the proposed t' would be expected to be seen. No evidence for such quarks is found; lower limits on the t' mass between 350 and 560 GeV are obtained.

[a] As this is an inclusive quantity, representing the fraction of events with activity above a certain threshold, the points are highly correlated.

Fourth generation bottom-like quarks Searches are also carried out for fourth generation bottom-like quarks (b') decaying to a W-boson and a top quark. Such events would have a very high multiplicity; thus in order to reduce the contribution from the SM background one can select same-sign dilepton events, tri-lepton events or lepton+jet events with semi-boosted W-bosons. In these analyses [?,?,?], lower limits on the mass of the b' have been set between 450 and 495 GeV. One of the ATLAS results can also be interpreted in terms of anomalous production of quarks and is able to exclude most of the phase-space of the Z' hypothesis used to explain the Tevatron A_{fb} measurement for Z' masses from 0.1 to 1 TeV.

t$\bar{\mathbf{t}}$ events with large missing transverse energy In some extensions of fourth generation-like quarks, one can have massive top-like quarks decaying to a top quark and a weakly interacting particle, $T \to tA_0$. The pair-production of such quarks will result in signatures similar to those of $t\bar{t}$ events but with additional missing transverse energy. One can thus look for the presence of such events in the tails of the missing transverse energy distribution of events in the lepton+jets decay mode. Limits are placed by the ATLAS collaboration in the plane of the mass of the T and the A_0 particles, with limits extending out to 420 and 150 GeV, respectively [?].

Flavour changing neutral current in fourth-generation-like top Another possible signature for these T quarks would be flavour changing neutral current decays $T \to Zt$ resulting in $t\bar{t}$-like signatures with two extra Z-bosons. By reconstructing events with three or more leptons and requiring two opposite sign leptons to form a Z-peak, the CMS Collaboration was able to place limits on the mass of the T up to 475 GeV [?].

References

1. The CMS Collaboration, CMS-PAS-TOP-11-031.
2. The ATLAS Collaboration, ATLAS-CONF-2011-141.
3. The ATLAS Collaboration, Phys. Rev. Lett. **108**, 212001 (2012).
4. The ATLAS Collaboration, Accepted by EPJC [arXiv:1203.4211].
5. The CMS Collaboration, CMS-PAS-TOP-11-030.
6. The CDF Collaboration, Phys. Rev. D **83** 112003 (2011) .
7. The D0 Collaboration, Phys. Rev. D **84**, 112005 (2011).
8. The ATLAS Collaboration, Accepted by JHEP [arXiv:1205.2484].
9. The CMS Collaboration, CMS-PAS-TOP-11-020.
10. The ATLAS Collaboration, Accepted by EPJC [arXiv:1203.5015].
11. The CMS Collaboration, CMS-PAS-TOP-11-029.
12. The ATLAS Collaboration, Submitted to JHEP [arXiv:1206.0257].
13. The CMS Collaboration, CMS-PAS-TOP-11-028.
14. The ATLAS Collaboration, Phys. Lett. **B712** (2012) 351-369 [arXiv:1203.0529].
15. The ATLAS Collaboration, Accepted by Phys. Rev. Lett. [arXiv:1202.3076].
16. The CMS Collaboration, CMS-PAS-EXO-11-099.
17. The ATLAS Collaboration, Submitted to Phys. Ref. D. [arXiv:1202.3389].
18. The ATLAS Collaboration, Accepted by Phys. Rev. Lett. [arXiv:1202.6540].
19. The ATLAS Collaboration, Submitted to JHEP [arXiv:1202.5520].
20. The CMS Collaboration, Submitted to JHEP [arXiv:1204.1088].
21. The ATLAS Collaboration,*Phys. Rev. Lett.* **108**, 041805 (2012).
22. The CMS Collaboration, *Phys. Rev. Lett.* **107**, 271802 (2011).

SINGLE TOP PRODUCTION AT THE TEVATRON

ZHENBIN WU
(on behalf of the CDF and D0 collaborations)
Department of Physics, Baylor University,
One Bear Place #97316, Waco TX 76798-7316, USA

We present recent results of single top quark production in the lepton plus jet final state, performed by the CDF and D0 collaborations based on 7.5 and 5.4 fb^{-1} of $p\bar{p}$ collision data collected at $\sqrt{s} = 1.96$ TeV from the Fermilab Tevatron collider. Multivariate techniques are used to separate the single top signal from the backgrounds. Both collaborations present measurements of the single top quark cross section and the CKM matrix element $|V_{tb}|$. A search for anomalous Wtb coupling from D0 is also presented.

1 Introduction

In the Standard Model (SM), the top quark can be produced via the strong interaction as a $t\bar{t}$ pair. The SM also allows for the top quark to be produced through the electroweak interaction as a single top quark plus jets. This is referred to as single top. As illustrated in Figure 1, there are three production modes: the t-channel (tbq), the s-channel (tb) and the Wt-channel processes. Single top quark production was first observed simultaneously by the CDF and D0 experiments in 2009.[1,2] The study of single top quark events will provide access to the properties of the Wtb coupling. Within the SM, the single top signal allows for a direct measurement of the Cabibbo-Kobayashi-Maskawa (CKM) matrix element V_{tb}.[3] Furthermore, since the top quark decays before hadronization, its polarization can be directly observed in the angular correlations of its decay products.[4,5] Single top processes are expected to be sensitive to several kinds of new physics such as flavor-changing neutral currents (FCNC).

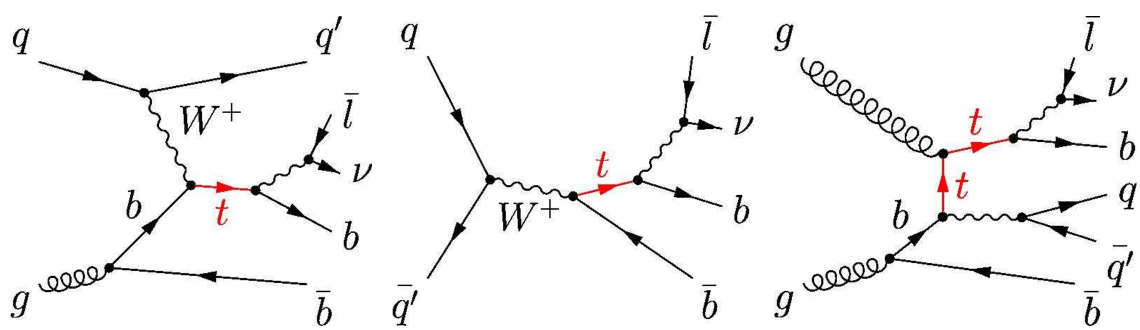

(a) t-channel (b) s-channel (c) Wt-channel

Figure 1: Representative Feynman diagrams of single top quark production channels: (a) t-channel $2 \rightarrow 3$ process at NLO with initial-state gluon splitting, (b) s-channel at leading order, and (c) Wt associated production at next-to-leading order (NLO) with initial-state gluon splitting.

2 Event Selection

The CDF collaboration performed the analysis on a lepton + jets dataset corresponding to an integrated luminosity of 7.5 fb^{-1}. Events are required to have an isolated electron or muon with $p_{\mathrm{T}} > 20$ GeV, $\not\!\!E_T > 25$ GeV, and 2–3 jets with $p_{\mathrm{T}} > 20$ GeV where at least one jet is b-tagged. By selecting a high quality, high-p_{T} isolated track, the signal acceptance increases by 15% compared to the previous CDF analysis. In this analysis, the CDF collaboration uses the POWHEG generator[9] for single top signal modeling with NLO accuracy.

The D0 collaboration uses 5.4 fb^{-1} of data collected with a logical OR of many trigger conditions, which together are fully efficient for the single top quark signal. The main event selection criteria applied is similar to the previous analysis:[2] an isolated electron or muon with $p_{\mathrm{T}} > 15$ GeV, $\not\!\!E_T > 20$ GeV, 2–4 jets with $p_{\mathrm{T}} > 15$ GeV out of which one jet has $p_{\mathrm{T}} > 25$ GeV and at least one jet tagged with a neural-network-based b-tagging algorithm. Additional selection criteria remove multijet background events with misidentified leptons.

Both collaborations use similar methods for signal and background modeling. They normalized the $t\bar{t}$, diboson and Z + jets processes to the SM prediction. The QCD models are derived from the data with a non-isolated lepton (D0) or anti-lepton (CDF). Before b–tagging, the W + jets and QCD backgrounds are normalized to the data using the $\not\!\!E_T$ variable (CDF) or several kinematic variables (D0).

3 Signal-Background Separation

After the event selection, additional multivariate techniques are used by both collaborations to further separate signal from backgrounds. Each multivariate technique constructs a powerful discriminant variable from different input variables that is proportional to the probability of an event being signal. The discriminant distribution is used as input to the cross section measurement. Several validation tests are conducted by studying the discriminant output distributions in background-enriched control samples.

The CDF collaboration uses a neural network (NN) multivariate technique to obtain a single top discriminant. By using 11–14 input variables, four separate NNs are constructed for different analysis channels based on the number of jets and b-tags. For each of the four different channels, the NN is optimized separately. In the channel with 2 jets and 2 b-tags, the NN is trained for the s-channel process as signal without knowledge of the t-channel. The remaining analysis channels are trained for the t-channel process as signal without knowledge of the s-channel. To further constrain the cross section measurement uncertainty, the CDF collaboration trained the NNs with samples that include a small fraction of events with variations in the jet energy scale and Q^2 scales. This method is expected to yield a 3% improvement in the uncertainty of the single top cross section measurement.

The D0 collaboration uses three individual techniques to separate single top quark events from the background, namely boosted decision trees (BDT), bayesian neural networks (BNN), and a neuroevolution of augmented topologies (NEAT).[6] All three methods use the same data and background models, and are trained separately for two channels: for the tb discriminant, which treats the tb process as the signal and the tqb process as a part of the background, and vice versa for the tbq discriminant. With 70% correlations among the outputs of the individual methods, a second BNN is used to construct a combined discriminant from the three discriminant outputs to increase sensitivity.

4 Measurement of Cross Section and $|V_{tb}|$

Both experiments measure the single top quark production cross section from the discriminant output distributions using a Bayesian-binned likelihood technique. The statistical uncertainty and all systematic uncertainties and their correlations are considered in these calculations. The single top cross section measured by the CDF collaboration is $3.04^{+0.57}_{-0.53}$ pb. The D0 collaboration measured the single top cross section for $tb + tqb$ to be $3.43^{+0.73}_{-0.74}$ pb.[6] Both of the measurements are shown in Figure 2.

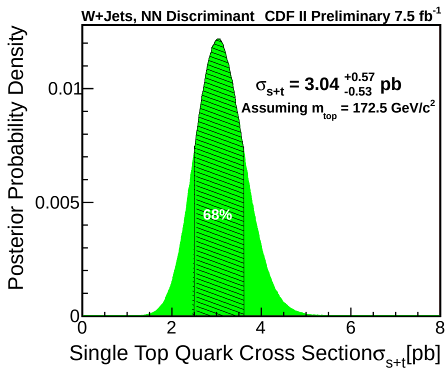

(a)

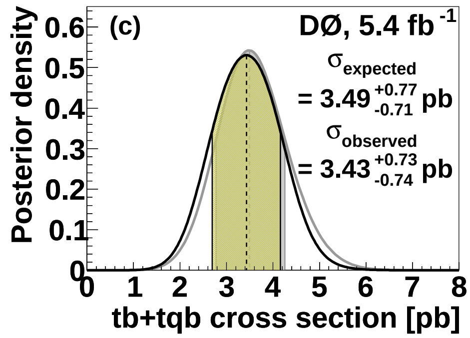

(b)

Figure 2: The posterior curve of the cross section measurement for the (a) CDF and (b) D0 collaborations.

Since the single top cross section is directly proportional to $|V_{tb}|^2$, both collaborations use the cross section measurements to extract $|V_{tb}|$. By restricting the measurement to the SM interval [0, 1], CDF measures $|V_{tb}| = 0.96 \pm 0.09$ (stat+syst) ± 0.05 (theory), and sets a limit of $|V_{tb}| > 0.78$ at 95% C.L. Using the same interval [0, 1], D0 extracts the limit of $|V_{tb}| > 0.79$ at 95% C.L.; after removing the upper constraint of the interval, D0 measures $|V_{tb} f_1^L| = 1.02^{+0.10}_{-0.11}$, where f_1^L is the strength of the left-handed Wtb coupling.

5 t-Channel Observation

With the same multivariate discriminant for the t-channel process, D0 computes the significance of the t-channel cross section using a log-likelihood ratio approach, which tests the compatibility of the data with two hypotheses: a null hypothesis with only background and a test hypothesis with background plus signal. The computation of the distributions for these two hypotheses is given by an asymptotic Gaussian approximation. With this approximation, the significance of the measured t-channel cross section is independent of any assumption on the production rate of s-channel.[8] The estimated probability corresponds to an observed significance of 5.5 standard deviations with an expected significance of 4.6 standard deviations.

6 Two-Dimensional Fit Results

The combined signal cross section (σ_{s+t}) is extracted by constructing a one-dimensional Bayesian posterior. An extension is to form a two-dimensional posterior probability density as a function of the cross sections for the s- and t-channel as in Figure 3. The best-fit cross section is the one for which the posterior is maximized without assuming the SM-predicted ratio between the cross section for the s- and t-channels.

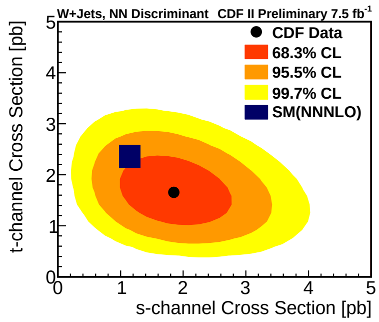

(a)

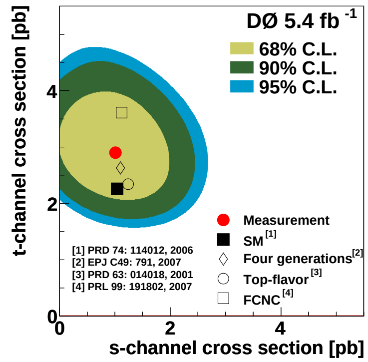

(b)

Figure 3: The results of the two-dimensional fit for σ_s and σ_t. The circle point shows the best fit value and the 68%, 95%, and 99% credibility regions are shown as shaded areas. The SM prediction is also indicated with theoretical uncertainties included.

7 Anomalous Wtb Coupling

Within the SM theory, the top quark coupling to the bottom quark and the W boson (tWb) has the V–A form of a left-handed vector interaction. Deviations from the SM expectation in the coupling form factors can manifest themselves by altering the fraction of W boson from top quark decays or by changing the rate and kinematic distributions of electroweak single top quark production. Three separate scenarios are investigated and upper limits are set with the same dataset by D0 for f_V^R, f_T^L, and f_T^R.[7]

8 Summary

The CDF and D0 collaborations have performed precise measurements of the electroweak single top quark production cross section and the CKM matrix element $|V_{tb}|$ using 7.5 and 5.4 fb^{-1} of data, respectively. An anomalous Wtb coupling search by D0 investigates three separate scenarios and sets an upper limit on each of them.

Acknowledgments

We thank the Fermilab staff, the technical staffs of the participating institutions, and the funding agencies for their vital contributions.

References

1. T. Aaltonen *et al.* [CDF Collaboration], *Phys. Rev. Lett.* **103**, 092002 (2009).
2. V.M. Abazov *et al.* [D0 Collaboration], *Phys. Rev. Lett.* **103**, 092001 (2009).
3. Johan Alwall *et al.*, *Eur. Phys. J.* C **49**, 791 (2007).
4. Gregory Mahlon and Stephen J. Parke, *Phys. Rev.* D **55**, 7249–7254 (1997).
5. Gregory Mahlon and Stephen J. Parke, *Phys. Lett.* B **476**, 323–330 (2000).
6. V. M. Abazov *et al.* [D0 Collaboration], *Phys. Rev.* D **84**, 112001 (2011).
7. V. M. Abazov *et al.* [D0 Collaboration], *Phys. Lett.* B **708**, 21 (2012).
8. V. M. Abazov *et al.* [D0 Collaboration], *Phys. Lett.* B **705**, 313 (2011).
9. S. Alioli, P. Nason, C. Oleari and E. Re, *J. High Energy Phys.* **0909**, 111 (2009).

SINGLE TOP PRODUCTION AT $\sqrt{s} = 7$ TeV

REBECA GONZALEZ SUAREZ, on behalf of the CMS and ATLAS collaborations
IIHE - VUB, Pleinlaan 2
1050 Brussels, Belgium

The production of single top quarks occurs via three processes: t-channel, s-channel and tW associated production. The LHC experiments have observed single top production via t-channel at 7 TeV and measured its cross section, providing a measurement of $|V_{tb}|$ with an uncertainty at the 10% level. Studies are in place to observe tW associated production with a sensitivity close to 3σ and the first limits on the production cross section for s-channel are set. Other studies based on single top topologies, like flavor changing neutral currents (FCNC) are also being performed.

1 Introduction

In hadronic colliders, top quarks are mostly produced in pairs via strong interaction. An alternative production via the weak interaction, that involves a Wtb vertex, leading to a single top quark final state, proceeds by three different mechanisms: t-channel, associated production with a W boson (tW), and s-channel. The study of single top quark processes allows for a measurement of the CKM matrix element $|V_{tb}|$ without assumptions about the number of quark generations, single top processes are also sensitive to many models of new physics.Single top production was first observed at the Tevatron in 2009, in a combination of t and s-channel; the LHC experiments, ATLAS [1] and CMS [2], have observed single top in the t-channel and measure its production cross section. Studies are also in place to study of tW associated production and s-channel.

2 t-channel

The t-channel production is the process with the highest cross section at the LHC, $\sigma_t = 64.6^{+3.3}_{-2.6}$pb [3]. This process is studied in final states with lepton+jets signature. The signal is characterized by one isolated muon or electron and missing transverse energy (E_T^{miss}), plus a central jet coming from the decay of a b quark and an additional light jet from the hard scattering process, that is often forward. A second b-jet produced in association to the top quark can be present as well, with a softer p_T spectrum with respect to the one coming from top decay.

2.1 Selection criteria

To define the signal region, events with exactly 1 isolated lepton (e,μ) and 2 or 3 jets, one of them identified as coming from the decay of a b-quark (b-tagged) are selected. ATLAS [4] applies a cut on the missing E_T of the event, $E_T^{miss} > 25$ GeV; while CMS [5] selects events with $E_T^{miss} > 35$ GeV in final states with electrons and applies a cut on the transverse mass of the

W boson, $m_T(W) > 40$ GeV, in the final states with muons. Then ATLAS applies a triangular cut: $m_T(W) >$(60 GeV - E_T^{miss}), while CMS uses the invariant mass of the reconstructed top quark, $130 < m_t < 220$ GeV. Other jet and b-tagging multiplicities are used in background estimations and as control regions. The main backgrounds that contribute to the analysis are W boson production in association with jets (W+jets), top pair ($t\bar{t}$) production and multijets (QCD) events. Background from $t\bar{t}$ and other processes like Z+jets, other single-top processes, and di-boson production, are estimated from simulation and normalized to their theoretical cross sections, while dedicated methods are applied to estimate the W+jets and QCD contributions.

2.2 Background estimation and Signal extraction

The QCD contribution is estimated via a maximum likelihood fit to the E_T^{miss} (e, μ ATLAS, e CMS) or $m_T(W)$ distribution (μ CMS). The template for QCD is obtained in data by inverting the isolation on muons and either requiring the electron to fail some of the quality requirements (CMS), or replacing it by a jet passing similar requirements (jet-electron model, ATLAS). For all other processes ($t\bar{t}$, W/Z+jets, di-bosons), the templates are obtained from simulation.
To estimate the W+jets background, ATLAS uses the distributions from simulation and extracts an overall normalization factor and the flavor composition from data. CMS extracts the W+jets shapes and the normalization from the events that fail the reconstructed top quark mass cut, subtracting other backgrounds.
For the signal extraction, ATLAS uses a set of discriminant variables as input to a cut based analysis and a Neural Network multivariate analysis. The main variables are the reconstructed top quark mass, the pseudorapidity of the light (untagged) jet, $|\eta_j|$ and the transverse energy of the light (untagged) jet. CMS carries out the extraction in a different way, performing a maximum likelihood fit to the distribution of $|\eta_j|$.

2.3 Results

The dominant sources of systematic uncertainty arise from detector simulation and object modeling, where the higher effect comes from jet energy scale (9%) b-tagging (18% ATLAS, 3% CMS), and jet energy resolution (]6% ATLAS, 1% CMS). Another main source of uncertainty are theoretical uncertainties. In the case of CMS the renormalization and factorization scale Q^2 (7%) is the most important, while for ATLAS, the effect of initial and final state radiation (14%) is the dominant one, followed by the choice of generator (11%) and parton shower modeling (10%).
The baseline result for ATLAS comes from the analysis based on cuts, that uses final states with 2 and 3 jets, and has a slightly smaller overall expected uncertainty. The value of the cross section measured by this analysis on 0.7fb^{-1} of data is: $\sigma_t = 90^{+9}_{-9}(stat)^{+31}_{-20}(syst) = 90^{+32}_{-22}$pb.
The cross section measured by CMS, using 1.14 fb^{-1} in final states with muons and 1.5 fb^{-1} in final states with electrons, is: $\sigma_t = 70.2 \pm 5.2(stat) \pm 10.4(syst) \pm 3.4(lumi)$pb, and from this value, CMS provides an estimation of $|V_{tb}|$, assuming $|V_{ts}|, |V_{td}| << |V_{tb}|$: $|V_{tb}| = \sqrt{\frac{\sigma_t}{\sigma_t^{th}}} = 1.04 \pm 0.09(exp.) \pm 0.02(th.)$

3 tW associated production

The associated production of single top quarks with a W boson (tW), inaccessible at the Tevatron, is the second in terms of cross section at the LHC, with $\sigma_{tW} = 15.7^{+1.3}_{-1.4}$pb [6]. It has an interesting topology, background to $H \rightarrow WW$searches; and has never been observed.
The leptonic decays of the W bosons are studied at the LHC, in signatures with two leptons, E_T^{miss} and one jet originating from the hadronization of a b-quark. The main backgrounds for

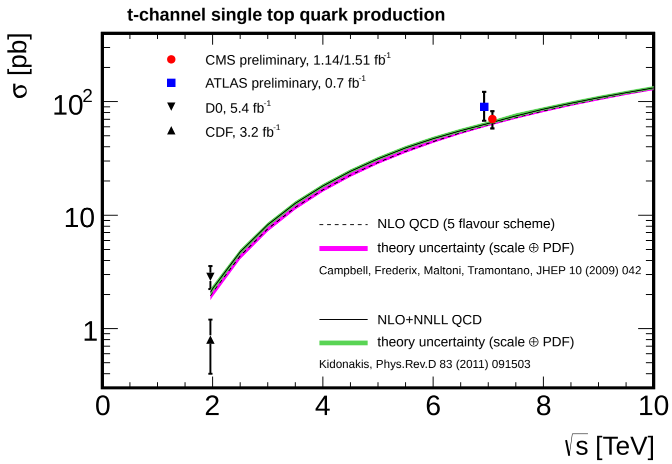

Figure 1: Single top t-channel cross section measurements from ATLAS and CMS, including CDF and D0 results.

this final state are $t\bar{t}$ production and Z+jets, with small contributions from di-bosons, other single top channels, W+jets and QCD.

3.1 Event Selection and background estimation

Events with two leptons, electrons or muons, and one jet are selected [7,8]. The analysis performed by CMS requires the jet to be b-tagged. A substantial amount of E_T^{miss} is expected to be present in the event, due to the presence of two neutrinos in the final state, therefore a cut on the E_T^{miss} of the event is applied: $E_T^{miss} > 50$ (30) ATLAS (CMS). To remove Z+jets background, events inside the Z mass window, $81 < m_{ll} < 101$ GeV, are rejected in the ee and $\mu\mu$ final states.
To complete the definition of the signal region CMS applies cuts on two extra variables, the p_T of the system formed by the leptons, the jet and E_T^{miss}, and H_T, defined as the scalar sum of the p_T of the leptons, the p_T of the jet and E_T^{miss}. ATLAS has a dedicated anti $Z \to \tau\tau$ cut: $\Delta\phi(l_1, E_T^{miss}) + \Delta\phi(l_2, E_T^{miss}) > 2.5$.
CMS estimates the Z+jets background from data, using events in and out of the Z mass window, and uses two $t\bar{t}$ enriched control regions (events with two jets with either one or both of them b-tagged) that are considered in the significance calculation to constrain $t\bar{t}$ contamination and b-tagging efficiency. ATLAS also estimates Z+jets background from data, using the so called ABCDEF method, where orthogonal cuts on 2 variables (m_{ll} and E_T^{miss}) define signal and background enriched regions. The contribution from fake leptons coming from W+jets (single) and QCD (double-fake) is estimated in ATLAS using the matrix method ($< 1\%$ effect). Finally, an estimation of the $Z \to \tau\tau$ background from data is performed and a scale factor for $t\bar{t}$ is obtained from events with two jets.

3.2 Results

The main sources of systematic uncertainty for CMS are the ones associated to the b-tagging (10%) and Q^2 (10%); while for ATLAS, the jet energy scale (35%) and resolution (32%), and background normalization are dominant.
ATLAS set a 95% CL limit on the production of tW of $\sigma_{tW} < 39.1(40.6)$pb obs.(exp.) with an observed significance of 1.2σ, estimating a value of the cross section of $\sigma_{tW} = 14^{+5.3}_{-5.1}(stat.)^{+9.7}_{-9.4}(syst.)$ pb using 0.7 fb^{-1} of data.
CMS, with 2.1fb^{-1} has an observed (expected) significance of 2.7σ ($1.8\pm0.9\sigma$), with a measured

value of the cross section and 68% CL interval of $\sigma_{tW} = 22^{+9}_{-7}(stat + sys)$pb.

4 s-channel

The s-channel, $\sigma_s = 4.6 \pm 0.3$pb [9] , is a process sensitive to several models of new physics, like W' bosons or charged Higgs bosons. Similar to tW production, it has not been observed yet. It has a very challenging lepton+jets signature, difficult to separate from the backgrounds ($t\bar{t}$, W+jets and QCD). At the LHC, ATLAS performs an analysis [10] using similar objects and preselection as for the t-channel; as well as the same background estimations for QCD and W+jets. After the final selection, made with a set of cuts, the signal purity is 6%. An upper limit on the production cross section is set at 95% CL, $\sigma_t < 26.5(20.5)$ pb observed (expected) with 0.7 fb^{-1} of data.

5 Other single top studies: FCNC single top quark production

ATLAS performs a search for Flavor Changing Neutral Currents (FCNC) [11] in the 1 jet bin, using leptonic decays. Events are classified using a neural network where the most significant variables are the p_T of the W boson, $\Delta R_{(b-jet,lepton)}$ and lepton charge. Over an integrated luminosity of 2.05 fb^{-1}, no excess is observed over the Standard Model expectations and limits are set on the coupling constants κ_{ugt}/Λ and κ_{cgt}/Λ, and on the branching fractions $t \to ug$ and $t \to cg$: $\sigma(qg \to t) \cdot B(t \to Wb) < 3.9$pb (95% CL), $B(t \to ug) < 5.7 \cdot 10^{-5}$, $B(t \to cg) < 2.7 \cdot 10^{-4}$.

6 Conclusion and outlook

ATLAS and CMS have a broad program of single top physics: the cross section of the t-channel production has been measured, allowing to also measure $|V_{tb}|$ at the 10% level; the first hints of tW associated production have been studied with a significance close to 3σ; the first upper limits on s-channel production have also been set; and finally, there are already results from other single top studies, the latest concerning the FCNC single top quark production.

References

1. ATLAS Collaboration, JINST 3 (2008) S08003.
2. CMS Collaboration, JINST 3 (2008) S08004.
3. N. Kidonakis, *Phys. Rev.* D **83**, 091503 (2011)
4. ATLAS Collaboration, *"Measurement of the t-channel Single Top-Quark Production Cross Section in 0.70 fb^{-1} of pp Collisions at $\sqrt{s} = 7$ TeV collected with the ATLAS detector"*, ATLAS-CONF-2011-101(2011).
5. CMS Collaboration, *"Measurement of the single top t-channel cross section in pp collisions at $\sqrt{s} = 7$ TeV using 2011 data"*, CMS PAS TOP-11-021 (2012).
6. N. Kidonakis, *Phys. Rev.* D **82**, 054018 (2010).
7. ATLAS Collaboration, *"Search for Wt associated production in dilepton final states with 0.70 fb^{-1} of $\sqrt{s} = 7$ TeV pp collision data in ATLAS"*, ATLAS-CONF-2011-104 (2011).
8. CMS Collaboration, *"Search for single top tW associated production in the dilepton decay channel in pp collisions at $\sqrt{s} = 7$ TeV "*, CMS PAS TOP-11-022 (2011).
9. N. Kidonakis, *Phys. Rev.* D **81**, 054028 (2010).
10. ATLAS Collaboration, *"Search for s-channel single top-quark production in pp collisions at $\sqrt{s} = 7$ TeV"*, ATLAS-CONF-2011-118 (2011).
11. ATLAS Collaboration, *"Search for FCNC single top-quark production at $\sqrt{s} = 7$ TeV with the ATLAS detector"*, Submitted to Phys. Lett. B, arXiv:1203.0529 (2012).

5.
Heavy Ion

RECENT ELLIPTIC FLOW MEASUREMENTS AT RHIC

HIROSHI MASUI FOR THE STAR COLLABORATION
Lawrence Berkeley National Laboratory, 1 Cyclotron Road, Berkeley, CA 94720

We present recent STAR measurements of elliptic flow v_2 in Au + Au collisions at $\sqrt{s_{NN}} = 7.7$ - 39 GeV from Bean Energy Scan at RHIC. We observe that the relative difference of v_2 between baryons and anti-baryons significantly increases with decreasing the beam energy, and the v_2 for ϕ mesons is deviated from other hadrons at $\sqrt{s_{NN}} = 11.5$ GeV. These results are the possible implication where hadronic phase is dominated at lower energies.

1 Introduction

Elliptic flow is one of the key observables to study the properties of the Quark Gluon Plasma (QGP) created in heavy ion collisions [1]. It is characterized by the second harmonic coefficient of azimuthal particle distribution

$$v_2 = \langle \cos\left(2[\phi - \Psi_{\rm RP}]\right)\rangle\,, \qquad (1)$$

where ϕ denotes the azimuth of produced particles, $\Psi_{\rm RP}$ is the azimuth of reaction plane made by the beam direction and the impact parameter vector, and brackets denote the average over particles of interest and over events.

The Beam Energy Scan (BES) program at Relativistic Heavy Ion Collider (RHIC) has begun since 2010 in order to search for the phase boundary as well as for the critical point by exploring the QCD phase diagram [2]. There are two main groups of signatures proposed to achieve these goals; (1) disappearance of QGP signatures and (2) critical point induced fluctuations. One of the main signatures is the number of constituent quark (NCQ) scaling of elliptic flow (v_2) observed at top RHIC energies [3,4], where the measured v_2 for identified particles shows the scaling behavior by number of constituent quarks at $p_T > 2$ GeV/c. The results indicate that the large amount of elliptic flow is developed at partonic phase prior to the hadronization. It is also important to point out that the ϕ mesons show the same magnitude of v_2 and also follow the NCQ scaling [5]. If the hadron phase is dominated in heavy ion collisions, their v_2 is expected to be small due to the small hadronic cross section of ϕ meson with other hadrons and hence the NCQ scaling for ϕ is broken [6]. Therefore, the measurements of elliptic flow are critical to study the structures of QCD phase diagram and to search for the possible phase boundary at low beam energies.

In this article, we present the recent STAR measurements of v_2 for unidentified charged particles as well as identified π, K, p, ϕ and Λ in Au + Au collisions at $\sqrt{s_{NN}} = 7.7$ - 39 GeV from RHIC BES, and discuss the implications of dominance of hadronic phase at low energies.

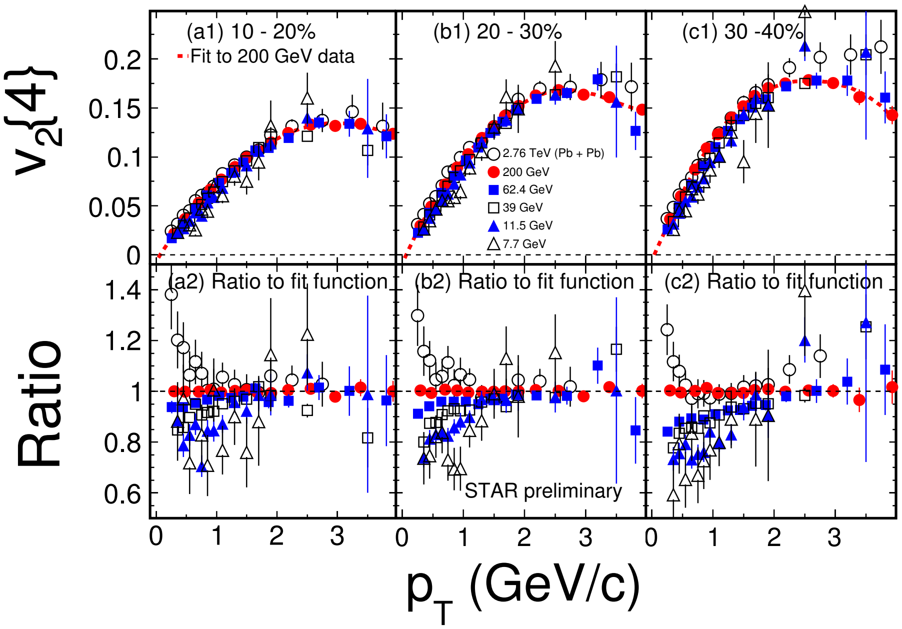

Figure 1: Top three panels show p_T dependence of v_2 for unidentified charged particles at $\sqrt{s_{NN}}$ = 7.7 - 200 GeV from STAR, and 2.76 TeV from ALICE in 10-20%, 20-30% and 30-40% centrality classes. Bottom panels show the ratio of v_2 to the polynomial fit of that at $\sqrt{s_{NN}}$ = 200 GeV. The error bars are statistical errors only.

2 STAR detector at RHIC

The first phase of Beam Energy Scan was accomplished in the year 2010 and 2011 at RHIC by varying the beam energies from 7.7 to 62.4 GeV in $\sqrt{s_{NN}}$. The main tracking detector at the STAR, Solenoid Tracker At RHIC, is the Time Projection Chamber (TPC) [7], which covers the full azimuth and pseudorapidity $|\eta| < 1.8$. The measurements of v_2 are carried out in $|\eta| < 1$ to ensure the uniform acceptance across the different beam energies. The TPC is also used to determine the collisions centrality by measuring the charged particle multiplicity distribution in $|\eta| < 0.5$. The event plane method is used to estimate the reaction plane using the TPC. A minimum $|\eta|$ gap 0.05 is used between particle of interest and event plane to avoid self-correlation of particles, and to reduce the non-flow effects. The π, K and p are identified by using the specific energy loss in the TPC together with the mass square from the Time-Of-Flight detector [8]. Other hadrons are measured through their hadronic decay channel; $K_S^0 \to \pi^+ + \pi^-$, $\phi \to K^+ + K^-$ and $\Lambda \to p + \pi^-$ ($\bar{\Lambda} \to \bar{p} + \pi^+$) with additional topological cuts to improve the signal to background ratio for weak decays.

3 Unidentified charged particles

Figure 1 shows the comparison of v_2 for unidentified charged particles at $\sqrt{s_{NN}}$ = 7.7 - 2760 GeV as a function of transverse momentum p_T in three different centrality classes, 10-20%, 20-30% and 40-40% [9]. The results from $\sqrt{s_{NN}}$ = 7.7 - 39 GeV are compared to the previously published STAR measurements at $\sqrt{s_{NN}}$ = 62.4 [10] and 200 GeV [11], and also to the results at $\sqrt{s_{NN}}$ = 2.76 TeV from ALICE [12]. The $v_2\{4\}$ in the y-axis title indicates that the results are obtained by using the four particle cumulant method [13,14] in order to reduce the background contributions from direct two particle correlations, such as di-jets, resonance decays and so on. Bottom panels show the ratio of $v_2\{4\}$ to the polynomial fit of that at 200 GeV. In $p_T > 2$ GeV/c, the $v_2\{4\}$ are consistent within statistical errors from 7.7 to 2.76 TeV, whereas the

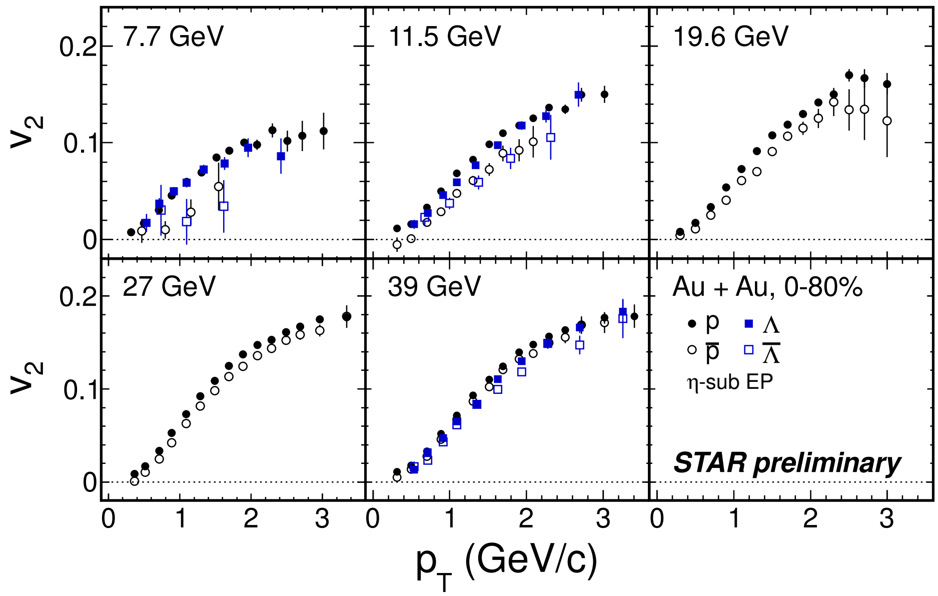

Figure 2: The v_2 for protons (circles) and Λ's (squares) as a function of p_T in 0-80% Au + Au collisions at $\sqrt{s_{NN}}$ = 7.7 - 39 GeV. The error bars are statistical errors only.

magnitude of $v_2\{4\}$ increase from 7.7 to 2.76 TeV in $p_T < 2$ GeV/c. The 20-40% decrease of $v_2\{4\}$ in low beam energies could be understood as different particle compositions, where the baryons (mesons) are dominated at low (high) energies with small (large) v_2 for a given p_T bin. In order to understand the systematics of v_2 in low beam energies, it is important to measure the v_2 for identified hadrons.

4 Identified hadrons

Figure 2 shows the v_2 for protons and Λ's as a function of p_T in 5 different collisions energies[9,15]. One can see that the magnitude of v_2 increases as a function of $\sqrt{s_{NN}}$, and the difference of v_2 between baryons and antibaryons increase with decreasing $\sqrt{s_{NN}}$. The measured v_2 for protons and Λ's are similar in terms of both magnitude and difference of v_2. One can argue that the NCQ scaling is broken between particles and antiparticles at $\sqrt{s_{NN}}$ = 7.7 and 11.5 GeV as a consequence of the significant difference of v_2. In order to quantify the difference of v_2 between particles and antiparticles, the relative difference of v_2 is calculated from the average v_2 in the measured p_T range. Figure 3 (a) shows the excitation function of the relative difference of v_2 for baryons and mesons. There are about 50-60% differences on v_2 for baryons at low beam energies, while the difference for mesons exhibit relatively smaller ($\sim$ 10%) than that for baryons. Several attempts to interpret the data have been made by baryon number transport[16], and by effects of hadronic potentials[17] but there are no quantitative conclusions to understand the difference of v_2 at low energies. Figure 3 (b) shows the ratio of v_2 for ϕ mesons to the protons as a function of p_T in 3 different $\sqrt{s_{NN}}$[18]. In $p_T < 2$ GeV/c, the ratio $v_2(\phi)/v_2(p)$ appears to decrease more than 50% at 11.5 GeV as compared to the results at 200 GeV. The decrease of v_2 for ϕ meson could be an indication that the hadronic phase is dominated at $\sqrt{s_{NN}} = 11.5$ GeV as predicted[6].

5 Conclusions

We present the STAR measurements of elliptic flow in Au + Au collisions at $\sqrt{s_{NN}}$ = 7.7 - 39 GeV from Beam Energy Scan at RHIC. Relative difference of v_2 between particles and

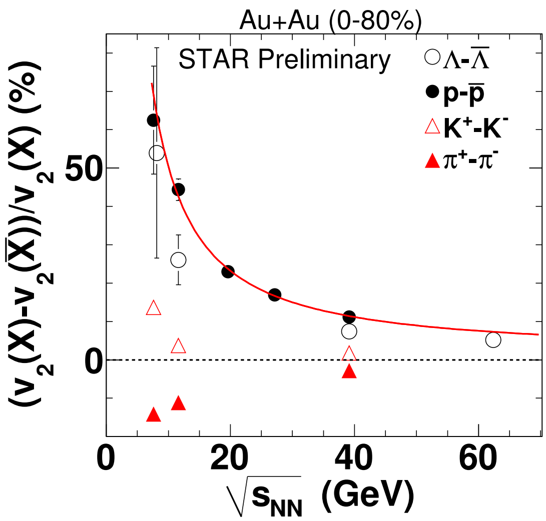

(a)

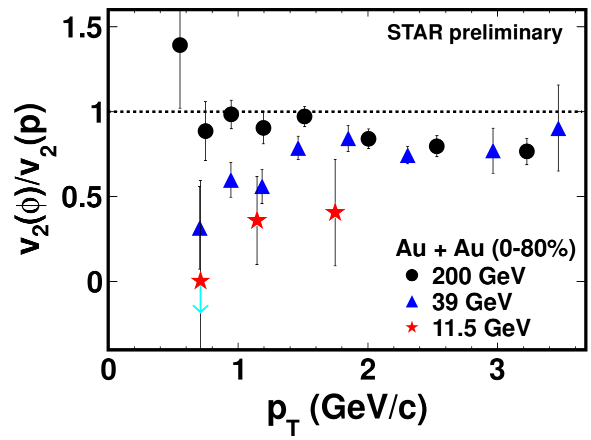

(b)

Figure 3: (a) Relative difference of v_2 between particles and antiparticles as a function of $\sqrt{s_{NN}}$ in 0-80% Au + Au collisions for Λ's (open circles), protons (solid circles), kaons (open triangles) and pions (solid triangles). Solid line just guides your eyes for proton results. (b) Ratio of v_2 for ϕ mesons to the protons as a function of p_T in 0-80% Au + Au collisions at $\sqrt{s_{NN}}$ = 11.5 (stars), 39 (triangles) and 200 GeV (circles). The error bars are statistical errors only for both figures.

antiparticles is found to increase with decreasing the beam energies. The number of constituent quark scaling of v_2 is broken between particles and antiparticles at $\sqrt{s_{NN}} = 7.7$ and 11.5 GeV as a consequence of the difference of v_2. The v_2 for ϕ mesons decreases with decreasing beam energies and is deviated from other hadrons at $\sqrt{s_{NN}} = 11.5$ GeV. These results might suggest that the hadronic phase is dominated at $\sqrt{s_{NN}} = 7.7$ and 11.5 GeV.

1. S. A. Voloshin, A. M. Poskanzer and R. Snellings, arXiv:0809.2949 [nucl-ex].
2. M. M. Aggarwal *et al.* [STAR Collaboration], arXiv:1007.2613 [nucl-ex].
3. S. S. Adler *et al.* [PHENIX Collaboration], Phys. Rev. Lett. **91**, 182301 (2003)
4. J. Adams *et al.* [STAR Collaboration], Phys. Rev. Lett. **92**, 052302 (2004)
5. B. I. Abelev *et al.* [STAR Collaboration], Phys. Rev. Lett. **99**, 112301 (2007)
6. B. Mohanty and N. Xu, J. Phys. G **36**, 064022 (2009)
7. M. Anderson *et al.*, Nucl. Instrum. Meth. A **499**, 659 (2003)
8. W. J. Llope [STAR Collaboration], Nucl. Instrum. Meth. A **661**, S110 (2012).
9. S. Shi [for the STAR Collaboration], arXiv:1201.3959 [nucl-ex].
10. B. I. Abelev *et al.* [the STAR Collaboration], Phys. Rev. C **75**, 054906 (2007)
11. B. I. Abelev *et al.* [STAR Collaboration], Phys. Rev. C **77**, 054901 (2008)
12. K. Aamodt *et al.* [The ALICE Collaboration], Phys. Rev. Lett. **105**, 252302 (2010)
13. N. Borghini, P. M. Dinh and J. -Y. Ollitrault, Phys. Rev. C **63**, 054906 (2001)
14. N. Borghini, P. M. Dinh and J. -Y. Ollitrault, Phys. Rev. C **64**, 054901 (2001)
15. A. Schmah [STAR Collaboration], J. Phys. G **38**, 124049 (2011).
16. J. C. Dunlop, M. A. Lisa and P. Sorensen, Phys. Rev. C **84**, 044914 (2011)
17. J. Xu, L. -W. Chen, C. M. Ko and Z. -W. Lin, Phys. Rev. C **85**, 041901 (2012)
18. X. Zhang [STAR Collaboration], arXiv:1203.5193 [nucl-ex].

Flow Phenomena in Pb-Pb Collisions at CMS

Rylan Conway for the CMS Collaboration
Department of Physics, University of California, 1 Shields Ave,
Davis, CA 95616 U.S.A.

This proceeding reports the results from azimuthal angle correlations of charged hadrons measured in $\sqrt{s}_{NN} = 2.76$ TeV PbPb collisions by the CMS experiment. The azimuthal distributions exhibit anisotropies that are correlated with the event-by-event orientation of the participant plane (the plane that contains the beam axis and the short direction of the lenticular overlap region). In general, the participant plane will not contain the reaction impact parameter vector because of fluctuations that arise from having a finite number of nucleons. The second Fourier coefficient of the charged hadron azimuthal distributions was measured as a function of transverse momentum, pseudorapidity, and centrality in a broad kinematic range. In addition, results on higher-order Fourier components are presented and their connection to the hydrodynamic medium will be discussed.

1 Introduction

In non-central heavy ion collisions, the interaction region is spatially anisotropic, often characterized as an "almond shape". This anisotropy in the initial collision geometry leads to a final-state momentum azimuthal anisotropy with respect to the participant plane. This anisotropy can be characterized with a Fourier expansion of the azimuthal distribution of charged particles. The resulting Fourier coefficients are known as anisotropy or flow parameters and provide information about the collective behavior of the medium. The second coefficient, v_2, is referred to as elliptic flow and is one of the most important measurements we have that can probe the hydrodynamic properties of the quark-gluon plasma. v_2 can also be used to constrain parton energy-loss models. In particular, the path-length of a jet traversing the medium will be correlated with its angle with respect to the participant plane, since the short-axis of the "almond" will be in the participant plane. It is expected that there will be more high-p_T particles emitted closer to the participant plane giving a non-zero value for v_2, the actual value of which will depend on the exact path-length dependence of the energy loss mechanism.

2 The Event Plane Method

Since the participant plane is not experimentally observable, we have to estimate with the event plane, which is the plane that contains the beam axis and the direction of maximum transverse energy [1]. Once the event plane has been calculated for each event and corrected for detector inefficiencies the average correlation of the particles in each event is calculated and gives us an estimate of v_2 as a function of p_T, η, and centrality. Finally, due to the finite resolution of the detector, the measurements must be corrected by a resolution factor to give the actual elliptic flow values.

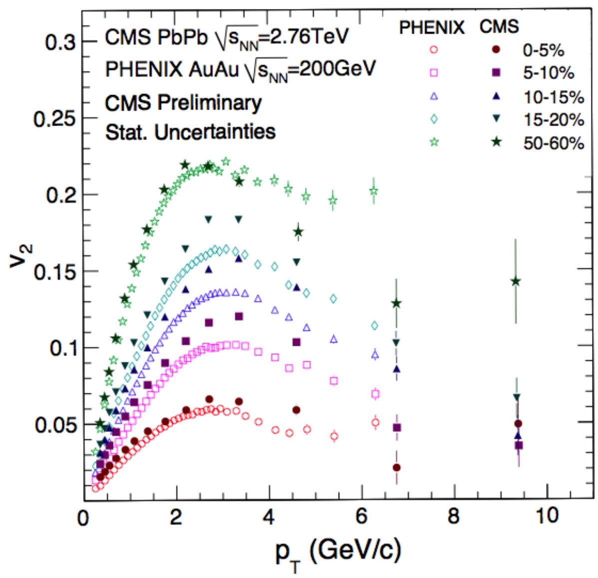

Figure 1: The single-particle azimuthal anisotropy, v_2, as a function of p_T at mid-rapidity ($|\eta| < 0.8$ for five different centrality classes measured with the event plane (EP) method. CMS data from PbPb collisions at $\sqrt{s_{NN}} = 2.76$ TeV is shown with the solid markers and PHENIX data from AuAu collisions at $\sqrt{s_{NN}} = 200$ GeV is shown with the open markers. Only statistical uncertainties are shown.

Fig. 2 shows a direct comparison between CMS and PHENIX results for v_2 as a function of p_T in five different centrality classes at mid-rapidity ($|\eta| < 0.8$) using the event plane method. Even though there is an increase in center-of-mass energy by a factor of 14 from RHIC (PHENIX) to the LHC (CMS), there is only a slight increase in the observed differential v_2 values. In both cases we see v_2 reach a maximum at 3 GeV/c. This is expected since at higher momentum hard processes begin to dominate and hydrodynamic effects become less significant [1].

3 Dihadron Correlations

Dihadron correlations are another way of investigating flow properties of the QGP. Since these measurements do not rely on the reaction plane and the systematic uncertainties associated with finding the event plane, they are a useful alternative. The associated yield, shown in Fig. 2(a), shows the two-particle correlation plotted as a function of $\Delta\eta$ and $\Delta\phi$ between the two particles. The correlated particles are each chosen such that a "trigger" particle in a given p_T^{trig} range is paired with all of the "associated" particles in a given event that are in a specified p_T^{assoc} range [2].

By looking at the long-range region of the associated yield, $2 < |\Delta\eta| < 4$, and projecting onto the $\Delta\phi$ axis, we can again Fourier expand the 1-D associated yield and extract the coefficients, $V_{n\Delta}(p_T^{trig}, p_T^{assoc})$. It has been shown [2] that these Fourier coefficients from dihadron correlations can be factored into the product of the single-particle azimuthal anisotropy harmonics: $V_{n\Delta}(p_T^{trig}, p_T^{assoc}) = v_n(p_T^{trig}) \times v_n(p_T^{assoc})$. With this relationship we can use dihadron correlations to compare with other techniques such as the event plane method. We can also measure higher-order harmonics, which are shown as a function of N_{part} in Fig. 2(b). One can see an obvious centrality dependence of v_2. However, v_3 - v_5 are largely independent of centrality.

4 v_2 at high p_T

Flow effects are only expected to be significant up to $p_T \approx 3$ GeV/c. At higher transverse momentum, recombination effects and hard processes begin to dominate [1]. Despite the absence of hydrodynamic flow at high p_T, we can still use the anisotropy parameter v_2 to constrain the

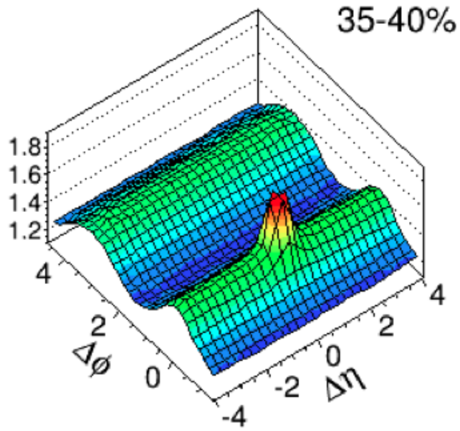

(a) The associated yield

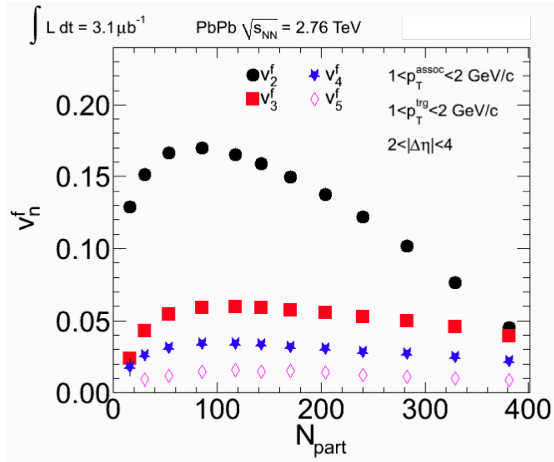

(b) Higher-order flow harmonics

Figure 2: Subfigure (a) shows the associated yield in PbPb collisions at $\sqrt{s_{NN}} = 2.76$ TeV in $35-40\%$ centrality class with $4 < p_T^{trig} < 6$ GeV/c and $2 < p_T^{assoc} < 4$ GeV/c. A $\cos(2\Delta\phi)$ modulation is clearly visible away from the jet region $(2 < |\eta| < 4)$, which is indicative of elliptic flow. Subfigure (b) shows the single-particle azimuthal harmonics, $v_2 - v_5$, from the long range $(2 < |\eta| < 4)$ azimuthal dihadron correlations as a function of N_{part} in PbPb collisions at $\sqrt{s_{NN}} = 2.76$ TeV for $1 < p_T^{assoc} < 2$ GeV/c and $1 < p_T^{trig} < 2$ GeV/c. $v_3 - v_5$ are essentially independent of the collision centrality, as expected if they are caused by fluctuations in the initial collision geometry.

path-length dependence of parton energy-loss mechanisms in a QGP medium [3]. Fig. 3(a) shows v_2 as a function of transverse momentum up to $p_T \approx 60$ GeV/c in six different centrality classes at mid-rapidity $(|\eta| < 1)$ with the event plane method. The data is also compared to 2010 CMS data (blue open circles) and ATLAS data (black open squares). This is the first accurate measurement of v_2 at such high p_T. Fig. 3(b) shows v_2 as a function of centrality in six different p_T ranges for $|\eta| < 1$ (red circles) and $1 < |\eta| < 2$ (blue open squares). You can see that in all centrality classes a non-zero v_2 persists up to $p_T \approx 40$ GeV/c.

5 Conclusions

Detailed measurements of charged hadron azimuthal anisotropies in PbPb collisions at $\sqrt{s_{NN}} = 2.76$ TeV have been presented. The results cover a broad kinematic range in different centrality classes. In particular, v_2 measurements from the event plane method were shown at a p_T range much higher then any previously published results. The data indicate that the elliptic flow at mid-rapidity at LHC energies is comparable to that at RHIC energies. It was also shown that non-zero higher-order Fourier coefficients exist and are independent of centrality. These results will be useful in comparison to hydro models and will help us to better understand the hydrodynamic properties of the QGP. The high-p_T v_2 data indicates that there is parton energy-loss occurring in the medium that is correlated with the reaction plane, thus implying a path-length dependence. Further studies will be useful for constraining this path-length dependence in energy-loss models.

References

1. CMS Collaboration, arXiv:1204.1409v1 [nucl-ex] 6 Apr 2012.
2. CMS Collaboration, arXiv:submit/0398170 [nucl-ex] 16 Jan 2012.
3. CMS Collaboration, arXiv:1204.1850v1 [nucl-ex] 9 Apr 2012

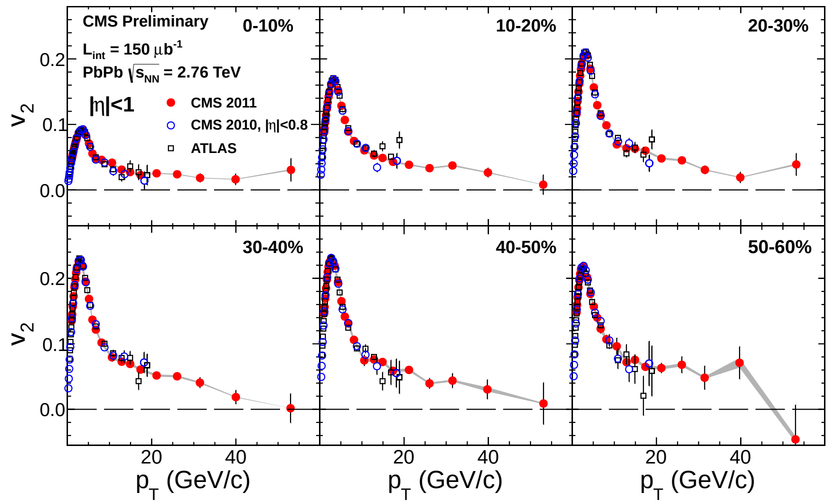

(a) v_2 as a function of p_T for six different centrality classes.

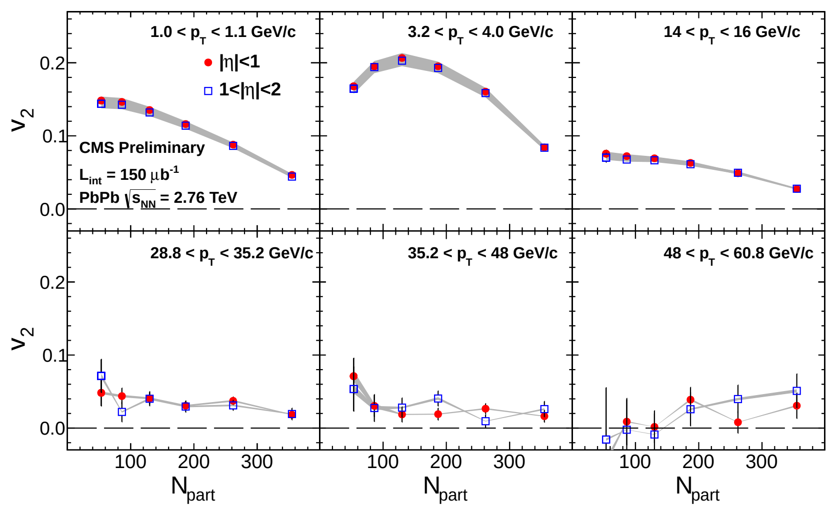

(b) v_2 as a function of N_{part} for six different p_T ranges.

Figure 3: Subfigure (a) shows the single-particle azimuthal anisotropy, v_2, as a function of the charged particle transverse momentum from $1 - 60$ GeV/c with $|\eta| < 1$ in six different centrality ranges in PbPb collisions at $\sqrt{s_{NN}} = 2.76$ TeV/c. Results from the data collected in 2011 by the CMS experiment are shown (red solid markers) as well as ATLAS (black open squares) and 2010 CMS data (blue open circles). Error bars denote the statistical uncertainty while the grey bands correspond to the systematic uncertainty. Subfigure (b) shows v_2 as a function of N_{part} in six different p_T ranges with $|\eta| < 1$ (red circles) and $1 < |\eta| < 2$ (blue open squares) in PbPb collisions at $\sqrt{s_{NN}} = 2.76$ TeV. Error bars denote the statistical uncertainty while the grey bands correspond to the systematic uncertainty.

Di-lepton production at STAR

Lijuan Ruan for the STAR Collaboration
Physics Department, Brookhaven National laboratory, Upton NY 11973

The recent results on di-electron production in $p+p$ and Au+Au collisions at $\sqrt{s_{NN}} = 200$ GeV are presented. The cocktail simulations of di-eletrons from light flavor meson decays and heavy flavor decays are reported and compared with data. The perspectives for di-lepton measurements in lower energy Au+Au collisions and with future detector upgrades are discussed.

1 Introduction

Ultra-relativistic heavy ion collisions provide a unique environment to study properties of strongly interacting matter at high temperature and high energy density [1]. One of the crucial probes of this strongly interacting matter are di-lepton measurements in the low and intermediate mass region. Di-leptons are not affected by the strong interaction once produced, therefore they can probe the whole evolution of the collision. The di-lepton spectra in the intermediate mass range ($1.1 < M_{ll} < 3.0$ GeV/c^2) are directly related to thermal radiation of the Quark-Gluon Plasma (QGP) [2,3]. In the low mass range ($M_{ll} < 1.1$ GeV/c^2), we can study vector meson in-medium properties through their di-lepton decays, where any modifications observed may relate to the possibility of chiral symmetry restoration.

Anisotropic flow, an anisotropy in the particle production relative to the reaction plane, leads to correlations among particles and have been studied by analysis of these correlations [4]. The elliptic flow v_2 is the second harmonic of the azimuthal distribution of particles with respect to the reaction plane. It is believed that di-lepton v_2 measurements will provide another independent way to study medium properties. Specifically, the v_2 as a function of transverse momentum (p_T) in different mass regions will enable us to probe the properties of medium from hadron-gas dominated to QGP dominated [5].

At STAR, the newly installed Time-of-Flight detector (TOF) offers high acceptance and efficiency [6]. The TOF, combined with measurements of ionization energy loss (dE/dx) from the Time Projection Chamber (TPC) [7,8,9], enables electron identification with high purity from low to intermediate p_T [10,11,12]. In this article we present the di-electron mass spectra in $p+p$ and Au+Au collisions at $\sqrt{s_{NN}} = 200$ GeV. The elliptic flow v_2 measurements are also reported in 200 GeV Au+Au collisions. Future capabilities for di-lepton measurements at STAR in lower energy Au+Au collisions and with detector upgrades are discussed.

2 Recent results on di-electron production

We utilize 107 million, 270 million and 150 million events for $p+p$, minimum-bias (0-80%) Au+Au, and central (0-10%) Au+Au di-electron analyses, respectively. The $p+p$ events were taken in 2009 and 72% of the full TOF system was installed and operational while the Au+Au events were taken in 2010 with full TOF system coverage. By applying velocity and dE/dx cuts on tracks with $p_T > 0.2$ GeV/c, we can achieve the purity for the electron candidates at 99% in $p+p$ collisions and 97% in minimum-bias Au+Au collisions.

The di-electron signals may come from light flavor hadron decays and heavy flavor hadron decays, for example, π^0, η, and η' Dalitz decays: $\pi^0 \to \gamma e^+e^-$, $\eta \to \gamma e^+e^-$, and $\eta' \to \gamma e^+e^-$; vector meson decays: $\omega \to \pi^0 e^+e^-$, $\omega \to e^+e^-$, $\rho^0 \to e^+e^-$, $\phi \to \eta e^+e^-$, $\phi \to e^+e^-$, and $J/\psi \to e^+e^-$; heavy flavor decays: $c\bar{c} \to e^+e^-$ and $b\bar{b} \to e^+e^-$; and Drell-Yan contributions. In Au+Au collisions, we look for additional vector meson in-medium modifications in the low mass region and possible QGP thermal radiations in the intermediate mass range.

The e^+ and e^- pairs from the same events are combined to reconstruct the invariant mass distributions (M_{ee}) marked as unlike-sign distributions. The unlike-sign distributions contain both signal and background. The background contains the random combinatorial pairs and correlated pairs. The electron candidates are required to be in the range of $|\eta| < 1$ and $p_T > 0.2$ GeV/c while e^+e^- pairs are required to be in the rapidity range of $|y_{ee}| < 1$. Two methods are used for background estimation, based on same-event like-sign and mixed-event unlike-sign techniques. In the like-sign technique, electron pairs with the same charge sign are combined from the same events. In the mixed-event technique, unlike-sign pairs are formed from different events. In $p+p$ collisions, we subtract the like-sign background at $M_{ee} < 0.4$ GeV/c^2 and mixed-event background in the higher-mass region. In Au+Au collisions, we subtract the like-sign background at $M_{ee} < 0.7$ GeV/c^2 and mixed-event background in the higher-mass region. The detailed analysis procedures can be found in [13,14].

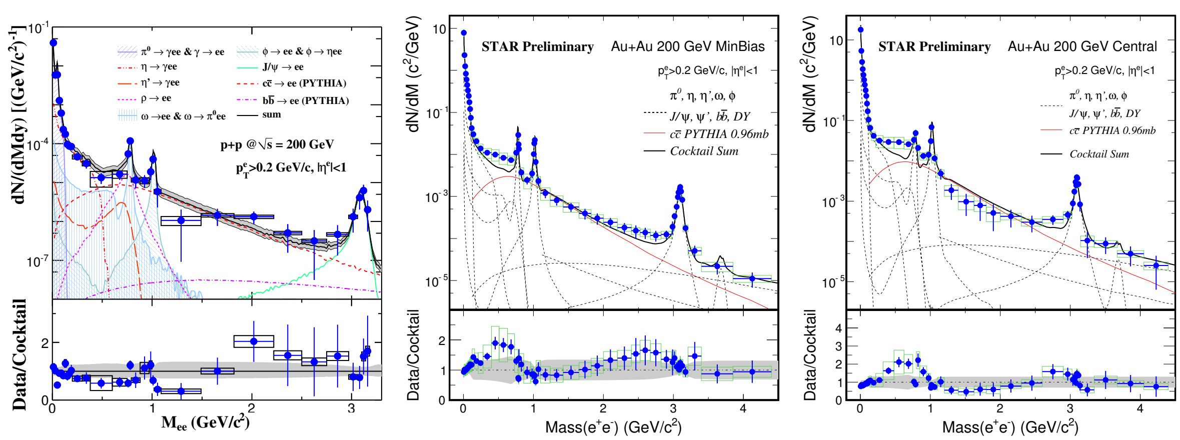

Figure 1: The comparison for di-electron continuum between data and simulation after efficiency correction within the STAR acceptance in $p+p$ (left panel), minimum-bias (middle panel) Au+Au and central (right panel) Au+Au collisions at $\sqrt{s_{NN}} = 200$ GeV. The di-electron continuum from simulations with different source contributions are also shown. The bars and boxes (bands) represent statistical and systematic uncertainties, respectively.

After the efficiency correction, the di-electron mass spectra within the STAR acceptance are shown in Fig. 1 for $p+p$, minimum-bias Au+Au and central Au+Au collisions at $\sqrt{s_{NN}} = 200$ GeV. The di-electron mass spectra are not corrected for momentum resolution and radiation energy loss effect. The ratios of data to cocktail simulations are shown in the lower panels. In $p+p$ collisions, the cocktail simulation, which includes the expected components from light flavor meson and heavy flavor meson decays, is consistent with the measured di-electron continuum within uncertainties. We also find that the $c\bar{c} \to e^+e^-$ contribution is dominant in the intermediate mass region. In Au+Au collisions, the ρ^0 contribution is not included and the $c\bar{c} \to e^+e^-$ contribution is from PYTHIA simulation, scaled by the number of underlying binary nucleon-nucleon collisions. In the low mass region $0.15 < M_{ee} < 0.75$ GeV/c^2, the possible enhancement factors, the ratios of the data to the cocktail simulations, are $1.53 \pm 0.07 \pm 0.41$ and $1.72 \pm 0.10 \pm 0.50$ in minimum-bias and central collisions, respectively. This suggests for possible vector meson in-medium modification in this low mass region. Differential measurements as a function of p_T and centrality are on-going.

The di-lepton v_2 measurements provide another independent way to study the medium properties. We use event-plane method to obtain the di-electron v_2. The event-plane is reconstructed using the tracks from the TPC. The details of the method are in Refs. [4,15]. We report the v_2 of di-electron signals in Fig. 2 (left panel) as a function of M_{ee} in minimum-bias Au+Au collisions at $\sqrt{s_{NN}} = 200$ GeV. The differential v_2 of di-electron pairs in the mass regions of $M_{ee} < 0.14$ GeV/c^2 and $0.14 < M_{ee} < 0.30$ GeV/c^2 are shown in the middle and right panels of Fig. 2 as a function of p_T in minimum-bias Au+Au collisions at $\sqrt{s_{NN}} = 200$ GeV. Also shown are the charged [16] and neutral pion [17] v_2. The dominant contribution sources to di-electrons at $M_{ee} < 0.14$ GeV/c^2 and $0.14 < M_{ee} < 0.30$ GeV/c^2 are π^0 Dalitz decay and η Dalitz decay, respectively. We parameterize pion v_2 from low to high p_T, do the Dalitz decay simulation, and obtain the expected di-electron v_2 from π^0 Dalitz decay shown by the solid curve. The simulated v_2 is consistent with the measured di-electron v_2 at $M_{ee} < 0.14$ GeV/c^2. We repeat the same exercise in the η mass region. We assume that η has the same v_2 as K^0_S [15] since the mass of η is close to that of K^0_S. The simulated v_2 of di-electrons from η Dalitz decay, shown by the solid curve, is consistent with the measured di-electron v_2 at $0.14 < M_{ee} < 0.30$ GeV/c^2. The current precision of our v_2 data does not allow to further study a possible deviation from the solid curve due to the other contributions in this mass region. The consistency between the expectations and measurements demonstrates the credibility of our method to obtain the di-electron v_2.

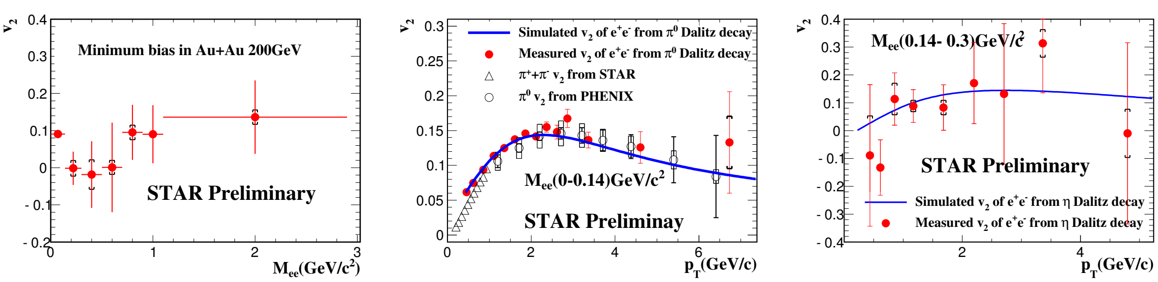

Figure 2: (left panel) The di-electron v_2 as a function of M_{ee} in minimum-bias Au+Au collisions at $\sqrt{s_{NN}} = 200$ GeV. (middle panel) The v_2 of di-electron at $M_{ee} < 0.14$ GeV/c^2 (solid symbol) as a function of p_T in minimum-bias Au+Au collisions at $\sqrt{s_{NN}} = 200$ GeV. Also shown are the charged and neutral pion v_2 and the expected v_2 (solid curve) of di-electrons from π^0 Dalitz decay. (right panel) The v_2 of di-electron at $0.14 < M_{ee} < 0.30$ GeV/c^2 as a function of p_T in minimum-bias Au+Au collisions at $\sqrt{s_{NN}} = 200$ GeV. Also shown is the expected v_2 (solid curve) of di-electrons from η Dalitz decay. The bars and boxes represent statistical and part of systematic uncertainties, respectively.

3 Future perspectives

A factor of two more data taken in 2011 will significantly improve the measurements of mass spectra and elliptic flow in Au+Au collisions at $\sqrt{s_{NN}} = 200$ GeV. In addition, in 2010 and 2011, STAR has taken a few hundred million minimum-bias events in Au+Au collisions at $\sqrt{s_{NN}} = 19.6, 27, 39, 62$ GeV with full TOF azimuthal coverage and low conversion material budget, which will enable us to systematically study the energy dependence of the following physics topics: 1) di-electron enhancement in the low mass region [18,19]; 2) in-medium modifications of vector meson decays; 3) virtual photons [20]; 4) $c\bar{c}$ medium modifications; and 5) possible QGP thermal radiation in the intermediate mass region. With the current data sets, it will be difficult to measure 4) or 5) since they are coupled to each other and one is the other's background for the physics case. So far at RHIC, there is no clear answer about thermal radiation in the intermediate mass region. The future detector upgrade with the Heavy Flavor Tracker at STAR, to be completed in 2014, will provide precise charm cross section measurements [21], however the measurements of $c\bar{c}$ correlations will still be challenging if not impossible. An independent approach is proposed with the Muon Telescope Detector upgrade [22], $\mu - e$ correlations, to measure the contribution from heavy flavor correlations to the di-electron or di-muon continuum. This will make it possible to access the thermal radiation in the intermediate mass region.

4 Summary

In summary, the di-electron mass spectra are measured in 200 GeV $p+p$ and Au+Au collisions at STAR. The cocktail simulations are consistent with the data in 200 GeV $p+p$ collisions. In Au+Au collisions, we observe a possible enhancement by comparison between data and cocktail simulation in the low mass region $0.15 < M_{ee} < 0.75$ GeV/c^2. The first elliptic flow measurements of di-electrons are presented in 200 GeV minimum-bias Au+Au collisions. The v_2 of di-electrons at $M_{ee} < 0.14$ GeV/c^2 and $0.14 < M_{ee} < 0.30$ GeV/c^2 are in agreement with the expectations from previous measurements.

References

1. J. Adams *et al.*, Nucl. Phys. A **757**, 102 (2005).
2. R. Rapp and J. Wambach, Adv. Nucl. Phys. 25 (2000) 1.
3. G. David, R. Rapp and Z. Xu, Phys. Rept. **462**, 176 (2008).
4. A.M. Poskanzer and S.A. Voloshin, Phys. Rev. C **58**, 1671 (1998).
5. R. Chatterjee *et al.*, Phys. Rev. C **75**, 054909 (2007).
6. B. Bonner *et al.*, Nucl. Instr. Meth. A **508**, 181 (2003); M. Shao *et al.*, Nucl. Instr. Meth. A **492**, 344 (2002); J. Wu *et al.*, Nucl. Instr. Meth. A **538**, 243 (2005).
7. M. Anderson *et al.*, Nucl. Instr. Meth. A **499**, 659 (2003).
8. H. Bichsel, Nucl. Instr. Meth. A **562**, 154 (2006).
9. Y. Xu *et al.*, Nucl. Instr. Meth. A **614**, 28 (2010).
10. M. Shao *et al.*, Nucl. Instr. Meth. A **558**, 419 (2006).
11. J. Adams *et al.*, Phys. Lett. B **616**, 8 (2005).
12. J. Adams *et al.*, Phys. Rev. Lett. **94**, 062301 (2005).
13. L. Adamczyk *et al.*, arXiv:1204.1890; L. Ruan *et al.*, Nucl. Phys. A **855**, 269 (2011).
14. J. Zhao *et al.*, J. Phys. G **38**, 124134 (2011).
15. B.I. Abelev *et al.*, Phys. Rev. C **77**, 054901 (2008).
16. Y. Bai, Ph.D. Thesis, NIKHEF and Utrecht University, 2007, http://drupal.star.bnl.gov/STAR/files/Bai_Yuting.pdf .
17. S. Afanasiev *et al.*, Phys. Rev. C **80**, 054907 (2009).
18. A. Adare *et al.*, Phys. Rev. C **81**, 034911 (2010).
19. S. Afanasiev *et al.*, nucl-ex/0706.3034.
20. A. Adare *et al.*, Phys. Rev. Lett. **104**, 132301 (2010).
21. http://rnc.lbl.gov/hft/docs/hft_final_submission_version.pdf; S. Kleinfelder *et al.*, Nucl. Instr. Meth. A **565**, 132 (2006).
22. http://drupal.star.bnl.gov/STAR/system/files/MTD_proposal_v14.pdf; Z. Xu, BNL LDRD project 07-007; L. Ruan *et al.*, J. Phys. G **36**, 095001 (2009); Y. Sun et al., Nucl. Instr. Meth. A **593**, 307 (2008); Y. Wang et al., Nucl. Instr. Meth. A **640**, 85 (2011).

Direct photon measurements at RHIC-PHENIX

K.Okada for the PHENIX collaboration
RIKEN BNL Research Center, BNL Bldg.510A Upton, NY 11973, USA

Recent progress in direct photon measurements at RHIC-PHENIX detector is presented. In $p+p$ collisions, direct photons were measured in the transverse momentum range up to 25 GeV/c at $\sqrt{s} = 200$ GeV at mid-rapidity, extending the range beyond previous measurements. Next-to-leading order perturbative QCD calculations give a good description of the spectrum. It also provides a reference for the heavy ion collisions. A new virtual photon measurement in d+Au collisions indicates no or little cold nuclear effects. In Au+Au collisions, an unexpectedly large positive elliptic flow was observed. It provides information about the formation process of the hot and dense media produced in heavy ion collisions.

Direct photons are defined as photons that do not originate from hadronic decays. Once produced, a photon emerges from the reaction with little disturbance since it only interacts electromagnetically. Hence the direct photon is a unique probe to look deeply into the interaction. The partonic hard interaction is the dominant source of direct photons with large transverse momentum, p_T. The production rate in heavy ion collisions is expected to be consistent with ones in $p+p$ collisions with the average nuclear thickness function unless there is a nuclear effect modifying the parton distribution function. The direct photon production is a good reference to evaluate the jet quenching effect. At low transverse momentum, there are several production mechanisms in heavy ion collisions. It can be produced from $q+\bar{q}$ annihilation in sQGP and from hadron annihilation in the hadronic phase. Also by the interaction with the medium, the parton bremsshtraulung and fragmentation process might be modified compared to the case of $p+p$ collisions.

Up to now, direct photon measurements at PHENIX have been performed with the central arm spectrometers. Real photons are detected in electromagnetic calorimeters (EMCal). Each of two EMCals covers 0.5π rad in azimuthal angle (ϕ) and $|\eta| < 0.35$ in pseudorapidity. The charged particle tracking was performed by the drift chambers and the pad chambers. The ring imaging Cherenkov counter (RICH) provides a powerful electron identification capability. For event classification, there are global detectors. The beam-beam counters (BBCs) positioned at pseudorapidities $3.1 < |\eta| < 3.9$ are used for the minimum bias trigger and for the determination of the centrality class and the reaction plane. The reaction plane detector (RXP) located at $1.0 < |\eta| < 2.8$ was installed for the 2007 data taking period. The PHENIX detector is described in detail elsewhere [1].

The p_T reach in the measurement of the direct photon production in $p+p$ collisions at $\sqrt{s} = 200$ GeV is up to 25 GeV/c. The NLO pQCD calculation shows a good agreement with the data. Figure 1 shows a collection of direct photon cross section measurements in $p+p$ and $p+\bar{p}$ collisions from various experiments. Except a couple of experiments, they are all on a universal curve as a function of $x_T = 2p_T/\sqrt{s}$ with a multiplication of $\sqrt{s}^{4.5}$ to the cross section for a wide range of collision energy. Surprisingly, the PHENIX measurements of low p_T points with virtual photon method [2,3] are also on the same curve.

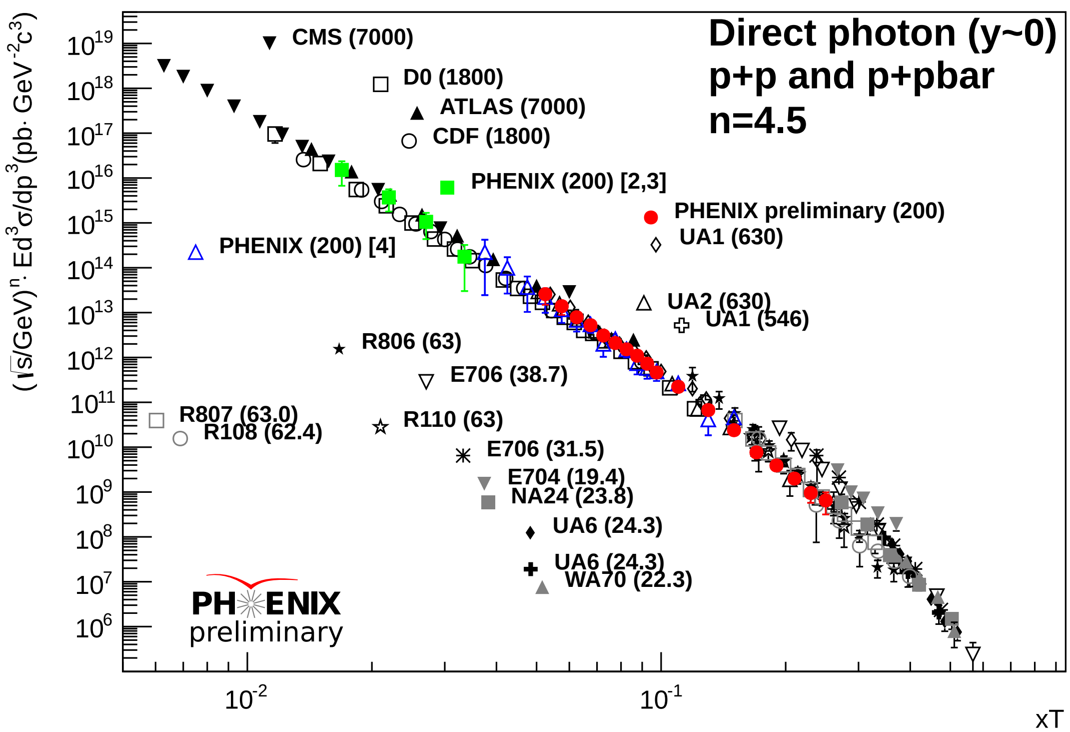

Figure 1: Various direct photon cross section measurements in $p+p$ and $p+\bar{p}$ collisions scaled by $\sqrt{s}^{4.5}$ on $x_T \equiv 2p_T/\sqrt{s}$. The legend shows the experiment and the center of mass energy [GeV] in parenthesis.

When the p_T goes high enough that the valence quark effect is dominant, we expect less direct photon production rate in heavy ion collisions than in the scaled $p+p$ collisions. It is because in a heavy ion d quark is dominant to u quark, while in the proton it is 1:2, and the rate is proportional to charge square in the $q+g$ scattering. The measurement of direct photon production in Au+Au collisions at $\sqrt{s} = 200$ GeV will be finalized soon.

As going to lower p_T ($p_T \lesssim 5$ GeV/c), experimentally it gets harder to extract the direct photon signal because of large background contribution of decay photons. Another way to access the direct photon is to measure the electron pair from its internal conversion. In this approach, the contribution of decay photons (mainly from π^0) is suppressed by applying a threshold on the pair invariant mass. However it requires a large integrated luminosity in compensation for the small conversion probability ($\sim 1\%$). We measured the direct photon production in $p+p$ and Au+Au at $\sqrt{s} = 200$ GeV with this virtual photon method [2,3]. In central Au+Au collisions, the excess of direct photon yield over $p+p$ is exponential in p_T. From the inverse slope, the average temperature was extracted. For the cold nuclear effect, direct photons in $d+$Au collisions are also measured (Fig. 2). The fact that they agree with scaled $p+p$ data indicates little or no nuclear effects. The spectrum provides an important information for the initial condition of the high energy heavy ion collisions.

The azimuthal anisotropy with respect to the reaction plane is an additional probe to explore the development of the medium. The lowest Fourier component that appears in the symmetric

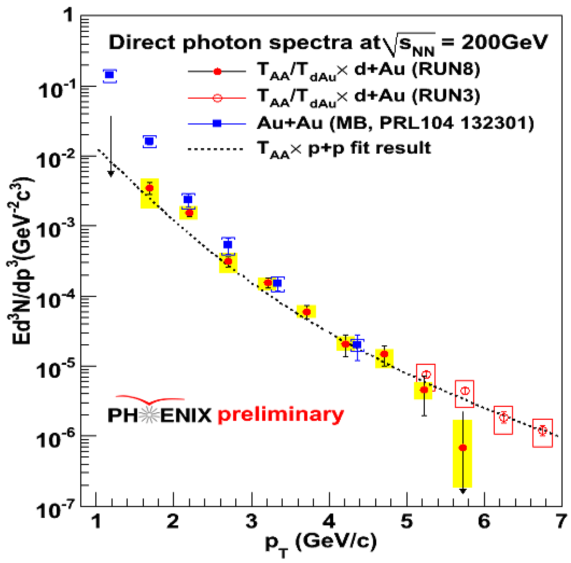

Figure 2: Direct photons in $d+$Au with the virtual photon method are scaled and compared with the data points in Au+Au collisions. Scaled $p+p$ fit result is also shown.

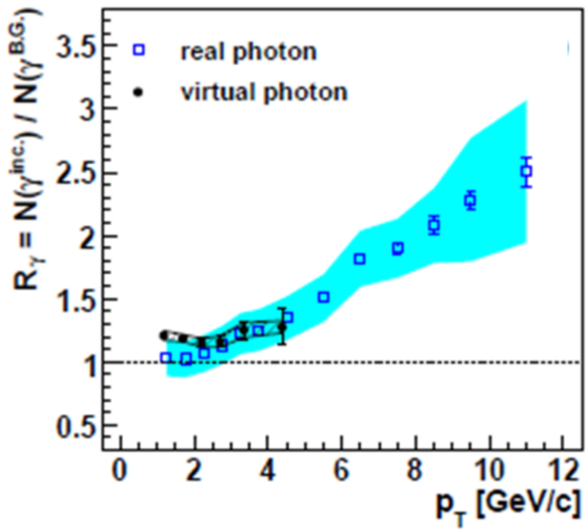

Figure 3: The direct photon excess ratio (R_γ) in Au+Au collisions. They are measured with virtual photons [2] (solid black circles) and real photons in the EMCal [5] (open blue squares).

geometry is the second term (called as ν_2 or elliptic flow). Eq. 1 shows the definition.

$$\frac{dN}{d(\phi - \Phi_{RP})} = N_0[1 + 2\nu_2 \cos 2(\phi - \Phi_{RP})], \tag{1}$$

where the azimuthal angle Φ_{RP} is defined by the reaction plane of the two nuclei. There are several approaches to measure the ν_2. Among them the simplest concept is to determine the Φ_{RP} with soft particles and to measure the particle production with respect to the Φ_{RP}. It is important to avoid or to correct the self correlation between the particle production ϕ and the reaction plane Φ_{RP}. At PHENIX, several global detectors were used to determine the Φ_{RP}. The resolution of Φ_{RP} was determined by the comparison of subsets in two side of the interaction point. It works as a dilution factor of the azimuthal dependence.

For the direct photon ν_2 (ν_2^{dir}), since we are not able to identify the direct photon event by event, we need to subtract the background components. The ν_2^{dir} is then obtained from the inclusive photon ν_2^{inc} and the background photon ν_2^{BG} as

$$\nu_2^{dir} = \frac{R_\gamma \nu_2^{inc} - \nu_2^{BG}}{R_\gamma - 1}, \tag{2}$$

where R_γ is a direct photon excess ratio defined by N^{inc}/N^{BG}. It depends on p_T as shown in Fig. 3. Both measurements with virtual photons and with real photons in the EMCal agree each other. At low p_T region ($p_T < 4$ GeV/c), the virtual photon method gives smaller systematic uncertainties and R_γ have non-zero values. The ν_2^{BG} is calculated from the measured ν_2 of π^0 ($\nu_2^{\pi^0}$). Other hadronic decay components are also derived from $\nu_2^{\pi^0}$.

Figure 4 shows the measurement of direct photon ν_2 for different centrality bins in Au+Au collisions at $\sqrt{s} = 200$ GeV [6]. At high p_T ($\gtrsim 5$ GeV/c), the ν_2^{dir} is consistent with zero, which is expected from hard scattering source. However a possible (small) elliptic flow cannot be rejected with the current uncertainties. At low p_T, the ν_2^{dir} is large, as much as the ones of hadrons [7]. In this region the size of ν_2^{dir} is sensitive to the formation time of the dense medium [8]. Larger ν_2^{dir} indicates later formation time. Currently as shown in Fig. 4 (d), the theoretical calculations are too small to the data.

The next step is to measure the ν_2^{dir} fully with electron pairs. It reduces the systematic uncertainties related to the π^0 background and the non photon contribution. However the yields go down by a factor of 200. Even in the lowest p_T region ($1 < p_T < 3$ GeV/c), it is a challenge with the current data sample. Note that there is an interesting suggestion about the enhancement of electron pair production in a strong magnetic field in heavy ion collisions[9]. If it is true, the assumption used to connect the yield of the electron pair to one of the direct photon needs to be revisited.

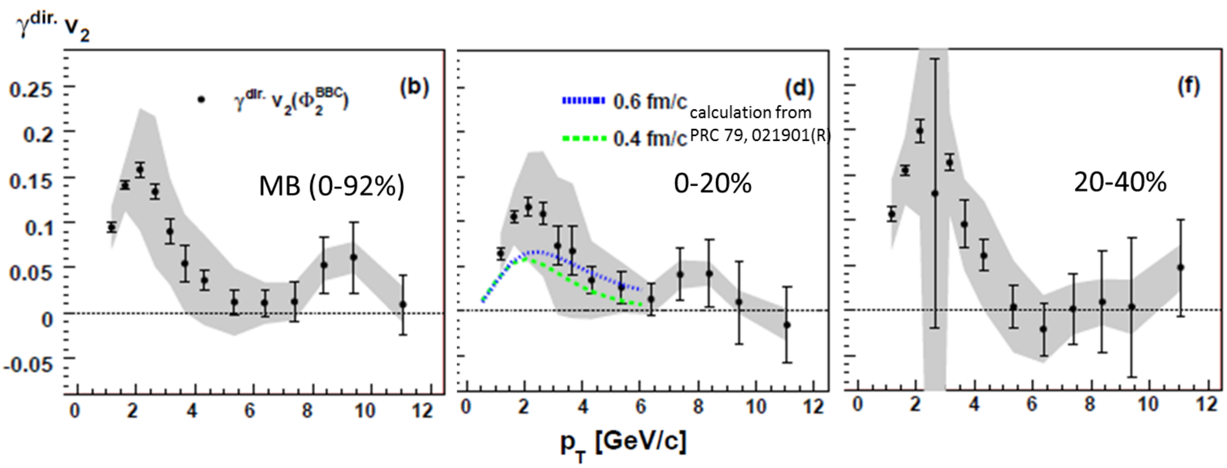

Figure 4: Direct photon ν_2^{dir} for different centrality classes[6]. In (d), theoretical calculations for different formation times are shown.

In summary, the PHENIX detector measured the direct photons over a wide p_T range at mid-rapidity in $p+p$, d+Au, and Au+Au collisions. The EMCal with high granularity were able to separate single photons from merged π^0 photons. In $p+p$ collisions, the direct photon spectrum was measured up to $p_T = 25$ GeV/c. The high rate capability of the data acquisition system and the excellent electron identification enabled us to access the direct photon production in the low p_T thermal production region via the virtual photon method.

We measured an unexpectedly large positive elliptic flow in the thermal production region. No theoretical explanation assuming the flow development in the QGP state exists yet.

For the future, the PHENIX collaboration plans to upgrade the detector. The immediate design is for the jet reconstruction, but its large acceptance will open new possibilities for the direct photon measurement. The physics cases of the upgrade detectors are measurements in large rapidity coverage, direct photon and jet correlation for the constraint of the kinematics, and a collection of a large statistics of electron pairs for virtual photon analysis.

References

1. K. Adcox *et al.*: *Nucl. Instrum. Methods* A **499**, 469 (2003).
2. S. Afanasiev *et al.*: *Phys. Rev. Lett.* **104**, 132301 (2010).
3. S. Afanasiev *et al.*: *Phys. Rev.* C **81**, 034911 (2010).
4. S. S. Adler *et al.*: *Phys. Rev. Lett.* **98**, 012002 (2007).
5. S. S. Adler *et al. Phys. Rev. Lett.* **94**, 232301 (2005).
6. S. Adare *et al.*: arXiv:1105.4126 (2011).
7. A. Adare *et al.*: *Phys. Rev. Lett.* **105**, 142301 (2010).
8. R. Chatterjee and D. K. Srivastava: *Phys. Rev.* C **79**, 021901 (2009).
9. K. Tuchin: *Phys. Rev.* C **83**, 017901 (2011).

Heavy flavour and quarkonia production measurement in pp and Pb–Pb collisions at LHC energies with the ALICE detector

Renu Bala, for the ALICE Collaboration
University of Jammu, Jammu, India

ALICE is the dedicated heavy-ion experiment at the LHC. Its main physics goal is to study the properties of strongly-interacting matter at conditions of high energy density and high temperature expected to be reached in central Pb–Pb collisions. Charm and beauty quarks are well-suited tools to investigate this state of matter since they are produced in initial hard scatterings and are therefore generated early in the system evolution and probe its hottest, densest stage. ALICE recorded pp data at $\sqrt{s}$ = 7 TeV and 2.76 TeV and Pb–Pb data at $\sqrt{s_{NN}}$=2.76 TeV in 2010 and 2011. We present the latest results on heavy flavour and J/ψ production at both central and forward rapidity.

1 Introduction

The main goal of the ALICE [1,2] experiment is to study the strongly interacting matter in conditions of high density and temperature. In such conditions lattice QCD calculations predict quark de-confinement and the formation of the so called Quark-Gluon Plasma (QGP) [3]. Heavy flavour particles are sensitive to the properties of the medium formed in heavy-ion collisions. In particular: open charm and beauty mesons are sensitive to the energy density, through the mechanism of in-medium energy loss of heavy quarks; quarkonium production suppression (which is expected to give information on the medium temperature) by colour screening was one of the first proposed signatures for QGP formation [4]; charmonium regeneration due to the recombination of initially uncorrelated c and $\bar{c}$ quarks may occur at LHC energies [5,6]. A detailed description of the physics motivations for heavy flavour measurements in heavy-ion collisions can be found in [2].

2 Heavy flavour detection in the ALICE experiment

The ALICE apparatus [1] has excellent capabilities for heavy flavour measurements, for both open heavy flavour hadrons and quarkonia. It is composed of a central barrel and a forward muon arm. In the central region ($|\eta| < 0.9$), the heavy flavour capability of ALICE relies in a high granularity tracking system made of the Inner Tracking System (ITS), the Time Projection Chamber (TPC) and the Transition Radiation Detector (TRD). The particle identification is performed via dE/dx measurement in the TPC, via time of flight measurement in the Time Of Flight detector (TOF). Electrons are identified at low p_t ($p_t < 6$ GeV/c) by TPC and TOF, while at intermediate and high p_t ($p_t > 2$ GeV/c), the TRD and the Electromagnetic Calorimeter (EMCal) is used. At forward rapidity, heavy flavour production is measured with the muon spectrometer ($-4 < \eta < -2.5$).

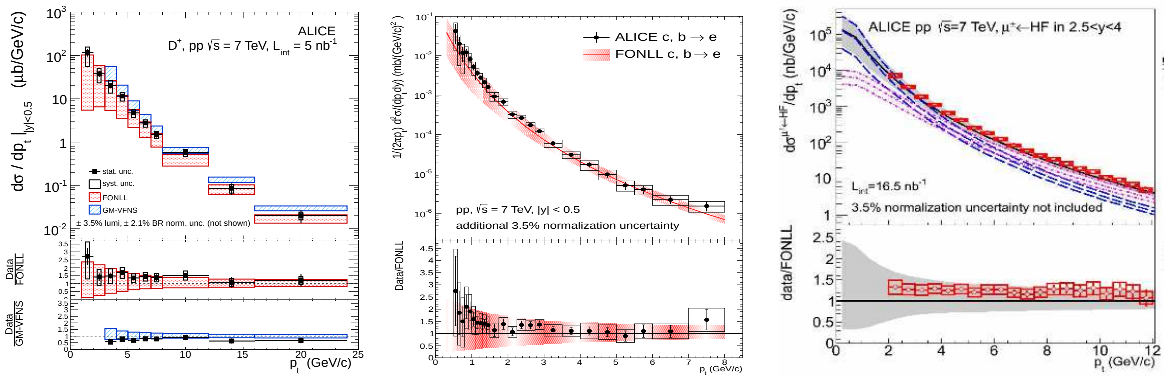

Figure 1: p_t differential cross section for D^+ mesons in pp collisions at $\sqrt{s} = 7$ TeV, compared to perturbative QCD predictions from FONLL [10,11] and GM-VFNS [12] calculations (left) [9]. p_t differential cross section of electrons from heavy flavour decays compared to FONLL calculations (middle) [14]. p_t differential cross section of muons from heavy flavour decays compared to FONLL calculations (right) [15].

The analysis is based on proton-proton collisions at $\sqrt{s} = 7$ TeV and 2.76 TeV and Pb–Pb collisions at $\sqrt{s_{NN}} = 2.76$ TeV. The proton-proton data sample consists of Minimum Bias (MB) and muon triggers. The former is defined by the presence of a signal in the Silicon Pixel Detector (two innermost layers of the ITS) or in either of the two VZERO scintillator arrays, in coincidence with the beam-beam counters placed at both sides of the interaction point. The muon trigger requires, in addition to a MB event, that a muon with transverse momentum above about 0.5 GeV/c reaches the muon trigger stations. In Pb–Pb collisions, the MB trigger requires the coincidence of signals in the two arrays of the VZERO and in the SPD. The measurement of the centrality is based on the distribution of signals in the VZERO hodoscopes, modeled with a Glauber calculation [7].

3 Open heavy flavour in pp collisions at $\sqrt{s} = 2.76$ TeV and 7 TeV

3.1 D mesons via hadronic decays

The detection strategy for D mesons at central rapidity is based, for both pp and Pb–Pb collisions, on the selection of displaced-vertex topologies, i.e. discrimination of tracks from the secondary vertex from those originating from the primary vertex, large decay length (normalized to its estimated uncertainty), and good alignment between the reconstructed D meson momentum and flight-line. The identification of the charged kaon in the TPC and TOF detectors helps to further reduce the background at low p_t. Figure 1 (left) shows the p_t differential cross section for prompt D^+ mesons at $\sqrt{s} = 7$ TeV. Similar results were obtained for D^0 and D^{*+} [9]. The feed down from beauty decays is calculated from theory (FONLL) and gives a contribution of 10-15%. The data are well described by pQCD calculations at Fixed-Order Next-to-leading Logarithm level (FONLL) [10,11] and GM-VFNS [12] predictions. The D mesons cross sections were also measured at $\sqrt{s} = 2.76$ TeV but with limited statistical precision [13].

3.2 Heavy flavour decay electrons and muons

At central rapidity, heavy flavour production is measured also using semi-electronic decays. The key tool for this analysis is the excellent electron PID capability of the ALICE experiment. The TPC dE/dx measurements together with the TOF information allows to identify electrons in the low and intermediate p_t region (up to ~ 4 GeV/c). The analysis includes (at present only for pp data) also the TRD detector to suppress the π background. The contribution of electrons from the decay of heavy flavours was extracted from the inclusive electron spectrum by subtracting

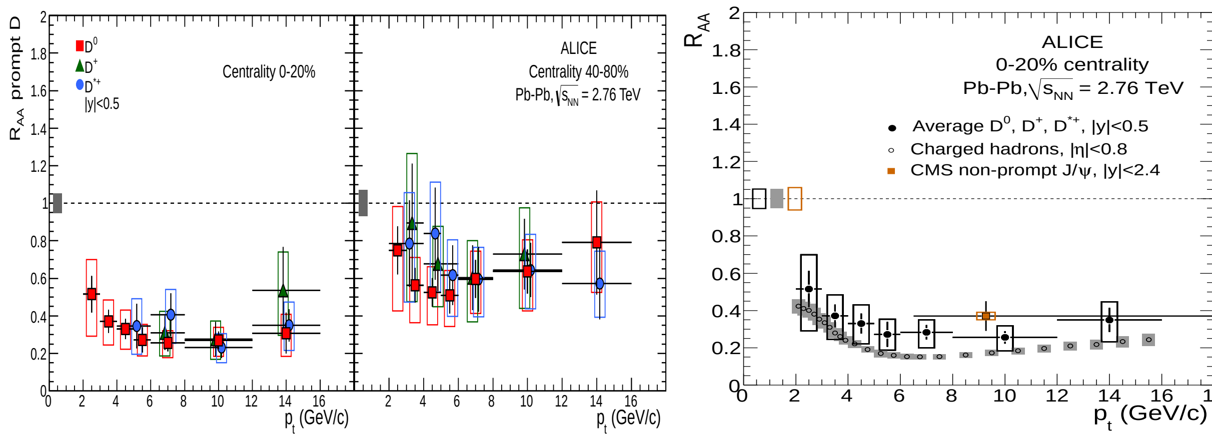

Figure 2: Prompt D^0, D^+ and D^{*+} R_{AA} as a function of p_t in 0-20% and 40-80% centrality classes (left). Averaged R_{AA} of D-mesons in 0-20% centrality class compared to the R_{AA} of charged hadrons and non-prompt J/ψ from B-decays (right) [17].

a cocktail simulation of the non heavy flavour electron sources. Figure 1 (middle) shows the heavy flavour electron cross section at $\sqrt{s} = 7$ TeV compared with FONLL pQCD calculations [14]. The data are well described by the theory within uncertainties. Heavy flavour production at forward rapidities can be studied in ALICE with single muons. Muons are measured in the muon spectrometer and identified by requiring that the reconstructed track matches a tracklet in the trigger system, placed behind an iron wall. This condition allows to efficiently remove the background contribution of hadrons punching through the frontal absorber. The main source of background consists of muons from the decay-in-flight of pions and kaons produced at the interaction point. In pp collisions, such contribution is subtracted through simulations, while in Pb–Pb collisions, it was estimated by extrapolating to forward rapidities the p_t distributions of pions and kaons measured at central rapidity. The measured differential production cross sections of muons from heavy flavour decays as a function of p_t in the rapidity region $2.5 < y < 4$ at $\sqrt{s} = 7$ TeV is shown in Fig. 1 (right) [15]. Also in this case, the results are well described by FONLL predictions. The muon cross section from heavy flavour decays at $\sqrt{s} = 2.76$ TeV were also measured and details can be found here [19].

4 Open heavy flavour in Pb–Pb collisions at $\sqrt{s} = 2.76$ TeV

The nuclear modification factor is sensitive to the interaction of hard partons with the medium. It is defined as the ratio of the transverse momentum spectrum measured in nucleus-nucleus (AA) collisions to the one measured in pp collisions at the same centre of mass energy, rescaled by the average number of binary nucleon-nucleon collisions (N_{coll}) expected in heavy-ion collisions. The ratio can be expressed also in terms of nuclear overlap integral (T_{AA}) estimated within the Glauber-model [7].

$$R_{AA}(p_t) = \frac{1}{<N_{coll}>} \cdot \frac{dN_{AA}/dp_t}{dN_{pp}/dp_t} = \frac{1}{<T_{AA}>} \cdot \frac{dN_{AA}/dp_t}{d\sigma_{pp}/dp_t}$$

For D mesons and electrons from heavy flavour decays, the pp reference is scaled from 7 to 2.76 TeV using pQCD calculations (FONLL) [8]. The scaled results for D mesons were cross

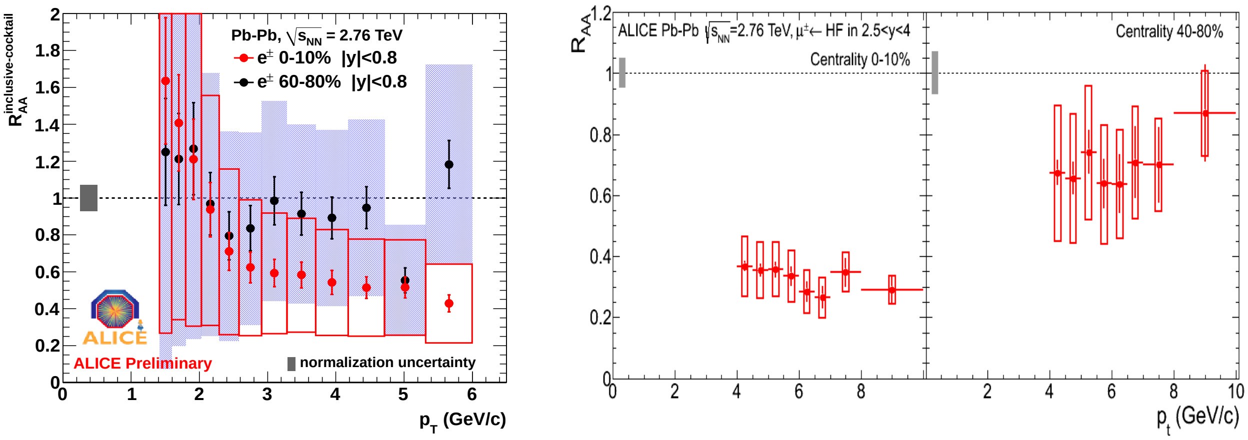

Figure 3: Comparison of the R_{AA} of background subtracted electrons for central and peripheral Pb–Pb collisions (left). R_{AA} of muons from heavy flavour decays in $2.5 < y < 4$ as a function of p_t in 0-10% and 40-80% centrality classes (right) [19].

checked with the available measurement in pp collisions at $\sqrt{s} = 2.76$ TeV [13] (this sample was not used in R_{AA} due to the limited statistics). The systematic uncertainties were obtained by taking into account the full theoretical uncertainties, and assuming no dependence of the quark mass and scales with $\sqrt{s}$.

For the muon R_{AA}, the pp reference was obtained from the analysis of muon triggered events collected during a pp run at $\sqrt{s} = 2.76$ TeV

4.1 D mesons via hadronic decays

The transverse momentum dependence of the nuclear modification factor for D-mesons is shown in Fig. 2 (left) for the central (0-20% centrality class) and semi-peripheral (40-80%) events. R_{AA} for the three species agree with each other in both centrality classes. A clear increase in the R_{AA} is visible for more peripheral collisions. A comparison of the averaged D meson R_{AA} with the charged hadrons R_{AA} was carried out and is shown in Fig. 2 (right). Since at high p_t ($p_t >$ 5 GeV/c) it is shown that the charged hadron R_{AA} coincides with that for charged pions [16], the comparison would allow to test the prediction about the colour charge and mass dependence of energy loss, according to which heavy quarks would lose less energy than gluons, translating into $R_{AA}^{D} > R_{AA}^{charged}$. The results show comparable suppression for heavy and light hadrons R_{AA} especially at $p_t > 5$ GeV/c. Nevertheless, there are some indications that R_{AA}^{D} may be higher than $R_{AA}^{charged}$ at low p_t (up to $\sim$ 30% at 3 GeV/c). Also in the same figure, R_{AA} measured by the CMS Collaboration for non-prompt J/ψ mesons (from B decays) with $p_t > 6.5$ GeV/c [18] is shown. The non-prompt J/ψ suppression is clearly weaker than that of charged hadrons, while the comparison with D mesons require more differential and precise measurements of the transverse momentum dependence. Comparisons with different theoretical models have also been carried out. Several models describe reasonably well both the charm R_{AA} and the light flavour R_{AA}. For more details on the analysis, see [17].

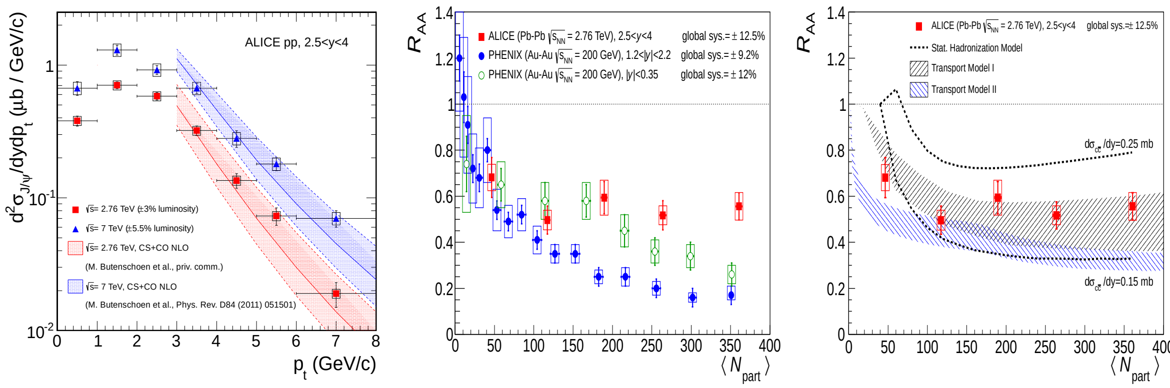

Figure 4: p_t differential cross section for inclusive J/ψ compared to NRQCD calculation (left) [20]. Inclusive J/ψ R_{AA} as a function of the average number of participating nucleons measured in Pb–Pb collisions at $\sqrt{s_{NN}} = 2.76$ TeV compared to PHENIX results in Au–Au collisions at $\sqrt{s_{NN}} = 200$ GeV (middle) [25]. Inclusive J/ψ R_{AA} compared to the predictions by Statistical Hadronization Model [26], Transport Model I [27] and II [28] (right).

4.2 Single muons and electrons

Figure 3 (left) shows the nuclear modification factor of electrons from heavy flavour decays for the centrality ranges 0-10% (central events) and 60-80% (peripheral events). In peripheral Pb-Pb collisions, R_{AA} is compatible with one, whereas a suppression by a factor 1.2-5 is observed for the most central collisions in the p_t region 3.5-6 GeV/c, where charm and beauty decays dominates. Figure 3 (right) presents the R_{AA} of muons from heavy flavour decays in $2.5 < y < 4$, as a function of p_t in central (0-10%) and peripheral (40-80%) collisions [19]. A larger suppression is observed in central collisions than in peripheral collisions with no significant dependence on p_t within uncertainties. These heavy flavour decay lepton measurements indicates a strong coupling of heavy quarks to the medium created in heavy-ion collisions.

5 Quarkonia production measurement in pp and Pb–Pb collisions

The inclusive J/ψ measurements was performed at $\sqrt{s} = 2.76$ TeV and 7 TeV. The integrated and differential cross sections were evaluated down to $p_t = 0$ in two rapidity ranges, $|y| < 0.9$ and $2.5 < y < 4$, in the dielectron and dimuon decay channel, respectively. The measurement at $\sqrt{s} = 2.76$ TeV provides a crucial reference for the study of hot nuclear matter effects on J/ψ production. Figure 4 (left) shows the differential cross section, averaged over the interval $2.5 < y < 4$ in the transverse momentum range $0 < p_t < 8$ for the two measured energies [20,21]. The results are compared with the predictions of a NRQCD calculation [22] that is in agreement with the data.
The inclusive J/ψ R_{AA} is shown in Fig. 4 (middle), for $p_t > 0$ and $2.5 < y < 4$, as a function of the average number of nucleons participating to the collision. The comparison with the results from PHENIX in Au–Au collisions at $\sqrt{s_{NN}} = 0.2$ TeV [23,24], which are also shown in the figure, indicates a smaller suppression at LHC than at RHIC in central collisions. Models based on statistical hadronization, or including J/ψ regeneration from charm quarks in the QGP phase can describe the data as shown in Fig. 4 (right) and as describe in [25].

6 Conclusions

The latest ALICE results on open heavy flavour and quarkonium measurements in pp and Pb–Pb were presented. In pp collisions, the open heavy flavour production measurements are well described by NLO pQCD calculations. The J/ψ cross sections were measured in a wide rapidity range down to $p_{\mathrm{t}} = 0$. The $\mathrm{R_{AA}}$ measurement shows a large suppression for D mesons in the centrality 0-20% as well as for electrons and muons from heavy flavour decays. The D mesons suppression at $p_{\mathrm{t}} > 5$ GeV/c is compatible with that of charged hadrons. Below 5 GeV/c, there is hint of possible hierarchy in the values of $\mathrm{R_{AA}}$ i.e. $\mathrm{R^{D}_{AA}} > \mathrm{R^{charged}_{AA}}$. The higher statistics from 2011 Pb–Pb run should allow for a firm conclusion. In addition, the comparison data from p–Pb collisios should allow to disentangle initial-state nuclear effects, which could be different for light and heavy flavours. A significant suppression is also observed in the inclusive J/ψ production in Pb–Pb collisions. The J/ψ $\mathrm{R_{AA}}$ is larger than the one measured at RHIC in central collisions, which could be an indication of (re)generation of J/ψ in the QGP. A better knowledge of the cold nuclear matter effects, to be studied by means of p–Pb collisions, will be required to constrain suppression/regeneration models.

References

1. K. Aamodt et al. (ALICE Collaboration), J. Instrum. 3, (2008) S08002.
2. B. Alessandro et al. (ALICE Collaboration), J. Phys. G: Nucl. Part. Phys. 32, (2006) 1295.
3. F. Karsch, Nucl. Phys. A698, (2002) 199.
4. T. Matsui, H. Satz, Phys. Lett. B 178 (1986) 416.
5. P. Braun-Munziger, J. Stachel Phys. Lett. B 490 (2000) 196.
6. R.L. Thews et al., Phys. Rev. C 63 (2001) 054905.
7. K. Aamodt et al. (ALICE Collaboration), Phys. Rev. Lett. 106 (2011) 032301.
8. R. Averbeck et. al, arxiv:1107.3243.
9. B. Abelev et al. (ALICE Collaboration), JHEP 01 (2012) 128.
10. M. Cacciari, M. Greco and P. Nason, JHEP 9805 (1998) 007.
11. M. Cacciari, S. Frixione, N. Houdeau, M.L. Mangano, P. Nason, and G. Ridolfi, CERN-PH-TH/2011-227.
12. B.A. Kniehl et al., Phys. Rev. Lett. 96 (2006) 012001.
13. B. Abelev et al. (ALICE Collaboration), arxiv:1205.4007.
14. B. Abelev et al. (ALICE Collaboration), arxiv:1205.5423.
15. B. Abelev et al. (ALICE Collaboration), Phys. Lett. B 708 (2012) 265.
16. H. Appelshauser (ALICE Collaboration), J. Phys. G 38 (2011) 124014.
17. B. Abelev et al. (ALICE Collaboration), arXiv:1203.2160v1.
18. CMS Collaboration, arXiv:1201.5069.
19. B. Abelev et al. (ALICE Collaboration), arXiv:1205.6443.
20. B. Abelev et al. (ALICE Collaboration), arXiv:1203.3641.
21. B. Abelev et al. (ALICE Collaboration), Phys. Lett. B 704 (2011) 442.
22. M. Butenschoen and B. A. Kniehl, Phys. Rev. D 84 (2011) 051501 and priv. comm.
23. A. Adare et al. (PHENIX Collaboration), Phys. Rev. Lett. 98 (2007) 232301.
24. A. Adare et al. (PHENIX Collaboration), Phys. Rev. C 84 (2011) 05491.
25. B. Abelev et al. (ALICE Collaboration), arxiv:1202.1383.
26. A. Andronic, P. Braun-Munzinger, K. Redlich, and J. Stachel, J. Phys. G: Nucl. Part. Phys 38 (2011) 124081.
27. X. Zhao and R. Rapp, Nucl.Phys. A 859, (2011) 114.
28. Y. P. Liu, Z. Qu, N. Xu, and P. F. Zhuang, Phys.Lett. B678 (2009) 72.

GEOMETRICAL SCALING IN HIGH ENERGY HADRONIC COLLISIONS

MICHAL PRASZALOWICZ
M. Smoluchowski Inst. of Physics, Jagellonian University
Krakow, Poland

After introducing the concept of geometrical scaling (GS) on the example of deep inelastic ep scattering, we show that GS is also present in the $p_{\rm T}$ spectra measured by the LHC. We discuss simple phenomenological signatures of GS and its applications.

It is known that gluonic parton density rapidly increases at low Bjorken x [1]. Such growth has to be tamed at some point. The scale at which this happens is called saturation scale $Q_{\rm s}(x)$ and it depends on the Bjorken x. The explicit form of the saturation scale follows from the fact that $Q_{\rm s}^2(x)$ is related to the gluon distribution in the proton at low x [2]:

$$Q_{\rm s}^2(x) = Q_0^2\,(x/x_0)^{-\lambda} \tag{1}$$

where $Q_0 \sim 1$ GeV and $x_0 \sim 10^{-3}$ are free parameters whose precise values can be extracted from fits to the HERA data. Power λ is known to be of the order $\lambda \sim 0.2 \div 0.3$ and Bjorken x is defined as

$$x = Q^2/(Q^2 + W^2 - M_p^2) \tag{2}$$

where M_p stands for the proton mass.

Geometrical scaling [3] consists in the fact that for sufficiently low x the reduced $\gamma^* p$ cross section $\sigma_{\gamma^* p}(W, Q^2) \sim F_2(x, Q^2)/Q^2$ depends in fact only on the scaling variable τ:

$$\sigma_{\gamma^* p} = \text{function}(\tau),\ \text{where}\ \tau = Q^2/Q_{\rm s}^2(x). \tag{3}$$

This is depicted in Fig.1. where the combined HERA data [1] for different scattering energies W are plotted in terms of Q^2(left) and in terms of τ (right). Quantitative analysis of the combined HERA data and the details of the W binning will be presented elsewhere [4].

In pp collisions particles of low and moderate $p_{\rm T}$ (and given rapidity y) are produced mainly from scattering of gluons carrying longitudinal momentum fractions $x_{1,2}$:

$$x_{1,2} = e^{\pm y}\, p_{\rm T}/W \quad \text{with} \quad W = \sqrt{s}. \tag{4}$$

If gluonic densities in pp collisions are characterized by the saturation scale (1), then also $dN/d\eta d^2 p_{\rm T}$ should scale. Therefore geometrical scaling for the multiplicity distribution in pp collisions [5,6] states that particle spectra depend on the scaling variable

$$\tau = p_{\rm T}^2/Q_{\rm s}^2(p_{\rm T}, W) \tag{5}$$

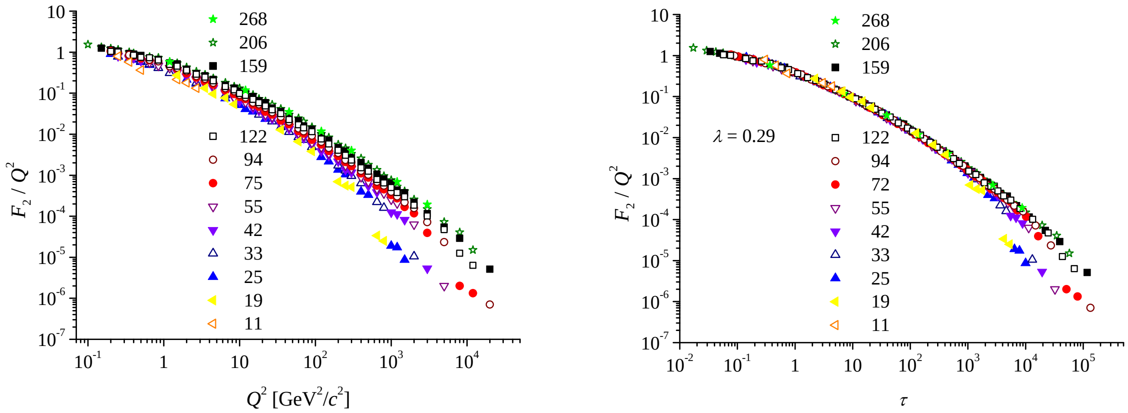

Figure 1: Geometrical scaling in DIS.

where $Q_{\mathrm{s}}^2(p_{\mathrm{T}}, W)$ is the saturation scale (1) at $x_1 \sim x_2$ (4):

$$Q_{\mathrm{s}}^2(p_{\mathrm{T}}, W) = Q_0^2 \left(p_{\mathrm{T}}/(W \times 10^{-3})\right)^{-\lambda} \tag{6}$$

where we have neglected rapidity dependence of $x_{1,2}$. Factor 10^{-3} corresponds to the choice of the energy scale (arbitrary at this moment x_0 in Eq.(1)). Hence

$$N_{\mathrm{ch}}(W, p_{\mathrm{T}}) = \left.\frac{dN_{\mathrm{ch}}}{d\eta d^2 p_{\mathrm{T}}}\right|_W = \frac{1}{Q_0^2} F(\tau) \tag{7}$$

with $Q_0 \sim 1$ GeV. Here $F(\tau)$ is a universal function of τ. This is depicted in Fig. 2 where the p_{T} spectra measured by CMS [7] ale plotted in terms of p_{T}^2 (left) and τ (right).

In order to examine the quality of geometrical scaling in pp collisions in Ref.[8] we have considered ratios R_{W_1/W_2}

$$R_{W_1/W_2}(p_{\mathrm{T}}) = \frac{N_{\mathrm{ch}}(W_1, p_{\mathrm{T}})}{N_{\mathrm{ch}}(W_2, p_{\mathrm{T}})}. \tag{8}$$

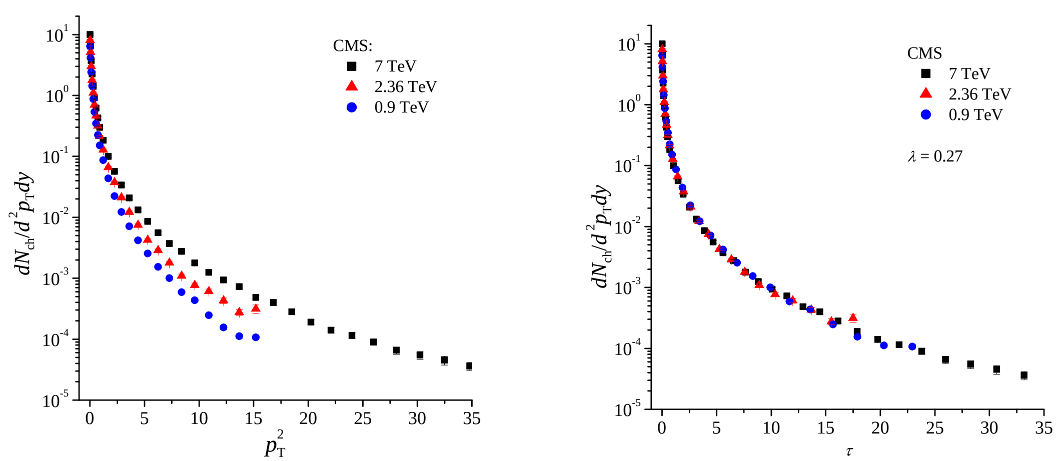

Figure 2: Geometrical scaling in pp.

Here, following Ref.[9] we shall discuss another way of establishing geometrical scaling, at least qualitatively. Note that if at two different energies W_1 and W_2 multiplicity distributions are equal

$$N_{\rm ch}(W_1, p_{\rm T}^{(1)}) = N_{\rm ch}(W_2, p_{\rm T}^{(2)}) \tag{9}$$

then this means that they correspond to the same value of variable τ (5). As a consequence

$$p_{\rm T}^{(1)\,2}\left(p_{\rm T}^{(1)}/W_1\right)^{\lambda} = p_{\rm T}^{(2)\,2}\left(p_{\rm T}^{(2)}/W_2\right)^{\lambda} \tag{10}$$

for constant λ. Equation (10) implies

$$S_{W_1/W_2}^{p_{\rm T}} = p_{\rm T}^{(1)}/p_{\rm T}^{(2)} = (W_1/W_2)^{\frac{\lambda}{2+\lambda}}\,. \tag{11}$$

Ratios $S_{W_1/W_2}^{p_{\rm T}}$ for pp non-single diffractive spectra measured by the CMS [7] collaboration at the LHC are plotted in Fig. 3 together with the straight horizontal lines corresponding to the r.h.s. of Eq.(11) for $\lambda = 0.27$. We see approximate constancy of $S_{W_1/W_2}^{p_{\rm T}}$ over the wide range of $N_{\rm ch}$. A small rise of $S_{W_1/W_2}^{p_{\rm T}}$ with decreasing $N_{\rm ch}$ corresponds to the residual $p_{\rm T}$-dependence [6] of the exponent λ.

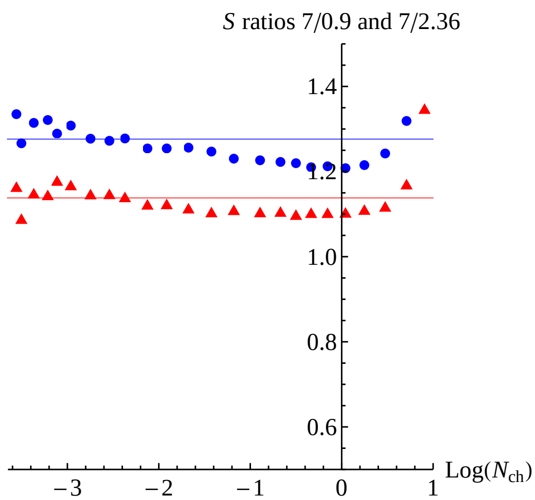

Figure 3: $S_{W_1/W_2}^{p_{\rm T}}$ ratios for CMS pp spectra

This is the simplest way of looking for GS in the $p_{\rm T}$ spectra. An obvious advantage is that it is very easy to do. An obvious disadvantage consists in the fact that it is difficult to attribute sensible error to the ratios $S_{W_1/W_2}^{p_{\rm T}}$, so for quantitative purposes it is better to consider ratios R_{W_1/W_2}.

One of the immediate applications of GS is its ability to *predict* $p_{\rm T}$ spectra at yet unmeasured energies. This was a crucial problem in calculating the so called nuclear modification factor R_{AA} for Pb-Pb collisions at the LHC. R_{AA} is essentially a ratio of nuclear to pp spectra at the same scattering energy normalized by the number of binary collisions. In the first heavy ion LHC run the c.m.s. energy per nucleon was 2.76 GeV and there was no data for pp collisions at this energy until the late run in 2011. In Fig. 4 we plot R_{AA} as published by ALICE [10]. Black (upper) stars correspond the 2010 data where proton spectrum has been interpolated from the measurements at other energies (two solid grey lines correspond to the estimated uncertainty). Pink (lower) stars in turn correspond to the preliminary data where pp spectrum has been measured in a dedicated 2.76 GeV run [11]. Triangles and circles correspond to our rough estimate of R_{AA} where ALICE measured Pb-Pb spectrum [10] has been divided by the theoretical pp spectrum obtained from the hypothesis of geometrical scaling for two different values of λ.

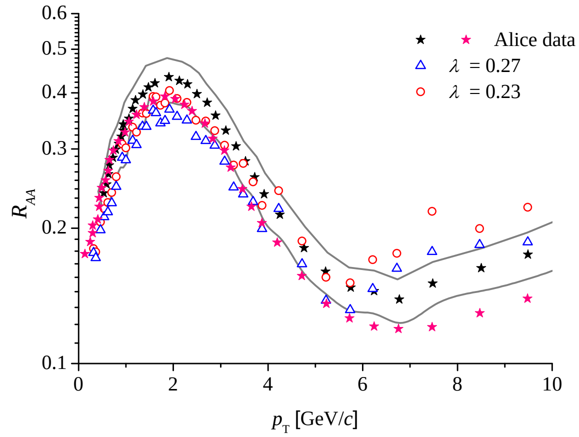

Figure 4: R_{AA} measured by ALICE (stars) and GS prediction (triangles and circles, see text) .

In this talk we have argued that geometrical scaling is a universal phenomenon observed in DIS and in pp scattering at the LHC (for theoretical background see lectures by L. McLerran [12]). After illustrating how GS works in these two processes we have proposed a simple procedure to look for geometrical scaling in the p_{T} spectra, namely to construct ratios of transverse momenta corresponding to the same multiplicity. We have used GS to predict the p_{T} spectra at yet unmeasured energies.

Many aspects of GS require further studies. Firstly, new data at higher energies (to come) have to be examined. Secondly, more detailed analysis including identified particles and rapidity dependence has to be performed. On theoretical side the universal shape $F(\tau)$ has to be found and its connection to the unintegrated gluon distribution has to be studied. That will finally lead to perhaps the most difficult part, namely to the breaking of GS in pp.

Acknowledgements

The author wants to thank Larry McLerran and Andrzej Bialas for stimulating discussions. This work was supported in part by the Polish NCN grant 2011/01/B/ST2/00492.

References

1. F. D. Aaron *et al.* [H1 and ZEUS Collaboration], JHEP **1001** (2010) 109.
2. K.J. Golec-Biernat, M. Wüsthoff, Phys. Rev. D **59** (1998) 014017, D **60** (1999) 114023.
3. A.M. Stasto, K.J. Golec-Biernat, J. Kwiecinski, Phys. Rev. Lett. **86** (2001) 596.
4. M. Praszalowicz, T. Stebel, in preperation.
5. L. McLerran, M. Praszalowicz, Acta Phys. Pol. B **41** (2010) 1917 and **42** (2011) 99.
6. M. Praszalowicz, Phys. Rev. Lett. 106 (2011) 142002.
7. V. Khachatryan *et al.* [CMS Collaboration], JHEP **1002** (2010) 041, Phys. Rev. Lett. **105** (2010) 022002, JHEP **1101** (2011) 079.
8. M. Praszalowicz, Acta Phys. Pol. **B42** (2011) 1557.
9. M. Praszalowicz, arXiv:1112.0997 [hep-ph].
10. K. Aamodt *et al.* [ALICE Collaboration], Phys. Lett. B **696** (2011) 30.
11. For pp spectra at 2.76 GeV see talk of M.L. Knichel, this proceedings.
12. L. McLerran, Acta Phys. Pol. B **41** (2010) 2799.

Hard Probes in Heavy Ion Collisions with CMS

Yetkin Yilmaz, on behalf of the CMS Collaboration
Massachusetts Institute of Technology
77 Massachusetts Avenue, Cambridge, MA02139, USA

Heavy Ion collisions at LHC energies allow studies of high density medium in kinematic ranges where vacuum reference is well understood and reproduced with perturbative calculations. High transverse momentum particles from the medium provide information on the amount of energy loss they suffered in the medium, which is known as "jet quenching". Using the capabilities of the CMS detector, the analyses of jets and various types of correlations between reconstructed jets and hadrons provide a detailed picture of this mechanism.

Studies of heavy ion collisions have provided evidence for a new state of matter that is formed in . Previous studies at RHIC have examined certain properties of this matter, of which an interesting one is the opacity, which is the resistance displayed by the material to a fast moving color-charged particle which traverses it through. This phenomenon was referred to as jet quenching, and it was quantified through the modification in the production rates of high transverse momentum probes. Since the cross sections of the production channels of these probes significantly increase in $\sqrt{s_{NN}} = 2.76$ TeV [1] compared to earlier accelerators, the study of PbPb collisions at LHC provide a great opportunity to both test the conclusions of the studies from RHIC, and extend the measurements into a lot larger kinematic ranges.

With its tracking, calorimetry and lepton identification capabilities, CMS is an excellent detector for measurements for a variety of probes at high transverse momenta, such as charged hadrons, jets, photons, vector bosons and quarkonia, in both pp and PbPb collisions. With the availability of pp data at the same $\sqrt{s}$, one can observe the modifications to any process when produced in PbPb environment. One such measurement is the nuclear modification factor, R_{AA} is defined as:

$$R_{\mathrm{AA}} = \frac{dN_{\mathrm{PbPb}}/dm_{\mathrm{T}}}{\langle T_{\mathrm{AA}} \rangle \times d\sigma_{\mathrm{pp}}/dm_{\mathrm{T}}}$$

where $m_{\mathrm{T}} = \sqrt{m^2 + p_{\mathrm{T}}^2}$ is the transverse mass of the particle.

The CMS measurements of the R_{AA} [2,3,4,5] are summarized in Fig. 1. While confirming the charged hadron results of earlier experiments, extends the p_{T} range significantly, and provide results of new color-neutral probes such as vector bosons. Although the production of color-neutral probes are consistent with the N_{coll} scaled expectation, the products of color-charged particles exhibit a suppression which is attributed to effects due to interaction of partons with the medium.

The studies with CMS detector can further investigate this effect with fully reconstructed jets, which provide a more direct comparison to the initial state of the hard scattering in pp

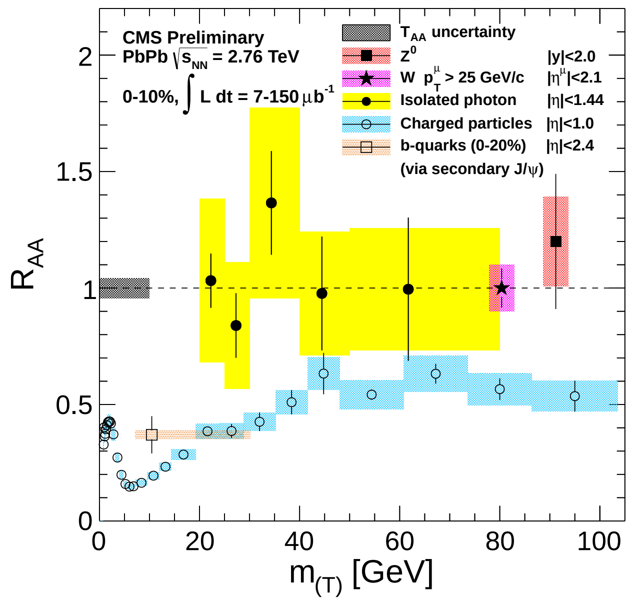

Figure 1: R_{AA} results in various CMS measurements, as a function of transverse mass (m_{T}) for charged particles, photons and b-quarks, and mass (m) for W and Z bosons.

collisions and perturbative calculations. Earlier results from CMS [6], with the dataset of the 2010 LHC run with PbPb ions, have revealed various aspects of the energy loss mechanism. While the jets lost a significant fraction of their energy in the medium, their azimuthal correlations are not modified significantly. The energy that is deposited in the medium is redistributed over a large angular region [6] and the hadron composition of the reconstructed jets [7] resemble the same pattern as those in pp collisions.

With the availability of a large dataset from the 2011 LHC run with PbPb ions, earlier studies of dijets were repeated and more details are investigated through a more differential approach [8]. When correlating jets with highest reconstructed p_{T} values in each event, one observes that the distributions of the azimuthal angle between the two jets ($\Delta\phi_{1,2}$) are similar to those in PYTHIA simulations at each range of jet p_{T}. However, an offset in these distributions due to background fluctuations which are reconstructed as low p_{T} jets, appears in different magnitudes in data and MC. This is consistent with the quenching effect, since when the p_{T} of the true subleading jet of the event is lower it is more likely for a background fluctuation to have higher p_{T}. The analysis of the dijet imbalance selects dijets with $\Delta\phi_{1,2} > 2\pi/3$ and the residual contamination is subtracted by estimating the effects from dijets with $\Delta\phi_{1,2} < \pi/3$.

It is observed that when the leading jet of the event has high enough p_{T}, it is always accompanied by a recoiled partner in the opposite direction in azimuth. The fraction of such correlated events after background subtraction and the fraction of the estimated background are shown in Fig. 3 as a function of leading jet p_{T} and event centrality.

In Fig. 4, the average ratio of subleading jet p_{T} to the leading jet p_{T}, $\langle p_{\mathrm{T},2}/p_{\mathrm{T},1}\rangle$, is shown as a function of leading jet p_{T} in different bins of centrality. In the central events, a significant shift of the $\langle p_{\mathrm{T},2}/p_{\mathrm{T},1}\rangle$ with respect to the MC and pp results is observed. This shift, while changing monotonically with centrality, does not show a significant dependence on the leading jet p_{T}. Since both data and MC include effects from detector resolution, the implications on the absolute amount of energy loss should be extracted via realistic models of quenching.

In summary, LHC has opened up a new territory for studies of the hard probes of the hot and dense medium. Although this paper discusses mainly the jet quenching related measurements,

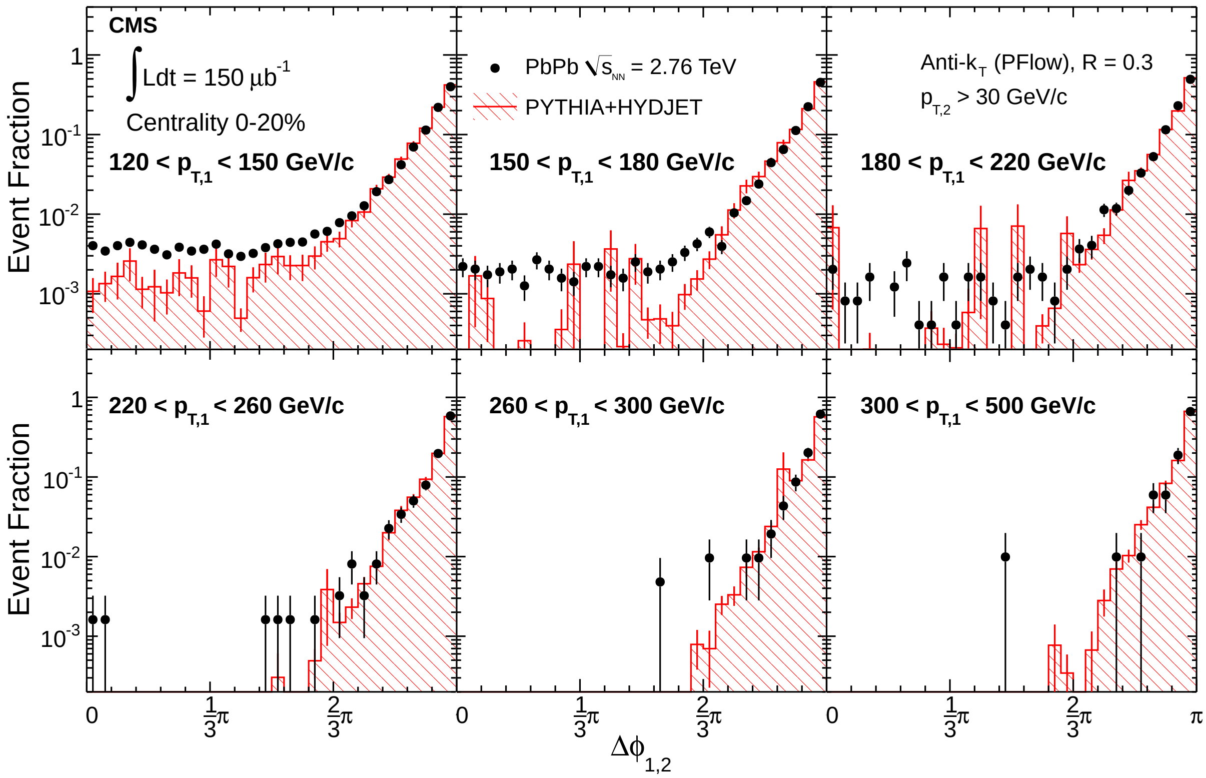

Figure 2: Distribution of the angle $\Delta\phi_{1,2}$ between the leading and subleading jets in bins of leading jet transverse momentum from $120 < p_{\mathrm{T},1} < 150$ GeV/c to $p_{\mathrm{T},1} > 300$ GeV/c for subleading jets of $p_{\mathrm{T},2} > 30$ GeV/c. Results for 0–20% central PbPb events are shown as points while the histogram shows the results for PYTHIA dijets embedded into HYDJET PbPb simulated events. The error bars represent the statistical uncertainties.

CMS also has measurements of quarkonia [5] which probe the color-screening phenomena. The variety of early results from LHC illustrate the potential for the future studies in the field of heavy ion collisions.

References

1. D. d'Enterria, (2009), arXiv:0902.2011 [nucl-ex].
2. CMS Collaboration, Eur. Phys. J. C **72**, 1945 (2012) [arXiv:1202.2554 [nucl-ex]].
3. CMS Collaboration, Phys. Lett. B **710**, 256 (2012) [arXiv:1201.3093 [nucl-ex]].
4. CMS Collaboration, Phys. Rev. Lett. **106**, 212301 (2011) [arXiv:1102.5435 [nucl-ex]].
5. CMS Collaboration, JHEP **1205**, 063 (2012) [arXiv:1201.5069 [nucl-ex]].
6. CMS Collaboration, Phys. Rev. C **84**, 024906 (2011) [arXiv:1102.1957 [nucl-ex]].
7. CMS Collaboration, CMS Physics Analysis Summary CMS-PAS-HIN-11-004, (2011).
8. CMS Collaboration, Phys. Lett. B **712**, 176 (2012) [arXiv:1202.5022 [nucl-ex]].

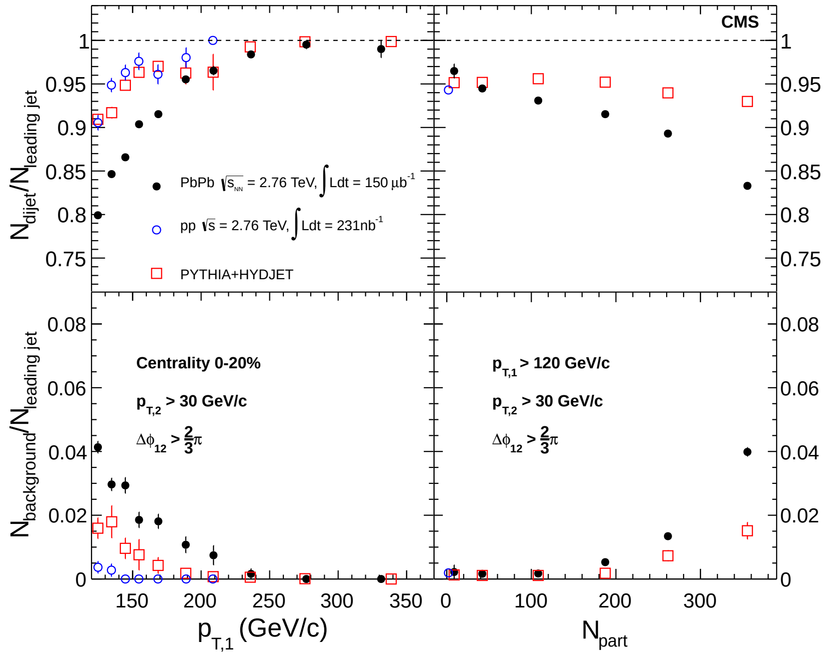

Figure 3: Fraction of events with a genuine subleading jet with $\Delta\phi_{1,2} > 2\pi/3$, as a function of leading jet $p_{\mathrm{T},1}$ (left) and N_{part} (right). The background due to underlying event fluctuations is estimated from $\Delta\phi_{1,2} < \pi/3$ events and subtracted from the number of dijets. The fraction of the estimated background is shown in the bottom panels. The error bars represent the statistical uncertainties.

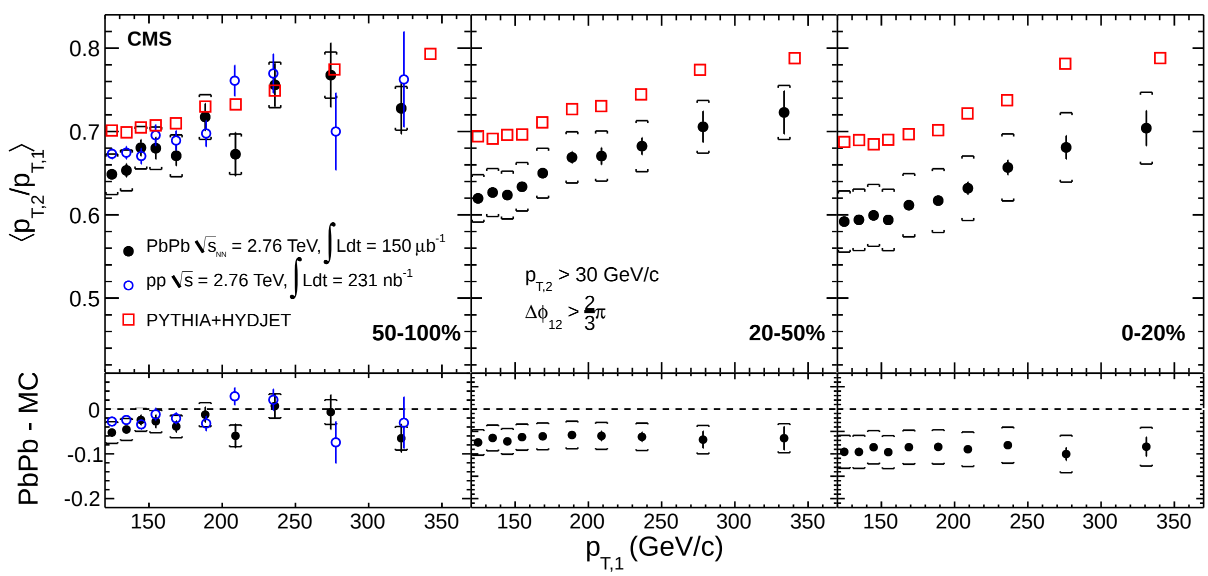

Figure 4: Average dijet momentum ratio $p_{\mathrm{T},2}/p_{\mathrm{T},1}$ as a function of leading jet $p_{\mathrm{T}}$for three bins of collision centrality, from peripheral to central collisions, corresponding to selections of 50–100%, 30–50% and 0–20% of the total inelastic cross section. Results for PbPb data are shown as points with vertical bars and brackets indicating the statistical and systematic uncertainties, respectively. Results for PYTHIA+HYDJET are shown as squares. In the 50–100% centrality bin, results are also compared with pp data, which is shown as the open circles. The difference between the PbPb measurement and the PYTHIA+HYDJET expectations is shown in the bottom panels.

HARD PROBES IN PB-PB COLLISIONS AT ATLAS

I. GRABOWSKA-BOLD
for the ATLAS Collaboration
AGH University of Science and Technology, Al. Mickiewicza 30,
Kraków, Poland

This document discusses the measurements from the lead-lead run at $\sqrt{s_{NN}} = 2.76$ TeV based on a minimum bias data sample of $5-7$ μb^{-1} collected by the ATLAS experiment at the LHC. In particular, the results on jet quenching and W production are reviewed. Jet yields are found to be suppressed by a factor of two in the most central collisions showing no modification to the jet internal structure in 10% most central events comparing to the 40-80% centrality bin. The W boson yield is proportional to the number of binary collisions.

1 Introduction

Collisions between lead ions at the Large Hadron Collider (LHC) are thought a way to create strongly interacting matter at temperatures well above the QCD critical temperature. The Relativistic Heavy Ion Collider (RHIC) has established [1] that at such temperatures, strongly interacting matter is expected to take the form of quark-gluon plasma (QGP). The energetic color charge carriers generated in hard-scattering processes during the initial stages of the nuclear collisions, and penetrating such a medium, are supposed to lose energy in the QGP. Both RHIC and LHC experiments have reported a suppression of charged hadron yields in heavy-ion (HI) collisions [2,3,4]. On the other hand particles which are created in hard scatterings and whose products do not interact via the strong forces, provide the means to investigate a phenomenon of energy loss in the QGP. The PHENIX experiment at RHIC measured the properties of highly energetic photons [5] while the ATLAS and CMS experiments at the LHC provided in addition the first measurements of Z, W at the LHC energy [6,7,8]. In this context measurements of hard probes at the LHC are very important as they may become a valuable source of information on the matter produced in the ultra-relativistic lead-lead collisions.

The LHC commenced a HI program in two lead-lead runs which took place in 2010 and 2011 at $\sqrt{s_{NN}} = 2.76$ TeV per colliding nucleon pair. In this document a report on jet and W boson measurements based on a minimum bias sample of $5-7$ μb^{-1} from the ATLAS experiment will be given. These results give some more insight into behavior of jets in the QGP and also establish a first evidence of W boson production with rates which follow the scaling with a number of binary collisions.

2 Inclusive jets

Jets are considered to be one of the most direct probes to study hot matter through the process of *jet quenching*. Jet quenching generally refers to the phenomenon by which a quark or a gluon can lose energy and/or have its parton shower modified in a medium of high color-charge density. This can occur through stimulated emission of gluon bremsstrahlung, collisional energy loss due to elastic scattering, or a variety of other processes [9,10].

The modification of the dijet asymmetry distribution reported in the first ATLAS Pb-Pb jet paper [11] strongly suggests, but does not yet prove, quenching of jets in the hot medium produced in the collisions. The dijet asymmetry analysis demonstrated that transverse energies (E_T) of pairs of jets produced in the back-to-back configuration had a significant E_T imbalance in central events. That imbalance can arise from jet quenching if one of the jets travels a longer path in the medium than the other. However, an intrinsic limitation of the dijet asymmetry observable is that it is less sensitive to events where each jet in a dijet pair loses a comparable amount of energy i.e. where each jet from both jets is comparably quenched. In this document proceeding the measurements on inclusive jets will be reported [12].

In ATLAS jets are reconstructed using the anti-kt algorithm with the jet size chosen to be $R = 0.2$ and $R = 0.4$. The jet reconstruction is based on "towers" composed of calorimeter cells integrated over regions of size $\Delta\eta \times \Delta\phi = 0.1 \times 0.1$. The underlying-event background is removed at the cell level. An iterative procedure is applied to remove any residual effect of the jets on the background subtraction. The final jets are corrected for the energy scale and resolution based on PYTHIA jets embedded into HIJING. The analysis of jets is restricted to $|\eta| < 2.8$, to stay within the barrel and endcap regions of the calorimeter.

2.1 Central-to-peripheral ratio for jets

Experimentally, the most direct way to measure modifications in the yield of jets at a given E_T value is to compare Pb-Pb jet measurement results to similar measurements in p-p collisions. A correction for the expected enhancement in the jet rate increase due to nuclear geometry also needs to be taken into account. A parameter which is responsible for the geometric factor is the number of binary collisions between the nucleons of the colliding nuclei which is termed as N_{coll}. Unfortunately the 2.76 TeV sample of p-p collisions obtained by the ATLAS experiment in 2011 has not been fully analyzed yet. In the absence of p-p one can use "peripheral" HI collisions for normalization. Jet quenching effects are expected to be minimal in peripheral collisions in which there is only a small overlap between the incoming nuclei and therefore only a small volume of hot medium created. Such peripheral collisions can provide a baseline for the jet spectrum at 2.76 TeV against which the jet yield in more central collisions can be compared. For this purpose, an observable called *central-to-peripheral ratio*, R_{cp} has been defined as a ratio of the jet yield in a given centrality bin to the jet yield in the reference peripheral centrality bin [3].

The obtained R_{cp} values as a function of centrality for fixed E_T values are shown in Fig. 1 for $R = 0.2$ and $R = 0.4$ jets. A suppression of the jet yield of approximately a factor of two in central Pb-Pb collisions for both $R = 0.4$ and $R = 0.2$ jets is observed. Within the errors no deviation from an E_T-independent R_{cp} for $R = 0.2$ jets with $E_T > 50\,GeV$ and for $R = 0.4$ jets with $E_T > 100\,GeV$ is seen. The suppression strength is comparable for two jet sizes.

2.2 Jet fragmentation functions

Different models of jet quenching predict different levels of modification of the jet internal structure. Both transverse and longitudinal structure of the jet are expected to be modified due to the gluon radiation inside the medium. To quantify the effect of the jet modification the jet fragmentation functions have been measured as a function of j_T - the transverse momentum of charged particles with respect to the jet axis, and z - the longitudinal fraction of the jet momentum carried by the charged particles. The j_T distribution has a soft core governed by non-perturbative physics and a power law tail resulting from hard radiation of the parton shower. In-medium jet energy loss is expected to modify the distribution of hard particles associated

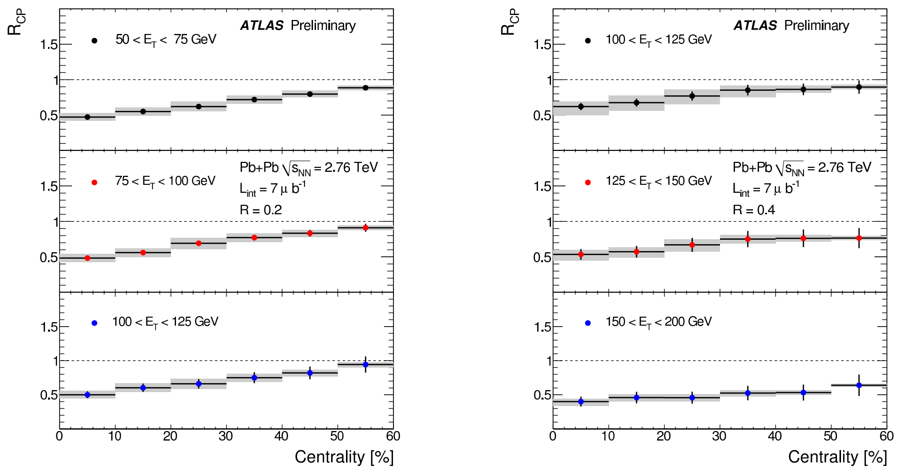

Figure 1: R_{CP} for $R = 0.2$ (left) and $R = 0.4$ (right) jets as a function of centrality for three E_T intervals. Error bars on the data points indicate statistical uncertainties, shaded errors represent combined systematic uncertainties.

with the jet and can be detected as a modification of the j_T distribution. Also the interaction of the jet with the medium may lead to a softening of the fragmentation function by reducing the number of charged particles at large z values and increasing the number of charged particles at small z. Direct measurements of the transverse and longitudinal fragmentation functions for tracks with $p_T > 2$ GeV in the ATLAS experiment, shown in the left and right panels respectively of Fig. 2, confirm that no substantial modification of the fragmentation function can be observed when comparing peripheral and central events. In other words, the suppression of the jet rates is not accompanied by any evident modification of the jets themselves.

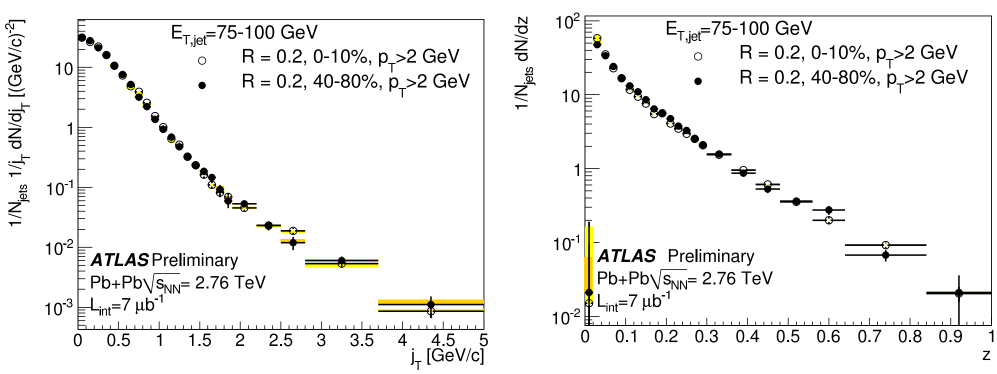

Figure 2: (left) Transverse fragmentation function for $R = 0.2$ anti-kt jets, comparing central 0-10% events with peripheral 40-80%. (right) The similar comparison for the longitudinal fragmentation function.

3 W bosons

The ATLAS experiment has performed a measurement of W boson production as a function of the collisions centrality [13]. Since vector bosons are produced in the nucleon-nucleon collisions and along with their decay products they do not interact with the color medium, they provide a reference for jets and quarkonia production which are known to be suppressed [6]. The left panel of Fig. 3 shows the inclusive muon p_T spectrum. The W yields are obtained by fitting a template using simulations of W decaying into a muon plus a neutrino in p-p collisions and using a functional form to describe the background. A sample of approximately 400 W bosons has been extracted. The binary scaling of the measured yields is studied using the variable R_{pc}, defined as the ratio of yields measured in different centrality classes to the yield measured in the

10% most central events, with all yields scaled by the corresponding number of binary nucleon-nucleon collisions. The right panel of Fig. 3 shows R_{pc} as a function of centrality. Using a fit to a constant value, giving $R_{pc} = 0.99 \pm 0.10$ with a $\chi^2 = 3.02$ for 3 degrees of freedom, a significant consistency with binary scaling is observed. Therefore this observation is an indication that W bosons are indeed produced at the initial phase of the collisions and neither $W's$ nor their decay products interact with the medium.

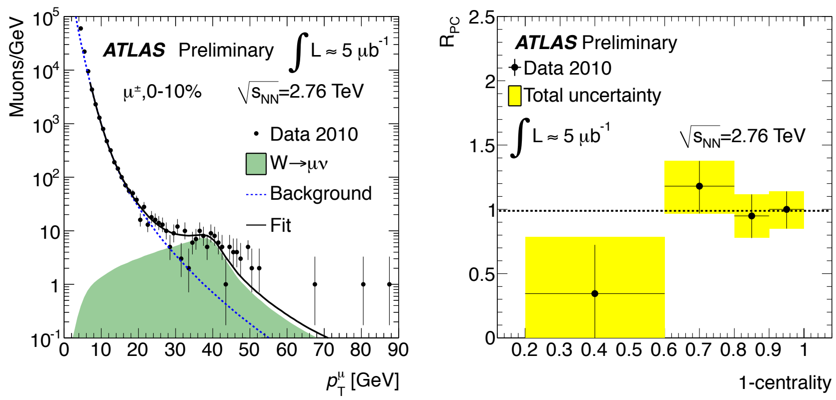

Figure 3: (left) Single muon spectrum measured for the 0-10% most central events. The templates for W bosons and heavy flavor (indicated as "Background") are also shown to illustrate the yield extraction procedure. (right) R_{pc} for W bosons as a function of centrality, showing consistency with binary collision scaling. The dotted line is a fit to a constant.

4 Summary

Results from the ATLAS detector based on lead-lead collisions from the 2010 LHC heavy-ion run have been presented. Jets are found to be suppressed in central events by a factor of two relative to peripheral events, with no significant dependence on the jet transverse energy. At the same time jet fragmentation functions are also found to be consistent in central and peripheral events. Single muons at high transverse momentum are used to extract the yields of W bosons as a function of centrality, which are found to be consistent with the binary collision scaling.

Acknowledgments

The author would like to thank the Heavy Ion session organizers for the invitation to speak at Moriond 2012, and the ATLAS collaboration for their continued strong support of the ATLAS heavy-ion physics program.

1. PHENIX Collaboration, *Nucl. Phys.* **A757**, 184-283 (2005).
2. PHENIX Collaboration, *Phys. Rev. Lett.* **93**, 152302 (2004).
3. ATLAS Collaboration, ATLAS-CONF-2011-079.
4. CMS Collaboration, *Eur. Phys. J.* **C72**, 1945 (2012).
5. PHENIX Collaboration, *Nucl. and Part. Phys.* **34**, no. 8, S1015 (2007).
6. ATLAS Collaboration, *Phys. Lett.* **B697**, 294-312 (2011).
7. CMS Collaboration, *J. Phys.* **G38**, 124132 (2011).
8. CMS Collaboration, *Phys. Lett.* **B710**, 256-277 (2012).
9. X.-N. Wang, M. Gyulassy, M. Plumer, *Phys. Rev.* **D51**, 3436-3446 (1995).
10. R. Baier, Y. L. Dokshitzer, A. H. Mueller, D. Schiff, *Phys. Rev.* **C58**, 1706-1713 (1998).
11. ATLAS Collaboration, *Phys. Rev. Lett.* **105**, 252303 (2010).
12. ATLAS Collaboration, ATLAS-CONF-2011-075.
13. ATLAS Collaboration, ATLAS-CONF-2011-074.

Particle production in pp and Pb–Pb collisions with the ALICE experiment at the LHC

F. Bellini* for the ALICE Collaboration
*Department of Physics, University of Bologna and I.N.F.N
Via Irnerio 46, 40126 Bologna - Italy

The performance and capabilities of the ALICE experiment allow to study the hadron production over a wide range of momenta both in pp and Pb–Pb collisions at the LHC. ALICE, with respect to the other LHC experiments, contributes especially with the measurement of identified particles, resonances and multi-strange baryons down to very low p_{t}. A review of the most recent results obtained in Pb–Pb collisions at $\sqrt{s_{\mathrm{NN}}} = 2.76$ TeV is reported. Transverse momentum spectra allow to characterize the dynamical evolution of the system produced in nuclear collisions, while production yields and ratios are discussed from a thermodynamical point of view. Results are finally compared to measurements at lower energies and predictions for the LHC.

1 Introduction

The ALICE experiment [1] has been taking data in pp collisions at $\sqrt{s} = 0.9$, 2.76 and 7 TeV and Pb–Pb collisions at $\sqrt{s_{\mathrm{NN}}} = 2.76$ TeV. The ALICE detector has been designed and optimized to allow particle identification (PID) with different techniques, especially in the central barrel. A six-layer silicon Inner Tracking System (ITS) provides precise tracking and vertex determination and allow PID down to 100 MeV/c via a dE/dx measurement in the 4 external layers, with a resolution of 10-15% on the dE/dx. A large-volume Time Projection Chamber (TPC) provides the global tracking and PID through the measurement of the specific energy loss in gas, with a resolution of 5%. The Time-Of-Flight system is a large Multigap Resistive Plate Chamber (MRPC) array. Its PID is based on the measured particle time-of-flight for matched tracks extrapolated from the TPC. Thanks to a resolution on the particle time-of-flight of $\sigma_{TOF} = 86$ ps, there is a 2σ separation for π/K up to $\mathrm{p_t} = 3.0$ GeV/c and a 2σ separation for K/p up to $\mathrm{p_t} = 5.0$ GeV/c. At higher particle energies the relativistic rise of the Bethe-Bloch distribution of the dE/dx in the TPC can be used for PID. Finally, topological reconstruction of V-shaped decays is exploited for the reconstruction of strange and multi-strange baryons in their "cascade" decays.
This contribution focuses in particular on Pb–Pb collisions results, referring to the available literature for the results in pp [2, 3].

2 Identified particle p_{t} spectra

The study of primary hadron transverse momentum (p_{t}) spectra and particle ratios gives insights on the medium properties at the freeze-out. Primary π/K/p p_{t} spectra have been measured by ALICE for different collision centrality in the following ranges: 0.1–3.0 GeV/c for pions, 0.2–3.0

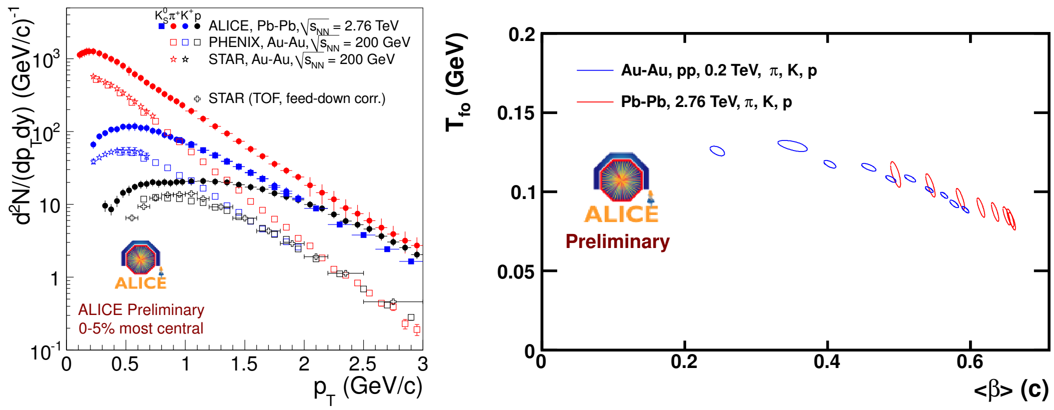

Figure 1: Positive π/K/p p_t spectra in the 0–5% most central Pb–Pb events, measured by ALICE at $\sqrt{s_{NN}} = 2.76$ TeV (left) and the freeze-out temperature (T$_{fo}$) and radial flow parameter ($\langle\beta\rangle$) resulting from a blast-wave fit to the primary hadron spectra for different centrality bins. The comparison with RHIC measurements is shown.

GeV/c for kaons, 0.3–3.0 GeV/c for protons. Fig. 1 (left) shows the comparison to similar measurements performed at RHIC in Au–Au collisions at $\sqrt{s_{NN}} = 200$ GeV [4, 5]. At the LHC the spectral shapes look much flatter at low p_t and spectra are harder, indicating a stronger radial flow at the LHC. A blast-wave fit [6] has been performed simultaneously on the π, K and p spectra for each centrality in order to extract the kinetic freeze-out temperature and radial flow ($\langle\beta\rangle$ parameter), as shown in Fig. 1 (right). While the former seems slightly lower than at RHIC, ALICE measures $\langle\beta\rangle = 0.66c$, which corresponds to a value about 10% higher than the one measured by STAR [4] for the most central collisions.

3 Multi-strange baryon production and strangeness enhancement

As observed at the SPS and then at RHIC, the enhancement of multi-strange hadron production supported the hypothesis that the state of matter produced in ultra-relativistic nucleus-nucleus collisions was different from a hadron gas created at the same energy in nucleon-nucleon collisions. It suggested instead the presence of a medium with large correlation volume and fast equilibration phase [7]. The measurement of multi-strange baryon p_t spectra has been performed at mid-rapidity in four centrality classes via the topological reconstruction of the following weak decays: $\Xi^- \to \pi^- + \Lambda$, $\Omega^- \to K^- + \Lambda$, where $\Lambda \to \pi^- + p$, and similarly for the anti-particle decay, where the corresponding branching ratios for Ξ and Ω are 63.9% and 43.3% respectively. The spectra integrated over all centralities are reported in Fig. 2 (left). It has been verified that the anti-particle to particle ratio is close to unity, as expected at the LHC where the baryochemical potential (μ_B) is close to zero. The yields which were extracted with a Blast-wave fit, are further used to estimate particle ratios, which have been compared with thermal model predictions [8]. The measured values for kaon and multi-strange baryons over pion are compatible with a model prediction that assumes a chemical freeze-out temperature of the medium T = 160-170 MeV. The p/π ratio is in better agreement with T = 148 MeV, which however fails for multi-strange.

The comparison between the yields of multi-strange hadrons in pp and Pb–Pb collisions has been carried out through the definition of the enhancement factors which are reported in Fig. 2 (right) for different hyperon species as a function of $\langle N_{part}\rangle$. Several experiments at different energies, WA97/NA57 at the SPS ($\sqrt{s_{NN}} = 17.2$ GeV) [9, 10], STAR at RHIC ($\sqrt{s_{NN}} = 200$ GeV) [11] and finally ALICE ($\sqrt{s_{NN}} = 2.76$ TeV) are compared. Details can be found in the original references. The enhancement increases with centrality, and follows the hierarchy of the

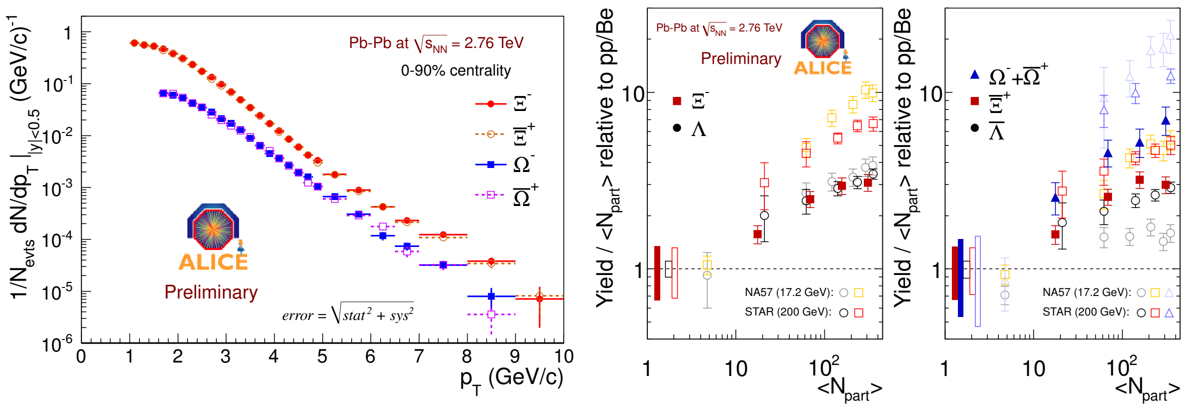

Figure 2: Transverse momentum spectra for Ξ^-, $\bar{\Xi}^+$, Ω^- and $\bar{\Omega}^+$ in the 0-90% centrality range, on the left. On the right: enhancement for hyperon yields measured at mid-rapidity and for different centralities by ALICE (filled points), compared with SPS and RHIC data (open points). The vertical bars indicate the quadratic sum of statistical and systematic error. ALICE's measurement of the Λ enhancement is not reported, as still in progress.

strangeness content in terms of valence quarks of the hyperons. Moving from SPS to LHC the relative enhancements seem to decrease with increasing collision energy, although it must be stressed that the absolute production of hyperons in heavy-ion collisions increases with energy from the SPS to the LHC, as expected.

4 Λ and K^0_S production

It was firstly observed at RHIC [12] that in Au–Au collisions the baryon (anti-baryon) production at intermediate p_t becomes comparable to that of mesons and that the maximum value of the Λ/K^0_S ratio in central collisions exceeds unity. In nucleus-nucleus (A-A) collisions the interplay between soft and hard processes involved in particle production is a candidate to explain this “baryon-to-meson anomaly”. In ALICE, the K^0_S and Λ particles are reconstructed via their V0 decay topology in a wide momentum range, the spectra of Λ being feed-down corrected for the contribution of Λ coming from the weak decays of Ξ^- and Ξ^0. ALICE measured the Λ/K^0_S ratio as function of p_t in five centrality bins, as reported in Fig. 3 (left). Baryon/meson ratio decreases from central to peripheral events, where it reaches the value measured in pp collisions. For most central Pb–Pb collisions it well goes above unity, reaching it maximum for $p_t \simeq 3$ GeV/c. A direct comparison with RHIC result indicates a dependence of the Λ/K^0_S both from the centrality and the collision energy. At higher p_t, up to 20 GeV/c, a suppression of a factor 4 in the Λ and K^0_S production in Pb–Pb collisions with respect to pp is observed. The suppression, measured in terms of the nuclear modification factor, R_{AA}, is seen to increase with the centrality of the collision. As shown in Fig. 3 (right), relative to collision centrality 0–5 %, the Λ exhibits an enhancement at intermediate p_t then a suppression for $p_t \geq 3$ GeV/c, while the K^0_S exhibits suppression in the full range. The mesons appear to be more suppressed than the baryons, up to $p_t = 8$ GeV/c. Above this value, the suppression is similar to that of the charged particles. This suppression effect has been interpreted as resulting from the energy loss by the partons that once produced with high energy in hard-scattering processes, traverse the hot and dense medium created with the collision. A common behaviour shared by the strange baryons, mesons and the other charged particles, suggests that the parton energy loss may not be strongly dependent by the (light) flavour of the parton involved. The significantly higher R_{AA} of Λ at intermediate p_t could be related to the presence of other hadronization mechanisms, as suggested by the Λ/K^0_S ratio.

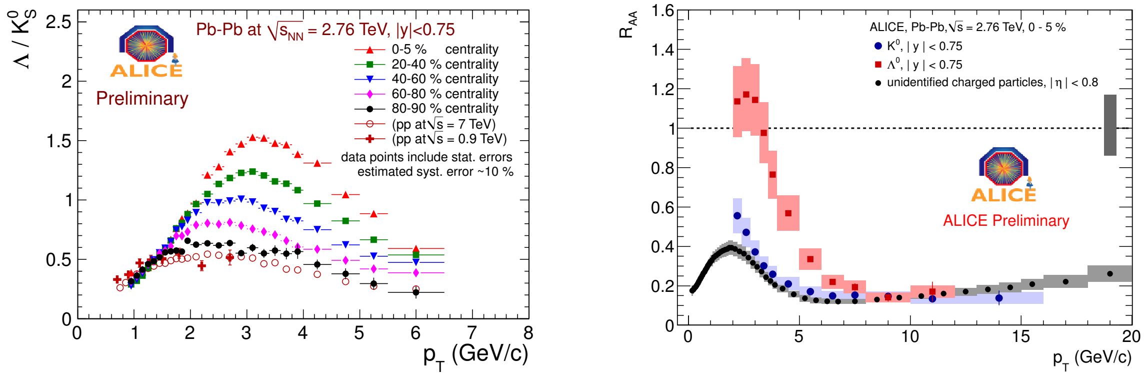

Figure 3: Strange baryon over meson ratio as function of p_t and centrality in Pb–Pb collisions at $\sqrt{s_{NN}} = 2.76$ TeV and compared with minimum bias pp collisions at $\sqrt{s_{NN}} = 0.9$ and 7 TeV, on the left. On the right: nuclear modification factor for Λ, K^0_S and charged particles in 0–5 % central Pb–Pb collisions. Vertical error bars represent statistical error, while rectangles represent systematic errors. The grey bar indicates the uncertainty in the calculation of the mean number of binary collisions.

5 Summary

We have presented the measurements of several observables that contribute to the investigation of the properties of the strongly interacting matter created in heavy-ion collisions at $\sqrt{s_{NN}} = 2.76$ TeV at the LHC. Identified π, K, p and multi-strange baryon p_t spectra have been measured for different centralities and compared to results at lower energies. The radial flow measured at the LHC is stronger that the one measured at RHIC. ALICE's measurement has been compared to the previous experiments to describe the excitation functions of the strange hyperons enhancement: the relative values seem to decrease with increasing energy, confirming the trend observed at the SPS and between the SPS and RHIC. Moreover we have reported the observation of the "baryon-to-meson anomaly" in most central Pb–Pb collisions. Finally the nuclear modification factor of Λ and K^0_S exhibits for $p_T \geq 8$ GeV/c a similar behaviour to that of the charged particles, suggesting no strong light flavour dependence of the parton energy loss in the medium produced in Pb–Pb collisions at the LHC.

References

1. K. Aamodt *et al.* [ALICE Collaboration], JINST **3**, S08002 (2008).
2. M. Chojnacki (Quark Matter 2011 proceedings), arXiv:1109.6744 [hep-ex].
3. B. Abelev *et al.* [ALICE Collaboration], arXiv:1204.0282v1 [nucl-ex].
4. B. I. Abelev *et al.* [STAR Collaboration], Phys. Rev. C **79**, 034909 (2009).
5. S. S. Adler *et al.* [PHENIX Collaboration], Phys. Rev. C **69**, 034909 (2004).
6. E. Schnedermann, J. Sollfrank and U. W. Heinz, Phys. Rev. C **48**, 2462 (1993).
7. J. Rafelski and B. Muller, Phys. Rev. Lett. **48**, 1066 (1982).
8. A. Andronic *et al.* Phys. Lett. B **673**, 142 (2009).
9. E. Andersen *et al.* [WA97 Collaboration], Phys. Lett. B **449**, 401 (1999).
10. F.. Antinori *et al.* [WA97/NA57 Collaboration], Nucl. Phys. A **698**, 118c (2002).
11. B. I. Abelev *et al.* [STAR Collaboration], Phys. Rev. C **77**, 044908 (2008).
12. J. Adams *et al.* [STAR and STAR-RICH Collaborations], arXiv:0601042 [nucl-ex].

HEAVY QUARK STRUCTURE FUNCTIONS IN THE ACOT SCHEME

T. Stavreva
Laboratoire de Physique Subatomique et de Cosmologie, UJF, CNRS/IN2P3, INPG, 53 avenue des Martyrs, 38026 Grenoble, France

We compute the structure functions F_2 and F_L in the ACOT scheme for heavy quark production. We use the complete ACOT results to NLO, and make use of the $\overline{MS}$ massless results at NNLO and N^{3}LO to estimate the higher order mass-dependent corrections. The dominant heavy quark mass effects can be taken into account using massless Wilson coefficients together with an appropriate rescaling prescription. Combining the exact NLO ACOT scheme with these expressions should provide a good approximation to the full calculation in the ACOT scheme at NNLO and N^{3}LO.These proceedings are based on Ref. [1], and further details can be found therein.

1 Introduction

The production of heavy quarks in high energy processes has become an increasingly important subject of study both theoretically and experimentally. The theory of heavy quark production in perturbative Quantum Chromodynamics (pQCD) is more challenging than that of light parton (jet) production because of the new physics issues brought about by the additional heavy quark mass scale. The correct theory must properly take into account the changing role of the heavy quark over the full kinematic range of the relevant process from the threshold region (where the quark behaves like a typical "heavy particle") to the asymptotic region (where the same quark behaves effectively like a parton, similar to the well known light quarks $\{u, d, s\}$).

With the ever-increasing precision of experimental data and the progression of theoretical calculations and parton distribution function (PDF) evolution to next-to-next-to-leading order (NNLO) of QCD there is a clear need to formulate and also implement the heavy quark schemes at this order and beyond. The most important case is arguably the heavy quark treatment in inclusive deep-inelastic scattering (DIS) since the very precise HERA data for DIS structure functions and cross sections form the backbone of any modern global analysis of PDFs. Here, the heavy quarks contribute up to 30% or 40% to the structure functions at small momentum fractions x. Extending the heavy quark schemes to higher orders is therefore necessary for extracting precise PDFs and hence for precise predictions of observables at the LHC. However, we would like to also stress the theoretical importance of having a general pQCD framework including heavy quarks which is valid to all orders in perturbation theory over a wide range of hard energy scales and which is also applicable to other observables than inclusive DIS in a straightforward manner.

An example, where higher order corrections are particularly important is the structure function F_L in DIS. The leading order ($\mathcal{O}(\alpha_S^0)$) contribution to this structure function vanishes for massless quarks due to helicity conservation (Callan-Gross relation). This has several consequences: 1) F_L is useful for constraining the gluon PDF via the dominant subprocess $\gamma^* g \to q\bar{q}$.

The heavy quark mass effects of order $\mathcal{O}(\frac{m^2}{Q^2})$ are relatively more pronounced.[a] 3) Since the first non-vanishing contribution to F_L is next-to-leading order (up to mass effects), the NNLO and N^{3}LO corrections are more important than for F_2. The purpose of this study is to calculate the leading twist neutral current DIS structure functions F_2 and F_L in the ACOT factorization scheme up to order $\mathcal{O}(\alpha_S^3)$ (N^{3}LO) and to estimate the error due to approximating the heavy quark mass terms $\mathcal{O}(\alpha_S^2 \times \frac{m^2}{Q^2})$ and $\mathcal{O}(\alpha_S^3 \times \frac{m^2}{Q^2})$ in the higher order corrections.

2 ACOT Scheme

The ACOT renormalization scheme [4,3] provides a mechanism to incorporate the heavy quark mass into the theoretical calculation of heavy quark production both kinematically and dynamically. In 1998 Collins [5] extended the factorization theorem to address the case of heavy quarks; this work provided the theoretical foundation that allows us to reliably compute heavy quark processes throughout the full kinematic realm. The key ingredient provided by the ACOT scheme is the subtraction term (SUB) which removes the "double counting" arising from the regions of phase space where the LO and NLO contributions overlap. Specifically, at NLO order, we can express the total result as a sum of

$$\sigma_{TOT} = \sigma_{LO} + \{\sigma_{NLO} - \sigma_{SUB}\} \tag{1}$$

where the subtraction term for the gluon-initiated processes is

$$\sigma_{SUB} = f_g \otimes \tilde{P}_{g\to Q} \otimes \sigma_{QV\to Q}. \tag{2}$$

σ_{SUB} represents a gluon emitted from a proton (f_g) which undergoes a collinear splitting to a heavy quark ($\tilde{P}_{g\to Q}$) convoluted with the LO quark-boson scattering $\sigma_{QV\to Q}$. Here, $\tilde{P}_{g\to Q}(x,\mu) = \frac{\alpha_s}{2\pi}\ln(\mu^2/m^2)\,P_{g\to Q}(x)$ where $P_{g\to Q}(x)$ is the usual $\overline{MS}$ splitting kernel, m is the quark mass and μ is the renormalization scale which we typically choose to be $\mu = Q$. An important feature of the ACOT scheme is that it reduces to the appropriate limit both as $m \to 0$ and $m \to \infty$ as we illustrate below. Specifically, in the limit where the quark Q is relatively heavy compared to the characteristic energy scale ($\mu \lesssim m$), we find $\sigma_{LO} \sim \sigma_{SUB}$ such that $\sigma_{TOT} \sim \sigma_{NLO}$. In this limit, the ACOT result naturally reduces to the Fixed-Flavor-Number-Scheme (FFNS) result. In the FFNS, the heavy quark is treated as being extrinsic to the hadron, and there is no corresponding heavy quark PDF ($f_Q \sim 0$); thus $\sigma_{LO} \sim 0$. We also have $\sigma_{SUB} \sim 0$ because this is proportional to $\ln(\mu^2/m^2)$. Thus, when the quark Q is heavy relative to the characteristic energy scale μ, the ACOT result reduces to $\sigma_{TOT} \sim \sigma_{NLO}$. Conversely, in the limit where the quark Q is relatively light compared to the characteristic energy scale ($\mu \gtrsim m$), we find that σ_{LO} yields the dominant part of the result, and the "formal" NLO $\mathcal{O}(\alpha_S)$ contribution $\{\sigma_{NLO} - \sigma_{SUB}\}$ is an $\mathcal{O}(\alpha_S)$ correction. In this limit, the ACOT result will reduce to the $\overline{MS}$ Zero-Mass Variable-Flavor-Number-Scheme (ZM-VFNS) limit exactly without any finite renormalizations. The quark mass m no longer plays any dynamical role and purely serves as a regulator. The σ_{NLO} term diverges due to the internal exchange of the quark Q, and this singularity is canceled by σ_{SUB}.

In the limit $Q^2 \gg m^2$ the mass simply plays the role of a regulator. In contrast, for $Q^2 \sim m^2$ the value of the mass is of consequence for the physics. The mass can enter dynamically in the hard-scattering matrix element, and kinematically in the phase space of the process. As is demonstrated in Ref. [1] for the processes of interest the primary role of the mass is kinematic and not dynamic. It was this idea which was behind the original slow-rescaling prescription of

[a] Similar considerations also hold for target mass corrections (TMC) and higher twist terms. We focus here mainly on the kinematic region $x < 0.1$ where TMC are small [2]. An inclusion of higher twist terms is beyond the scope of this study.

Ref. [6] which considered DIS charm production (e.g., $\gamma c \to c$) introducing the shift $x \to \chi = x[1 + (m_c/Q)^2]$. This prescription accounted for the charm quark mass by effectively reducing the phase space for the final state by an amount proportional to $(m_c/Q)^2$.

This idea was extended in the χ-scheme by realizing that (in most cases) in addition to the observed final-state charm quark, there is also an anti-charm quark in the beam fragments since all the charm quarks are ultimately produced by gluon splitting ($g \to c\bar{c}$) into a charm pair. For this case the scaling variable becomes $\chi = x[1 + (2m_c/Q)^2]$. This rescaling is implemented in the ACOT$_\chi$ scheme [7,8]. As mentioned above, the dominant mass effects are those coming from the phase space, i.e. kinematic mass, these can be taken into account via a generalized slow-rescaling $\chi(n)$-prescription. Assuming that a similar relation remains true at higher orders one can construct the following approximation to the full ACOT result up to N^{3}LO ($\mathcal{O}(\alpha_S^3)$):

$$\mathrm{ACOT}[\mathcal{O}(\alpha_S^{0+1+2+3})] \simeq \mathrm{ACOT}[\mathcal{O}(\alpha_S^{0+1})] + \mathrm{ZMVFNS}_\chi[\mathcal{O}(\alpha_S^{2+3})]. \tag{3}$$

Here, the massless Wilson coefficients at $\mathcal{O}(\alpha\,\alpha_S^2)$ and $\mathcal{O}(\alpha\,\alpha_S^3)$ are substituted for the Wilson coefficients in the ACOT scheme as the corresponding massive coefficients have not yet been computed.

3 Results

In Figures 1a) and 1b) we display the fractional contributions for the final-state quarks (j) to the structure functions F_2 and F_L, respectively, for selected x values as a function of Q; here we have used $n = 2$ scaling. Reading from the bottom, we have the cumulative contributions from the $\{u, d, s, c, b\}$. We observe that for large x and low Q the heavy flavor contributions are minimal, but these can grow quickly as we move to smaller x and larger Q.

In Figure 2a) we display the results for F_2 vs. Q computed at various orders. For large x (c.f. $x = 0.1$) we find the perturbative calculation is particularly stable; we see that the LO result is within 20% of the others at small Q, and within 5% at large Q. The NLO is within 2% at small Q, and indistinguishable from the NNLO and N^{3}LO for Q values above ~ 10 GeV. The NNLO and N^{3}LO results are essentially identical throughout the kinematic range. For smaller x values (10^{-3}, 10^{-5}) the contribution of the higher order terms increases. Here, the NNLO and N^{3}LO coincide for Q values above ~ 5 GeV, but the NLO result can differ by $\sim 5\%$.

In Figure 2b) we display the results for F_L vs. Q computed at various orders. In contrast to F_2, we find the NLO corrections are large for F_L; this is because the LO F_L contribution (which violates the Callan-Gross relation) is suppressed by (m^2/Q^2) compared to the dominant gluon contributions which enter at NLO. Consequently, we observe (as expected) that the LO result for F_L receives large contributions from the higher order terms. Essentially, the NLO is the first non-trivial order for F_L, and the subsequent contributions then converge. For example, at large x (c.f. $x = 0.1$) for $Q \sim 10$ GeV we find the NLO result yields ~ 60 to 80% of the total, the NNLO is a $\sim 20\%$ correction, and the N^{3}LO is a $\sim 10\%$ correction. For lower x values (10^{-3}, 10^{-5}) the convergence of the perturbative series improves, and the NLO results is within $\sim 10\%$ of the N^{3}LO result. Curiously, for $x = 10^{-5}$ the NNLO and N^{3}LO roughly compensate each other so that the NLO and the N^{3}LO match quite closely for $Q \geq 2$ GeV.

4 Conclusions

The results of this study form the basis for using the ACOT scheme in NNLO global analyses and for future comparisons with precision data for DIS structure functions.

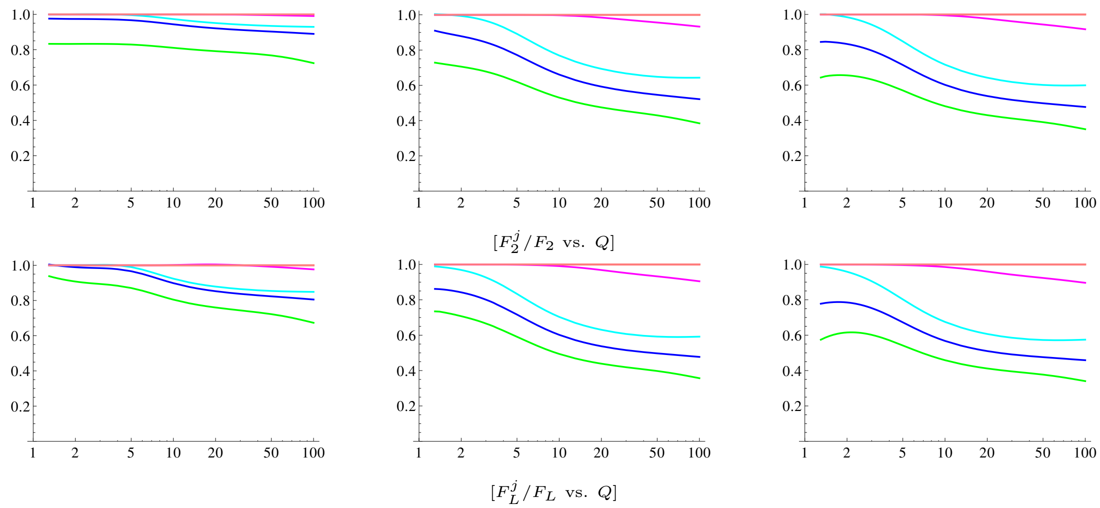

Figure 1: Fractional contribution for each quark flavor to $F_{2,L}^j/F_{2,L}$ vs. Q at N^{3}LO for fixed $x = \{10^{-1}, 10^{-3}, 10^{-5}\}$ (left to right). Results are displayed for $n = 2$ scaling. Reading from the bottom, we have the cumulative contributions from the $\{u, d, s, c, b\}$ (green, blue, cyan, magenta, pink).

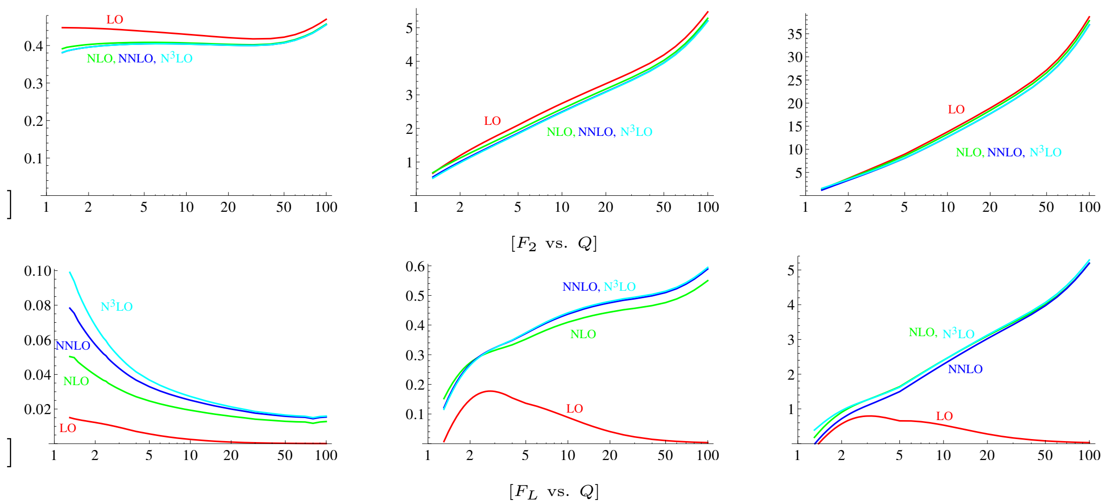

Figure 2: $F_{2,L}$ vs. Q at {LO, NLO, NNLO, N^{3}LO} (red, green, blue, cyan) for fixed $x = \{10^{-1}, 10^{-3}, 10^{-5}\}$ (left to right) for $n = 2$ scaling.

References

1. T. Stavreva *et al.* *Preprint* `arXiv:1203.0282 [hep-ph]` 2012.
2. I. Schienbein *et al.* J.Phys.G **G35**, 053101 (2008).
3. M. A. G Aivazis *et al.* Phys.Rev. **D50**, 3102 (1994).
4. M. A. G Aivazis *et al.* Phys.Rev. **D50**, 3085 (1994).
5. J. C. Collins, Phys.Rev. **D58**, 094002 (1998).
6. R. M. Barnett, PRL **36**, 1163 (1976).
7. W. K. Tung *et al.* J.Phys. **G28**, 983 (2002).
8. M. Guzzi *et al.* *Preprint* `arXiv:1108.5112 [hep-ph]` 2011.

Deeply Virtual Compton Scattering and Higgs Production Using the Pomeron in AdS

Richard C. Brower[a]
Department of Physics, Boston University, Boston MA 02215

Miguel S. Costa
Centro de Física do Porto, Universidade do Porto, 4169-007 Porto, Portugal

Marko Djurić[a]
Centro de Física do Porto, Universidade do Porto, 4169-007 Porto, Portugal

Chung-I Tan
Physics Department, Brown University, Providence RI 02912

In the past decade overwhelming evidence has emerged for a conjectured duality between a wide class of gauge theories in d dimensions and string theories on asymptotically AdS_{d+1} spaces. We apply this duality to scattering processes that occur via Pomeron exchange. First we develop the Pomeron in string theory, as done by Brower, Polchinski, Strassler and Tan,[1] showing that it naturally emerges as the Regge Trajectory of the AdS graviton. Next we apply the AdS Pomeron to the study of Deeply Virtual Compton Scattering (DVCS), and see that our model gives good results when compared to HERA data.[2] We then show how we can extend our results to double Pomeron exchange, and apply it to developing a formalism for the study of double diffractive Higgs production.[3]

Pomeron-Graviton Duality: In the Regge limit, $s \gg t$, it can be shown for a wide range of scattering processes that the amplitude is dominated by Pomeron exchange. Traditionally this has been modeled at weak coupling using perturbative QCD, but we will use here a formulation based on gauge/gravity duality, or the AdS/CFT correspondence, of which one particular example is the duality between $\mathcal{N} = 4$ SYM and Type IIB string theory on $AdS_5 \times S^5$. This approach has the advantages of allowing us to study the strong coupling region, providing a unified soft and hard diffractive mechanism, and as we will see it also fits well the experimental data.

In lowest order in weak 't Hooft coupling for QCD, a bare Pomeron was first identified by Low and Nussinov as a two gluon exchange corresponding to a Regge cut in the J-plane at $j_0 = 1$. Going beyond the leading order, Balitsky, Fadin, Kuraev and Lipatov (BFKL) summed all the diagrams for two gluon exchange to first order in $\lambda = g^2 N_c$ and *all* orders in $(g^2 N_c \log s)^n$, thus giving rise to the so-called BFKL Pomeron. The position of this J-plane cut is at $j_0 = 1 + \log(2) g^2 N_c/\pi^2$, recovering the Low-Nussinov result in the $\lambda \to 0$ limit. In a holographic approach to diffractive scattering [1,16,17,19], the weak coupling Pomeron is replaced by the "Regge graviton" in AdS space, as formulated by Brower, Polchinski, Strassler and Tan

[a] speaker

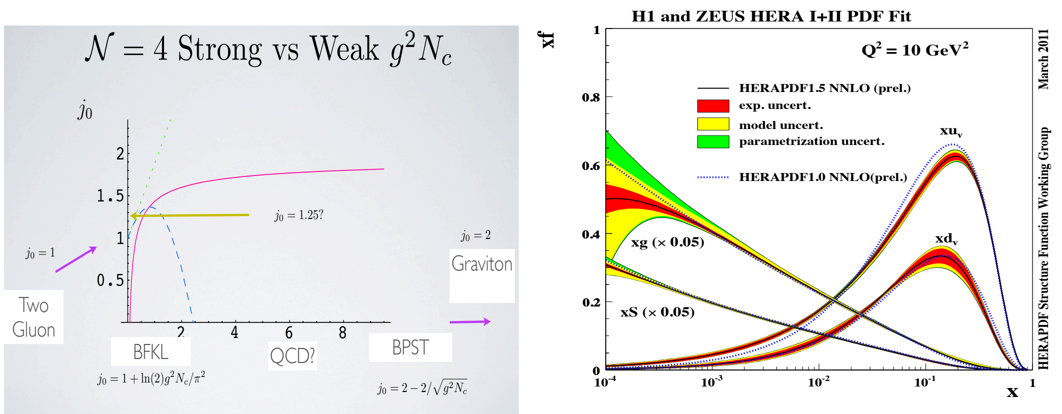

Figure 1: On the left, intercept j_0 in $\mathcal{N}=4$ YM shown as a function of 't Hooft coupling λ for the BPST Pomeron (solid red) and for BFKL (dotted and dashed to first and second order in λ respectively). On the right, a typical partonic fit to HERA DIS data demonstrating the dominance for gluon dynamics at small x.

(BPST)[1,17] which has both hard components due to near conformality in the UV and soft Regge behavior in the IR. Corrections to the strong coupling lower the intercept from $j = 2$ to

$$j_0 = 2 - 2/\sqrt{g^2 N_c}\,. \tag{1}$$

In Fig. 1, we compare this with the weak coupling BFKL intercept to second order. A typical phenomenological estimates for this parameter for QCD is about $j_0 \simeq 1.25$, which suggests that the physics of diffractive scattering is in the cross over region between strong and weak coupling. A corresponding treatment for Odderons has also been carried out [18]. We also show in Fig. 1 the dominance of gluons, in a conventional partonic approach, thus further justifying the large N_c approximation, where quark constituents are suppressed.

Holographic Treatment of Deeply Virtual Compton Scattering: Previously, we have applied the AdS/CFT correspondence to deep inelastic scattering[4,11,6] (see for example [5] for more references and the report from the previous Moriond conference). DVCS is the scattering between an off-shell photon and a proton, with the outgoing photon being on-shell. We make use of the fact that the DVCS cross section and differential cross section can be related to the Pomeron exchange amplitude, $A(s,t)$ via

$$\frac{d\sigma}{dt}(x, Q^2, t) = \frac{|A|^2}{16\pi s^2}\,, \tag{2}$$

and

$$\sigma(x, Q^2) = \frac{1}{16\pi s^2}\int dt\, |A|^2\,. \tag{3}$$

In the holographic approach, the impact parameter space $(b_\perp, z)$ is 3 dimensional, where $z \geq 0$ is the warped radial 5th dimension. Conformal dilatations ($\log z \to \log z + \text{const}$) take one from the UV boundary at $z = 0$ deep into the IR $z =$ large. The near forward elastic amplitude takes the eikonal form,

$$A(s,t) = 2is \int d^2b\, e^{i\vec{q}\cdot\vec{b}} \int dz dz'\, P_{13}(z) P_{24}(z') \{1 - e^{i\chi(s,b,z,z')}\}\,. \tag{4}$$

where $t = -q_\perp^2$ and the eikonal function, χ, is related to a BPST Pomeron kernel in a transverse AdS_3 representation, $\mathcal{K}(s, b, z, z')$, by

$$\chi(s, b, z, z') = \frac{g_0^2}{2s}\left(\frac{R^2}{zz'}\right)^2 \mathcal{K}(s, b, z, z'). \tag{5}$$

An important unifying features for the holographic map is factorization in the AdS space. For hadron-hadron scattering, $P_{ij}(z) = \sqrt{-g(z)}(z/R)^2\phi_i(z)\phi_j(z)$ involves a product of two external normalizable wave functions for the projectile and the target respectively. For DVCS, states 1 and 3 are replaced by currents for an off-shell and on-shell photon respectively, and we can simply replace P_{13} by product of the appropriate unnormalized wave-functions. We can calculate these by evaluating the R-current - graviton Witten diagram in AdS, and we get

$$P_{13}(z) = -C\,\frac{\pi^2}{6}\,z^3\,K_1(Qz). \tag{6}$$

Here C is a normalization constant that can be calculated in the strict conformal limit. When expanded to first order in χ, Eq. (4) provides the contribution from exchanging a single Pomeron. When χ is large equation (4) can be replaced by an AdS black disk model.[2]. In the conformal limit, a simple expression can be found. Confinement can next be introduced, eg., via a hardwall model $z < z_{cut-off}$. The effect of saturation can next be included via the full transverse AdS_3 eikonal representation (4).

Pomeron Kernel: The leading order BFKL Pomeron has remarkable properties. It enters into the first term in the large N_c expansion with zero beta function. Thus it is in effect the weak coupling cylinder graph for the Pomeron for a large N_c conformal theory, the same approximations used in the AdS/CFT approach albeit at strong coupling. Remarkable BFKL integrability properties allows one to treat the BFKL kernel as the solution to an $SL(2,\mathcal{C})$ conformal spin chain. Going to strong coupling, the two gluon exchange evolves into a close string of infinitely many tightly bound gluons but the same underlying symmetry persists, referred to as Möbius invariance in string theory or the isometries of the transverse AdS_3 impact parameter geometry. The position of the j-plane cut moves from $j_0 = 1 + \log(2)g^2N_c/\pi^2$ up to $j_0 = 2 - 2/\sqrt{g^2N_c}$ and the kernel obeys a Schrödinger equation on AdS_3 space for the Lorentz boost operators M_{+-} ,

$$\Big[(-\partial_u^2 - te^{-2u})/2 + \sqrt{\lambda}(j - j_0)\Big]\, G_j(t, z, z') = \delta(u - u'), \tag{7}$$

with $z = e^{-u}$. In the conformal limit, $G_j(t, z, z') = \int dq\; q\; J_{\tilde{\Delta}(j)}(zq)J_{\tilde{\Delta}(j)}(qz')/(q^2 - t)$, $\tilde{\Delta}(j)^2 = 2\lambda(j - j_0)$, and the Pomeron kernel is obtained via an inverse Mellin transform. From here we can obtain χ using (5). The solution for χ exhibits diffusion

$$\chi(\tau, L) = (\cot(\frac{\pi\rho}{2}) + i)g_0^2 e^{(1-\rho)\tau}\,\frac{L}{\sinh L}\,\frac{\exp(\frac{-L^2}{\rho\tau})}{(\rho\tau)^{3/2}}, \tag{8}$$

in the "size" parameter $\log z$ for the exchanged closed string, analogous to the BFKL kernel at weak coupling, with diffusing taking place in $\log(k_\perp)$, the virtuality of the off shell gluon dipole. The diffusion constant takes on $\mathcal{D} = 2/\sqrt{g^2N_c}$ at strong coupling compared to $\mathcal{D} = 7\zeta(3)g^2N_c/2\pi^2$ in weak coupling. The close analogy between the weak and strong coupling Pomeron suggests the development of a hybrid phenomenology leveraging plausible interpolations between the two extremes.

Fit to HERA Data We now apply equations (2) and (3) to compare our model to the measurements at HERA.[22,23] Related papers using AdS/CFT correspondence applied to DVCS include [12,13,14]. We use equation (6) for the photon wavefunctions and a delta function for the proton. Note that equation (8) is for the conformal model, and the hard wall expression would include another term with the contribution due to the presence of the hard wall. See [2] for the explicit form. We obtain a good agreement with experiment, with χ^2 varying from

$0.51 - 1.33$ depending on the particular data and model we are considering. We find that confinement starts to play a role at small $|t|$, and the hardwall fits the data better in this region. Explicitly, the parameter values we get for the hard wall model are $g_0^2 = 2.46 \pm 0.70$, $z_* = 3.35 \pm 0.41$ GeV^{-1}, $\rho = 0.712 \pm 0.038$, $z_0 = 4.44 \pm 0.82$ GeV^{-1} for the differential cross section, and $g_0^2 = 6.65 \pm 2.30$, $z_* = 4.86 \pm 2.87$ GeV^{-1}, $\rho = 0.811 \pm 0.036$, $z_0 = 8.14 \pm 2.96$ GeV^{-1}, with $\chi^2_{d.o.f} = 0.51$ and 1.03 respectively. In figure we present the plots corresponding to these parameters.

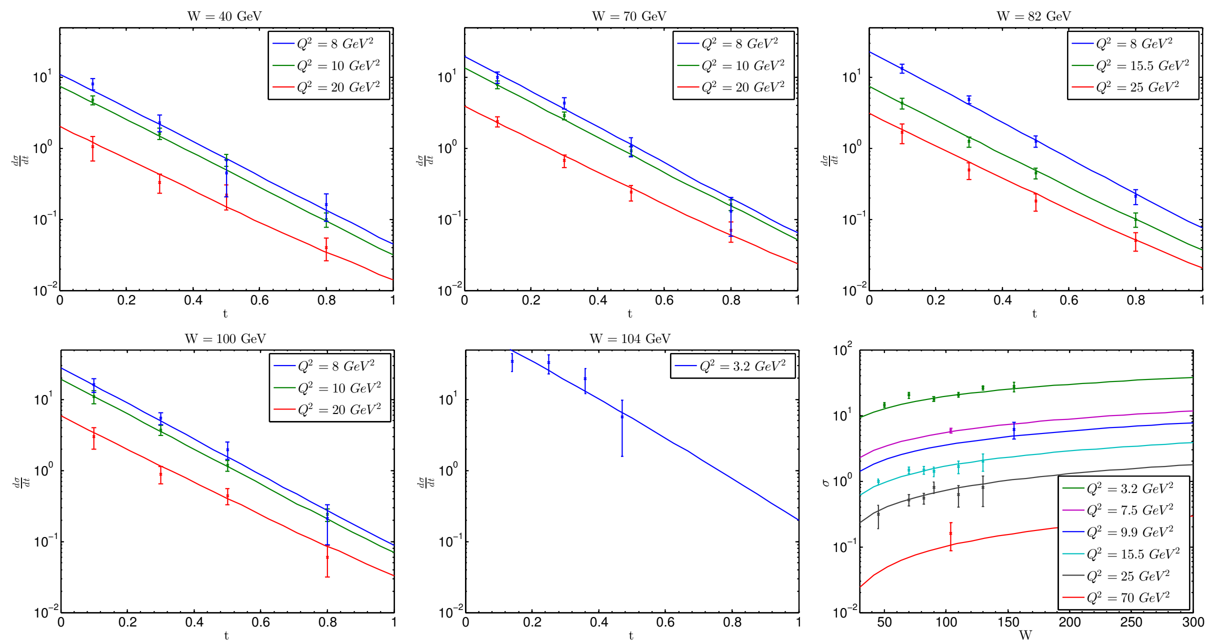

Figure 2: The plots of the hard wall pomeron compared to HERA data. The first 5 correspond to the differential cross section, and the last one to the cross section where we omit some values of Q^2 to avoid cluttering the graph.

Double Diffractive Higgs Production We would now like to extend these methods to double diffractive Higgs production from forward proton-proton scattering, $pp \to pHp$.[3] The protons scatter through very small angles with a large rapidity gaps separating the Higgs in the central region. The Higgs subsequently decays into large transverse momentum fragments. Although this represents a small fraction of the total cross section, the exclusive channel should provide an exceptional signal to background discrimination by constraining the Higgs mass to both the energy of decay fragments and the energy lost to the forward protons [24]. To extend our previous methods to this process, first notice that after expanding equation (4) to single pomeron exchange, we can schematically represent it as

$$A(s,t) = \Phi_{13} * \widetilde{\mathcal{K}}_P * \Phi_{24}\ . \tag{9}$$

A holographic treatment of Higgs production amounts to a generalization of our previous AdS treatment for 2-to-2 amplitudes to one for 2-to-3 amplitudes, e.g., from Fig. 3a to Fig. 3b. A more refined analysis for Higgs production requires a careful treatment for that depicted in Fig. 3c. A particularly useful paper for the diffractive Higgs analysis is the prior work by Herzog, Paik, Strassler and Thompson [25] on holographic double diffractive scattering. In this analysis, one generalizes (9) to 2-to-3 amplitude where

$$A(s, s_1, s_2, t_1, t_2) = \Phi_{13} * \widetilde{\mathcal{K}}_P * V_H * \widetilde{\mathcal{K}}_P * \Phi_{24}\ , \tag{10}$$

schematically represented by Fig. 3b. However, a new aspect, not addressed in [25], is the issue of scale invariance breaking. A proper accounting for a non-vanishing gluon condensate $\langle F^2 \rangle$ turns out to be a crucial ingredient in understanding the strength of diffractive Higgs production. We now must pause to realize that in any conformal theory the is no dimensional parameter to allow for such a dimensionful two-graviton-dilaton coupling, $M^2 \phi h_{\mu\nu} h^{\mu\nu}$, emerging in an expansion of the AdS gravity action if scale invariance is maintained. However since QCD is not a conformal theory this is just one of many reasons to introduce conformal symmetry breaking. To model an effective QCD background we will for the most part introduce two modifications of the pure AdS background: (1) an IR hardwall cut-off beyond $z = 1/\Lambda_{qcd}$ to give confinement and linear static quark potential at large distances and (2) a slow deformation in the UV ($z \to 0$) to model the logarithmic running for asymptotic freedom. Both break conformal invariance, which as we will argue is required to couple the two gravitons to the dilaton and produce a Higgs in the central rapidity region.

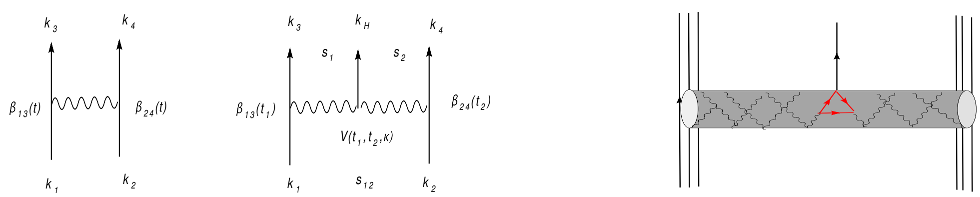

Figure 3: (a) Kinematics for single-Regge limit for 2-to-2 amplitudes, (b) Double-Regge kinematics for 2-to-3 amplitudes. (c) Cylinder Diagram for large N_c Higgs Production.

Pomeron-Pomeron Fusion Vertex We are now in a position to focus on the Higgs vertex, V_H. It is important to stress that our general discussion in moving from single-Pomeron exchange processes, (9), to double-Pomeron exchange, (10), applies equally well for both diffractive glueball production and for Higgs production. The difference lies in how to treat the new central vertex. For the production of a glueball, the vertex will be proportional to a normalizable AdS wave-function. There will also be an overall factor controlling the strength of coupling to the external states, e.g., the Pomeron-Pomeron-glueball couplings. For Higgs production, on the other hand, the central vertex, V_H, involves a non-normalizable bulk-to-boundary propagator, appropriate for a scalar external current. This in turns leads to coupling to a Higgs scalar. This is analogous to the use of a non-normalizable current for $P_{13}(z)$ in equation (6).

A Higgs scalar in the standard model couples exclusively to the quarks via Yukawa coupling, which for simplicity we will assume is dominated by the top quark, with $\mathcal{L} = -\frac{g}{2M_W} m_t \, \bar{t}(x) t(x) \phi_H(x)$. Taking advantage of the scale separations between the QCD scale, the Higgs mass and the top quark mass, $\Lambda_{qcd} \ll m_H \ll 2m_t$, heavy quark decoupling allows one to replace the Yukawa coupling by direct coupling of Higgs to gluons, which is treated as an external source in the AdS dictionary. Consequently V_H, in a coordinate representation, is replaced by the vertex for two AdS Pomerons fusing at $(x'_{1\perp}, z'_1)$ and $(x'_{2\perp}, z'_2)$ and propagating this disturbance to the $\bar{t}(x)t(x)$ scalar current at the boundary of AdS. The double diffractive Higgs vertex V_H can then be obtained in a two-step process.

First, since the Yukawa Higgs quark coupling is proportional to the quark mass, it is dominated by the top quark. Assuming $m_H \ll m_t$, this can be replaced by an effective interaction by evaluating the two gluon Higgs triangle graph in leading order $O(M_H/m_t)$. Second, using the AdS/CFT dictionary, the external source for $F^a_{\mu\nu} F^a_{\mu\nu}(x)$ is placed at the AdS boundary ($z_0 \to 0$) connecting to the Pomeron fusion vertex in the interior of AdS_3 at $\mathbf{b}_H = (x'_H, z'_H)$, by a scalar bulk-to-boundary propagator, $K(x'_H - x_H, z'_H, z_0)$.

We are finally in the position to put all the pieces together. Although we eventually want to go to a coordinate representation in order to perform eikonal unitarization, certain simplification can be achieved more easily in working with the momentum representation. The Higgs production amplitude, schematically given by (10), can then be written explicitly as

$$
\begin{aligned}
A(s,s_1,s_2,t_1,t_2) &\simeq \int dz_1 dz dz_2 \sqrt{-g_1}\sqrt{-g}\sqrt{-g_2}\ \Phi_{13}(z_1) \\
&\times \ \widetilde{\mathcal{K}}_P(s_1,t_1,z_1,z)\ V_H(q^2,z)\ \widetilde{\mathcal{K}}_P(s_2,t_2,z,z_2)\ \Phi_{24}(z_2)\ .
\end{aligned}
$$

where $q^2 = -m_H^2$. For this production vertex, we will keep it simple by expressing it as

$$
V_H(q^2,z) = V_{PP\phi} K(q^2,z) L_H\ . \tag{11}
$$

where $K(q^2,z)$ is the conventionally normalized bulk to boundary propagator, $V_{PP\phi}$ serves as an overall coupling from two-Pomeron to F^2, and L is the conversion factor from F^2 to Higgs, i.e., $L_H = L(-m_H^2) \simeq \frac{\alpha_s g}{24\pi M_W}$. By treating the central vertex $V_{PP\phi}$ as a constant, which follows from the super-gravity limit, we have ignored possible additional dependence on κ, as well as that on t_1 and t_2. This approximation gives an explicit factorizable form for Higgs production.

Strategy for Phenomenological Estimates As a first step in making a phenomenological estimate for the cross section, we ask how the central vertex, V_H, or equivalently, $V_{PP\phi}$, via (11), can be normalized, following the approach of Kharzeev and Levin [24] based on the analysis of trace anomaly. We also show how one can in principle use the elastic scattering to normalize the bare BPST Pomeron coupling to external protons and the 't Hooft coupling $g^2 N_c$.

We start from Eq. (11). When nearing the respective tensor poles at $t_1 \simeq m_0^2$ and $t_2 \simeq m_0^2$, the amplitude can be expressed as

$$
A(s,s_1,s_2,t_1,t_2) \ \simeq \ g_{13}\, \frac{\Gamma_{GGH}\ s^2}{(t_1 - m_0^2)(t_2 - m_0^2)}\, g_{24} \tag{12}
$$

We have performed the z_1 and z_2 integrations, and have also made use of the fact that $s_1 s_2 \simeq \kappa\ s \simeq m_H^2 s$. Here Γ_{GGH} is the effective on-shell glueball-glueball-Higgs coupling, which can also be expressed as $\Gamma_{GGH} = L_H F(-m_H^2)$ where $L_H = \frac{\alpha_s g}{24\pi M_W}$ and F is a scalar form factor $F(q^2) =< G,++,q_1|F^a_{\mu\nu}F^a_{\mu\nu}(0)|G,--,q_2>$. That is, in the high energy Regge limit, the dominant contribution comes from the maximum helicity glueball state [1], with $\lambda = 2$. In this limit, this form factor, is given by the overlap of the dilaton bulk to boundary propagator

$$
F(q^2) \ = \ (\alpha' m_H^2)^2 V_{PP\phi} \int dz \sqrt{-g(z)} e^{-4A(z)} \phi_G(z) K(q,z) \phi_G(z) \tag{13}
$$

What remains to be specified is the overall normalization, $F(0)$.

We next follow D. Kharzeev and E. M. Levin [24], who noted that, from the SYM side, $F(q^2)$ at $q^2 = 0$, can be considered as the glueball condensate. Consider matrix elements of the trace-anomaly between two states, $|\alpha(p)>$ and $|\alpha'(p')>$, with four-momentum transfer $q = p - p'$. In particular, for a single particle state of a tensor glueball $|G(p)>$, this leads to $< G(p)|\Theta^\alpha_\alpha|G(p')> = \frac{\widetilde{\beta}}{2g} < G(p)|F^a_{\mu\nu}F^{a\mu\nu}|G(p')>$. At $q = 0$, the forward matrix element of the trace of the energy-momentum tensor is given simply by the mass of the relevant tensor glueball, with $< G|\Theta^\alpha_\alpha|G> = M_G^2$, this directly yields

$$
F(0) =< G|F^a_{\mu\nu}F^{a\mu\nu}|G> = -\frac{4\pi M_G^2}{3\widetilde{\beta}} \tag{14}
$$

where $\widetilde{\beta} = -b\alpha_s/(2\pi)$, $b = 11 - 2n_f/3$, for $N_c = 3$. In what follows, we will use $n_f = 3$. Note that heavy quark contribution is not included in this limit. Since the conformal scale breaking is due the running coupling constant in QCD, there is apparently a mapping between QCD scale breaking and breaking of the AdS background in the IR, which gives a finite mass to the glueball and to give a non-zero contribution to the gauge condensate.

Let us turn next to the non-forward limit. We accept the fact that, in the physical region where $t < 0$ and small, the cross sections typically have an exponential form, with a logarithmic slope which is mildly energy-dependent. We therefore approximate all amplitudes in the near forward region where $t < 0$ and small, $A(s,t) \simeq e^{B_{eff}(s)\,t/2}\,A(s,0)$ where $B_{eff}(s)$ is a smoothly slowly increasing function of s, (we expect it to be logarithmic). We also assume, for $t_1 < 0$, $t_2 < 0$ and small, the Higgs production amplitude is also strongly damped so that

$$A(s,s_1,s_2,t_1,t_2) \simeq e^{B'_eff(s_1)\,t_1/2} e^{B'_eff(s_2)\,t_2/2}\,A(s,s_1,s_2,t_1 \simeq 0, t_2 \simeq 0) \tag{15}$$

We also assume $B'_{eff}(s) \simeq B_{eff}(s) +$ b. With these, both the elastic, the total pp cross sections and the Higgs production cross section can now be evaluated. Various cross sections will of course depend on the unknown slope parameter, B_{eff}, which can at best be estimated based on prior experience with diffractive estimates. One can relate B_{eff} directly in terms of the experimentally smooth dimensionless ratio, $R_{el}(s) = \sigma_{el}/\sigma_{total} = \frac{(1+\rho^2)\sigma_{total}(s)}{16\pi B_{eff}(s)}$. Upon squaring the amplitude, $A(s,s_1,s_2,t_1,t_2)$, (15), the double-differential cross section for Higgs production can now be obtained. After integrating over t_1 and t_2 and using the fact that, for m_H^2 large $s \simeq s_1 s_2/m_H^2$, one finds

$$\frac{d\sigma}{dy_H} \;\simeq\; (1/\pi) \times C' \times |\Gamma_{GGH}(0)/\widetilde{m}^2|^2 \times \frac{\sigma(s)}{\sigma(m_H^2)} \times R_{el}^2(m_H\sqrt{s}) \tag{16}$$

The value of the above result is model dependent, and with our model is $\sim 1pb$. This is of the same order as estimated in [24]. However, as also pointed in [24], this should be considered as an over-estimate. The major source of suppression will come from absorptive correction, which can lead to a central production cross section in the femtobarn range. A lot of details have been glossed over in the above derivation, see [3].

Conclusions: We have presented the phenomenological application of the AdS/CFT correspondence to the study of high energy diffractive scattering for QCD. Fits to the HERA DVCS data at small x demonstrates that the strong coupling BPST Graviton/Pomerons [1] does allow for a very good description of diffractive DVCS with few phenomenological parameters, the principal one being the intercept to the bare Pomeron fit to be $j_0 \simeq 1.2$. Encouraged by this, we plan to undertake a fuller study of several closely related diffractive process: total and elastic cross sections, DIS, virtual photon production, vector meson production and double diffraction production of heavy quarks. The goal is that by over constraining the basic AdS building blocks of diffractive scattering, this framework will give a compelling phenomenology prediction for the double diffractive production of the Higgs in the standard model to aid in the analysis of LHC data.

Acknowledgments The work of M.S.C. and M.D. was partially funded by grants PTDC/FIS/ 099293/2008 and CERN/FP/ 116358/2010. *Centro de Física do Porto* is partially funded by FCT. The work of M.D. is supported by the FCT/Marie Curie Welcome II program. The work of R.C.B. was supported by the Department of Energy under contract DE-FG02-91ER40676, and that of C.-IT. by the Department of Energy under contract DE-FG02-91ER40688, Task-A. R.B. and C.-IT. would like to thank the Aspen Center for Physics for its hospitality during the early phase of this work.

References

1. R. C. Brower, J. Polchinski, M. J. Strassler, C. -I Tan, JHEP **0712**, 005 (2007).
2. M. S. Costa and M. Djuric, arXiv:1201.1307 [hep-th].
3. R. C. Brower, M. Djuric and C. -ITan, arXiv:1202.4953 [hep-ph].
4. R. C. Brower, M. Djurić, I. Sarcevic, C. -I Tan, JHEP **1011**, 051 (2010).
5. R. C. Brower, M. Djuric, I. Sarcevic and C. -ITan, arXiv:1106.5681 [hep-ph].
6. L. Cornalba and M. S. Costa, Phys. Rev. D **78** (2008) 096010, `arXiv:0804.1562 [hep-ph]`.
7. J. M. Maldacena, Adv. Theor. Math. Phys. **2**, 231 (1998)
8. E. Witten, Adv. Theor. Math. Phys. **2**, 253-291 (1998).
9. F.E. Low, *Phys. Rev.* D **12**, 163 (1975)
10. S. Nussinov, *Phys. Rev. Lett.* **34**, 1286 (1975)
11. L. Cornalba, M. S. Costa, J. Penedones, Phys. Rev. Lett. **105**, 072003 (2010).
12. J. H. Gao and B. W. Xiao, Phys. Rev. D **81** (2010) 035008, `arXiv:0912.4333 [hep-ph]`.
13. C. Marquet, C. Roiesnel, S. Wallon, JHEP **1004** (2010) 051, `arXiv:1002.0566 [hep-ph]`.
14. R. Nishio and T. Watari, Phys. Rev. D **84** (2011) 075025, `arXiv:1105.2999 [hep-ph]`. R. Nishio and T. Watari, `arXiv:1105.2907 [hep-ph]`.
15. J. Polchinski, M. J. Strassler, JHEP **0305**, 012 (2003).
16. R. C. Brower, M. J. Strassler, C. -I Tan, JHEP **0903**, 050 (2009).
17. R. C. Brower, M. J. Strassler, C. -I Tan, JHEP **0903**, 092 (2009).
18. R. C. Brower, M. Djuric and C-I Tan, JHEP **0907**, 063 (2009).
19. L. Cornalba, M. S. Costa, J. Penedones, R. Schiappa, Nucl. Phys. **B767**, 327-351 (2007).
20. L. Cornalba, M. S. Costa, J. Penedones, JHEP **0806**, 048 (2008).
21. L. Cornalba, M. S. Costa, J. Penedones, JHEP **0709**, 037 (2007).
22. S. Chekanov *et al.* [ZEUS Collaboration], JHEP **0905** (2009) 108, `arXiv:0812.2517 [hep-ex]`.
23. F. D. Aaron *et al.* [H1 Collaboration], Phys. Lett. B **681** (2009) 391, `arXiv:0907.5289 [hep-ex]`.
    F. D. Aaron *et al.* [H1 Collaboration], Phys. Lett. B **659** (2008) 796, `arXiv:0709.4114 [hep-ex]`.
24. D. Kharzeev and E. Levin, Phys. Rev. D **63**, 073004 (2001) [arXiv:hep-ph/0005311].
25. C. P. Herzog, S. Paik, M. J. Strassler and E. G. Thompson, JHEP **0808**, 010 (2008) [arXiv:0806.0181 [hep-th]].

$K_{l3}^{\pm}$ FORM FACTOR MEASUREMENT AT NA48/2

MANUEL HITA-HOCHGESAND
Institut für Physik, Johannes Gutenberg-Universität, Staudingerweg 7,
55099 Mainz, Germany

In 2003/2004 the NA48/2 experiment collected a large sample of $K^{\pm}$ decays. Using a run with minimal trigger conditions, samples of 2.5×10^6 $K_{\mu 3}^{\pm}$ and 4.0×10^6 $K_{e3}^{\pm}$ events were selected. These samples allow precise measurements of the form factors in various parametrizations. This report describes the event selections and the fitting procedure and gives a preliminary result.

1 Introduction

Semileptonic decays of the kaon ($K_{l3}^{\pm}$, $l = \quad, e$) provide the most accurate and theoretically cleanest way to measure the CKM matrix element $|V_{us}|$. In addition, stringent constraints on new physics can be given by testing lepton universality. The hadronic matrix element of these decays is described by two dimensionless form factors $f_{\pm}(t)$, which depend on the squared four-momentum $t = (p_K \quad p_\pi)^2$ transferred to the lepton system. The form factors are important input parameters to the phase space integrals of those decays for the determination of $|V_{us}|$.

The $K_{l3}^{\pm}$ decays are usually described in terms of the vector form factor f_+ and the scalar form factor f_0 defined as [1]:

$$f_0(t) = f_+(t) + \frac{t}{m_k^2 \quad m_\pi^2} f \quad (t). \tag{1}$$

The functions f_+ and f_0 are related to the vector ($1 \quad$) and scalar (0^+) exchange to the lepton system, respectively. Being proportional to the lepton mass squared, the contribution of $f \quad$ can be neglected in K_{e3} decays. By construction, $f_0(0) = f_+(0)$. Since $f_+(0)$ is not directly measurable, it is customary to factor out $f_+(0)$ and to normalize to this quantity all the form factors, so that:

$$\bar{f}_+(t) = \frac{f_+(t)}{f_+(0)}, \ \bar{f}_0(t) = \frac{f_0(t)}{f_+(0)}. \tag{2}$$

To describe the form factors, two different parametrizations are used in this report. Widely known and most common is the Taylor expansion, called quadratic parametrization in the following:

$$\bar{f}_{+,0}(t) = 1 + \lambda'_{+,0} \frac{t}{m_\pi^2} + \frac{1}{2} \lambda''_{+,0} \frac{t^2}{m_\pi^4}, \tag{3}$$

where $\lambda'_{+,0}$ and $\lambda''_{+,0}$ are the slope and the curvature of the form factors, respectively. The disadvantage of this parametrization is related to the strong correlations between the parameters and

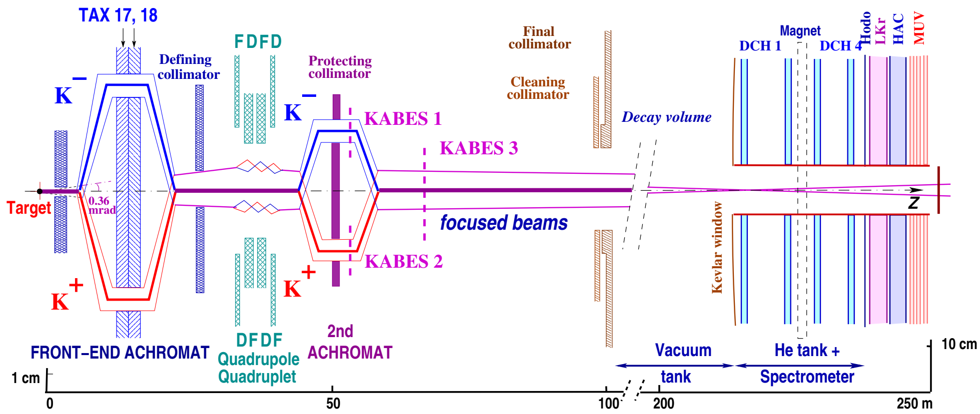

Figure 1: Schematic side view of the NA48/2 beam line, decay volume, and detectors.

the absence of a physical meaning. To reduce the parameters and to add a physical motivation, the pole parametrization is used:

$$\bar{f}_{+,0} = \frac{M_{V,S}^2}{M_{V,S}^2 \quad t}. \tag{4}$$

In this parametrization, dominance of a single resonance is assumed and the corresponding pole masses $M_{V,S}$ are the only free parameters.

2 The NA48/2 Experiment

In the years 2003 and 2004, the NA48/2 experiment collected data from charged kaon decays. Two simultaneous K^+ and K beams were produced by 400 GeV/c primary protons delivered by the CERN SPS. The layout of beams and detectors is shown in Fig. 1. The NA48/2 beamline selected kaons with a momentum range of (60 3) GeV/c. The data used for the $K^\pm_{\mu 3}$ form factor analysis were collected in 2004 during a dedicated run with a special minimum bias trigger setup which required one or more tracks in the magnetic spectrometer and an energy deposit of at least 10 GeV/c in the electromagnetic calorimeter. Also the intensity of the beam was lowered and the momentum spread was reduced.

The main components of the NA48/2 detector were a magnetic spectrometer, composed of four drift chambers and a dipole magnet deflecting the charged particles in the horizontal plane and providing a momentum resolution of 1.4% for 20 GeV/c charged tracks, and a liquid krypton electromagnetic calorimeter (LKr) with an energy resolution of about 1% for 20 GeV photons and electrons. For the selection of $K^\pm_{\mu 3}$ decays, a muon veto system (MUV) was essential to distinguish muons from pions. It consisted of three planes of scintillator strips with alternating horizontal and vertical orientation. Each plane was shielded by a 80 cm thick iron wall. The inefficiency of the system was at the level of one per-mil for muons with momenta greater than 10 GeV/c, and the time resolution was below 1 ns. The NA48 detector is described in detail elsewhere [2].

3 $K^\pm_{l3}$ event selection

The detector can measure only the charged lepton and the two photons from the instant decay of the neutral pion; the neutrino leaves the detector unseen. To select the decay, one track in the magnetic spectrometer and at least two clusters in the electromagnetic calorimeter were required. The track had to be inside the geometrical acceptance of the detector, and needed a good reconstructed decay vertex, proper timing and a momentum $p > 5$ GeV/c in case of electrons. For muons, the momentum needed to be greater than 10 GeV/c to ensure proper efficiency of the MUV system. To identify the track as a muon, an associated hit in the MUV system and a ratio $E/p > 0.2$ was required, where E is the energy deposited in the calorimeter and p is the track momentum. For electrons, a range of $0.95 < E/p < 1.05$ and no associated hit in the MUV system were required. At least two photon clusters were needed to reconstruct the neutral pion. They were required to be well isolated from any track hitting the calorimeter, to have an energy $E_\gamma > 3$ GeV/c, and to be in time with the track in the spectrometer. Finally, a kinematical constraint was applied, requiring the missing mass squared ($K^{\pm}_{l3}$ hypothesis) to satisfy $m^2_{\text{miss}} < (10\ \text{MeV/c}^2)^2$.

For $K^{\pm}_{\mu 3}$, the background from $K^{\pm} \to\ {}^{\pm}\ {}^{0}$ events with a decay in flight of the charged pion was suppressed by using a combined requirement on the invariant mass $m_{\pi^\pm\pi^0}$ (under ${}^{\pm}$ hypothesis) and on the ^{0} transverse momentum. This cut reduces the contamination to 0.5%, but causes a loss of statistics of about 24%. Another source of background is due to $K^{\pm} \to\ {}^{\pm}\ {}^{0}\ {}^{0}$ events with ${}^{\pm}$ decaying in flight and a ^{0} not being reconstructed. The estimated contamination amounts to only about 0.1%, so no specific cut was applied. For $K^{\pm}_{e3}$, only the background from $K^{\pm} \to\ {}^{\pm}\ {}^{0}$ significantly contributes to the signal. A cut in the transverse momentum of the event reduced this background to less than 0.1%, while losing only about 3% of the signal. The selected samples amount to 2.5×10^6 $K^{\pm}_{\mu 3}$ and 4.0×10^6 $K^{\pm}_{e3}$ events.

4 Fitting procedure

To extract the form factors, a two-dimensional fit to the Dalitz plot density was performed. The reconstructed four-momenta of the pion and the lepton were boosted into the kaon rest frame. The calculation of the kaon energy was done by assuming no transverse component of the momentum of the kaon, which leaves only two solutions for the longitudinal component of the neutrino momentum. The solution which fits better to the designed kaon momentum of 60 GeV/c was used. In this way, the energy resolution in the Dalitz plot is improved, especially for high pion energies. The reconstructed Dalitz plot was then corrected for remaining background, detector acceptance and distortions induced by radiative effects. The radiative effects were simulated by using a special Monte Carlo generator developed by the KLOE collaboration [3]. For the fit, the Dalitz plot was subdivided into 5 MeV × 5 MeV cells. Cells which do cross or are outside of the kinematical border were not used in the fit.

Table 1: Preliminary form factor fit results for the quadratic and the pole parametrization. The first error is statistical, the second systematic. For the combined result, statistical and systematic uncertainties were combined.

Quadratic $(\times 10\ ^{3})$	λ'_+	λ''_+	λ_0
$K^{\pm}_{\mu 3}$	26.3 3.0 2.2	1.2 1.1 1.1	15.7 1.4 1.0
$K^{\pm}_{e3}$	27.2 0.7 1.1	0.7 0.3 0.4	
combined	27.0 1.1	0.8 0.5	16.2 1.0
Pole (MeV/c^2)	m_V		m_S
$K^{\pm}_{\mu 3}$	873 8 9		1183 31 16
$K^{\pm}_{e3}$	879 3 7		
combined	877 6		1176 31

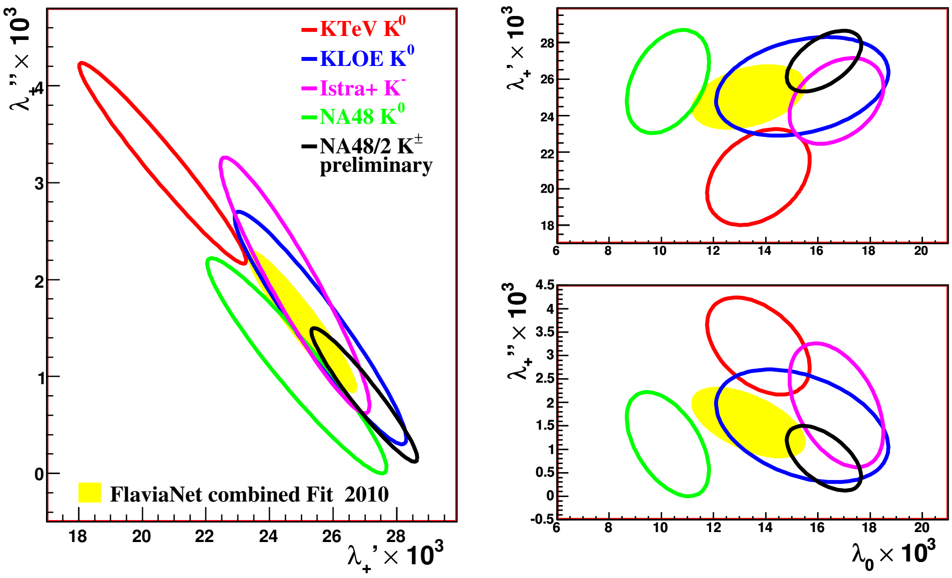

Figure 2: Combined quadratic fit results for K_{l3} decays. The ellipses are 68% confidence level contours. For comparison, the combined fit from the FlaviaNet kaon working group is shown[1].

5 Preliminary result

The fit results for the quadratic and the pole parametrization are listed in Table 1. The systematic uncertainty was evaluated by changing the cuts defining the vertex quality and the geometrical acceptance by small amounts. In addition, we applied variations to the resolutions of pion and muon energies in the kaon center of mass system, we varied the $\to$ background and took into account the differences in the results of two independent analyses that were performed in parallel.

For comparison, the combined $K^{\pm}_{l3}$ quadratic fit results as reported by recent experiments is shown in Fig. 2 [1]. The 68% confidence level contours are displayed for both neutral (KLOE, KTeV and NA48) and charged K_{l3} decays (ISTRA+ studied K only). The preliminary NA48/2 results presented here are the first high precision measurements done with both K^+ and K mesons. The form factors are in good agreement with most measurements done by the other experiments and compatible with the combined fit done by FlaviaNet [1].

6 Future perspectives for form factors at NA62

Using the beam line and detector of the NA48/2 experiment, the new NA62 collaboration collected data in 2007 for the measurement of $R_K = \Gamma(K_{e2})/\Gamma(K_{\mu 2})$ and made tests for the future NA62 $K^+ \to \ {}^+\nu\bar{\nu}$ experiment. The collected data contain K^+_{e3} and $K^+_{\mu 3}$ samples of $\simeq 40$ and 20×10^6 events, respectively. A special K_L run was also taken: it provides K^0_{e3} and $K^0_{\mu 3}$ samples of about 4×10^6 events. With these statistics, NA62 is able to realize high precision measurements of the form factors of all K_{l3} channels, providing important inputs to further reduce the uncertainty on $|V_{us}|$.

References

1. M. Antonelli et al., *Eur. Phys. J.* C **69**, 399 (2010).
2. V. Fanti et. al. [NA48 Collaboration], *Nucl. Instrum. Methods* A **574**, 433 (2007).
3. C. Gatti, *Eur. Phys. J.* C **45**, 417 (2006).

HADRON PHYSICS AT KLOE AND KLOE-2

C. Di Donato on Behalf of KLOE and KLOE-2 Collaborations
I.N.F.N., Complesso Universitario M.S.A. ed. 6,
Via Cintia 80126-Napoli, Italy

KLOE data allow to study many interesting processes related to light mesons. Several item have been investigated, among them we present the recently published search for the U boson produced with η meson and the last results on the dynamics of the $\eta \to \pi^+\pi^-\gamma$ decay. The KLOE-2 project aims to extend the KLOE program with detector upgrades and increased statistics: we describe the status of the art.

1 KLOE and DAΦNE

The e^+e^- collider DAΦNE, designed to operate at the center of mass energy $\sqrt{s} \simeq 1.02$ GeV, the ϕ meson mass, has delivered to the KLOE experiment an integrated luminosity of about $2.5fb^{-1}$ on peak of the ϕ meson and also about $240pb^{-1}$ at $\sqrt{s} \simeq 1$ GeV. The KLOE detector consists of a large volume cylindrical drift chamber [1] (DC), 3.3 m length and 2 m radius, surrounded by a calorimeter [2] (EMC) made of lead and scintillating fibers. A superconducting coil produces an axial field $B = 0.52$ T. In the DC charged particle momenta are reconstructed with resolution $\sigma_p/p \simeq 0.4\%$, while in the EMC energy clusters are reconstructed grouping calorimeter cells close in space and in time with energy and time resolution of $\sigma_E/E = 5.7\%/\sqrt{E(GeV)}$ and $\sigma_t = 57ps/\sqrt{E(GeV)} \oplus 100$ ps.

1.1 U Boson Search: $\phi \to \eta e^+e^-/\eta U$

In recent years several unexpected astrophysical observations have failed to find a common interpretation in terms of standard astrophysical or particle sources. All these unexpected observations [a] can be interpreted assuming the existence of a light hidden sector interacting with Standard Model particles through the mixing (ϵ) between a new gauge vector boson U, with mass lighter than O(GeV), and the photon. The U boson can be produced at e^+e^- colliders via different processes [3], we present the analysis of the process $\phi \to \eta U$, where the η meson is tagged by the $\eta \to \pi^+\pi^-\pi^0$ channel. The Dalitz decay $\phi \to \eta l^+l^-$, having the same signature, is an irreducible background for the U boson search. The SND [4] and CMD-2 [5] collaborations measured the branching fraction of $BR(\phi \to \eta e^+e^-) = O(10^{-4})$, which corresponds to a cross section of $\sigma(\phi \to \eta l^+l^-) \sim 0.7$ nb. For the signal the expected cross section is $\sigma(\phi \to \eta U) \sim 40$ fb, in the hypothesis of a mixing $\epsilon = 10^{-3}$ and a $\phi\eta\gamma^*$ transition form factor $|F_{\phi\eta}(m_U^2)|^2 = 1$. Even though the ratio between the overall cross section of the $\phi \to \eta U$ and $\phi \to \eta l^+l^-$ is not favorable to the signal, the di-lepton invariant mass should be different allowing to test the kinetic mixing parameter ϵ. We searched for the U boson in the e^+e^- final state, because the

[a] For an exhaustive list of references see the KLOE-2 paper [3]

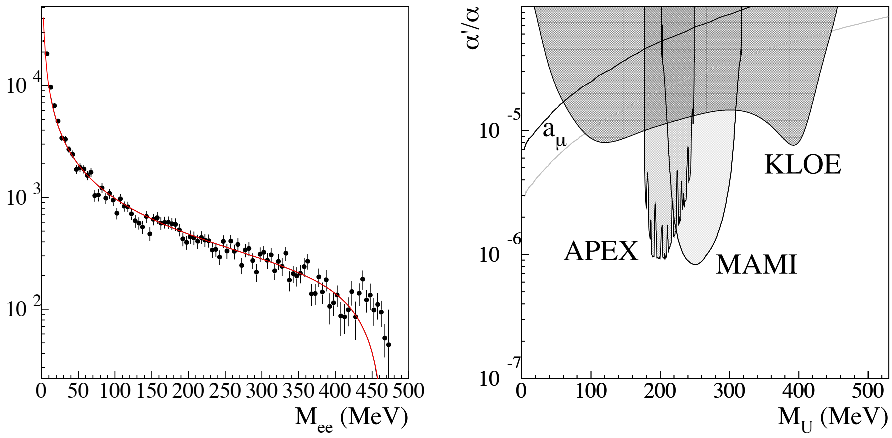

Figure 1: Left: Fit to the corrected M_{ee} spectrum for the Dalitz decays $\phi \to \eta e^+e^-$; Right: Exclusion plot at 90% C.L. for the parameter $\alpha'/\alpha = \epsilon^2$, compared with existing limits in our region of interest.

channel $U \to e^+e^-$ allow to search the U boson in a wider mass range and the $e^\pm$ are easily identified using TOF technique.
The M_{ee} spectrum has been studied using an integrated luminosity of 1.5 fb^{-1} of ϕ decays: about 14,000 $\phi \to \eta e^+e^-$, $\eta \to \pi^+\pi^-\pi^0$ candidates are present in the analyzed data set, with a negligible background contamination.

The background shape is extracted directly from our data. A fit is performed to the M_{ee} distribution, after a bin-by-bin subtraction of $\phi \to \eta\gamma$ background and efficiency correction, using the following parametrization as from Vector Meson Dominance (VMD) model [6]

$$\frac{d\Gamma(\phi \to \eta e^+e^-)}{dq^2} = \frac{\alpha}{3\pi}\frac{|F_{\phi\eta}(q^2)|^2}{q^2}\sqrt{1-\frac{4m^2}{q^2}}\left(1+\frac{2m^2}{q^2}\right)\lambda^{3/2}\left(m_\phi^2, m_\eta^2, m_U^2\right) \tag{1}$$

with $q = M_{ee}$ and the transition form factor described by:

$$F_{\phi\eta}(q^2) = \frac{1}{1-q^2/\Lambda^2} \tag{2}$$

Free parameters of the fit are Λ and an overall normalization factor. A good description of the M_{ee} shape is obtained except at the high end of the spectrum see fig.(1.left), because of the contamination of a residual background from multi-pion events. The $\phi \to \eta U$ Monte Carlo signal has been produced according to Reece-Wang model [7], with a flat distribution of the U mass, M_U. The sample has been used to evaluate the resolution on the e^+e^- invariant mass as a function of M_U: resolution is ~ 2 MeV for $M_U < 350$ MeV and then improves to 1 MeV for higher values. The upper limit on $\phi \to \eta U$ as a function of M_U has been reported in terms of the kinetic mixing parameter $\epsilon^2 = \alpha'/\alpha$, where α' is the coupling of U boson to electrons and α is the fine structure constant. We include the opening $U \to \mu^+\mu^-$ threshold, in the hypothesis that the U boson decay only to lepton pairs and assuming equal coupling to e^+e^- and $\mu^+\mu^-$. The smoothed exclusion plot at 90% C.L. on α'/α, see fig.(1.right), is compared with existing limits from the muon anomalous magnetic moment a_μ and from recent measurement of MAMI [8] and APEX [9]. The gray line is where the U boson parameters should lay to account for the observed discrepancy between measured and calculated a_μ values. Our result improves existing limits in a wide mass range, resulting in an U.L. on $\alpha'/\alpha \leq 2 \times 10^{-5}$ @ 90% C.L. for $50 < M_U < 420$ MeV. Our result excludes that the existing a_μ discrepancy is due to U boson with mass ranging between 90 and 450 MeV. Preliminary study for $U-$boson search looking at

$\eta \to \gamma\gamma$ and $\eta \to 3\pi^0$ looks promising and they should in principle allow to improve U.L. by a factor 2.

1.2 Light Mesons: $\eta \to \pi^+\pi^-\gamma$

The decays $\eta \to \pi^+\pi^-\gamma$ and $\eta' \to \pi^+\pi^-\gamma$ are expected to get contribution from the anomaly accounted for by the Wess Zumino Witten (WZW) term into the ChPT Lagrangian [10]. Those anomalous processes are referred to as box anomalies which proceed through a vector meson resonant contribution, described by VMD. According to effective theory [10] the contribution of the direct term should be present together with VMD. In case of $\eta \to \pi^+\pi^-\gamma$ the ρ contribution is not dominant, this makes the partial width sensitive to the presence of the direct term. Recently CLEO [12] has measured the ratio $R_\eta = \Gamma(\eta \to \pi^+\pi^-\gamma)/\Gamma(\eta \to \pi^+\pi^-\pi^0) = 0.175 \pm 0.007_{stat} \pm 0.006_{syst}$, which differs by more than 3σ from the average result [15] of previous measurements [13,14], $R_\eta = 0.207 \pm 0.004$. We present a preliminary measurement with the highest statistics and the smallest systematic error ever achieved.

The final state under study is $\pi^+\pi^-\gamma\gamma$, since at KLOE, the η mesons are produced together with a monochromatic recoil photon ($E_\gamma = 363$ MeV) through the radiative decay $\phi \to \eta\gamma$. In the considered data sample there are about $\simeq 25 \times 10^6$ η's. The main background comes from $\phi \to \pi^+\pi^-\pi^0, \pi^0 \to \gamma\gamma$ decaying to the same final state. Other backgrounds are $\phi \to \eta\gamma \to \pi^+\pi^-\pi^0 \to \pi^+\pi^-3\gamma$ with one photon lost, and $\phi \to \eta\gamma, \eta \to e^+e^-\gamma$ when both electrons are mis-identified as pions. The process $\phi \to \eta\gamma$ with $\eta \to \pi^+\pi^-\pi^0$ represents a good control sample, due to the similar topology. Moreover the ratio $\Gamma(\eta \to \pi^+\pi^-\gamma)/\Gamma(\eta \to \pi^+\pi^-\pi^0)$ is not affected by the uncertainties on the luminosity, the $\phi \to \eta\gamma$ partial width and the ϕ production cross section cancel in the ratio. We use the same preselection as for the $\eta \to \pi^+\pi^-\gamma$ signal. Concerning the control sample we select $N(\eta \to \pi^+\pi^-\pi^0) = 1190 \cdot 10^3$, with a selection efficiency of $\varepsilon = 0.2277 \pm 0.0002$ and a background contamination of 0.65%; concerning the signal we select $N(\eta \to \pi^+\pi^-\gamma) = 204950 \pm 450$ with $\varepsilon = 0.2131 \pm 0.0004$ and a background contamination of 10%. Combining our results we obtain the ratio:

$$R_\eta = \frac{\Gamma(\eta \to \pi^+\pi^-\gamma)}{\Gamma(\eta \to \pi^+\pi^-\pi^0)} = 0.1856 \pm 0.0005_{stat} \pm 0.0028_{syst} \tag{3}$$

Our measurement is in agreement with the most recent result from CLEO [12], $R_\eta = 0.175 \pm 0.007_{stat} \pm 0.006_{syst}$. Combining our measurement with the world average value [11] $\Gamma(\eta \to \pi^+\pi^-\pi^0) = (295 \pm 16)$ eV, we get $\Gamma(\eta \to \pi^+\pi^-\gamma) = (55 \pm 3)$ eV, which is in agreement with the value expected taking into account the direct term [10], providing a strong evidence in favor of the box anomaly.

The $M_{\pi^+\pi^-}$ dependence of decay width has been parametrized in different approaches, in which VMD has been implemented in effective Lagrangians [10,16]. Recently a model independent method, based on ChPT and dispersive analysis, has been developed [17]. In this approach, the relative strength between tree level and resonance contribution are not fixed. The function proposed to describe the partial width as function of $s_{\pi\pi} = m^2_{\pi\pi}$ is the following:

$$\frac{d\Gamma(\eta \to \pi^+\pi^-\gamma)}{ds_{\pi\pi}} = \left|AP(s_{\pi\pi})F(s_{\pi\pi})\right|^2 \Gamma_0(s_{\pi\pi}) \tag{4}$$

where A is a normalization factor; $\Gamma_0(s_{\pi\pi}) = \frac{1}{3 \cdot 2^{11} \cdot \pi^3 m_\eta^3}\left(m_\eta^2 - s_{\pi\pi}\right)^3 s_{\pi\pi}\sigma(s_{\pi\pi})^3$ with $\sigma(s_{\pi\pi}) = \sqrt{1 - 4m_\pi^2/s_{\pi\pi}}$; $F_V(s_{\pi\pi})$ is the pion vector form factor, the function $P(s_{\pi\pi}) = 1 + \alpha s_{\pi\pi}$ is reaction specific. For more details see Stoll's paper [17].

The α parameter was measured also by the WASA@COSY collaboration [18]: $\alpha = (1.89 \pm 0.25_{stat} \pm 0.59_{syst} \pm 0.02_{th})$ GeV^{-2}. Fig.2 shows the observed $M_{\pi^+\pi^-}$ spectrum, background subtracted, compared with the theoretical prediction of eq.(4) with the value $\alpha = (1.31 \pm 0.08_{stat} \pm 0.40_{syst} \pm 0.02_{th})$ coming as output of the fit to the $M_{\pi\pi}$ shape, corrected for acceptance and smearing.

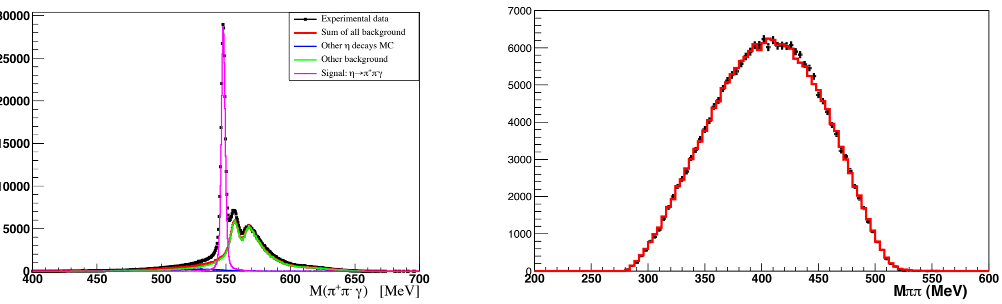

Figure 2: Left: The $\pi^+\pi^-\gamma_\eta$ invariant mass distribution: Data-MC comparison. Dots are data, Magenta is MC signal $\eta \to \pi^+\pi^-\gamma$, Red is all MC background contribution; Right:Measured spectrum $m_{\pi\pi}$ (dots); histogram is the prediction from eq.(4) with α as from the output of the fit, corrected for acceptance and experimental resolution

1.3 KLOE-2

High statistic samples of light mesons produced at KLOE allowed to perform precision measurement and to look for very rare decays. A new DAΦNE interaction region, with large beam crossing angle and sextupoles for crab waist, improved the performance of the collider: a factor 3 in the luminosity has been gained. Minimal detector upgrade for first KLOE-2 run are already available as taggers to detect momentum of leptons in $e^+e^- \to e^+e^-\gamma^*\gamma^* \to e^+e^-X$. Work is in progress to insert an Inner Tracker, a 4 layers of cylindrical triple GEM, and new calorimeters around the beam pipe to increase acceptance for γ's from interaction point. Nowadays a new data taking at KLOE-2 is waiting for stable run conditions.

References

1. M. Adinolfi *et al.*, *Nucl. Instrum. Methods* A **488**, 51 (2002)
2. M. Adinolfi *et al.*, *Nucl. Instrum. Methods* A **482**, 364 (2002)
3. F. Archilli *et al.*, *Phys. Lett.* B **706**, 251 (2002)
4. M. N. Achasov *et al.*, *Phys. Lett.* B **504**, 275 (2001)
5. R. R. Akhmetshin *et al.*, *Phys. Lett.* B **501**, 191 (2001)
6. L. G. Landsberg, PRep **128**, 301 (1985)
7. M. Reece, L. T. Wang,JHEP **0907**, 051 (2009)
8. H. Merkel,*et al.*, *Phys. Rev. Lett.* **106**, 251802 (2011)
9. S. Abrahamyan,*et al.*, *Phys. Rev. Lett.* **107**, 191804 (2011)
10. M. Benayoun *et al.*, *E. Phys. Journal* C **31**, 525 (2003)
11. K. Nakamura et al. (PDG), Review of Particle Physics, *J. Phys.* G **37**, 075021 (2010)
12. A. Lopez et al., *Phys. Rev. Lett.* **99**, 122001 (2007)
13. M. Gormley et al., *Phys. Rev.* D **2**, 501 (1970)
14. J. C. Layter et al., *Phys. Rev.* D **7**, 2565 (1973)
15. W.-M. Yao et al. (PDG), Review of Particle Physics, *J. Phys.* G **33**, 1 (2006)
16. C. Picciotto, *Phys. Rev.* D **45**, 1569 (1992)
17. Stollenwer, Hanhart, Kupsc, Meisner and Wirzba, *Phys. Lett.* B **707**, 184 (2012)
18. WASA-at-COSY Collaboration: P. Adlarson et al., *Phys. Lett.* B **707**, 243 (2012)

Status of the proton radius puzzle

Richard J. Hill
Enrico Fermi Institute and Department of Physics
The University of Chicago, Chicago, Illinois, 60637, USA

This talk reviews the status of the proton radius puzzle, i.e., the discrepancy between inferred values for the proton charge radius. The focus is on a discussion of the uncertainties in extrapolations of electron scattering data, and of the uncertainties due to proton structure corrections in the muonic hydrogen bound state.

1 Introduction

In 2010 the CREMA collaboration reported a first measurement of the Lamb shift in muonic hydrogen [1]. Interpreted as a measurement of the proton charge radius, the result differs significantly from extractions based on electronic hydrogen, and extractions from electron-proton scattering, as summarized in Fig. 1. This $\sim 5\sigma$ anomaly is perplexing. It is an obstacle to precise determination of the Rydberg constant R_∞, [a] and it brings into question the reliability of electron scattering data.[b] It has also led to speculations on new forces acting in the muon-proton system [21], inadequate treatment of proton charge density correlations [22], and modifications of offshell photon vertices [23].

This talk begins by discussing effective field theory formalism for proton structure effects in atomic bound states. Dispersive analysis to constrain electron scattering determinations of coefficients in the effective theory is then described, and the status of the proton radius puzzle is summarized.

2 Proton structure in NRQED

Non-relativistic QED (NRQED) [24] is a field theory describing the interactions of photons and nonrelativistic matter. The NRQED lagrangian is constructed to yield predictions valid to any fixed order in small parameters α and $|\boldsymbol{q}|/M$, where $|\boldsymbol{q}|$ denotes a typical bound state momentum, and M is a mass scale for the nonrelativistic particle. NRQED provides a rigorous framework to study the effects of proton structure, avoiding problems of double counting in bound state energy computations [25]; eliminating difficulties of interpretation for the polarizability of a strongly interacting particle [26]; and providing trivial derivations of universal properties, such as the low

[a] "Data from muonic hydrogen are so inconsistent with the other data that they have not been included in the determination of r_p and thus do not have an influence on R_∞" [19].

[b] Until the difference between the e p and p values is understood, it does not make much sense to average all the values together. For the present, we stick with the less precise (and provisionally suspect) CODATA 2006 value. It is up to workers in this field to solve this puzzle [20].

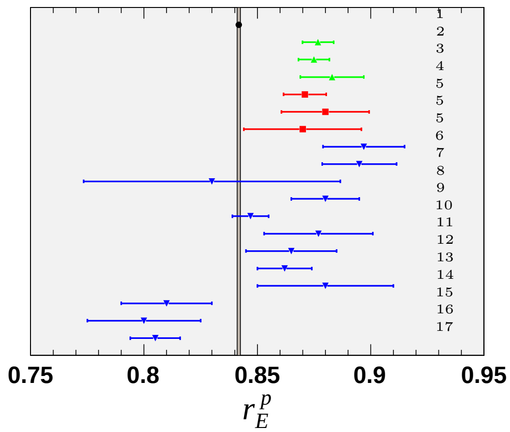

Figure 1: Values of the proton charge radius (in fm) extracted from muonic hydrogen (circle and vertical band); electronic hydrogen (green triangles); electron scattering employing the z expansion (red squares); and previous electron scattering extractions (blue downward triangles).

	Ref. [1]	Ref. [28]	
vertex correction	-0.0096 meV	-0.0108 meV	mismatch in r_E^p definition
two photon correction	0.051 meV	$\sim 0.05 \pm 0.05$ meV	model dependence
recoil finite size	0.013 meV	0	double counting
total	210.0011(45) - 5.2262 r^2 meV	209.987(50) - 5.2262 r^2 meV	
extracted radius	0.8421(6) fm	0.841(6) fm	

Table 1: Comparison between this and previous works for proton structure corrections to the $2P-2S$ Lamb shift in muonic hydrogen, in meV.

energy theorems of Compton scattering [27]. Neglecting the pure photon sector, the NRQED lagrangian has the expansion,

$$\mathcal{L}_e = \psi_e^\dagger \Big\{ iD_t + \frac{\boldsymbol{D}^2}{2m_e} + \frac{\boldsymbol{D}^4}{8m_e^3} + c_F e \frac{\boldsymbol{\sigma}\cdot\boldsymbol{B}}{2m_e} + c_D e \frac{[\boldsymbol{\partial}\cdot\boldsymbol{E}]}{8m_e^2} + ic_S e \frac{\boldsymbol{\sigma}\cdot(\boldsymbol{D}\times\boldsymbol{E}-\boldsymbol{E}\times\boldsymbol{D})}{8m_e^2}$$
$$+ c_{W1} e \frac{\{\boldsymbol{D}^2, \boldsymbol{\sigma}\cdot\boldsymbol{B}\}}{8m_e^3} - c_{W2} e \frac{D^i \boldsymbol{\sigma}\cdot\boldsymbol{B} D^i}{4m_e^3} + c_{p'p} e \frac{\boldsymbol{\sigma}\cdot\boldsymbol{D}\boldsymbol{B}\cdot\boldsymbol{D} + \boldsymbol{D}\cdot\boldsymbol{B}\boldsymbol{\sigma}\cdot\boldsymbol{D}}{8m_e^3} + ic_M e \frac{\{\boldsymbol{D}^i, [\boldsymbol{\partial}\times\boldsymbol{B}]^i\}}{8m_e^3}$$
$$+ c_{A1} e^2 \frac{\boldsymbol{B}^2 - \boldsymbol{E}^2}{8m_e^3} - c_{A2} e^2 \frac{\boldsymbol{E}^2}{16m_e^3} + \dots \Big\} \psi_e + d_1 \frac{\psi_p^\dagger \boldsymbol{\sigma} \psi_p \cdot \psi_e^\dagger \boldsymbol{\sigma} \psi_e}{m_e m_p} + d_2 \frac{\psi_p^\dagger \psi_p \psi_e^\dagger \psi_e}{m_e m_p} + \dots . \quad (1)$$

Here ψ_e is a two-component spinor representing the nonrelativistic electron field, $\boldsymbol{\sigma}$ is the Pauli spin matrix, D_t and $\boldsymbol{D}$ are covariant derivatives and $\boldsymbol{E}$, $\boldsymbol{B}$ are the electric and magnetic fields. The proton charge radius is defined by the matching condition for c_D, while structure-dependent contributions to two-photon exchange enter the contact interactions d_1,d_2.

Once a regularization scheme for the field theory is specified, and coefficients $c_D, d_2, \dots$ are determined, spectroscopic intervals can be computed. The bound state computation is not essentially different for a point particle nucleus (e.g. a muon-electron bound state) versus a composite nucleus (e.g. a proton-electron bound state). Some discrepancies between the tabulation of Ref. [1] are noted in Table 1. For details, see Ref. [28].

3 Electron scattering

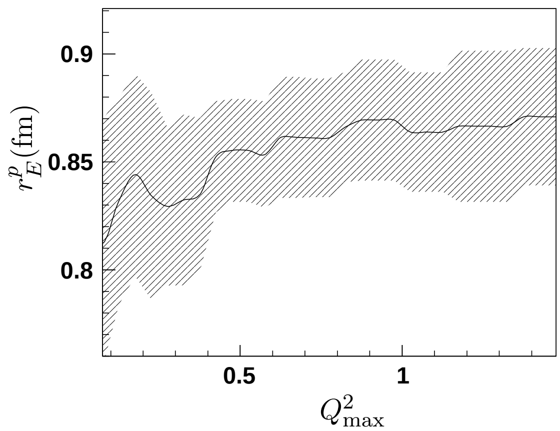

Figure 2: Variation of the fitted proton charge radius as a function of maximum Q^2. Fits of the proton data were performed with $k_{\rm max} = 10$, $\phi = 1$, $t_0 = 0$, $|a_k| \le 10$. Data from Ref. [33].

Electron scattering is a promising method to determine structure-dependent constants in the NRQED lagrangian. Let us consider the electromagnetic form factors satisfying $F_1(0) = 1$, $F_2(0) = a_p$, and

$$F_1'(0) = \frac{1}{6}(r_E^p)^2 - \frac{a_p}{4m_p^2} + \frac{Z^2\alpha}{3\pi m_p^2}\log\frac{m_p}{\lambda}\,, \quad F_2'(0) = \frac{1}{6}\left[(1+a_p)(r_M^p)^2 - (r_E^p)^2\right] + \frac{a_p}{4m_p^2}\,, \qquad (2)$$

where λ is a photon mass introduced for convenience. When extracting the form factor slope we must account for the unknown form factor shape while retaining predictive power. This problem can be addressed using constraints from analyticity [32], both to constrain the functional form of $F_i(q^2)$, and to allow systematic inclusion of electron-neutron scattering data and $\pi\pi \to N\bar{N}$ data [5]. Figure 2 illustrates the radius extraction from a representative dataset [33], as a function of the maximum momentum transfer included in the fit. The corresponding radius, for $Q^2_{\rm max} = 0.5\,{\rm GeV}^2$, is displayed in Fig. 1, together with more precise determinations including neutron and $\pi\pi$ data. For details see Ref. [5].

4 Outlook

			Ref. [1]	Ref. [28]
H	CODATA06	0.876(8)	4.2σ	3.5σ
ep	Sick 2005	0.895(18)	2.9σ	2.8σ
	JLab 2011	0.875(10)	3.3σ	2.9σ
	Mainz 2011	0.879(8)	4.6σ	3.8σ
H, ep	CODATA10	0.8775(51)	6.9σ	4.6σ
ep	this work	0.870(26)	1.1σ	1.1σ
ep, en	this work	0.880(20)	1.9σ	1.9σ
ep, en, $\pi\pi \to N\bar{N}$	this work	0.871(10)	2.9σ	2.6σ

Table 2: Discrepancy between the proton charge radius from muonic hydrogen and from other determinations.

The proton radius remains a puzzle. Table 2 displays the discrepancy between the proton charge radius from muonic hydrogen, and other determinations. The final two columns of the table correspond to the reference values in the final row of Table 1. Future work should provide a more robust estimation of uncertainties due to radiative corrections in the electron scattering determination. New measurements in electronic hydrogen are being undertaken to assess the possibility of systematic effects in the Rydberg and proton radius determinations. Proposed muon-proton scattering measurements could provide an independent determination of the proton radius, and directly measure the poorly constrained contact interaction parameterized by d_2.

Acknowledgments

The work reported here summarizes Refs. [5,28], done in collaboration with Gil Paz. Research supported by NSF Grant 0855039.

References

1. R. Pohl *et al.*, Nature **466**, 213 (2010).
2. P. J. Mohr, B. N. Taylor and D. B. Newell, Rev. Mod. Phys. **80**, 633 (2008).
3. P. J. Mohr and B. N. Taylor, Rev. Mod. Phys. **77**, 1 (2005).
4. K. Melnikov and T. van Ritbergen, Phys. Rev. Lett. **84**, 1673 (2000).
5. R. J. Hill and G. Paz, Phys. Rev. D **82**, 113005 (2010).
6. P. G. Blunden and I. Sick, Phys. Rev. C **72**, 057601 (2005).
7. I. Sick, Phys. Lett. B **576**, 62 (2003).
8. I. M. Gough Eschrich *et al.* [SELEX Collaboration], Phys. Lett. B **522**, 233 (2001).
9. R. Rosenfelder, Phys. Lett. B **479**, 381 (2000).
10. P. Mergell, U. G. Meissner and D. Drechsel, Nucl. Phys. A **596**, 367 (1996).
11. C. W. Wong, Int. J. Mod. Phys. E **3**, 821 (1994).
12. M. McCord *et al.*, Nucl. Instrum. Meth. B **56/57**, 496 (1991).
13. G. G. Simon, C. Schmitt, F. Borkowski and V. H. Walther, Nucl. Phys. A **333**, 381 (1980).
14. F. Borkowski, P. Peuser, G. G. Simon, V. H. Walther and R. D. Wendling, Nucl. Phys. A **222**, 269 (1974).
15. Yu. K. Akimov *et al.*, Sov. Phys. **JETP35**, 651 (1972).
16. D. Frerejacque, D. Benaksas and D. J. Drickey, Phys. Rev. **141**, 1308 (1966).
17. L. N. Hand, Rev. Mod. Phys. **35**, 335 (1963).
18. V. Lyubushkin *et al.* [NOMAD Collaboration], Eur. Phys. J. C **63**, 355 (2009).
19. P. J. Mohr, B. N. Taylor and D. B. Newell, arXiv:1203.5425 [physics.atom-ph]].
20. K. Nakamura *et al.* [Particle Data Group Collaboration], J. Phys. G G **37**, 075021 (2010).
21. V. Barger, C. -W. Chiang, W. -Y. Keung and D. Marfatia, Phys. Rev. Lett. **106**, 153001 (2011). D. Tucker-Smith and I. Yavin, Phys. Rev. D **83**, 101702 (2011). B. Batell, D. McKeen and M. Pospelov, Phys. Rev. Lett. **107**, 011803 (2011).
22. A. De Rujula, Phys. Lett. B **693**, 555 (2010). A. De Rujula, Phys. Lett. B **697**, 26 (2011). I. C. Cloet and G. A. Miller, Phys. Rev. C **83**, 012201 (2011).
23. G. A. Miller, A. W. Thomas, J. D. Carroll and J. Rafelski, Phys.Rev. A**84**, 020101 (2011).
24. W. E. Caswell and G. P. Lepage, Phys. Lett. B **167**, 437 (1986).
25. U. D. Jentschura, Eur. Phys. J. D **61**, 7 (2011).
26. A. I. Lvov, Int. J. Mod. Phys. A **8**, 5267 (1993).
27. S. Ragusa, Phys. Rev. D **47**, 3757 (1993).
28. R. J. Hill and G. Paz, Phys. Rev. Lett. **107**, 160402 (2011).
29. K. Pachucki, Phys. Rev. A **60**, 3593 (1999).
30. E. Borie, Phys. Rev. A **71**, 032508 (2005).
31. C. E. Carlson and M. Vanderhaeghen, Phys. Rev. A **84**, 020102 (2011).
32. For a review and references see: R. J. Hill, [arXiv:hep-ph/0606023].
33. J. Arrington, W. Melnitchouk and J. A. Tjon, Phys. Rev. C **76**, 035205 (2007).

6.
From Space

STUDIES OF HADRONIC INTERACTIONS AT ULTRA-HIGH ENERGIES WITH THE PIERRE AUGER OBSERVATORY

DIEGO GARCIA-GAMEZ[1] FOR THE PIERRE AUGER COLLABORATION[2]
[1]*Laboratoire de l'Accélérateur linéaire (LAL), Université Paris 11, CNRS-IN2P3, Orsay, France*
[2]*Observatorio Pierre Auger, Av. San Martin Norte 304, 5613 Malargüe, Argentina*
(Full author list: http://www.auger.org/archive/authors_2012_01.html)

The hybrid design of the Pierre Auger Observatory allows one to measure the longitudinal profile of ultra-high energy air showers and the depth at which the shower reaches its maximum size, $X_{\rm max}$. It also provides a record of the shower front by sampling the secondary particles at ground level. These measurements give a variety of independent experimental observables with information about the nature of the primary particle and its interactions. In this contribution we present a comparison of our mass sensitive observables with the prediction of different hadronic interaction models. Furthermore we show how the analysis of the tail of the distribution of $X_{\rm max}$ allows one to estimate the proton-air cross-section for particle production at center-of-mass energies of 57 TeV.

1 Introduction

The Pierre Auger Observatory is the largest cosmic ray observatory ever built. It was conceived to study the properties of ultra-high energy cosmic rays (UHECR). It is a hybrid detector that combines both surface and fluorescence detectors at the same site [1]. The Surface Detector (SD) [2] consists of a triangular grid of over 1600 water Cherenkov detectors spaced 1.5 km and covering a surface of about 3000 km^2. The purpose of these detectors is to measure the density of particles at the ground. The Fluorescence Detector (FD) [3,4] consists of 27 telescopes placed at four sites surrounding the SD and looking to the atmosphere. Their aim is to collect the UV light track emitted by the de-excitation of air molecules. The detection of this radiation is only possible during dark nights without moon. That results in a small duty cycle of about 13 %, which contrasts with the nearly 100 % of the SD. As the atmosphere is where extensive air showers (EAS) develop, a good knowledge of its state is of great importance for an experiment like the Pierre Auger Observatory. In any FD measurement, the atmosphere is the medium where emission and transmission of recorded light occur. The particle density at ground sampled by the SD, particularly the electromagnetic component, is also sensitive to the amount of matter traversed. Hence, fluctuations in the atmospheric conditions have an effect over both the longitudinal [5] and the lateral [6] developments of the showers. Different monitoring devices are placed at the observatory site to record atmospheric conditions. This is crucial to be able to understand the functioning of the detector and correct the different measurements.
The goal of any UHECR detector is to measure the development of EAS. This development is extremely sensitive to the hadronic interaction properties at ultra-high energies. Although the results coming from LHC will be of great help, the range of energies that governs the features of these showers is not accessible by any current accelerator. Therefore the different models are

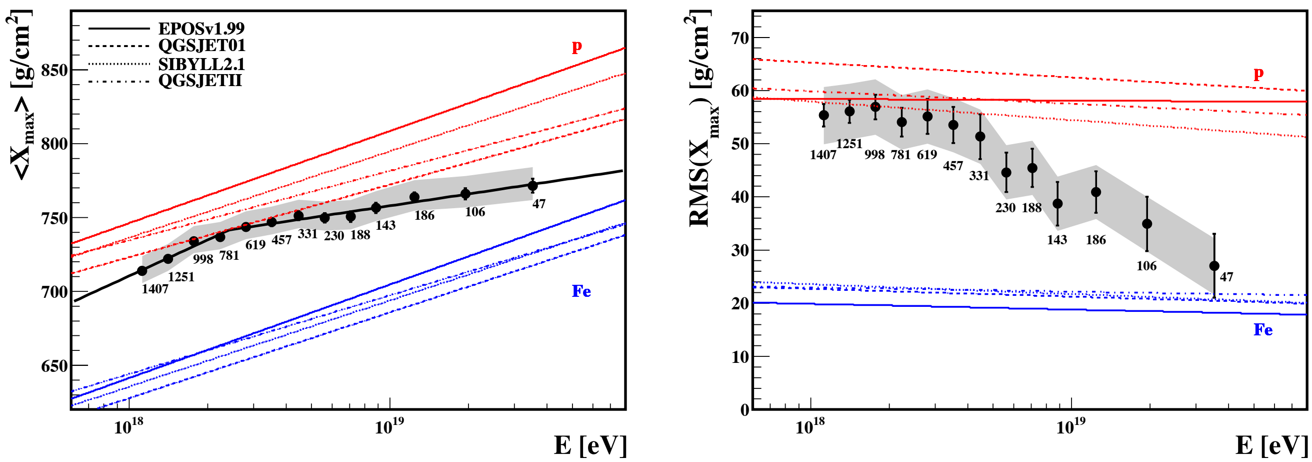

Figure 1: $\langle X_{\max} \rangle$ (left) and RMS($X_{\max}$) (right) as a function of the energy. The number of real data events in each energy bin is indicated. The predictions for proton and iron, following different hadronic models, are shown as well. The shaded region represents the systematic uncertainties.

built over different extrapolations and approximations [7,8,9]. Differences in multi-particle production models are directly reflected in shower observables like $X_{\max}$ and the number of muons at ground level. Other hadronic interaction features like the particle production cross-section, elasticity or charge-ratio (fraction of particles going into the electromagnetic (EM) cascade) have also their own impact on the different shower observables. They have been studied in detail in [10]. This interconnection allows the study of hadronic interactions at ultra-high energies using cosmic ray data. The main problem for this kind of analysis is that the cosmic ray composition is unknown at these energies. Furthermore, the mass of the primary particles can only be determined by comparing air shower observables with simulations. All this, along with their origin and mechanisms of acceleration, is the complex cosmic ray puzzle that experiments like the Pierre Auger Observatory try to solve. In Sec. 2 we describe the main observables and analysis carried out by the Auger collaboration to infer the mass of the primary particles measured with both the FD and the SD. The measurement of the proton-air cross-section from the tail of the $X_{\max}$ distribution is discussed in Sec. 3. We finish this document (in Sec. 4) with different studies that highlight the muon deficit found in simulations when compared with real data.

2 Measurements of the Longitudinal Shower Development

2.1 Fluorescence Detector Measurements

With the fluorescence detector of the Pierre Auger Observatory it is possible to measure the longitudinal development of cosmic rays in the atmosphere. The preferred observable used for composition studies is the depth of the maximum in the shower development, $X_{\max}$. A simple way to understand the sensitivity of this variable to the mass of the primary particle is the superposition model. It states that the interaction of a nucleus with mass A and energy E can be seen as the superposition of A nucleons interacting with an energy E/A. All this, in the framework of the extended Heitler model [11,12], leads to the following expresion where the mass dependence is shown:

$$\langle X^A_{\max} \rangle = c + D_p \ln(E/A). \tag{1}$$

The elongation rate $D_p = dX_{\max}/dlnE$ and the parameter c contain the dependency on the hadronic interaction properties. Also the fluctuations in $X_{\max}$ carry information about the pri-

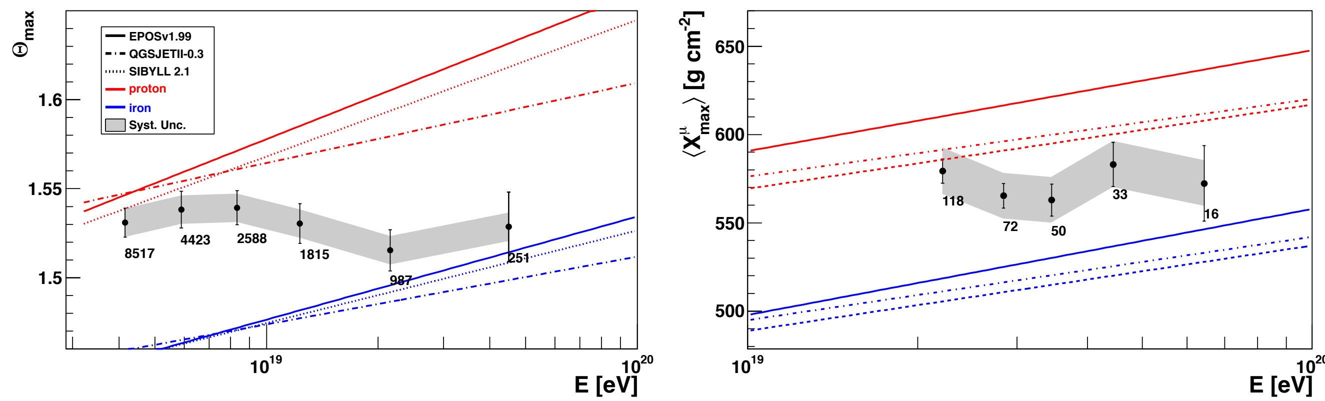

Figure 2: The azimuthal rise-time asymmetry Θ_{max} (left panel) and $\langle X^{\mu}_{\max} \rangle$ (right panel) as a function of the energy. The number of events in each bin is indicated.

mary particles. They are supposed to be smaller for heavy than for light nuclei.
When we analyse real data we have to compare them with simulations. Given that accelerator data do not cover the energy range of the first interactions produced in the cascade development, models must rely in theoretical extrapolations. Differences between them are often used as an estimation of the systematic uncertainties due to the lack of knowledge in the hadronic interactions at ultra-high energies.
The measurement of the longitudinal profile of the energy deposited in the atmosphere with the Pierre Auger Observatory is described in [14]. Only hybrid events (showers measured with the FD and at least one SD station in coincidence) are considered in this analysis, to provide an accurate reconstruction of the geometry. To ensure a good $X_{\max}$ resolution and an unbiased mean measurement (not undersampling the tails of the $X_{\max}$ distributions) different set of cuts are applied over the data sample [15]. Figure 1 shows the results for the $\langle X_{\max} \rangle$ analysis. Along with the predictions for different hadronic interaction models and primaries, the mean values (left panel) and the RMS (right panel) of the $X_{\max}$ distributions are shown as a function of the primary energy. The elongation rate is well described with a linear fit broken at $\log(\mathrm{E/eV}){=}18.38^{+0.07}_{-0.17}$ [16]. This change in the elongation rate can be interpreted as a transition from lighter to heavier primaries as the energy increases. The values for the $X_{\max}$ fluctuations shown in Figure 1 have been corrected by the detector resolution [16]. Again, assuming that the hadronic interaction properties do not change much within the observed energy range, this result is an independent signature of an increasing average mass of the primary particles with energy. The compatibility of the Auger results for $\langle X_{\max} \rangle$ and RMS($X_{\max}$) with different hadronic interaction models has been studied in [17]. A direct comparison between the shape of the measured $X_{\max}$ distributions with different hadronic models and primaries is discussed in [16].

2.2 Surface Detector Measurements

In the development of EAS, the atmosphere acts as a huge calorimeter absorbing part of the EM component in its path to ground. This means that the number of these particles at ground relates with the depth of the shower maximum. Furthermore, the arrival time for the muon component is earlier than for EM particles, since they travel in almost straight lines with smaller multiple scattering. Based on this, it is possible to find observables relating to primary particle composition in the time structure of particles at ground, recorded by the water Cherenkov detectors of the Pierre Auger Observatory.

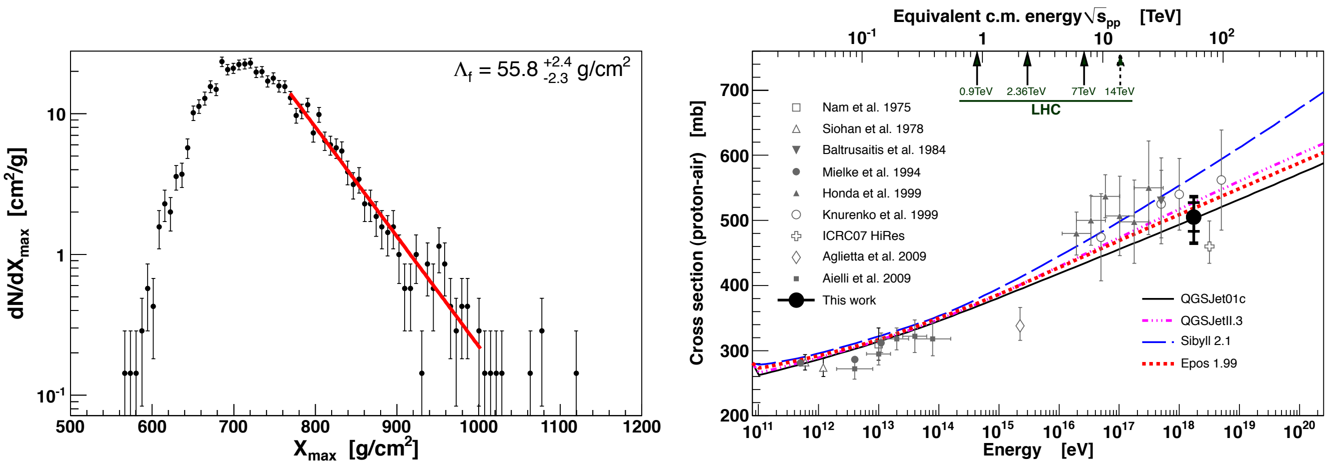

Figure 3: Left: Unbinned likelihood fit of the tail of X_{max} distribution in the energy interval 10^{18}-$10^{18.5}$ eV. Right: Proton-air cross-section measured by Auger and other cosmic ray experiments along with different model predictions.

The so called rise-time of the signal (the time to go from the 10% to the 50% of the total integrated signal), $t_{1/2}$, is a measurement of the muon to electron ratio in a SD detector. It depends on the primary mass, the zenith angle θ and the distance to the shower axis r. The azimuthal asymmetry of $t_{1/2}$ for non vertical events carries information about the longitudinal development of the shower [18]. The maximum of this asymmetry, Θ_{max}, has been used to study the composition of cosmic rays.

Using signals dominated by muons (in inclined events and far from the shower core) it is possible to reconstruct the muon production depth distribution (MPD) [19]. In this technique the arrival times of the muons are converted into their production distances along the shower axis assuming they travel undeflected from birth until reaching the ground. These distributions carry information about the hadronic longitudinal development of the shower. The maximum $X^{\mu}_{\max}$ of these profiles is strongly correlated with the depth of the first interaction X_1, and $X_{\max}$, so it is also sensitive to the nature of primary particles.

Figure 2 shows the values of Θ_{max} and $\langle X^{\mu}_{\max}\rangle$ as a function of the energy. Both results are compatible with showers that develop earlier than pure proton showers in the highest energy region.

3 Proton-air cross-section

The Pierre Auger Collaboration has measured the proton-air cross-section, σ_{p-air}, for particle production at ultra-high energies using hybrid data. This cross-section is directly related with the exponential distribution of X_1. The strong correlation between X_1 and $X_{\max}$ makes the tail of the $X_{\max}$ distribution still sensitive to the proton-air cross-section. This quality was first exploited for this purpose by the Fly's Eye Collaboration [20]. The idea is to fit the deep tail of the $X_{\max}$ distribution with an exponential function and use the slope as an estimator of σ_{p-air}. The translation to a cross-section is done using Monte Carlo simulations with a consistent rescaling of the original cross-section to reproduce the value of the measurement [21].

One of the main difficulties in this analysis is the poor knowledge of mass composition at these energies. The tail of $X_{\max}$ distribution is supposed to be proton-rich as protons are the most penetrating nuclei. However we cannot exclude the presence of other primaries, mainly helium and photons. The possible photon impact is almost under control thanks to the strong limits reported on the photon fraction in Auger data [22]. But no limit exists on the helium fraction of cosmic rays at these energies. This lack of knowledge translates into the main contribution to

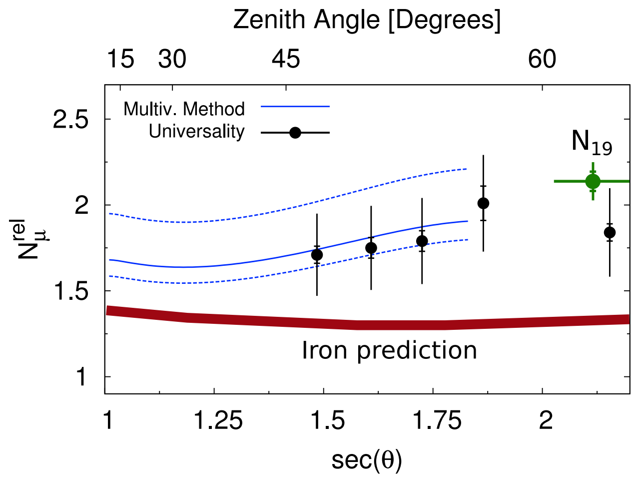

Figure 4: Data from the Pierre Auger Observatory showing the measured number of muons at 1000 m from the shower axis and 10^{19} eV relative to the predictions of the hadronic model QGSJETII for proton initiated showers (N_μ^{rel}) as a function of the zenith angle. The figure shows the results derived from the multivariate, shower universality and inclined events (N_{19}) methods. The result for pure iron simulations is also shown.

the systematic uncertainty of this measurement. Figure 3 left panel shows the selected $X_{\max}$ distribution and the fit of its exponential tail. Only events with E$\in [10^{18}eV, 10^{18.5}eV]$ are used in this analysis, resulting in an averaged center-of-mass energy of $\sqrt{s} = 57$ TeV. If we neglect the possible presence of helium in our data sample, then the measured proton-air cross-section is

$$\sigma_{p-air} = (505 \pm 22_{stat} \pm (^{+20}_{-15})_{sys})mb. \tag{2}$$

Using simulations we find that a 50 % fraction of helium would reduce the actual value of the measured cross-section by 80 mb [21]. In Figure 3, right panel, we show the measured σ_{p-air} together with different model predictions and other measurements derived from cosmic ray data. Our result favors a moderately slow rise of the cross-section towards higher energies.

4 Muon shower content

A good description of shower data is essential to draw the right conclusions when comparing the measurements with simulations. As mentioned in the text, the number of muons at ground depends on several properties of hadronic interactions [10], becoming a powerful tool in the difficult task of validate the various existing models. Different methods have been developed to derive the fraction of the signals, collected by the surface detectors, coming from the muonic or the electromagnetic component of the shower using the Auger data. Some of these methods are based on the different time structure showed by both components [23]. Muons typically deposit more energy in the water Cherenkov detectors than electrons and photons, producing spikes over the smoother EM contribution in the signals. The multivariate method exploits this feature in the time traces to build an estimator correlated with the number of muons. The universality method uses a recently found shower universality property which relates the muon to electromagnetic signal ratio with the maximum in the shower development [24]. This property can be described by a simple parameterization for showers with zenith angle between 45° and 65°. Then, for hybrid events, this method derives the muonic signal in a SD detector from the shower maximum depth and the total signal. The most direct way to investigate the muon content of cosmic ray showers is by studying very inclined events, where the dominant particles at ground are muons because most of the electrons and photons have been absorbed in the atmosphere [25]. Using hybrid inclined events, the measured shower size N_{19}, which is a muon estimator itself, can be calibrated with the calorimetric energy reconstructed by the FD. This calibration procedure can be used to obtain the number of muons as a function of energy. A summary of the results obtained when we apply these methods to real data is presented in Figure 4. It shows the estimated number of muons at 1000 m in data relative to the predictions of simulations using the hadronic model QGSJETII [7] with proton primaries. In view of this figure, the considered simulations are found to present underestimations of the muon fraction at ground level for the events measured with the Pierre Auger Observatory. The observed relative excess is angle dependent, growing from about 1.6 [23], at the lower zenith angles, to more than 2 [25], for the more inclined events. Understanding this discrepancy is critical to an appropriate interpretation of cosmic ray data. Different efforts are focused on that. For example, it has been recently demonstrated that a larger baryon anti-baryon pair production yields to a higher number of low energy muons [8].

Acknowledgments

This work was supported by the ANR-2010-COSI-002 grant of the French National Research Agency.

References

1. J. Abraham *et al*, (Pierre Auger Collab.), *Nucl. Instr. and Meth. A*, **523**, 50-95, (2004)
2. J. Abraham *et al*, (Pierre Auger Collab.), *Nucl. Instr. and Meth. A*, **613**, 29-39, (2010)
3. J. Abraham *et al*, (Pierre Auger Collab.), *Nucl. Instr. and Meth. A*, **620**, 2-3, (2010)
4. H.-J. Mathes *et al*, (Pierre Auger Collab.), *Proc. 32nd ICRC*, (2011), arXiv:1107.4807v1
5. J. Abraham *et al*, (Pierre Auger Collab.), *Astropart. Phys.* **33**, 108-129, (2010)
6. J. Abraham *et al*, (Pierre Auger Collab.), *Astropart. Phys.* **32**, 88-99, (2009)
7. S.S Ostapchenko, *Nucl. Phys.* B **151**, 143-146 (2006)
8. T. Pierog and K. Werner, *Phys. Rev. Lett.* **101**, 171101 (2008)
9. E.J. Ahn *et al*, *Phys. Rev.* D **80**, 094003 (2009)
10. R. Ulrich *et al*, *Phys. Rev.* D **83**, 054026 (2011)
11. W. Heitler, *Oxford University Press*, (1954)
12. J. Matthews, *Astropart. Phys.* **22**, 387, (2005)
13. N.N. Kalmykov and S.S. Ostapchenko, *Phys. Atom. Nucl.* **56**, 346-353 (1993)
14. J. Abraham *et al*, (Pierre Auger Collab.), *Phys. Rev. Lett.* **104**, 091101 (2010)
15. M. Unger *et al*, (Pierre Auger Collab.), *Nucl. Phys. B Proc. Suppl.* **190**, 240, (2009)
16. P. Facal *et al*, (Pierre Auger Collab.), *Proc. 32nd ICRC*, (2011), arXiv:1107.4804v1
17. Karl-Heinz Kampert and Michael Unger, *Astropart. Phys.* **35**, 660-678, (2012)
18. M.T. Dova *et al*, *Astropart. Phys.* **31**, 312-319, (2009)
19. D. Garcia-Gamez *et al*, (Pierre Auger Collab.), *Proc. 32nd ICRC*, (2011), arXiv:1107.4804v1
20. R. Ellsworth *et al*, *Phys. Rev.* D **26**, 336 (1982)
21. R. Ulrich *et al*, (Pierre Auger Collab.), *Proc. 32nd ICRC*, (2011), arXiv:1107.4804v1
22. M. Settimo *et al*, (Pierre Auger Collab.), *Proc. 32nd ICRC*, (2011), arXiv:1107.4805v1
23. J. Allen *et al*, (Pierre Auger Collab.), *Proc. 32nd ICRC*, (2011), arXiv:1107.4804v1
24. A. Yushkov *et al*, *Phys. Rev.* D **81**, 123004 (2010)
25. G. Rodriguez *et al*, (Pierre Auger Collab.), *Proc. 32nd ICRC*, (2011), arXiv:1107.4809v1

TESTS OF FUNDAMENTAL SYMMETRIES THROUGH THE CMB: FROM WMAP TO PLANCK

A. GRUPPUSO[1,4], N. MANDOLESI[1] AND P. NATOLI[2,1,3]
[1] *INAF-IASF Bologna, Istituto di Astrofisica Spaziale e Fisica Cosmica di Bologna via Gobetti 101, I-40129 Bologna, Italy*
[2] *Dipartimento di Fisica and Sezione INFN, Universitęgli Studi di Ferrara, via Saragat 1, I-44100 Ferrara, Italy*
[3] *ASI Science Data Center, c/o ESRIN, via G. Galilei, I-00044, Frascati, Italy*
[4] *INFN, Sezione di Bologna, Via Irnerio 46, I-40126 Bologna, Italy*

We review some constraints about Parity violating models that go beyond the Maxwell electromagnetism. The observable, that is already considered as a standard tracer of such violations, is the in vacuo Cosmological Birefringence angle that can be obtained from the Angular Power Spectra of the Cosmic Microwave Background (henceforth CMB) pattern. This angle, that represents the rotation of the polarization plane that a CMB photon experiences traveling from the last scattering surface to us, is different from zero only if there is a Parity violating coupling in the Maxwell Lagrangian. We also review the claimed Parity anomaly found at large scales of the TT spectrum of the WMAP data by Kim and Naselsky in 2010. We finally forecast the capabilities of Planck in tightening the present constraints.

1 Introduction

The observed properties of the Cosmic Microwave Background (henceforth CMB) pattern can be used to constrain Parity (P) symmetry. P violations arise in many models, as modification of electromagnetism[1,2,3](hence deviations from the Standard Model of Particle Physics) or as modification of the standard picture of the Inflationary mechanism (where P is broken for primordial gravitational waves). In the latter case, we refer to Chiral Gravity[4,5,6,7] and in former we generally talk of Cosmological Birefringence. Both of these classes of models predict cross-correlations between E and B modes and T and B modes different from zero. However Chiral Gravity induces such correlations at the CMB last scattering surface whereas the Cosmological Birefringence effect induces them by rotating the primordial polarization during the CMB photon journey from the last scattering to us[8].

In this proceeding, we focus on the Cosmic Birefringence case reporting mainly from [9]. Moreover we review the claimed P anomaly found at large scales of the TT spectrum of the WMAP data by Kim and Naselsky in 2010 [10,11,12,13]. Since, up to our knowledge, there is no P violating model capable to explain such deviation from the expected cosmological standard model, the reader might find the use of the "P violation" term in this context not proper. However since such anomaly highlights a difference in the even and odd multipoles (that behave differently under P transformation, see Section 2), it is commonly use such terminology, i.e. TT P anomaly. It is not known yet if this come from fundamental physics or it is due to some spurious effect, like systematics or foreground not removed [14]. Supposing it is due to fundamental physics, since it shows up in the WMAP temperature map at large angular scales one may naturally think about the possibility that a P violating mechanism is responsible for such an effect during the early universe evolution. For a more conservative approach see [11] where under the hypothesis that the early universe evolution is unchanged from the standard inflationary mechanism, it is concluded that we live in a special location of the universe, such that translational invariance is violated for scales larger than 4 Gpc leading to a sort of breaking of the Copernican principle.

2 Parity symmetry in CMB

All-sky temperature maps, $T(\hat{n})$, are usually expanded in terms of Spherical Harmonics $Y_{\ell m}(\hat{n})$, with $\hat{n}$ being a direction in the sky, namely depending on the couple of angles (θ, ϕ), $a_{T,\ell m} = \int d\Omega\, Y^{\star}_{\ell m}(\hat{n})\, T(\hat{n})$, where $a_{T,\ell m}$ are the coefficients of the Spherical Harmonics expansion and $d\Omega = d\theta d\phi \sin\theta$. Under reflection (or P) symmetry ($\hat{n} \to -\hat{n}$), these coefficients behave as $a_{T,\ell m} \to (-1)^{\ell}\, a_{T,\ell m}$. Analogously for polarizations maps, taking into account the usual combination of Stokes parameters ($Q(\hat{n})$ and $U(\hat{n})$) one obtains $a_{\pm 2,\ell m} = \int d\Omega\, Y^{\star}_{\pm 2,\ell m}(\hat{n})\,(Q(\hat{n}) \pm iU(\hat{n}))$, where $Y_{\pm 2,\ell m}(\hat{n})$ are the Spherical Harmonics of spin 2 and $a_{\pm 2,\ell m}$ are the corresponding coefficients. It is possible to show that under P, $a_{E,\ell m} \to (-1)^{\ell}\, a_{E,\ell m}, \quad a_{B,\ell m} \to (-1)^{\ell+1}\, a_{B,\ell m}$, where $a_{E,\ell m} = -(a_{2,\ell m} + a_{-2,\ell m})/2$ and $a_{B,\ell m} = -(a_{2,\ell m} - a_{-2,\ell m})/2i$. If P is conserved, combining the previous transformation one immediately derives that the cross-correlations $C_\ell^{TB} = C_\ell^{EB} = 0$. Further details can be found for example in [15,16] and explicit algebra is present in the Appendix of [12].

3 Cosmological Birefringence

The CMB is a powerful probe for constraining the Cosmological Birefringence angle (and therefore exploring possible P violations of Maxwell Lagrangian) for two main reasons. First, it is generated in the early universe, when the physics at the stake was not obviously identical to present. Secondly, the long look-back time of CMB photons may render tiny violations to the electromagnetic Lagrangian observable, since such effects usually accumulate during propagation. CMB polarization arises at two distinct cosmological times: the recombination epoch ($z \sim 1100$) and the reionization era ($z \sim 11$ or less [17]). When the CMB field is expanded in spherical harmonics, the first signal mostly shows up at high multipoles, since polarization is generated through a causal process and the Hubble horizon at last scattering only subtends a degree sized angle. The later reionization of the cosmic fluid at lower redshift impacts the low ℓ instead. These two regimes need to be taken into account when probing for cosmological birefringence, since they can be ascribed to different epochs and, hence, physical conditions.

Recent polarization oriented CMB observations [18,19,20,21] have been capable to measure TB and EB correlations, other than TT, TE and EE correlations. While no detection has been claimed to date, polarization data have been used to derive constraints on the birefringence angle [19,22,23,24].

In the limit of constant birefringence angle, α, the angular power spectra of CMB anisotropies, assuming $C_\ell^{TB} = C_\ell^{EB} = 0$, are given by [4,22,25,26] [a],

$$C_\ell^{TE,obs} = C_\ell^{TE} \cos(2\alpha)\,, \tag{1}$$

$$C_\ell^{TB,obs} = C_\ell^{TE} \sin(2\alpha)\,, \tag{2}$$

$$C_\ell^{EE,obs} = C_\ell^{EE} \cos^2(2\alpha) + C_\ell^{BB} \sin^2(2\alpha)\,, \tag{3}$$

[a] See [27,28] as an example of computation that takes into account the time dependence of α in a specific model of pseudoscalar fields coupled to photons. See [29,30,31] as examples of non-isotropic birefringence effect.

$$C_\ell^{BB,obs} = C_\ell^{BB}\rangle \cos^2(2\alpha) + C_\ell^{EE}\sin^2(2\alpha)\,, \quad (4)$$
$$C_\ell^{EB,obs} = \frac{1}{2}\left(C_\ell^{EE} + C_\ell^{BB}\right)\sin(4\alpha)\,. \quad (5)$$

The WMAP team [19], using a Markov Chain Monte Carlo (MCMC) method, at high ℓ (from 24 to 800) find $\alpha^{\mathrm{WMAP}\,7yr} = -0.9^\circ \pm 1.4^\circ$ at 68% C.L.. Our constraint, obtained at low resolution [9] and considering the same estimator that has been used in [24], reads $\alpha = -1.6^\circ \pm 1.7^\circ$ (3.4°) at 68% (95%) C.L. for $\Delta\ell = 2-47$. Considering $\Delta\ell = 2-23$ we obtain $\alpha = -3.0^{\circ}{}^{+2.6^\circ}_{-2.5^\circ}$ at 68% C.L. and $\alpha = -3.0^{\circ}{}^{+6.9^\circ}_{-4.7^\circ}$ at 95% C.L.. This is the same multipole range considered by the WMAP team at low resolution in [19] (the only other result available in the literature at these large angular scales) where with a pixel based likelihood analysis they obtain $\alpha^{\mathrm{WMAP}\,7yr} = -3.8^\circ \pm 5.2^\circ$ at 68% C.L.. In [32] it is claimed that the improvement expected for the Planck satellite [33] in terms of sensitivity [34] is around 15. Almost the same number is obtained in [9]. Both the forecasts are provided considering just the nominal sensitivity whereas the uncertainties coming from the systematic effects are not taken into account.

4 TT Parity anomaly

The starting consideration for this analysis is that CMB physics does not distinguish between even and odd multipoles [10,11]. Therefore the power contained in even and odd multipoles must be statistically the same. For this reason we define the ratio $R^X = C_+^X/C_-^X$, as in [10,11,12] and the difference $D^X = C_+^X - C_-^X$, , as in [12,35], where $C_\pm^X$ is the band power average contained in the even (+) or odd (-) multipoles with X standing for one of the six CMB spectra. See [13] for other estimators. In Fig. 1 we plot the percentage related to the WMAP 7 year P anomaly

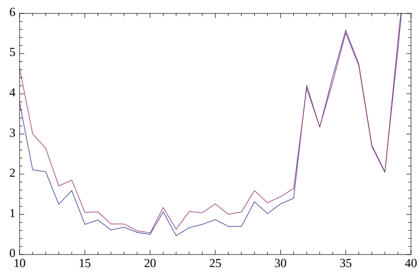

Figure 1: TT. Percentage of the WMAP 7 year value (y-axis) vs ℓ_{max} (x-axis). Blue line is for the ratio and the red line for the difference.

for TT versus ℓ_{max} in the range $10-40$ for the two considered estimators. As evident there is not a single ℓ_{max} for which the TT anomaly shows up, but rather a characteristic scale in the ℓ range $[15, 25]$. We confirm the previously reported P anomaly in TT in the range $\Delta\ell = [2, 22]$ at $> 99.5\%$ C.L.. Planck will not improve the signal-to-noise ratio in this range for the TT spectrum, since it is already cosmic variance dominated in the WMAP data. However Planck has a wider frequency coverage and this will improve the component separation layer in the data analysis pipeline. Moreover Planck is observing the sky with a totally different scanning strategy and this represents a benefit from the systematic effects analysis point of view.

Acknowledgments

This work has been done in the framework of the Planck LFI activities. In particular we acknowledge the use of the Planck LFI DPC code, BolPol, described in [9,12]. We acknowledge support by ASI through ASI/INAF agreement I/072/09/0 for the Planck LFI activity of Phase E2. We acknowledge the use of computing facilities at NERSC. We acknowledge the use of the

Legacy Archive for Microwave Background Data Analysis (LAMBDA [b]). Support for LAMBDA is provided by the NASA Office of Space Science. Some of the results in this paper have been derived using the HEALPix [36] package [c].

References

1. S. M. Carroll, G. B. Field and R. Jackiw, *Phys. Rev.* D **41**, 1231 (1990)
2. S. M. Carroll and G. B. Field, *Phys. Rev.* D **43**, 3789 (1991)
3. S. M. Carroll, *Phys. Rev. Lett.*, **81**, 3067, (1998)
4. A. Lue, L. -M. Wang, M. Kamionkowski, *Phys. Rev. Lett.* **83**, 1506 (1999)
5. C. R. Contaldi, J. Magueijo and L. Smolin, *Phys. Rev. Lett.* **101**, 141101 (2008)
6. S. Saito, K. Ichiki and A. Taruya, *JCAP* **0709**, 002 (2007)
7. L. Sorbo, *JCAP* **1106**, 003 (2011)
8. V. Gluscevic and M. Kamionkowski, *Phys. Rev. D* **81**, 123529 (2010)
9. A. Gruppuso, P. Natoli, N. Mandolesi, A. De Rosa, F. Finelli and F. Paci, *JCAP* **1202**, 023 (2012)
10. J. Kim and P. Naselsky, *Astrophys. J.* **714**, L265 (2010)
11. J. Kim and P. Naselsky, *Phys. Rev. D* **82**, 063002 (2010)
12. A. Gruppuso, F. Finelli, P. Natoli, F. Paci, P. Cabella, A. De Rosa and N. Mandolesi, *Mon. Not. Roy. Astron. Soc.* **411**, 1445 (2011)
13. P. K. Aluri and P. Jain, *Mon. Not. Roy. Astron. Soc.* **419**, 3378 (2012)
14. M. Maris, C. Burigana, A. Gruppuso, F. Finelli and J. M. Diego, *Mon. Not. Roy. Astron. Soc.* **415**, 2546 (2011)
15. M. Zaldarriaga, *Astrophys. J.* **503**, 1 (1998)
16. M. Zaldarriaga and U. Seljak, *Phys. Rev.* D **55**, 1830 (1997)
17. S. Dodelson, "Modern Cosmology", Academic Press, Elsevier (2003)
18. C. Pryke *et al.* [QUaD Collaboration], *Astrophys. J.* **692**, 1247-1270 (2009).
19. E. Komatsu *et al.* [WMAP Collaboration], *Astrophys. J. Suppl.* **192**, 18 (2011).
20. F. Piacentini *et al.*, *Astrophys. J.* **647**, 833 (2006).
21. T. E. Montroy *et al.*, *Astrophys. J.* **647**, 813 (2006).
22. B. Feng, M. Li, J. -Q. Xia, X. Chen, X. Zhang, *Phys. Rev. Lett.* **96**, 221302 (2006).
23. P. Cabella, P. Natoli, J. Silk, *Phys. Rev. D* **76**, 123014 (2007).
24. E. Y. S. Wu *et al.* [QUaD Collaboration], *Phys. Rev. Lett.* **102**, 161302 (2009).
25. B. Feng, H. Li, M. -z. Li, X. -m. Zhang, *Phys. Lett.* **B620**, 27-32 (2005).
26. E. Komatsu *et al.* [WMAP Collaboration], *Astrophys. J. Suppl.* **180**, 330-376 (2009).
27. M. Galaverni, F. Finelli, *Nucl. Phys. Proc. Suppl.* **194**, 51-56 (2009).
28. F. Finelli, M. Galaverni, *Phys. Rev. D***79**, 063002 (2009).
29. M. Li, X. Zhang, *Phys. Rev. D* **78**, 103516 (2008).
30. M. Kamionkowski, *Phys. Rev. D* **82**, 047302 (2010).
31. G. Gubitosi *et al.*, [arXiv:1106.6049 [astro-ph.CO]].
32. G. Gubitosi *et al.*, *JCAP* **0908**, 021 (2009)
33. P. A. R. Ade *et al.* [Planck Collaboration], *Astronomy & Astrophysics*, **536**, id.A1
34. Planck Collaboration, *ESA publication* ESA-SCI (2005)/1 [arXiv:astro-ph/0604069].
35. F. Paci *et al.*, *Mon. Not. Roy. Astron. Soc.* **407**, 399 (2010)
36. K.M. Gorski, E. Hivon, A.J. Banday, B.D. Wandelt, F.K. Hansen, M. Reinecke and M. Bartelmann, *Astrophys. J.* **622**, 759 (2005)

[b] http://lambda.gsfc.nasa.gov/
[c] http://healpix.jpl.nasa.gov/

7.
QCD

EXTENDING THE MATRIX ELEMENT METHOD TO NEXT-TO-LEADING ORDER

JOHN M. CAMPBELL, WALTER T. GIELE, CIARAN WILLIAMS
Fermilab, Pine St. and Kirk Road, Batavia, IL 60510 USA.

We discuss the extension of the matrix element method (MEM) to Next-to-Leading Order (NLO) in perturbation theory. In particular we focus on the production of a Standard Model Higgs boson which decays into four leptons.

1 Introduction

The matrix element method uses fixed order matrix elements to calculate probabilities for exclusive experimental events [1,2]. By varying the underlying theoretical parameters of the matrix element one can determine the best fit values between theory and data. The ensemble data set can then be used to define a likelihood associating the input parameters with the experimental data set. By varying the underlying theoretical parameters used in the matrix elements one can obtain multiple likelihoods, the maximum likelihood corresponds to the best fit parameters linking the theory model to data. The MEM has been extensively used in experimental analyses, see e.g. ref. [3] for a review of the MEM's application to the measurement of the top mass. This talk illustrates how this can be extended to NLO in perturbation theory [4].

2 The Matrix Element Method at LO and NLO

The primary difficulty inherent in modeling experimental events with fixed order matrix elements occurs when attempting to map an experimentally observed set of objects $\tilde{p}$ to a Born phase space point p in which the beams are along the z-axis. We define the sum over the particles identified with the Born final state as X, i.e. $X = -\sum_{i=1}^{n} \tilde{p}_i$. For a generic event X_x and $X_y \neq 0$, which is incompatible with our assumption that the initial state partons are aligned with the beam. In order to overcome this obstacle we perform a Lorentz transformation to a frame in which $X_T = 0$. This preserves all of the Lorentz invariant quantities associated with the experimental event. We now need to construct the longitudinal components of the initial state particles which are fixed through the corresponding components of the final state particles. However the Lorentz boost which we performed does not uniquely fix these components. In other words, there are multiple frames in which the final state particles are balanced in p_T connected to each other by longitudinal boosts. We refer to this collection of frames as the MEM frame. In order to provide an unbiased weight we must integrate over all allowed boosts. We note that the matrix element is a Lorentz scalar and as such the only boost dependent term we need to consider for the MEM is the integration over parton distribution functions

$$\mathcal{L}_{ij}(s_{ab}, x_l, x_u) \quad = \quad \int_{x_l}^{x_u} dx_a \, \frac{f_i(x_a) f_j(s_{ab}/(s x_a))}{s x_a s_{ab}} \, . \tag{1}$$

Combining this boost integration with the boost invariant matrix element $\mathcal{B}^{ij}$ allows us to construct the probability density function for the MEM accurate to LO,

$$\mathcal{P}(\mathbf{x}|\Omega) = \frac{1}{\sigma_\Omega^{LO}} \int d\mathbf{y} \, \mathcal{L}_{ij}(s_{ab}, x_l, x_u) \mathcal{B}_\Omega^{ij}(p_a, p_b, \mathbf{y}) W(\mathbf{x}, \mathbf{y}) \, . \tag{2}$$

Here $W(\mathbf{x},\mathbf{y})$ represents the experimental transfer function which models the detector effects. We will assume that $W(\mathbf{x},\mathbf{y}) = \delta(\mathbf{x}-\mathbf{y})$, which is valid for identified muons and electrons.

In order to extend the MEM formalism to NLO we need to incorporate both virtual and real contributions into the weight under the constraint that the weight should be evaluated for a fixed experimental input event. We imagine that we have performed the Lorentz boost described above such that the experimental event has the kinematics of a Born phase space point $\mathbf{x}$. In this setup our NLO calculation should be formulated as follows,

$$\frac{d\,\sigma_{\Omega}^{NLO}(\mathbf{x})}{d\mathbf{x}} = R_{\Omega}(\mathbf{x}) + V_{\Omega}(\mathbf{x})\ . \tag{3}$$

That is, we define the virtual $V_{\Omega}(\mathbf{x})$ and real $R_{\Omega}(\mathbf{x})$ parts of the calculation separately as a function of the Born phase space point $\mathbf{x}$. Summing over the Born phase results in the usual NLO cross section. Defining the virtual phase space is straightforward since this piece shares the same phase space as the Born contribution, the virtual piece is thus,

$$\begin{aligned} V_{\Omega}(\mathbf{x}) \quad &= \quad \mathcal{L}_{ij}(s_{ab},x_l,x_u)\Big(\mathcal{B}_{\Omega}^{ij}(p_a,p_b,\mathbf{x}) + \mathcal{V}_{\Omega}^{ij}(p_a,p_b,\mathbf{x})\Big) \\ &\quad + \sum_{m=0}^{2}\int dz\Big(\mathcal{D}_m(z,\mathbf{x})\otimes\mathcal{L}_m(z,s_{ab},x_l,x_u)\Big)_{ij}\mathcal{B}_{\Omega}^{ij}(p_a,p_b,\mathbf{x}). \end{aligned} \tag{4}$$

Here the first line represents the contributions from the Born matrix element and the virtual-born interference terms which occur at one-loop $\mathcal{V}_{\Omega}^{ij}$. These pieces contain divergences which are regulated through a subtraction scheme. These subtractions are denoted in the second line and factor onto the Born matrix element. We observe that since we are considering electro-weak final states the subtractions are for initial state singularities. This results in convolution integrals between the dipole parameter z and the boost integration. This is shown schematically by the sum over m in the above equation.

In addition to the virtual contributions we must also define the real corrections associated with the radiation of an additional parton. These pieces are more troublesome since they reside in a higher dimensional phase space than the Born. In order to maintain the desired mapping to the Born phase space point we use a Forward Branching Phase Space generator (FBPS) [5], this provides the following factorisation.

$$d\Phi(p_a+p_b\to Q+p_r) = d\,\Phi(\widehat{p}_a+\widehat{p}_b\to Q)\times d\,\Phi_{\text{FBPS}}(p_a,p_b,p_r)\times\theta_{\text{veto}}\ . \tag{5}$$

Hatted momentum represent an underlying Born topology whilst the un-hatted momenta are the real phase space point. We note that the observed particles Q are identical to their Born counterparts. In terms of the kinematic invariants the FBPS is given by,

$$d\,\Phi_{\text{FBPS}}(p_a,p_b,p_r) = \frac{1}{(2\pi)^3}\left(\frac{\widehat{s}_{ab}}{s_{ab}}\right)d\,t_{ar}d\,t_{rb}d\,\phi\ . \tag{6}$$

Using the FBPS we can now explicitly define $R_{\Omega}(\mathbf{x})$ as,

$$\begin{aligned} R_{\Omega}(\mathbf{x}) = \int d\,\Phi_{\text{FBPS}}(p_a,p_b,p_r)\Big(&\mathcal{L}_{ij}(s_{ab},x_l,x_u)\mathcal{R}_{\Omega}^{ij}(p_a,p_b,\mathbf{x},p_r) \\ &-\sum_m \mathcal{L}_{ij}(s_{ab},x_l^m,x_u^m)D^m(p_a,p_b,p_r)\mathcal{B}_{\Omega}^{ij}(\hat{p}_a,\hat{p}_b,\mathbf{x})\Big). \end{aligned} \tag{7}$$

The first term in the above equation represents the integration over the FBPS of the real matrix elements $\mathcal{R}^{ij}$. In certain regions of phase space these terms develop singularities which are regulated by the subtraction terms defined in the second line of the equation.

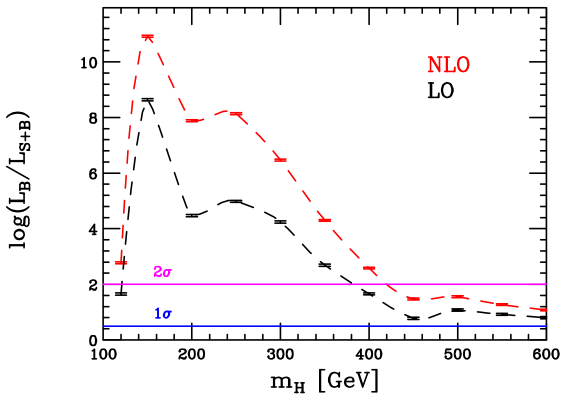

Figure 1: The log-likelihood difference for background only and signal plus background, for a Higgs boson search in the channel, $H \to ZZ^\star \to 4$ leptons. Positive values of the difference indicate that the background-only hypothesis is more likely than the signal plus background one. The blue and magenta lines represent the 1- and 2-σ limits respectively.

We are now in a position to define the NLO probability density to be used in the MEM,

$$\mathcal{P}(\mathbf{x}|\Omega) = \frac{1}{\sigma_\Omega^{NLO}}\Big(V_\Omega(\mathbf{x}) + R_\Omega(\mathbf{x})\Big) \, . \tag{8}$$

We have suppressed the dependence on the transfer functions, assuming perfectly resolved particles. In the next section we will present an application for which this assumption is reasonable, namely the production of a SM Higgs boson and its decay to four charged leptons. The future applications of the method for LHC physics are widespread.

3 The Search for the SM Higgs boson

The search for the Higgs boson is one of the most pressing in experimental particle physics. Current LHC limits indicate that, if it exists, then the SM Higgs has a mass in the range 120-125 GeV [6,7]. One of the most promising decay modes in which to extract the Higgs properties is the decay of the Higgs to ZZ which subsequent decays to charged leptons $ZZ \to 4\ell$. In this instance the final state is fully reconstructed and contains particles which the general purpose detectors can measure accurately [8,9]. In this example we generate samples of unweighted events produced from a NLO sample, directly in the MEM frame. The underlying physics is identical to that implemented in MCFM [10]. We assume that no Higgs boson exists and proceed to set limits using the MEM. In Fig. 1 we present a results from a single pseudo-experiment for around 250 events. In this example we sweep over a range of Higgs masses and set limits. NLO sets a limit of $100 < m_H < 430$ GeV, whilst LO sets a limit of $120 < m_H < 380$ GeV. In Fig. 2 we generate multiple pseudo experiments and test a single hypothesis ($m_H = 200$ GeV). As such we are able to discern the differences between LO and NLO in a more systematic nature. We observe that in general there are observable differences between LO and NLO. The NLO results set better limits, however this is hardly surprising given that the underlying sample is NLO.

4 Conclusions

We have illustrated how the matrix element method may be extended to NLO in perturbation theory. As an example we have considered the decay of the SM Higgs boson to four charged leptons.

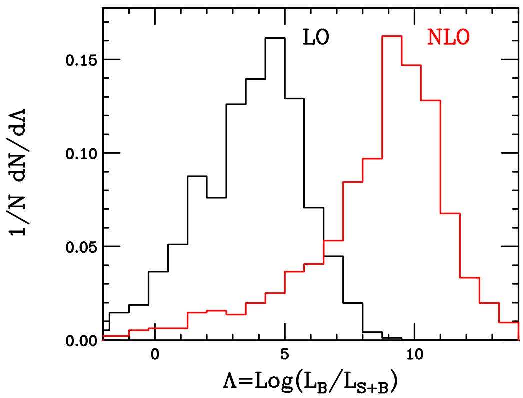

Figure 2: Pseudo experiments testing the hypothesis that there is a Higgs boson with $m_H = 200$ GeV. We generate pseudo-experiments which consist only of background and no Higgs signal. As such the most common outcome is that the signal plus background hypothesis is less likely than the background only.

Acknowledgments

CW would like to thank the organisers of the Moriond conference for a grant providing financial support. Fermilab is operated by Fermi Research Alliance, LLC under Contract No. DE-AC02-07CH11359 with the United States Department of Energy.

1. K. Kondo, *Dynamical likelihood method for reconstruction of events with missing momentum. 2: Mass spectra for 2 → ; 2 processes*, *J.Phys.Soc.Jap.* **60** (1991) 836–844.
2. R. Dalitz and G. R. Goldstein, *The Decay and polarization properties of the top quark*, *Phys.Rev.* **D45** (1992) 1531–1543.
3. F. Fiedler, A. Grohsjean, P. Haefner, and P. Schieferdecker, *The Matrix Element Method and its Application in Measurements of the Top Quark Mass*, *Nucl.Instrum.Meth.* **A624** (2010) 203–218, [arXiv:1003.1316].
4. J. M. Campbell, W. T. Giele, and C. Williams, *The Matrix Element Method at Next-to-Leading Order*, arXiv:1204.4424.
5. W. T. Giele, G. C. Stavenga, and J.-C. Winter, *A Forward Branching Phase-Space Generator*, arXiv:1106.5045.
6. **ATLAS Collaboration** Collaboration, G. Aad *et. al.*, *Combined search for the Standard Model Higgs boson using up to 4.9 fb-1 of pp collision data at sqrt(s) = 7 TeV with the ATLAS detector at the LHC*, *Phys.Lett.* **B710** (2012) 49–66, [arXiv:1202.1408].
7. **CMS Collaboration** Collaboration, S. Chatrchyan *et. al.*, *Combined results of searches for the standard model Higgs boson in pp collisions at sqrt(s) = 7 TeV*, arXiv:1202.1488.
8. **ATLAS Collaboration** Collaboration, G. Aad *et. al.*, *Search for the Standard Model Higgs boson in the decay channel H→ZZ(*)→4l with 4.8 fb-1 of pp collision data at sqrt(s) = 7 TeV with ATLAS*, *Phys. Lett.* **B710** (2012) 383–402, [arXiv:1202.1415].
9. **CMS Collaboration** Collaboration, S. Chatrchyan *et. al.*, *Search for the standard model Higgs boson in the decay channel H to ZZ to 4 leptons in pp collisions at sqrt(s) = 7 TeV*, arXiv:1202.1997.
10. J. M. Campbell, R. K. Ellis, and C. Williams, *Vector boson pair production at the LHC*, *JHEP* **07** (2011) 018, [arXiv:1105.0020].

W/Z+jet results from the Tevatron

D.V. Bandurin (for the D0 and CDF Collaborations)
Department of Physics, Florida State University, Tallahassee, Florida 32306, USA

Selected quantum chromodynamics (QCD) measurements performed at the Fermilab Run II Tevatron $p\bar{p}$ collider running at $\sqrt{s} = 1.96$ TeV by D0 and CDF Collaborations are presented. Events with W/Z+jets productions are used to measure many kinematic distributions allowing extensive tests and tunes of predictions from perturbative QCD at next-to-leading (NLO) order and Monte-Carlo (MC) event generators.

1 Introduction

The D0 and CDF collaborations have extensively studied the W/Z+jet productions since these events are the main background to top-quark, Higgs boson, SUSY and many other new physics production channels. To make discoveries at the Tevatron and the LHC, these processes need to be measured and simulated with a level of accuracy that will be comparable to the significance of the new physics signals.

There are several programs on the market that can simulate hadronic interactions at NLO accuracy, but the processes included in these programs are limited. Matrix element plus parton shower (ME+PS) programs simulate a more comprehensive set of processes, typically at leading-log (LL) or leading order (LO) accuracy, and rely on models to simulate emissions and fragmentation associated with higher order processes. These programs have been employed regularly for background simulation at the Tevatron in recent years, notably in the Higgs searches [?] and the discovery of the production of single top quarks [?]. The Tevatron measurements presented here are compared to predictions by NLO pQCD in MCFM [?], BLACKHAT+SHERPA [?] and ROCKET+MCFM [?], ME+PS programs ALPGEN [?] and SHERPA [?], and PS programs HERWIG [?] and PYTHIA [?]. The most of measurements have been published [?,?,?,?,?] or approved as preliminary results [?,?,?] at the time these proceedings were written. ALPGEN employs the MLM algorithm to ensure jets originating from the matrix element and the parton shower are not double counted. SHERPA is a CKKW-inspired model which uses a re-weighting of the matrix elements to achieve the same appropriate jet configurations. A detailed description of these programs can be found in [?].

In this paper we review some of the recent Tevatron results on the W/Z+jet and W/Z+heavy flavor jet productions.

1.1 W/Z+jet production

Both collaborations have extensively studied the W/Z+jet productions with Z and W decaying via electron and muon decay modes. The leptonic decay of the Z/W provides a clean signal for reconstruction of the events, and small background contamination. The test of pQCD is made by comparing the measurements to NLO pQCD predictions. The W/Z + jets final states also make up a major background of many new physics searches at both the Tevatron and LHC. Therefore, these data measurements unfolded to the particle level are useful for tuning LO simulation programs which are heavily relied upon to model background processes.

Fig. **??** shows the inclusive cross section for Z/γ^*+jets production measured by CDF [?] as a function of leading and 3rd jet p_T (jets are ordered in descending p_T) in $Z+\geq$1 jet and in $Z+\geq$3 jet events. Also shown are dijet invariant mass and azimuthal angle between the two leading jets in $Z+\geq 2$ jet events. The measurements are in agreement with NLO pQCD predictions (BLACKHAT+SHERPA and MCFM) within theoretical scale uncertainties which are about 25%, obtained by variation of the default scale by a factor 2.

D0 measured jet p_T inclusive cross sections of $W+n$-jet production for jet multiplicities $n = 1-4$ [?]. The measurements are compared to the NLO predictions for $n = 1-3$ and to LO predictions for $n = 4$. The measured cross sections are generally found to agree with the NLO calculation although certain regions of phase space are identified where the calculations could be improved.

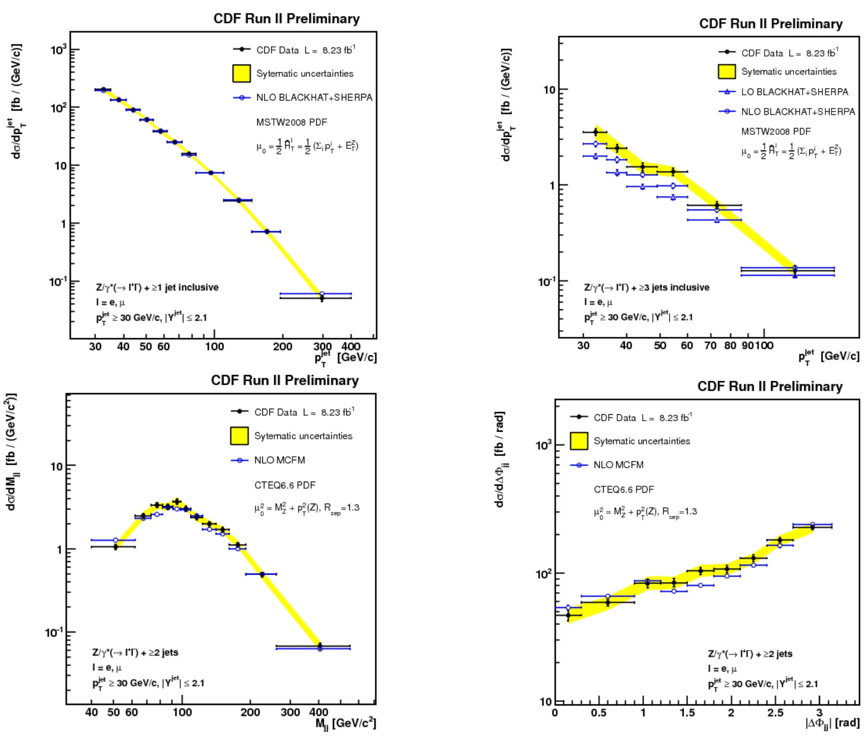

Figure 1: Two top plots show measured inclusive cross section for Z/γ^*+jets production as a function of leading jet p_T in $Z+\geq$1 jet events (top left) and 3rd jet p_T in $Z+\geq$3 jet events (top right) compared to NLO pQCD predictions using BLACKHAT+SHERPA. Two bottom plots show measured cross section as a function of dijet invariant mass (bottom left) and azimuthal angle between two jets (bottom left) in $Z+\geq$2 jet events; results are compared to NLO pQCD predictions using MCFM.

1.2 W/Z+heavy flavor jet production

D0 recently published the measured cross section ratio $\sigma(Z{+}b)/\sigma(Z{+}\text{jet}) = 0.0193 \pm 0.0022(\text{stat}) \pm 0.0015(\text{syst})$ for events with jet $p_T > 20$ GeV and $|\eta| < 2.5$ [?]. This most precise measurement of the $Z + b$ fraction is consistent with the NLO theory prediction, 0.0192 ± 0.0022, done with MCFM, renormalization and factorization scales set at m_Z, and the CDF result $0.0208 \pm 0.0033(\text{stat}) \pm 0.0034(\text{syst})$ [?]. The CDF collaboration measured the cross section of $W + b$-jet production $\sigma(W + b) \cdot Br(W \to l\nu) = 2.74 \pm 0.27(\text{stat}) \pm 0.42(\text{syst})$ pb with jet

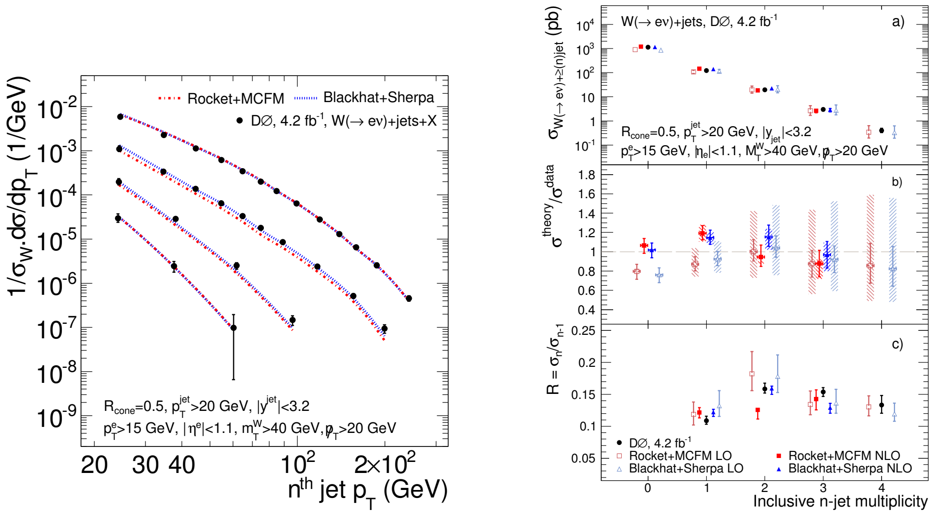

Figure 2: Left: measured $W + n$ jet differential cross section as a function of jet p_T for $n = 1-4$, normalized to the inclusive $W \to e\nu$ cross section. The $W + 1$ jet inclusive spectra are shown by the top curve, the $W + 4$ jet inclusive spectra by the bottom curve. The measurements are compared to the fixed-order NLO predictions for $n = 1-3$ and to LO predictions for $n = 4$. Right: (a) total inclusive n-jet cross sections σ_n as a function of n, (b) the ratio of the theory predictions to the measurements, and (c) σ_n/σ_{n-1} ratios for data, Blackhat+Sherpa and Rocket+MCFM. The hashed areas represent the theoretical uncertainty arising from the choice of renormalization and factorization scale.

$p_T > 20$ GeV, $|\eta| < 2.0$ and $l = e, \mu$. The measurement significantly exceeds the NLO prediction 1.2 ± 0.14 pb. The fit results for the b-jet fractions for both the measurements are shown in Fig. **??**.

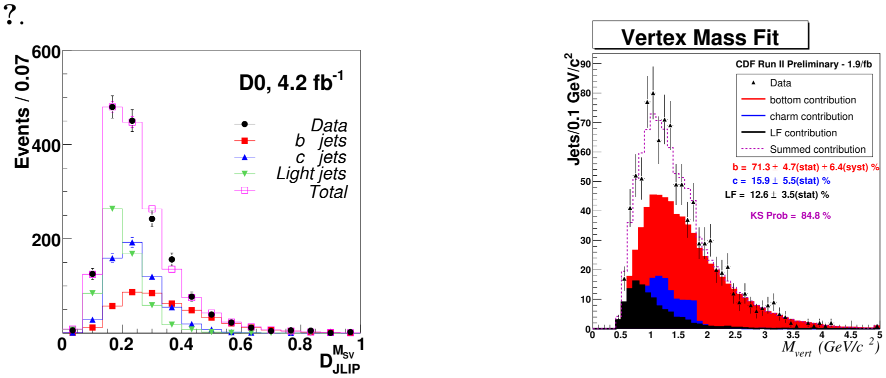

Figure 3: Left (D0): the distributions of the b, c, light jets and data over the $b-$jet discriminant; MC templates are weighted by the fractions found from the fit to data. Right (CDF): the secondary vertex mass fit for the tagged jets in the selected sample.

The CDF collaboration has also measured differential cross section of $Z + b$-jet production versus b-jet p_T and η[?]. Results are shown in Fig. **??**. The following cross sections ratio have been also measured, $\sigma(Z + b)/\sigma(Z) = 0.293 \pm 0.030(\text{stat}) \pm 0.036(\text{syst})\%$ and $\sigma(Z + b)/\sigma(Z + jet) = 2.31 \pm 0.23(\text{stat}) \pm 0.32(\text{syst})\%$.

Both experiments measured $W + c$ production cross section using the soft lepton tagging technique [?,?]. The D0 collaboration measured ratio $\sigma(W + c)/\sigma(W + jet)$ and found it to be $0.074 \pm 0.019(\text{stat})^{+0.012}_{-0.014}(\text{syst})\%$, what is higher than ALPGEN+PYTHIA predictions 0.044 ± 0.003. The CDF collaboration measured total cross section (electron and muon channels combined) and found $\sigma(W + c) \times Br(W \to l\nu, l = e, \mu) = 13.3^{+3.3}_{-2.9}$ pb what is in agreement with pQCD NLO predictions 11.3 ± 2.2 pb.

Summary

Several differential cross sections of W/Z + jet+X events measured with the D0 and CDF detectors have been presented. The data are generally consistent with predictions from NLO

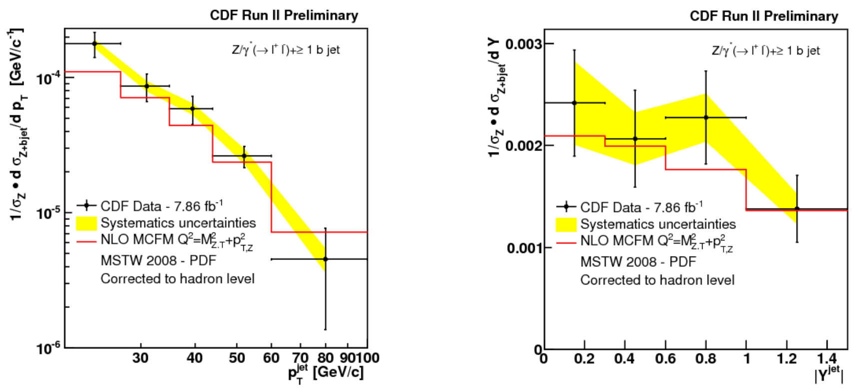

Figure 4: Differential cross section of $Z + b$ production as a function of b-jet p_T (left) and rapidity (right).

pQCD, although some LO programs can also reproduce the shape of the data, sometimes better than NLO, due either to their inclusion of higher parton multiplicity matrix elements than can be currently included in a fixed order pQCD calculation, or an optimized tune of MC. These data should be useful for continued tuning of these and other MC programs used at the Tevatron and LHC experiments.

Acknowledgments

The author would like to thank Mike Strauss and Christina Mesropian for a help in preparing the conference talk and this paper.

References

1. V.M. Abazov *et al.* [D0 Collaboration], *Phys. Lett.* B **663**, 26 (2008).
2. V.M. Abazov *et al.* [D0 Collaboration], *Phys. Rev. Lett.* **103**, 092001 (2009).
3. J.M. Campbell and R.K. Ellis, *Phys. Rev.* D **65**, 113007 (2002).
4. C.F. Berger *et al.*, arXiv:0905.2735 [hep-ph].
5. R.K. Ellis *et al.*, JHEP **01**, 012 (2009); W.T. Giele and G. Zanderighi, JHEP **06**, 038 (2008).
6. M.L. Mangano *et al*, JHEP **0307**, 001 (2003).
7. T. Gleisberg, S. Hoche, F. Krauss, M. Schonherr, S. Schumann, F. Siegert and J. Winter, JHEP **0902**, 007 (2009).
8. G. Corcella *et al.*, JHEP **0101**, 010 (2001).
9. T. Sjostrand, *et al* Comput. Phys. Commun. **135**, 238 (2001). [arXiv:hep-ph/0010017].
10. V.M. Abazov *et al.* [D0 Collaboration], *Phys. Lett.* B **669**, 278 (2008); *Phys. Lett.* B **682**, 370 (2010).
11. V.M. Abazov *et al.* [D0 Collaboration], *Phys. Lett.* B **705**, 200 (2011).
12. V.M. Abazov *et al.* [D0 Collaboration], *Phys. Rev.* D **83**, 031105 (2011)
13. T. Aaltonen *et al.* [CDF Collaboration], Phys.Rev. D **79**, 052008 (2009).
14. V.M. Abazov *et al.* [D0 Collaboration], *Phys. Lett.* B **666**, 23 (2008)
15. T. Aaltonen*et al.* [CDF Collaboration], *Phys. Rev. Lett.* **104**, 131801 (2010).
16. CDF Collaboration, http://www-cdf.fnal.gov/physics/new/qcd/zjets10fb/index.html
17. CDF Collaboration, http://www-cdf.fnal.gov/physics/new/qcd/wcharm2011/publicWc.html
18. CDF Collaboration, http://www-cdf.fnal.gov/physics/new/qcd/zbjet2012/index.html
19. J. Alwall *et al.*, EPJ **53**, 473 (2008).

W/Z + JETS AND W/Z + HEAVY FLAVOR PRODUCTION AT THE LHC

A.A. PARAMONOV
for the ATLAS and CMS collaborations
High Energy Physics Division, Argonne National Laboratory,Argonne, Illinois 60439, USA

The ATLAS and CMS experiments at the LHC conduct an extensive program to study production of events with a $W^{\pm}$ or Z^0 boson and particle jets. Dedicated studies focus on final states with the jets containing decays of heavy-flavor hadrons (b-tagged jets). The results are obtained using data from proton-proton collisions at $\sqrt{s} = 7$ TeV from the LHC at CERN. The set of measurements constitute a stringent test of the perturbative QCD calculations.

1 Introduction

Production of jets in association with a massive vector boson ($W^{\pm}$ or Z^0) is a well-understood process that provides tests of calculations based on quantum chromodynamics (QCD). These events are also substantial backgrounds to standard model (SM) measurements and searches for new physics. The studies of the associated production constitute a foundation for development of perturbative QCD (pQCD) calculations and Monte Carlo (MC) simulations. The ATLAS [1] and CMS [2] experiments at the LHC have reported their results using data from proton-proton collisions at $\sqrt{s} = 7$ TeV collisions in Refs. [3,4,5,6]. Previously, the associated production of a massive vector boson and jets was studied at the Tevatron using $p\bar{p}$ collisions at $\sqrt{s} = 1.96$ TeV. The measurements at the LHC offer wider reach in momenta of the jets than the previous studies.

Production of jets containing heavy-flavor hadrons in association with a massive boson is of special interest. The results of these studies are presented in Refs. [7,8,9,10,11]. Identification of jets with decays of heavy flavor hadrons, b-tagging, was performed via reconstruction of a secondary vertex within a jets. In Ref. [10] jets were not used but B-mesons were identified via secondary vertices from $B \to D + X$ decays. The associated production of heavy-flavor hadrons is less understood than of that of light particle jets. Therefore, the experimental input is of key importance for development of the MC simulations and pQCD calculations. Also, these measurements can provide constraints on the parton density functions (PDF's).

The measurements with a $W^{\pm}$ boson and a Z^0 boson are complementary. Both final states are sensitive to similar physics processes but they are different from the experimental point of view. The experimental signatures of the two bosons are different. Identification of a $W^{\pm}$ boson requires a well-identified lepton (an electron or a muon) and large imbalance of the vector sum of transverse momenta of all reconstructed objects in event (missing-p_{T}). Identification of a Z^0 requires two oppositely-charged leptons of the same flavor (two electrons or two muons).

All the experimental results have been corrected for all known instrumental effects and are often quoted is a specific range of jet and lepton kinematics, similar to the detector acceptance. That is done to avoid prediction-dependent extrapolation and to facilitate comparisons with theoretical predictions. Theoretical calculations at next-to-leading order (NLO) in pQCD are presented for final states with a vector boson and up to four jets.

2 Backgrounds and Systematic Uncertainties

Reconstruction of the di-lepton invariant mass allows significant reduction of backgrounds to events with a Z^0 boson. The majority of observed events are from the associated production of a Z^0 and jets. The irreducible backgrounds are the top quark pair production ($t\bar{t}$), dibosons, and Wt. These are estimated using MC simulations normalized with the measured luminosity and predicted cross sections. Background with one or two non-prompt ("fake") leptons are from events with a $W^{\pm}$ bosons and associated jets and multi-jet events, correspondingly. Rates of events with "fake" leptons are obtained using control regions in data. The requirement for a jet with decay of a heavy-flavor hadron enhances the fraction of events from the $t\bar{t}$ production.

Events with a $W^{\pm}$ boson and jets are produced at a higher rate than with a Z^0 boson. The major background with a non-prompt lepton is from the multi-jet production. The background is evaluated using orthogonal control regions in data. The contribution from multi-jet events is different for the electron and muon decay modes of $W^{\pm}$ bosons. Therefore, comparison of the measured cross section from the two decay modes can provide information of biases related to the evaluation of the backgrounds. The backgrounds with a prompt lepton are from $t\bar{t}$ production, dibosons, and events with a Z^0 boson and jet. The top pair production becomes the dominant background in final states with four or more jets (the jets are counted when $p_{\mathrm{T}} > 20$, 25, or 30 GeV). The top pair production is also substantial for events with a b-tagged jet. The top pair production is the dominant background that limits our ability to measure cross section for events with a $W^{\pm}$ and two b-jets. The top background is less prominent for measurements involving a Z^0 boson in the final state.

The major systematic uncertainties are from the jet energy scale (JES) calibration and efficiency of b-tagging. The uncertainty on the JES grows rapidly when the absolute value of jet rapidity is above two.

3 Results

The high cross section of the associated production of a massive boson and jets allows detailed studies of the kinematic distributions using differential and inclusive cross sections. Such studies have been performed by the CMS [3] and ATLAS [4,5,6] collaborations. Figs. 1 and 2 illustrate the cross sections measured as a function of inclusive jet multiplicity and transverse momentum of the leading jet. The studies have been conducted for a variety of kinematic observables such as invariant mass of multiple jets, angular and rapidity separation between jets, and so on. The measured ratios of cross sections allow cancellation of major systematic uncertainties.

The measured cross sections are compared to the NLO calculations from BlackHat-Sherpa and MC simulations from Pythia, Sherpa and Alpgen matched to Herwig. The NLO pQCD predictions are found in good agreement with data. Leading-order (LO) matrix element calculations for final states with a vector boson and up to five partons are matched to parton showering in Sherpa and Alpgen+Herwig. These two generators are also in good agreement with data.

Production of a charm hadron in a jet and a $W^{\pm}$ boson is reported in Ref. [11]. The study has sensitivity to the strange quark PDF. Ratios of cross sections were measured to be $\sigma(W^+\bar{c}+X)/\sigma(W^-c+X) = 0.92\pm0.19(\text{stat.})\pm0.04(\text{syst.})$ and $\sigma(Wc+X)/\sigma(W+jet+X) = 0.143 \pm 0.015(\text{stat.})\pm0.024(\text{syst.})$. The ratios are measured in the kinematic region $p_{\mathrm{T}}^{\mathrm{jet}} > 20$ GeV, $|\eta^{\mathrm{jet}}| < 2.1$ for $W \to \mu\nu$ decays. The measured results are in agreement with theoretical predictions at NLO based on available parton distribution functions.

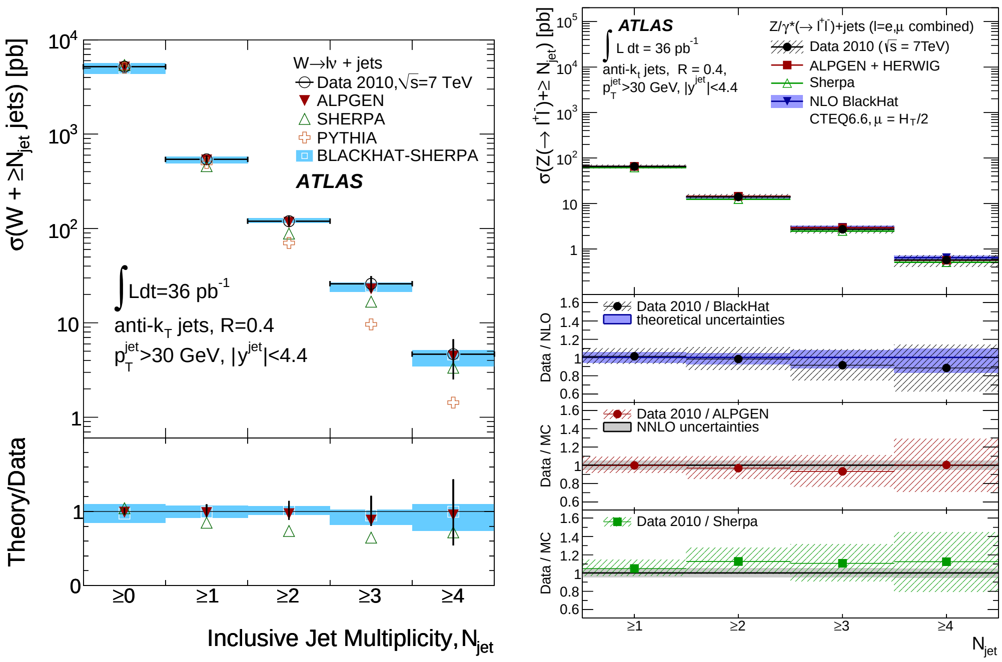

Figure 1: Measured cross sections as a function of jet multiplicity for events with a $W^{\pm}$ boson [6] (left) and with a Z^0 boson [5] (right). The solid bands correspond to the systematic uncertainties on the predicted cross sections.

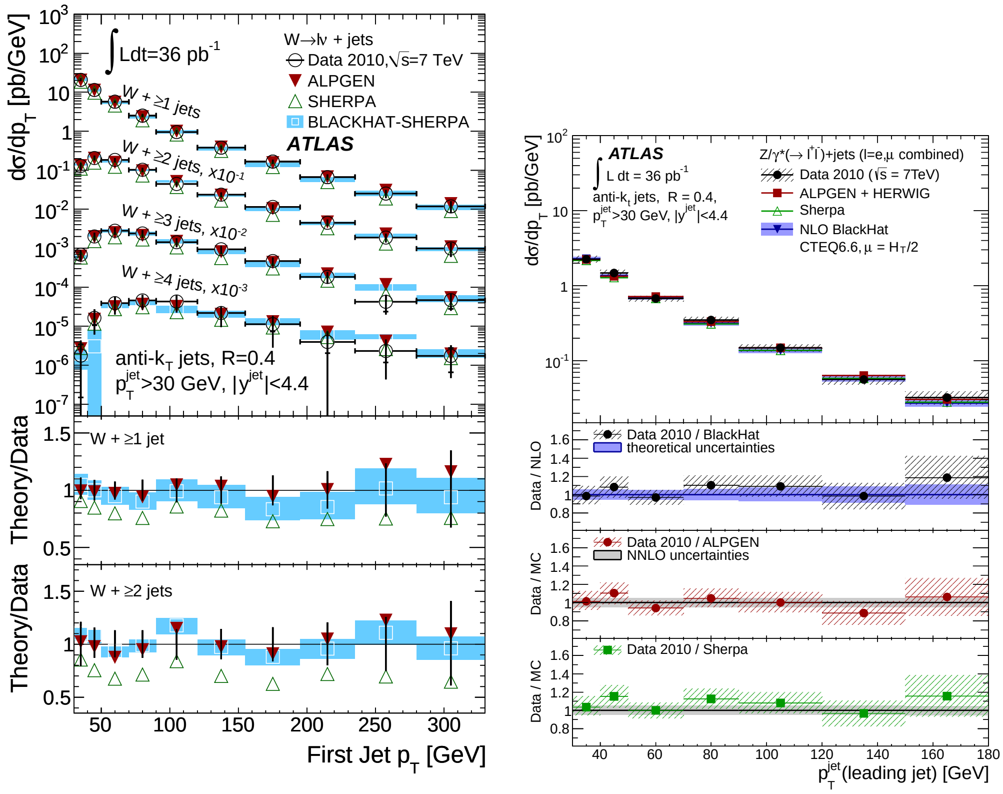

Figure 2: Measured cross sections as a function of p_T of the leading jet for events with a $W^{\pm}$ boson [6] (left) and with a Z^0 boson [5] (right). The solid bands correspond to the systematic uncertainties on the predicted cross sections.

Studies of the associated production of jets with decays of B mesons (b-jets) are described in Refs. [7,8,9]. These final state are backgrounds to the associated Higgs production; $pp \to HW$ and $pp \to HZ$, where $h \to b\bar{b}$. The results for production of a b-jet and a $W^{\pm}$ boson are presented in Fig. 3. The measured cross section slightly exceeds the predicted value for final states with a single b-jet and another jet. Ref. [7] presents cross sections for one and two b-jets with $p_T^{\mathrm{jet}} > 25$ GeV and $\eta^{\mathrm{jet}} < 2.1$. The measured cross sections are $\sigma(Z^0 + 2\ b\mathrm{-jets} + X) = 0.37 \pm 0.02(\mathrm{stat.}) \pm 0.07(\mathrm{syst.}) \pm 0.02(\mathrm{theory})$ pb and $\sigma(Z^0 +\ b\mathrm{-jet} + X) = 3.78 \pm 0.05(\mathrm{stat.}) \pm 0.31(\mathrm{syst.}) \pm 0.11(\mathrm{theory})$ pb. The cross section for two b-jets is in agreement with LO pQCD predictions.

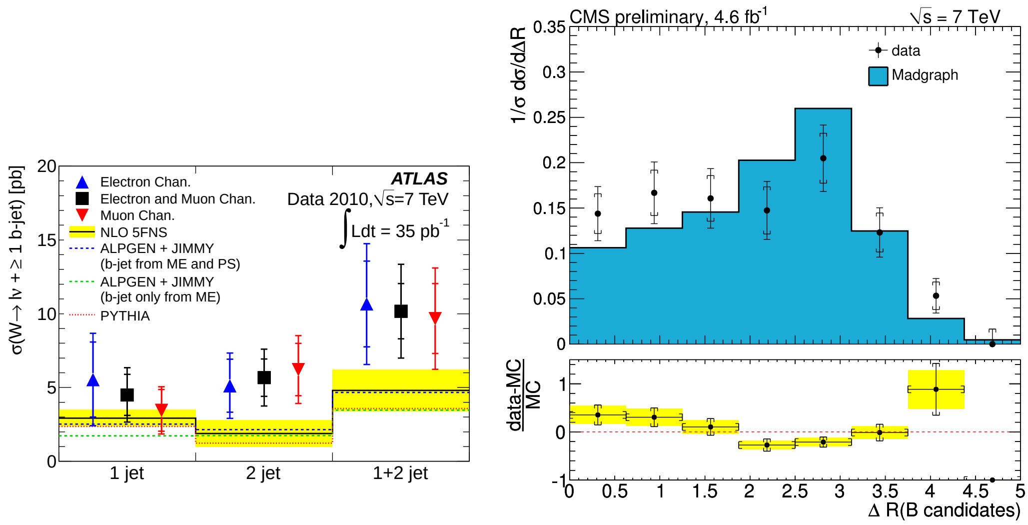

Figure 3: Exclusive cross sections for events with a b-jet and a $W^{\pm}$ (left) from ATLAS [8]. Distribution in angular separation, ΔR, between B meson candidates in events with a Z^0 (right) from CMS [10].

The study of the angular correlations between two B hadrons produced in association with a Z^0 boson is presented in Ref. [10]. Identification of B-hadron candidates utilizes displaced secondary vertices without involving jets. That allows to analyze production of B hadrons at small angular separation. The normalized production cross section as function of the angular separation is compared with QCD predictions at tree-level in Fig 3. The measurement is performed in the kinematic region defined for B hadrons with $p_{\mathrm{T}} > 15$ GeV and $|\eta| < 2$. This study gives further insight into the properties of heavy quark pair-production in association with a neutral vector bosons.

References

1. ATLAS Collaboration, JINST **3**, S08003 (2008)
2. CMS Collaboration, JINST **3**, S08004 (2008)
3. CMS Collaboration, JHEP **1201**, 010 (2012).
4. ATLAS Collaboration, *Phys. Lett.* B **708**, 221 (2012).
5. ATLAS Collaboration, *Phys. Rev.* D **85**, 032009 (2012).
6. ATLAS Collaboration, *Phys. Rev.* D **85**, 092002 (2012).
7. CMS Collaboration, CMS-PAS-SMP-12-003 (2012).
8. ATLAS Collaboration, *Phys. Lett.* B **707**, 418 (2012).
9. ATLAS Collaboration, *Phys. Lett.* B **706**, 295 (2012).
10. CMS Collaboration, CMS-PAS-EWK-11-015 (2012).
11. CMS Collaboration, CMS-PAS-EWK-11-013 (2011).

LATEST RESULTS ON JET PRODUCTION AND PROPERTIES FROM THE LHC

G. JONES
on behalf of the ATLAS and CMS collaborations
Department of Physics, University of Warwick, Gibbet Hill Road,
Coventry CV4 7AL, UK

Investigations of jets performed by the ATLAS and CMS collaborations using collisions at $\sqrt{s} = 7$ TeV are described. Topics of interest are jet performance, production and the precision measurement of their properties. Comparison of the results to theoretical predictions are discussed and areas with poor agreement identified.

1 Introduction

The LHC has made amazing progress in the past few years to provide the experiments with a tremendous increase in the amount of data available for analysis, where 2011 brought approximately 4.7 fb^{-1} of data. The study of jets at the LHC is an important topic for many analysis, not simply due to the nature of the hadron collider environment, but also because the signature of many processes involves the production of jets. The kinematic properties of a jet are believed to reflect those of the progenitor particle, and thus provides a window into the hard process of the original scatter. Therefore measurements of jets provide important tests of the Standard Model of particle physics.

2 Performance

Both collaborations have performed extensive performance studies for the measurement of jets. [1] [2] ATLAS reconstructs jets using the anti-kT jet algorithm [3] using recombination parameters equal to 0.4 and 0.6, which can be crudely thought of as the jet radius. The jet energy scale uncertainty was determined to be less than 5% in the central region for 2010 data. Additional interactions have so far been seen to contribute little to the overall jet uncertainty, with the dominant contribution being from the single particle calorimeter response. In situ techniques have been used to cross check the calibration of jets, where results have shown the simulation and MC based techniques are consistent within the derived uncertainties, as illustrated in figure 1b. The CMS collaboration has chosen to use the same jet algorithm but different recombination parameters, 0.5 and 0.7. In addition to the clustering of energy collected by the calorimeters CMS use information from other parts of the detector, such as the tracker, creating objects known as particle flow jets. This improves the resolution and response for jet measurements. The performance of these particle flow jets can be seen in figure 1a, where there is a low uncertainty in the jet energy calibration down to low jet transverse momentum, p_T.

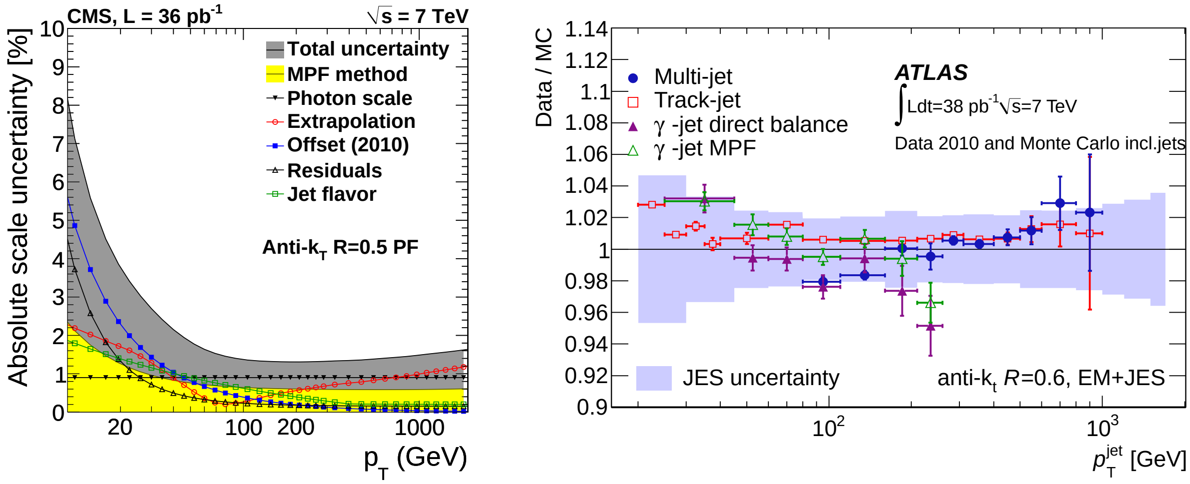

(a) (b)

Figure 1: The absolute uncertainty of the jet energy calibration as a function of jet p_T for particle flow jets in 2010 data is shown in figure (a). [2] The ratio of jet p_T to the reference jet using data and MC for a number of data driven techniques with the jet energy scale uncertainty shown as a reference in figure (b). [1]

3 Cross Section

The ATLAS and CMS collaborations have both published analysis [4 5] of the inclusive single jet and dijet cross sections using data samples corresponding to approximately 35 pb^{-1}, collected during 2010 running. The inclusive jet cross section was measured for jet p_T, between 20 GeV and 1.5 TeV, and split into absolute rapidity regions up to $|y| = 4.4$. The dijet mass cross section measurement has also been extended with masses observed between 70 GeV and 5 TeV. Good agreement was seen with the latest theoretical NLO jet predictions over many orders of magnitude, with no sign of physics beyond the Standard Model evident. Using the detailed information released about the correlations amongst the different systematic uncertainties it should be possible to use the data to provide new constraints on parton distribution functions. The larger integrated luminosity collected during 2011 is still undergoing analysis, however initial results are looking promising. Using the full dataset from 2011 ATLAS has measured the dijet mass cross section, in figure 2a, which has improved experimental uncertainties. Whilst figure 2b shows CMS has extended the single jet cross section to $p_T = 2$ TeV.

Analysis of the cross section for events containing both a forward and central jet allowed the study of collisions where one of the colliding partons could carry a small fraction of the total proton momentum, and so gave an opportunity to test different models of parton evolution. Results showed a large disagreement in the predicted and measured cross section for these events for many Monte Carlo generators. [6]

4 Jet Flavour

ATLAS has measured the $D^{*\pm}$ meson production rate in jets. Figure 3b shows the significant disagreement at low values of z, the fraction of jet momentum which the meson comprises. This indicated that current modelling of fragmentation by Monte Carlo generators is incorrect. An improved understanding of flavour composition would aid many analysis, given the large dependence of many of the jets properties on flavour.

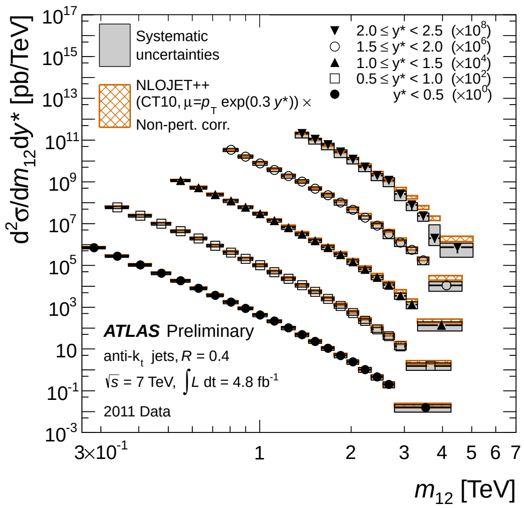

(a)

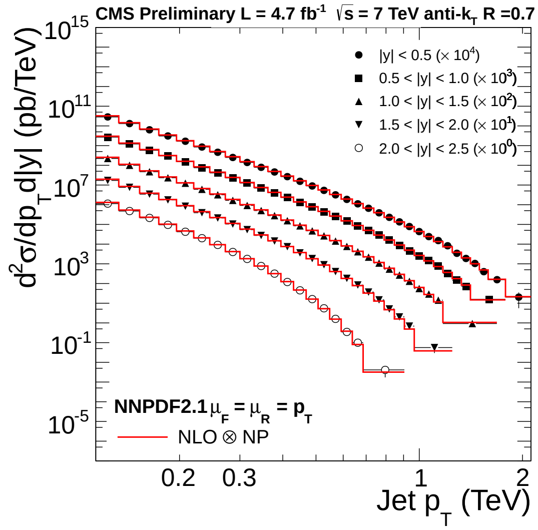

(b)

Figure 2: The mass of the dijet system measured in different regions of $y^* = |y_1 - y_2|/2$ in figure (a).[7] The inclusive single jet cross section measured in regions of absolute rapidity in figure (b).[8]

5 The Third Jet

Increasingly more complex final states have been analysed. Both the detection and prediction of these states is challenging. Even relatively simple $N_{\text{jet}} > 2$ events, which probe higher orders of QCD, are fraught with difficulties. The inclusive three to two jet cross section ratio has been measured by CMS up to a total transverse momentum sum of 2.5 TeV [10], see figure 3a. There is a general trend for the Monte Carlo simulations to predict too many three jet events at low total transverse momenta.

Studies have also been carried out with the restriction that any third jet must to be in a rapidity region bounded by the two highest p_T jets in an event [11]. A measurement was made of the probability of an event not containing a third jet with $p_T > 20$ GeV, resulting in a quantity known as the gap fraction. When the rapidity region or the average p_T of the leading jets was large, huge variations in theoretical predictions for the gap fraction were observed compared to the small experimental uncertainties. This precision measurement should prove useful for future theoretical development related to wide angle radiation.

6 Conclusions

A significant number of results have been published by each experiment at the LHC using data collected in both 2010 and 2011 involving jets. A wide range of precision jet measurements have been made, which required many detailed performance studies. Properties of jets are still understood even in the highest pile-up conditions seen so far. The jet measurements performed have shown good agreement with Standard Model predictions in many areas, however weaknesses such as in the large rapidity limit and the modelling of fragmentation are evident.

At the time of writing the LHC has started producing data at a new collision energy of $\sqrt{s} = 8$ TeV for the 2012 programme. The new running conditions will prompt yet another rediscovery of the Standard Model for many measurements involving jets and allow extensions to searches for exotic physics. Given the quantity and quality of results already available, the

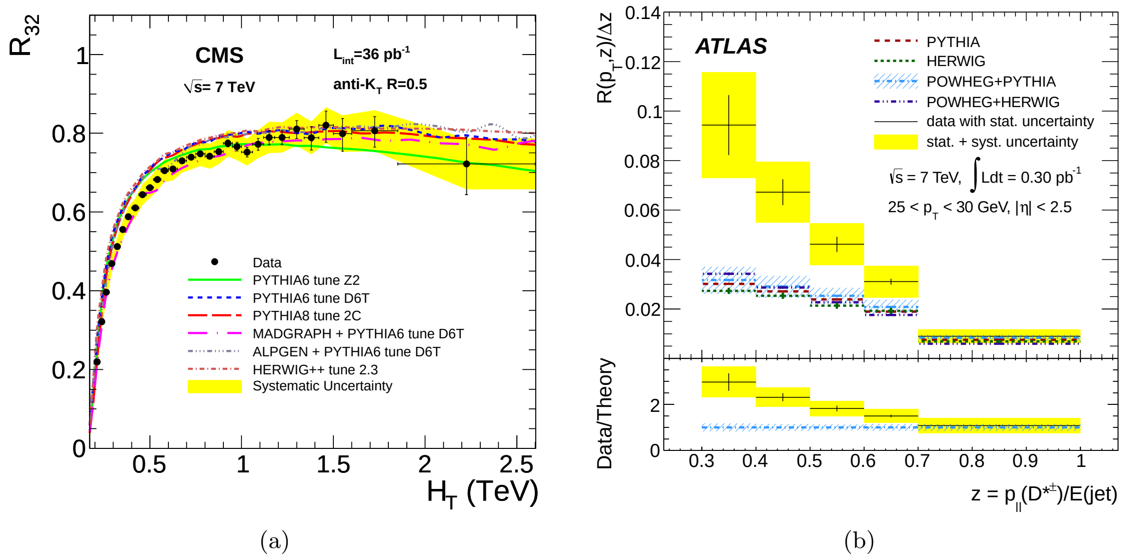

Figure 3: The inclusive three to two jet cross section ratio, R_{32}, shown as a function of the total transverse energy of the event, H_T in figure (a). [10] The production rate of $D^{*\pm}$ mesons, R, as a function of the fractional momentum of the jet it resided in, z in figure (b) . [9]

future is certainly bright for extending our knowledge of QCD and the Standard Model into previously unreachable territories.

Acknowledgements

This work was supported by the Science & Technology Facilities Council. I would also like to thank the organisers of Recontres de Moriond QCD 2012 for giving me the opportunity to present this work and hear so many interesting talks.

References

1. ATLAS Collaboration, CERN-PH-EP-2011-191 (2011), `https://cdsweb.cern.ch/record/1409965`.
2. CMS Collaboration, *JINST* **6**, 11002 (2011).
3. Cacciari et al., *JHEP* **4**, 63 (2008)
4. ATLAS Collaboration, CERN-PH-EP-2011-192 (2011), `https://cdsweb.cern.ch/record/1409964`.
5. CMS Collaboration, *Phys. Rev. Lett.* **107**, 132001 (2011).
6. CMS Collaboration, CMS-FWD-11-002; CERN-PH-EP-2011-179 (2012), `https://cdsweb.cern.ch/record/1421692`.
7. ATLAS Collaboration, ATLAS-CONF-2012-021 (2012), `https://cdsweb.cern.ch/record/1430730`.
8. CMS Collaboration, CMS-PAS-QCD-11-004 (2012), `https://cdsweb.cern.ch/record/1431022`.
9. ATLAS Collaboration, *Phys. Rev.* D **85**, 052005 (2012).
10. CMS Collaboration, *Phys. Lett.* B **702**, 336-354 (2011).
11. ATLAS Collaboration, *JHEP* **53**, 1109 (2011)

Subtraction method for parton shower to $2 \to 2$ matrix element matching in $k_\perp$-factorisation

M. Deák
Departamento de Física de Partículas, Facultade de Física,
Universidade de Santiago de Compostela, Campus Sur,
15706 Santiago de Compostela, Spain

We present a subtraction method for including next to leading order corrections to a 2 to 2 jet production process in kt-factorisation equivalent to a jet matching procedure in Monte Carlo generators. We study the improvement in soft cut dependance.

1 Motivation

Motivation for this work is to increase the precision of the fixed order calculation of multi-jet in $k_\perp$-factorisation by going beyond the fixed order of the QCD perturbation theory for the matrix element of the hard subprocess. The calculation is done in the context of a Monte Carlo generator, but the ideas have a general application. We push the ideas of[1] to take a step forward to inclusion of higher order corrections to this process.

The goal is to remove the dependence of observable cross sections on the soft cutoff. The soft cutoff is necessary to regularise matrix elements of $2 \to 2$ processes which exhibit collinear singularities [1]. The cutoff is applied in a form of cutoffs on each of the final state transversal momenta $p_{3\perp}, p_{4\perp} > p_{cut\perp}$. In $k_\perp$-factorisation the transversal momenta of the final state are not compensated and the contribution to the observed cross section of one jet depends on $p_{cut\perp}$ since $p_{3\perp}$, although fixed, does not fix $p_{4\perp}$. Consequently $p_{4\perp}$ can run through the integration region near the cutoff $p_{cut\perp}$ and generate big contributions to the observed cross section $\sigma(p_{3\perp})$.

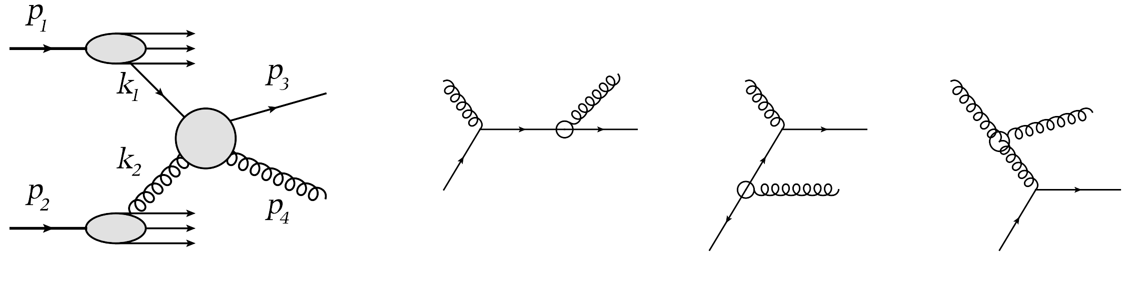

Figure 1: The notation and diagrams for the process.

One can express the above using simple formula. In $k_\perp$-factorisation on the other hand

(notation in the figure 1)

$$\frac{d^2\sigma(\mathbf{p}_3)}{d\mathbf{p}_3^2} = \int_0^1 d\xi_1 \int_0^1 d\xi_2 \int_{p_{cut\perp}} d^2\mathbf{p}_4 \, \frac{d^2\hat{\sigma}(\xi_1, \xi_2, \mathbf{p}_3, \mathbf{p}_4)}{d\mathbf{p}_3^2 d\mathbf{p}_4^2} \times \tilde{H}(\xi_1, \xi_2, \mathbf{p}_3 + \mathbf{p}_4, \mu^2(\mathbf{p}_3, \mathbf{p}_4)) \ . \tag{1}$$

In the equations above, H and $\tilde{H}$ are the non-perturbative factors related to the initial state radiation, μ^2 is the hard scale of the subprocess and ξ_1 and ξ_2 are the proton momentum fractions carried by the initial state partons.

A solution of the problem sketched above is regularisation of the hard $2 \to 2$ subprocess by virtual corrections.

A way to regularise the cross section is matrix element-shower jet matching. It has to be applied when including loop corrections or match parton showers with hard subprocesses with multi-jet final states in Monte Carlo generators based on collinear factorisation [2]. The peculiarity of $k_\perp$-factorisation causes that it has to be applied already for $2 \to 2$ processes.

In next chapters we describe regularisation of the cross section by the inclusion of virtual corrections using a Monte Carlo program framework and study of the cut dependence before and after regularisation.

2 Finite terms – Leading order shower versus the exact tree level matrix element

From previous introductory section follows, that calculations we are about to perform are mostly important for cases when we want to look at production of one or more jets using a $2 \to 2$ hard subprocess. For this purpose we are going to concentrate on one simplified example of the partonic subprocess $qg^* \to qg$. Note, that for simplification we made the quark on-shell. The chosen process $qg^* \to qg$ gives a very important contribution to forward jet production – a process important from the point of view of small-x physics [1].

We are going to take the leading order in α_S matrix element of the example process $qg^* \to qg$. Then we calculate the limits corresponding to all the collinear divergencies interpreting them as leading order in α_S parton shower of $2 \to 1$ process-generated $2 \to 2$ matrix elements. This allows us to remove the divergencies present in the full $2 \to 2$ matrix element and replace them with the full parton shower in which the divergencies are regulated by virtual corrections.

3 Virtual corrections

To calculate the virtual corrections we use a Monte Carlo parton shower implementation of the CCFM equation in the Monte Carlo program CASCADE [3].

Using a Monte Carlo implementation of the CCFM equation, we can generate extra external legs to a $2 \to 1$ process with above mentioned virtual corrections included. It is important to mention that we are going to calculate $qg^* \to qg$ convoluted with unintegrated parton density functions.

For the diagrams with emitted quark in the initial state we have used Monte Carlo implementation of the one loop CCFM equation and for a quark emitted from the final state leg an implementation of the DGLAP equation [3]. The virtual corrections in the latter cases are calculated in a similar way using corresponding final state or initial state evolution equation.

Using formulas from the previous section we can calculate the difference between the leading α_s approximation of the first emission from the $2 \to 1$ matrix element, figure 1, and the $2 \to 2$ process generated from $2 \to 1$ process by an extra emission in a shower algorithm. By doing the latter we calculate the virtual corrections present in the shower in form of the Sudakov and Non-Sudakov formfactors by

$$d\sigma^{virtual}_{qg^*\to qg} = d\sigma^{shower}_{qg^*\to qg} - d\sigma^{0}_{qg^*\to qg}, \tag{2}$$

where $d\sigma^{shower}_{qg^*\to qg}$ is the differential cross section of the $2 \to 2$ process calculated using the full shower algorithm and $d\sigma^{0}_{qg^*\to qg}$ is the leading α_s part of the emission.

In the next step we add add the difference $d\sigma^{virtual}_{qg^*\to qg}$ to the exact $2 \to 2$ matrix element:

$$d\sigma^{corrected}_{qg^*\to qg} = d\sigma^{exact}_{qg^*\to qg} + d\sigma^{virtual}_{qg^*\to qg}. \tag{3}$$

The differential cross section $d\sigma^{corrected}_{qg^*\to qg}$ includes virtual corrections resummed in Sudakov and Non-Sudakov formfactors present in parton showers.[a]

4 Results of the Monte Carlo implementation

We have studied the dependence of the transversal momenta cross sections of final state quark and gluon on the cut $p_{q\perp}, p_{g\perp} > p_{cut\perp}$. We have chosen values of $p_{cut} = 1$ and $2\ GeV$ and we have plotted ratios of cross sections for these two choices. We have fixed a cut on $|\mathbf{Q}| > p^{\mathbf{Q}}_{cut\perp} = 1\ GeV$ (defined by $\mathbf{Q} = (1-\nu)\mathbf{p}_4 - \nu\mathbf{p}_3$ and $\nu = (p_2 \cdot p_4)/(p_2 \cdot k_1)$ and related to final state collinear singularity).

A general feature of the plots in figures 2 to 3 is that the transverse momentum spectra of the quark and the gluon, calculated using the exact matrix element and the leading order shower, agree very well.

From the plots one can also see that the inclusion of the virtual corrections present in the parton showers reduces the dependence on the regulation cut. The reduction of the dependence on the cut is a consequence of cancelation of this dependence in equation (2), this result shows that the contribution of finite terms is relatively small.

We observe reduction of the dependence on the cutoff around $40-50\%$ in the quark case, figure 3 left, and even bigger reduction of the dependence, $70-80\%$ in the gluon case, figure 3 right.

The steep rise of the gluon transversal momentum spectrum explains the remaining dependence on the cut in the transversal momentum spectrum of the quark and other features of our plots, exactly in the spirit of the equation 1. A small change in cut on $p_{g\perp}$ produces a big change in the integral 1 which causes a shift in the observed cross section. This does not happen in the gluon case since the $p_{q\perp}$ spectrum exhibits a turnover at larger transversal momentum value.

5 Summary and Outlook

We have presented a simple prescription based on subtraction of cross sections for including loop corrections and IR regularisation of a $2 \to 2$ process in $k_\perp$-factorisation. We have also shown a successful application of the prescription to the process $qg^* \to qg$ important for forward jet production. We have studied transversal momentum cross sections for 2 produced jets with different cuts applied.

We observe a decrease in the dependence of the observed transversal momentum cross sections on the transversal momentum cutoff. In the case of the quark transversal momentum the improvement is around $40-50\%$. In the case of the gluon momentum even around $70-80\%$.

[a] Other way how to see equation (3) is by defining $d\sigma^{finite}_{qg^*\to qg} = d\sigma^{exact}_{qg^*\to qg} - d\sigma^{0}_{qg^*\to qg}$ and rewriting $d\sigma^{corrected}_{qg^*\to qg} = d\sigma^{shower}_{qg^*\to qg} + d\sigma^{finite}_{qg^*\to qg}$.

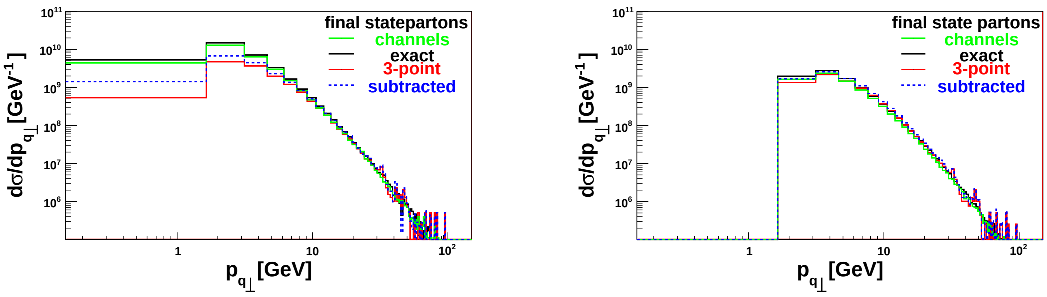

Figure 2: Transversal momentum of the quark $p_{q\perp}$ when cuts on $p_{q,g\perp} > 1\ GeV$. The dashed line labeled subtracted shows the result of equations (2) and (3).

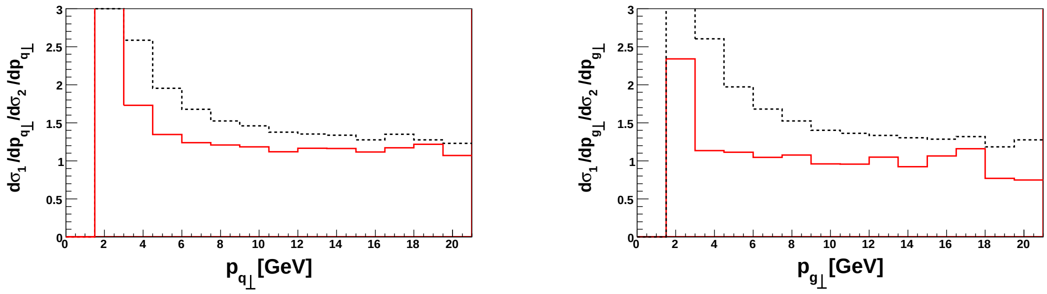

Figure 3: Ratios of the cross section of the quark transversal momentum $p_{q\perp}$ when cuts on $p_{q,g\perp} > 1\ GeV$ and $2\ GeV$. Red being the result of subtraction and black the full $2 \to 2$ matrix element. The dashed line labeled subtracted shows the result of equations (2) and (3).

A side observation of the calculation is that the contribution of the finite terms of the matrix element to the transversal momentum spectra is relatively small.

Next steps should involve application of the method to forward jet phenomenology. For this purpose extension to more complicated matrix elements will be necessary. For practical reasons and to remove the cutoff dependence completely it will be also good to formulate a prescription for jet matching on an event-by-event basis and implement it in a Monte Carlo generator.

6 Acknowledgements

1. M. Deak, F. Hautmann, H. Jung, and K. Kutak. Forward Jet Production at the Large Hadron Collider. *JHEP*, 09:121, 2009.
   M. Deak, F. Hautmann, H. Jung, and K. Kutak. Forward-Central Jet Correlations at the Large Hadron Collider. 2010.
2. S. Catani, F. Krauss, R. Kuhn, and B. R. Webber. QCD Matrix Elements + Parton Showers. *JHEP*, 11:063, 2001.
3. H. Jung, S. Baranov, M. Deak, A. Grebenyuk, F. Hautmann, et al. The CCFM Monte Carlo generator CASCADE version 2.2.03. *Eur.Phys.J.*, C70:1237–1249, 2010.

DIBOSON PRODUCTION CROSS SECTION AT THE TEVATRON

JESUS VIZAN
(On behalf of the CDF and D0 Collaborations)
CP3, Université catholique de Louvain,
Chemin du Cyclotron 2 bte L7.01.01, B-1348 Louvain-la-Neuve, Belgium

Recent results in diboson production in diverse final states from the CDF and D0 experiments in $p\bar{p}$ collisions at $\sqrt{s} = 1.96$ TeV at the Tevatron are reviewed. Special emphasis is given to the recent combined CDF and D0 measurement of WZ and ZZ production in final states with b-tagged jets. Assuming the ratio of the production cross sections $\sigma(WZ)$ and $\sigma(ZZ)$ as predicted by the standard model, the sum of the WZ and ZZ cross sections is measured to be $\sigma(WZ+WZ) = 4.47 \pm 0.64(\mathrm{stat.})^{+0.73}_{-0.72}$ (syst.) pb. This is consistent with the standard model prediction and corresponds to a significance of 4.6 standard deviations above the background-only hypothesis.

1 Introduction

Studies on the production of VV (V = W, Z) boson pairs provide an important test of the electroweak sector of the standard model (SM). In $p\bar{p}$ collisions at $\sqrt{s} = 1.96$ TeV, the next-to-leading order (NLO) SM cross sections for these processes are $\sigma(WW) = 11.3 \pm 0.8$ pb, $\sigma(WZ) = 3.2 \pm 0.2$ pb and $\sigma(ZZ) = 1.2 \pm 0.1$ pb [1]. These cross sections assume both $\gamma^\star$ and Z^0 components in the neutral current exchange and corresponding production of dilepton final states in the region $75 \leq m_{l^+l^-} \leq 105$ GeV/c^2. Measuring a significant departure in cross section or deviations in the predicted kinematic distributions would indicate the presence of anomalous gauge boson couplings [2] or new particles in extensions of the SM [3]. Diboson production is an important background in studies of the top quark, and searches for the Higgs boson and SUSY particles. Thus, precise knowledge of diboson processes and their proper modeling is important for current and future studies.

In the following sections, some of the most important measurements of the diboson production cross sections and of the trilinear gauge boson couplings (TGCs) [4] in different final states in $p\bar{p}$ collisions at the Fermilab Tevatron Collider will be presented.

2 $W\gamma$ and $Z\gamma$ Production

The cross section and the difference in rapidities between photons and charged leptons for inclusive $W(\rightarrow l\nu)+\gamma$ production in $e\gamma$ and $\mu\gamma$ final states is measured using D0 data corresponding to an integrated luminosity of 4.2 fb^{-1}. The measured cross section times branching fraction for the process $pp \rightarrow W\gamma + X \rightarrow l\nu\gamma + X$ and the distribution of the charge-signed photon-lepton rapidity difference are found to be in agreement with the standard model. These results provide limits on anomalous $WW\gamma$ couplings: $-0.4 < \Delta\kappa_\gamma < 0.4$ and $-0.08 < \lambda_\gamma < 0.07$ at the 95% confidence level [5].

The total and the differential production cross section, $d\sigma/dp_T^\gamma$, for $p\bar{p} \to Z\gamma \to l^+l^-\gamma$ ($l = e, \mu$) is measured with a D0 data sample corresponding to an integrated luminosity of 6.2 fb^{-1}. The results obtained are consistent with the standard model predictions from next-to-leading order calculations. The transverse momentum spectrum of the photon is used to place limits at 95% confidence level on anomalous $ZZ\gamma$ and $Z\gamma\gamma$ couplings for $\Lambda = 1.2$ TeV, $|h_{03}^Z| < 0.050$, $|h_{04}^Z| < 0.0033$, $|h_{03}^\gamma| < 0.052$, $|h_{04}^\gamma| < 0.0034$; and for $\Lambda = 1.5$ TeV, $|h_{03}^Z| < 0.041$, $|h_{04}^Z| < 0.0023$, $|h_{03}^\gamma| < 0.044$, $|h_{04}^\gamma| < 0.0023$ [6]. Another search for potential anomalous $Z\gamma$ couplings [7] is performed using 4.9 (5.1) fb^{-1} of CDF data using $Z\gamma$ candidates in the $Z \to \nu\bar{\nu}$ ($Z \to l^+l^-$, $l = e, \mu$) decay channel. Using an energy scale of $\Lambda = 1.5$ TeV the limits on the CP-conserving parameters that describe $Z\gamma$ couplings are set to $|h_{03}^{Z,\gamma}| < 0.022$ and $|h_{03}^{Z,\gamma}| < 0.0009$.

3 VV Production in Fully Leptonic Final States

VV production has been observed both by CDF and D0 collaborations in all of the 3 production modes (WW, WZ, ZZ) in fully leptonic final states. The W boson pair-production is observed using an integrated luminosity as low as 252 pb^{-1} of D0 data in the $l^+\nu l^-\bar{\nu}$ final state [8]. A more recent result using 3.6 fb^{-1} of CDF data [9] measures a W boson pair-production cross section of $\sigma(p\bar{p} \to W^+W^- + X) = 12.1 \pm 0.9(\text{stat.})^{+1.6}_{-1.4}(\text{syst.})$ pb using the same final state. The WZ production cross section is measured in the three charged lepton (e, μ) and one neutrino final state using 7.1 fb^{-1} of CDF data [10]. The measured cross section is $3.96^{+0.6}_{-0.5}(\text{stat.})^{+0.6}_{-0.4}(\text{syst.})$ pb. The ZZ production cross section is measured using the $l^+l^-l^+l^-$ and the $l^+l^-\nu\bar{\nu}$ final states using 8.6 fb^{-1} of D0 data [11]. The measured cross section is $1.44^{+0.35}_{-0.34}$ pb. All the previously described results are in good agreement with the standard model predictions.

4 VV Production in Semileptonic Final States

VV production has been observed as well at the Tevatron in semileptonic final states. The WW and WZ production with $l\nu q\bar{q}$ final states has been studied both by the CDF and D0 collaborations. Using matrix-element calculations a signal significance for $WW + WZ$ of 5.4 standard deviations is measured using 2.7 fb^{-1} of CDF data [12]. A complementary analysis uses the dijet invariant mass distribution and 3.9 fb^{-1} of data. Combining the results for both methods gives $\sigma(WW + WZ) = 16.0 \pm 3.3$ pb. Another analysis using 4.3 fb^{-1} of D0 data [13] rejects the background-only hypothesis at a level of 7.9 σ and measures a cross section of $\sigma(WW + WZ) = 19.6^{+3.2}_{-3.0}$ pb. Another analysis is performed using 3.5 fb^{-1} of CDF data [14] on a sample of events with large transverse momentum imbalance and two jets. This signature is sensitive not only to $l\nu q\bar{q}$, but also to $\nu\bar{\nu}q\bar{q}$ decays because no explicit requirement on the presence of identified charged leptons is applied. A cross section of $\sigma(p\bar{p} \to VV + X) = 18.0 \pm 2.8(\text{stat.}) \pm 2.4(\text{syst.}) \pm 1.1(\text{lumi.})$ pb, in agreement with the standard model prediction, is measured.

5 WZ and ZZ Production in Final States with b-tagged Jets

During the last years, the CDF and D0 experiments have studied the WZ and ZZ production in semileptonic decays with heavy flavor jets in the final state. The use of b-tagging requirements allows to separate the WW from the WZ and ZZ components. Assuming the ratio between the production cross sections $\sigma(WW)$ and $\sigma(WZ)$ as predicted by the standard model, the $WZ+ZZ$ signal is seen with a significance of 2.2 σ above the background-only hypothesis in the $l\nu q\bar{q}$ final state using 4.3 fb^{-1} of D0 data [13]. A similar CDF analysis [15] measures a significance of 1.08 σ using 7.5 fb^{-1} of data, while 1.9 σ are measured in a CDF search in the $\nu\nu q\bar{q}$ final state using 5.2 fb^{-1} of data [16]. More recently, the CDF and D0 collaborations have presented

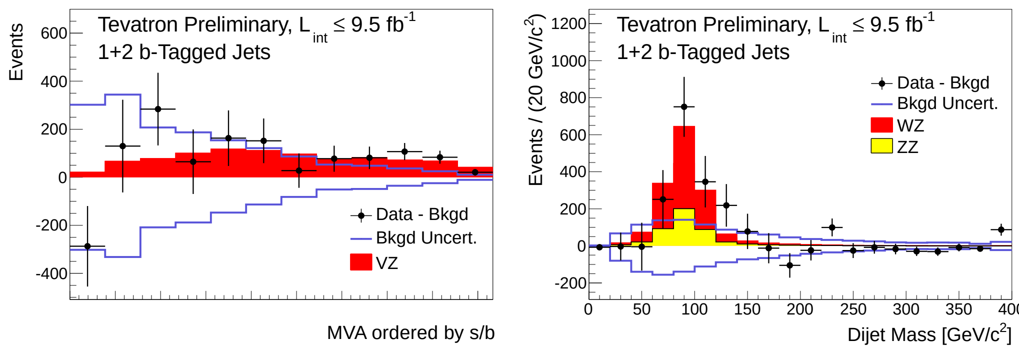

Figure 1: Comparison of the measured VZ signal (filled histograms) to background-subtracted data (points) after the maximum likelihood fit. Distributions of a variable that combines all final discriminants, where the bins are ordered by their expected signal to background ratio (s/b), and bins of comparable s/b are combined for display purposes (left), and of the dijet mass (right). Also shown is the ± 1 standard deviation uncertainty on the fitted background.

a combined measurement showing evidence for WZ and ZZ production in semileptonic decays with a b-tagged final state [17]. This analysis is relevant as a proving ground for the combined Tevatron search for a low-mass Higgs boson produced in association with a weak boson and decaying into a $b\bar{b}$ pair [18] since it shares the same selection criteria as well as analysis and combination techniques.

This result is a combination of the CDF and D0 searches in the $l\nu b\bar{b}$, $l^+l^-b\bar{b}$, and $\nu\bar{\nu}b\bar{b}$ final states. The total VZ cross section is determined from a maximum likelihood fit of the distributions of the multivariate discriminants (MVA) for the background and signal samples from the contributing analyses to the data. The cross section for the signal $(WZ + ZZ)$ is a free parameter in the fit, but the ratio of the WZ and ZZ cross sections is fixed to the SM prediction. The combined fit for the total VZ cross section distributions yields $\sigma(WW+WZ) = 4.47 \pm 0.64(\text{stat.})^{+0.73}_{-0.72}(\text{syst.})$ pb. This measurement is consistent with the NLO SM prediction of $\sigma(WW+WZ) = 4.4 \pm 0.3$ pb [1]. Based on the measured central value for the VZ cross section and its uncertainties, the observed significance is estimated to be 4.6 σ, while the expected significance is 4.8 σ.

To visualize the sensitivity of the combined analysis, the expected signal over background (s/b) is calculated in each bin of the MVA distributions from the contributing analyses. Bins with similar s/b are then combined to produce a single distribution, shown in Figure 1. The background subtracted dijet mass distribution is also shown in Figure 1 demonstrating the presence of a hadronic resonance in the data consistent with the SM expectation, both in shape and normalization.

Summary

A wealth of results about diboson production in diverse final states from the CDF and D0 experiments in $p\bar{p}$ collisions at $\sqrt{s} = 1.96$ TeV at the Tevatron has been presented. In the most recent one, the combined CDF and D0 measurement of WZ and ZZ production in final states with b-tagged jets, a diboson production cross section of $\sigma(WW+WZ) = 4.47 \pm 0.64(\text{stat.})^{+0.73}_{-0.72}(\text{syst.})$ pb, in good agreement with the standard model prediction, is measured. This result validates the analysis techniques applied to the Tevatron search for a low-mass Higgs boson produced in association with a weak boson and decaying into a $b\bar{b}$ pair.

Acknowledgments

We thank the Fermilab staff and the technical staffs of the participating institutions for their contributions, and we acknowledge support from the DOE and NSF (USA); CONICET and UBACyT (Argentina); ARC (Australia); CNPq, FAPERJ, FAPESP and FUNDUNESP (Brazil); CRC Program and NSERC (Canada); CAS, CNSF, and NSC (China); Colciencias (Colombia); MSMT and GACR (Czech Republic); Academy of Finland (Finland); CEA and CNRS/IN2P3 (France); BMBF and DFG (Germany); INFN (Italy); DAE and DST (India); SFI (Ireland); Ministry of Education, Culture, Sports, Science and Technology (Japan); KRF, KOSEF and World Class University Program (Korea); CONACyT (Mexico); FOM (The Netherlands); FASI, Rosatom and RFBR (Russia); Slovak R&D Agency (Slovakia); Ministerio de Ciencia e Innovacion, and Programa Consolider-Ingenio 2010 (Spain); The Swedish Research Council (Sweden); Swiss National Science Foundation (Switzerland); STFC and the Royal Society (United Kingdom); and the A.P. Sloan Foundation (USA).

References

1. J. M. Campbell and R. K. Ellis, *Phys. Rev.* D **60**, 113006 (1999). We used MCFM v6.0. Cross sections are computed using a choice of scale $\mu_0^2 = M_V^2 + P_T^2(V)$, where V is the vector boson, and the MSTW2008 PDF set.
2. K. Hagiwara, S. Ishihara, R. Szalapski, and D. Zeppenfeld, *Phys. Rev.* D **48**, (1993).
3. J. C. Pati and A. Salam, *Phys. Rev.* D **10**, 275 (1974); 11 703(E) (1975);
   G. Altarelli, B. Mele, and M. Ruiz-Altaba, *Z. Phys.* C **45**, 109 (1989); 47, 676(E) (1990);
   L. Randall and R. Sundrum, *Phys. Rev. Lett.* **83**, 3370 (1999);
   H. Davoudiasl, J. L. Hewett, and T. G. Rizzo, *Phys. Rev.* D **63**, 075004 (2001);
   H. He et al., *Phys. Rev.* D **78**, 031701 (2008).
4. K. Hagiwara, J. Woodside, and D. Zeppenfeld, *Phys. Rev.* D **41**, 2113 (1990);
   U. Baur, and E. Berger, *Phys. Rev.* D **47**, 4889 (1993).
5. V. M. Abazov *et al* (D0 Collaboration), *Phys. Rev. Lett.* **107**, 241803 (2011).
6. V. M. Abazov *et al* (D0 Collaboration), *Phys. Rev.* D **85**, 052001 (2012).
7. T. Aaltonen *et al* (CDF Collaboration), *Phys. Rev. Lett.* **107**, 051802 (2011).
8. V. M. Abazov *et al* (D0 Collaboration), *Phys. Rev. Lett.* **94**, 151801 (2005).
9. T. Aaltonen *et al* (CDF Collaboration), *Phys. Rev. Lett.* **104**, 201801 (2010).
10. CDF Collaboration, "Measurement of the WZ Production Cross Section in $p\bar{p}$ Collisions $\sqrt{s} = 1.96$ TeV using 7.1 fb^{-1} of CDF Run II Data", CDF Conference Note 10176 (2011).
11. D0 Collaboration, "A measurement of the WZ and ZZ production cross sections using leptonic final states in 8.6 fb^{-1} of $p\bar{p}$ collisions", FERMILAB-PUB-12-022-E (2012).
12. T. Aaltonen *et al* (CDF Collaboration), *Phys. Rev. Lett.* **104**, 101801 (2010).
13. V. M. Abazov *et al* (D0 Collaboration), *Phys. Rev. Lett.* **108**, 181803 (2012).
14. T. Aaltonen *et al* (CDF Collaboration), *Phys. Rev. Lett.* **103**, 091803 (2009).
15. CDF Collaboration, "Evidence for $WZ/WW \to l\nu +$ Heavy Flavor Vector Boson Production in 7.5 fb^{-1} of CDF data", CDF Conference Note 10598 (2011).
16. T. Aaltonen *et al* (CDF Collaboration), *Phys. Rev.* D **85**, 012002 (2012).
17. The CDF and D0 Collaborations and the TEVNPH Working Group, "Combined CDF and D0 measurement of WZ and ZZ production in final states with b-tagged jets", FERMILAB-CONF-12-068-E, arXiv:1203.3782v1 [hep-ex] (2012).
18. The CDF and D0 Collaborations and the TEVNPH Working Group, "Combined CDF and D0 Search for Standard Model Higgs Boson Production with up to 10.0 fb^{-1} of Data", FERMILAB-CONF-12-065-E, arXiv:1203.3774v1 [hep-ex] (2012).

DIBOSON PRODUCTION CROSS SECTION AT $\sqrt{s} = 7$ TEV

J. MALCLES on behalf of the ATLAS and CMS experiments at the LHC
CEA-Saclay SPP-IRFU, 91191 GIF-SUR-YVETTE

We present the latest measurements of diboson production cross sections in pp collisions at a center-of-mass energy of 7 TeV, based on data recorded by the ATLAS and CMS detectors at the LHC in 2010 and 2011. New measurements are highlighted. Updated WW and ZZ production cross-sections are presented. The search for a resonant enhancement in the dijet mass spectrum in W plus 2 or 3 jets events and the first observation of Z decaying to 4 leptons at hadron colliders are shown. The results are compared to SM predictions.

1 Introduction

The Standard Model (SM) gauge sector stands explicitely the interactions between gauge bosons. Triple terms and quartic terms appear in the lagrangian density after the spontaneous electroweak symmetry breaking and determine the gauge structure of the interactions between bosons. The strength of these interactions is a non trivial prediction of the electroweak theory and a unique signature of the non abelian nature of the gauge symmetry. Anomalous effects in triple gauge couplings (TGCs) would lead to an increase of the diboson production cross-section with regard to the SM, specially for large invariant masses of the diboson system. Diboson production measurement is thus a direct probe of the Standard Model. Diboson production is also a major background in many searches, namely the SM Higgs boson search in four leptons.

Production cross sections of WW, $W\gamma$ and $Z\gamma$ were measured by both ATLAS and CMS for Moriond 2011 [1] with approximately 35 pb^{-1}. For summer conferences, with 1 fb^{-1}, WW production measurement was updated [2] and WZ and ZZ production cross sections were measured [3]. These results are in good agreement with the SM. We focus here on updates of WW and ZZ production cross sections by ATLAS [4,5]. The study of the dijet mass spectra and the observation of $Z \to 4\ell$ by CMS [7,6] are also shown. These results are based on 4.7 fb^{-1}.

Despite their small branching ratio, the boson decays considered in these analyses are leptonic decays, as they have clean signatures and low QCD backgrounds. The main backgrounds are QCD multijets or W plus jets with jets faking leptons, top ($t\bar{t}$ or Wt, $t \to Wb$), Drell-Yan and other diboson modes. Major backgrounds are determined with data-driven techniques.

2 Update on WW production with 4.7 fb^{-1} (ATLAS)

The signal is selected in three different channels: ee, $e\mu$ and $\mu\mu$, with leptons of opposite charges and $p_T > 20$ GeV. The event is required to have large M_{ET} from the undetected neutrinos. The leading lepton p_T has to be greater than 25 GeV for the ee and $\mu\mu$ modes, whereas the electron p_T has to be greater than 25 GeV in the $e\mu$ mode. QCD and W+jets backgrounds are reduced by tight lepton identification and isolation criteria. Drell-Yan and other diboson backgrounds are suppressed by applying a veto on events with a dilepton invariant mass around the Z mass ±15 GeV for same flavor events. The top background is reduced by requiring no jet with $p_T > 25$ GeV ("jet veto"), and further suppressed by requiring no b-tagged jet with $p_T > 20$ GeV ("top veto"). Backgrounds from jets faking leptons are estimated from a fake rate measurement in data used to extrapolate the background yield from a W+jets control region to the signal region. The top background is estimated with Monte-Carlo (MC) and corrected with a data/MC factor for the jet veto efficiency. The Drell-Yan is also taken from MC with a data/MC correction determined from the M_{ET} tail in the Z peak region. The acceptance and efficiencies from simulation are corrected with data/MC ratio for lepton ID and jet veto efficiencies determined on Z events with the "tag-and-probe" method. The systematic uncertainty is about 8% and comes mainly from the W+jets and top backgrounds knowledge ($\simeq$ 5%) and the signal efficiencies ($\simeq$ 7%). The measured cross section is given in equation 1 and is in good agreement with previous measurements [1,2] and with the prediction from theory: $\sigma_{WW}^{\text{theo}} = 45.1 \pm 2.8$ pb.

$$\sigma_{WW} = 53.4 \pm 2.1 \text{ (stat.)} \pm 4.5 \text{ (syst.)} \pm 2.1 \text{ (lumi.) pb} \tag{1}$$

3 Update on ZZ production with 4.7 fb^{-1} (ATLAS)

The ZZ production cross section is measured using the four-lepton decay channel, where the term lepton is used for electrons and muons. Events are selected by requiring four leptons with $p_T > 7$ GeV, forming two opposite-sign same-flavour lepton pairs with $66 < m_{\ell^+\ell^-} < 116$ GeV, with the leading lepton required to have $p_T > 20\,(25)$ GeV if it is a muon (electron). Leptons are required to be isolated and well identified. Heavy flavor decays are rejected by cutting on the leptons impact parameters. The sample after selection is almost background free, as it is shown in figure 1. The number of observed candidate events in the acceptance is 62 for a background expectation of 0.7 ± 1.8. The efficiencies are determined from MC and corrected for eventual differences with data using the "tag-and-probe" method on Z events. The systematic uncertainty is about 5%. The total ZZ production cross section measurement, extrapolated to the full phasespace using SM predicted kinematic distributions and corrected for the $ZZ \to \ell^+\ell^-\ell^+\ell^-$ branching fraction, is given by equation 2 and is consistent with the SM prediction: $\sigma_{ZZ}^{\text{tot, theo}} = 6.5 \pm 0.3$ pb.

$$\sigma_{ZZ}^{\text{tot}} = 7.2^{+1.1}_{-0.9} \text{ (stat.)}^{+0.4}_{-0.3} \text{ (syst.)} \pm 0.3 \text{ (lumi.) pb} \tag{2}$$

4 Dijet mass spectra in W plus 2 or 3 jets events 4.7 fb^{-1} (CMS)

This section presents the study of the invariant mass spectrum m_{jj} of the two jets with the highest transverse momentum in events with two or three jets produced in association with a W boson. In events with a lepton plus jets, the CDF collaboration reported evidence for an excess around 150 GeV over the m_{jj} distribution expected from the SM processes [8]. The D0 collaboration did not confirm this result [8]. The analysis is performed in the e and μ W boson decay channels. The muon (electron) is required to have $p_T > 25\,(35)$ GeV, with $M_{ET} > 25\,(30)$ GeV, and a transverse mass $m_T = \sqrt{2p_T^\ell M_{ET}(1 - cos(\Delta\phi(\ell, M_{ET})))} > 50$ GeV. Events with a second lepton passing looser quality criteria and with $p_T > 10\,(20)$ GeV for muon (electron) are disregarded to reduce the Drell-Yan contribution. Furthermore, we require the presence of exactly two or three jets in the event with $p_T > 40$ GeV for the leading p_T jet and $p_T > 30$ GeV for the second and third jets. The selected jets and the lepton from the W decay are required to originate from the same primary vertex. Jet energy corrections are applied versus p_T and η to account for jet energy resolution variations and pile-up. The selected data sample is dominated

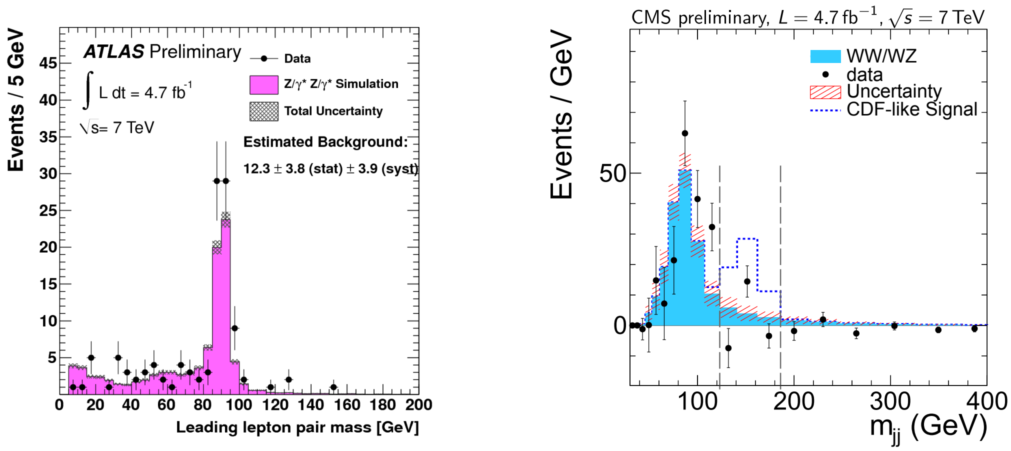

Figure 1: Leading lepton pair mass distribution for ZZ candidates in all four-lepton channels (left), without applying the dilepton mass requirements. Dijet invariant mass spectrum after substraction of the major backgrounds (right): the diboson signal is the only background left and there is no evidence for a resonant enhancement.

by events with W plus two or more jets. Smaller contributions come from top pairs, single top, Drell-Yan plus two or more jets, and multijet production. A small fraction of events is due to WW and WZ diboson production. We determine the relative contribution of the known SM processes to the observed m_{jj} spectrum using an unbinned maximum likelihood fit in the range between 40 GeV and 400 GeV.

The m_{jj} region between 123 and 186 GeV is excluded from this fit. The templates used in the fit are taken from MC except for the multijets background taken from a control sample with the lepton failing the isolation criteria. The normalisation of the W+jets background is free in the fit. As shown on the right in figure 1, there is no evidence for a resonant enhancement in the background substracted dijet mass spectrum.

The dominant systematic uncertainties arise from the jet energy scale, the M_{ET} resolution and the trigger and lepton ID efficiencies. A potential signal is excluded by testing a generic gaussian signal hypothesis around 150 GeV, with a width 15 GeV corresponding to a CDF-like signal with the CMS resolution. An upper limit on the cross section times branching fraction is set at 95% of confidence level at 1.3 pb, to be compared with the CDF excess of 3.4 pb.

5 First observation of $Z \to 4\ell$ at hadron colliders with 4.7 fb^{-1} (CMS)

All four LEP collaborations reported observations of four-fermion production $e^+e^- \to 4f$, which includes $e^+e^- \to Z \to 4f$ [9]. However, the observation of $Z \to 4\ell$ decays in pp collisions is of special interest. The clean resonant peak in the four-lepton invariant mass distribution at $m_{4\ell} = m_Z$ can be used as a standard candle for direct calibration of the four-lepton mass scale, the four-lepton mass resolution, and the overall four-lepton reconstruction efficiency in phase space similar to the Higgs boson four-lepton decays, $H \to ZZ \to 4\ell$.

The main irreducible background, $q\bar{q} \to Z\gamma^\star \to 4\ell$ is an initial state radiation whereas the signal $q\bar{q} \to Z \to 4\ell$ is a final state radiation. The interference term between signal and background is negligible in the analysis range, which allows to discuss the two production mechanisms separately. We define signal events as those with four leptons ($4e$, 4μ, $2e2\mu$), with $80 < m_{4\ell} < 100$ GeV and di-lepton masses for all pairings of leptons satisfying $m_{\ell\ell} > 4$ GeV. Lepton are selected with $p_T > 7\,(5)$ GeV and $|\eta| < 2.5\,(2.4)$ GeV for $e(\mu)$. The two hardest leptons are required to have a p_T greater than 20 GeV and 10 GeV. Isolation requirement are applied, after correcting the isolation for pile-up and other leptons. Heavy-flavour decays are rejected by cutting on the leptons impact parameters. We observe 26 events, in agreement with

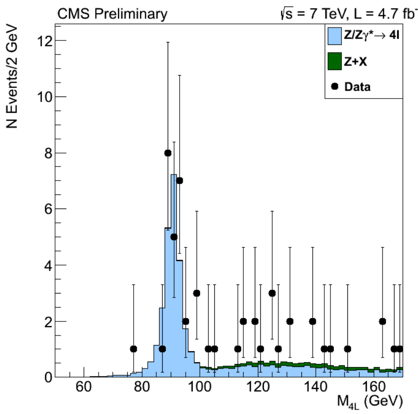

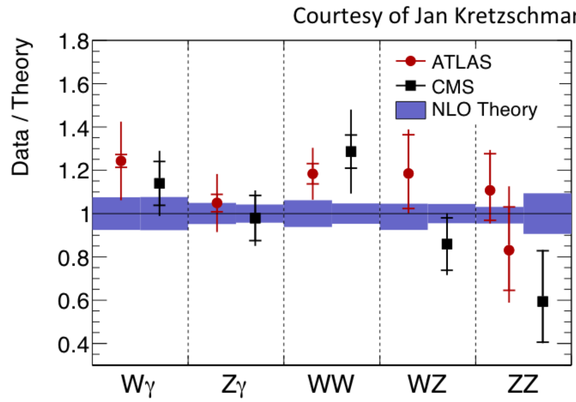

Figure 2: Left: four lepton mass distribution in data (black points) and simulation (blue). Right: up-to-date data over theory ratio for several diboson channels and both experiments.

the expected rate of 25.0 events, this analysis being almost background free (0.4 ± 0.1 expected background events). A pronounced resonance peak is observed in the $m_{4\ell}$ distribution (figure 2, right). The efficiencies are determined from MC and corrected with data using Z events and the "tag-and-probe" technique. The measured cross section times branching fraction is given in equation 3 and is consistent with the standard model prediction of 120 fb. The measured branching fraction of $Z \to 4\ell$ decays with a cut on the minimum dilepton mass $m_{2\ell} > 4$ GeV is given in equation 4 and agrees with the SM expectation 4.45×10^{-6}. With the current data, a fit to the observed four lepton mass leads to a precision on the mass scale of about 0.5%.

$$(\sigma \times BR)_{Z\to 4\ell} = 125^{+26}_{-23}\ (\mathrm{stat.})^{+9}_{-6}\ (\mathrm{syst.})^{+7}_{-5}\ (\mathrm{lumi.})\ \mathrm{fb} \tag{3}$$

$$BR_{Z\to 4\ell} = 4.4^{+1.0}_{-0.8}\ (\mathrm{stat.}) \pm 0.2\ (\mathrm{syst.}) \times 10^{-6} \tag{4}$$

6 Conclusion

Diboson studies at the LHC are now beyond the observation phase and all the results are in good agreement with SM expectations so far (see figure 2, right). With more statistics, precision will keep on increasing and interpretations of the latest results in terms of limits on TGCs are still to come.

References

1. ATLAS, ATLAS-CONF-2011-015 (2011); CMS, CMS-EWK-10-009, CERN-PH-EP-2011-015 (2011); ATLAS, ATLAS-CONF-2011-013 (2011); CMS, *Phys. Lett.* B **701**, 535 (2011).
2. ATLAS, ATLAS-CONF-2011-110 (2011); CMS, CMS-EWK-11-010 (2011).
3. ATLAS, ATLAS-CONF-2011-099 (2011); CMS, CMS-EWK-11-010 (2011); ATLAS, ATLAS-CONF-2011-107 (2011); CMS, CMS-EWK-11-010 (2011).
4. ATLAS, ATLAS-CONF-2012-025 (2012).
5. ATLAS, ATLAS-CONF-2012-026 (2012).
6. CMS, CMS-SMP-12-009 (2012).
7. CMS, CMS-EWK-11-017 (2012).
8. CDF, *Phys. Rev. Lett.* **106**, 171801 (2011); D0, *Phys. Rev. Lett.* **107**, 011804 (2011).
9. ALEPH, *Phys. Lett.* B **263**, 112 (1991); OPAL, *Phys. Lett.* B **287**, 389 (1992); L3, *Phys. Lett.* B **321**, 283 (1994); DELPHI, *Nucl. Phys.* B **403**, 3 (1993).

Precision Multiboson Phenomenology

G. Bozzi[1], F. Campanario[2, a], C. Englert[3], M. Rauch[2], M. Spannoswky[3], D. Zeppenfeld[2]
[1] *Dipartimento di Fisica, Università di Milano and INFN, Sezione di Milano*
Via Celoria 16, I-20133 Milano, Italy
[2] *Institute für Theoretische Physik, Universität Karlsruhe, KIT,*
76128 Karlsruhe, Germany
[3] *Institut for Particle Physics Phenomenology, Department of Physics, Durham University, Durham, United Kingdom*

We present recent results in precision multiboson (+jet) phenomenology at the LHC. Results for diboson + jet, triboson, and also for $W^{\pm}\gamma\gamma$+ jet will be discussed focusing on the impact of the perturbative corrections on the expected phenomenology.

1 Introduction

Processes with multiple electroweak bosons are important channels to test the Standard Model (SM) at the LHC. They are important backgrounds to SM and also to beyond standard physics searches. As a signal, they allow us to obtain information on triple and quartic couplings, and therefore, to quantify deviations from the SM prediction through, e.g., anomalous couplings.

To match the experimental accuracy, precise and reliable predictions beyond the leading order (LO) perturbative expansion are required not only for cross sections but also for differential distributions. As part of such a program we have, in the past, determined next-to-leading-order (NLO) QCD corrections for the production cross sections of all combinations of three electroweak bosons [1,2], to $W\gamma$ + jet [3,4] , WZ + jet [5,6] and also to $W^{\pm}\gamma\gamma$+ jet [7], available in the VBFNLO package [8]. In all cases, leptonic decays of the electroweak bosons were included in the calculations. For the production of three weak bosons and also for $W^{\pm}\gamma\gamma$, these results were verified against independent calculations [9,10,11] which are available for on-shell bosons and neglecting Higgs boson exchange.

In these proceedings, we review results for $W^{\pm}\gamma\gamma$, $W^{\pm}\gamma\gamma$ + jet and $W^{\pm}\gamma/W^{\pm}Z$ +jet, including their leptonic decays and full off-shell effects, in Section 2, 3 and 4, respectively, for the LHC at 14 TeV. We summarize in Section 5.

2 $W^{\pm}\gamma\gamma$

Among the triple vector boson production channels, $W^{\pm}\gamma\gamma$ has turned out to be of particular interest. $W^{\pm}\gamma\gamma$ production is sensitive to the $WW\gamma$ and $WW\gamma\gamma$ vertices [12]. In addition, a final state with two photons and missing transverse energy is relevant in a variety of beyond

[a]Speaker, based on a talk given at the 47th Rencontres de Moriond on QCD and High Energy Interactions, March 10-17, 2012, La Thuile, Italy.

the standard model scenarios [13]: in gauge-mediated supersymmetry breaking, for instance, the neutralino is often the next-to-lightest supersymmetric particle and decays into a photon plus a gravitino, giving a signal of two photons and missing E_T. In Ref. [14], a study of the backgrounds for supersymmetry motivated di-photon production searches has been performed, pointing out the relevance of the $W^{\pm}\gamma\gamma$ production process as a SM background in case of electron misidentification. Another possible application is an estimate of backgrounds when searching for WH production, followed by Higgs decay to two photons.

We compute the NLO hadronic cross section by straightforward application of the Catani-Seymour dipole subtraction [15]. The loop contributions are evaluated using the Passarino-Veltman scheme up to four-point functions [16] and the Denner-Dittmaier reduction [17] for five point integrals and we perform various cross checks to validate our implementation, Refs. [2,18].

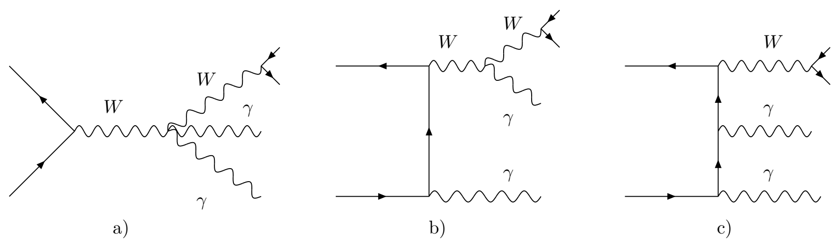

Figure 1: Example of the three topologies contributing to $pp \to l\nu\gamma\gamma$ + X

The NLO virtual corrections result from one-loop diagrams obtained by attaching a gluon line to the quark-antiquark line in diagrams like the ones depicted in Fig. 1. We combine the virtual corrections into three different groups, which include all loop diagrams derived from a given Born level configuration. This leaves us with three universal building blocks, namely factorizable corrections (Virtual-born) and corrections to two (Virtual-box) or three (Virtual-Pentagons) vector bosons attached to the quark line. For our numerical results, we use the CT10 parton distribution set [19] with $\alpha_s(m_Z) = 0.118$ at NLO, and the CTEQ6L1 set [20] with $\alpha_s(m_Z) = 0.130$ at LO. We impose a set of minimal cuts on leptons, photons and jets, namely,

$$p_{T\ell(\gamma)} > 20 \text{ GeV} \qquad |y_{\ell(\gamma)}| < 2.5 \qquad R_{\gamma\gamma} > 0.4 \qquad R_{\ell\gamma} > 0.4 \qquad R_{j\ell} > 0.4 \qquad R_{j\gamma} > 0.7 \quad (1)$$

as well as an isolation criteria à la Frixione [21] for the photons,

$$\Sigma_i \, E_{T_i} \, \theta(\delta - R_{i\gamma}) \, \leq \, p_{T\gamma} \, \frac{1-\cos\delta}{1-\cos\delta_0} \qquad (\text{for all} \quad \delta \leq \delta_0), \qquad (2)$$

where δ_0 is a fixed separation which is set to 0.7. We consider $W^{\pm}$ decays to the first two lepton generations, i.e., $W \to e\nu_e(+\gamma), \mu\nu_\mu(+\gamma)$ and these contributions have been summed in Fig. 2, where we show numerical results for $W^{+}\gamma\gamma$ production within the cuts of Eqs. (1, 2). On the left panel, we show the overall scale variation of our numerical predictions at LO and NLO: the NLO K-factor is large both in absolute value (~ 3) and compared to the LO scale variation. The NLO scale uncertainty is about 10% when varying the factorization and the renormalization scale $\mu = \mu_F = \mu_R$ up and down by a factor 2 around the reference scale $\mu_0 = m_{W\gamma\gamma}$ and is mainly driven by the dependence on μ_R. The large size of the NLO corrections partially originates from new gluon induced channels entering first at NLO, $gq \to W^{\pm}\gamma\gamma \; q$, which are α_s suppressed, but enhanced by the large gluon pdfs at the LHC. Since these 1-jet contributions to the $\mathcal{O}(\alpha_s)$ cross section are only determined at LO, and are unbalanced against the virtual part, their scale variation is large. In fact, most of the scale variation of the total NLO result is accounted for by the real emission contributions, defined here as the real emission cross section

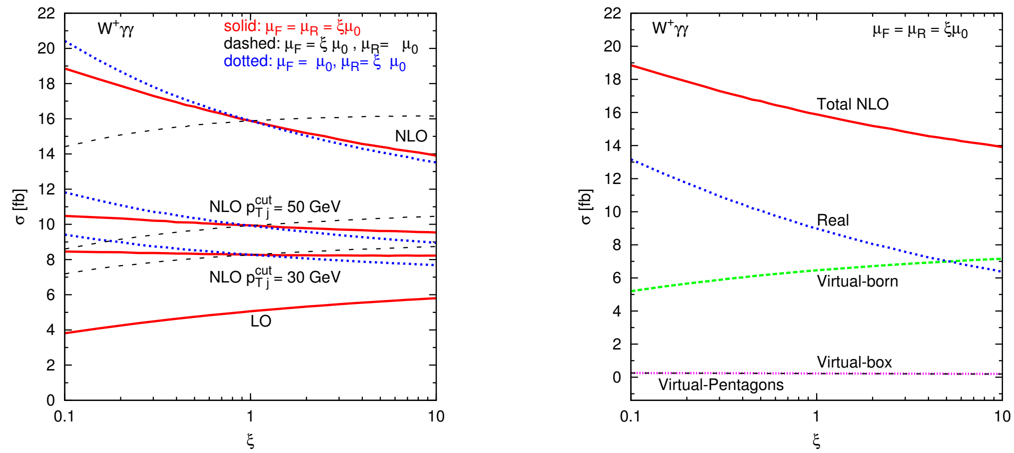

Figure 2: *Left:* Scale dependence of the total LHC cross section for $pp \to \ell^+\gamma\gamma + \not{p}_T + X$ at at LO and NLO, within the cuts of Eqs. (1,2). The factorization and renormalization scales are varied in the range from $0.1 \cdot \mu_0$ to $10 \cdot \mu_0$. *Right:* Same as in the left panel but for the different NLO contributions at $\mu_F = \mu_R = \xi\mu_0$.

minus the Catani-Seymour subtraction terms plus the finite collinear terms. This is more visible in the right panels, where we show the scale dependence and compare the size of the different parts of the NLO calculation. As for the relative size of the NLO terms, the real emission contributions dominate and are even larger than the LO terms plus virtual terms proportional to the Born amplitude. Non-trivial virtual contributions, namely the interference of the Born amplitude with virtual-box and virtual-pentagon contributions, represent less than 1% of the total result and their scale dependence is basically flat. In the left panels, we also show results for additional jet veto cuts, requiring $p_{Tj} < 50$ GeV or $p_{Tj} < 30$ GeV. While it is evident that the renormalization scale variation is highly reduced by a jet veto, this reduction should not be interpreted as a smaller uncertainty of the vetoed cross section: a similar effect in $W^\pm\gamma j$ and WZj and $W^\pm\gamma\gamma j$ production could be traced to cancellations between different regions of phase space and, thus, the small variation is cut-dependent [5] as shown in the following sections.

Among the triple vector boson production channels, $W^\pm\gamma\gamma$ production is the one with the largest K-factor for the integrated cross section. In Ref.[2] (see also [11]), it was shown that this is due to cancellations at LO driven by a radiation zero [22]. The radiation zero at NLO is obscured, similar to $W^\pm\gamma$ production [25], by additional real QCD radiation, $W^\pm\gamma\gamma$ +jet, as part of the NLO contributions. An additional jet veto-cut might help in the detection of the radiation zero, while reducing also the scale uncertainties for the relevant distributions. However, this procedure raises the question of the reliability of the predictions due to the aforementioned problem with the exclusive vetoed samples. Furthermore, the remaining scale uncertainties at NLO QCD are due to unbalanced gluon-induced real radiation computed at LO, e.g., $gq \to W^\pm\gamma\gamma\, q$. To realistically asses the uncertainties, also concerning anomalous coupling searches, and as an important step towards a NNLO QCD calculation of $W^\pm\gamma\gamma$, we have calculated $W^\pm\gamma\gamma$ +jet at NLO QCD.

3 $W^\pm\gamma\gamma$+ jet

This is the first calculation falling in the category of $VVV + j$, which includes the evaluation of the complex hexagon virtual amplitudes, which poses a challenge not only at the level of the analytical calculation, but also concerning the CPU time required to perform a full $2 \to 4$ process at NLO QCD.

For the virtual contributions we use the routines computed in Ref. [18]. At the numerical evaluation level, we split the virtual contributions into fermionic loops (Virtual-fermionbox) and bosonic contributions with one (Virtual-box), two (Virtual-pentagons) and three (Virtual-hexagons) electroweak vector bosons attached to the quark line. This procedure allows us to drastically reduce the time spent in evaluating the part containing hexagon diagrams as explained in Refs. [7,18]. The numerical stability of the hexagons' contributions is discussed in detail in Ref. [18].

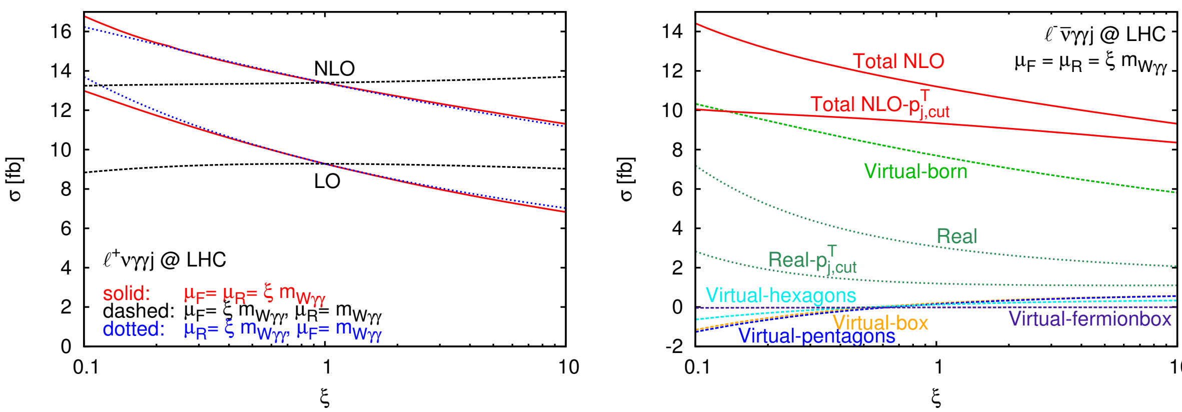

Figure 3: Scale variation of the $\ell^{\pm}\nu\gamma\gamma$+jet production cross sections at the LHC ($\ell = e, \mu$). The cuts are described in the text and we choose $\mu_R = \mu_F = m_{W\gamma\gamma}$ as central dynamical reference scale. The right panel shows the individual contributions to the NLO cross section according to our classification of topologies. We also show results where we have applied a veto on events with two identified jets having both $p_T^j > 50$ GeV

We use the same input parameters as for $W^{\pm}\gamma\gamma$ production and apply the cuts of Eqs. (1,2). Further details on the parameter choices can be found in Ref. [7]. Again, we consider $W^{\pm}$ decays to the first two lepton generations, i.e, $W \to e\nu_e(+\gamma), \mu\nu_\mu(+\gamma)$ and these contributions have been summed in Fig 3 and 4.

We compute total K factors of 1.43 (1.48) for $W^+\gamma\gamma$+jet ($W^-\gamma\gamma$+jet) production at the LHC, values which are quite typical for multiboson+jet production as found in Refs. [4,6,24] and partially originated by new e.g, gg and qq induced channels. This moderate K-factor (as compared to corrections of $\sim 300\%$ for $W^{\pm}\gamma\gamma$ production) indicates, as expected, that the $W^{\pm}\gamma\gamma$ + jet production channel is not affected by radiation zero cancellations.

The scale dependences of the $W^+\gamma\gamma j$ and $W^-\gamma\gamma j$ production cross sections turn out to be modest: when comparing $\mu_R = \mu_F = \xi m_{W\gamma\gamma}$ for $\xi = 0.5$ and $\xi = 2$, we find differences of 10.8% (12.0%), respectively, see Fig. 3.

The phase space dependence of the QCD corrections is non-trivial and sizable (we again choose $\mu_R = \mu_F = m_{W\gamma\gamma}$). Vetoed real-emission distributions are plagued with large uncertainties (Fig.4, left) — a characteristic trait well-known from VV+jet phenomenology [5,24]. Additional parton emission modifies the transverse momentum and invariant mass spectra in particular. The leading jet becomes slightly harder at NLO as can be inferred from the differential K factor in the bottom panel of Fig. 4. When comparing precisely measured distributions in this channel against LO Monte Carlo predictions, the not-included QCD corrections could be misinterpreted for anomalous electroweak trilinear or quartic couplings [4,6,25] arising from new interactions beyond the SM.

4 $W^{\pm}\gamma/W^{\pm}Z$ + jet

NLO corrections to $pp \to W^{\pm}\gamma/W^{\pm}Z$ +jet cross section have been computed in Refs. [3,5], and including anomalous couplings in Refs. [4,6]. All off-shell effects were included. Similar observations as in $W^{\pm}\gamma\gamma$ + jet were found. When varying the factorization and renormalization scale by a

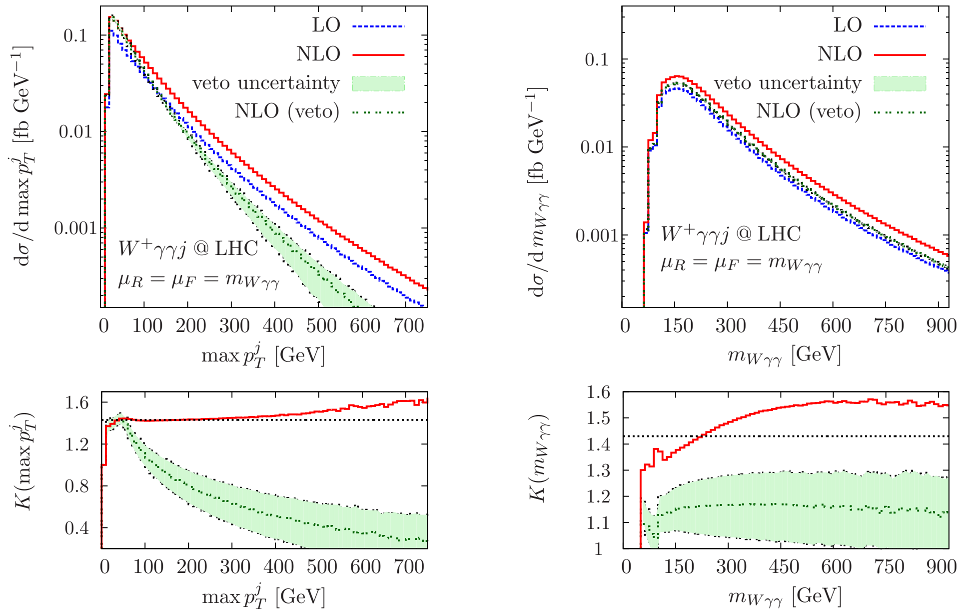

Figure 4: Differential $\max p_T^j$ and $m_{W\gamma\gamma}$ distribution for inclusive and exclusive $l^+\bar{\nu}\gamma\gamma$+jet production.

factor 2 around fixed values of μ_0=100 GeV, one finds modest scale variations. Vetoed samples pick up large uncertainties (Fig.5, left). K-factors are around 1.4 at the LHC and they vary over phase space. Two examples are shown for these processes in Fig. 5, including the sensitivity to anomalous couplings in the p_T^γ differential distributions for $W^\pm\gamma$ +jet production for different choices of anomalous parameters (λ_0, k_0).

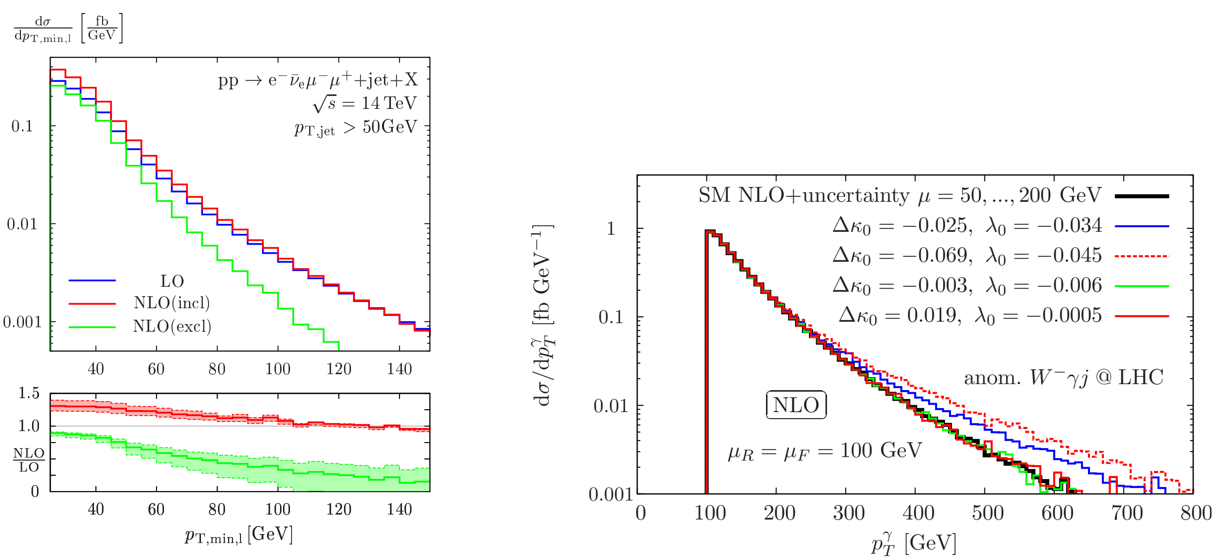

Figure 5: *Left:* Differential distribution for $p_{T,min,l}$ for inclusive and exclusive W^-Z+jet production. *Right:* Sensitivity to anomalous couplings for $l^-\nu\gamma$ + jet in the p_T^γ distribution.

5 Summary

The QCD corrections for vector boson production in the diboson + jet, triboson and triboson + jet channels are large and exceed the expectations driven by LO scale uncertainties. Total K-factors up to 3 for $W^\pm\gamma\gamma$ have been reported. The size of the QCD corrections for $W^\pm\gamma/W^\pm Z$ + jet and $W^\pm\gamma\gamma$ + jet production is around the 40% level. Corrections can be larger for differential distributions and therefore have to be considered for a precise comparison of data to SM predictions for all these processes. Finally, we have shown that the diboson + jet production channels are sensitive to anomalous coupling searches through differential distributions.

References

1. V. Hankele and D. Zeppenfeld, Phys. Lett. B **661** (2008) 103; F. Campanario, V. Hankele, C. Oleari, S. Prestel and D. Zeppenfeld, Phys. Rev. D **78** (2008) 094012; G. Bozzi, F. Campanario, V. Hankele and D. Zeppenfeld, Phys. Rev. D **81** (2010) 094030; G. Bozzi, F. Campanario, M. Rauch, H. Rzehak and D. Zeppenfeld, Phys. Lett. B **696**, 4 (2011); G. Bozzi, F. Campanario, M. Rauch and D. Zeppenfeld, Phys. Rev. D **84** (2011) 074028.
2. G. Bozzi, F. Campanario, M. Rauch and D. Zeppenfeld, Phys. Rev. D **83** (2011) 114035.
3. F. Campanario, C. Englert, M. Spannowsky and D. Zeppenfeld, Europhys. Lett. **88** (2009) 11001.
4. F. Campanario, C. Englert and M. Spannowsky, Phys. Rev. D **83** (2011) 074009.
5. F. Campanario, C. Englert, S. Kallweit, M. Spannowsky and D. Zeppenfeld, JHEP **1007** (2010) 076.
6. F. Campanario, C. Englert and M. Spannowsky, Phys. Rev. D **82** (2010) 054015.
7. F. Campanario, C. Englert, M. Rauch and D. Zeppenfeld, Phys. Lett. B **704** (2011) 515.
8. K. Arnold *et al.*, Comput. Phys. Commun. **180** (2009) 1661; arXiv:1107.4038 [hep-ph].
9. A. Lazopoulos, K. Melnikov and F. Petriello, Phys. Rev. D **76** (2007) 014001.
10. T. Binoth, G. Ossola, C. G. Papadopoulos and R. Pittau, JHEP **0806** (2008) 082.
11. U. Baur, D. Wackeroth and M. M. Weber, PoS **RADCOR2009**, 067 (2010) [arXiv:1001.2688 [hep-ph]]; M. M .Weber, private communication.
12. S. Godfrey, arXiv:hep-ph/9505252; P. J. Dervan, A. Signer, W. J. Stirling and A. Werthenbach, J. Phys. G **26** (2000) 607; O. J. P. Eboli, M. C. Gonzalez-Garcia, S. M. Lietti and S. F. Novaes, Phys. Rev. D **63** (2001) 075008; P. J. Bell, arXiv:0907.5299 [hep-ph]; M. Dobbs, AIP Conf. Proc. **753** (2005) 181-192.
13. J. M. Campbell, J. W. Huston and W. J. Stirling, Rept. Prog. Phys. **70**, 89 (2007).
14. CMS Collaboration, CMS-PAS-SUS-09-004, (2009).
15. S. Catani and M. H. Seymour, Nucl. Phys. B **485** (1997) 291 [Erratum-ibid. B **510** (1998) 503].
16. G. Passarino and M. J. G. Veltman, Nucl. Phys. B **160**, 151 (1979).
17. A. Denner and S. Dittmaier, Nucl. Phys. B **658**, 175 (2003); Nucl. Phys. B **734**, 62 (2006).
18. F. Campanario, JHEP **1110** (2011) 070.
19. H. -L. Lai, M. Guzzi, J. Huston *et al.*, Phys. Rev. **D82** (2010) 074024.
20. J. Pumplin, D. R. Stump, J. Huston, H. L. Lai, P. Nadolsky and W. K. Tung, JHEP **0207** (2002) 012.
21. S. Frixione, Phys. Lett. B **429**, 369 (1998).
22. R. W. Brown, K. L. Kowalski, S. J. Brodsky, Phys. Rev. **D28** (1983) 624.
23. U. Baur, T. Han, J. Ohnemus, Phys. Rev. **D48** (1993) 5140-5161.
24. V. Del Duca, F. Maltoni, Z. Nagy and Z. Trocsanyi, JHEP **0304** (2003) 059. S. Dittmaier, S. Kallweit and P. Uwer, Phys. Rev. Lett. **100**, 062003 (2008); Nucl. Phys. B **826** (2010) 18. T. Binoth, T. Gleisberg, S. Karg, N. Kauer and G. Sanguinetti, Phys. Lett. B **683**, 154 (2010).
25. U. Baur, T. Han and J. Ohnemus, Phys. Rev. D **48** (1993) 5140. J. M. Campbell, R. K. Ellis and C. Williams, JHEP **1107**, 018 (2011).

MEASUREMENT OF THE STRONG COUPLING α_S FROM THE 3-JET RATE IN e^+e^- ANNIHILATION USING JADE DATA

S. KLUTH
Max-Planck-Institut für Physik, Föhringer Ring 6, 80805 Germany

We describe a measurement of the strong coupling $\alpha_S(m_{Z^0})$ from the 3-jet rate in hadronic final states of e^+e^- annihilation recorded with the JADE detector at centre-of-mass energies of 14 to 44 GeV. The jets are reconstructed with the Durham jet clustering algorithm. The JADE 3-jet rate data are compared with QCD predictions in NNLO combined with resummed NNLA calculations. We find good agreement between the data and the prediction and extract

$$\alpha_S(m_{Z^0}) = 0.1199 \pm 0.0010(\text{stat.}) \pm 0.0021(\text{exp.}) \pm 0.0054(\text{had.}) \pm 0.0007(\text{theo.}) \ .$$

1 Introduction

We report on the first measurement of $\alpha_S(m_{Z^0})$ from the 3-jet rate with the Durham algorithm with matched NNLO+NLLA QCD calculations [1]. The first measurement of α_S from R_3 with NNLO QCD calculations was shown in [2].

2 JADE Detector and Data

The JADE detector was a universal and hermetic detector covering a solid angle of almost 4π. The interaction point was surrounded by a large tracking detector (jet chamber) of 1.6 m diameter and 2.4 m length inside a solenoid magnet coil with a magnetic field of 0.48 T. Outside of the magnetic coil was the electromagnetic calorimeter consisting of 2520 lead glass blocks in the barrel section and 96 lead glass blocks in each endcap with a total acceptance of 90% of 4π. The measurement of hadronic final states relies mainly on these two detector systems. More details can be found e.g. in [3].

The data used in the analysis are from the JADE experiment which operated at the PETRA e^+e^- collider at DESY in Hamburg, Germany, from 1979 to 1986. The main data samples were collected at centre-of-mass (cms) energies of 14, 22, 35, 38 and 44 GeV. The integrated luminosities range from about 1/pb at 14 and 22 GeV to about 100/pb at 35 GeV and correspond to sample sizes of $O(10^3)$ events at 14, 22, 38 and 44 GeV and $O(10^5)$ events at 35 GeV.

3 QCD Predictions

The Durham jet clustering algorithm [4] defines $y_{ij} = 2\min(E_i, E_j)^2(1 - \cos\theta_{ij})/s$ as distance in phase space between a pair of particles or jets i and j with energies E_i, E_j and angle θ_{ij} between them. The pair with the smallest y_{ij} is combined by adding their 4-vectors, the particles or jets i, j are removed and the combined 4-vector is added. This procedure is repeated until all

$y_{ij} > y_{\mathrm{cut}}$. The 3-jet rate for a given value of y_{cut} at a cms energy $Q = \sqrt{s}$ is defined as $R_3(y_{\mathrm{cut}}, Q) = N_{3-jet}(y_{\mathrm{cut}}, Q)/N(Q)$, where N_{3-jet} is the number of 3-jet events and N is the total number of events in the sample. The 3-jet rate is a measurement of $\sigma_{3-jet}(y_{\mathrm{cut}}, Q)/\sigma_{had}(Q)$ where $\sigma_{3-jet}(y_{\mathrm{cut}}, Q)$ is the exclusive 3-jet cross section and $\sigma_{had}(Q)$ is the total hadronic cross section.

The NNLO QCD prediction [5,6] can be written as:

$$R_{3,NNLO}(y_{\mathrm{cut}}, Q) = A(y_{\mathrm{cut}})\hat{\alpha}_{\mathrm{S}}(Q) + B(y_{\mathrm{cut}})\hat{\alpha}_{\mathrm{S}}^2(Q) + C(y_{\mathrm{cut}})\hat{\alpha}_{\mathrm{S}}^3(Q) \tag{1}$$

with $\hat{\alpha}_{\mathrm{S}}(Q) = \alpha_{\mathrm{S}}(Q)/(2\pi)$. The coefficient functions $A(y_{\mathrm{cut}})$, $B(y_{\mathrm{cut}})$ and $C(y_{\mathrm{cut}})$ are obtained by numerical integration of the QCD matrix elements in LO, NLO or NNLO. The resummed NLLA calculations use an improved resummation scheme [7] and are matched to the NNLO prediction [1]. Figure 1 (left) shows these QCD predictions as black band with renormalisation scale uncertainty defined by multiplying the renormalisation scale μ by a factor of 1/2 or 2. The other bands show NLO and NLO+NLLA predictions for comparison. The theoretical uncertainties of the NNLO+NLLA prediction are significantly smaller compared to the less advanced predictions.

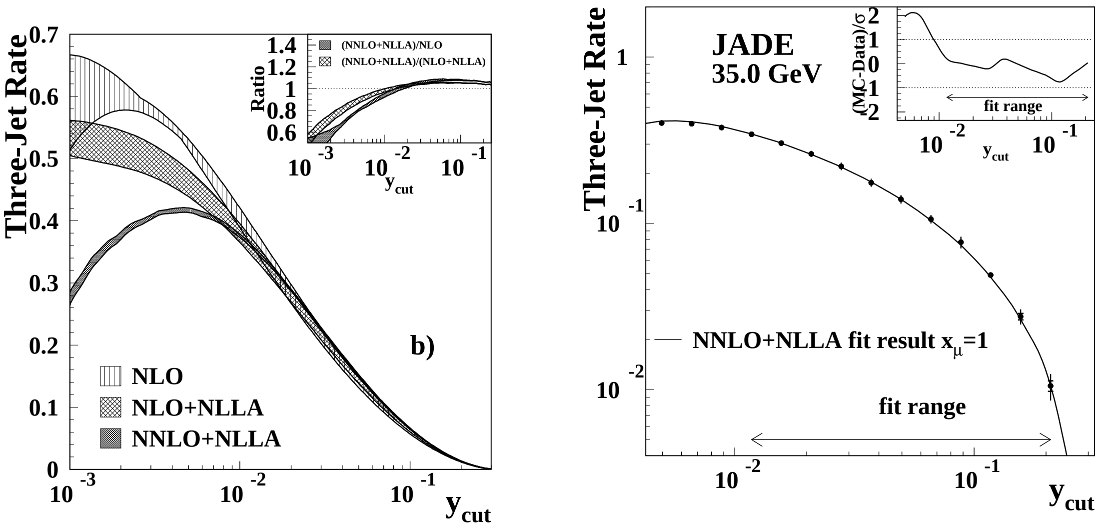

Figure 1: (left) QCD predictions for R_3 in NLO, NLO+NLLA and NNLO+NLLA are shown by bands as indicated on the figure. The widths of the bands reflect the renormalisation scale uncertainty. (right) Fit of the NNLO+NLLA prediction to the R_3 data at $\sqrt{s} = 35$ GeV corrected for experimental effects. The data points included in the fit are indicated by the horizontal arrow. The insert shows the difference between data and fitted QCD prediction divided by the combined statistical and experimental error [1].

4 Data Analysis

The data for the 3-jet rate R_3 are corrected for the effects of detector resolution and acceptance and for photon initial state radiation to the so-called hadron-level using samples of simulated events. The expected contributions from $e^+e^- \to b\bar{b}$ events are subtracted. The Monte Carlo generators PYTHIA 5.7, HERWIG 6.2 or ARIADNE 4.11 with parameter settings from OPAL are used to produce the simulated events together with a full simulation of the JADE detector. The corrected data for R_3 are well described by the simulations.

The QCD predictions have to be corrected for effects of the transition from the partons (quarks and gluons) of the theory to the particles of the hadronic final state. These so-called hadronisation corrections are taken from the samples of simulated events by comparing R_3 values after the parton shower has stopped (parton-level) and the hadron-level consisting of all particles with a lifetime larger than 300 ps. OPAL has compared for the observable[a] y_{23} the parton-level predictions of the theory and the simulation and found agreement within the differences between the three simulations [8]. Thus it is justified to use the simulations to derive the hadronisation corrections, since the hadronisation systematic uncertainty evaluated by comparing the three simulations covers any discrepancies.

The theory is compared with the data using a χ^2-fit with α_S as a free parameter. The statistical correlations between the data points for $R_3(y_{\mathrm{cut}})$ are taken into account. Only data points within a restricted range of y_{cut} are used in the fits to ensure that the experimental and hadronisation corrections are under control and that the QCD predictions are reliable.

Several sources of systematic uncertainty are investigated. Experimental uncertainties are evaluated by repeating the analysis with different event selection cuts, reconstruction calibration versions, corrections for experimental effects, and with different fit ranges. The experimental uncertainties are dominated by the different detector calibrations and the detector corrections based on PYTHIA or HERWIG. Hadronisation uncertainties are estimated by changing the Monte Carlo generator for hadronisation corrections from PYTHIA to HERWIG or ARIADNE. The differences between PYHTIA and HERWIG determine this uncertainty. Theoretical systematic uncertainties are found by repeating the fits with the renormalisation scale factor $x_\mu = \mu/Q$ changed from $x_\mu = 1$ to 0.5 or 2.

5 Results

The fit of the NNLO+NLLA QCD prediction to the 3-jet rate data at $\sqrt{s} = 35$ GeV is shown in figure 1 (right). The fitted prediction agrees well with the data corrected to the hadron-level within the fit range. The extrapolation to the other data points also gives a good description of the data. For this fit based on statistical errors we find $\chi^2/\mathrm{d.o.f.} = 1.2$. The fits at the other cms energies are similar with $1.2 < \chi^2/\mathrm{d.o.f.} < 3.8$ except at $\sqrt{s} = 14$ GeV where we have $\chi^2/\mathrm{d.o.f.} = 6.3$. At the lowest cms energy the hadronisation corrections are significantly larger compared to the other cms energies. The individual fit results for α_S are shown in figure 2 (left) as a function of the cms energy where they were obtained.

The individual results for α_S are evolved to $\alpha_S(m_{Z^0})$ using the 3-loop evolution equations. Then they are combined into a single value taking account of correlated experiental, hadronisation and theory uncertainties as described in [1]. The result from $\sqrt{s} = 14$ GeV is excluded from the combined value since it has a much larger value of $\chi^2/\mathrm{d.o.f.}$ and larger hadronisation corrections compared to the other results. The combined value is

$$\alpha_S(m_{Z^0}) = 0.1199 \pm 0.0010(\mathrm{stat.}) \pm 0.0021(\mathrm{exp.}) \pm 0.0054(\mathrm{had.}) \pm 0.0007(\mathrm{theo.}) \quad . \tag{2}$$

The errors are dominated by the hadronisation correction uncertainties.

As a cross check the analysis is repeated with NNLO QCD predictions using the same fit ranges with $x_\mu = 1$. We find larger values of $\chi^2/\mathrm{d.o.f.}$, a less satisfactory description of the R_3 data and larger uncertainties from variations of the fit ranges compared to the NNLO+NLLA fits. The NNLO predictions do not reproduce the slope of the $R_3(y_{\mathrm{cut}})$ data as well as the NNLO+NLLA predictions. A similar observation can be made in the analysis of [2].

In figure 2 (right) the result of this analysis is compared with other measurements of $\alpha_S(m_{Z^0})$ using the 3-jet or 4-jet rate based on the Durham algorithm. The JADE measurement with y_{23} is highly correlated with our measurement using R_3 and the good agreement of the results is a strong consistency check. The agreement with the other results and with the world average value is also satisfactory within the uncertainties.

[a] The distribution of y_{ij} values for which events change from 2 jets to 3 jets.

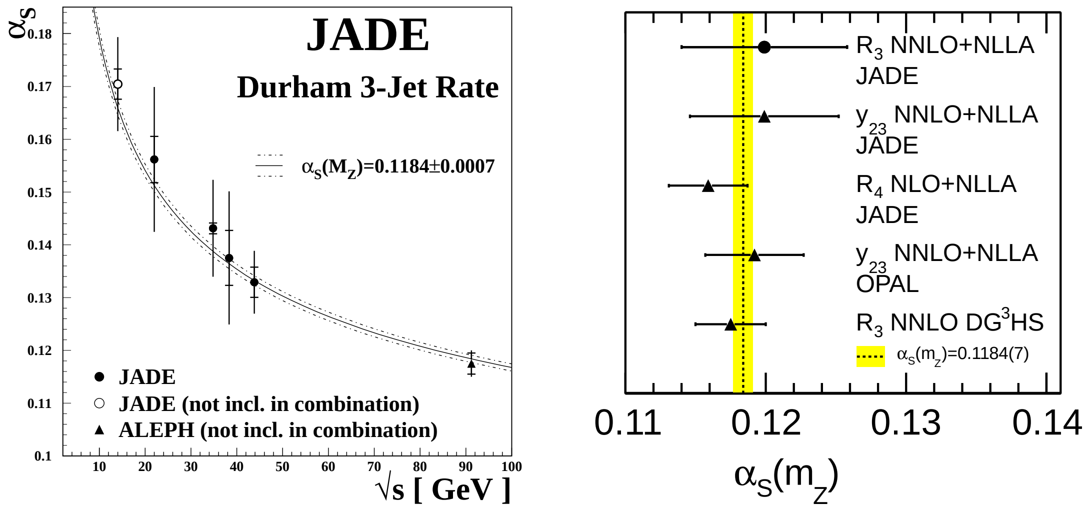

Figure 2: (left) Results for α_S from the JADE energy points are shown. The lines give the prediction from the 3-loop QCD evolution with uncertainties for the value of $\alpha_S(m_{Z^0})$ as indicated on the figure. (right) The result for $\alpha_S(m_{Z^0})$ from this analysis (solid point) is compared with results from [9,10,8,2] (solid triangles) and the current world average value [11,12].

6 Conclusion

We have shown the first measurement of $\alpha_S(m_{Z^0})$ using the 3-jet rate with the Durham algorithm and matched NNLO+NLLA QCD calculations and data from the JADE experiment. The agreement between data and the NNLO+NLLA QCD prediction is improved compared to less advanced predictions. The errors are dominated by the hadronisation correction uncertainties as expected at the low cms energies of the JADE experiment. However, the data of the JADE experiment at comparatively small cms energies can now be analysed with rather good precision thanks to the progress in perturbative QCD calculations and Monte Carlo simulations made since the data were recorded. Our analysis provides an independent and strong cross check on those recent QCD calculations made for the LHC which have related Feynman diagrams or share calculation techniques.

References

1. J. Schieck, S. Bethke, S. Kluth, C. Pahl, Z. Trocsanyi, 1205.3714, sub. to Eur. Phys. J. C
2. G. Dissertori, A. Gehrmann-De Ridder, T. Gehrmann, E.W.N. Glover, G. Heinrich et al., Phys. Rev. Lett. **104**, 072002 (2010)
3. B. Naroska, Phys. Rep. **148**, 67 (1987)
4. S. Catani et al., Phys. Lett. B **269**, 432 (1991)
5. A. Gehrmann-De Ridder, T. Gehrmann, E.W.N. Glover, G. Heinrich, Phys. Rev. Lett. **100**, 172001 (2008)
6. S. Weinzierl, J. High Energy Phys. **0906**, 041 (2009)
7. Z. Nagy, Z. Trocsanyi, Nucl. Phys. Proc. Suppl. **74**, 44 (1999)
8. OPAL Collaboration Coll., G. Abbiendi et al., Eur. Phys. J. C **71**, 1733 (2011)
9. JADE Coll., S. Bethke, S. Kluth, C. Pahl, J. Schieck, Eur. Phys. J. C **64**, 351 (2009)
10. JADE Coll., J. Schieck et al., Eur. Phys. J. C **48**, 3 (2006), Erratum-ibid.C50:769,2007
11. S. Bethke, Eur. Phys. J. C **64**, 689 (2009)
12. PDG Coll., K. Nakamura et al., J. Phys. G **37**, 075021 (2010)

NEW MEASUREMENTS WITH PHOTONS AT THE TEVATRON

J.R. DITTMANN
(on behalf of the CDF and D0 collaborations)
Department of Physics, Baylor University,
One Bear Place #97316, Waco TX 76798-7316, USA

We present three recent photon analyses from data collected at the Fermilab Tevatron: measurements of the direct photon pair production cross section at CDF and D0, measurements of azimuthal decorrelations and multiple parton interactions in γ + 2 jet and γ + 3 jet events at D0, and an observation of exclusive diphoton production at CDF.

1 Introduction

With the recent completion of Run II at the Fermilab Tevatron, the CDF and D0 experiments are publishing results based on challenging measurements that probe quantum chromodynamics (QCD) and are sensitive to next-to-leading-order (NLO) and next-to-next-to-leading-order (NNLO) effects and non-perturbative physics. A superior understanding of parton distribution functions and QCD backgrounds will improve the sensitivity of searches for new phenomena at the LHC and reduce uncertainties in a multitude of future measurements.

2 Prompt Diphoton Production at CDF and D0

Precise measurements of the diphoton production cross section are important as a test of perturbative QCD and soft gluon resummation. Furthermore, the production of prompt photon pairs in hadron collisions is a large background in many ongoing searches including low-mass Higgs decays to diphotons, new heavy resonances, extra spatial dimensions, and cascade decays of heavy new particles. The measurement of prompt photon pair production at $\sqrt{s} = 1.96$ TeV was performed by CDF using 5.36 fb^{-1} of data and by D0 using 4.2 fb^{-1} of data.

Prompt photons are produced directly from the hard scattering or fragmentation process as opposed to photons from the decay of particles such as π^0, η, or K_s^0. At a much smaller rate ($< 1\%$), photon pairs may come from Higgs boson decay, graviton decay (extra dimensions), or

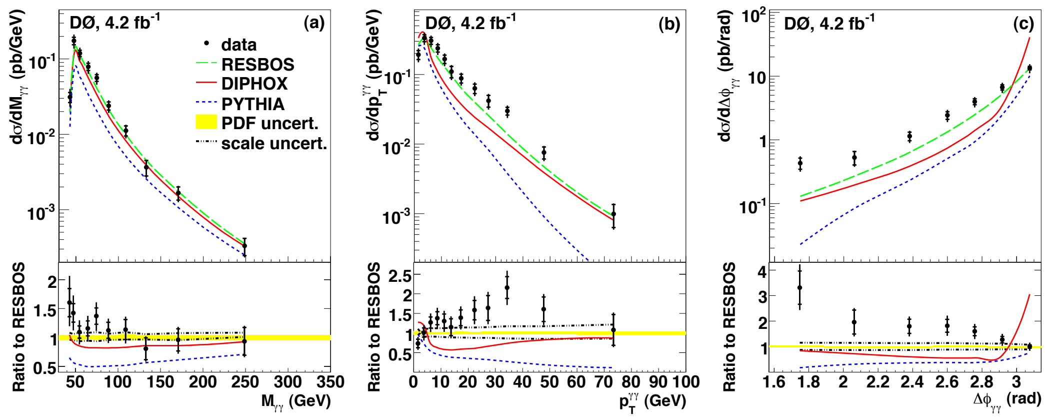

Figure 1: The measured differential diphoton production cross sections at D0 as a function of (a) $M_{\gamma\gamma}$, (b) $p_T^{\gamma\gamma}$, and (c) $\Delta\phi_{\gamma\gamma}$. The data are compared to theoretical predictions from RESBOS, DIPHOX, and PYTHIA.

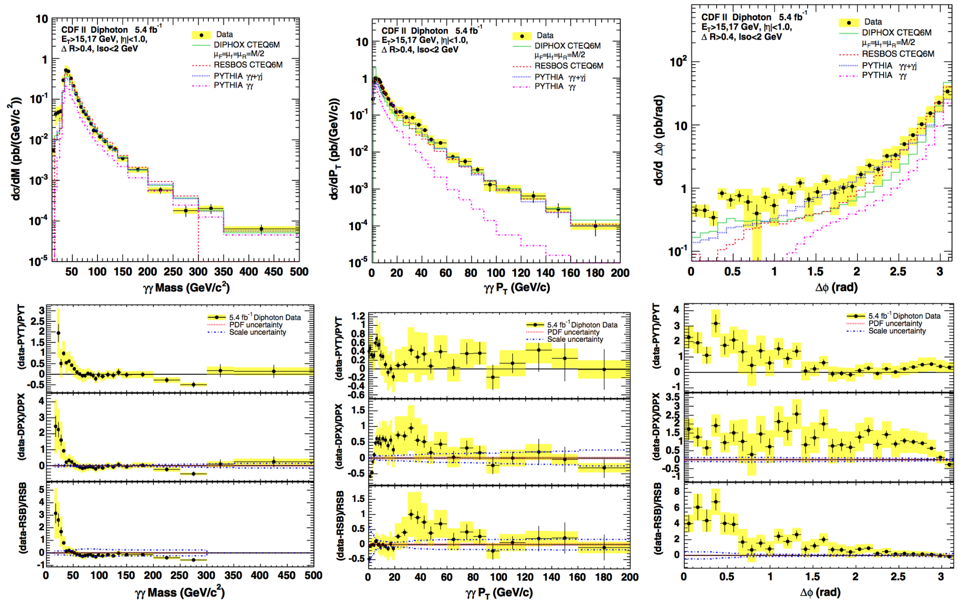

Figure 2: The measured differential diphoton production cross sections at CDF as a function of (left) $M_{\gamma\gamma}$, (center) $p_T^{\gamma\gamma}$, and (right) $\Delta\phi_{\gamma\gamma}$. Top: the absolute cross section values. Bottom: the relative deviations of the data from predictions using RESBOS, DIPHOX, and PYTHIA.

neutralino decay (SUSY). A variety of theoretical predictions are available (e.g. PYTHIA, DIPHOX, and RESBOS), where each includes a different set of Feynman diagrams in the calculation.[1]

The CDF[2] and D0[3] analyses both identify two isolated, high E_T (p_T) photons in the central region. Diphotons are identified with a purity of about 70% among backgrounds consisting mainly of γ + jet, dijet, and $Z/\gamma^* \to e^+e^-$ production. Whereas the CDF diphoton selection is cut-based, the D0 analysis uses a neural net discriminant to separate jets and photons.

The results of the analyses are shown in Figures 1 and 2 for three kinematic variables: the diphoton invariant mass $M_{\gamma\gamma}$, the transverse momentum of the diphoton system $p_T^{\gamma\gamma}$, and the azimuthal angle between the photons $\Delta\phi_{\gamma\gamma}$. All three calculations studied (PYTHIA, DIPHOX, and RESBOS) reproduce the main features of the data within their known limitations, but none of them describes all aspects of the data. In the D0 analysis, RESBOS shows the best agreement with data, although systematic discrepancies are observed at low $M_{\gamma\gamma}$, high $p_T^{\gamma\gamma}$, and low $\Delta\phi_{\gamma\gamma}$. The results from CDF are similar, and it is observed that the inclusion of photon radiation in the initial and final states significantly improves the PYTHIA parton shower calculation. The

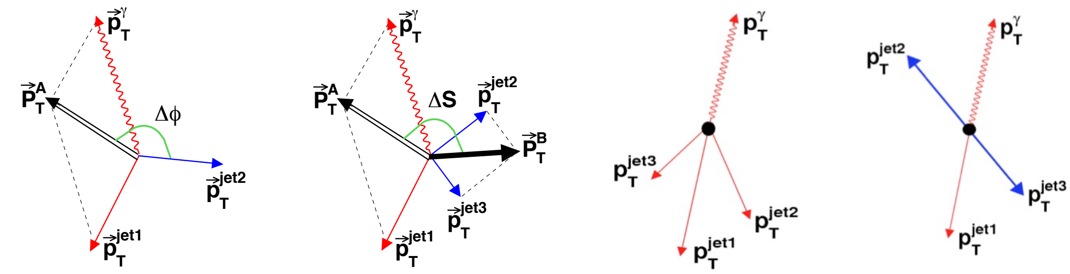

(a) (b) (c) (d)

Figure 3: (a) Diagram illustrating the definition of $\Delta\phi$ as the azimuthal angle between the p_T vector of the γ + leading jet system and the p_T vector of jet2 in γ + 2 jet events, (b) Diagram illustrating the definition of ΔS as the azimuthal angle between the p_T vectors of the γ + leading jet system and the jet2 + jet3 system in γ + 3 jet events, (c) Single parton-parton (SP) interactions yield $\Delta\phi$ and ΔS distributions that are peaked at π, (d) Double parton (DP) interactions yield $\Delta\phi$ and ΔS distributions that are flat because there is no correlation between the separate parton-parton interactions.

comparison between data and theory clearly indicates the necessity of including higher-order corrections beyond NLO, as well as the resummation of soft and collinear initial-state gluons to all orders.

3 Angular Decorrelations in γ + 2 and γ + 3 Jet Events at D0

The D0 collaboration uses data corresponding to 1.0 fb^{-1} of integrated luminosity to measure differential cross sections versus azimuthal angles in γ + 2 and γ + 3 jet events.[4] The purpose of this analysis is (1) to better understand non-perturbative QCD and to improve multiple parton interaction (MPI) models, (2) to learn new and complementary information about the spacial distribution of partons within the proton and correlations between them, and (3) to obtain better background estimates for other analyses such as Higgs boson searches.

In this analysis, two kinematic quantities ($\Delta\phi$ and ΔS) are defined that distinguish between single parton-parton (SP) interactions, in which the photon and all jets originate from the same hard scattering process with gluon bremsstrahlung in the initial or final state, and double parton (DP) interactions, in which two independent parton-parton interactions produce the photon + jets final state (see Figure 3).

The results are summarized in Figure 4, which shows (1) the normalized differential cross

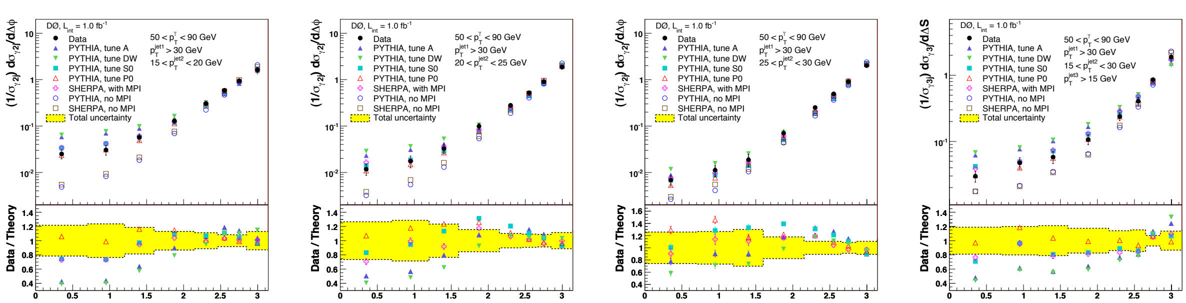

(a) (b) (c) (d)

Figure 4: (a)–(c) The measured normalized differential cross section in γ + 2 jet events, $(1/\sigma_{\gamma 2j})d\sigma_{\gamma 2j}/d\Delta\phi$, compared to MC models for the ranges (a) $15 < p_T^{\rm jet2} < 20$ GeV, (b) $20 < p_T^{\rm jet2} < 25$ GeV, and (c) $25 < p_T^{\rm jet2} < 30$ GeV. The ratio of data over theory is also provided (only for models including MPI). (d) The measured normalized differential cross section in γ + 3 jet events, $(1/\sigma_{\gamma 3j})d\sigma_{\gamma 3j}/d\Delta S$, compared to MC models for the range $15 < p_T^{\rm jet2} < 30$ GeV. The ratio of data over theory is also provided (only for models including MPI).

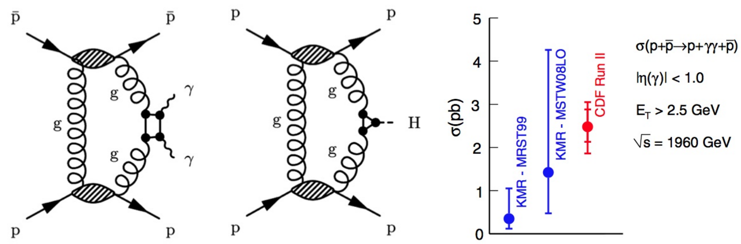

(a) (b) (c)

Figure 5: (a) Leading-order diagram for central exclusive $\gamma\gamma$ production in $p\overline{p}$ collisions. (b) Leading-order diagram for central exclusive Higgs boson production in pp collisions. (c) Comparison of the measured cross section for exclusive $\gamma\gamma$ production in $p\overline{p}$ collisions at $\sqrt{s} = 1.96$ TeV with theoretical predictions.

section versus $\Delta\phi$ in γ + 2 jet events for three bins of p_T^{jet2}, and (2) the normalized differential cross section versus ΔS in γ + 3 jet events. Comparisons to theoretical predictions using PYTHIA and SHERPA reveal that the predictions of SP models alone do not provide an adequate description of the data; additional DP models are required. The new PYTHIA MPI models with p_T-ordered showers are favored, as well as the default SHERPA showers.

4 Exclusive Diphoton Production at CDF

The CDF collaboration performed a search for exclusive $\gamma\gamma$ production via $p\overline{p} \to p + \gamma\gamma + \overline{p}$ in data from 1.11 fb^{-1} of integrated luminosity.[5] This process is intrinsically interesting as a QCD process; moreover, it tests the theory of exclusive Higgs boson production in pp collisions at the LHC. Feynman diagrams of these processes are shown in Figure 5 (a) and (b). Three features are evident in these events: (1) the proton and antiproton emerge intact with no hadrons produced, (2) the outgoing proton and antiproton have nearly the beam momentum ($p_T < 1$ GeV/c), and (3) rapidity gaps are located adjacent to the proton and antiproton. The event selection requires two well reconstructed central ($|\eta| < 1.0$) photons with $E_T > 2.5$ GeV and an absence of other activity in the detector. Events with pileup are rejected.

After a careful treatment of background processes that produce an exclusive $\gamma\gamma$ final state (e.g. $q\overline{q} \to \gamma\gamma$), exclusive diphoton production was observed and the cross section for $p\overline{p} \to p + \gamma\gamma + \overline{p}$ with $|\eta(\gamma)| < 1.0$ and $E_T(\gamma) > 2.5$ GeV was measured to be $2.48^{+0.40}_{-0.35}$(stat)$^{+0.40}_{-0.51}$(syst) pb. As shown in Figure 5 (c), this cross section is in agreement with the only theoretical prediction, based on g + g $\to \gamma + \gamma$, with another gluon exchanged to cancel the color and with the p and $\overline{p}$ emerging intact. If a Higgs boson exists, it should be produced by the same mechanism and the cross sections are related.

Acknowledgments

We thank the Fermilab staff, the technical staffs of the participating institutions, and the funding agencies for their vital contributions.

References

1. C. Balázs *et al.*, *Phys. Rev.* D **76**, 013009 (2007).
2. T. Aaltonen *et al.* (CDF Collaboration), *Phys. Rev. Lett.* **107**, 102003 (2011); T. Aaltonen *et al.* (CDF Collaboration), *Phys. Rev.* D **84**, 052006 (2011).
3. V.M. Abazov *et al.* (D0 Collaboration), *Phys. Lett.* B **690**, 108 (2010).
4. V.M. Abazov *et al.* (D0 Collaboration), *Phys. Rev.* D **83**, 052008 (2011).
5. T. Aaltonen *et al.* (CDF Collaboration), *Phys. Rev. Lett.* **108**, 081801 (2012).

TRANSVERSE-MOMENTUM RESUMMATION: VECTOR BOSON PRODUCTION AND DECAY AT HADRON COLLIDERS

G. FERRERA

Dipartimento di Fisica, Università di Milano and INFN, Sezione di Milano, I-20133 Milan, Italy

We consider the W and Z/γ^* bosons transverse-momentum (q_T) distribution at hadron colliders. We include the leptonic decay of vector bosons with the corresponding spin correlations, the finite width effects and the fully-differential dependence on leptonic variables. At small values of q_T, we resum to all-orders the logarithmically-enhanced perturbative QCD contributions up to next-to-next-to-leading logarithmic accuracy. Resummed results are consistently combined with the next-to-leading fixed-order result at intermediate and large values of q_T. We present a preliminary comparison with some of the available LHC data.

1 Introduction

The Drell-Yan (DY) mechanism, i.e. the hadroproduction of vector bosons which decay in lepton pairs, plays a crucial role in physics studies at hadron colliders. It is thus a major task to provide accurate theoretical predictions to the DY cross section and the related kinematical distributions. This requires, in particular, the computation of perturbative QCD corrections[1,2,3,4].

A particularly relevant observable is the transverse-momentum (q_T) distribution of the vector boson. In the large-q_T region ($q_T \sim m_V$), where the transverse momentum is of the order of the vector boson mass m_V, QCD corrections are known up to the next-to-leading order (NLO) [5,6]. However the bulk of the vector boson events is produced in the small-q_T region ($q_T \ll m_V$), where the reliability of the fixed-order expansion is spoiled by the presence of large logarithmic corrections of infrared and collinear origin of the form $\alpha_S^n\, m_V^2/q_T^2 \ln^m(m_V^2/q_T^2)$ (with $1 \leq m \leq 2n-1$). In order to obtain reliable predictions, these logarithmically-enhanced terms have to be systematically resummed to all orders in perturbation theory [7]. The resummed and fixed-order approaches have to be be consistently matched at intermediate values of q_T to achieve a uniform theoretical accuracy for the entire range of transverse momenta. Experiments can directly measure only the decay products of vector bosons, in finite kinematical regions, it is thus important to include in the theoretical calculations the vector boson leptonic decay.

In this paper we show some preliminary results on DY q_T resummation, based on Refs. [8], taking into account the full dependence on the lepton decay variables with the corresponding spin correlations. This allows us to include the typical kinematical cuts on the final state leptons applied in the actual experimental analyses. We combine the most advanced perturbative information that is available at present: next-to-next-to-leading logarithmic (NNLL) resummation at small q_T and the NLO calculation at large q_T. Our results contain all the $\mathcal{O}(\alpha_S^2)$ corrections in the entire q_T range and implements a unitarity constraint that guarantees to reproduce the exact value of the corresponding fixed order cross section after integration over the q_T variable. Other phenomenological studies of DY q_T distribution can be found in Refs. [9].

2 Transverse-momentum resummation

We follow the transverse-momentum resummation formalism proposed and discussed in detail in Refs.[10]. We consider the production of a vector boson V ($V = W^+, W^-, Z/\gamma^*$) that subsequently decays in a lepton pair

$$h_1(p_1) + h_2(p_2) \;\to\; V(\boldsymbol{q_T}, M, y) + X \;\to\; l_1 l_2(\boldsymbol{q_T}, M, y, \theta, \phi) + X, \tag{1}$$

where h_1 and h_2 are the colliding hadrons (with momenta p_1 and p_2), V is the vector boson, $l_1 l_2$ is the lepton pair and X is an arbitrary and undetected final state. The kinematical variables we use to give a complete description of the leptons in the final state are the two-dimension transverse-momentum vector $\boldsymbol{q_T}$, the invariant mass M and the rapidity y of the vector boson (dilepton system) and the polar θ and azimuthal ϕ lepton angular variables[a].

According to the QCD factorization theorem the multi-differential cross section $d\sigma^V$ can be written as

$$\begin{aligned}\frac{d\sigma^V}{d^2\boldsymbol{q_T}\, dM^2\, dy\, d\cos\theta\, d\phi}(\boldsymbol{q_T}, M, y, \theta, \phi, s) \;&=\; \sum_{a_1,a_2}\int_0^1 dx_1 \int_0^1 dx_2\, f_{a_1/h_1}(x_1,\mu_F^2)\, f_{a_2/h_2}(x_2,\mu_F^2) \\ &\times\; \frac{d\hat{\sigma}^V_{a_1a_2}}{d^2\boldsymbol{q_T}\, dM^2\, d\hat{y}\, d\cos\theta\, d\phi}(\boldsymbol{q_T}, M, \hat{y}, \theta, \phi, \hat{s}; \alpha_S, \mu_R^2, \mu_F^2)\end{aligned} \tag{2}$$

where $f_{a/h}(x,\mu_F^2)$ are the parton densities of the colliding hadrons at the factorization scale μ_F^2, $d\hat{\sigma}^V_{a_1a_2}/dq_T^2$ are the perturbative QCD computable partonic cross sections, s ($\hat{s} = x_1 x_2 s$) is the hadronic (partonic) centre-of-mass energy, $\hat{y} = y - \ln\sqrt{x_1/x_2}$ is the partonic rapidity and μ_R^2 is the renormalization scale.

The resummation is performed at the level of the partonic cross section, which is decomposed as

$$d\hat{\sigma}^V_{a_1a_2} = d\hat{\sigma}^{V\,(\mathrm{res.})}_{a_1a_2} + d\hat{\sigma}^{V\,(\mathrm{fin.})}_{a_1a_2}\,. \tag{3}$$

The first term on the right hand side, the *resummed* component, contains all the logarithmically enhanced contributions (at small q_T) which have to be resummed to all orders in α_S, while the second term, the *finite* component, is free of such contributions and can thus be evaluated at fixed order in perturbation theory.

Resummation holds in the impact parameter space (Fourier conjugated to $\boldsymbol{q_T}$), where the resummed component can be expressed in an exponential form collecting the large logarithmic contributions at leading (LL), next-to-leading (NLL), next-to-next-to-leading accuracy (NNLL) and so forth[10].

We evaluated the finite component starting from the usual fixed order perturbative truncation of the partonic cross section and subtracting the expansion of the resummed part at the same perturbative order:

$$\left[d\hat{\sigma}^{V\,(\mathrm{fin.})}_{a_1a_2}\right]_{f.o.} = \left[d\hat{\sigma}^{V}_{a_1a_2}\right]_{f.o.} - \left[d\hat{\sigma}^{V\,(\mathrm{res.})}_{a_1a_2}\right]_{f.o.}\,. \tag{4}$$

In the case of $q\bar{q}$ initiated process, as the DY process, the resummed component depends on $q_T \equiv |\boldsymbol{q_T}|$ and it does not contain any dependence on the azimuthal angle $\phi_{\boldsymbol{q_T}}$. The azimuthal correlations are contained in the standard fixed-order component (and thus also the finite component).

[a] The angles θ and ϕ are referred to the lepton l_1, with respect to the direction of the hadron h_1, in the rest of frame of the dilepton system.

3 Numerical results

In this section we present selected numerical results for Z/γ^* and W production at NNLL+NLO accuracy and we compare them with some of the available LHC data. We compute the hadronic cross sections using the NNLO MSTW2008 parton distributions[11], with α_S evaluated at 3-loop order.

Our calculation implements the leptonic decays $Z/\gamma^* \to l^+l^-$ and $W \to l\nu_l$ with the corresponding spin correlations and the full dependence on the final state leptons variables. This allows us take into account the typical kinematical cuts on final state leptons considered in the experimental analyses. Moreover, we include the effects of the $\gamma^* Z$ interference and of the W and Z finite-width effects.

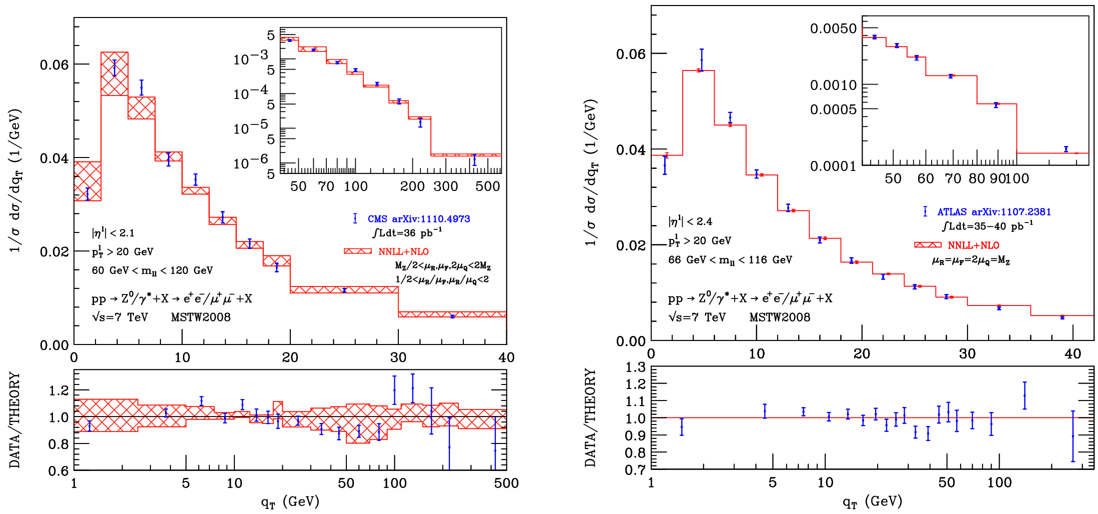

Figure 1: CMS data (left) and ATLAS data (right) for the Z/γ^* q_T spectrum compared with NNLL+NLO result.

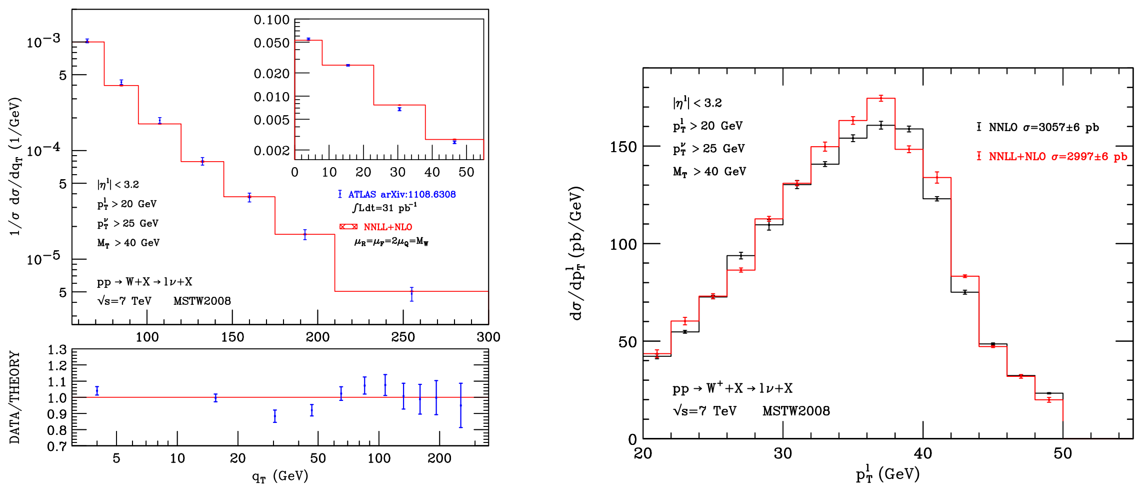

Figure 2: ATLAS data for W q_T spectrum compared with the NNLL+NLO result (left) and NNLL+NLO result compared with the NNLO result for the lepton p_T spectrum from W^+ decay (right).

In Fig. 1 we show the NNLL+NLO q_T spectrum for Z/γ^* production at the LHC [12,13]. The kinematical cuts on the final state leptons are reported in the plots. In the left panel of Fig. 1 we also give an estimate of the perturbative uncertainty considering the independent variation of the factorization, renormalization and resummation (Q) scale by a factor two around their central values, $\mu_F = \mu_R = 2Q = m_Z$, with the constraints [8]: $1/2 \leq \{\mu_F/\mu_R, Q/\mu_R\} \leq 2$. The perturbative uncertainty is roughly around $\pm 5\%$ for $5 \lesssim q_T \lesssim 30$GeV, while it reaches $\pm 10\%$ for $q_T \lesssim 5$GeV and $q_T \gtrsim 30$GeV.

In the left panel of Fig. 2 we show the NNLL+NLO q_T spectrum for W production at the LHC [14]. The kinematical cuts on the final state leptons are reported in the plots.

In the case of the W production, because of the neutrino in the final state, the q_T of the vector boson can only be reconstructed through a measure of the hadronic recoil. In this case it is thus specially relevant the transverse-momentum distribution of the final state charged lepton. In the right panel of Fig. 2 we show the resummed and fixed-order predictions for the lepton transverse-momentum distribution from W decay: the difference between the NNLL+NLO and the next-to-next-to-leading order (NNLO) distribution can reach the 10% level.

In summary we observe an overall good agreement of the NNLL+NLO results with the LHC data for the W/Z q_T distribution without the inclusion of any model for non-perturbative effects and we find a moderate effect of the q_T-resummation on the lepton p_T distribution from W decay.

References

1. R. Hamberg, W. L. van Neerven and T. Matsuura, Nucl. Phys. B **359** (1991) 343 [Erratum-ibid. B **644** (2002) 403]; R. V. Harlander and W. B. Kilgore, Phys. Rev. Lett. **88** (2002) 201801.
2. C. Anastasiou, L. J. Dixon, K. Melnikov and F. Petriello, Phys. Rev. D **69** (2004) 094008.
3. K. Melnikov and F. Petriello, Phys. Rev. Lett. **96** (2006) 231803, Phys. Rev. D **74** (2006) 114017.
4. S. Catani, L. Cieri, G. Ferrera, D. de Florian and M. Grazzini, Phys. Rev. Lett. **103** (2009) 082001; S. Catani, G. Ferrera and M. Grazzini, JHEP **1005** (2010) 006.
5. R. K. Ellis, G. Martinelli and R. Petronzio, Nucl. Phys. B **211** (1983) 106; P. B. Arnold and M. H. Reno, Nucl. Phys. B **319** (1989) 37 [Erratum-ibid. B **330** (1990) 284]; R. J. Gonsalves, J. Pawlowski and C. F. Wai, Phys. Rev. D **40** (1989) 2245.
6. E. Mirkes, Nucl. Phys. B **387** (1992) 3; E. Mirkes and J. Ohnemus, Phys. Rev. D **51**, 4891 (1995).
7. Y. L. Dokshitzer, D. Diakonov and S. I. Troian, Phys. Lett. B **79** (1978) 269, Phys. Rep. **58** (1980) 269; G. Parisi and R. Petronzio, Nucl. Phys. B **154** (1979) 427; G. Altarelli, R. K. Ellis, M. Greco and G. Martinelli, Nucl. Phys. B **246** (1984) 12; J. C. Collins, D. E. Soper and G. Sterman, Nucl. Phys. B **250** (1985) 199; J. Kodaira and L. Trentadue, Phys. Lett. B **112** (1982) 66, report SLAC-PUB-2934 (1982); S. Catani, D. de Florian and M. Grazzini, Nucl. Phys. B **596** (2001) 299; S. Catani and M. Grazzini, Nucl. Phys. B **845** (2011) 297.
8. G. Bozzi, S. Catani, G. Ferrera, D. de Florian and M. Grazzini, Nucl. Phys. B **815** (2009) 174; Phys. Lett. B **696** (2011) 207.
9. P. B. Arnold and R. P. Kauffman, Nucl. Phys. B **349** (1991) 381; C. Balazs, J. w. Qiu and C. P. Yuan, Phys. Lett. B **355** (1995) 548; C. Balazs and C. P. Yuan, Phys. Rev. D **56** (1997) 5558; R. K. Ellis, D. A. Ross and S. Veseli, Nucl. Phys. B **503** (1997) 309; F. Landry, R. Brock, P. M. Nadolsky and C. P. Yuan, Phys. Rev. D **67** (2003) 073016.
10. G. Bozzi, S. Catani, D. de Florian and M. Grazzini, Nucl. Phys. B **737** (2006) 73; Nucl. Phys. B **791** (2008) 1; Phys. Lett. B **564** (2003) 65.
11. A. D. Martin, W. J. Stirling, R. S. Thorne and G. Watt, Eur. Phys. J. C **63** (2009) 189.
12. S. Chatrchyan *et al.* [CMS Collaboration], Phys. Rev. D **85** (2012) 032002.
13. G. Aad *et al.* [ATLAS Collaboration], Phys. Lett. B **705** (2011) 415.
14. G. Aad *et al.* [ATLAS Collaboration], Phys. Rev. D **85** (2012) 012005.

QCD measurements in the forward region at LHCb

Cédric Potterat, on behalf of the LHCb collaboration
Departament de Estructura i Constituents de la Materia, Universitat de Barcelona, Barcelona, Spain

The LHCb experiment does have a unique pseudorapidity coverage in the forward region among the LHC detectors. Due to its unique angular range, it can provide QCD measurements complementary to the other LHC experiments. The measurement of the ratio of prompt χ_c to J/ψ production, the measurement of $\psi(2S)$ meson production, the observation of double charm production are presentedThe charge track distribution at $\sqrt{s} = 7\,\mathrm{TeV}$ and the ratio of anti-proton to proton production at $\sqrt{s} = 7\,\mathrm{TeV}$ and 900 GeV are also reported.

1 Introduction

The LHCb experiment is dedicated to the b-hadron sector and aims to study CP-violation processes and rare decays involving b and c hadrons. The $b\bar{b}$ pair production are strongly correlated at small angle with respect to the beam line, therefore the LHCb detector [1] has been designed as a single-arm forward spectrometer covering a pseudo-rapidity range $2 < \eta < 5$. The detector consists of a silicon vertex detector, a dipole magnet, a tracking system, two ring-imaging Cherenkov (RICH) detectors, a calorimeter system and a muon system.

2 Measurement of the ratio of prompt χ_c to J/ψ production at $\sqrt{s} = 7\,\mathrm{TeV}$

The prompt production of charmonium χ_c and J/ψ is studied [2] in pp collision at $\sqrt{s} = 7\,\mathrm{TeV}$ using an integrated luminosity of $36\,\mathrm{pb}^{-1}$ recorded by LHCb. The ratio of prompt χ_c to J/ψ, $\sigma(\chi_c \to J/\psi\gamma)/\sigma(J/\psi)$, is determined as a function of the $p_T^{J/\psi}$ in the range $2 < p_T^{J/\psi} < 15\,\mathrm{GeV/c}$. The χ_c particles are reconstructed through the $J/\psi\gamma$ channel. The J/ψ's are selected using the dimuon channel and the photons are reconstructed in the calorimeter.

Since we measure the ratio of cross sections, many systematic uncertainties cancel. The gamma efficiency is the main difference entering the ratio calculation. It has been determined on Monte Carlo (MC) and validated on data using the ratio of two siblings channels: $B^+ \to J/\psi K^+$ and $B^+ \to \chi_c K^+$, including charge conjugate. The candidates are selected keeping as many of the selection criteria in common as possible with the main analysis.

The ratio, $\sigma(\chi_c \to J/\psi\gamma)/\sigma(J/\psi)$, is in agreement with the NLO NRQCD [4] calculations over the full $p_T^{J/\psi}$ range as shown in Fig. 1. This measurments is complementary from the cross-section ratio $\sigma(\chi_{c2})/\sigma(\chi_{c1})$ for prompt production measured by LHCb [5] also shown in Fig. 1.

The polarization was not simulated in the χ_c and J/ψ MC samples, thus a systematic uncertainty has been computed using all the possible configurations for both decays and is shown separately from other uncertainties in Fig. 1.

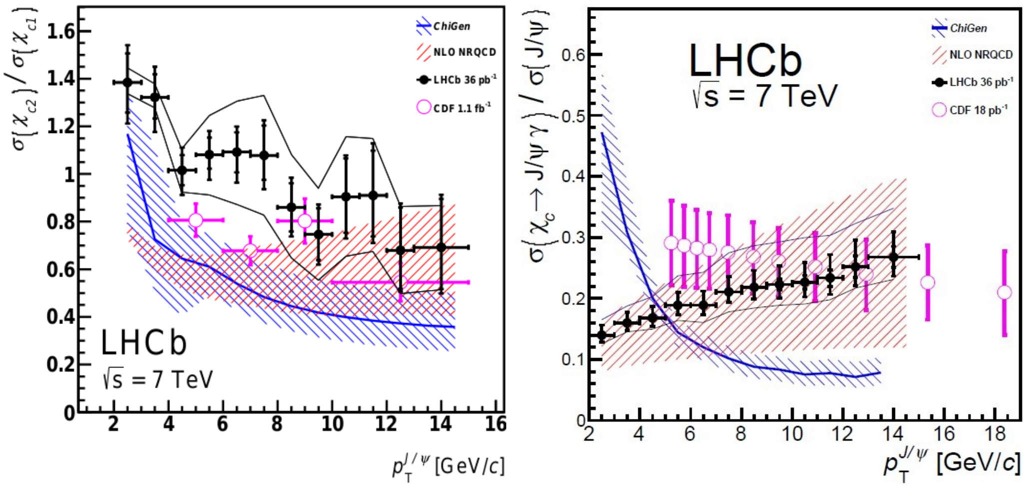

Figure 1: (Left) Ratio $\sigma(\chi_{c2})/\sigma(\chi_{c1})$ and (Right) ratio $\sigma(\chi_c \to J/\psi\gamma)/\sigma(J/\psi)$ in bins of $p_T^{J/\psi}$ in the range $2 < p_T^{J/\psi} < 15\,\mathrm{GeV}/c$. The LHCb results, in the rapidity range $2.0 < y^{J/\psi} < 4.5$ and assuming the production of unpolarized J/ψ and χ_c mesons, are shown with solid black circles and the error bars correspond to the statistical and systematic uncertainties (apart from the polarization). The lines surrounding the data points show the maximum effect of the unknown J/ψ and χ_c polarizations on the result. The CDF data points, at $\sqrt{s} = 1.96\,\mathrm{TeV}$ in $p\bar{p}$ collisions and in the η pseudo-rapidity range $|\eta^{J/\psi}| < 1.0$, are shown in with open pink circles. The two hatched bands correspond to the ChiGen Monte Carlo generator [3] and NLO NRQCD [4] predictions.

3 Measurement of $\psi(2\mathrm{S})$ meson production at $\sqrt{s} = 7\,\mathrm{TeV}$

The differential cross-section for the inclusive production of $\psi(2\mathrm{S})$ mesons in pp collisions at $\sqrt{s} = 7\,\mathrm{TeV}$ has been measured [6] using an integrated luminosity of $36\,\mathrm{pb}^{-1}$. The decay channels $\psi(2\mathrm{S}) \to \mu^+\mu-$ and $\psi(2\mathrm{S}) \to (J/\psi \to \mu^+\mu^-)\pi^+\pi^-$ are reconstructed using prompt $\psi(2\mathrm{S})$ and $\psi(2\mathrm{S})$ decaying from a b-hadron (delayed). The separation between the two samples is done using a pseudo-decay-time distribution defined as $t = d_z(M/p_z)$, where d_z is the separation along the beam axis between the $\psi(2\mathrm{S})$ decay vertex and the primary vertex, M is the nominal $\psi(2\mathrm{S})$ mass and p_z is the component of its momentum along the beam axis. The polarization of promptly reconstructed $\psi(2\mathrm{S})$'s is not measured here, therefore a systematic uncertainty is computed separately for the unknown state of the polarization. This does not effect the delayed $\psi(2\mathrm{S})$.

The differential cross-sections for prompt $\psi(2\mathrm{S})$ and delayed $\psi(2\mathrm{S})$ mesons are measured in the kinematic range $p_T(\psi(2\mathrm{S})) \leq 16\,\mathrm{GeV/c}$ and $2 < y(\psi(2\mathrm{S})) \leq 4.5$:

$$\sigma_{\mathrm{prompt}}(\psi(2\mathrm{S})) = 1.44 \pm 0.01(\mathrm{stat}) \pm 0.12(\mathrm{sys})^{+0.20}_{-0.40}(\mathrm{pol})\,\mu\mathrm{b}$$

$$\sigma_b(\psi(2\mathrm{S})) = 0.25 \pm 0.01(\mathrm{stat}) \pm 0.02(\mathrm{sys})\,\mu\mathrm{b}$$

Recent QCD calculation on the differential cross-sections are found to be in a good agreement with these results as shown in Fig. 2. Combining this result with the LHCb J/ψ measurement, the inclusive branching ratio has been determined to be:

$$\mathcal{B}(b \to \psi(2\mathrm{S})X) = (2.73 \pm 0.06(\mathrm{stat}) \pm 0.16(\mathrm{syst}) \pm 0.24(\mathrm{BR})) \times 10^{-3}$$

where the last uncertainty is due to the $\mathcal{B}(b \to J/\psi X)$, $\mathcal{B}(J/\psi \to \mu^+\mu^-)$ and $\mathcal{B}(\psi(2\mathrm{S}) \to e^+e^-)$ branching fraction uncertainties. The later branching fraction is used and justified by the leptons universalities.

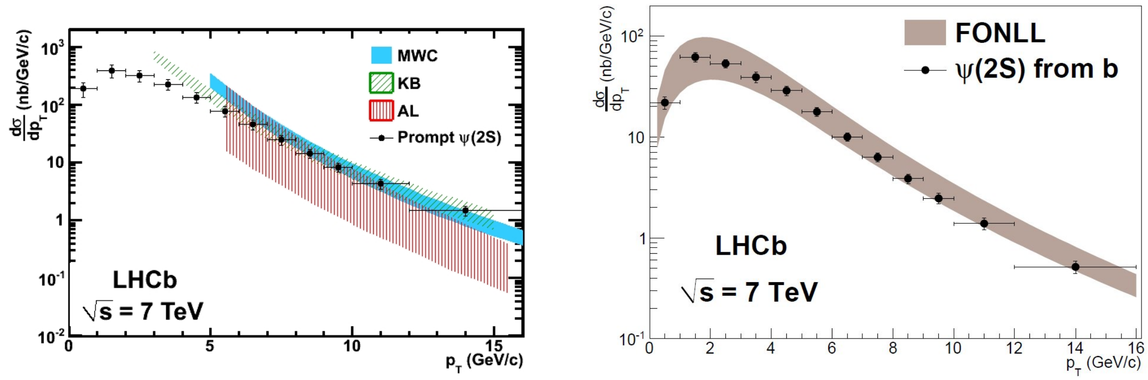

Figure 2: (Left) Differential production cross-section vs. p_T for prompt $\psi(2S)$. The predictions of three non-relativistic QCD models are also shown for comparison. MWC [7] and KB [8] are NLO calculations including colour-singlet and colour-octet contributions. AL [9] is a colour-singlet model including the dominant NNLO terms. (Right) Differential production cross-section vs. p_T for delayed $\psi(2S)$. The shaded band is the prediction of a FONLL calculation [10].

4 Observation of double charm production involving open charm

The production of a J/ψ accompanied by open charm and pairs of open charm (C) hadrons are observed [11] in pp collisions at $\sqrt{s} = 7\,\text{TeV}$ using an integrated luminosity of $355\,\text{pb}^{-1}$. Leading order calculation in perturbative QCD and Double Parton Scattering (DPS) predictions [12,13] give significantly different prediction, $\sigma(J/\psi C + J/\psi \bar{C}) \sim 18\,\text{nb}$ and $\sim 280\,\text{nb}$ respectively. The DPS predictions can also be tested through the ratios of cross sections of the charm hadrons involved: in a DPS senario $\sigma(C_1) \times \sigma(C_2)/\sigma(C_1 C_2)$ should be equal (twice bigger if $C_1 \neq C_2$) to the effective DPS cross-section measured at the Tevatron [14].

The open charm hadrons considered here are: D^0, D^+, D_s^+ and Λ_c^+, while the $C\bar{C}$ are used as control channels. Selected charged tracks are combined to form $J/\psi \to \mu^+\mu^-$, $D^0 \to K^-\pi^+$, $D^+ \to K^-\pi^+\pi^+$, $D_s^+ \to K^-K^+\pi^+$ and $\Lambda_c^+ \to pK^+\pi^+$. Subsequently these candidates are combined into $J/\psi C$, CC and $C\bar{C}$. The combinations are requested to come from the same primary vertex and in the rapidity range $2 < y^{J/\psi,C} < 4$ while the $p_t^{J/\psi} < 12\,\text{GeV/c}$ and $3 < p_t^C < 12\,\text{GeV/c}$. In additon a flight distance $c\tau > 100\mu\text{m}$ is required for the C.

Signals with a statistical significance over five standard deviations have been observed for the four $J/\psi C$, for six CC modes: $D^0 D^0$, $D^0 D^+$, $D^0 D_s^+$, $D^0 \Lambda_c^+$, $D^+ D^+$ and $D^+ D_s^+$, and for seven $C\bar{C}$ channels: $D^0 \bar{D}^0$, $D^0 D^-$, $D^0 D_s^-$, $D^0 \bar{\Lambda}_c^-$, $D^+ D^-$, $D^+ D_s^-$ and $D^+ \bar{\Lambda}_c^-$.

In Fig. 3 the cross-sections are shown on the left and the DPS fraction on the right. Results favour the DPS model using the effective cross-section measured at Tevatron, which is also favoured with the absence of azimuthal and rapidity correlations.

The transverse momentum of these events has also been studied. In the $J/\psi C$ case we can see an harder $p_T^{J/\psi}$ spectra compared to the prompt J/ψ production.

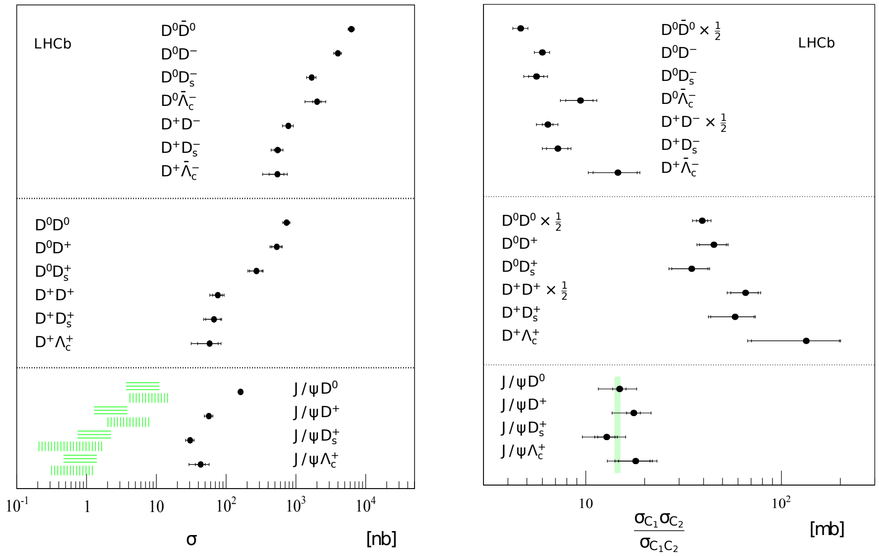

Figure 3: (Left) Measured cross-sections $\sigma_{J/\psi C}$, σ_{CC} and $\sigma_{C\bar{C}}$ (points with error bars) compared, in $J/\psi C$ channels, to the calculations in Refs. [15] (vertical hatched areas) and Ref. [16] (horizontal hatched areas). The inner error bars indicate the statistical uncertainty whilst the outer error bars indicate the sum of the statistical and systematic uncertainties in quadrature. (Right) Measured ratios $\sigma_{C_1}\sigma_{C_2}/\sigma_{C_1C_2}$ (points with error bars) in comparison with the expectations from DPS using the cross-section measured at Tevatron for multi-jet events (light green shaded area). For the D^0D^0, $D^0\bar{D}^0$, D^+D^+ and D^+D^- cases the ratios are rescaled with the symmetry factor of one half. The inner error bars indicate the statistical uncertainty whilst the outer error bars indicate the sum of the statistical and systematic uncertainties in quadrature. For the $J/\psi C$ case the outermost error bars correspond to the total uncertainties including the uncertainties due to the unknown polarization of the prompt J/ψ mesons.

References

1. LHCb collaboration, JINST **3**, S08005 (2008)
2. LHCb Collaboration, arXiv:1204.1462
3. L. A. Harland-Lang and W. J. Stirling, http://projects.hepforge.org/superchic/chigen.html
4. Y.-Q. Ma, K. Wang, and K.-T. Chao, Phys. Rev. D **83**, 111503 (2011)
5. LHCb Collaboration, arXiv:1202.1080
6. LHCb Collaboration, arXiv:1204.1258, submitted to EPJ
7. Y.-Q. Ma, K. Wang and K.-T. Chao, arXiv:hep-ph/1012.1030
8. B. Kniehl and M. Butenschön, Phys. Rev. Lett **106**, 022003 (2011)
9. Phys. Rev. Lett **101**, 152001 (2008) and Eur. Phys J. C **61**, 693 (2009)
10. JHEP **9805**, 007 (1998) and JHEP **0407**, 033 (2004)
11. LHCb Collaboration, arXiv:1205.0975, submitted to JHEP
12. Phys. Rev. D **57**, 4385 (1998) and Phys. Rev. D **73**, 074021 (2006)
13. Phys. Rev. Lett. **107**, 082002 (2011), Phys. Rev. B **705**, 116 (2011), arXiv:1106.2184 and arXiv:1111.3255
14. CDF collaboration Phys. Rev. D **56**, 3811 (1997)
15. Phys. Rev. D **57**, 4385 (1998) and Phys. Rev. D **73**, 074021 (2006)
16. J.-P. Lansberg, Eur. Phys. Rev. J. C **61**, 693 (2009)

LHC data and the proton strangeness

N.P. Hartland
Tait Institute, School of Physics and Astronomy,
University of Edinburgh, EH9 3JZ, UK.

The LHC has already provided many relevant measurements for the determination of parton distribution functions (PDFs). Measurements of the W and Z lepton distributions are of interest for flavor separation and in particular for the determination of the relatively poorly constrained strange quark distribution. In this contribution we shall discuss the computational developments that allow for the efficient inclusion of LHC data into the NNPDF framework consistently at NLO for all observables, and we study the constraints of the LHC W and Z data on the strangeness content of the proton.

There have been a number of experimental measurements of direct relevance to PDF determination performed by LHC collaborations. Measurements of inclusive jet and dijet cross sections[1,2,3] and electroweak vector boson production[4,5,6] provide information on PDFs in previously unexplored kinematical regions. While the importance of including LHC data in future determinations is clear, of particular interest is the potential impact of these data sets upon collider only fits, where existing determinations tend to be poorly constrained. This necessitates the inclusion into PDF determinations low energy data with potential contamination from nuclear corrections or higher twist effects.

However, including collider measurements into a PDF fit on a large scale requires substantial computational resources. NNPDF parton sets are fitted by genetic algorithm minimisation over a large number of generations,[7] therefore the NNPDF methodology requires a fast method of computing collider observables. Although LHC data was previously included in NNPDF2.2[8] by a reweighting method, the constraining power of the LHC dataset makes adding a large quantity of data in this manner impractical. We shall here describe a fast convolution method that has been developed to enable the inclusion of new hadronic data in NNPDF fits, before going on to discuss some preliminary results from fits including LHC data (NNPDF2.3 preliminary). There has been particular interest in the usefulness of the recent ATLAS measurements of W/Z production[4] in providing information on the strange content of the proton.[9] We shall discuss here some preliminary results on the proton strangeness fraction using the updated fit.

A number of tools are available for the computation of hadronic observables that allow for a straightforward variation of the input PDF *a posteriori*, a prerequisite for utility in parton fitting. In particular, the FastNLO[10] and APPLGrid[11] projects provide software which is well suited for use in fitting. The principle of these projects is to store the required perturbative coefficients for a process as weights upon an interpolating grid in x and Q space. The convolution required to calculate the observable is then reduced to a simple product, the PDF in the product may be straightforwardly varied along with the chosen value of α_S. For example, to compute a hadronic cross section in the APPLGrid framework, the following calculation is performed,

$$\sigma = \sum_{p} \sum_{l=0}^{N_{\rm sub}} \sum_{\alpha,\beta}^{N_x} \sum_{\tau}^{N_Q} W_{\alpha\beta\tau}^{(p)(l)} \left(\frac{\alpha_s \left(Q^2_\tau\right)}{2\pi} \right)^p F^{(l)} \left(x_\alpha, x_\beta, Q^2_\tau \right), \tag{1}$$

where the indices α, β run over points in the x-space grid. τ runs over points in Q^2, p denotes the perturbative order of the contribution, and l denotes the specific parton level subprocess. The W table contains the values of the Monte Carlo weights for a particular subprocess point, and the $F^{(l)}$ are the incoming subprocess parton densities constructed as a combination of PDFs as appropriate for the process in consideration. This method of computing observables is fast, but substantial speed improvements can be gained by combining PDF evolution with this procedure. For a set of flavour basis PDFs f, we write a general subprocess density as,

$$F^{(l)} \left(x_\alpha, x_\beta, Q^2_\tau \right) = \sum_{i,j}^{13} C^{(l)}_{ij} \left(f_i(x_\alpha, Q^2_\tau) f_j(x_\beta, Q^2_\tau) \right). \tag{2}$$

Where i, j denote the PDF flavour, and the $C^{(l)}_{ij}$ are coefficients specifying how the subprocess density l is to be built. The evolution of the initial state PDF to the required scale Q^2_τ can be performed in an analogous fashion to the convolution in Eqn 1 by evaluating the matrix of DGLAP evolution kernels upon an interpolation grid as per the FastKernel method.[7] Obtaining the evolved PDF is reduced once again to a product,

$$f_i(x_\alpha, Q^2_\tau) = \sum_{j}^{13} R_{ij} N_j(x_\alpha, Q^2_\tau) = \sum_{j}^{13} \sum_{\gamma}^{N_x} \sum_{k}^{N_{\rm pdf}} R_{ij} E^\tau_{\alpha\gamma jk} N^0_k(x_\gamma). \tag{3}$$

Where the N are PDFs in a suitable evolution basis that diagonalises the matrix of DGLAP evolution kernels. The matrix E^τ_{jk} holds the values of the DGLAP evolution kernel $\Gamma_{jk} \left(x, Q^2_0, Q^2_\tau \right)$ convoluted with the interpolating basis functions as in reference [7], and the matrix R is the rotation matrix from the evolution to the flavour basis. Here we adopt the notation N^0 for the $N_{\rm pdf}$ light evolution basis PDFs parameterised at the initial fitting scale Q^2_0. It is now simple to construct the subprocess density using these matrices,

$$F^{(l)} \left(x_\alpha, x_\beta, Q^2_\tau \right) = \sum_{i,j}^{13} \sum_{k,l}^{N_{\rm pdf}} C^{(l)}_{ij} A^\tau_{\alpha\gamma ik} A^\tau_{\beta\delta jl} N^0_k(x_\gamma) N^0_l(x_\delta), \qquad A^\tau_{\alpha\gamma ik} = \sum_{j}^{13} R_{ij} E^\tau_{\alpha\gamma jk}. \tag{4}$$

With the PDF evolution factorized, the computation in Eqn 1 is now reduced to a much simpler form particularly suited to a fitting application,

$$\sigma = \sum_{i,j}^{N_{\rm pdf}} \sum_{\alpha,\beta}^{N_x} \widetilde{W}_{\alpha\beta ij} N^0_i(x_\alpha) N^0_j(x_\beta), \tag{5}$$

where

$$\widetilde{W}_{\alpha\beta ij} = \sum_{p} \sum_{l=0}^{N_{\rm sub}} \sum_{k,l}^{13} \sum_{\gamma,\delta}^{N_x} \sum_{\tau}^{N_Q} W_{\gamma\delta\tau}^{(p)(l)} \left(\frac{\alpha_s \left(Q^2_\tau\right)}{2\pi} \right)^p C^{(l)}_{kl} A^\tau_{\gamma\alpha ki} A^\tau_{\delta\beta lj}, \tag{6}$$

is the weight matrix containing all the values that may be precomputed and stored prior to a PDF fit. The calculation of a hadronic observable is then simply a matter of a sum of products over a grid in x-space, and the now reduced flavour basis of $N_{\rm pdf}$ light PDFs. Through this method we are able to reproduce the results of the original APPLGrid/FastNLO calculation at the same level of precision and with a substantial improvement in speed.

Using this technique, we can now present results on the strangeness fraction with recent preliminary NNPDF fits including LHC data. $R_s(x, Q^2) = (s+\bar{s})/(\bar{u}+\bar{d})$ has been determined from a number of NNPDF fits at NLO to different datasets. Firstly a fit (here denoted NNPDF2.3 prelim) to the full NNPDF2.1 dataset with the addition of ATLAS 35 pb^{-1} inclusive jet measurements,[3] ATLAS 35 pb^{-1} W and Z rapidity distributions,[4] and CMS 840 pb^{-1} W electron asymmetry data.[14] Secondly, a fit exclusively to the NNPDF2.3 collider data subset (NNPDF2.3 Collider), and finally, a fit to the HERA-I combined dataset[13] and ATLAS W/Z measurement only (NNPDF2.3 HERA+ATLASWZ). For comparison, the value of $R_s(x, Q^2)$ determined by the NNPDF2.1[12] fit is also provided.

A study by the ATLAS collaboration on the strange content of the proton,[9] based upon fits to the same dataset as NNPDF2.3 HERA+ATLASWZ suggest that the ratio of strange to non-strange PDFs may be underestimated by previous determinations from global fits. In Figure 1 we examine the ratio of strange to non strange PDFs for the NLO fits NNPDF2.3 prelim, NNPDF2.3 HERA+ATLASWZ, and NNPDF2.1. From this figure it is clear that the recent ATLAS W/Z measurements provide a valuable constraint, however at medium to large-x the HERA and ATLAS data alone is insufficient to provide a precise determination of the strangeness.

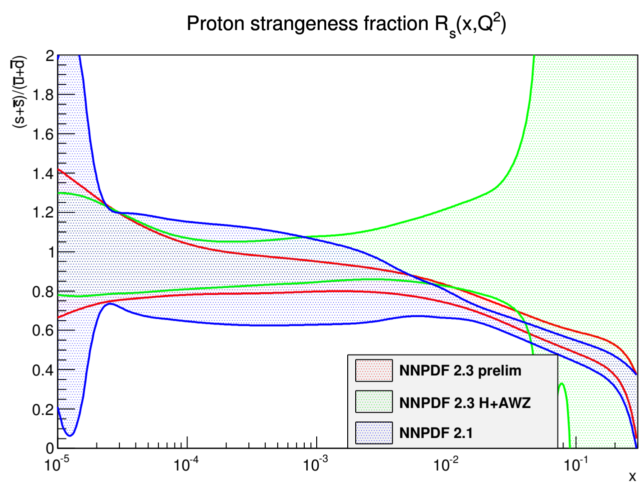

Figure 1: Comparison of the proton strangeness fraction determined from fits to various datasets.

In Table 1 we compare the values obtained by the different sets at specific values of (x, Q^2) and see a similar pattern. Fits to reduced datasets, such as the collider only and HERA + ATLAS W/Z fits suggest a higher value of R_s, however the data provides little constraint and therefore the uncertainties are substantially larger than in the determinations provided by the global fits. The values all broadly agree within the large uncertainties of the HERA + ATLAS W/Z fit as shown in the comparison in Figure 2. We can therefore conclude that the collider data alone is not yet sufficiently constraining to provide a precise determination of the proton strangeness fraction, and that the uncertainty on R_s in the ATLAS determination[9] has been underestimated.

Acknowledgments

The author would like to thank the organisers of the Rencontres de Moriond 2012 for the opportunity to present this work. This contribution made use of resources provided by the Edinburgh Compute and Data Facility (ECDF) (http://www.ecdf.ed.ac.uk/). The ECDF is partially supported by the eDIKT initiative (http://www.edikt.org.uk).

PDF Set	$R_s(0.013, M_z^2)$	$R_s(0.023, 1.9\mathrm{GeV}^2)$
NNPDF2.1	0.61 ± 0.09	0.24 ± 0.09
NNPDF2.3 preliminary	0.68 ± 0.06	0.36 ± 0.10
NNPDF2.3 HERA+ATLAS WZ only	1.00 ± 0.33	1.40 ± 2.20
NNPDF2.3 Collider only	1.00 ± 0.28	0.95 ± 0.60

Table 1: Table of R_s values determined from several PDF fits and at two choices of (x, Q^2)

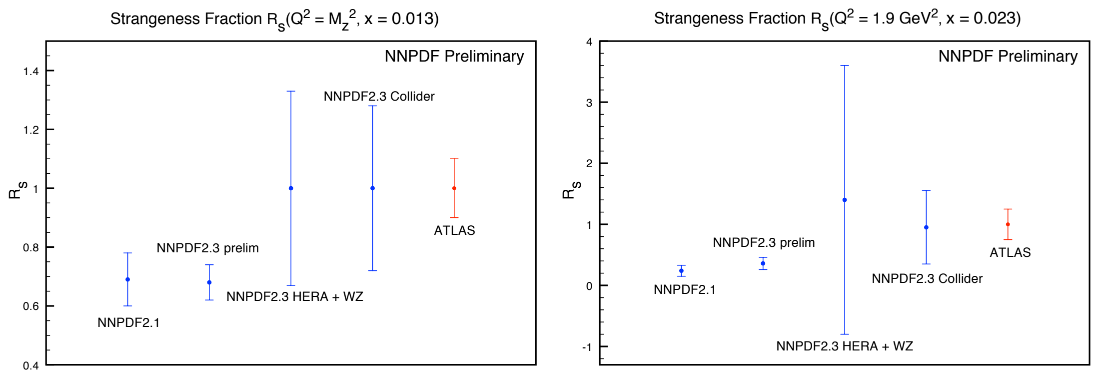

Figure 2: Value of R_s determined with different PDF sets at two choices of (x, Q^2).

References

1. S. Chatrchyan *et al.* [CMS Collaboration], Phys. Rev. Lett. **107** (2011) 132001 [arXiv:1106.0208 [hep-ex]].
2. S. Chatrchyan *et al.* [CMS Collaboration], Phys. Lett. B **700** (2011) 187 [arXiv:1104.1693 [hep-ex]].
3. G. Aad *et al.* [Atlas Collaboration], Eur. Phys. J. C **71** (2011) 1512 [arXiv:1009.5908 [hep-ex]].
4. G. Aad *et al.* [ATLAS Collaboration], Phys. Rev. D **85** (2012) 072004 [arXiv:1109.5141 [hep-ex]].
5. R. Aaij *et al.* [LHCb Collaboration], arXiv:1204.1620 [hep-ex].
6. S. Chatrchyan *et al.* [CMS Collaboration], JHEP **1104** (2011) 050 [arXiv:1103.3470 [hep-ex]].
7. R. D. Ball, L. Del Debbio, S. Forte, A. Guffanti, J. I. Latorre, J. Rojo and M. Ubiali, Nucl. Phys. B **838** (2010) 136 [arXiv:1002.4407 [hep-ph]].
8. R. D. Ball, V. Bertone, F. Cerutti, L. Del Debbio, S. Forte, A. Guffanti, N. P. Hartland and J. I. Latorre *et al.*, Nucl. Phys. B **855** (2012) 608 [arXiv:1108.1758 [hep-ph]].
9. G. Aad *et al.* [ATLAS Collaboration], arXiv:1203.4051 [hep-ex].
10. T. Kluge, K. Rabbertz and M. Wobisch, hep-ph/0609285.
11. T. Carli, D. Clements, A. Cooper-Sarkar, C. Gwenlan, G. P. Salam, F. Siegert, P. Starovoitov and M. Sutton, Eur. Phys. J. C **66** (2010) 503 [arXiv:0911.2985 [hep-ph]].
12. R. D. Ball, V. Bertone, F. Cerutti, L. Del Debbio, S. Forte, A. Guffanti, J. I. Latorre and J. Rojo *et al.*, Nucl. Phys. B **849** (2011) 296 [arXiv:1101.1300 [hep-ph]].
13. F. D. Aaron, H. Abramowicz, I. Abt and L. Adamczyk, *et al.* [H1 and ZEUS collaborations] Journal of High Energy Physics, 2010, Volume 2010, Number 1, 109.
14. CMS Collaboration, CMS-PAS-SMP-12-001, 2012.

SOFT QCD AT THE LHC

A. D. Pilkington (on behalf of the ATLAS and CMS Collaborations)
School of Physics and Astronomy, University of Manchester, Oxford Road, Manchester, M13 9PL
Institute of Particle Physics Phenomenology, University of Durham, South Road, Durham DH1 3LE

Recent ATLAS and CMS measurements related to non-perturbative QCD are presented. The multiple parton scattering model is tested using two different analysis methods and the data is compared to the predictions of general purpose Monte Carlo event generators. Studies of charged particle correlations are discussed in the context of the physics models commonly used to simulate particle production. Measurements of the inelastic cross section within the fiducial acceptance of the detectors are presented and the issues with extrapolating this cross section to the complete inelastic phase space are discussed. Finally, the latest measurements of soft- and hard- diffractive processes are shown.

1 Introduction

Several phenomenological models have been formulated to explain the dynamics of soft particle production in high-energy hadron-hadron interactions. These models are incorporated in general purpose Monte Carlo (MC) event generators and attempt to describe the features of QCD that cannot be calculated using perturbative techniques alone; features such as hadronisation and multiple parton-parton scattering. The first measurements at the LHC tested the phenomenological models by focussing on the multiplicity and transverse momentum of charged particles produced in inclusive proton-proton interactions[1,2]. A reasonable description of the data was obtained after the internal model parameters had been retuned to fit the data[3], although discrepancies remained in some regions of phase space suggesting that the modelling and/or tuning procedures were incomplete. Recent measurements performed at ATLAS[4] and CMS[5] examined increasingly complicated event topologies in order to push the phenomenological models to breaking point. A selection of those measurements are presented in these proceedings.

2 Multiple parton scattering and the underlying event

Proton-proton collisions are typically pictured as containing a short-distance hard partonic scatter, which produces high transverse momentum objects such as jets, accompanied by additional soft processes that produce extra particle activity in the event, which are collectively called the underlying event. One major source of underlying event activity is that of multiple parton interactions (MPI), which is the scattering between spectator partons in the protons. The CMS Collaboration has recently tested whether the event generator tunes, derived in the early leading-track[6] and leading-jet analyses[7], reliably predict the charged particle multiplicity in events containing a Z-boson[8]. CMS measured the particle activity in various azimuthal ($\Delta\phi$) regions with respect to the Z-boson direction, observing a good agreement between the tuned event generators and the data in distributions such as the summed transverse momentum of

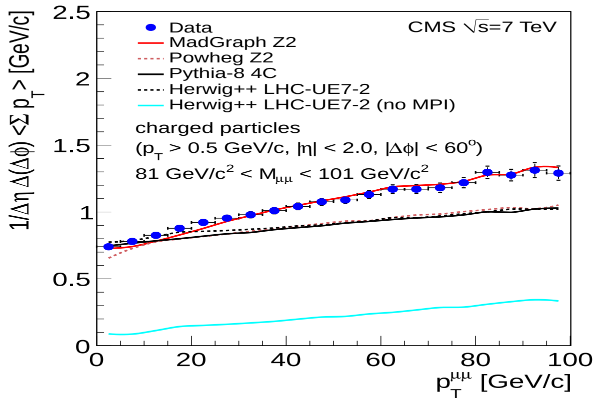

(a)

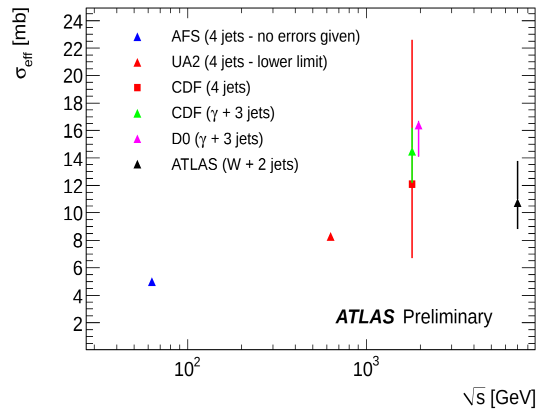

(b)

Figure 1: (a) Measurement of the summed charged particle transverse momentum in events containing a Z-boson candidate. Charged particles are used in the summation if they are nearby the Z-boson in azimuth ($\Delta\phi < 60^\circ$). (b) The measurement of $\sigma_{\rm eff}$ performed at various hadron colliders in a variety of different final state topologies.

charged particles produced within $\Delta\phi < 60^\circ$ of the Z-boson direction (Figure 1 (a)).

If the MPI model is correct, then the production of hard scale objects from the additional scatters must be possible. For example, the cross section for the production of $pp \to X + Y$ can be written as the sum of direct (dir) and double parton scattering (DPI) components, that is

$$\sigma^{(\rm tot)}_{X+Y} \quad = \quad \sigma^{(\rm dir)}_{X+Y} + \sigma^{(\rm dpi)}_{X+Y} \quad \approx \quad \sigma^{(\rm dir)}_{X+Y} + \frac{\sigma_X\, \sigma_Y}{\sigma_{\rm eff}}. \tag{1}$$

The quantity $\sigma_{\rm eff}$ is introduced to parameterize the cross section of DPI in terms of the cross sections for the production of X and Y separately. The ATLAS Collaboration has recently measured $\sigma_{\rm eff}$ at the LHC using W + 2j events, by examining the fraction of these events in which the jets are balanced in transverse momentum[9]. The result was $\sigma_{\rm eff}\,(7\,{\rm TeV}) = 11 \pm 1\,({\rm stat})\,^{+3}_{-2}\,({\rm syst})$ mb. Figure 1 (b) shows the ATLAS result compared to measurements performed at previous colliders. The scaling of $\sigma_{\rm eff}$ with the centre-of-mass energy ($\sqrt{s}$) is compatible with (i) no scaling and (ii) a simple Regge-type scaling of the form $\sigma_{\rm eff} \propto s^{0.12}$.

3 Charged particle correlations

ATLAS performed a spectral analysis of correlations between longitudinal and transverse components of the momentum of charged particles, driven by the search for phenomena related to the structure of the QCD field[10]. One particular observable of interest was the power spectrum,

$$S_\eta\,(\xi) = \frac{1}{n_{\rm event}} \sum_{\rm event} \frac{1}{n_{\rm ch}} \left| \sum_j^{n_{\rm ch}} \exp\left(i\left(\xi\eta_j - \phi_j\right)\right) \right|^2, \tag{2}$$

where the summation 'j' runs over a set of charged particles, η and ϕ are the pseudo-rapidity and azimuthal angle of those particles, and ξ is a parameter. Figure 2 shows the power spectrum obtained using charged particles with (a) $p_{\rm T} > 0.5$ GeV and (b) $0.1 < p_{\rm T} < 1$ GeV. The event generators predict too strong a correlation in case (a), but too weak a correlation in case (b). Varying model parameters to increase/decrease the underlying event or initial state radiation impacts upon both distributions in the same way. It may not be possible to achieve good agreement in both phase space regions simultaneously by tuning the existing models.

ATLAS and CMS also studied two particle angular correlations, assessing the probability that, for a given particle, there is another particle at a specified distance in pseudo-rapidity and

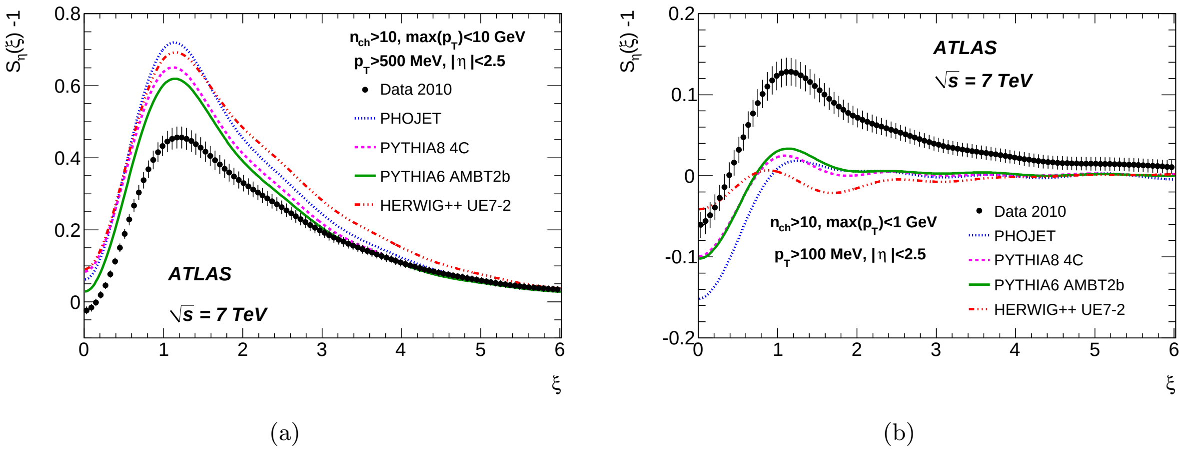

Figure 2: Power spectrum obtained using charged particles with (a) $p_T > 0.5$ GeV and (b) $0.1 \leq p_T < 1$ GeV.

azimuth[11,12]. The CMS measurement at high charged particle multiplicity uncovered a ridge in the correlation function for particles separated by a long distance in pseudo-rapidity but nearby in azimuth. This ridge is not predicted by any of the general purpose event generators. ATLAS also studied correlations between the charged particle multiplicity measured in forward and backward pseudo-rapidity bins[13]. The latest MC tunes give a reasonable description of the data, although they do not completely describe the observed correlation strength as the interval between pseudo-rapidity bins is increased.

4 Diffractive processes

ATLAS measured the inelastic cross section differential in forward rapidity gap size[14]. The forward rapidity gap ($\Delta\eta_F$) was measured from the edge of the calorimeters at $|\eta| = 4.9$ and defined as containing no particle activity with $p_T > 200$ MeV. Figure 3 (a) demonstrates that each of the event generators is incapable of describing the data across the full $\Delta\eta_F$ spectrum. The slope of the distribution at large gap sizes was used to extract a value of the pomeron intercept to be $\alpha_{\mathbb{P}}(0) = 1.058 \pm 0.003(\text{stat})\,^{+0.034}_{-0.039}(\text{syst})$. The measurement was repeated after changing the minimum transverse momentum cut used to define the rapidity gap, to probe different hadronisation models[15].

CMS has made the first measurements of hard diffraction at the LHC, most recently with the measurement of diffractive dijet production[16]. Figure 3 (b) shows the cross section for dijet production measured differentially in $\tilde{\xi}^{\pm} = \sum_i \left(E^i \pm p_z^i\right)/\sqrt{s}$ and the contribution from diffractive dijet production is observed at low $\tilde{\xi}^{\pm}$. CMS used this measurement to place constraints on the rapidity gap survival factor, $S^2 < 0.21 \pm 0.07$. This is on the upper edge of the theoretical expectations. CMS also provided the first indication of diffractive $W \to l\nu_l$ production at the LHC[17]. The diffractive component was observed as an excess of events with the lepton in the hemisphere opposite to a forward rapidity gap.

5 The inelastic cross section

Both experiments made detailed studies of visible and total (extrapolated) inelastic cross sections. ATLAS measured the visible inelastic cross section ($\xi > 5\times10^{-6}$) to be $\sigma_{\text{inel}}^{\text{vis}} = 60.3 \pm 0.05(\text{stat}) \pm 0.5(\text{syst}) \pm 2.1(\text{lumi})$ mb, by measuring the event rate for particle activity in the Minimum Bias Trigger Scintillators[18]. The variable $\xi = M^2/s$ is used by the experiments to quantify the phase space that is covered by the detector. CMS measured $\sigma_{\text{inel}}^{\text{vis}} = 60.2 \pm 0.2(\text{stat}) \pm$

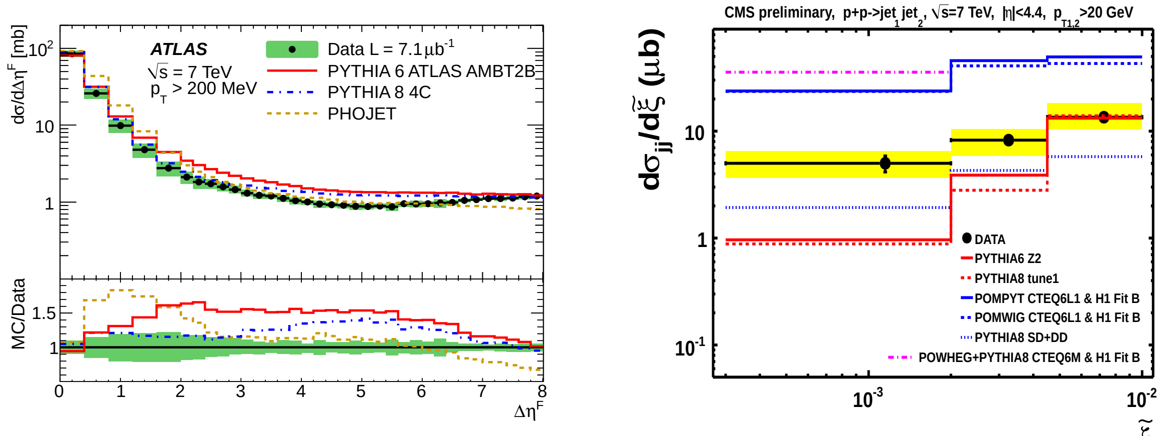

(a) (b)

Figure 3: (a) Inelastic cross section as a function of forward rapidity gap size. (b) Measurement of the dijet cross section as a function of $\tilde{\xi}$; the contribution from diffractive dijet production is observed at low $\tilde{\xi}^{\pm}$.

1.1(syst) $\pm$ 2.4(lumi) mb, for $\xi > 5\times10^{-6}$, by counting the event rate for activity in the forward calorimeters [19]. Both experiments used event generator models to extrapolate the measurement to the full inelastic cross section ($\xi > m_p^2/s$), finding $\sigma_{\text{inel}} = 69.4 \pm 2.4(\text{exp}) \pm 6.9(\text{extr})$ mb and $\sigma_{\text{inel}} = 64.5 \pm 1.1(\text{syst}) \pm 2.6(\text{lumi}) \pm 1.5(\text{extr})$ mb for ATLAS and CMS, respectively.

The extrapolation from visible to total cross section carries a large theoretical uncertainty due to the poorly known cross section for low mass diffraction. The TOTEM result[20] of $\sigma_{\text{inel}} = 73.5 \pm 0.6(\text{stat})\,^{+1.8}_{-1.3}(\text{syst})$ (for $\xi > m_p^2/s$), inferred from the measured elastic and total cross sections, indicates that the majority of the event generators and theory calculations underestimate low mass diffraction and cannot be reliably used in the extrapolations[14].

References

1. ATLAS Collaboration, New J. Phys. **13** (2011) 053033
2. CMS Collaboration, Phys. Rev. Lett. **105** (2010) 022002
3. ATLAS Collaboration, ATLAS-CONF-2010-031; ATLAS Collaboration, ATL-PHYS-PUB-2010-014; R. Field, arXiv:1010.3558 [hep-ph].
4. ATLAS Collaboration, JINST 3 S08003 (2008)
5. CMS Collaboration, JINST 3 S08004 (2008)
6. ATLAS Collaboration, Phys. Rev. D **83** (2011) 112001
7. CMS Collaboration, JHEP **1109** (2011) 109
8. CMS Collaboration, arXiv:1204.1411 [hep-ex].
9. ATLAS Collaboration, ATLAS-CONF-2011-160
10. ATLAS Collaboration, arXiv:1203.0419 [hep-ex].
11. CMS Collaboration, JHEP **1009** (2010) 091
12. ATLAS Collaboration, arXiv:1203.3549 [hep-ex].
13. ATLAS Collaboration, arXiv:1203.3100 [hep-ex].
14. ATLAS Collaboration, Eur. Phys. J. C **72** (2012) 1926
15. V. A. Khoze *et al.*, Eur. Phys. J. C **69** (2010) 85
16. CMS Collaboration, CMS-PAS-FWD-10-004
17. CMS Collaboration, Eur. Phys. J. C **72** (2012) 1839
18. ATLAS Collaboration, Nature Commun. **2** (2011) 463
19. CMS Collaboration, CMS-PAS-QCD-11-002
20. TOTEM Collaboration, Europhys. Lett. **96** (2011) 21002

8.
Structure function,
Spin,
Diffraction
and
Forward Physics

PROTON STRUCTURE MEASUREMENTS AT HERA

D. LONTKOVSKYI ON BEHALF OF THE H1 AND ZEUS COLLABORATIONS
DESY, Notkestrasse 85,
22607 Hamburg, Germany

A QCD analysis HERAPDF1.7 of the combined HERA inclusive neutral and charged current deep inelastic scattering data, including reduced proton energy data as well as charm and jet production data is presented. Predictions for different observables at LHC energies based on proton parton density functions (PDFs) extracted from the HERA data only are competitive with predictions based on parton distributions extracted from more diverse processes. The program for determination of the proton PDFs HERAFITTER is also presented.

1 Introduction

The precision of predictions of the Standard Model processes in high energy experiments with protons is often limited by the precision of the proton PDFs, therefore an accurate extraction of the pPDFs is vital. The measurements from HERA provide one of the main sources of information about the proton structure. The phase space coverage by the HERA experiments is complementary to the one by fixed target experiments and overlaps with the Tevatron and the LHC. The HERA PDF sets are based on using HERA data only. So far the HERAPDF1.5 [1,2] provides the reference set. It is based on the combined HERAI and preliminary combined HERAII inclusive neutral current (NC) and charged current (CC) data [1,2]. The kinematic range of the combined HERA data is $0.045 < Q^2 < 30000$ GeV^2 and $6 \times 10^{-5} < x < 0.65$. In the HERAPDF1.6 [3] set jet production data from H1 and ZEUS are used in addition. This allowed a simultaneous PDF and $\alpha_s\,(M_Z)$ fit with good precision. Here a new PDF set HERAPDF1.7 [4] is presented, exploiting a large variety of different data and processes at HERA. In addition to the data used for HERAPDF1.6 it also uses combined preliminary $F_2^{c\bar{c}}$ data [5] and combined NC data from runs with lower proton energy.

2 QCD analysis settings

The QCD analysis procedure can be summarised as follows. At the starting scale below the charm mass threshold the proton PDFs are parametrised as functions of x. The following flavour decomposition is used: the valence distributions xu_v and xd_v; the gluon distribution xg; the u-type and d-type sea quark distributions $x\bar{U} = x\bar{u}, x\bar{D} = x\bar{d} + x\bar{s}$. These PDFs are then evolved to higher scales using the NLO DGLAP equations, by means of the QCDNUM program [6]. The predictions for the observables are computed by the convolution of the evolved PDFs with perturbative coefficient functions. Heavy flavours were treated in the general mass variable flavour number scheme [7]. In case of jet observables the FastNLO [8] convolution engine was used. It has been shown in previous studies [2,3] that more data allow for more flexible gluon and sea quark PDF parametrisatons, therefore the flexible 14 parameters fit of HERAPDF1.5f was adopted in this analysis.

3 Results and predictions

The result of the HERAPDF1.7 fit is presented in Fig. 1. A detailed error analysis was performed in order to obtain the best estimate for the PDF uncertainties. The consistency of the combined measurements allows the estimation of experimental uncertainties on the proton PDFs by a $\delta\chi^2 = 1$ tolerance criterion. Variations of the strangeness fraction, charm and bottom quark masses, minimal Q^2 of the measurements account for the model uncertainty. The variation of the starting scale of the evolution and modification of the PDFs parametrisations is included in the parametrisation uncertainty. The experimental uncertainty accounts for the precision of the data. The HERAPDF1.7 fit is also compared to the previous proton PDF determination HERAPDF1.6 in Fig. 1. It is found that additional data used in HERAPDF1.7 prefers a slightly softer gluon distribution, however the difference between different HERAPDF sets is within the PDF uncertainty.

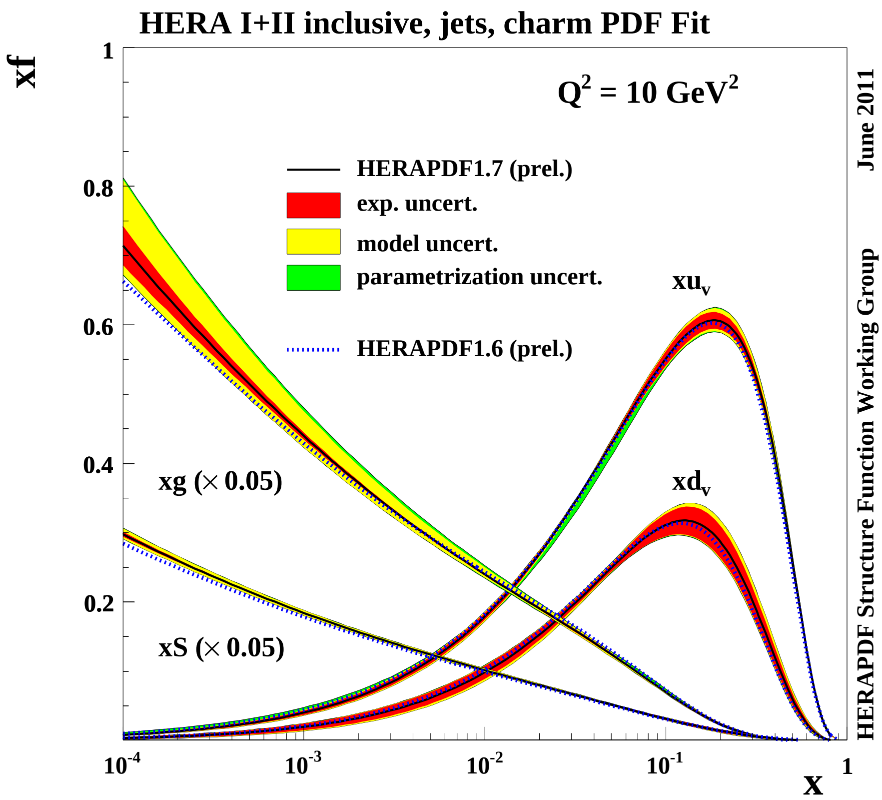

Figure 1: The proton PDFs HERAPDF1.7 at $Q^2 = 10$ GeV^2 extracted from a fit to the data and compared to the HERAPDF1.6. Solid and dashed lines represent central values of the HERAPDF 1.7 and HERAPDF 1.6 fits, respectively. The bands represent various contributions to the PDFs uncertainties.

The predictions based on HERAPDFs as well as those from other PDF fitter groups have been confronted with the recent measurements at the LHC. Exemplary results [9,10] from ATLAS and CMS are shown in Fig. 2. The predictions are found to be in reasonable agreement with the data.

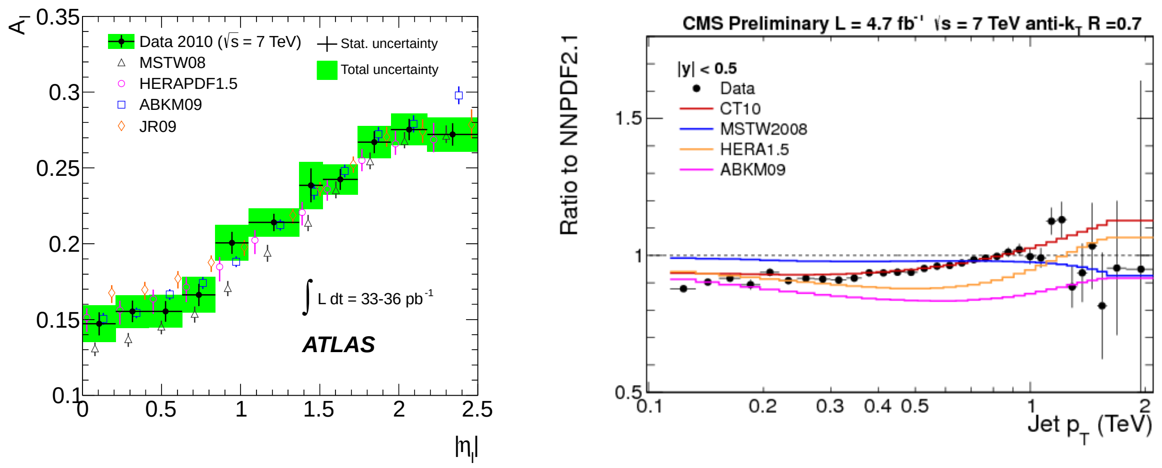

(a) (b)

Figure 2: Measured W charge asymmetry at ATLAS as a function of lepton pseudorapidity $|\eta_l|$ compared with theoretical predictions calculated to NNLO and based on different proton PDF sets (a). Ratio of CMS inclusive jet cross section to NLO predictions based on different proton PDF sets for $|y| < 0.5$ (b)

4 HERAFITTER project

Various measurements at the LHC will reach a precision allowing further constrains on the proton PDFs. The aim of the HERAFITTER project is to provide the necessary infrastructure for PDF studies. The framework covers processes from a wide area: ep (inclusive DIS, jets), $p\bar{p}$ (jets, Drell-Yan) with a clear possibility to extend to new processes and theories. An open source program for the PDF determination HERAFITTER is available [11].

5 Summary

The NLO QCD analysis HERAPDF1.7 of extended datasets of measurements from HERA experiments provides a new precise determination of the proton PDFs. This determination is consistent with previous determinations at HERA and has smaller uncertainty. The predictions based on different variants of HERAPDF provide a reasonable description of different observables at the LHC energy. The new open source project HERAFITTER combines all necessary ingredients for further theoretical and experimental studies of the proton PDFs in advent of new precise measurements by LHC experiments.

References

1. H1 and ZEUS Collaboration, H1prelim-10-142, ZEUS-prel-10-018.
2. H1 and ZEUS Collaboration, H1prelim-11-042, ZEUS-prel-11-002.
3. H1 and ZEUS Collaboration, H1prelim-11-034, ZEUS-prel-11-001.
4. H1 and ZEUS Collaboration, H1prelim-11-143, ZEUS-prel-11-010.
5. H1-prelim-10-143, ZEUS-prel-10-019
6. M. Botje, *Comput. Phys. Commun.* **182**, 490 (2011).
7. R. S. Thorne code, revised in 2008.
8. D. Britzger *et al*, arXiv:1109.1310.
9. ATLAS Collaboration, CERN-PH-EP-2011-143.
10. CMS Collaboration, CMS-PAS-QCD-11-004.
11. H1 and ZEUS Collaboration, https://znwiki3.ifh.de/HERAFitter/HERAFitter.

DIFFRACTION AND PRECISE QCD MEASUREMENTS AT HERA

M.KAPISHIN for the H1 and ZEUS Collaborations
Joint Institute for Nuclear Research, Joliot Curie 6,
141980 Dubna, Moscow region, Russia

Results are reported on precision measurements of jet and diffractive cross sections in *ep* deep-inelastic scattering (DIS) and photoproduction at HERA. The inclusive jet and multi-jet cross sections are used in QCD calculations at next-to-leading order (NLO) to determine the strong coupling α_s. The cross section measurements for diffractive inclusive DIS processes with a leading proton in the final state are combined for the H1 and ZEUS experiments to improve the precision and extend the kinematic range. The dijet cross sections are measured in diffractive DIS with a leading proton and compared with QCD predictions based on diffractive parton densities in the proton. The cross sections for heavy vector meson photoproduction processes are studied in terms of the momentum transfer at the proton vertex and of the photon-proton centre of mass energy.

1 Jets in DIS and photoproduction

Processes of inclusive *ep* DIS, described at leading order (LO) by quark-parton model (QPM), are sensitive to valence and see quark parton distribution functions (PDF) in the proton. At next-to-leading order (NLO) inclusive DIS processes become sensitive to the gluon PDF and strong coupling α_s via scaling violations. But these quantities extracted from a NLO QCD fit to inclusive DIS data are strongly correlated. Jets with large P_T produced in DIS in the Breit frame are sensitive to the gluon density and α_s already in LO via boson-gluon fusion (BGF). BGF process dominates at low and medium values of photon virtuality, Q^2 (up to $Q^2 \sim 10^3\mathrm{GeV}^2$). The QCD-Compton process dominates at higher values of Q^2 and provides sensitivity to α_s and the quark density. Contrary to BGF and QCD-Compton, processes described by QPM generate no jets with large P_T in the Breit frame. Therefore, the inclusion of inclusive jet data into a NLO QCD fit disentangle α_s and the gluon density.

The H1 Collaboration measured inclusive-jet, 2-jet and 3-jet production in the Breit frame at high Q^2 ($150 < Q^2 < 15000$ GeV^2) [1] using DIS data, which correspond to the integrated luminosity of 351 pb^{-1}. The ultimate 1% jet energy scale uncertainty is achieved to minimise the experimental uncertainty of α_s extracted from a NLO QCD analysis. The double-differential 3-jet cross section measured as a function of the averaged P_T of jets in bins of Q^2 is shown in Fig. 1(left). The data are well described by a NLO calculation with the hard scale defined as $\mu_r^2 = (Q^2 + < P_T >^2)/2$. The value of the strong coupling evaluated at the mass of Z^0 from a NLO QCD fit to the 3-jet cross sections is:

$$\alpha_s(M_Z) = 0.1196 \pm 0.0016(\mathrm{exp}) \pm 0.0010(\mathrm{pdf}) \pm^{0.0055}_{0.0039} (\mathrm{theory}), \qquad (1)$$

where the theory uncertainty due to missing higher orders in the NLO calculation dominates over the experimental uncertainty and the uncertainty of the proton PDF parameterisation.

In photoproduction processes ($Q^2 \sim 0$ GeV^2) a hard scale is provided by E_T of the hardest jet in the laboratory frame. These processes are directly sensitive to α_s, the gluon and photon PDFs. The cross section for direct photoproduction of n-jets, where photon interacts as a point-like object, is proportional in LO to α_s^{n-1}. In resolved photoproduction process, where photon interacts by its constituents, the cross section for n-jet production is proportional in LO to α_s^n.

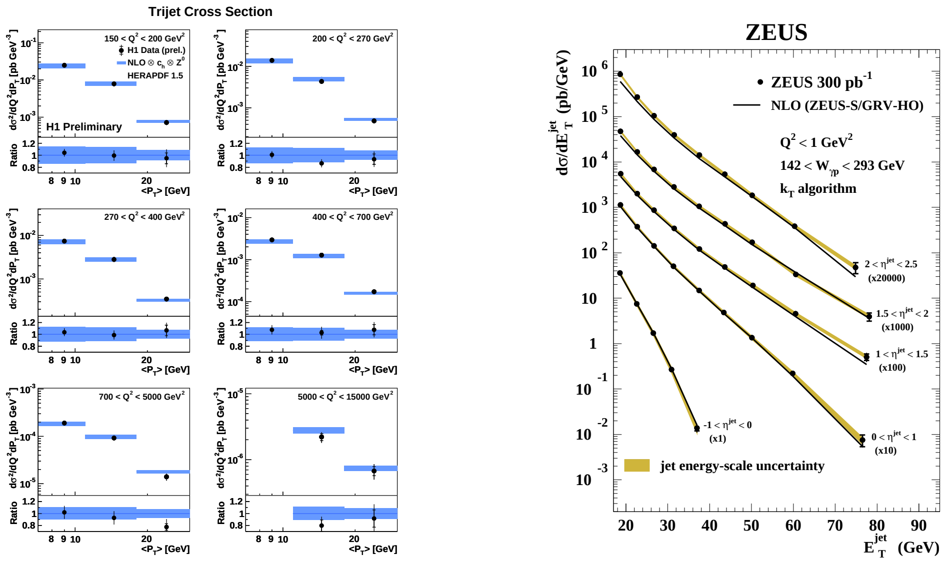

Figure 1: Differential 3-jet cross section by H1, shown as a function of jet $< P_T >$ in Q^2 bins (left). The differential cross section for inclusive jet photoproduction by ZEUS, shown as a function of jet E_T in η bins (right).

The ZEUS Collaboration measured inclusive-jet photoproduction [2] using data based on luminosity of 300 pb^{-1}. The differential cross sections on the jet E_T are measured in bins of pseudo-rapidity η, as it is shown in Fig. 1(right). The 1% jet energy scale uncertainty is achieved. The value of $\alpha_s(M_Z)$ is extracted using a NLO calculation performed in the range $21 < E_T < 70$ GeV, where non-perturbative effects from multiple-interactions are small. The result is:

$$\alpha_s(M_Z) = 0.1206 \pm^{0.0023}_{0.0022} \text{ (exp)} \pm 0.0030\text{(pdf)} \pm^{0.0042}_{0.0033} \text{ (theory)}, \tag{2}$$

where the uncertainties due to the proton and photon PDFs are added in quadrature. The uncertainties due to PDFs and missing orders in the NLO calculation dominate over the experimental uncertainty.

A NLO QCD fit to inclusive DIS data alone with $\alpha_s(M_Z)$ treated as a free fit parameter leads to a very large uncertainty on the gluon density. Combined H1 and ZEUS inclusive NC and CC cross sections together with inclusive jet DIS cross sections are used in the NLO QCD fit HERAPDF1.6 [3] for the simultaneous determination of the proton PDF and $\alpha_s(M_Z)$. The addition of jet data into the fit significantly reduces the correlation between the gluon density and $\alpha_s(M_Z)$ compared to the fit without jet data. The uncertainty of the gluon density at low

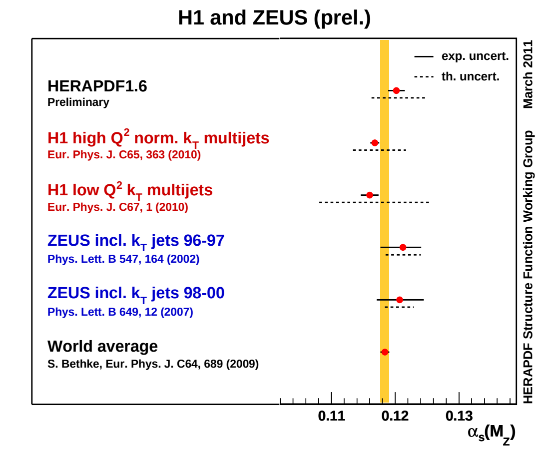

Figure 2: Recent $\alpha_s(M_Z)$ values obtained from the NLO QCD fit HERAPDF1.6 and from the H1 and ZEUS jet measurements.

fractional momenta is considerably decreased and an unbiased evaluation of $\alpha_s(M_Z)$ is achieved. The results on $\alpha_s(M_Z)$ obtained from the HERAPDF1.6 fit and from the jet cross sections measured by H1 and ZEUS in DIS are shown in Fig. 2. The values are consistent with each other and with the world average.

2 Diffraction at HERA

Diffractive processes such as $ep \to eXp$ constitute about $\sim 10\%$ of the DIS cross section measured at low Bjorken x at HERA. The photon virtuality Q^2 provides a hard scale for perturbative QCD to be applicable, so that diffractive DIS events can be viewed as processes in which the photon probes a net colour singlet combination of exchanged partons. In processes of diffractive production of jets and heavy vector mesons (VM), the P_T of jets and the mass of heavy quarks provide a hard scale for perturbative calculations.

Diffractive processes are characterised by the absence of hadron activity in the rapidity interval between the central rapidity range and the leading proton (or the proton dissociation system). Therefore, diffractive events are selected at HERA by the requirement of a large rapidity gap between the leading proton and hadrons in the central rapidity range (LRG method) or by the measurement of the leading proton using the forward proton spectrometers (PS method). The LRG method is limited by the systematics related to the missing leading proton and the proton dissociation contribution. The PS method is limited by the low acceptance and proton tagging systematics. The diffractive DIS variables are the momentum fraction of the proton carried by the diffractive exchange ($x_{I\!P}$), the momentum fraction of the diffractive exchange carried by the struck quark ($\beta = x/x_{I\!P}$) and the squared 4-momentum transfer at the proton vertex t.

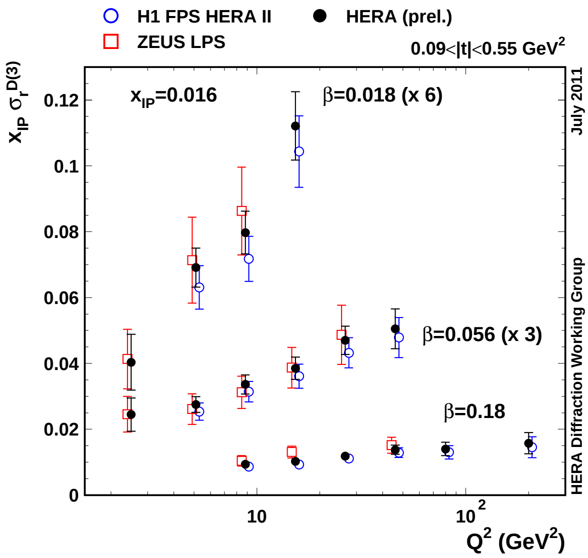

Figure 3: Diffractive reduced cross section σ_r^D, shown as a function of Q^2 for selected values of $x_{I\!P}$ and β. The H1, ZEUS and combined cross sections are presented.

The H1 and ZEUS Collaborations performed the first combination of the diffractive DIS cross sections measured using their proton spectrometers in the range $0.09 < |t| < 0.55$ GeV^2 [4]. The diffractive reduced cross sections are presented in Fig. 3 as a function of Q^2 for selected values of β and $x_{I\!P}$. A reasonable agreement is found between the H1 and ZEUS data in the shape and normalisation taking into account that the H1 and ZEUS normalisation uncertainties are 4.5% and 7%, respectively. The H1 and ZEUS diffractive DIS cross sections are combined to extend the phase space in $x_{I\!P}$ and Q^2 and reduce the uncertainties compared to those for one experiment. The combination method [5] uses the iterative χ^2 minimisation and takes into account correlations of systematic errors of the data points. The two experiments calibrate each other resulting in the reduction of systematic uncertainties. The combined data have $\sim 27\%$ smaller total uncertainties with respect to the most precise H1 data set.

In recent H1 analyses [6,7], dijets are selected in events with a leading proton measured in the forward and very forward proton spectrometers. The measurements cover new regions of the phase space in which there are jets at rapidity beyond the LRG range. These dijet data are reasonably described by NLO QCD predictions based on the diffractive PDF sets H1 Jets and H1 FitB [8,9] supporting the universality of the diffractive PDFs.

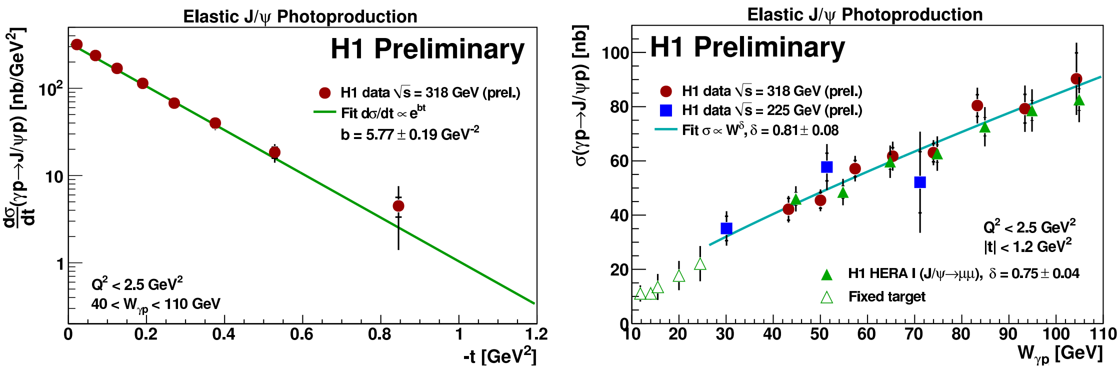

Figure 4: Cross section for J/ψ photoproduction by H1, shown as a function of t (left) and γp centre of mass energy (right).

The H1 Collaboration performed a simultaneous measurement of J/ψ photoproduction in elastic and proton dissociation processes[10] using the LRG method. The cross section is measured as a function of t and the γp centre of mass energy, $W_{\gamma p}$. The measurement is also performed at the reduced proton energy to extend the kinematic range to lower $W_{\gamma p}$ values. The cross sections for elastic J/ψ photoproduction are presented in Fig. 4.

In a colour dipole approach the exclusive VM is produced at leading order via a 2-gluon colour-singlet exchange between the $\gamma \to q\bar{q}$ dipole and the proton. The cross section is proportional to the square of the gluon density in the proton. The J/ψ photoproduction cross section rises steeply with W as $\propto W^{\delta}$ with $\delta \sim 0.8$. This can be explained by the rapid increase of the gluon density with decreasing of the fractional momentum x, where $x \propto 1/W^2$.

In an optical model approach the exponential slope b of the t-dependence of the exclusive VM production is related to the sum of the squared radii of the $\gamma \to q\bar{q}$ dipole and that of the proton. At high values of the VM mass M_V or photon virtuality Q^2 the $q\bar{q}$ contribution decreases as $b_{q\bar{q}} \propto 1/(Q^2 + M_V^2)$ and the slope of the t-dependence saturates at $b \sim 5$ GeV^{-2}, which corresponds to the gluonic radii of the proton. The H1 results on the t-dependence of the J/ψ photoproduction and the recently published ZEUS results on the $\Upsilon(1S)$ photoproduction [11] are consistent with this approach.

References

1. H1 Collaboration, `H1-preliminary-11-032`.
2. ZEUS Collaboration, H.Abramowicz *et al.*, DESY-12-045.
3. H1 and ZEUS Collaborations, HERAPDF1.6, `H1-preliminary-11-034, ZEUS-preliminary-11-001`.
4. H1 and ZEUS Collaborations, `H1-preliminary-11-111, ZEUS-preliminary-11-011`.
5. A. Glazov, AIP Conf.Proc 792 (2005) 237.
6. H1 Collaboration, F.D.Aron *et al*, DESY 11-166 [arXiv:1111.0584].
7. H1 Collaboration, `H1prelim-11-013`.
8. H1 Collaboration, A. Aktas *et al.*, EPJC **48**, 715 (2006) [hep-ex/0606004].
9. H1 Collaboration, A. Aktas *et al.*, JHEP 0710:042 (2007) [arXiv:0708.3217].
10. H1 Collaboration, `H1prelim-11-011`.
11. ZEUS Collaboration, H.Abramowicz *et al.*, *Phys. Lett.* B **708**, 14 (2012).

Evidence for the higher twists effects in diffractive DIS at HERA

M. Sadzikowski[a], L. Motyka, W. Słomiński
Institute of Physics, Jagiellonian University, Reymonta 4, 30-059 Kraków, Poland

We study a twist decomposition of diffractive structure functions in the diffractive deep inelastic scattering at HERA. At low Q^2 and at large energy the data exhibit a strong deviation from the twist-2 NLO DGLAP description. It is found that this deviation in consistent with higher twist effects. We conclude that the DDIS at HERA provides the first, strong evidence of higher twist effects in DIS.

1 Introduction

The QCD description of the diffractive deep inelastic scattering processes $ep \to epX$ (DDIS) is based on the series expansion of the scattering amplitudes in the inverse powers of a large scale Q^2, defined as a negative squared four-momentum transfer from the electron to the proton carried by the virtual photon γ^*. In the leading twist-2 approximation the diffractive proton structure functions $F_{L,T}^{D(3)}$ can be calculated using diffractive parton distribution functions (DPDFs) due to the Collins factorization theorem[?], whereas the DPDFs dependence on the hard scale is governed by the celebrated DGLAP evolution equation. Despite of great efficiency of this approximation in the data description this approach has an obvious limitation that follows from negligence of the higher twists contributions. Certainly, the higher twists contribute at any energy scale and become relevant for data description below some virtuality Q^2, which depends on the process and required precision. In this presentation we point out that in the case of DDIS the DGLAP description breaks down at the scale $Q^2 \simeq 5$ GeV^2 and to show that these deviations are consistent with a higher twists contribution.

2 Cross section and the DGLAP description

The DDIS is an quasi-elastic electron-proton scattering process $e(k)p(P) \to e(k')p(P')X(P_X)$ in which the final hadronic state X with four-momentum P_X is separated in rapidity from the proton, that scatters elastically (see Fig. 1). The t-integrated ep cross-section reads:

$$\frac{d\sigma}{d\beta dQ^2 d\xi} = \frac{2\pi\alpha_{\rm em}^2}{\beta Q^4}[1+(1-y)^2]\sigma_r^{D(3)}(\beta, Q^2, \xi) \tag{1}$$

where the invariants read $y = (kq)/(kP)$, $Q^2 = -q^2$, $\xi = (Q^2+M_X^2)/(W^2+Q^2)$ and $t = (P'-P)^2$. The quantity $W^2 = (P+q)^2$ is the invariant mass squared in photon-proton scattering, and M_X^2 is the invariant mass of the hadronic state X. The reduced-cross-section may be expressed in

[a]Talk presented during the conference Rencontres de Moriond, "QCD and High Energy Interactions", 2012.

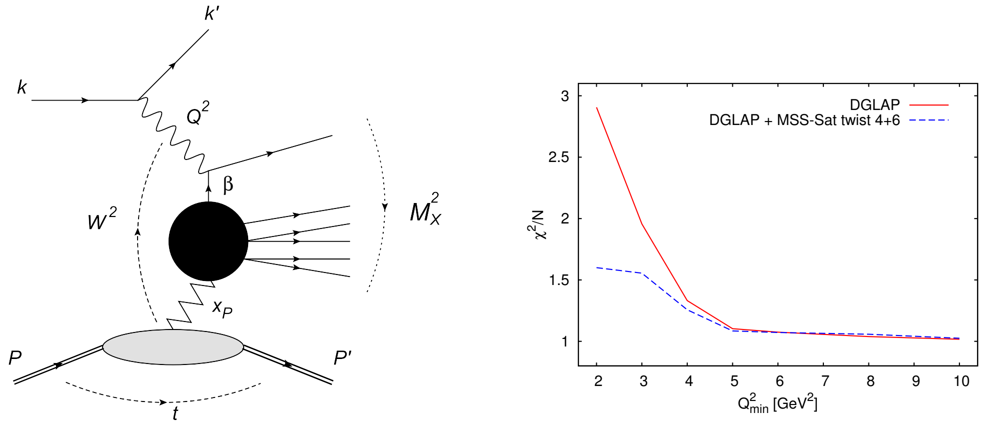

Fig. 1. Left panel - kinematics of the DDIS scattering. Right panel - the $\chi^2/$d.o.f. for NLO DGLAP and NLO DGLAP + HT fits to ZEUS LRG data [?] with $Q^2 < Q^2_{\rm min}$.

terms of the diffractive structure functions

$$\sigma_r^{D(3)}(\beta, Q^2, \xi) = F_T^{D(3)} + \frac{2-2y}{1+(1-y)^2} F_L^{D(3)}, \tag{2}$$

whereas the structure functions T, L may be, respectively, expressed through transversally and longitudinally polarized γ^* - proton cross sections $F_{L,T}^{D(3)} = (Q^4/4\pi^2\alpha_{\rm em}\beta\xi) d\sigma_{L,T}^{\gamma^* p}/dM_X^2$.

In the recent analysis [?] the ZEUS diffractive data were fitted within NLO DGLAP approximation. A satisfactory description was found only for $Q^2 > Q^2_{\rm min} = 5$ GeV^2. The ZEUS fits were performed above $Q^2_{\rm min}$ and then extrapolated to lower photon virtualities. The deviations of the fits rapidly grow with decreasing ξ and Q^2 reaching 100 percent effect at the minimal $Q^2 = 2.5$ GeV^2 and $\xi \simeq 4 \cdot 10^{-4}$. We confirmed this result throug the calculation of $\chi^2/$d.o.f. for subsets of ZEUS LRG data with $Q^2 > Q^2_{\rm min}$ and $\beta > 0.035$ [?] (see Fig. 1, right panel). The cut-off in β is imposed to reject part of the data with significant contributions from higher Fock states not included in our model. It is clear from this discussion that the leading twist DGLAP evolution is unable to describe the DDIS data below $Q^2 \simeq 5$ GeV^2 and at the low ξ.

3 Estimation of the higher twist contributions

The large energy limit of the DDIS scattering may be described within the framework of the colour dipole model [?,?]. In this approach the $\gamma^* p$ process is factorized into an amplitude of photon fluctuation into the partonic debris and then scattering of these states off the proton by the multiple gluon exchange. We take into account the contributions from the fluctuation of the photon into a colour singlet quark-antiquark pair $q\bar{q}$ and into $q\bar{q}$-gluon triple (see Fig. 2). This gives the t-integrated $\gamma^* p$ cross section $d\sigma_{L,T}^{\gamma^* p}/dM_X^2 = d\sigma_{L,T}^{q\bar{q}}/dM_X^2 + d\sigma_{L,T}^{q\bar{q}g}/dM_X^2$.

Assuming an exponential t-dependence of diffractive cross-section, one finds for the $q\bar{q}$ component (see Fig.2, left panel)

$$\frac{d\sigma_{L,T}^{q\bar{q}}}{dM_X^2} = \frac{1}{16\pi b_D} \int \frac{d^2 p}{(2\pi)^2} \int_0^1 dz \delta\left(\frac{p^2}{z\bar{z}} - M_x^2\right) \sum_f \sum_{spin} \left| \int d^2 r e^{i\vec{p}\cdot\vec{r}} \psi^f_{h\bar{h},\lambda}(Q, z, \vec{r}) \sigma_d(r, \xi) \right|^2 . \tag{3}$$

where b_D is a diffractive slope, $z\bar{z} = z(1-z)$ and the first sum runs over the three light flavours. The second sum of (**??**) means summation over massless (anti)quark helicities $(\bar{h})h$ in the case

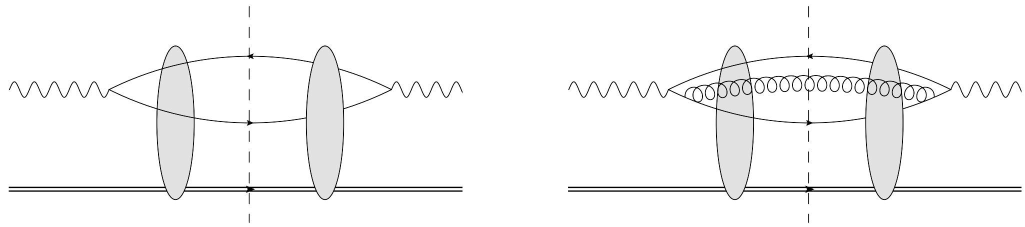

Fig. 2. Left panel - the quark box contribution. Right panel - the $q\bar{q}g$ contribution.

of longitudinal photons whereas for transverse photons there is an additional average over initial photon polarizations λ. The squared photon wave functions can be found in literature[?].

We use the GBW parametrization [?] for the dipole-proton cross section $\sigma_d(r,\xi) = \sigma_0(1 - \exp(-r^2/4R_\xi^2))$ where the saturation radius in DDIS $R_\xi = (\xi/x_0)^{\lambda/2}$ GeV^{-1} and $\sigma_0 = 23.03$ mb, $\lambda = 0.288$, $x_0 = 3.04 \cdot 10^{-4}$. The contribution of the $q\bar{q}g$ component of γ^* (see Fig. 2, the right panel) is calculated at $\beta = 0$ and in the soft gluon approximation (the longitudinal momentum carried by the gluon is much lower then carried by the $q\bar{q}$ pair). This approximation is valid in the crucial region of $M_X^2 \gg Q^2$ or $\beta \ll 1$, where the deviations from DGLAP are observed. The correct β-dependence is then restored using a method described by Marquet [?], with kinematically accurate calculations of Wšthoff [?]. With these approximations one obtains:

$$\begin{aligned} \frac{d\sigma_{L,T}^{q\bar{q}g}}{dM_x^2} &= \frac{1}{16\pi b_D}\frac{N_c\alpha_s}{2\pi^2}\frac{\sigma_0^2}{M_x^2}\int d^2r_{01}N_{q\bar{q}g}^2(r_{01},\xi)\sum_f\sum_{spin}\int_0^1 dz|\psi_{h\bar{h},\lambda}^f(Q,z,r_{01})|^2, \qquad (4)\\ N_{q\bar{q}g}^2(r_{01}) &= \int d^2r_{02}\frac{r_{01}^2}{r_{02}^2r_{12}^2}\left(N_{02}+N_{12}-N_{02}N_{12}-N_{01}\right)^2 \end{aligned}$$

where $N_{ij} = N(\vec{r}_j - \vec{r}_i)$, $\vec{r}_{01}, \vec{r}_{02}, \vec{r}_{12} = \vec{r}_{02} - \vec{r}_{01}$ denote the relative positions of quark and antiquark (01), quark and gluon (02) in the transverse plain. The form of N_{qqg}^2 follows from the Good-Walker picture of the diffractive dissociation of the photon[?]. The factor $1/M_X^2$ is a remnant of the phase space integration under the soft gluon assumption. The twist decomposition of (**??**) is performed through the Taylor expansion in the inverse powers of QR whereas that of (**??**) using Mellin transform technic [?].

4 Discussion

In Fig. 3 we compare selected results with data. The saturation model (MSS model) results are obtained using the original GBW parameters λ and σ_0, and three massless quark flavours. In our approach we modified the GBW parameter x_0 to $\xi_0 = 2x_0$ in order to account for the difference between Bjorken x and pomeron ξ, the variables used in GBW dipole cross-section in DIS and DDIS respectively. We chose $\alpha_s = 0.4$ that provides a good description of the data. The conclusion from the analysis and from Fig. 3 is that a combination of the DGLAP fit and twist-4 and twist-6 components of the model gives a good description of the data at low Q^2. Inclusion of these higher twist terms improves the fit quality in the low Q^2 region (see the dashed curve at Fig. 1 right panel). Indeed, the maximal value of χ^2/d.o.f. $\simeq 1.5$ at $Q^2_{min} = 2$ GeV^2 is significantly lower then χ^2/d.o.f. $\simeq 3$ of the DGLAP fit. Nevertheless, it is important to stress that a truncation of the twist series (up to twist-6) is required to have a good description of the data. The truncation of this kind, however, may be motivated in QCD. Let us recall that in BFKL, at the leading logarithmic approximation, only one reggeized gluon may couple to a fundamental colour line. Since DGLAP and BFKL approximations have the same double logarithmic ($\ln x \ln Q^2$) limit, one concludes that also in DGLAP couplings of more than two

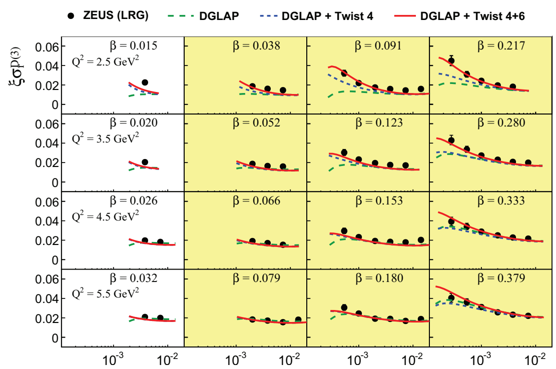

Fig. 3. The LRG ZEUS data for $\xi\sigma_r^{D(3)}$ at low Q^2 compared to a DGLAP fit [?] and the DGLAP fit with included twist-4 and twist-4 and 6 corrections from the MSS saturation model. In yellow (gray) — the region of β where the correction due to $q\bar{q}gg$ may be neglected.

gluons to a colour dipole is much weaker than in the eikonal picture. Thus one can couple only two gluons to a colour dipole and up to four gluons to $q\bar{q}g$ component (two colour dipoles in the large N_c limit) without BFKL constraint. This means that one may expect a suppression beyond twist-8 if only the $q\bar{q}$ and $q\bar{q}g$ components are included in the calculations.

In conclusion, the DDIS data at low Q^2 provide the first evidence for higher twists effects in DIS in the perturbative domain and opens a possibility for further theoretical and experimental investigations.

Acknowledgments

The work is supported by the Polish National Science Centre grant no. DEC-2011/01/B/ST2/03643.

References

1. J. Collins, Phys. Rev. **D57** (1998) 3051.
2. S. Chekanov et al. [ZEUS Collaboration], Nucl. Phys. **B831** (2010) 1; Nucl. Phys. **B816** (2009) 1.
3. L. Motyka, M. Sadzikowski and W. Slominski, arXiv:hep-ph/1203.5461 (2012).
4. N. N. Nikolaev and B. G. Zakharov, Z. Phys. **C49** (1991) 607.
5. K. J. Golec-Biernat and M. Wüsthoff, Phys. Rev. **D59** (1998) 014017, Phys. Rev. **D60** (1999) 114023.
6. H. Kowalski, L. Motyka and G. Watt, Phys. Rev. **D74** (2006) 074016.
7. C. Marquet, Phys. Rev. **D76** (2007) 094017.
8. M. Wüsthoff, Phys. Rev. **D56** (1997) 4311.
9. S. Munier and A. Shoshi, Phys. Rev. **D69** (2004) 074022.

Unintegrated sea quark at small x and vector boson production

F. Hautmann
University of Oxford, Oxford OX1 3NP

Martin Hentschinski
Instituto de Física Teórica UAM/CSIC, Universidad Autónoma de Madrid, E-28049 Madrid

H. Jung
Deutsches Elektronen Synchrotron, D-22603 Hamburg,
CERN, Physics Department, CH-1211 Geneva 23

Parton-shower event generators that go beyond the collinear-ordering approximation at small x have so far included only gluon and valence quark channels at transverse momentum dependent level. In this contribution we provide a definition of a transverse momentum depend (TMD) sea quark distribution valid in the small x region, which is based on the TMD gluon-to-quark splitting function. As an example process we consider vector boson production in the forward direction of one of the protons. The $qq^* \to Z$ matrix element (with one off-shell quark) is calculated in an explicit gauge invariant way, making use of high energy factorization.

1 Introduction

Scattering processes with a single hard scale are well described within the framework of collinear factorization. The treatment of multi-scale processes is on the other hand more involved. In this case, generalized factorization formula are needed to gain control over large logarithms in higher orders of perturbation theory [?]. Such generalized factorization formulas typically involve transverse-momentum dependent (TMD), or "unintegrated" parton distribution and parton decay functions. A broad class of such multiple-scale events is given by small-x processes. The latter are one of the main sources of final states in the central region at the LHC and lead to sizeable rates of forward large-$p_\perp$ jet production at the LHC [?,?]. At small x, TMD parton distributions arise naturally as a consequence of high energy factorization and BFKL evolution [?]. k_T-factorization[?,?] provides then the matching of these high energy factorized TMD distributions to collinear factorized distributions. For Monte Carlo applications a convenient description is given in terms of the CCFM evolution equation [?] which interpolates for inclusive observables between DGLAP and BFKL evolution [?]. It therefore provides a natural basis for a Monte-Carlo realization of k_T-factorization which is provided by the Monte Carlo event generator Cascade [?].

Computational tools based on TMD parton densities have so far been developed within a quenched approximation where only gluons and valence quarks are taken into account [?,?]. While this captures correctly the leading contributions at small x, it is mandatory to go beyond this approximation in order to include preasymptotic effects and to treat final states associated with quark-initiated processes such as Drell-Yan production.

In this contribution we present first steps in this direction, through providing a definition for a TMD sea quark distribution at small x. As an example process we examine forward Drell-Yan production. For a detailed description we refer to [?].

2 Definition of a TMD sea quark distribution and off-shell $qq^* \to Z$ coefficient

The following definition of an unintegrated sea-quark distribution at small x is based on the off-shell TMD gluon-to-quark splitting function [?]. It is obtained by generalizing the expansion in two-particle irreducible kernels of [?] to finite transverse momenta. It reads

$$P_{qg}\left(z, \frac{\boldsymbol{k}^2}{\boldsymbol{\Delta}^2}\right) = T_R \left(\frac{\boldsymbol{\Delta}^2}{\boldsymbol{\Delta}^2 + z(1-z)\boldsymbol{k}^2}\right)^2 \left[(1-z)^2 + z^2 + 4z^2(1-z)^2 \frac{\boldsymbol{k}^2}{\boldsymbol{\Delta}^2}\right]. \tag{1}$$

Here $\boldsymbol{\Delta} = \boldsymbol{q} - z\cdot\boldsymbol{k}$ with $\boldsymbol{k}$ and $\boldsymbol{q}$ transverse momenta of the off-shell gluon and quark respectively, while z is the fraction of the 'minus' light cone momentum of the gluon which is carried on by the t-channel quark. Although evaluated off-shell, the splitting probability is universal. In combination with the gluon Green's function, it takes into account the full small x enhanced transverse momentum dependence to all orders in the strong coupling. The transverse momenta of the sea quark arises therefore as a consequence of subsequent small x enhanced branchings which are not strongly ordered in their transverse momenta. To relate this parton splitting

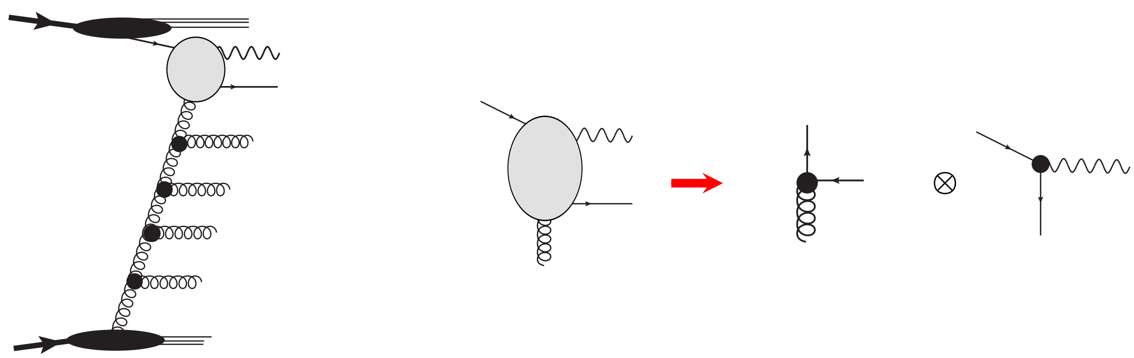

(a) (b)

Figure 1: (a): If the vector boson is produced in the forward region, the sea quark density becomes sensitive to multiple small x enhanced gluon emissions, leading to a k_T-dependent gluon density (b): Schematic factorization of the partonic $qg^* \to Zq$ process of a) into the $g^* \to q^*$ splitting and the $qq^* \to Z$ coefficient.

kernel to forward vector boson production, we analyze the flavor exchange process $g^*q \to Zq$, see Fig. **??**. At high (partonic) center of mass energy, this process can be treated according to the "reggeized quark" calculus [?,?]. The latter extends the effective action formalism [?], currently explored at NLO [?], to amplitudes with quark exchange in terms of effective degrees of freedom, the so-called reggeized quarks [?,?]. The use of the effective vertices [?,?] ensures gauge invariance of the coefficients relevant to perform the high-energy factorization [?,?] for vector boson production, despite the off-shell parton. If taken literally, the reggeized quark calculus leads for the $g^*q \to Zq$ process to a rather crude approximation to the $g^* \to q^*$ splitting function. This is due to a strong ordering condition which sets the 'plus' momenta of the off-shell quark for the $g^* \to q^*$ splitting to zero. For Eq. (**??**) this corresponds to the limit $z \to 0$. It is however possible to relax this kinematic restriction and to keep z finite, while maintaining the gauge invariance properties of the original vertex. For the $g^* \to q^*$ splitting this yields then precisely the splitting function Eq. (**??**).

For the $qq^* \to Z$ coefficient, the high energy limit sets the 'minus' component of the quark momentum to zero. While it is possible to relax the ordering prescription also in this case, both versions are in agreement with collinear factorization and will be therefore considered in the following. We obtain

$$\hat{\sigma}_{qq^* \to Z} = \sqrt{2} G_F M_Z^2 (V_q^2 + A_q^2) \frac{\pi}{N_c} \delta(z x_1 x_2 s + T - M_Z^2). \tag{2}$$

Here the variable T parametrizes the off-shellness of the t-channel quark. In the collinear limit $T = 0$ and Eq. (**??**) agrees with the conventional $qq \to Z$ coefficient. For the general off-shell case, T coincides with the squared transverse momentum of the off-shell quark if strong minus momentum ordering is fulfilled. If this condition is on the other hand relaxed, T agrees with the absolute value of the squared four momentum of the off-shell quark. These two possibilities then factorize the $qg^* \to qZ$ process as convolutions in the modulus of transverse (k_T) and four momentum (t) respectively. For further details we refer to the paper [?].

3 Numerical analysis

In the following section we compare the different off-shell factorized expressions with the full $qg^* \to qZ$ matrix element result and an expression which uses only the collinear splitting function. For small $|\boldsymbol{\Delta}|$, the differences between t and k_T-factorized expressions are numerically

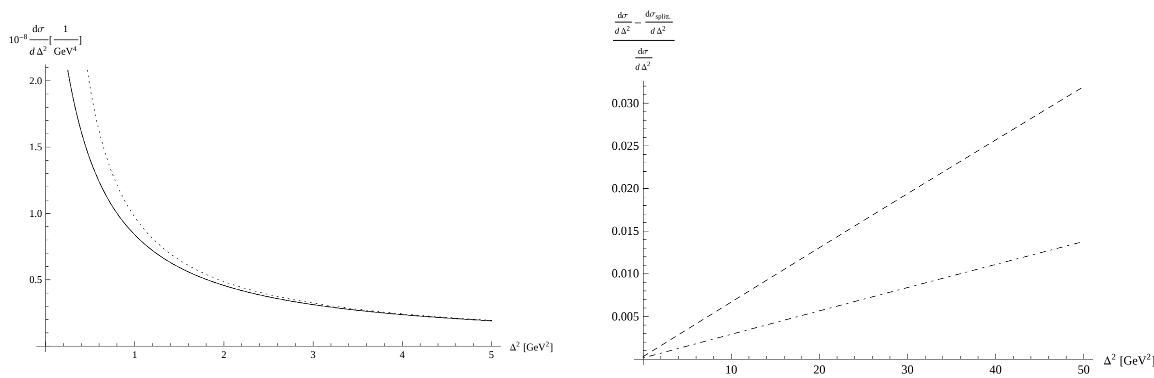

(a) (b)

Figure 2: (a): $\boldsymbol{\Delta}^2$ dependence of the differential cross section $d\sigma/d\boldsymbol{\Delta}^2$ for small $|\boldsymbol{\Delta}|$: (solid) full; (dashed) no plus-momentum ordering; (dot-dashed) no plus-momentum and minus-momentum ordering; (dotted) collinear approximation. All but the last curve overlap in this region. We set $x_1 x_2 s = 2.5 M_Z^2$, $\boldsymbol{k}^2 = 2$ GeV^2. (b): Relative deviations in the differential cross section $d\sigma/d\boldsymbol{\Delta}^2$: (dashed) no plus-momentum ordering; (dot-dashed) no plus-momentum and minus-momentum ordering.

small. Both expressions are close to the full result; as $|\boldsymbol{\Delta}|$ increases, we find that the deviations due to the kinematic contributions by which both versions differ become non-negligible, and that the t-factorized expression gives a better approximation to the full result.

Future extensions of the above results concern at first large-x corrections, likely to be important for Drell-Yan phenomenology, see [?,?,?,?]. Another direction addresses the inclusion of full quark emissions to the evolution of the unintegrated parton densities. The latter are naturally contained in both leading-order DGLAP evolution and unintegrated parton densities which taken into account full next-to-leading order BFKL evolution, see [?] for related work. The results in this paper can be implemented in a parton shower Monte Carlo generator including transverse-momentum dependent branching, such as [?]. Work along these lines is in progress.

Acknowledgments

We thank the organizers for the opportunity to present this work at the meeting. M. H. is grateful for financial support from the German Academic Exchange Service (DAAD), the MICINN under grant FPA2010-17747, the Research Executive Agency (REA) of the European Union under the Grant Agreement number PITN-GA-2010-264564 (LHCPhenoNet) and the Helmholtz Terascale Analysis Center.

References

1. J.C. Collins, *Foundations of perturbative QCD*, CUP 2011.
2. M. Deak *et al.*, JHEP **0909** (2009) 121; arXiv:0908.1870 [hep-ph]; F. Hautmann, arXiv:0909.1250 [hep-ph]; PoS ICHEP2010 (2010) 108; arXiv:1101.2656 [hep-ph].
3. M. Deak *et al.*, arXiv:1012.6037 [hep-ph]; arXiv:1112.6354 [hep-ph]; arXiv:1112.6386 [hep-ph].
4. V. S. Fadin, E. A. Kuraev and L. N. Lipatov, Phys. Lett. B **60** (1975) 50, I. I. Balitsky and L. N. Lipatov, Sov. J. Nucl. Phys. **28** (1978) 822 [Yad. Fiz. **28** (1978) 1597].
5. S. Catani, M. Ciafaloni and F. Hautmann, Phys. Lett. B**307** (1993) 147; Nucl. Phys. B**366** (1991) 135; Phys. Lett. B**242** (1990) 97.
6. S. Catani and F. Hautmann, Nucl. Phys. B**427** (1994) 475; Phys. Lett. B**315** (1993) 157.
7. M. Ciafaloni, Nucl. Phys. B **296** (1988) 49, S. Catani, F. Fiorani and G. Marchesini, Nucl. Phys. B **336** (1990) 18.
8. F. Hautmann and H. Jung, Nucl. Phys. B Proc. Suppl. **184** (2008) 64; arXiv:0808.0873 [hep-ph]; F. Hautmann, Acta Phys. Polon. B **40** (2009) 2139; PoS ICHEP2010 (2010) 150.
9. H. Jung *et al.*, Eur. Phys. J. C **70** (2010) 1237.
10. F. Hautmann and H. Jung, JHEP **0810** (2008) 113; arXiv:0804.1746 [hep-ph].
11. F. Hautmann, M. Hentschinski and H. Jung, arXiv:1205.1759 [hep-ph], F. Hautmann, M. Hentschinski and H. Jung, in preparation.
12. G. Curci, W. Furmanski and R. Petronzio, Nucl. Phys. B**175** (1980) 27.
13. L. N. Lipatov and M. I. Vyazovsky, Nucl. Phys. B**597** (2001) 399.
14. A. V. Bogdan and V. S. Fadin, Nucl. Phys. B**740** (2006) 36.
15. L.N. Lipatov, Nucl. Phys. B**452** (1995) 369; Phys. Rept. **286** (1997) 131.
16. M. Hentschinski and A. Sabio Vera, Phys. Rev. D **85** (2012) 056006 [arXiv:1110.6741 [hep-ph]]; M. Hentschinski, Nucl. Phys. B **859** (2012) 129 [arXiv:1112.4509 [hep-ph]]; G. Chachamis, M. Hentschinski, J. D. Madrigal Martinez and A. Sabio Vera, Nucl. Phys. B **861** (2012) 133 [arXiv:1202.0649 [hep-ph]].
17. V. S. Fadin and V.E. Sherman, Zh. Eksp. Teor. Fiz. 72 (1977) 1640;
18. B.A. Kniehl, V. A. Saleev, A.V. Shipilova and E.V. Yatsenko, Phys. Rev. D **84** (2011) 074017; B.A. Kniehl, V. A. Saleev and A.V. Shipilova, Phys. Rev. D **79** (2009) 034007; V. A. Saleev, Phys. Rev. D **80** (2009) 114016; Phys. Rev. D **78** (2008) 114031. Pisma Zh. Eksp. Teor. Fiz. 23 (1976) 599.
19. M. Hentschinski, arXiv:1112.6339 [hep-ph], G. Chachamis, M. Hentschinski, A. Sabio Vera and C. Salas, arXiv:0911.2662 [hep-ph], M. Hentschinski, A. Sabio Vera and C. Salas, in preparation.
20. M. Garcia-Echevarria, A. Idilbi and I. Scimemi, arXiv:1111.4996 [hep-ph]; Phys. Rev. D**84** (2011) 011502; A. Idilbi and I. Scimemi, arXiv:1012.4419; Phys. Lett. B **695** (2011) 463.
21. F.A. Ceccopieri, Mod. Phys. Lett. A**24** (2009) 3025; arXiv:1006.4731 [hep-ph]; F.A. Ceccopieri and L. Trentadue, Phys. Lett. B**660** (2008) 43; Phys. Lett. B**636** (2006) 310.
22. I.O. Cherednikov and N.G. Stefanis, Nucl. Phys. B**802** (2008) 146; Phys. Rev. D**77** (2008) 094001; Phys. Rev. D**80** (2009) 054008; arXiv:0911.1031 [hep-ph]; I.O. Cherednikov, A.I. Karanikas and N.G. Stefanis, Nucl. Phys. B**840** (2010) 379.
23. J.C. Collins and F. Hautmann, JHEP **0103** (2001) 016; Phys. Lett. B **472** (2000) 129; F. Hautmann, Nucl. Phys. B**604** (2001) 391; Phys. Lett. B **655** (2007) 26; arXiv:0708.1319 [hep-ph].

New measurements of transverse spin asymmetries at COMPASS

F. Sozzi on behalf of the COMPASS Collaboration
INFN, Sezione di Trieste
via Valerio 3, 34128, Italy

The study of transverse momentum effects and transverse spin structure of the nucleon is an important part of the scientific program of COMPASS, a fixed target experiment at the CERN SPS. The transverse effects are investigated via semi inclusive DIS reactions with a 160 GeV/c muon beam impinging on transversely polarised targets. The hadrons produced in the reactions are detected in a wide momentum and angular range by a two-stage spectrometer. A deuterium target has been used in the first part of COMPASS data taking from 2002 to 2004, while a proton target has been used in 2007 and 2010. Here we present the recent results obtained from the 2010 data on different channels, involving the azimuthal distribution of single hadrons and the azimuthal dependence of the plane containing hadron pairs. The results confirm the published results of the 2007 data taking with an improved statistical significance; the measured azimuthal asymmetries are clearly non zero, at variance with those measured on a deuterium target.

1 Introduction

To fully specify the quark structure of the nucleon at twist two level, three parton distribution functions (PDF) are needed: the well known momentum and helicity distribution $q(x)$ and $\Delta q(x)$, and the transversity distribution $\Delta_T q(x)$. Transversity describes the probability density of finding transversely polarised quarks in a transversely polarised nucleon. In the past years it has received a lot of attention, both from the experimental and from the theoretical point of view.

Transversity is chiral odd, thus it must be coupled to another chiral-odd function in order to build an observable. It can be measured in semi-inclusive DIS experiments (SIDIS), where at least one hadron in the final state is detected. In particular, two channels investigated by the COMPASS Collaboration are described in this contribution: the azimuthal distribution of single hadrons and the azimuthal dependence of hadron pairs.

2 The COMPASS experiment

COMPASS [1] is a fixed target experiment at the CERN SPS, with a physics program focused on the study of the nucleon spin structure and of hadron spectroscopy. The nucleon spin structure is investigated using a high energy muon beam of 160 GeV/c on targets that are either longitudinally polarised (in order to access gluon polarisation and helicity PDF) or transversely polarised (to access the transversity PDF and transverse momentum dependent PDFs).

The detection and the identification of hadrons for SIDIS measurements is done in a two-stage spectrometer, that allows to cover a large kinematic range in momentum and angular acceptance. The spectrometer comprises several type of trackers, as well as electromagnetic and hadronic calorimeters, muon walls for the muon identification, and a RICH detector.

Different periods of the COMPASS data taking has been devoted to transversity measurements:

- 20% of the time in the years 2002, 2003 and 2004; the target material was ^{6}LiD, characterised by polarisation values P_t of the order of 50% and dilution factor f around 0.38;
- 50% of the time of year 2007; the material was NH_3 ($P_t \sim 90\%$ and $f \sim 0.15$);
- full 2010 year: a NH_3 target was used again, to improve the precision of the results from the 2007 run.

The most recent results from the 2010 data taking are shown in this contribution.

3 Collins asymmetries

In SIDIS on a transversely polarised target the so called Collins effect [2] gives origin to azimuthal asymmetries in the single hadron production. In this mechanism the Collins fragmentation function, describing the correlation between the fragmenting quark spin and the momentum of the produced hadron, introduces a left-right asymmetry in the distribution of the hadron. The hadron yield can be written as:

$$N = N_0 \cdot (1 + f \cdot P_t \cdot D_{nn} \cdot A_C \cdot \sin(\phi_C)) \tag{1}$$

where f and P_t have been already introduced, and $D_{nn} = (1-y)/(1-y+y^2/2)$ is the transverse spin transfer coefficient from the initial to the struck quark. The Collins angle ϕ_C is defined as $\phi_h - \phi_{s'}$, where ϕ_h is the angle of the transverse momentum of the outgoing hadron and $\phi_{s'} = \pi - \phi_s$ is the azimuthal angle of the struck quark spin (ϕ_s is the azimuthal angle of quark before the hard scattering). A_C is the Collins asymmetry, proportional to the convolution of the Collins fragmentation function and the transversity distribution. Comparing the number of hadrons produced in SIDIS reactions on nucleons polarised transversely in opposite directions, the modulation given by the Collins angle gives access to the asymmetry A_C.

The results obtained from the 2010 data are shown in fig. 1, as a function of x, of the hadron relative energy z, and of the transverse momentum of the hadron p_T; the bands in the picture represent the systematic uncertainties, that are 50% of the statistical errors. The Collins asymmetries confirm the results from 2007 data [3], with an improved statistical precision, around a factor of 2. In the valence region, for x larger than 0.03, there is a large signal of opposite sign for positive and negative hadrons. This result is in agreement with the other existing measurement on a proton target, by the HERMES experiment [4]; since the Q^2 values in the last x bins are higher in COMPASS of a factor 2-3 with respect to HERMES's, the agreement between the two experiments implies a negligible Q^2 dependence for the Collins effect. In the small x region, not covered by the HERMES experiment, the asymmetries are compatible with zero, for both hadron charges.

Transversity has been already extracted performing global fit [5] using Collins asymmetries from COMPASS on deuterium data [8,7,6] and from HERMES on proton data, as well as azimuthal asymmetries in $e^+e^- \to \pi^+\pi^-$ annihilation from Belle [9], that give independent information on the Collins FF. The Collins asymmetries from the 2010 data are of particular importance and interest since they can be used in the global fits, providing precise data, in a large x and Q^2 range.

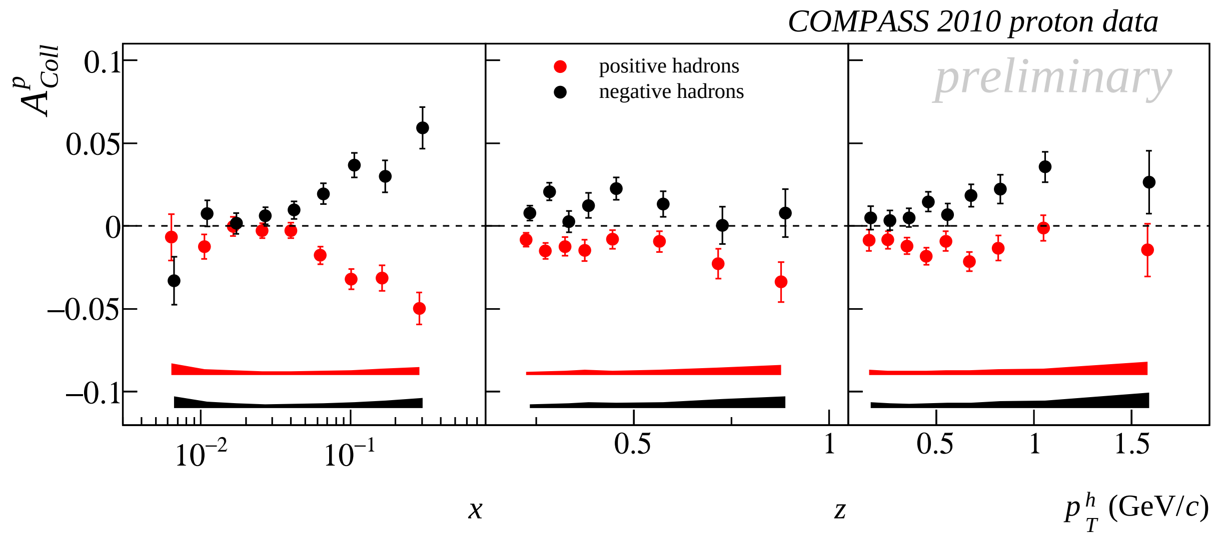

Figure 1: Collins asymmetries for positive and negative hadrons as a function of x, z and p_T.

4 Hadron pair asymmetries

The transversity PDF can be accessed also via the hadron pair asymmetries. In this case, transversity is coupled to another chiral odd function, the di-hadron fragmentation function, describing the correlation between the transverse polarisation of the fragmenting quark and the azimuthal angle of the plane containing the hadron pair.

The hadron pair asymmetries from the 2010 run are shown in fig. 2, as a function of x, the sum of the relative energies of the two hadrons z, and their invariant mass M. The bands represent the systematic uncertainties, equal to 0.8 of the statistical errors. As for the Collins asymmetries, the statistical precision has been improved of a factor 2 with respect to the 2007 results [10]. In the small x region the asymmetry is compatible with zero, while a large signal up to 5-10% in the valence region is visible. Also in this case, in the overlap region there is agreement with the HERMES result [11].

Recently a first extraction of transversity from the hadron-pair asymmetries measured by HERMES or COMPASS has been done. The extraction [12] has been made possible by the first available asymmetries in $e^+e^- \to (\pi^+\pi^-)(\pi^+\pi^-)$ channel by the Belle Collaboration [13]. This way to access transversity is interesting since it provides independent information with respect to the Collins channel. Although with still large error uncertainty, the results extracted from the hadron pair asymmetries are in agreement with the parametrisation obtained in the global fit of the one hadron channel. The new measurement of hadron pair asymmetries from 2010 can be used to improve the significance of the extraction.

5 Conclusions

From 2005 onwards, results on Collins and hadron-pair asymmetries have been produced by COMPASS, using a deuterium target in 2002-2004 and a proton target in 2007 and 2010. The most recent results from the 2010 data confirm the 2007 results with improved statistical uncertainties, and can be used to extract the transversity PDFs in global fits.

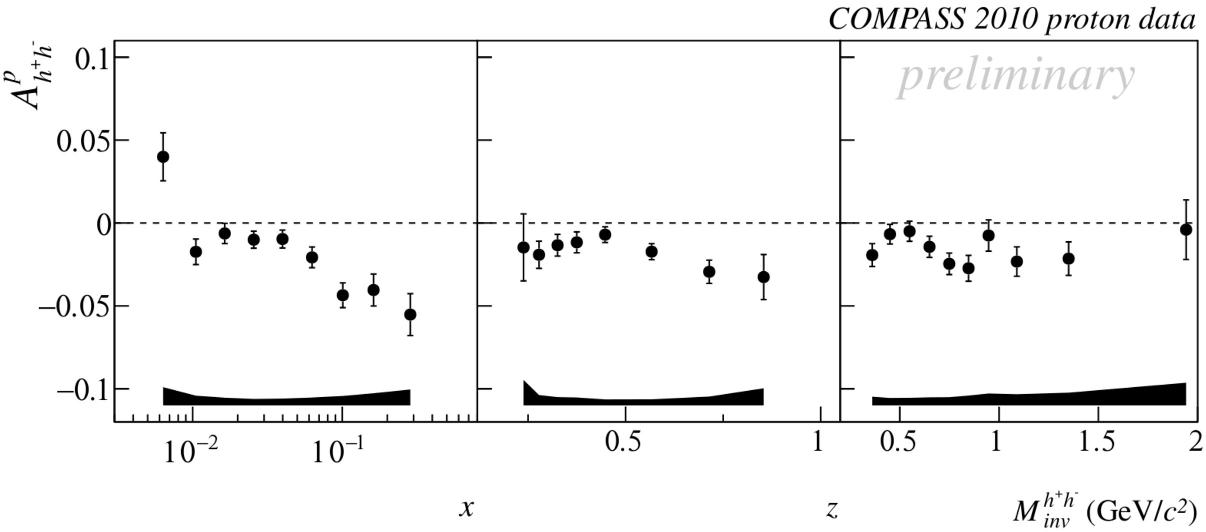

Figure 2: Hadron-pair asymmetries as a function of x, z and M_h.

References

1. P. Abbon *et al.* [COMPASS Collaboration], Nucl. Instrum. Meth. A **577**, 455 (2007).
2. J. C. Collins, Nucl. Phys. B **396**, 161 (1993).
3. M. G. Alekseev *et al.* [COMPASS Collaboration], Phys. Lett. B **692** (2010) 240
4. A. Airapetian *et al.* [HERMES Collaboration], Phys. Lett. B **693**, 11 (2010)
5. M. Anselmino, M. Boglione, U. D'Alesio, A. Kotzinian, F. Murgia, A. Prokudin and C. Turk, Phys. Rev. D **75**, 054032 (2007)
6. V. Y. Alexakhin *et al.* [COMPASS Collaboration], Phys. Rev. Lett. **94**, 202002 (2005).
7. E. S. Ageev *et al.* [COMPASS Collaboration], Nucl. Phys. B **765**, 31 (2007).
8. M. Alekseev *et al.* [COMPASS Collaboration], Phys. Lett. B **673** (2009) 127
9. R. Seidl *et al.* [Belle Collaboration], Phys. Rev. D78 (2008) 032011.
10. C. Adolph *et al.* [COMPASS Collaboration], Phys. Lett. B **713** (2012) 10
11. A. Airapetian *et al.* [HERMES Collaboration], JHEP **0806**, 017 (2008)
12. A. Bacchetta, A. Courtoy and M. Radici, Phys. Rev. Lett. **107**, 012001 (2011)
13. A. Vossen *et al.* [Belle Collaboration], Phys. Rev. Lett. **107**, 072004 (2011)

Progress in top-pair production at hadron colliders [a]

Peter Bärnreuther, Michał Czakon
Institut für Theoretische Teilchenphysik und Kosmologie, RWTH Aachen University, D-52056 Aachen, Germany

Alexander Mitov [b]
Theory Division, CERN, CH-1211 Geneva 23, Switzerland

We review recently derived NNLO QCD results for top-pair production at hadron colliders. We compare the size of the NNLO corrections in $q\bar{q} \to t\bar{t}+X$ with the LO and NLO ones, and address the question of convergence of perturbative series. We compare the NLO and NNLO K-factors for the Tevatron.

1 Introduction

The speed with which the LHC, complemented by the measurements from the Tevatron, is reshaping the landscape of particle physics is remarkable. In two short years a number of constraints on new physics have been placed and the search for a light Standard Model Higgs boson has narrowed down to a small window around $m_{\text{Higgs}} = 126$ GeV. An important lesson from these searches is the need for precise knowledge of Standard Model signals and backgrounds.

During the last several years, similarly profound advances in our ability to tame perturbative QCD and describe with increasing precision and confidence hadron collider observables were made. These developments are nowhere more evident than in top physics.

First, the advances in NLO calculations of the recent past [?,?,?,?] made possible fully exclusive calculations for final states with large multiplicities ($t\bar{t}$ + up to 2 jets), including top decays and even accounting for non-factorizable effects [?,?,?,?,?,?,?,?,?,?,?]. Only few years ago such progress seemed like an impossible task.

Second, also in the last several years, a renewed, massive push for describing the higher order (i.e. NNLO) corrections in top pair production was undertaken. It is an approach based on approximating the NNLO cross-section with its threshold behavior [?,?,?]. A number of phenomenological predictions were made [?,?,?,?,?,?,?,?,?,?], and compared in [?,?,?]. We have concluded [?] that the ability of such an approach to unambiguously solve the question of higher order (NNLO) effects in top-pair production is limited. To resolve this, we have undertaken the task of computing the complete NNLO result for top-pair production at hadron colliders. The result for the $q\bar{q} \to t\bar{t} + X$ reaction appeared in [?], which we describe next. Very recently, also the so-called BLM/PMC approach was applied to top production at NNLO [?].

[a]Preprint numbers: CERN-PH-TH/2012-155, TTK-12-24.
[b]Speaker.

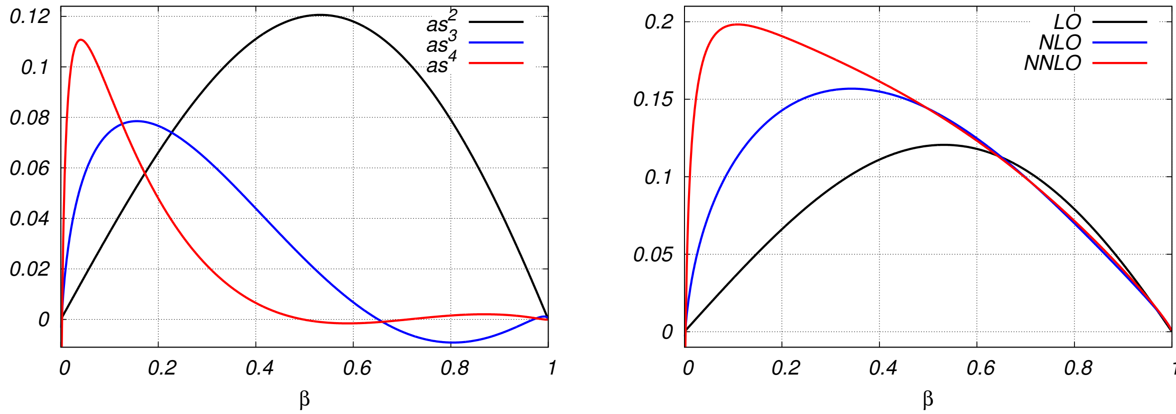

Figure 1: (Left plot) the functions $f_{\alpha_S^2}$ (black), $f_{\alpha_S^3}$ (blue) and $f_{\alpha_S^4}$ (red) as defined in Eq. (**??**). (Right plot) their contribution to $\hat{\sigma}$ at LO ($f_{\alpha_S^2}$), NLO ($f_{\alpha_S^2} + f_{\alpha_S^3}$) and NNLO ($f_{\alpha_S^2} + f_{\alpha_S^3} + f_{\alpha_S^4}$).

2 Results at NNLO

In [?] we calculate the NNLO corrections to the reaction $q\bar{q} \to t\bar{t} + X$. The calculation is based on the two-loop virtual corrections from [?], the analytical form for the poles [?] and the one-loop squared amplitude [?]. The real-virtual corrections are derived by integrating the one–loop amplitude with a counter-term that regulates it in all singular limits [?]. The finite part of the one-loop amplitude is computed with a code used in the calculation of $pp \to t\bar{t} + \text{jet}$ at NLO [?]. The most nontrivial part of the calculation are the double real corrections [?]. As in Ref. [?], we do not include the contribution from the reaction $q\bar{q} \to t\bar{t}q\bar{q}$ where the final state light pair has the same flavor as the initial state one. We expect the contribution from this reaction to be negligible. The explicit results for this contribution, as well as the remaining pure fermionic reactions qq, qq' and $q\bar{q}'$, with $q' \neq q$, will be presented elsewhere.

The dominant role of the $q\bar{q} \to t\bar{t} + X$ reaction to top-pair production at the Tevatron, makes it possible to use the results derived in [?] for a consistent, NNLO-level phenomenology at this collider of the hadronic total inclusive cross-section:

$$\sigma_{\text{had}}(\rho_h) = \int_0^{\beta_{\max}} d\beta \, \hat{\sigma}(\beta) \, \Phi_{\rho_h}(\beta) \,, \tag{1}$$

where $\rho_h \equiv 4m_{\text{top}}^2/s_{\text{collider}}$ and $\beta_{\max} \equiv \sqrt{1-\rho_h}$. The flux Φ reads:

$$\Phi_{\rho_h}(\beta) = \frac{2\beta}{1-\beta^2} \, \mathcal{L}\left(\frac{\rho_h}{1-\beta^2}\right) \,, \tag{2}$$

and $\mathcal{L}(x) = x\,(f_1 \otimes f_2)\,(x)$ is the usual partonic luminosity given as a convolution of two parton distributions. We have suppressed for short the partonic indices (and the sum over them) as well as factorization and renormalization scales (we set $\mu_F = \mu_R = m_{\text{top}}$ throughout).

Through NNLO the partonic cross-section $\hat{\sigma}$ has the following expansion:

$$\hat{\sigma}(\beta) \;=\; \frac{\alpha_S^2}{m^2}\left(\sigma^{(0)} + \alpha_S\sigma^{(1)} + \alpha_S^2\sigma^{(2)} + \dots\right) \equiv \frac{\alpha_S^2}{m^2}\left(f_{\alpha_S^2} + f_{\alpha_S^3} + f_{\alpha_S^4} + \dots\right) . \tag{3}$$

The functions $f_{\alpha_S^2}, f_{\alpha_S^3}$ and $f_{\alpha_S^4}$ for the reaction $q\bar{q} \to t\bar{t} + X$ and with $N_L = 5$ are plotted on the left Fig. (**??**), while on the right we present their contribution to the cross-section, i.e. $f_{\alpha_S^2}$ at LO, $f_{\alpha_S^2} + f_{\alpha_S^3}$ at NLO and $f_{\alpha_S^2} + f_{\alpha_S^3} + f_{\alpha_S^4}$ at NNLO.

The curves plotted on Fig. (**??**) naturally raise the question about the convergence of the perturbative series. We observe that the subsequent higher orders do not get smaller (for example in the naive sense of their integrals or maxima) and tend to get distributed closer and closer to the absolute threshold $\beta = 0$. The reason for this behavior is that the higher orders are more and more dominated by the soft gluon and Coulomb terms. One can anticipate that at even higher perturbative orders this trend will continue.

We would like to point out two important additions to this observation. First, it does not account for the fact that close to threshold (where the corrections are largest) perturbation theory breaks down and resummation of the soft-gluon corrections is needed to restore the predictivity of perturbation theory. A not-so-well-known example for an effect of this type is the fact that beyond order α_S^4, the Coulomb terms in the fixed order expansion will render the perturbative cross-section nonintegrable - a seemingly disastrous implication - that is resolved by the observation that Coulombic terms *must* be factorized and resummed; see [?] for details.

Second, the size of the curves on Fig. (**??**) does not directly determine the hadronic cross-section. For that one needs to multiply them with the partonic flux (**??**). Due to Jacobian factor $\sim \beta$ the flux vanishes at threshold as a power which dominates over the logarithmic rise of the partonic cross-section due to soft-gluon radiation. For example, for top production at Tevatron, the flux is roughly bell shaped with maximum around $\beta \approx 0.7$ thus making the behavior of the partonic cross-section away from threshold more relevant for the hadronic cross-section.

Finally, we discuss K-factors at the Tevatron. Introducing the shorthand notation I_n for the contribution of the functions $f_{\alpha_S^n}$, $n = 2, 3, 4$ (from all partonic reactions) to the cross-section $\sigma_{\rm had}$, and following the setup outlined in [?] implemented in the program `Top++` (ver. 1.2) [?], we get:

$$I_2 = 5.221\,[\text{pb}] \quad , \quad I_3 = 1.234\,[\text{pb}] \quad , \quad I_4 = 0.548\,[\text{pb}]\,. \tag{4}$$

From the above equation we derive the following K-factors for the Tevatron:

$$K_{\rm NLO/LO} = 1.24 \quad , \quad K_{\rm NNLO/NLO} = 1.08\,. \tag{5}$$

We use the MSTW2008nnlo68cl pdf set [?]. We note that the K-factors are not sensitive to the choice of pdf set (for example NNLO or NLO), or if NNLL resummation is included or not.

3 Conclusions and outlook

In [?] we have performed the first ever NNLO calculation of a hadron collider process with more than 2 colored partons (there are four) and/or massive fermions. The result exhibits remarkable stability with respect to scale variation and suggests very precise estimate of the total cross-section for top-pair production at the Tevatron. When supplemented with soft gluon resummation at NNLL the stability of the result further increases, as expected. The result calculated matches all partial checks available in the literature.

The K-factor derived from the NNLO result is modest and shifts the NLO result by about 8% (when both the NLO and NNLO are computed with the same pdf). The inclusion of the $q\bar{q} \to t\bar{t} + X$ reaction at NNLO improves also the prediction at the LHC [?]. While this is the most complete theoretical prediction available for the LHC, it is clear that substantial improvement for the Large Hadron Collider can be expected only upon inclusion of the $qg-$ and $gg-$initiated reactions. Our calculational method is well suited for the calculation of these reactions and, even more importantly, fully differential top-pair production, including the $\mathcal{O}(\alpha_S^4)$ correction to the top-pair charge asymmetry. We anticipate reporting these results in the near future.

Acknowledgments

The work of M.C. was supported by the Heisenberg and by the Gottfried Wilhelm Leibniz programmes of the Deutsche Forschungsgemeinschaft, and by the DFG Sonderforschungsbereich/Transregio 9 Computergestützte Theoretische Teilchenphysik.

References

1. Z. Bern, L. J. Dixon, D. C. Dunbar and D. A. Kosower, Nucl. Phys. B **425**, 217 (1994).
2. R. Britto, F. Cachazo and B. Feng, Nucl. Phys. B **725** (2005) 275 [hep-th/0412103].
3. G. Ossola, C. G. Papadopoulos and R. Pittau, Nucl. Phys. B **763**, 147 (2007).
4. W. T. Giele, Z. Kunszt and K. Melnikov, JHEP **0804**, 049 (2008) [arXiv:0801.2237].
5. S. Dittmaier, P. Uwer, S. Weinzierl, Phys. Rev. Lett. **98**, 262002 (2007) [hep-ph/0703120 [hep-ph]]; Eur. Phys. J. **C59**, 625-646 (2009) [arXiv:0810.0452 [hep-ph]].
6. A. Bredenstein, A. Denner, S. Dittmaier, S. Pozzorini, Phys. Rev. Lett. **103** (2009) 012002
7. K. Melnikov and M. Schulze, JHEP **0908**, 049 (2009) [arXiv:0907.3090 [hep-ph]].
8. G. Bevilacqua, M. Czakon, C. G. Papadopoulos, R. Pittau, M. Worek, JHEP **0909** (2009) 109 [arXiv:0907.4723 [hep-ph]].
9. A. Bredenstein, A. Denner, S. Dittmaier, S. Pozzorini, JHEP **1003** (2010) 021.
10. G. Bevilacqua, M. Czakon, C. G. Papadopoulos, M. Worek, Phys. Rev. Lett. **104** (2010) 162002 [arXiv:1002.4009 [hep-ph]].
11. A. Denner, S. Dittmaier, S. Kallweit, S. Pozzorini, Phys. Rev. Lett. **106** (2011) 052001.
12. G. Bevilacqua, M. Czakon, A. van Hameren, C. G. Papadopoulos, M. Worek, JHEP **1102** (2011) 083 [arXiv:1012.4230 [hep-ph]].
13. G. Bevilacqua, M. Czakon, C. G. Papadopoulos, M. Worek, Phys. Rev. D **84** (2011) 114017
14. M. Worek, JHEP **1202** (2012) 043 [arXiv:1112.4325 [hep-ph]].
15. M. Beneke, P. Falgari and C. Schwinn, Nucl. Phys. B **828**, 69 (2010) [arXiv:0907.1443].
16. M. Czakon, A. Mitov and G. F. Sterman, Phys. Rev. D **80**, 074017 (2009).
17. M. Beneke, M. Czakon, P. Falgari, A. Mitov and C. Schwinn, Phys. Lett. B **690**, 483 (2010) [arXiv:0911.5166].
18. U. Langenfeld, S. Moch and P. Uwer, Phys. Rev. D **80** (2009) 054009 [arXiv:0906.5273].
19. V. Ahrens, A. Ferroglia, M. Neubert, B. D. Pecjak and L. L. Yang, JHEP **1009**, 097 (2010)
20. M. Beneke, P. Falgari, S. Klein, C. Schwinn, Nucl. Phys. Proc. Suppl. **205-206** (2010) 20.
21. V. Ahrens, A. Ferroglia, M. Neubert, B. D. Pecjak and L. -L. Yang, JHEP **1109**, 070 (2011) [arXiv:1103.0550 [hep-ph]].
22. V. Ahrens, A. Ferroglia, M. Neubert, B. D. Pecjak and L. L. Yang, Phys. Lett. B **703**, 135 (2011) [arXiv:1105.5824 [hep-ph]].
23. N. Kidonakis and B. D. Pecjak, arXiv:1108.6063 [hep-ph].
24. M. Beneke, P. Falgari, S. Klein and C. Schwinn, Nucl. Phys. B **855**, 695 (2012).
25. M. Cacciari, M. Czakon, M. L. Mangano, A. Mitov and P. Nason, Phys. Lett. B **710**, 612 (2012) [arXiv:1111.5869 [hep-ph]].
26. M. Beneke, P. Falgari, S. Klein and C. Schwinn, arXiv:1112.4606 [hep-ph].
27. P. Baernreuther, M. Czakon and A. Mitov, arXiv:1204.5201 [hep-ph].
28. S. J. Brodsky and X. -G. Wu, arXiv:1204.1405 [hep-ph].
29. M. Czakon, Phys. Lett. B **664**, 307 (2008) [arXiv:0803.1400 [hep-ph]].
30. A. Ferroglia, M. Neubert, B. D. Pecjak and L. L. Yang, JHEP **0911**, 062 (2009).
31. J. G. Korner, Z. Merebashvili and M. Rogal, Phys. Rev. D **77**, 094011 (2008) [arXiv:0802.0106 [hep-ph]]; Phys. Rev. D **71**, 054028 (2005) [hep-ph/0412088].
32. Z. Bern, V. Del Duca, W. B. Kilgore and C. R. Schmidt, Phys. Rev. D **60**, 116001 (1999) [hep-ph/9903516]; S. Catani and M. Grazzini, Nucl. Phys. B **591**, 435 (2000) [hep-ph/0007142]; S. Catani, S. Dittmaier and Z. Trocsanyi, Phys. Lett. B **500**, 149 (2001); I. Bierenbaum, M. Czakon and A. Mitov, Nucl. Phys. B **856**, 228 (2012) [arXiv:1107.4384].
33. M. Czakon, Phys. Lett. B **693**, 259 (2010) [arXiv:1005.0274]; Nucl. Phys. B **849**, 250 (2011) [arXiv:1101.0642 [hep-ph]].
34. M. Czakon and A. Mitov, arXiv:1112.5675 [hep-ph].
35. A. D. Martin, W. J. Stirling, R. S. Thorne and G. Watt, Eur. Phys. J. C **63**, 189 (2009).

9.
Summary Talks

MORIOND 2012, QCD AND HIGH ENERGY INTERACTIONS -EXPERIMENTAL SUMMARY-

G. Dissertori
Institute for Particle Physics, ETH Zurich,
Schafmattstr. 20, 8093 Zurich, Switzerland

The Moriond conference on QCD and High Energy Interactions has been a most exciting and interesting event once more. This year's edition has been characterized by a very large amount of new results from the LHC experiments. However, also the experiments at other present or past accelerators are still giving extremely important input to our quest for the understanding of nature at shortest distance scales. In this review I will attempt to summarize the main experimental highlights of this conference.

1 Introduction

The focus of the Moriond "QCD and High Energy Interactions" conference series is on theoretical and experimental advances in our understanding of the Standard Model (SM), by studying processes up to the highest achievable energy scales, together with searching for physics beyond the SM. Particular attention is given to the many aspects of Quantum Chromodynamics (QCD), the theory of strong interactions. Phenomena ranging from strongly interacting matter at high energy densities, to scattering processes at highest energies and thus shortest distance scales, are being probed at unprecedented experimental precision and thus provide extremely valuable input to the theoretical community. Furthermore, the study of hadrons containing heavy quarks provides deep insights into phenomena related to the CP-violating sector of the SM.

This year's conference [1] has been characterized by a most impressive amount of results presented by the LHC experiments. Most of these new measurements are based on the statistics collected during the 2011 LHC run. Also the TEVATRON experiments continue to be an important player in the field, with new results appearing, which are based on the full Run II dataset of about 10 fb^{-1}. These being hadron (as well as heavy ion) colliders, obviously a deep understanding of QCD at many energy scales is necessary. The rich spectrum of LHC and TEVATRON physics is complemented by new results from past and present accelerators. Here an overview of the most recent developments will be given, which by the nature of the vast richness of the field cannot be complete. The author thus apologizes for any important omission.

The structure of this summary is the following. Our main tools, namely accelerators and detectors, are listed in Section 2. Section 3 is dedicated to Heavy Ion Physics, and in Section 4 we discuss new results on the proton structure and inelastic proton scattering. Heavy Flavour Physics is addressed in Section 5, followed by a summary of recent tests of perturbative QCD in Section 6. Top Physics is discussed in Section 7. Finally, searches for Physics beyond the SM and for the Higgs boson are summarized in Sections 8 and 9, respectively. Regarding the status of theoretical advances in the field, we refer to a dedicated review [2] in these proceedings.

2 Our Tools

None of the results presented below would have been possible without the excellent performance of our tools, namely the accelerators and detectors. While at such conferences typically only the final results of long analysis chains are shown, it is easy to forget and praise all the immense work and ingenuity, which has gone into the design, construction, commissioning and operation of the various accelerators and the corresponding experiments.

Currently, the world's spotlights are on the LHC and its experiments. As presented by Lamont [3], the LHC machine physicists and engineers had many special events to celebrate during the year 2011, because of several important milestones and even world records achieved, mostly in terms of beam intensities, instantaneous and integrated luminosities, both for the p-p and the heavy ion (HI) running. Overall, during the proton run the LHC has delivered about 12.5 fb^{-1} to its experiments, with the largest fraction (about 5.5 fb^{-1} each) to the two general purpose detectors ATLAS and CMS, and smaller amounts, because of luminosity leveling, to LHCb (1.2 fb^{-1}) and ALICE (0.005 fb^{-1}). This became possible thanks to an increase by a factor of 20 in the p-p peak luminosity, compared to the 2010 run. A similar factor of 20 increase has been achieved for the integrated luminosity of the HI run in 2011, compared to 2010, with 150 $\mu\mathrm{b}^{-1}$ of Pb-Pb collisions delivered.

For the 2012 run it has been decided to increase the centre-of-mass energy to 8 TeV and to stay with 50 ns bunch spacing. Very tight collimator settings should allow for regularly running at a β^* value of 0.6 m at the ATLAS and CMS interaction points. Combined with bunch intensities above the design value of 1.1×10^{11} it is planned to attain peak luminosities of close to $7 \times 10^{33}\mathrm{cm}^{-2}\mathrm{s}^{-1}$. Taking the planned $\sim$ 126 days of p-p running and the expected beam parameters above, integrated luminosities anywhere between 12 and 19 fb^{-1} can be expected for ATLAS and CMS at the end of 2012. For LHCb and ALICE a larger β^* value of 3 m is foreseen. Finally, at the end of the 2012 p-p run, currently some 22-24 days of p-Pb running are scheduled. It is worth noting that at the time of writing this review the LHC has already gone very close to the 2012 milestones in terms of peak luminosity, a fantastic achievement of the very short and smooth intensity ramp-up for this new 8 TeV run.

However, results shown at this conference were not only based on LHC data. Up to its end of operations in September 2011, the TEVATRON has delivered the impressive amount of 12 fb^{-1} of p-$\bar{\mathrm{p}}$ collisions, with 10 fb^{-1} recorded and already analyzed to a large extent by the CDF and DØ experiments. New results are still arriving from the HERA experiments, as well as from the B-factories and DAPHNE. The BESIII $\mathrm{e}^+\mathrm{e}^-$ ring by now has delivered the world's largest samples of J/ψ and ψ' mesons. The RHIC experiments have presented new results on HI collisions, and new measurements were presented based on data from the fixed-target SPS experiment COMPASS and even from the former JADE detector at PETRA.

3 Heavy Ion Physics

One of the main purposes of HI physics is to study the properties of a quark-gluon plasma (QGP), supposed to have existed during the initial stages of the Universe and to be created, under laboratory conditions, in HI collisions. More generally, the aim of HI experiments is to gain a better understanding of the many phases, which the strongly interacting matter undergoes from its initial creation in the HI collision to the freeze-out of colour-neutral hadrons. Having experiments at different centre-of-mass energies and with different colliding particles, such as at RHIC and LHC, gives additional handles for probing various areas in the phase diagram. Also, more and more (hard) probes are being studied, in particular at the LHC, where unprecedented measurements based on jets, photons, Z and W bosons have been made. Combining the information obtained by different probes and observables, the goal is to shed light on properties such as the hydrodynamic behaviour of the hot and dense medium, jet quenching, quarkonia suppression and the medium's "transparency" to colored partons or colour-neutral electromagnetically or weakly interacting particles.

An important class of measurements is given by the study of hydrodynamic *flow*. Starting from the simple fact that the initial state should exhibit a spatial anisotropy, due to non-central HI collisions, the pressure-driven expansion is expected to lead to an anisotropy in the distribution of final state momenta or correlations thereof. A standard approach to quantifying these anisotropies is by expanding such distributions in terms of a Fourier series in the angle w.r.t. the reaction plane. Whereas the 2nd order coefficient (v_2) captures the elliptic nature of the flow, and is well established since years, precise measurements of non-vanishing higher-order moments have become available only recently (see, e.g. Fig. 1, left), giving important insight [4]. Indeed, the fact that such higher harmonics are non-zero gives strong support to the hydrodynamic picture of the QGP as a perfect liquid, whereas a finite viscosity of the medium would smear out any anisotropies due to fluctuations in the initial state and only lead to a finite v_2 term. Quite a number of new results from flow studies have been shown by ATLAS, CMS, PHENIX, STAR and ALICE, with first measurements up to very high transverse momenta, flow distributions for identified hadrons and anti-particles, di-hadron correlations and first attempts to measure v_2 with di-leptons, photons and D mesons. We refer to the dedicated HI contributions in these proceedings for further details.

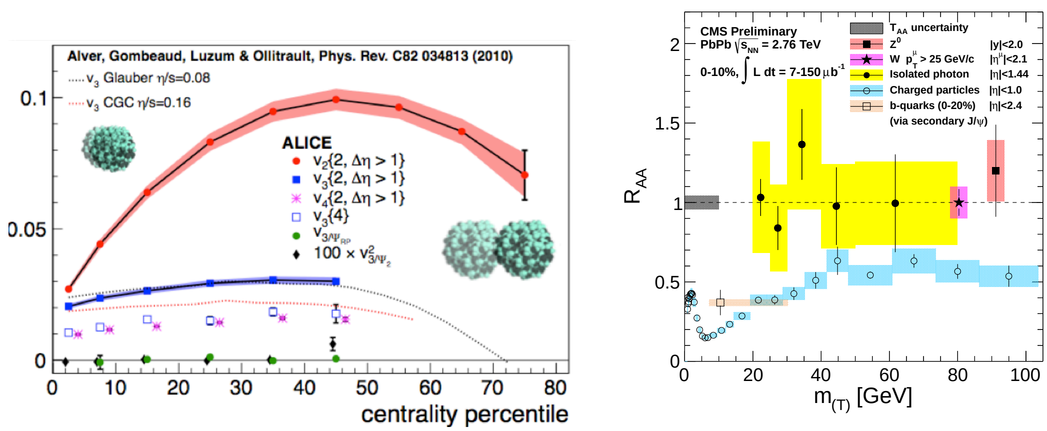

Figure 1: Left: Higher harmonics in flow measurements by ALICE, as a function of the centrality percentile; Right: R_{AA} measurements by CMS for charged particles, b-quarks, photons, W and Z bosons.

As mentioned above, hard probes have become quite a unique tool for the LHC experiments. Here the main observable is the so-called nuclear modification factor R_{AA}, a ratio of properly scaled A-A and p-p cross sections in order to account for the number of nucleon interactions in a single HI (A-A) collision. If a particular particle (probe) is not affected by the presence of the dense and hot medium, this ratio is expected to be unity. However, a strong suppression below 1 is expected and observed for hadrons, due to the influence of the medium on the colored constituents and thus on the hadron formation. Earlier RHIC measurements have been extended by the LHC experiments to p_T values up to 50 GeV [5] or higher [6], where the initial strong rise of the modification factor between 10 and 20 GeV is observed to flatten out above $\sim$ 40 GeV. This behaviour is captured by a large number of models, however, the large spread of model predictions indicates the need of still a better understanding to be obtained. First measurements of R_{AA} for photons, Z and W bosons have been presented by ATLAS [7] and CMS [6], cf. Fig. 1, right. As expected, R_{AA} values consistent with 1 within the still relatively large uncertainties are found. Interestingly, ATLAS has also measured the ratio for W and Z production, $R_{W/Z} = 10.5 \pm 2.3$ and found it to be consistent with the SM expectation, within the large uncertainty. Such types of measurements, with better statistics, should allow to obtain information on the parton distributions functions (pdfs) and their modifications in HI collisions. Concerning the observation of quarkonia suppression, it has been concluded that still a number of questions have to be clarified before firm statements can be made, in particular those related to the understanding of the initial conditions. Here dedicated RHIC studies at forward rapidity will give important input [8]. Finally, the clear observation of jet quenching by ATLAS and CMS, reported after the 2010 run, has been confirmed and studied in more detail thanks to the large 2011 statistics. For example, CMS has found that an enhanced imbalance exists at all jet transverse momenta [6], while at the same time no angular decorrelation and no significant modification of the jet fragmentation function is observed.

4 Proton Structure

The HERA and SPS experiments have presented some of their legacy measurements, in terms of unpolarized and polarized (spin-) structure functions and their interpretations. For example, a new and precise determination of HERA pdfs has been shown [9] (HERAPDF1.7, cf. Fig. 2 left). It is based on combined inclusive HERA I + HERA II neutral and charged current data, HERA jet data, which reduce the strong correlation between the strong coupling α_s and the gluon pdf, and a combined $F_2^{c\bar{c}}$ measurement, which gives sensitivity to the gluon and charm content of the proton. It is worth highlighting that predictions, based on such proton pdfs extracted from $e^{\pm}p$ data alone, actually provide a good description of the LHC data.

Extensive account of the wealth of pioneering HERMES and COMPASS measurements in polarized ep scattering has been given in the presentations by Riedl [10] and Sozzi [11]. Examples are inclusive spin structure functions, various amplitudes and asymmetries from exclusive samples of deeply virtual Compton scattering, and transverse spin asymmetries. The interpretation of such data is expected to lead to an improved understanding of the proton spin puzzle, of the related questions of orbital angular momentum carried by quarks and of the correlations among spin and transverse momentum, as well as between longitudinal momentum and transverse position, captured by transverse-momentum dependent or generalized parton distribution functions.

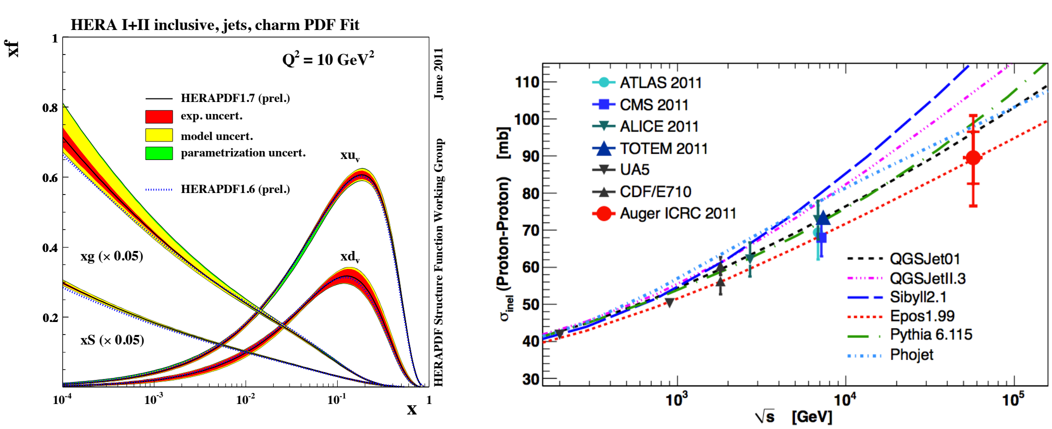

Figure 2: Left: Latest HERA pdf set, based on inclusive and charm structure functions and jet data; Right: Comparison of inelastic proton cross section data, from collider experiments and Auger, with various models.

Related to the basic understanding of the proton structure and of proton scattering cross sections are studies of the underlying event, multi-parton interactions, particle correlations and diffractive interactions [12]. Recent measurements of this kind are important input to the tuning of Monte Carlo generators. A fundamental observable is the total inelastic proton-proton cross section, with several new measurements from ATLAS, CMS and TOTEM. Typically they are presented for the fiducial acceptance region and extrapolated to full phase space, as well as differential in the forward rapidity gap size. In this context, Garcia-Gamez [13] has shown a very interesting comparison of the LHC results with an interpretation of shower observables from Auger data, see Fig. 2, right.

5 Heavy Flavour Physics

Heavy flavour physics as discussed at this conference can be divided into the following classes: (i) studies of quarkonia systems, (ii) production of heavy flavors at colliders and (iii) studies of the CKM matrix, CP violation and indirect searches for new physics with heavy flavor hadrons.

Addressing the first class, we have seen a large amount of new studies of charmonium and bottomonium states, with data from BESIII, BELLE, BABAR and the LHC experiments [14–18]. In particular, most of the efforts are concentrating on understanding and deciphering the origin of already known or completely new resonant states, such as $X(1835)$, $X(1870)$, $X(2120)$, $X(2370)$, $X(3815)$, $X(3872)$, $X(3823)$ and $\Upsilon(5S)$. The main questions still to be answered in a satisfactory manner are if these (or some of these) are indeed tetra-quark states, and/or (loosely-bound) "molecules" of meson-meson pairs, e.g. $D - D^*$ or $B - B^*$.

A review of heavy flavour production results from the LHC [19,20] reveals that, overall, perturbative QCD gives a rather satisfactory description, with still some discrepancies seen for particular phase space regions of p_T and/or rapidity distributions. Indeed, such measurements have been carried out for inclusive open b production, B hadron production as well as b-jet production. Furthermore, angular correlations in events with two B-tags have shown some need for improvements in the Monte Carlo modeling of gluon splitting into b quarks. Highlights at this conference comprise new results from CMS on Λ_b production, showing a steeper p_T spectrum than observed for B mesons, the first particle discovered at the LHC, namely the $\chi_b(3P)$ state, an observation by ATLAS now confirmed by DØ, as well as new LHCb measurements [21] of χ_c, $\psi(2s)$ and double charm production. Interestingly, the latter represents a very stringent test for models of double parton scattering.

An excellent review on probing new physics with heavy flavours, and the current experimental status, was given by Schopper [22]. These efforts can be subdivided in (i) attempts to constrain the CKM parameters, (ii) measurements of direct or mixing-induced CP violation and (iii) the searches for very rare decays. Some of the most important new results or updates presented at the conference, concerning these areas, are LHCb studies of direct CP violation in hadronic B decays [23,24] ($B \to hh'$), new results on CP violation in B_s mixing [25], a large number of new results on rare decays [25,26,27], such as $B_s \to \mu^+\mu^-$ from LHCb, CMS, ATLAS and CDF, as well as $B \to K^*\mu^+\mu^-$ and further rare decays from LHCb, e.g. $B^+ \to \pi^+\mu^+\mu^-$ and $B \to 4\mu$. In the case of $B \to K^*\mu^+\mu^-$, LHCb has presented the world's first measurement of the zero crossing point for the forward-backward asymmetry, giving nice agreement with the SM prediction. Finally, new results on the CP-asymmetry in charm have been presented [25], confirming values of this asymmetry around the -1% level and at $\sim 4\sigma$ from zero, thus indicating a larger value than expected from some of the currently available SM estimates.

The recent progress towards identification of rare decays attracts most of the current attention. Figure 3 (left) gives a summary of the most recent upper limits obtained on the branching ratio for $B_s \to \mu^+\mu^-$, which is very sensitive to contributions from new physics such as SUSY and predicted by the SM to be $(3.2 \pm 0.2) \times 10^{-9}$. The current world's best limit, obtained by LHCb from their 1 fb^{-1} dataset, is $BR(B_s \to \mu^+\mu^-) < 4.5 \times 10^{-9}$, closely followed by CMS which finds $BR(B_s \to \mu^+\mu^-) < 7.7 \times 10^{-9}$ from their full 2011 dataset (5 fb^{-1}). Also ATLAS has presented a first limit from an analysis of a 2.4 fb^{-1} data sample, and CDF has shown an update based on their full RunII statistics. Their new result does not further enhance, but rather reduce, a slight excess found in their 7 fb^{-1} sample. The strong power of this observable is nicely illustrated by Fig. 3 (right) and further discussed in Sec. 8 below, showing that these recent results exclude a very large portion of parameter space for SUSY models [28].

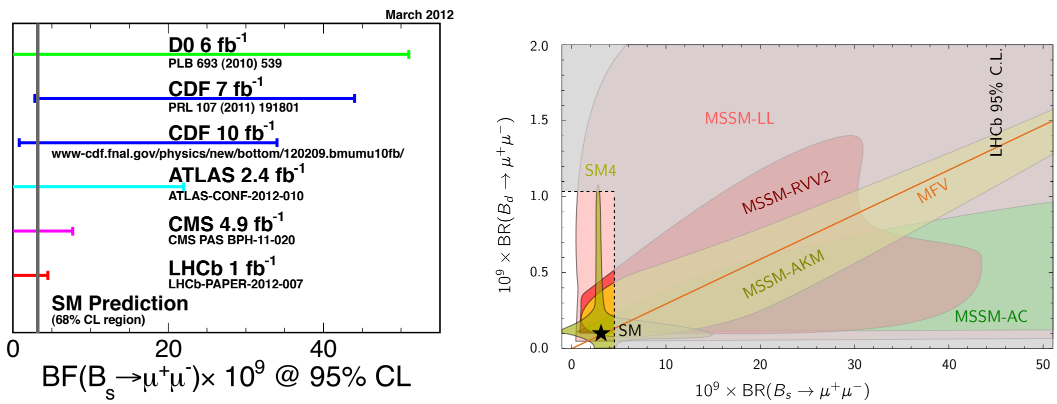

Figure 3: Left: Summary of upper limits on the branching ratio for $B_s \to \mu^+\mu^-$; Right: Impact of these limits on the parameter space of SUSY models (from D. Straub, Moriond EWK 2012).

In conclusion, the results on heavy flavour physics presented at this conference could be summarized by naming LHCb as an "anomaly terminator". This is because (i) earlier indications of a large phase Φ_s in B_s mixing have not been confirmed, the current results showing nice agreement with SM expectations; (ii) the measured forward-backward asymmetry and derived parameters in the $B \to K^*\mu^+\mu^-$ decay also agree with the SM, and thus do not confirm earlier hopes of possible signs of new physics in this decay; (iii) and finally the limit on the $B_s \to \mu^+\mu^-$ branching ratio is approaching the SM value, with a first measurement to be expected later in 2012. Nevertheless, for those believing in new physics showing up in heavy flavour systems, their is now some new hope due to the large CP-asymmetry found in charm. However, care should be taken here, since SM predictions in this area suffer from large long-distance (non-perturbative) QCD effects, thus are notoriously difficult to predict, i.e. in the end it could simply turn out that the observed large asymmetry could be ascribed to such QCD effects. Overall, the phenomenologists are more and more given a fantastic set of data and experimental constraints, which allow putting strong limits on new physics, in particular when combined with other observables, such as direct searches at colliders (see below).

6 Tests of perturbative QCD

Measurements of hard-scattering cross sections, with jets, photons or vector bosons in the final state, are interesting because of several reasons: (i) it allows probing higher-order predictions of perturbative QCD for the hard-scattering part of the overall process; (ii) parton distribution functions can be constrained; (iii) SM predictions can be tested, in particular QCD calculations, as implemented in various codes and MC generators, for processes which are important backgrounds for new physics searches. At this conference a large number of new results in these directions have been presented, in general showing a remarkable agreement of theory and data. We note in passing that a more extensive review of this subject has been published recently [29].

A central component of those measurements, which contain jets in the final state, is the excellent control of the systematic uncertainty due to the jet energy scale. This is essential because of the nature of the steeply falling cross sections as a function of the jet p_T. By now the LHC experiments master this effect already at a remarkable level of precision, e.g., around 2% or even better for central jets and a p_T range of about 50 to several hundred GeV.

Concerning jet production at the LHC, new results have been presented [30] for inclusive jet production, dijet production as a function of dijet invariant mass and jet rapidity separation, as well as third-jet activities. In particular, new measurements have appeared on the inclusive jet cross section as a function of jet p_T by CMS, and dijet production by ATLAS, based on the full 2011 dataset, cf. Fig. 4. Overall, the agreement of next-to-leading order (NLO) QCD predictions with data over many orders of magnitude is rather impressive. The inclusive jet cross section has been compared to predictions based on a large set of pdfs, showing in general good agreement within theoretical and experimental uncertainties. In the dijet case, where the data have an impressive reach up to about 4 TeV in dijet mass, some discrepancies are found at very large masses and large dijet rapidity separation, a region where NLO predictions probably reach their limit of applicability. A similar observation is made by a dedicated CMS analysis, which studied central jet production with the additional requirement of a second jet in the forward region. They found some significant disagreements among data and MC models. Finally, ATLAS has presented a measurement of the D^* fragmentation function, showing a sizable discrepancy, with MC clearly underestimating the yield in the data. This might point to a problem with the simulations for gluon splitting to charm, similarly to the observations for the b-quark case in an earlier CMS measurement of $B\bar{B}$ angular correlations [31].

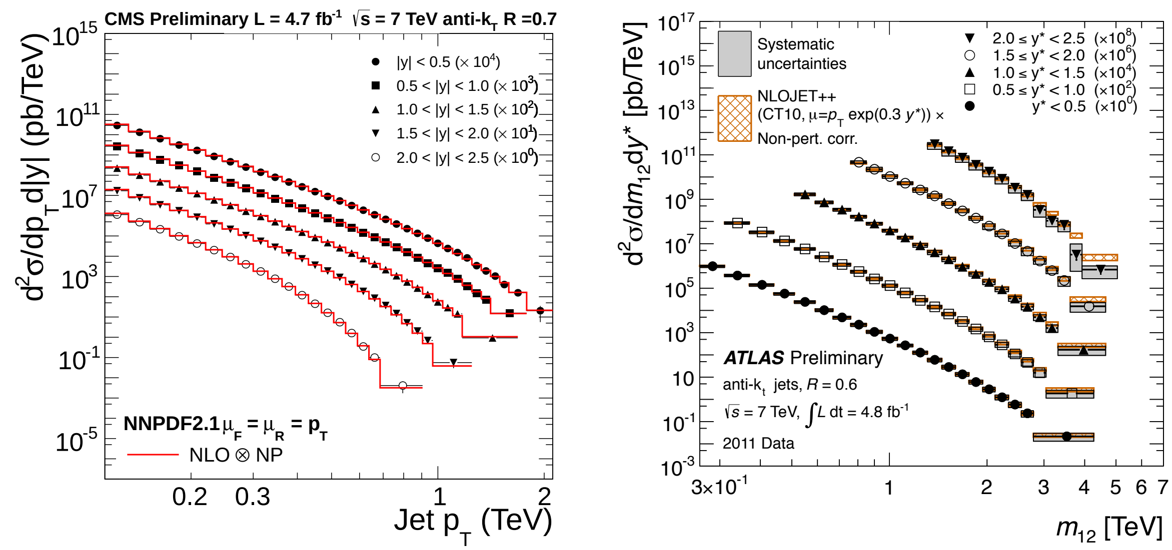

Figure 4: Left: Inclusive jet production, as a function of jet p_T and rapidity, measured by CMS; Right: ATLAS data on dijet production.

New results on inclusive photon, di-photon and photon plus jet production at the TEVATRON and the LHC have been presented by Dittmann [32] and Gascon-Shotkin [33]. Among the highlights of this year, there is a new calculation [34] at next-to-NLO (NNLO) level for di-photon production, which finally brings the theory into agreement with data in the region of small azimuthal separation (Fig. 5, left). In that region of phase space the previously available NLO calculation is effectively a leading order approximation, which underestimates the data obtained for this distribution both at the LHC and the TEVATRON. Thus here we have a spectacular example for the need of NNLO calculations, for the description of particular variables in specific regions of phase space, not only because of radiative corrections, but also because of the appearance of new partonic channels in the initial state only at a certain order of perturbation theory. Also worth mentioning is the first LHC measurement on photon plus jet production by ATLAS, as a function of several kinematic variables and differential in the photon-jet angular separation. This is a classical study for hadron colliders, in particular because of the sensitivity to the gluon pdf. The data are in good agreement with NLO predictions (Fig. 5, right), besides some deviations seen for photon p_T below 50 GeV. A similar observation had been made for inclusive photon production. Also worth mentioning is a measurement of angular decorrelations in photon plus 2 or 3 jets final states by DØ, showing nice evidence for the need to include double parton scattering contributions into the theoretical predictions.

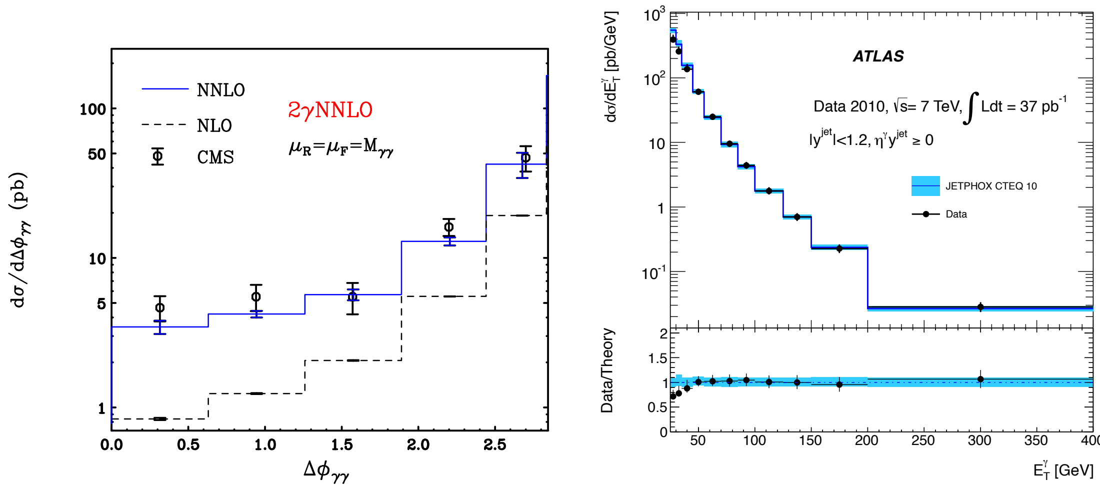

Figure 5: Left: Comparison of CMS data and QCD predictions for the di-photon azimuthal separation; Right: photon plus jet production cross section from ATLAS.

Whereas the excellent agreement of data with NNLO QCD predictions, for the inclusive production of W and Z bosons, had already been shown and discussed at earlier conferences, this year special focus has been put on the study of vector boson plus jet production [35,36]. These processes are extremely important backgrounds for searches of supersymmetry and the Higgs, especially for associated Higgs production in the low mass region. Furthermore, such measurements allow for testing different approaches to the implementation of perturbative QCD calculations into MC codes, such as at fixed order (NLO) or based on the matching of leading order matrix elements with parton showers, for example in MADGRAPH, ALPGEN or SHERPA. Thanks to important recent advances, NLO calculations are now available up to high jet multiplicities [2]. Concerning such jet multiplicities in W (or Z) plus jet production, as well as angular correlations among the jets, overall a very good agreement with the NLO and matched calculations is found. Also dijet masses and the H_T distribution (scalar sum of jet momenta) are well modeled over large regions of phase space, where the various calculations are applicable (Fig. 6, left). For the more specific case of vector boson plus heavy flavor production (b- or c-tagged jets), a rather consistent picture seems to appear from the TEVATRON and the LHC: data and NLO QCD predictions agree, within the sometimes sizable theoretical and experimental uncertainties, for $W+c$ and $Z+b$ production, whereas deviations are found for $W+b(b)$ (Fig. 6, right). This is interesting, again also because of the relevance of this process for the Higgs search. Finally, first studies of angular correlations in $Z+bb$ final states have been presented by CMS.

Going lower in production cross section for electro-weak particles, the most relevant and often studied processes are di-boson production ($W\gamma, Z\gamma$, WW, WZ, ZZ), for various decay channels of the vector bosons. An interesting new measurement of $VZ(\rightarrow b\bar{b})$ production at the TEVATRON [37] is further discussed in section 9 below. The large and by now rather complete set of LHC results is summarized in more detail in Ref. [38]. The picture arising is that all the aforementioned processes, measured with statistics up to 5 fb^{-1}, are in agreement with NLO QCD predictions, which then allows to put stringent constraints on anomalous trilinear gauge couplings. It has been remarked that the measured WW cross section appears to be slightly higher (however, not at a statistically significant level) both in ATLAS and CMS, compared to the NLO predictions. Since this process is particularly relevant for the understanding of

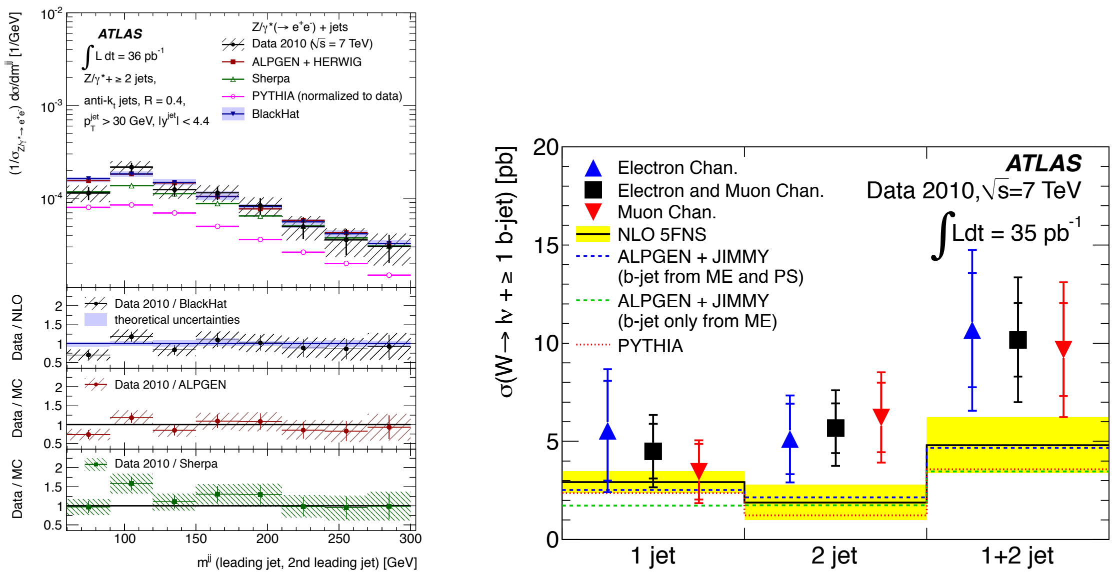

Figure 6: Left: Invariant mass of the leading and 2nd leading jet, measured by ATLAS in Z+jets final states; Right: ATLAS results on the production of a W boson in association with b-jets.

electro-weak symmetry breaking, it will be interesting to follow up on future results in this area. In the past, a bump in the dijet mass distribution for $W + 2$ jets production, observed by CDF, had caused a certain amount of excitement. However, at this conference both DØ and CMS presented results, which do not confirm that finding. Finally, an interesting new LHC measurement, related to the ZZ and $H \to ZZ$ processes, has been put forward by CMS, namely the first observation at a hadron collider of $Z \to 4\ell$. While interesting in itself, this process will turn out to be an extremely useful standard candle for controlling the absolute mass scale, the mass resolution and the reconstruction efficiencies for the Higgs search in the four-leptons channel.

We close this section on tests of perturbative QCD by mentioning a nice re-analysis of JADE data for the 3-jet rate, used to precisely determine the strong coupling constant at NNLO+NLLA approximation [39]. Indeed, it is shown that this measurement has an uncertainty due to higher order QCD corrections below the 1% level, and is dominated by hadronization model systematics. Similarly, new recent results were also shown on jet production and α_s determinations based on HERA data [40].

7 Physics of the Top Quark

The top quark is given special attention because of several reasons: it is by far the heaviest of all quarks, and with a mass of the order of the electro-weak scale it is conceivable that the top plays a special role in electro-weak symmetry breaking. Furthermore, it is considered to be a possibly important gateway to new physics. Until recently the TEVATRON has been the only player in the field. However, the LHC has quickly risen to the status of a "top factory" and the LHC experiments start to play the leading role more and more. A central test of SM predictions is the measurement of the top-pair production cross section. The LHC experiments have presented new results [41] for a large number of channels (leptons+jets, dileptons, $\tau+\mu$, τ+jets, all hadronic), analyzing data sets between 0.7 and 4.7 fb^{-1}. The currently combined best cross section values found by ATLAS and CMS are $\sigma_{t\bar{t}} = 177 \pm 3(\mathrm{stat})^{+8}_{-7}(\mathrm{syst}) \pm 7(\mathrm{lumi})$ pb and $\sigma_{t\bar{t}} = 165.8 \pm 2.2(\mathrm{stat}) \pm 10.6(\mathrm{syst}) \pm 7.8(\mathrm{lumi})$ pb, respectively. Here one should highlight that the experimental uncertainty has already achieved a level of 6%, which is smaller than the uncertainty on the theoretical predictions. It would be interesting to see an ATLAS-CMS combination, also in light of the very slight tension which appears from these two experimental results and the fact that most likely part of the systematic uncertainties are correlated. Nevertheless, both results are in agreement with expectations from perturbative QCD, and one should start considering the possible impact of this cross section on pdf determinations [42].

The studies of single top production are steadily progressing, both at the TEVATRON [43] and the LHC [44]. Thanks to the considerably enhanced cross section at the LHC compared to the TEVATRON, ATLAS and CMS have already reached an accuracy of $\sim 20\%$ in the measurement of t-channel production (Fig. 7, left). A clear wish has been expressed at the conference for harmonizing, among the LHC experiments, the treatment of theoretical uncertainties in this class of measurements. CMS has interpreted the cross section measurement in terms of $|V_{tb}|$ and extracted a measurement at the 10% accuracy level. Besides this production channel, a considerable effort is spent by all experiments, in order to close in on the tW and s channels.

What concerns the top mass, the TEVATRON is still leading, with the world's most precise measurement, from a TEVATRON combination, presented [45] to be $m_t = 173.2 \pm 0.6(\text{stat}) \pm 0.8(\text{syst})$ GeV, noteworthy a quark mass measurement with a relative uncertainty of 0.54%. Further improvements are still expected until the final analysis of the full Run II dataset. However, the LHC is catching up. For example, CMS has come up [46] with their latest best result of $m_t = 172.6 \pm 0.6(\text{stat}) \pm 1.2(\text{syst})$ GeV, thus already achieving the same statistical precision as the TEVATRON experiments. However, it was noted that this determination does not yet consider some systematic uncertainties, such as color reconnection and underlying event effects. There is certainly an interest in obtaining an LHC, and ultimately an LHC-TEVATRON, combination for this important parameter. Such an effort should then also help in synchronizing the treatment of systematic effects by the different experiments. A further observation made at the conference was that all experiments use the W mass as a kinematic constraint in their analyses, meaning that there is some correlation between the top and W mass measurements. On the other hand, in the electro-weak precision tests, where the consistency among m_t, m_W and m_H is tested (see also below), such a correlation is not taken into account. However, because of the largely different levels of precision achieved for these mass determinations, in the end this is not a serious issue, most likely. A somewhat "disturbing" aspect of the direct top mass determinations from kinematic reconstruction is the not really well defined meaning of the finally extracted parameter. While it is supposed to be close to a definition according to a pole-mass scheme, currently a theoretically sound understanding is not available, which triggers some experts to question if we really know this quark mass at the 0.5% accuracy level [2]. On the other hand, a theoretically very well defined approach is given by the extraction of the top mass (typically in the form of a running mass) from a top cross section measurement. In view of the ever improving precision on the latter (see above), this becomes more and more interesting. So far an accuracy of $\mathcal{O}(7\text{ GeV})$ is attained, mostly dominated by pdf uncertainties, and achieving a 5 GeV error seems to be viable [42].

Besides production cross sections and mass, an amazing amount of further top properties have been studied by the TEVATRON and LHC experiments [47,48]. These comprise spin correlations, W helicity and polarization in top decays, extractions of $|V_{tb}|$, the top width, $m_t - m_{\bar{t}}$, the electric charge of the top, the charge asymmetry, searches for anomalous couplings and flavour-changing neutral currents, as well as a first study of jet veto effects in top-pair production. Basically for all these properties and observables agreement is found among data and SM predictions, besides the well-known discrepancy found for the forward-backward asymmetry (A_{FB}) at the TEVATRON. CDF has presented a differential study of A_{FB} as a function of the invariant mass of the $t\bar{t}$ system, showing a steeper slope in data compared to theory. Probably further improved understanding, eg., of non-perturbative effects when correcting from particle to parton level, as well as from higher-order QCD, is needed before establishing this as a significant hint for new physics. This cautious approach appears to be supported by an interesting interpretation by ATLAS of their latest measurement of the top charge asymmetry, A_C. When comparing their measurement, as well as CDF's A_{FB} result, to predictions for $m_{t\bar{t}} > 450$ GeV, there appears to arise some tension, Fig. 7, right. For example, while some physics beyond the SM, such as a heavy Z boson, would still be consistent with the CDF measurement, its effect would lead to a larger A_C than observed by ATLAS.

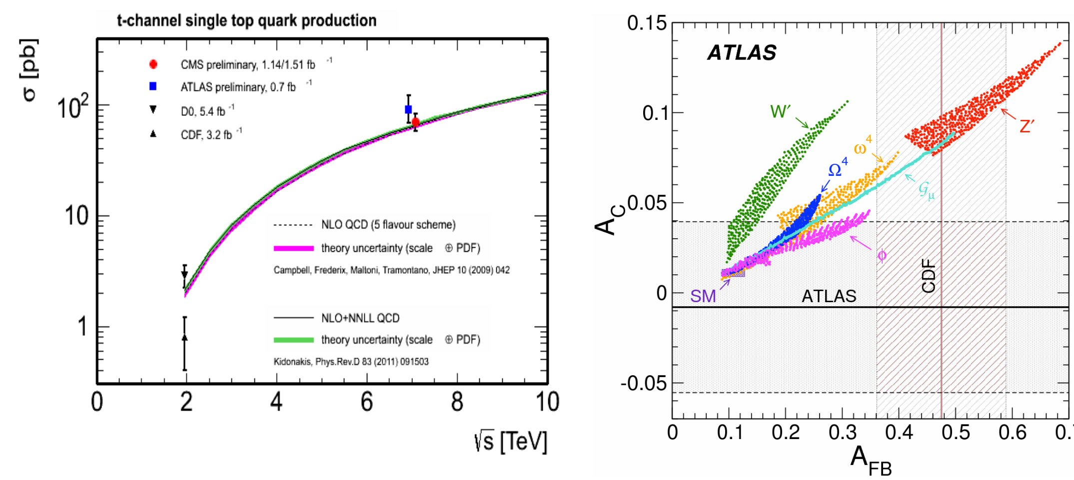

Figure 7: Left: Single top production cross section as a function of centre-of-mass energy; Right: Comparison of top asymmetry measurements by ATLAS and CDF, and interpretation in terms of new physics models.

8 Searches for New Phenomena

The searches for new physics, now dominated by the LHC results, can be roughly classified into two large sectors, namely (i) those concentrating on signatures of SUSY particles, and (ii) the large class of searches for other particles and interactions beyond the SM. The sheer amount of SUSY exclusion plots shown at this conference is testimony of the enormous efforts invested at the collider experiments, in order to get any hint of SUSY components in the data. Typical classifications of the analyses follow topological considerations, such as looking for events with large missing transverse energy (MET), due to the possible production of weakly interacting massive SUSY particles, accompanied by high-p_T jets, one or two opposite or same-sign leptons, more than two leptons or photons. The interpretation of the, so far unsuccessful, searches of any deviation from the SM predictions, is carried out in various manners; either in the context of since long established specific SUSY incarnations, with very constrained parameter sets, such as mSUGRA or cMSSM, or in a more general approach as implemented in so-called Simplified Models (see e.g. Ref.[50]). In this case basic properties of particle cascades, arising from the decays of heavy particles such as pair-produced gluinos, are explored. At the conference first results were presented based on the full 2011 statistics, showing the potential for big advances in terms of excluded parameter space. In simple terms, the current results of "generic" squark and gluino searches, in the topologies as mentioned before, allow setting limits around the TeV scale, if interpreted in scenarios such as the cMSSM [49]. Thus, with the first two years of LHC data this mass scale is pushed rather high, such that some start to consider giving up (at least to some extent) naturalness arguments. On the other hand, first attempts have already started, and will be pursued with much more vigor in 2012, regarding the searches for third generation squarks. So far limits in those cases are not too strong, roughly around 300 GeV. Such efforts are, e.g., motivated by models where the first generation squarks are pushed to very high mass scales, whereas only the third generation is kept light, around the electroweak scale, arguing that after all naturalness can be maintained if the effects from top loops, which dominate radiative corrections to the Higgs mass, are controlled by contributions from particles such as stops. These searches could turn out to be rather difficult, in particular if the mass separation between the top and third-generation spartners is not too large. Related to these SUSY searches, there are two further aspects worth mentioning: (i) when looking at the enormous amount of analyses, in the end always condensed into a few exclusion plots, one easily forgets to appreciate the large ingenuity and the many new ideas, which are at the basis of those results. In particular, during these last years a large set of new observables, which are differently sensitive to SM backgrounds and to the appearance of new heavy particles, have been established, as well as many clever, so-called data-driven, methods have been developed, in order to estimate SM background contributions to the search regions. In this context, also observables are studied, such as the ratio of Z+jet over γ+jet production as a function of H_T and/or jet multiplicity, which are interesting in itself from a SM point of view.

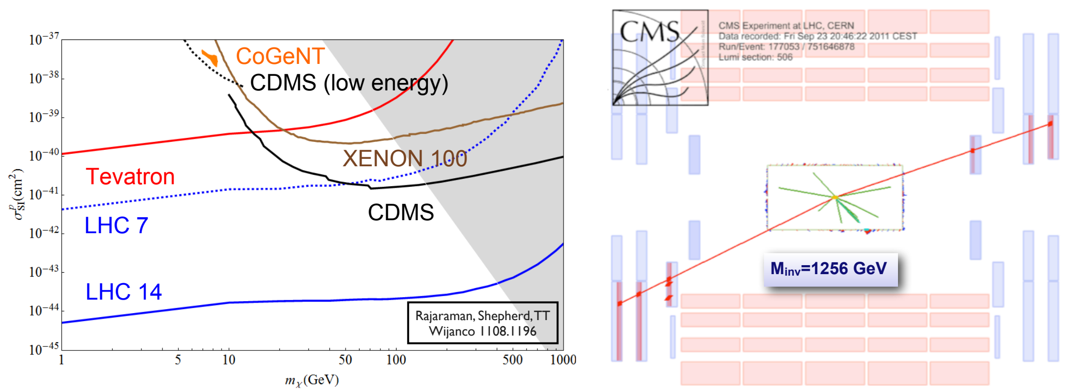

Figure 8: Left: Complementarity of the searches for DM candidates at colliders and by direct DM detectors: shown is an example of limits on the spin-independent WIMP-nucleon scattering cross section in an iso-spin violating scenario, with regions above the lines excluded; Right: Dimuon event with very large invariant mass as detected by the CMS experiment.

The discussions of SUSY searches have focused on two further highly-interesting aspects. Tait [51] highlighted the important complementarity of searches for dark matter (DM) candidates (in particular Weakly Interacting Massive Particles, WIMPs), as carried out at colliders, with direct DM searches. Whereas at colliders we probe the parton-DM couplings, in direct DM searches one explores the coherent nucleon-DM scattering. An advantage of collider searches is their reach towards very small DM masses, by e.g. looking for monojet signatures induced by direct DM pair-production and a jet from initial state radiation [52]. This complementarity is nicely expressed in exclusion plots as shown in Fig. 8, left. Another example of complementarity was underlined by Mahmoudi [53], who analyzed the constraining power, in terms of SUSY models, arising from heavy flavor physics, such as rare decays ($B \to K^* \mu^+\mu^-, B_s \to \mu^+\mu^-$) mentioned above, or from searches for (supersymmetric) Higgs bosons. In simple terms, the direct searches push the masses of (first generation) particles higher and higher, and rare decays such as $B_s \to \mu^+\mu^-$ strongly constrain $\tan\beta$ to lower values, therefore creating tension with other observables such as the muon $g-2$ result. Though, concerning the latter, participants at the conference highlighted the need for a still better understanding of the theory uncertainties, before taking this tension too seriously. Finally, if the current exclusion limits for a very light Higgs below about 120 GeV are taken at face value, particular implementations of SUSY breaking, such as gauge mediation (GMSB), can be considered to be ruled out.

Similarly to the SUSY searches, also other attempts to look for new physics are so numerous by now that a comprehensive summary is basically impossible. Many new LHC results have been presented [52], which show that exclusion limits for heavy objects, such as heavy vector bosons

(Z', W') or excited quarks, have reached the few-TeV range. Even higher scales are excluded in the context of certain large extra dimension models or the searches for miniature black holes. Typical exclusion limits for heavy fermions, such as 4th generation partners, are around half a TeV. A number of spectacular events, discovered by such analyses, have been shown at the conference (cf. Fig. 8, right). For sure, the philosophy of not leaving any stone unturned, will be pursued at the new 8 TeV LHC run, where the higher centre-of-mass energy leads to a significant increase of effective luminosity, in particular when searching for very heavy objects.

9 Searches for the Higgs Boson

A traditional approach to testing the electroweak sector of the SM is by looking at the overall consistency among direct measurements of the W and top quark masses, current limits on the Higgs mass m_H, and the SM relationship among m_W, m_t and m_H. The latest version of this test has been shown at this conference, Fig. 9, and can be considered as one of the real highlights. Indeed, we see that there is consistency, at the 1 sigma level, among these mass measurements and a possible existence of a SM Higgs with mass around 125 GeV. The two most important new ingredients to this test are an improved measurement of m_W at the TEVATRON and the strong Higgs exclusion limits, as discussed below. The latest, and the world's most precise, determination of the W mass [54] has been obtained by CDF, with an astonishing total uncertainty of 19 MeV, leading to an uncertainty on the latest TEVATRON combination (world average) of 17 MeV (15 MeV). An important contribution to the uncertainty of the final TEVATRON result, related to the knowledge of parton distribution functions, was estimated to be about 10 MeV. However, this error and its possible further reduction in the future, has been questioned by some of the theorists present [2].

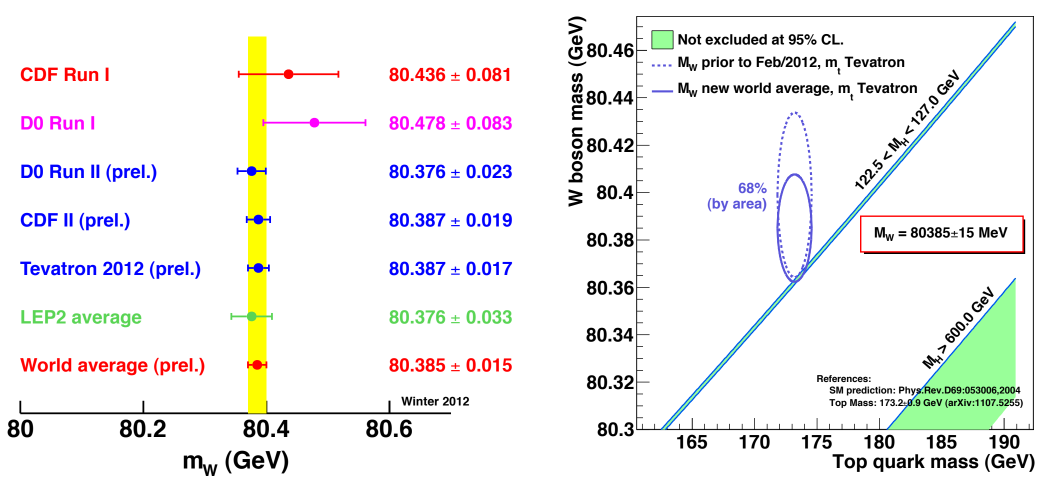

Figure 9: Left: Summary of recent measurements of the W mass; Right: Consistency check among the m_W, m_t measurements, the limits on the Higgs mass, and their relation in the context of the SM.

The LHC and TEVATRON experiments have presented the latest combinations of their Higgs searches [55,56,57], leading to the following executive summary: (i) ATLAS excludes, at 95% C.L., the mass ranges 110-117.5, 118.5-122.5 and 129-539 GeV, (ii) CMS excludes the range 127.5-600 GeV, and (iii) the TEVATRON has a 95% exclusion limit for $100 < m_H < 106$ and $147 < m_H < 179$ GeV. Very interestingly, all these combined results indicate a slight excess in the mass range of roughly 122-128 GeV, with the individual significances of those excesses somewhat above the 2 sigma level (cf. Figs. 10 and 11). When looking more closely at the updates presented at this conference, the following observations can be made:

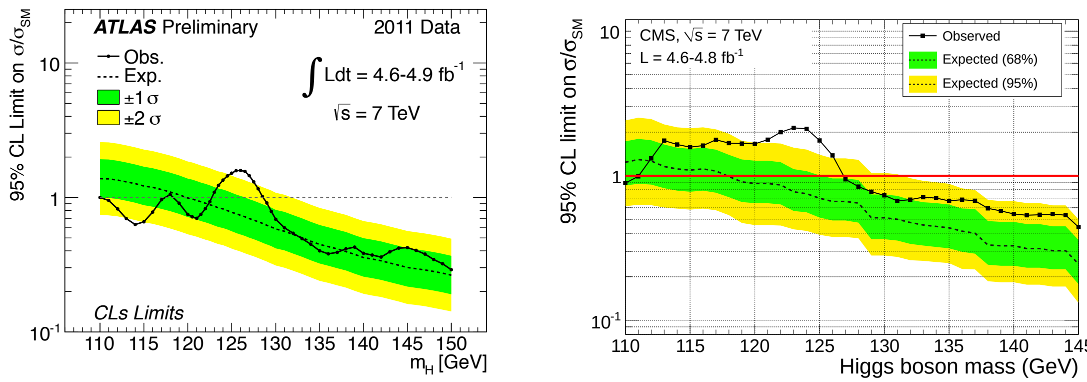

Figure 10: 95% C.L. exclusion limits on the SM Higgs cross section, as a function of the hypothetical Higgs mass, as derived from a combination of the ATLAS (left) and CMS (right) Higgs searches.

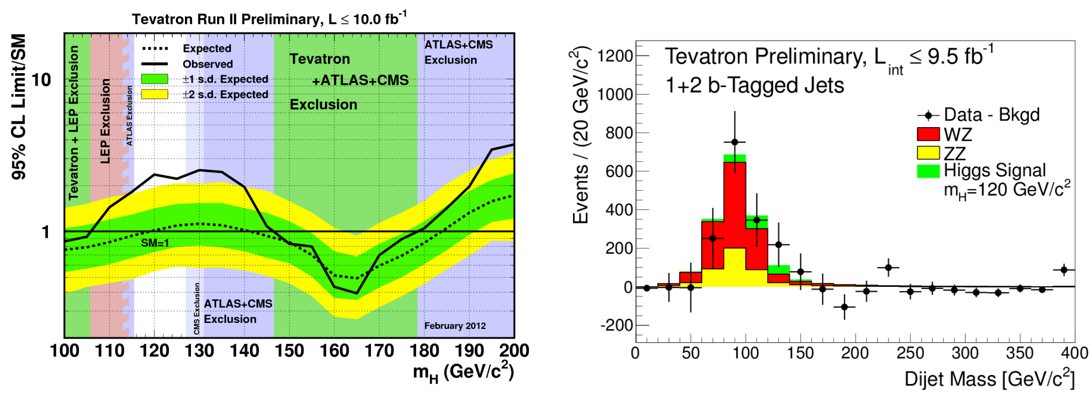

Figure 11: Left: 95% C.L. exclusion limits on the SM Higgs cross section, as a function of the hypothetical Higgs mass, as derived from a combination of the TEVATRON Higgs searches; ; Right: TEVATRON combination of the measurement of the cross section for $WZ(\to b\bar{b})$ production.

- at the CERN seminar on Dec. 13, 2011, CMS had presented already a complete set of Higgs searches in the various channels, based on the full 2011 statistics. In the meantime, they have performed a new, alternative analysis of the $H \to \gamma\gamma$ channel [56], now based on an event classification derived from a multi-variate approach to the measurement of photon properties. This leads to a $\sim 20\%$ improvement in the expected limit, leaving the overall conclusions from the observation on real data unchanged, compared to their earlier analysis. Furthermore, they have presented first results for the $WH \to WWW \to 3\ell 3\nu$ channel and for two new channels in the $H \to \tau\tau$ search.

- in contrast to CMS, previously ATLAS had shown full-2011 statistics results only for the $H \to \gamma\gamma$ and $H \to ZZ \to 4\ell$ channels, which are most sensitive in the low-m_H region and characterized by their excellent mass resolution. Now, at this conference [55], ATLAS has complemented those analyses with a full suite of analyses based on the full 2011 data sample, covering basically all relevant channels and mass regions;

- interestingly, when comparing all those ATLAS and CMS analyses, it is evident that currently both experiments have very similar sensitivity in basically all the channels.

- the most important recent changes at the TEVATRON [57] come from the $VH(\to b\bar{b})$ channel, in particular thanks to a considerable improvement in the CDF b-tagging performance. An interesting application of the improved tools, and at the same time an important "calibration" channel for the low-mass Higgs search, is their latest measurement of $WZ(\rightarrow b\bar{b})$ production, Fig. 11, showing excellent agreement with the SM prediction. When analyzing further the recently observed excess in the TEVATRON data, one finds that this excess is driven by the $H \rightarrow b\bar{b}$ search in CDF and by a contribution from DØ in the $H \rightarrow WW$ channel. The most significant channel for the CDF excess is $Z(\rightarrow e^+e^-)H(\rightarrow b\bar{b})$.

- a closer look at the LHC results reveals that there are downward fluctuations in the measurement of the signal strength modifier (Fig. 12, left) at the lower end of the search region, which should probably looked at with the same attention as the upward fluctuations around 125 GeV, since they tell us something about the (relatively little) statistics still involved. Furthermore, it was noted that the updated ATLAS result for the $H \rightarrow WW$ channel does not really confirm the excess in the di-photon and four-lepton channel, as for example seen in the distribution of the background-only probability, Fig. 12, right. However, obviously all these observations correspond to ~ 2 sigma effects only, thus should be taken with the appropriate grain of salt.

In conclusion, it is simply impressive to see what the LHC and TEVATRON experiments have delivered, in terms of Higgs results, over such a short time scale between the end of data taking in 2011 and the winter conferences in 2012. A rather solid conclusion appears to be that a SM Higgs boson is excluded, to very high level of confidence, for masses above ~ 130 GeV up to about 600 GeV, where the current searches stop. As mentioned above, all experiments observe some excess in the region around 125 GeV, which may be called *tantalizing* at this stage. However, we should not forget the still limited statistics available, correspondingly the still not overwhelming significance of these observations, and therefore try not to be carried away. Luckily, new data at 8 TeV start pouring in, the hope being that the increased statistics expected in 2012 will allow to make concluding statements on the existence (or exclusion) of a SM Higgs boson. The challenge is with the analyzers, who will have to avoid, at all costs, the (psychological) bias, which undeniably exists after having seen the 2011 results. Finally, it is also worth mentioning that a number of non-SM Higgs searches have been presented [58,59,60], eg. in the context of fermiophobic, (N)MSSM or doubly-charged Higgs scenarios, without any significant hints for a signal.

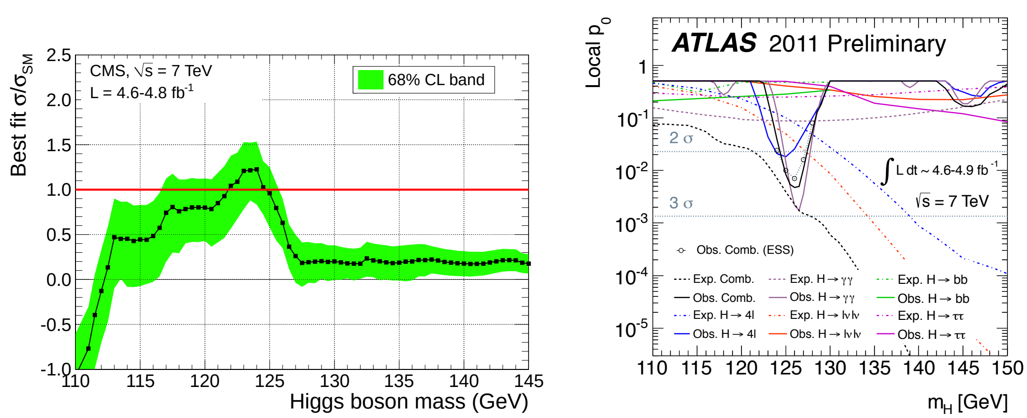

Figure 12: Left: Best fit of the signal strength modifier (relative to the SM Higgs cross section), as obtained from a combination of the CMS Higgs searches; Right: ATLAS results on the background-only probability for different Higgs search channels.

10 Conclusions

Following the 93 (!) presentations of this conference has been most interesting and allowed obtaining an excellent and rather complete overview of the present theoretical and experimental status in the field of QCD and high energy interactions. The wealth of new data, in particular arriving from the LHC experiments, is overwhelming and exciting at the same time. So far, the Standard Model appears to be as healthy as ever, with no really significant indication for a deviation from its predictions observed, and with the final missing building block, the Higgs boson, probably on the horizon. In a year from now, our big puzzle called "particle physics up to the TeV scale" will be even more complete than already seen this year, and we might know then if there is any space left for some missing piece of the puzzle, entitled "new physics".

Acknowledgments

My sincere thanks go to the organizers of this fantastic conference, for their kind invitation to give this experimental summary talk. It was a real honor for me. The organizers not only managed, as every year, to run a smooth and very high-quality conference, but also provided sun shine throughout the whole week (which unfortunately could not be exploited to the maximum by the summary speakers). I would also like to thank all the speakers and colleagues, who provided input for this summary and who answered my many questions. Finally, very special thanks go to B. Klima and D. Treille for their comments on the manuscript.

References

1. A direct weblink to the conference program, with links to the slides of all talks, is `http://moriond.in2p3.fr/QCD/2012/MorQCD12Prog.html`. Note that detailed references to notes and publications are given in those slides and in the corresponding contributions to these proceedings.
2. D. Soper, these proceedings.
3. M. Lamont, these proceedings.
4. R. Snellings, these proceedings.
5. M.L. Knichel, these proceedings.
6. Y. Yilmaz, these proceedings.
7. I. Grabowska-Bold, these proceedings.
8. M. Grosse Perdekamp, these proceedings.
9. D. Lontkovskyi, these proceedings.
10. C. Riedl, these proceedings.
11. F. Sozzi, these proceedings.
12. A. Pilkington, these proceedings.
13. D. Garcia-Gamez, these proceedings.
14. V. Bhardwaj (Nara), these proceedings.
15. N. Guttmann, these proceedings.
16. Z. Wang, these proceedings.
17. H.S. Zhao, these proceedings.
18. G. Tatishvili, these proceedings.
19. E. Aguilo', these proceedings.
20. A. Kozlinskiy, these proceedings.
21. C. Potterat, these proceedings.
22. A. Schopper, these proceedings.
23. J.v. Tilburg, these proceedings.

24. C. Jones, these proceedings.
25. M. Dorigo, these proceedings.
26. M. Smizanska, these proceedings.
27. C. Parkinson, these proceedings.
28. D. Straub, in the proceedings of the 2012 Recontres de Moriond on EW interactions and unified theories.
29. J. M. Butterworth, G. Dissertori and G. P. Salam, arXiv:1202.0583 [hep-ex], to be published in Annu. Rev. Nucl. Part. Sci. 2012, 62.
30. G. Jones, these proceedings.
31. V. Khachatryan *et al.* [CMS Collaboration], JHEP **1103** (2011) 136 [arXiv:1102.3194 [hep-ex]].
32. J.R. Dittmann, these proceedings.
33. S. Gascon-Shotkin, these proceedings.
34. S. Catani, L. Cieri, D. de Florian, G. Ferrera and M. Grazzini, Phys. Rev. Lett. **108** (2012) 072001 [arXiv:1110.2375 [hep-ph]].
35. D. Bandurin, these proceedings.
36. A. Paramonov, these proceedings.
37. J. Vizan, these proceedings.
38. J. Malcles, these proceedings.
39. S. Kluth, these proceedings.
40. M. Kapishin, these proceedings.
41. I. Aracena, these proceedings.
42. C. Schwinn, these proceedings.
43. Z. Wu, these proceedings.
44. R.G. Suarez, these proceedings.
45. O. Brandt, these proceedings.
46. S. Blyweert, these proceedings.
47. A. Lister, these proceedings.
48. D. Mietlicki, these proceedings.
49. L. Duflot, these proceedings.
50. D. Alves *et al.* [LHC New Physics Working Group Collaboration], arXiv:1105.2838 [hep-ph].
51. T. Tait, these proceedings.
52. L. Sonnenschein, these proceedings.
53. N. Mahmoudi, these proceedings.
54. R. Lopez de Sa, these proceedings.
55. R. Bernhard, these proceedings.
56. A. Bornheim, these proceedings.
57. D. Bortoletto, these proceedings.
58. P. Spagnolo, these proceedings.
59. J. Kroseberg, these proceedings.
60. F. Couderc, these proceedings.

THROUGH A GLASS, DARKLY: THEORY SUMMARY

DAVISON E. SOPER
Institute of Theoretical Science, University of Oregon,
Eugene, Oregon 97403, USA

This is a summary of the theoretical contributions to the QCD session of the 47th Rencontre de Moriond, including some perspectives on the implications of the reported experimental results on the status of our theoretical understanding.

For now we see through a glass, darkly, but then face to face:
now I know in part; but then shall I know ...

1 Introduction

The quote above is from 1 Corinthians 13 in the King James Bible. To my mind, it illustrates our situation at the 47th Rencontre de Moriond "QCD and High Energy Interactions" [1] as we heard of tantalizing hints from experiment of the existence of the Higgs boson, but wait to know whether these hints will take convincing form or recede into the dark mists in the 2012 running of the CERN Large Hadron Collider.

The question to be answered is whether we are confirming the Standard Model mechanism for electroweak symmetry breaking or are finding structures that lie beyond the Standard Model. In order to present a definite point of view on this, I take the Standard Model to be a renormalizable quantum field theory, viewed as a low energy effective field theory with a high cutoff energy scale.

With this view, there are good arguments that the Standard Model is wrong. The issues were nicely presented in the talk of G. Altarelli [2]. If the energy cutoff scale is very large, then it is difficult to understand why the Higgs boson mass not also very large. I will discuss this point when we come to the Higgs boson in Sec. 6. Also, there is solid astronomical evidence for dark matter particles that are not present in the Standard Model. Additionally, there are some experimental anomalies. For instance, the forward-backward asymmetry in $p\bar{p} \to t\bar{t}$ and the proton charge radius as measured from the energy levels of muonic hydrogen do not seem to fit well with Standard Model expectations. I will return to these issues in Sec. 5.

Despite these indications that the Standard Model is wrong, it has passed many, many experimental tests. I suppose that it seems as durable as the Roman Empire must have seemed to those living in La Thuile two thousand years ago. In contrast, physics beyond the Standard Model offers prospects that seem now unknown and largely unknowable until we find the sought indications from experiment.

My plan for this summary is to say something about each of several topics covered at the conference: emergent phenomena within the Standard Model (Sec. 2); testing Standard Model

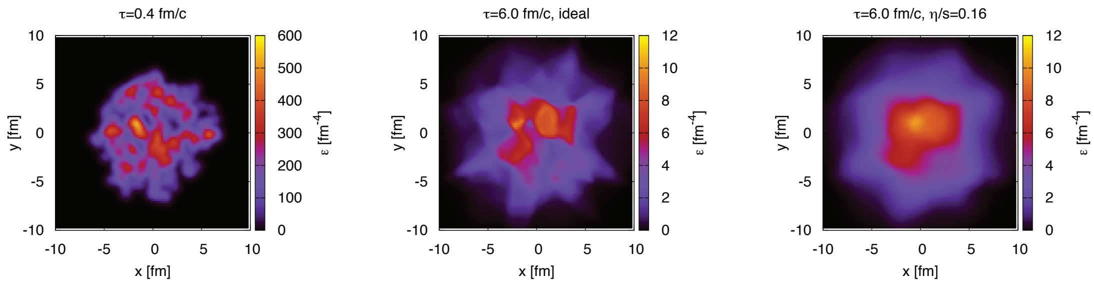

Figure 1: Modeled[7] energy density distribution in the transverse plane for one event at the initial time (left) and after a time of 6 fm/c for the ideal fluid case (middle) and with $\eta/s = 0.16$ (right), as reported in the talk of R. Snellings from ALICE.[4].

physics (Sec. 3); direct searches for new physics (Sec. 4); indirect searches for new physics using flavor physics (Sec. 5); and looking for the Standard Model Higgs boson (Sec. 6).

2 Emergent phenomena within the Standard Model

We heard about some kinds of phenomena that are presumed to arise from the Standard Model lagrangian but that do not come about in a simple way, so that highly non-trivial theoretical insights are needed if we are to have a real understanding of the observations. I discuss these in three categories.

2.1 Transverse flow in heavy ion collisions

In a heavy ion collision, one expects that the flow of energy in the plane transverse to the beam axis will not be symmetric under rotations but rather will depend on the angle between the measured momentum and the direction defined by the transverse vector $\vec{b}$ from the center of one of the nuclei to the center of the other. (One can measure $\vec{b}$ approximately from the total activity in the event and the geometry of this activity.) Experimental results on this flow were reported by STAR and PHENIX,[3] ALICE,[4] CMS,[5] and ATLAS.[6] These are an experimental results, but some comments about the theory may be helpful.

Suppose that $|\vec{b}|$ is not small compared to the nuclear radius R, but not close to R either. Then the region in the transverse plane in which constituents of the nuclei collide is almond shaped, with the long axis of the almond perpendicular to $\vec{b}$. Presumably, just after the collision, this region is filled with a hot plasma of some sort, with very high pressure in the middle and low pressure on the outside. (The use of this language implies a system that is locally not too far from thermodynamic equilibrium, but one has to judge from the data how close to reality such a hydrodynamic picture is.) Because the pressure gradient is greatest in the directions parallel or antiparallel to $\vec{b}$, one expects that the matter in the plasma will gain momentum in these directions. After the plasma has expanded and cooled, one then expects that the transverse particle flow as measured by $dN/d\phi$ will be biggest in the $\pm\vec{b}$ directions, producing a pattern $N_0[1 + 2V_2 \cos(2(\phi - \phi_b))]$ with nonzero V_2. This is what the experiments find. There are also contributions proportional to $V_n \cos(n(\phi - \phi_b))$. Many interesting results along these lines were presented. When interpreted using a model of hydrodynamic flow[7] with a model for the density fluctuations at the initial time, the results suggest that the viscosity is quite small, as illustrated in Fig. 1 from the talk of R. Snellings from ALICE.[4]. More generally, the experimental results suggest that the mean free path within the medium is small.

2.2 Jet quenching in heavy ion collisions

There were also interesting results from ATLAS [8] and CMS [9] about jet quenching in heavy ion collisions. Here one attempts to investigate back-to-back jets produced by parton-parton collisions with a transverse momentum given to the jets. If the partonic collision happens near the edge of the transverse collision region and if jet A is produced heading toward the edge of the hadronic matter while jet B is produced heading toward the middle, then it seems clear that jet B should suffer a substantial energy loss in the medium. This effect is seen in the data for high transverse momentum jets. The size of the effect and its dependence on the available event parameters should be able to test our understanding of the underlying physics. As a parton is passing through the nuclear matter, it scatters from the partons in the nuclear matter and emits bremsstrahlung gluons, which further scatter. Thus a jet develops quite differently from a jet that creates a parton shower in vacuum. It seems to me that developing a detailed picture of this, a picture that can match the data, will be a significant challenge to theorists.

2.3 Physics of the saturation scale

In QCD at small momentum fraction x, the saturation scale $Q_s(x)$ is a key concept. The saturation scale can be qualitatively defined by the relation $\alpha_s x f_g(x, Q_s^2)/[Q_s^2 R_p^2] = 1$. Here α_s/Q^2 is the cross section for a gluon in a proton to scatter from another parton with a momentum transfer of scale Q. Since $x f_g(x, Q^2)$ is the number of gluons per unit $\log(x)$, the product $\alpha_s x f_g(x, Q^2)/Q^2$ is the transverse area in the proton covered by gluons. The transverse area of the proton is proportional to the square of its radius, R_p. Thus $\alpha_s x f_g(x, Q^2)/[Q^2 R_p^2]$ measures the fraction of the proton's area covered by gluons. That is, for a given x, the proton appears black for scattering processes of scale Q_s and below. For small x, $x f_g(x, Q_s^2)$ is big enough that $Q_s(x)$ becomes greater than a GeV, so that the physics of the saturation scale is at least marginally perturbative.

We did not have a session devoted to physics of the saturation scale, but the idea was present in several talks. See, for instance, the talk of M. Perdekamp [10] on the suppression of hadrons at forward rapidity at RHIC.

M. Praszalowicz [11] proposed a scaling formula involving $Q_s(x)$ in which the p_T distribution of produced particles in hadron-hadron collisions becomes a function of one variable instead of the two variables p_T^2 and s.

I. Sarcevic [12] showed a calculation of the rate at which neutrinos are produced from the decay of charm produced in collisions of cosmic rays with air nuclei. Here x is very small, so she used a color dipole model that that incorporates $Q_s(x)$. The same color dipole/saturation model appeared in the talk of M. Sadzikowski.[13] The issue here is diffractive deeply inelastic electron scattering. This is governed by diffractive parton distribution functions that obey the DGLAP evolution equation at large Q^2, but at small Q^2 and very small momentum fraction, saturation effects take over.

2.4 Use of gauge-gravity duality

M. Djuric [?] reported on studies of the pomeron using the conjectured connection between field theory at large coupling and higher dimensional gravity at weak coupling (the AdS/CFT correspondence). Specifically, he analyzed deeply virtual Compton scattering from this point of view. R. Brower [?] reported on studies of diffractive Higgs production using this same picture.

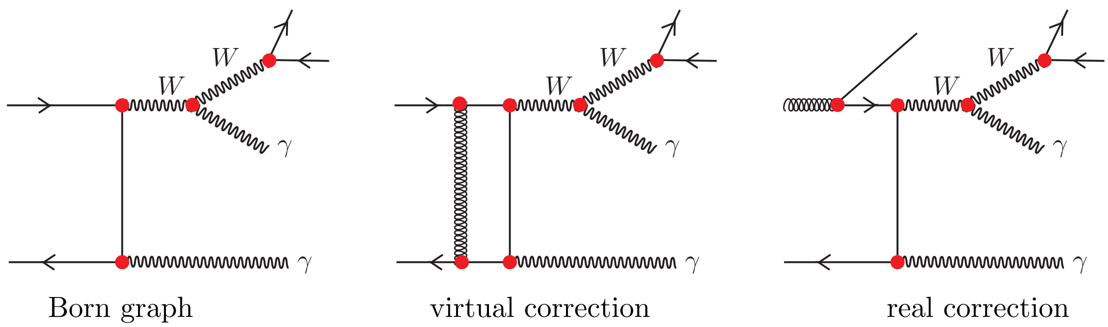

Figure 2: Graphs for production of a W and two photons plus anything.

3 Calculating and testing Standard Model physics

Calculations of Standard Model cross sections continue to improve. This is important because Standard Model processes are important backgrounds for many new physics signals that we are looking for. The better we know the background, the better we can find the signal. In addition, the same calculational techniques allow us to better calculate cross sections for possible new physics signals, particularly when the sought new particles carry color. Finally, we can compare calculated Standard Model cross sections to data. This tests our ability to calculate correctly and to measure correctly and has the potential to show us a deviation from the Standard Model induced by some new physics in a place where we might not have expected it. We heard about exciting examples of these efforts at the conference.

3.1 Calculation of multiple weak boson production

F. Campanario [16] presented calculations for multiple electroweak boson production at next-to-leading order (NLO). His talk illustrates some general points that are worth emphasizing. Consider first the inclusive production of $W\gamma\gamma$ (that is, production of $W\gamma\gamma$ plus any number of jets). One of the the Born level diagrams is illustrated in the left hand diagram in Fig. 2. Working to NLO, there are many diagrams to add that represent virtual corrections, as in the middle diagram. Then there are also diagrams representing real corrections, that is corrections in which one more parton is emitted, as in the right hand diagram. Of course, the real diagrams and the virtual diagrams have infrared divergences, which have to be cancelled against each other and against terms arising from evolution of the incoming partons. Some of the real emission corrections introduce a new process, in which there is an initial state gluon replacing an initial state quark. There are lots of initial state gluons, so even though the NLO corrections are suppressed by a factor α_s, they can still be large. In this case the ratio of the NLO cross section to the Born cross section (for a certain choice of scales) is as large as 3.3.

Unfortunately, that means one should go to NNLO. That is very difficult, but one can go part way there by considering the inclusive production of $W\gamma\gamma$ *jet*. Then the previous NLO real emission graph is now one of the Born graphs, as illustrated in Fig. 3. Working now to NLO for the inclusive production of $W\gamma\gamma$ *jet*, there are again virtual corrections and real corrections, as illustrated in Fig. 3. Again, there are new processes introduced, so the corrections need not be small. In this case the ratio of the NLO cross section to the Born cross section is as large as 1.4.

Note that this calculation contains some of the ingredients for a NNLO calculation of the inclusive production $W\gamma\gamma$, but more would be needed. As it stands, to compare the cross section for $W\gamma\gamma$ *jet* plus anything to experiment, one needs to require that the jet be measured and not have small transverse momentum.

Similar physics appeared in the talk of L. Cieri [17] on inclusive diphoton production from

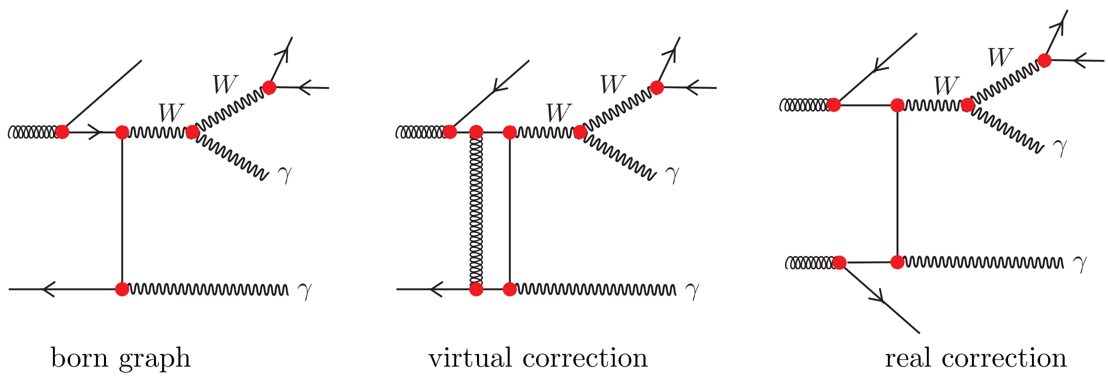

Figure 3: Graphs for production of a W, two photons, and a jet plus anything.

sources other than Higgs boson decay. This is evidently of interest with respect to the Higgs searches. Here we simply omit the W-boson from the previous discussion. The same issues appear. Also, this talk emphasized the issue of a final state quark splitting into a quark plus a photon, which I did not discuss above. The photon is required to be isolated from the quark using the so-called Frixione isolation criterion (also used in the calculation presented by Campanario). In this analysis, the authors have succeeded in carrying the calculation to NNLO. That is a remarkable result.

3.2 Progress in higher order perturbative calculations

Over the past few years there has been substantial progress in performing calculations at next-to-leading order or NNLO and also in matching NLO calculations to parton showers. An example of this was visible in the experimental talk of A. Paramonov [18] on W/Z plus jets or heavy flavor production at the LHC. Paramonov showed a graph for the inclusive production plus N jets for $N = 0, 1, 2, 3$ and 4, with data compared to NLO calculations from BlackHat-Sherpa. One notes two things: first, the estimated theory error is reasonably small and, second, the agreement with experiment is within the estimated error in each case. This situation represents a substantial improvement in the theory compared to the Rencontre de Moriond of, say, ten years ago.

There were some theoretical presentations along these lines. A. Lazopoulos [19] showed results from a calculation of inclusive Higgs production at NNLO in QCD (in the high top mass approximation). Improvements have been added to previous results. There are also (more difficult) calculations of differential distributions. One can estimate the uncertainty in the calculation due to having left out terms of yet higher perturbative order by checking how the calculated cross section depends on the renormalization and factorization scales. As we see in Fig. 4, as we go to higher order in perturbation theory, the estimated uncertainty decreases.

Similarly, A. Mitov [20] reported on progress in the calculation of the differential cross section for $p + p \to t + \bar{t} + X$ at NNLO. The goal is to have a NNLO parton level event generator for this process.

3.3 Summing large logarithms

For a cross section that depends on two momentum scales, say M_H and p_T, plain perturbation theory fails when $M_H^2 \gg p_T^2$ because it is an expansion in powers of $\alpha_s L^2$ where $L = \log(M_H^2/p_T^2)$. The diagrams that are responsible for the large logarithms are illustrated in Fig. 5.

M. Grazzini [21] showed an improved calculation for the Higgs transverse momentum distribution. This includes the full kinematical information on the Higgs decay products in $H \to \gamma\gamma$,

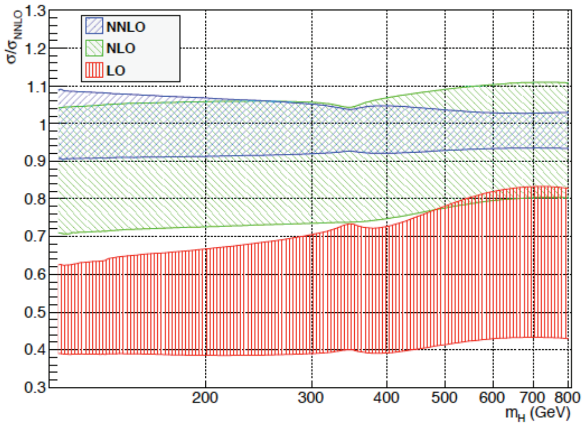

Figure 4: Dependence of the estimated uncertainty in the Higgs production cross section on the order of perturbation theory.[19]

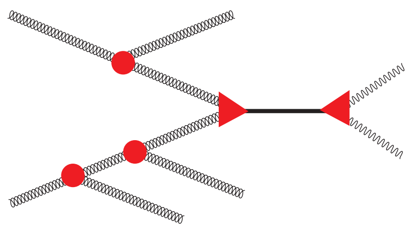

Figure 5: The transverse momentum of a produced Higgs boson can come from multiple gluon emission from the incoming partons. The same diagram also illustrates the source of threshold logarithms.

and $H \to VV$ where the vector bosons decay to leptons. It also includes matching at large P_T^2 to the perturbative expansion at NNLO.

G. Ferrera [22] showed an improved calculation for the transverse momentum of vector bosons, with the decay of the vector bosons included in the result.

M. Deak [23] discussed matching the transverse momentum dependent parton distributions used for summing small x logs to a parton shower.

C. Schwinn [24] showed an improved summation of threshold logs for top pair production. If the parton distributions are falling very quickly with x, then emission of real gluons (as in Fig. 5) is restricted. Inside of an integration over x there are large logarithms, known as threshold logarithms. For the observed cross section, the large parameter is effectively $d\log[f_{a/A}(x,\mu^2)]/dx$. For top or Higgs production at LHC, one can debate (and one did debate at the coffee breaks) the value of a summation of threshold logs compared to a full calculation at one higher order in α_s, as in the talks of Lazopoulos [19] and Mitov [20].

3.4 Jet cross section

There were many experimental presentations in which the data was compared to theoretical calculations. I have mentioned a couple of these, but it would not be useful to list many examples. Let me simply draw attention to one classic example that I think is exciting. G. Jones [25] presented jet data from the LHC. In Fig. 6, I show the Atlas data on the dijet mass distribution in $p + p \to jet + jet + X$, grouped in bins of the rapidity difference $2y^*$ between the two jets. The data extend to large mass values, about 3 TeV. The data are compared with the NLO cross section using NLOjet++. There is some disagreement in the bin of largest y^*, but this is a region with some difficulties in the NLO theory. Everywhere else, there is good agreement.

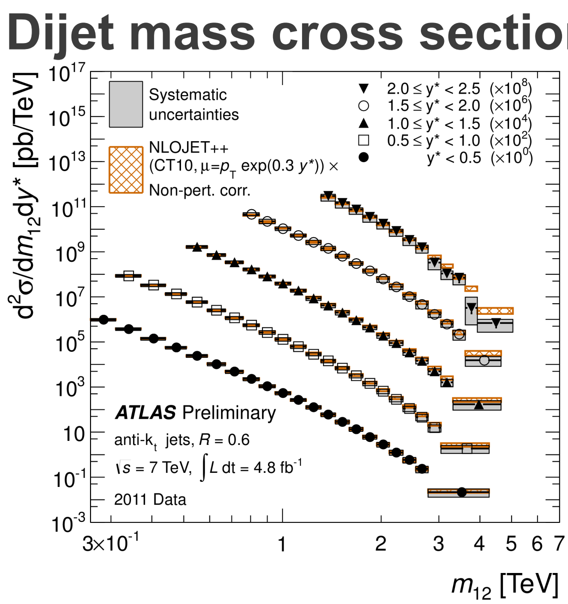

Figure 6: Dijet mass distribution from Atlas.[25]

Most relevant is the bin of smallest y^*. Here is where we would see a deviation if there were a heavy object that couples to color. No deviation is seen.

3.5 Top quark mass

We heard exciting results about direct measurements of the top quark mass. O. Brandt [26] presented a measurement from the Tevatron (D0 and CDF) of $m_t = (173.2 \pm 0.9)$ GeV, while S. Blyweert [27] presented a measurement from the CMS of $m_t = (172.6 \pm 1.3)$ GeV. The top mass is a parameter in the QCD lagrangian that is subject to renormalization. One can adopt different prescriptions for this, among them the $\overline{\rm MS}$ prescription and the pole prescription. At the level of precision of the measurements reported, the exact definition matters. Unfortunately, the data analysis methods that give the most precise results do not precisely define what mass one is measuring. It would seem that more attention to this issue from theorists is needed.

3.6 W boson mass

R. Lopez de Sa [28] reported very precise measurements of the mass of the W boson at the Tevatron: $M_W = (80387 \pm 19)$ MeV for CDF and $M_W = (80376 \pm 23)$ MeV for D0. He reported that at this level of precision, uncertainties in the parton distributions used in the theory are an important source of error. I asked Robert Thorne, who kindly advised me that the valence d quark distribution and the $\bar{u} - \bar{d}$ distribution are mostly responsible.[29] Perhaps LHC data can help a little to pin this down. The talk of N. Hartland [30] on neural net parton distributions suggests that there may be some impact.

4 Direct searches for new physics

Talks at the conference showed substantial progress in looking for new physics. No definitive signals have been seen, but there is lots more to do, looking for signals that are harder to see.

G. Altarelli [2] reviewed the status many of these searches and their relation to the theoretical possibilities. (I mention some of the points he raised elsewhere in this talk.) He emphasized that the null results of searches so far puts severe constraints on the parameters of the simplest models of supersymmetry, but that there is "plenty of room for more sophisticated versions of SUSY as a solution to the hierarchy problem." He noted that it is important to look for the partner particles of the third generation particles. I might suggest the motto "start with stop."

T. Tait [31] reviewed the status of searches for dark matter. Assuming that the dark matter seen in the universe from its gravitational effects consists of weakly interacting massive particles (WIMPs), the LHC has a chance to produce these particles in two ways. Either LHC proton collisions can produce the WIMPs directly, or they can produce sibling particles (perhaps squarks or gluinos) that decay into the WIMPs plus standard model particles. In either case, we look for events with missing transverse momentum. Tait explained the relation of LHC searches to non-accelerator searches: direct detection experiments that seek to discover dark matter particles from space interacting with matter on earth and indirect detection that looks, for example, for photons from dark matter annihilation in space.

M. Spannowsky [32] summarized theoretical tools for using jet substructure to find new particles and new interactions. The idea is that a very heavy particle produced approximately at rest can decay to lighter particles that have lots of transverse momentum. In fact, in many scenarios there is a chain of successive decays. The result is high transverse momentum jets that have lots of internal structure that is characteristic of particle decays instead of normal QCD interactions. One can use this internal structure to discover the new physics. For instance, S. Lee [33] presented one such method. A method based on the perturbative matrix elements was presented by C. Williams.[34]

5 Flavor physics

Flavor physics can provide a way to look for physics beyond the Standard Model. Andreas Schopper [35] discussed some of the main ideas and summarized recent progress, including CKM metrology, analysis of direct CP violation, mixing induced CP violation, searches for rare decays, and a surprising finding in direct CP violation in charm.

How can flavor physics can provide a way to look for physics beyond the Standard Model? In this talk, I view the Standard Model as a low energy effective field theory with a high cutoff energy scale. With this view, we may ask about the theory beyond the high cutoff energy scale. The parameters of the Standard Model come from the high energy theory, so the fermion mass hierarchy, the CKM matrix, and so forth are providing us clues to the high energy theory. There can be more clues. Besides the Standard Model lagrangian, we should have extra terms. For example, we might have a term

$$\Delta\mathcal{L} = \frac{g}{\Lambda^2}(\bar{\psi}\psi)^2 + \cdots \quad , \tag{1}$$

where ψ is a quark or lepton field. The extra terms are suppressed by powers of the cutoff scale Λ. We can look for the extra terms in rare processes.

This same analysis applies for the analysis of experiments at a few GeV scale even if Λ is on the order of a TeV. In that case, the Standard Model is already breaking down at the LHC energy scale and this breakdown is directly accessible at the LHC, the new physics at $E > \Lambda$ is indirectly accessible via flavor physics at lower energy.

This general approach was nicely outlined by Nazila Mahmoudi [36]. Consider B_s decay. We can use

$$\mathcal{H} = -\frac{4G_F}{\sqrt{2}}\, V_{tb}V_{ts}^* \sum_i C_i(\mu)\mathcal{O}_i(\mu) \quad . \tag{2}$$

The $\mathcal{O}_i$ here are operators for the light partons. The coefficients $C_i(\mu)$ are calculated at $\mu = M_W$ from $\mathcal{L} + \Delta\mathcal{L}$. Then they are translated from the scale M_W to the scale m_b using an

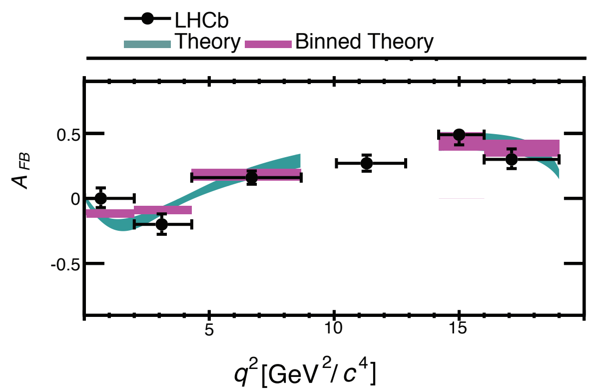

Figure 7: Forward-backward asymmetry in B_s decay.[38]

effective field theory in which the W and Z bosons are "integrated out." Using this approach, there are several observables of interest. For example, one can look at the forward backward asymmetry $A_{FB}(B \to K^* \mu^+ \mu^-)$. For each observable, we need hadronic matrix elements like $\langle K^*(p+q)|\mathcal{O}_i|B_s(p)\rangle$. For the hadronic matrix elements, we need a calculation. Thus there are several ingredients, but the net result contains the $C_i(\mu)$, which depend on $\Delta\mathcal{L}$, so in the end we have a chance to learn about the physics beyond the Standard Model contained in $\Delta\mathcal{L}$.

A nice example of this kind of program was presented by Cai-Dian Lu.[37] Corresponding data from LHCb was shown by Chris Parkinson.[38] In Fig. 7, I show the forward backward asymmetry $A_{FB}(B \to K^* \mu^+ \mu^-)$ as a function of the momentum transfer q^2. In this case, everything matches and we do not find evidence for a non-zero $\Delta\mathcal{L}$.

Sometimes the weakest link in this chain of argument is the assumptions that go into the calculation of the hadronic matrix elements. Joachim Brod[39] talked the uncertainty in the calculation of the hadronic matrix elements for direct CP violation in D meson decays. Within these uncertainties, he argued how due care with modeling can allow Standard Model to plausibly explain the data. The talk of of Giulia Ricciardi [40] illustrated how uncertainties in hadronic matrix elements can be controlled. Manuel Hita-Hochgesand [41] reported a measurement by NA48/2 of two of the hadronic form factors needed for the analysis of direct CP violation in $K^\pm$ decays. In general, getting at the hadronic matrix elements needed for flavor physics is not easy. However, we have good theoretical tools: lattice gauge theory, heavy quark effective theory, soft collinear effective theory, *etc.*

Richard Hill [42] reported on a possible clue to new physics that relates to the difference between electrons and muons. One can measure the proton charge radius from electron-proton scattering, or from the energy levels of the hydrogen atom, or from the energy levels of muonic hydrogen. Because a muon bound to a proton spends a lot of its time close to the proton, the measurement using the energy levels of muonic hydrogen is the most accurate. However, this measurement using muons does not agree with the two measurement methods using electrons. Hill reported that careful attention to the theory in electron-proton scattering and hydrogen energy levels does not rescue us from this discrepancy. Thus one wonders if there is some new physics that couples differently to muons and electrons. It is not so easy to see what this could be while remaining consistent with other constraints. Thus a mystery remains.

There was quite a lot of discussion about the forward backward asymmetry in top pair production at the Tevatron, which was reported by David Mietlicki.[43] Produced top quarks tend to follow the proton direction while top antiquarks tend to follow the antiproton direction. Alison Lister [44] reported analogous results from Atlas and CMS, but here measuring whether the top quark has larger $|y|$ than the antitop. While the LHC asymmetry result is inconclusive,

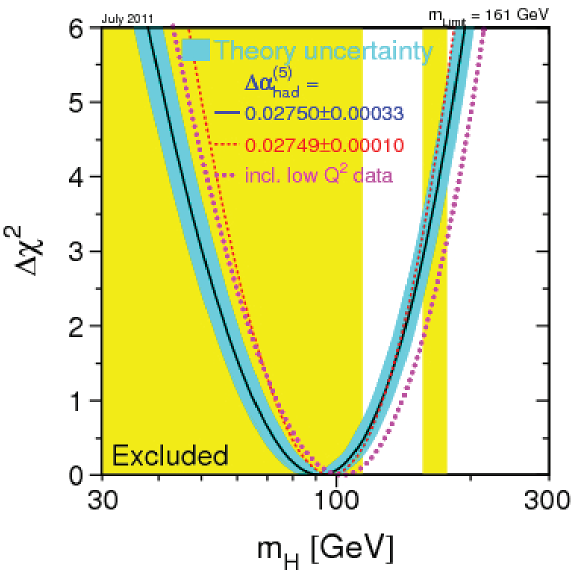

Figure 8: Effect of electroweak precision data on the mass of the Higgs boson (from the talk of Lopes de Sá [28]).

the observed Tevatron forward backward asymmetry is larger than predicted in the Standard Model, suggesting that top quarks may couple to something not included in the Standard Model. However, some caution is needed. The asymmetry vanishes at leading order in QCD, so that the asymmetry calculated at next-to-leading order is actually calculated at the leading order at which it is nonzero. Thus one needs a calculation at yet higher perturbative order. The presentation of A. Mitov [20] discussed some of these issues.

6 Looking for the Standard Model Higgs boson

The topic on everyone's mind at this Rencontre de Moriond was the Higgs boson. Is it possible that the mechanism for electroweak symmetry breaking is the fundamental scalar field posited in the Standard Model? Let me put this question more provocatively. Is it possible that the Standard Model, with its Higgs boson, is correct as an effective field theory up to a cutoff scale Λ that is very large compared to the Higgs field vacuum expectation value (about 250 GeV)? If so, the natural scale for the Higgs boson mass would be of order Λ and we need "fine tuning" to keep it small. To stick with the Standard Model in this sense, we choose to simply ignore this problem.

This picture brings with it some tight constraints. First, the Higgs boson mass cannot be just anything. If I say that Λ is at least as big as 100 TeV, then m_h is bounded from below at about 100 GeV because of vacuum stability arguments and it is bounded above at about 300 GeV so as to not to produce a Landau pole into perturbation theory. This issue was discussed by G. Altarelli.[2] There is more. The direct search for the Higgs boson at LEP puts a lower bound on m_h at 114 GeV. Moreover, electroweak precision data puts strong constraints on the Higgs boson mass, assuming that it is the Higgs boson of the Standard Model. This is illustrated in Fig. 8. Clearly $m_h > 200$ GeV is excluded.

Now the exciting news at this meeting was that the LHC experiments, with the Tevatron helping, exclude most of the available range for a Standard Model Higgs boson. A region around 125 GeV remains, as shown in Fig. 9. Furthermore, both CMS and Atlas see events that could

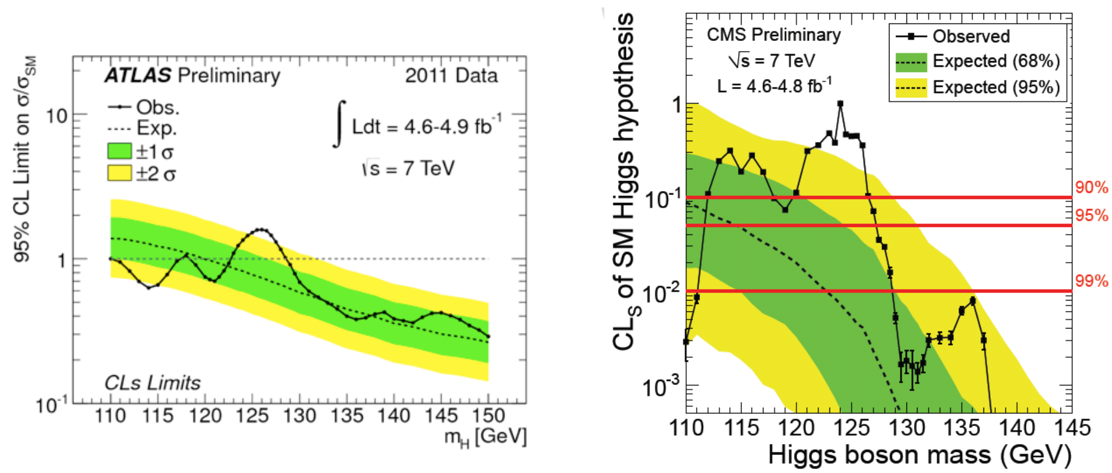

Figure 9: Higgs boson exclusion limits from Atlas [45] and CMS.[46]

match a SM Higgs with mass 125 GeV and that is unlikely to be a background fluctuation. See the talks of Ralf Bernhard [45] and Adi Bornheim.[46] The Tevatron experiments also report a signal that could be $H \to b + \bar{b}$ with a Higgs boson mass of about 125 GeV, as reported by Daniela Bortoletto.[47]

What looks like a signal for a 125 GeV Higgs boson could be a result of misestimated backgrounds and random fluctuations. It is not as convincing as the evidence for the top quark at the 1995 Rencontre de Moriond. Maybe the Standard Model Higgs boson will be ruled out with further data. If so, we will need to find a non-Standard-Model version. Then it will be significant that Atlas and CMS already can rule out a Standard-Model-like Higgs up to 540 to 600 GeV.

On the other hand, the seeming signal at around 125 GeV could well be real. Data in the 2012 LHC run will tell the story. If the signal is real, we will want to know if the found object is really the Standard Model Higgs boson. We will want to test whether there is more than one resonance seen. We will want to know whether the couplings of the resonance to W bosons, Z bosons, top quarks, bottom quarks, and tau leptons are in accordance with the Standard Model. We will want to know if the resonance really has spin zero. We will want to see if the effect of the Higgs field on W-W scattering works out as claimed in the Standard Model, with the W-W cross section not growing as the c.m. energy of the W-W system increases. Evidently, this is an ambitious program, which will not be accomplished by the end of 2012 even if the basic signal is confirmed.

This brings me back to the biblical passage that I quoted at the beginning of this talk: "For now we see through a glass, darkly; but then face to face: now I know in part; but then shall I know ...." For the Higgs boson and possible extensions of the Standard Model, the glass may be not so dark at Moriond 2013.

Acknowledgments

On behalf of, I think, all of the participants of Moriond QCD 2012, I would like to thank the organizing committee for putting this meeting together. It is a very big task to organize a meeting like this and even more of a challenge to do so while maintaining the spirit of free scientific exchange that characterizes the Rencontres de Moriond. This work was supported by the United States Department of Energy.

References

1. The conference program, with links to the slides of the talks, can be found at http://moriond.in2p3.fr/QCD/2012/MorQCD12Prog.html.
2. G. Altarelli, these proceedings.
3. H. Masui, these proceedings.
4. R. Snellings, these proceedings.
5. R. Conway, these proceedings.
6. A. Trzupek, these proceedings.
7. B. Schenke, S. Jeon and C. Gale, Phys. Rev. Lett. **106** (2011) 042301, [arXiv:1009.3244 [hep-ph]] INSPIRE.
8. I. Grabowska-Bold, these proceedings.
9. Y. Yilmaz, these proceedings.
10. M. Perdekamp, these proceedings.
11. M. Praszlowicz, these proceedings.
12. I. Sarcevic, these proceedings.
13. M. Sadzikowski, these proceedings.
14. R. Brower, M. Djuric, these proceedings.
15. F. Campanario, these proceedings.
16. L. Cieri, these proceedings.
17. A. Paramonov, these proceedings.
18. A. Lazopoulos, these proceedings.
19. A. Mitov, these proceedings.
20. M. Grazzini, these proceedings.
21. G. Ferrera, these proceedings.
22. M. Deak, these proceedings.
23. C. Schwinn, these proceedings.
24. G. Jones, these proceedings.
25. O. Brandt, these proceedings.
26. S. Blyweert, these proceedings.
27. R. Lopez de Sa, these proceedings.
28. R. Thorne, private communication.
29. N. Hartland, these proceedings.
30. T. Tait, these proceedings.
31. M. Spannowsky, these proceedings.
32. S. Lee, these proceedings.
33. C. Williams, these proceedings.
34. A. Schopper, these proceedings.
35. N. Mahmoudi, these proceedings.
36. C.-D. Lu, these proceedings.
37. C. Parkinson, these proceedings.
38. J. Brod, these proceedings.
39. G. Ricciardi, these proceedings.
40. M. Hita-Hochgesand, these proceedings.
41. R. Hill, these proceedings.
42. D. Mietlicki, these proceedings.
43. A. Lister, these proceedings.
44. R. Bernhard, these proceedings.
45. A. Bornheim, these proceedings.
46. D. Bortoletto, these proceedings.

List of Participants

Family name	First name	Instituition	Country	Email
Aguilo	Ernest	University of Zurich	Switzerland	Ernest.Aguilo@cern.ch
Altarelli	Guido	CERN	Switzerland	Guido.altarelli@cern.ch
Aracena	Ignacio	SLAC	USA	aracena@slac.stanford.edu
Augé	Etienne	CNRS/IN2P3	France	eauge@admin.in2p3.fr
Bala	Renu	Universitá di Torino - INFN	Italy	bala@to.infn.it
Bandurin	Dmitry	Florida State University	USA	bandurin@fnal.gov
Bellini	Francesca	Università degli Studi di Bologna & INFN	Italy	bellini@bo.infn.it
Bernhard	Ralf	University of Freiburg	Germany	bernhard@cern.ch
Bhardwaj	Vishal	Nara Women's University	Japan	vishstar@gmail.com
Blyweert	Stijn	Vrije Universiteit Brussel	Belgium	stijn.blyweert@gmail.com
Bornheim	Adolf	CALTECH	USA	bornheim@hep.caltech.edu
Bortoletto	Daniela	Purdue University	USA	bortolet@purdue.edu
Brandt	Oleg	U. of Goettingen	Germany	obrandt@fnal.gov
Brod	Joachim	University of Cincinnati	USA	joachim.brod@uc.edu
Brower	Richard	Boston University	USA	brower@bu.edu
Campanario	Francisco	KIT Fakultät für Physik	Germany	francisco.campanario@kit.edu
Cieri	Leandro	Univ. de Buenos Aires & INFN Firenze	Argentina	lcieri@df.uba.ar
Conway	Rylan	University of California	USA	Rylan.Towne.Conway@cern.ch
Couderc	Fabrice	CEA-Saclay/SPP	France	fabrice.couderc@cea.fr
Deak	Michal	Universidade de Santiago de Compostela	Spain	michal.deak@uam.es
Dell'Acqua	Andrea	CERN	Switzerland	dellacqu@mail.cern.ch
Di Donato	Camilla	INFN	Italy	didonato@na.infn.it
Dissertori	Guenther	ETH Zurich	Switzerland	dissertori@phys.ethz.ch
Dittmann	Jay	Baylor University	USA	Jay_Dittmann@baylor.edu
Djuric	Marko	Universidade do Porto	Portugal	djuric@fc.up.pt
Dorigo	Mirco	University of Trieste - INFN	Italy	mircodor@gmail.com
Duflot	Laurent	LAL	France	duflot@lal.in2p3.fr
Ferrera	Giancarlo	University of Milan	Italy	giancarlo.ferrera@mi.infn.it
Garcia-Gamez	Diego	LAL	France	gamez@lal.in2p3.fr
Gascon-Shotkin	Suzanne	IPN Lyon - Univ. Claude Bernard Lyon 1	France	smgascon@in2p3.fr
Gonzalez Suarez	Rebeca	Inter-University Institute for High Energies	Belgium	rebeca@cern.ch
Grabowska-Bold	Iwona	Applied Computer Science AGH	Poland	Iwona.Grabowskabold@gmail.com
Grazzini	Massimiliano	University of Zurich	Switzerland	grazzini@physik.uzh.ch
Grosse Perdekamp	Matthias	University of Illinois at Urbana Champaign	USA	mgp@illinois.edu
Gruenberg	Oliver	University of Rostock	Germany	oliver.gruenberg2@googlemail.com
Gruppuso	Alessandro	INAF - IASF Bologna	Italy	gruppuso@iasfbo.inaf.it
Guttman	Nir	Tel Aviv university	Israel	gutt@post.tau.ac.il
Hartland	Nathan	University of Edinburgh	UK	n.p.hartland@ed.ac.uk
Hentschinski	Martin	Institute of Theoretical Physics UAM/CSIC	Spain	martin.hentschinski@uam.es
Hill	Richard	University of Chicago	USA	richardhill@uchicago.edu
Hita-Hochgesand	Manuel	Johannes Gutenberg-Universität Mainz	Germany	hitahoch@uni-mainz.de
Hubacek	Zdenek	CEA Saclay	France	zdenek.hubacek@cea.fr
Hughes	Emlyn	Columbia University	USA	ewh42@columbia.edu
Jones	Christopher	HEP Group, Cavendish Laboratory	UK	jonesc@hep.phy.cam.ac.uk
Jones	Graham	The University of Warwick	UK	Graham.Jones@cern.ch
Jung	Andreas	Fermilab	USA	ajung@fnal.gov
Kapishin	Mikhail	Joint Institute for Nuclear Research (JINR)	Russia	kapishin@mail.desy.de
Karapostoli	Georgia	Imperial College	UK	georgia.karapostoli@cern.ch
Klima	Boaz	Fermilab	USA	klima@fnal.gov
Kluth	Stefan	MPI fuer Physik	Germany	skluth@mpp.mpg.de
Knichel	Michael Linus	EMMI GSI	Germany	m.l.knichel@gsi.de
Kozlinskiy	Alexandr	Nikhef	The Netherlands	akozlins@cern.ch
Krawczyk	Maria	University of Warsaw	Poland	krawczyk@fuw.edu.pl
Kroseberg	Jürgen	Bonn University	Germany	kroseberg@uni-bonn.de
Lazopoulos	Achilleas	ETH Zurich	Switzerland	lazopoli@phys.ethz.ch
Lebedev	Oleg	DESY	Germany	lebedev@mail.desy.de
Lee	Seung	Advaced Inst. of Science and Technology	South korea	sjjlee@kaist.ac.kr
Li	Shi-Yuan	Shandong University	China	lishy@sdu.edu.cn
Lister	Alison	Université de Genève	Switzerland	alison.lister@cern.ch
Lontkovskyi	Denys	DESY	Germany	denys.lontkovskyi@desy.de
Lopes de Sá	Rafael	Stony Brook University	USA	rafael.lopesdesa@stonybrook.edu
Lu	Cai-Dian	Institute of High Energy Physics, CAS	China	lucd@ihep.ac.cn

Family name	First name	Instituition	Country	Email
Mahmoudi	Farvah Nazila	CERN	Switzerland	mahmoudi@in2p3.fr
Malcles	Julie	CEA-SACLAY	France	julie.malcles@cea.fr
Masui	Hiroshi	Lawrence Berkeley National Laboratory	USA	hmasui@lbl.gov
Mietlicki	David	University of Michigan	USA	dmietl@umich.edu
Mitov	Alexander	CERN	Switzerland	alexander.mitov@cern.ch
Moyse	Edward	University of Massachusetts	USA	edward.moyse@cern.ch
Okada	Kensuke	RIKEN BNL Research Center	USA	okada@bnl.gov
Paramonov	Alexander	Argonne National Laboratory	USA	alexander.paramonov@cern.ch
Parkinson	Christopher J.	Imperial College	England	c.parkinson09@imperial.ac.uk
Pietrzyk	Bolek	LAPP	France	pietrzyk@lapp.in2p3.fr
Pilkington	Andrew	Manchester/IPPP	UK	Andrew.Pilkington@cern.ch
Pirumov	Hayk	PI Universität Heidelberg	Germany	hayk.pirumov@desy.de
Potterat	Cédric	Universitat de Barcelona	Spain	potterat@ecm.ub.es
Praszalowicz	Michal	Jagellonian University	Poland	michal@if.uj.edu.pl
Quiros	Mariano	ICREA/IFAE	Spain	quiros@ifae.es
Ricciardi	Giulia	Università di Napoli Federico II	Italy	giulia.ricciardi@na.infn.it
Riedl	Caroline	DESY	Germany	caroline.riedl@desy.de
Rimoldi	Adèle	University of Pavia & INFN	italy	adele.rimoldi@cern.ch
Ruan	Lijuan	Brookhaven National Laboratory	USA	ruanlj@rcf.rhic.bnl.gov
Sadzikowski	Mariusz	Institute of Physics, Jagiellonian University	Poland	sadzikowski@th.if.uj.edu.pl
Sarcevic	Ina	University of Arizona	USA	ina@physics.arizona.edu
Schoeffel	Laurent	CEA Saclay	France	laurent.schoeffel@cea.fr
Schopper	Andreas	CERN	Switzerland	Andreas.Schopper@cern.ch
Schwinn	Christian	Universitaet Freiburg	Germany	christian.schwinn@physik.uni-freiburg.de
Shipsey	Ian	Purdue University	USA	shipsey@purdue.edu
Smizanska	Maria	Lancaster University	UK	maria.smizanska@cern.ch
Snellings	Raimond	Utrecht University	The Netherlands	Raimond.Snellings@cern.ch
Sonnenschein	Lars	RWTH Aachen III.	Germany	Lars.Sonnenschein@cern.ch
Soper	Davison	Institute of Theoretical Science	USA	soper@uoregon.edu
Sozzi	Federica	INFN	Italy	federica.sozzi@cern.ch
Spagnolo	Paolo	INFN	italy	Paolo.Spagnolo@cern.ch
Spannowsky	Michael	Inst. for Particle Physics Phenomenology	UK	michael.spannowsky@durham.ac.uk
Stavreva	Tzvetalina	LPSC	France	stavreva@lpsc.in2p3.fr
Tait	Tim	University of California	USA	ttait@uci.edu
Tan	Chung-I	physics Department, Brown University	USA	Tan@het.brown.edu
Tatishvili	Gocha	Pacific Northwest National Laboratory	USA	Gocha.Tatishvili@pnnl.gov
Tran Thanh Van	Jean	Université Paris 11	France	jtrantv@gmail.com
Trzupek	Adam	Institute of Nuclear Physics PAN	Poland	Adam.Trzupek@ifj.edu.pl
van Tilburg	Jeroen	Physikalisches Institut Heidelberg	Germany	Jeroen.van.Tilburg@cern.ch
Vizan	Jesus	UC Louvain	Belgium	vizan@cern.ch
Wang	Jianxiong	Institute of High Energy Physics, CAS	China	jxwang@ihep.ac.cn
Wang	Zhiyong	Institute of High Energy Physics, CAS	China	wangzy@ihep.ac.cn
Williams	Ciaran	Fermilab	USA	ciaran@fnal.gov
Wu	Zhenbin	Baylor University	USA	zhenbin_wu@baylor.edu
Yilmaz	Yetkin	Massachusetts Institute of Technology	USA	yetkin.yilmaz@cern.ch
Zambelli	Laura	LPNHE	France	laura.zambelli@lpnhe.in2p3.fr
Zhao	Haisheng	Institute of High Energy Physics, CAS	China	zhaohs@ihep.ac.cn
Zivkovic	Lidija	Brown University	USA	lidiaz@fnal.gov